Imperial College London

Mechanical Engineering PhD Thesis

IMPERIAL COLLEGE LONDON

DEPARTMENT OF MECHANICAL ENGINEERING

Indentation and Impact Damage in Carbon Fibre-Reinforced Polymer Composite Materials

Name:

Richard Andrew Brooks

Supervisor:

Professor John P. Dear

Co-supervisor:

Dr Nan Li

May 2024

Abstract

The issue of climate change has led to an increased focus on efficiency and reduction of emissions in the aerospace sector. Large improvements in fuel efficiency have been achieved through the use of lightweight composite materials. The impact behaviour of these composite materials, particularly carbon fibre-reinforced polymers (CFRPs), is complex and highly dependent on a number of variables. Therefore, this thesis focuses on the impact behaviour of CFRP and the resulting damage formed by low-velocity impacts.

Low-velocity impacts usually initiate internal damage within CFRP which must be viewed and analysed using non-destructive testing (NDT) methods. In most cases, an indentation is also formed on the surface of the CFRP. The results of this thesis show that a larger surface indentation depth corresponds to a larger delamination damage area. However, an indentation appears to initiate before the development of any delamination damage.

The effect of previous damage within a structure was investigate by performing two low-velocity impacts in different locations on the same panel, separated by varying distances. The resulting delamination damage area and the residual compression-after-impact (CAI) strength were measured. The results highlight that multiple impacts close to each other are more detrimental to the structural integrity of a component than impacts separated by larger distances.

Once damage has been detected and analysed, a decision must be made on whether to replace the whole component or whether to perform a repair. A repair increases the complexity of the damage process, therefore this thesis has also focused on the impact behaviour of patch-repaired CFRP. Low-velocity impact testing in the centre of circular patch repairs highlighted that thicker patches show a lower delamination damage area than thinner patches. The greatest reductions in damage area were however seen through the addition of a plug of material beneath the patch.

Declaration of Originality

I confirm that the work presented in this thesis is my own and was all produced during the course of my PhD studies at Imperial College London. Any contributions from others have been highlighted and appropriately referenced. None of the work presented in this thesis has been submitted elsewhere for another qualification.

Copyright Declaration

The copyright of this thesis rests with the author. Unless otherwise indicated, its contents are licensed under a Creative Commons Attribution-Non Commercial 4.0 International Licence (CC BY-NC). Under this licence, you may copy and redistribute the material in any medium or format. You may also create and distribute modified versions of the work. This is on the condition that: you credit the author and do not use it, or any derivative works, for a commercial purpose. When reusing or sharing this work, ensure you make the licence terms clear to others by naming the licence and linking to the licence text. Where a work has been adapted, you should indicate that the work has been changed and describe those changes. Please seek permission from the copyright holder for uses of this work that are not included in this licence or permitted under UK Copyright Law.

Acknowledgements

First of all, I would like to thank my primary supervisor, Professor John P. Dear, for his guidance throughout this project. His support allowed me to investigate new ideas, develop my experimental skills and present research at high-quality conferences. I would also like to thank my co-supervisor, Dr Nan Li, for her guidance and detailed advice while working on my original project. Additionally, I would like to thank Professor Anthony J. Kinloch for sharing his vast experience and knowledge to help analyse experimental findings. The knowledge and dedication of all these people has allowed me to achieve the work presented in this thesis and the skills I have learnt from them will help me throughout my future career. For this I am exceedingly grateful.

Furthermore, I would like to thank everyone who has assisted me with my experimental work throughout this project. In particular, I would like to thank Dr Jun Liu, Dr Zoe Hall and Dr Yuzhe Ding for their assistance with impact testing and analysis and Mr Zerong Ding, Dr Hongyan Wang and Mr Chunyi Gao for their assistance with forming. I would also like to thank Dr Lee Harper and Dr Adam Joesbury at the University of Nottingham for manufacturing most of the composite panels used in this project.

I would like to acknowledge COMAC for providing the financial support necessary for this project.

I would like to thank my family and friends for their unwavering support throughout my PhD and for looking after me, both in college and at home. A very special thanks goes to my parents, my sister Helen and my girlfriend Susannah for helping with my recovery and supporting me to finish my PhD studies.

Last of all, I would like to thank all of the doctors, nurses and other healthcare workers who have looked after me over the last three years. I am extremely grateful for all the care and assistance they have provided.

List of Publications

Journal papers

1. Liu H, **Brooks RA**, Hall ZEC, Liu J, Crocker JWM, A. M. Joesbury AM, Harper LT, Blackman BRK, Kinloch AJ, Dear JP. Experimental and numerical investigations on the impact behaviour of pristine and patch-repaired composite laminates. *Phil. Trans. R. Soc. A.* 2022;380(2232): 20210340. https://doi.org/10.1098/rsta.2021.0340

2. Hall ZEC, Liu J, **Brooks RA**, Liu H, Crocker JWM, Joesbury AM, Harper LT, Blackman BRK, Kinloch AJ, Dear JP. The effectiveness of patch repairs to restore the impact properties of carbon-fibre reinforced-plastic composites. *Engineering Fracture Mechanics.* 2022;270: 108570. https://doi.org/10.1016/j.engfracmech.2022.108570

3. **Brooks RA**, Wang H, Ding Z, Xu J, Song Q, Liu H, Dear JP, Li N. A review on stamp forming of continuous fibre-reinforced thermoplastics*. International Journal of Lightweight Materials and Manufacture*. 2022;5(3): 411–30. Available from: https://doi.org/10.1016/j.ijlmm.2022.05.001

4. Liu H, Liu J, Hall ZEC, **Brooks RA**, Crocker JWM, Joesbury AM, Harper LT, Blackman BRK, Kinloch AJ, Dear JP. Modelling the effects of patch-plug configuration on the impact performance of patch-repaired composite laminates. *Composites Science and Technology*. 2023;233: 109917. https://doi.org/10.1016/j.compscitech.2023.109917

5. Ding Y, Liu J, Hall ZEC, **Brooks RA**, Liu H, Kinloch AJ, Dear JP. Damage and energy absorption behaviour of composite laminates under impact loading using different impactor geometries. *Composite Structures*. 2023;321: 117259. https://doi.org/10.1016/j.compstruct.2023.117259

6. Hall ZEC, Liu J, **Brooks RA**, Liu H, Dear JP. Impact Testing on the Pristine and Repaired Composite Materials for Aerostructures. *Applied Mechanics*. 2023;4(2): 421-444. https://doi.org/10.3390/applmech4020024

7. Evans EE, **Brooks RA**, Liu J, Hall ZEC, Liu H, Lowe TJE, Withers PJ, Kinloch AJ, Dear JP. Comparison of X-ray Computed Tomography and Ultrasonic C-Scan Techniques and Numerical Modelling of Impact Damage in a CFRP Composite Laminate. *Applied Composite Materials*. 2024;31: 249-264. https://doi.org/10.1007/s10443-023-10171-3

8. **Brooks RA**, Liu J, Hall ZEC, Joesbury AM, Harper LT, Liu H, Kinloch AJ, Dear JP. The Relationship Between the Extent of Indentation and Impact Damage in Carbon-Fibre Reinforced-Plastic Composites after a Low-Velocity Impact. *Applied Composite Materials.* 2024. https://doi.org/10.1007/s10443-024-10223-2

Conference papers

1. **Brooks RA**, Liu J, Hall ZEC, Liu H, Crocker JWM, Joesbury AM, Harper LT, Blackman BRK, Kinloch AJ, Dear JP. Impact and repair performance of CFRPs. In: *British Society for Strain Measurement Postgraduate Experimental Mechanics PGEM Conference (BSSM PGEM 2022), 7-8 April 2022, Bristol, UK.* Won 3rd place prize for best presentation.

2. **Brooks RA**, Liu J, Hall ZEC, Liu H, Blackman BRK, Kinloch AJ, Dear JP. Impact of composite repairs: indentation, plasticity, intralaminar and interlaminar damage. In: *20th European Conference on Composite Materials (ECCM20), 26-30 June 2022, Lausanne, Switzerland.*

3. **Brooks RA**, Liu J, Hall ZEC, Ding Y, Joesbury AM, Harper LT, Liu H, Blackman BRK, Kinloch AJ, Dear JP. C-scan visualisation of barely visible impact damage (BVID) in composites for airframes. In: *8th International Conference on Materials Science & Smart Materials (MSSM 2022), 11–13 July 2022, Brunel University London, UK.* Won 1st place prize for best presentation.

4. **Brooks RA**, Liu J, Hall ZEC, Ding Y, Joesbury AM, Harper LT, Liu H, Blackman BRK, Kinloch AJ, Dear JP. Impact of Repaired CFRPs: Ultrasonic Evaluation and Microscopic Analysis of Internal Damage. In: *British Society for Strain Measurement 16th International Conference on Advances in Experimental Mechanics, 6-8 September 2022, Oxford, UK.*

5. **Brooks RA**, Hall ZEC, Liu J, Ding Y, Joesbury AM, Harper LT, Liu H, Blackman BRK, Kinloch AJ and Dear JP. An Investigation into barely visible impact damage (BVID) and internal delamination damage formed during impact of CFRPs. In: *14th Sustainable Energy and Environmental Protection (SEEP2022), 11-15 September 2022, Brunel University London, UK.*

6. **Brooks RA**, Liu J, Hall ZEC, Joesbury AM, Harper LT, Liu H, Kinloch AJ and Dear JP. Internal Damage in CFRPs after Multiple Low-velocity Impacts. In: *15th Sustainable Energy and Environmental Protection (SEEP2023), 25-28 July 2023, Brunel University London, UK.*

7. **Brooks RA**, Liu J, Hall ZEC, Joesbury AM, Harper LT, Liu H, Kinloch AJ, Dear JP. The Role of Indentation on Impact Damage in CFRPs. In: *British Society for Strain Measurement 17th International Conference on Advances in Experimental Mechanics, 30 August-1 September 2023, Glasgow, UK.*

8. **Brooks RA**, Liu J, Hall ZEC, Joesbury AM, Harper LT, Liu H, Blackman BRK, Kinloch AJ, Dear JP. Delamination damage formed during multiple impacts in different locations on CFRP. In: *9th International Conference on Fracture of Polymers, Composites and Adhesives, 24-28 March 2024, Les Diablerets, Switzerland.*

Table of Contents

Abstract *2*

Declaration of Originality *3*

Copyright Declaration *4*

Acknowledgements *5*

List of Publications *6*

Table of Contents *9*

List of Figures *16*

List of Tables *30*

Nomenclature *31*

Abbreviations *33*

Chapter 1 Introduction *35*

1.1 Background **35**

1.2 Aims and Objectives **36**

1.3 Structure of the Thesis **37**

Chapter 2 Literature review *39*

2.1 Introduction **39**

2.2 Continuous FRPs **39**

2.3 Impact performance of FRPs **41**

2.3.1 Introduction 41

2.3.2 Impact damage 42

2.3.2.1 Intralaminar failure 42

2.3.2.2 Interlaminar failure 44

2.3.2.3 Impact damage summary 46

2.3.3 Effect of impact velocity 47

2.3.4 Effect of impactor hardness 50

2.3.5 Effect of impactor geometry 52

2.3.6 Effect of matrix type 57
2.3.7 Effect of reinforcement geometry and lay-up 60
2.3.8 Effect of multiple impacts 63
2.3.9 Surface indentation 65
2.3.10 Non-destructive testing (NDT) techniques for damage detection 68
2.3.10.1 Ultrasonic C-scanning 68
2.3.10.2 X-ray Computed Tomography (CT) 70
2.3.10.3 Thermography 71
2.3.10.4 Other 72
2.3.11 Impact summary 72
2.4 Repair of FRPs 72
2.4.1 Repair techniques 73
2.4.1.1 Scarf repair 73
2.4.1.1.1 Effect of scarf repair type 74
2.4.1.1.2 Effect of scarf angle 75
2.4.1.1.3 Effect of layer orientation 75
2.4.1.1.4 Effect of overplies 76
2.4.1.1.5 Manufacture 77
2.4.1.1.6 Effect of impact location 79
2.4.1.2 Patch repair 79
2.4.1.2.1 Single-sided 79
2.4.1.2.2 Double-sided 80
2.4.1.2.3 Effect of patch properties 80
2.4.1.3 Bonded and bolted repair 83
2.4.1.4 Resin injection repair 84
2.4.2 Other Parameters 85
2.4.3 Repair summary 85
2.5 Stamp forming of FRTPs 86
2.5.1 Introduction 86
2.5.1.1 Stamp forming vs. other thermoforming methods for FRTPs 87
2.5.1.2 A brief history of stamp forming for FRTPs 89
2.5.2 Mechanisms for stamp forming of FRTPs 91
2.5.2.1 Deformation mechanisms 91
2.5.2.2 Friction 94
2.5.2.2.1 Ply-ply friction 97
2.5.2.2.2 Tool-ply friction 100
2.5.2.2.3 Friction summary 103

2.5.2.3 Consolidation 104
2.5.3 Challenges and defects 105
2.5.3.1 Wrinkles 105
2.5.3.2 Voids 108
2.5.3.2.1 Formation mechanisms 109
2.5.3.2.2 Distribution 110
2.5.3.2.3 Effect on mechanical properties 111
2.5.3.2.4 Void reduction 111
2.5.4 Effect of process parameters on stamp formed parts 112
2.5.4.1 Temperature 112
2.5.4.2 Speed 114
2.5.4.3 Pressure 116
2.5.4.4 Holding time 118
2.5.4.5 Cooling rate 119
2.5.4.6 Effect of process parameters summary 120
2.5.5 Forming summary 122

Chapter 3 Materials and experimental procedures 124

3.1 Introduction 124

3.2 Materials and manufacturing processes 124
3.2.1 Thermoset matrix material (i.e. CF/Epoxy) 124
3.2.1.1 Pristine panels 124
3.2.1.2 Repaired panels 126
3.2.2 Thermoplastic matrix material (i.e. CF/PPS) 128

3.3 Overview of experiments 134
3.3.1 Low-velocity drop-weight testing 134
3.3.1.1 Drop-weight tower 134
3.3.1.2 High-speed cameras 135
3.3.2 Ultrasonic C-scanning 136
3.3.3 Indentation depth measurement 138
3.3.4 Compression-after-impact (CAI) testing 139
3.3.4 Microscopy 140
3.3.4.1 Preparation 140
3.3.4.2 Optical microscopy 142
3.3.4.3 Scanning electron microscopy (SEM) 143
3.3.5 Pull-out testing 144

Chapter 4 Study on the internal and external damage formed in CFRP thermoset laminates under low-velocity impact conditions 145

4.1 Introduction 145

4.2 Test specification and methods 146

4.2.1 Materials 146

4.2.2 Experimental methods 146

4.3 Experimental results and discussion 147

4.3.1 Delamination (i.e. interlaminar) damage 147

4.3.2 Load versus time and load versus displacement results 152

4.3.3 Indentation depth studies 157

4.3.4 Optical microscopy studies 165

4.4 Summary 168

Chapter 5 Study on the internal and external damage formed in CFRP thermoset laminates after multiple impacts in the same location 169

5.1 Introduction 169

5.2 Test specification and methods 169

5.2.1 Materials 169

5.2.2 Experimental methods 170

5.3 Experimental results and discussion 170

5.3.1 Delamination damage 170

5.3.2 Load versus time and load versus displacement results 186

5.3.3 Indentation depth studies 202

5.3.4 Optical microscopy studies 213

5.4 Summary 217

Chapter 6 Study on the internal and external damage formed in CFRP thermoplastic laminates under low-velocity impact conditions 219

6.1 Introduction 219

6.2 Test specification and methods 219

6.2.1 Materials 219

6.2.2 Experimental methods 220

6.3 Experimental results and discussion 220

6.3.1 Delamination damage 220
6.3.2 Load versus time and load versus displacement results 224
6.3.3 Indentation depth studies 229
6.3.4 Optical microscopy studies 233
6.4 Summary 237
Chapter 7 Study on the damage formed in CFRP thermoset laminates and the residual compressive strength after multiple impacts in different locations . 239
7.1 Introduction 239
7.2 Test specification and methods 239
7.2.1 Materials 239
7.2.2 Experimental methods 240
7.3 Experimental results and discussion 243
7.3.1 Delamination damage 243
7.3.2 Load versus time and load versus displacement results 247
7.3.3 Compression-after-impact (CAI) results 252
7.3.3.1 Effect of impact energy 252
7.3.3.2 Effect of separation distance 255
7.3.3.3 CAI summary 258
7.4 Summary 259
Chapter 8 Study on the impact behaviour of patch-repaired CFRP thermoset laminates 261
8.1 Introduction 261
8.2 Test specification and methods 262
8.2.1 Materials 262
8.2.2 Experimental methods 262
8.3 Experimental results and discussion 263
8.3.1 Summary of previous work 263
8.3.1.1 Effect of patch diameter 263
8.3.1.1.1 Patch only (No plug) 266
8.3.1.1.2 Patch + plug 269
8.3.1.2 Effect of patch thickness 272
8.3.1.3 Summary 275
8.3.2 Indentation 279

8.3.3 Microscopy 285
8.3.3.1 Patch-only repair versus patch + plug repair 285
8.3.3.2 Optical microscopy versus Scanning electron microscopy (SEM) 288
8.4 Summary 293
Chapter 9 Conclusions 295
9.1 Introduction **295**
9.2 Study on the internal and external damage formed in CFRP thermoset laminates under low-velocity impact conditions **295**
9.3 Study on the internal and external damage formed in CFRP thermoset laminates after multiple impacts in the same location **296**
9.4 Study on the internal and external damage formed in CFRP thermoplastic laminates under low-velocity impact conditions **298**
9.5 Study on the damage formed in CFRP thermoset laminates and the residual compressive strength after multiple impacts in different locations **299**
9.6 Study on the impact behaviour of patch-repaired CFRP thermoset laminates **300**
9.7 Summary **301**
Chapter 10 Future work 302
10.1 Introduction **302**
10.2 Measuring indentation depth in alternative CFRP materials after low-velocity impact **302**
10.3 Effects of impactor shape and size on the resulting indentation shape and depth ... **303**
10.4 Effects of high-velocity impact on the indentation depth in CFRP materials **304**
10.5 Multiple impacts of different energies in different locations **304**
10.6 Impact testing of formed CFRP components **305**
10.7 Testing of scarf repairs with similar dimensions to the patch repairs **305**
List of references 306
Appendices 343
Appendix A - Design of pull-out rig for inter-ply friction testing 343

A.1 Initial ideas for friction testing machine/rig..... 343
A.2 Detailed design for vertical pull-out rig..... 344
A.3 Testing..... 348

Appendix B - Repeat data for Chapter 4 349

Appendix C - Discussion of 2.3 mm thick CF/Epoxy panels impacted at 15 J 351

Appendix D - Load versus time and load versus displacement traces for multiple impacts at 2 J on CF/Epoxy.....357

Appendix E – Repeat data for Chapter 5 359

Appendix F - Additional data for Chapter 6.....360

Appendix G - Additional data for Chapter 7 361

List of Figures

Figure 2-1: Multi-scale structures of (a) unidirectional (UD) and (b) woven composite [21]. 40

Figure 2-2: Matrix cracking in composite laminates under: (a) tensile, (b) compressive and (c) shear loading [28]. 43

Figure 2-3: Diagram showing microbuckling of fibres and kink band geometry [31]. 43

Figure 2-4: Intralaminar and interlaminar damage in an impacted UD CF/Epoxy composite panel. ... 45

Figure 2-5: Modes of delamination induced buckling – (a) local, (b) global and (c) mixed (adapted from [41]). 46

Figure 2-6: Schematic representation of the impact response under (a) low-velocity and (b) high-velocity impact loading [44]. 48

Figure 2-7: C-scans of CF/PEEK and CF/Epoxy samples after impact at (a) low-velocity (2.56 $m.s^{-1}$) and (b) high-velocity (54.4 $m.s^{-1}$) [19]. 50

Figure 2-8: Ultrasonic scanning images of gelatine-impacted and HDPE-impacted CF/PEEK samples [53]. 52

Figure 2-9: Damage in jute/epoxy laminates of thicknesses 6 mm, 8 mm and 10 mm after impact at 8 $m.s^{-1}$ using (a) a conical, (b) a hemispherical and (c) a flat-ended impactor [59]. 53

Figure 2-10: C-scan maps obtained from the round-nosed and flat-ended impact tests performed at impact energies of 10, 15, 20, 25 and 30 J, respectively. (The footprint of the delamination area is highlighted by white dashed lines and the area is given in the bottom left of each map) [63]. 56

Figure 2-11: C-scan inspection of CF/PEEK, CF/PPS and CF/Epoxy samples after impact at 2, 6, 10.5, 17 and 25 J [65]. 58

Figure 2-12: Ultrasonic C-scanning images of the damage area of $[0/90]_{ns}$ cross-ply CF/Epoxy laminates showing the effect of impact energy and thickness on the impact damage area [79]. 61

Figure 2-13: Ultrasonic C-scanning images of the damage area of $[0/90]_{4s}$, $[\pm45]_{4s}$ and $[0/90/\pm45]_{2s}$ CF/Epoxy laminates subjected to an impact of energy 31.4 J [79]. 62

Figure 2-14: Delamination shapes and delamination areas (DA) in CF/Epoxy after (a) one, (b) two and (c) three impacts at 30 J [14]. 64

Figure 2-15: Diagram showing volumetric examination through A-scan, B-scan, C-scan and L-scan [98]. 69
Figure 2-16: Typical damage maps in an impacted CF/Epoxy panel from (a) an ultrasonic C-scan inspection technique and (b) an X-ray CT technique. Delaminations are colour-coded from the top (red) surface to the bottom (black) as indicated by the damage depth colour bar [103]. 70
Figure 2-17: Composite repair configurations utilising bonded joints – (a) scarf repair, (b) stepped scarf repair, (c) scarf doubler bonded repair and (d) patch repair (adapted from [109]). 73
Figure 2-18: A compact scarf repair with steps in the fibre direction only [140]. 78
Figure 2-19: Repair geometry used by Li et al. [141] for (a) a single-sided scarf repair and (b) a double-sided scarf repair. 78
Figure 2-20: Final failure pictures of adhesive in a patch repair showing shear failure of adhesive in patches of (a) 40 mm, (b) 50 mm, (c) 60 mm and (d) 70 mm in diameter [153]. 81
Figure 2-21: Through-thickness reinforcement technique pinning patterns: (a) 8 pins in one ring, (b) 18 pins in two rings and (c) 28 pins in three rings. Pins have equal circumferential spacing in each ring and the rings divide the distance uniformly between the edge of the central hole and that of the assumed 50 mm diameter delamination [165]. 84
Figure 2-22: Diagram of resin injection repair method, showing resin infiltration through the delaminations [167]. 85
Figure 2-23: Typical stamp forming process for FRTPs, showing stages: (a) heating, (b) transfer, (c) forming, (d) removal. 87
Figure 2-24: Example shapes formed by stamp forming: (a) hemisphere, (b) V-shape, (c) wing fixed leading edge stiffener, (d) square cup with two steps [181,191,211,215]. 90
Figure 2-25: Development of FRTP shapes/components formed by stamp forming and their approximate complexities [179,185,199–201,203,204,207–209,211,213–216]. 90
Figure 2-26: Deformation mechanisms required for different deformation modes (adapted from [178]). 93
Figure 2-27: Example pull-out experiment set-up to measure (a) inter-ply and (b) tool-ply friction. 95
Figure 2-28: Typical force-displacement curve for a pull-out test. 96
Figure 2-29: Stribeck curve [71]. 97

Figure 2-30: Laminate deformation behaviours when double curvature leads to excess material during forming [253]. 106
Figure 2-31: Wrinkles in final formed parts: (a) hemisphere and (b) shape containing cylindrical portion, quarter sphere and flat faces [218,257]. 107
Figure 2-32: Void content in GF/PA6 after preheating to: (a) 240 ºC, (b) 255 ºC and (c) 270 ºC [201] 109
Figure 2-33: Microscopic images of woven CF/PEEK laminates fabricated at: (a) 360ºC and 3 MPa, (b) 400ºC and 3 MPa, (c) 420ºC and 3 MPa, (d) 400ºC and 1 MPa, (e) 400ºC and 5 MPa and (f) 400ºC and 9 MPa [261]..... 110
Figure 2-34: Optical microscopy photographs of the cross section of woven CF/polycarbonate (CF/PC) laminates manufactured at 255 °C and 1 MPa with different dwell times: (a) 5 minutes, (b) 10 minutes and (c) 20 minutes [264]..... 111
Figure 2-35: Studied forming temperatures for different thermoplastic matrices in relation to their melting (T_m) and degradation temperatures (T_{deg}) [191,197,201,217,261,262,265–272]..... 113
Figure 2-36: General trends of the effect of an increase in a certain processing parameter on some post-form material properties. Increase in: (a) - temperature, (b) - speed, (c) - pressure, (d) - holding time, (e) - cooling rate [197,201,217,261–264,267–269,277–281]. 121
Figure 3-1: Diagram of a pristine CF/Epoxy panel. 126
Figure 3-2: Diagram of a repaired CF/Epoxy panel. 127
Figure 3-3: Repaired panel with a 65 mm diameter patch and no plug. 128
Figure 3-4: CF/PPS pre-preg and Teflon sheeting before forming into a laminate. 130
Figure 3-5: Stainless-steel mould (a) with all three parts laid out - base, plate and top and (b) with plate inside the base, ready for pre-preg to be placed inside. 131
Figure 3-6: LP_M4SH50 manual hot press with attached cooling unit. 132
Figure 3-7: Stainless-steel mould with CF/PPS pre-preg and teflon sheets positioned inside for forming. 132
Figure 3-8: Graph showing the temperature and pressure of the CF/PPS pre-preg during forming into a laminate using the manual hot press. 133
Figure 3-9: Optical microscope image of a pristine CF/PPS panel. 133

Figure 3-10: (a) Drop-weight tower and PC, (b) window cut-out in impact zone and (c) hemispherical impactor and clamped repaired panel. 135
Figure 3-11: Diagram showing the setup of the two high-speed cameras used to record impacts on the CFRP panels. 136
Figure 3-12: The equipment used for C-scanning the CFRP panels. 137
Figure 3-13: Photograph of a CF/Epoxy composite panel 150 mm x 100 mm in size with a thickness of 4.6 mm after an impact of 7.5 J showing a typical surface indentation [87]. 138
Figure 3-14: The indentation depth in CF/Epoxy composite panels impacted once, measured using the Confocal laser scanning microscope versus using the handheld gauge [87]. 139
Figure 3-15: CAI testing set-up, showing the CAI test rig in a 250 kN Instron Universal Testing Machine. 140
Figure 3-16: Photograph of the inside of the Brillant 220 cutting machine showing the general set-up used for cutting the panels with the diamond blade. 141
Figure 3-17: Grinding wheels set up for grinding (left) and polishing (right). 142
Figure 3-18: Zeiss Axio Scope.A1 optical microscope set-up with accompanying PC. 143
Figure 4-1: C-scan damage maps obtained from the CF/Epoxy replicate composite panels with a thickness of 2.3 mm with impact energies of 2, 5, 10 and 15 J. 148
Figure 4-2: C-scan damage maps obtained from the CF/Epoxy replicate composite panels with a thickness of 4.6 mm with impact energies of 2, 5, 10, 15 and 20 J. 149
Figure 4-3: Comparison of the C-scan damage maps obtained from the impacted CF/Epoxy composite panels with a thickness of 2.3 or 4.6 mm.. 151
Figure 4-4: (a) Load versus time traces and (b) load versus displacement traces for 2.3 mm and 4.6 mm thick CF/Epoxy composite panels impacted at 2, 5, 10, 15 and 20 J [87]. 153
Figure 4-5: Series of high-speed photographic images showing the indentation process for an impact of 15 J on a 2.3 mm thick CF/Epoxy composite panel (inter-frame time is 1.6 ms). The first image (top left) is captured just before the impact event and the total contact time is approximately 8 ms, with the last image (bottom right) showing the start of the rebounding of the impactor. The hemispherical stainless-steel impactor has a diameter of 16 mm. 155

Figure 4-6: Series of high-speed photographic images showing the indentation process for an impact of 15 J on a 4.6 mm thick CF/Epoxy composite panel (inter-frame time is 1 ms). The first image (top left) is captured just before the impact event and the total contact time is approximately 5 ms, with the last image (bottom right) showing the start of the rebounding of the impactor. The hemispherical stainless-steel impactor has a diameter of 16 mm [87]..... 156
Figure 4-7: Energy versus time traces for 2.3 mm and 4.6 mm thick CF/Epoxy composite panels for impact energies of 2, 5, 10, 15 and 20 J [87]..... 157
Figure 4-8: Typical indentation cross-section in (a) 2.3 mm thick and (b) 4.6 mm thick CF/Epoxy composite panels after an impact of 2, 5, 10, 15 and 20 J [87]. 158
Figure 4-9: The indentation depth versus impact energy, and delamination damage area versus impact energy, for the CF/Epoxy composite panels of (a) thickness 2.3 mm and (b) thickness 4.6 mm, for the two replicate cases presented in Figure 4-1 and Figure 4-2 and, in some cases, for a third replicate test [87]. 159
Figure 4-10: The indentation depth versus (a) the impact energy and (b) the interlaminar damage area for the 2.3 mm and 4.6 mm thick CF/Epoxy composite panels [87]. 160
Figure 4-11: The indentation depth versus normalised interlaminar damage area (i.e. damage area divided by thickness) for the CF/Epoxy composite panels [87]. 162
Figure 4-12: Optical microscopy images of a 4.6 mm thick CF/Epoxy composite panel after an impact of 15 J. (Showing a cross-section cut from the panel after grinding and polishing. The scale bars in the upper-left and upper-right micrographs represent 100 µm and 500 µm, respectively.) [87]. 166
Figure 4-13: Optical microscopy images of (a) a 2.3 mm and (b) a 4.6 mm thick CF/Epoxy composite panel after an impact at 5 J. (Showing a cross-section cut from the panel after grinding and polishing.) 167
Figure 4-14: Optical microscopy images of (a) a 2.3 mm and (b) a 4.6 mm thick CF/Epoxy composite panel after an impact at 15 J. (Showing a cross-section cut from the panel after grinding and polishing.) [87]. 167
Figure 5-1: C-scan damage maps obtained from the CF/Epoxy replicate composite panels with a thickness of 2.3 mm after two impacts at impact energies of 2, 5, 10 and 15 J. 172

Figure 5-2: C-scan damage maps obtained from the CF/Epoxy replicate composite panels with a thickness of 4.6 mm after two impacts at impact energies of 2, 5, 10, 15 and 20 J. 173
Figure 5-3: Comparison of the C-scan damage maps obtained from the impacted CF/Epoxy composite panels with a thickness of 2.3 or 4.6 mm after two impacts. 174
Figure 5-4: C-scan damage maps obtained from the CF/Epoxy replicate composite panels with a thickness of 2.3 mm after three impacts at impact energies of 2, 5, 10 and 15 J. 176
Figure 5-5: C-scan damage maps obtained from the CF/Epoxy replicate composite panels with a thickness of 4.6 mm after three impacts at impact energies of 2, 5, 10, 15 and 20 J. 177
Figure 5-6: Image of the rear surface of a 2.3 mm thick CF/Epoxy panel after three impacts at 15 J. The delamination damage area shown by this panel was 1454 mm^2. 178
Figure 5-7: Comparison of the C-scan damage maps obtained from the impacted CF/Epoxy composite panels with a thickness of 2.3 or 4.6 mm after three impacts..... 179
Figure 5-8: C-scan damage maps for 2.3 mm and 4.6 mm thick CF/Epoxy composite panels after one, two and three impacts at 5 J. The increase in delamination damage area (DA) between impacts is shown. 181
Figure 5-9: C-scan damage maps for 2.3 mm and 4.6 mm thick CF/Epoxy composite panels after one, two and three impacts at 10 J. The increase in delamination damage area (DA) between impacts is shown. 182
Figure 5-10: C-scan damage maps for 2.3 mm and 4.6 mm thick CF/Epoxy composite panels after one, two and three impacts at 15 J. The increase in delamination damage area (DA) between impacts is shown. 183
Figure 5-11: C-scan damage maps for a 4.6 mm thick CF/Epoxy composite panel after one, two and three impacts at 20 J. The increase in delamination damage area (DA) between impacts is shown. 184
Figure 5-12: Graph of delamination damage area versus accumulated impact energy for first, second and third impacts at 5, 10, 15 and 20 J on 2.3 mm and 4.6 mm thick CF/Epoxy composite panels.. 186
Figure 5-13: (a) Load versus time traces and (b) load versus displacement traces for first, second and third impacts at 5 J on 2.3 mm and 4.6 mm thick CF/Epoxy composite panels. 188
Figure 5-14: (a) Load versus time traces and (b) load versus displacement traces for first, second and third impacts at 10 J on 2.3 mm and 4.6 mm thick CF/Epoxy composite panels. 190

Figure 5-15: (a) Load versus time traces and (b) load versus displacement traces for first, second and third impacts at 15 J on 2.3 mm and 4.6 mm thick CF/Epoxy composite panels. 192
Figure 5-16: (a) Load versus time traces and (b) load versus displacement traces for first, second and third impacts at 20 J on 4.6 mm thick CF/Epoxy composite panels. 194
Figure 5-17: Series of high-speed photographic images showing the indentation process for an impact of 15 J on a previously impacted 2.3 mm thick CF/Epoxy composite panel (inter-frame time is 1.6 ms). The first image (top left) is captured just after the impact event and total contact time is approximately 8 ms, with the last image (bottom right) showing the start of the rebounding of the impactor. The hemispherical stainless-steel impactor has a diameter of 16 mm..... 196
Figure 5-18: Series of high-speed photographic images showing the indentation process for an impact of 15 J on a previously impacted 4.6 mm thick CF/Epoxy composite panel (inter-frame time is 1 ms). The first image (top left) is captured just after the impact event and total contact time is approximately 5 ms, with the last image (bottom right) showing the start of the rebounding of the impactor. The hemispherical stainless-steel impactor has a diameter of 16 mm..... 197
Figure 5-19: Energy versus time traces for first, second and third impacts at 2 J on 2.3 mm and 4.6 mm thick CF/Epoxy composite panels. 199
Figure 5-20: Energy versus time traces for first, second and third impacts at 5 J on 2.3 mm and 4.6 mm thick CF/Epoxy composite panels. 199
Figure 5-21: Energy versus time traces for first, second and third impacts at 10 J on 2.3 mm and 4.6 mm thick CF/Epoxy composite panels. 200
Figure 5-22: Energy versus time traces for first, second and third impacts at 15 J on 2.3 mm and 4.6 mm thick CF/Epoxy composite panels. 200
Figure 5-23: Energy versus time traces for first, second and third impacts at 20 J on 4.6 mm thick CF/Epoxy composite panels. 201
Figure 5-24: Graph of percentage of impact energy rebounded versus the impact energy for first, second and third impacts at 2, 5, 10, 15 and 20 J on 2.3 mm and 4.6 mm thick CF/Epoxy composite panels. 201
Figure 5-25: Indentation cross-section in (a) 2.3 mm thick and (b) 4.6 mm thick CF/Epoxy composite panels after one, two and three impacts at 5 J. 204

Figure 5-26: Indentation cross-section in (a) 2.3 mm thick and (b) 4.6 mm thick CF/Epoxy composite panels after one, two and three impacts at 10 J. 205
Figure 5-27: Indentation cross-section in (a) 2.3 mm thick and (b) 4.6 mm thick CF/Epoxy composite panels after one, two and three impacts at 15 J. Cross-sections from two panels are shown for the 2.3 mm thick third impact case. 206
Figure 5-28: The indentation depth in the CF/Epoxy composite panel measured using the Confocal laser scanning microscope versus using the handheld gauge, including measurements taken after first, second and third impacts..... 207
Figure 5-29: Summary of indentation cross-sections in 2.3 mm and 4.6 mm thick CF/Epoxy composite panels after one, two and three impacts at 5, 10 and 15 J. Cross-sections from two panels are shown for the 2.3 mm thick third impact case. 208
Figure 5-30: The indentation depth versus impact energy, and delamination damage area versus impact energy, for the 2.3 mm and 4.6 mm thick CF/Epoxy composite panels after (a) two impacts and (b) three impacts..... 209
Figure 5-31: The indentation depth versus the delamination damage area for the 2.3 mm and 4.6 mm thick CF/Epoxy composite panels after (a) two impacts and (b) three impacts. 211
Figure 5-32: The indentation depth versus normalised interlaminar damage area (i.e. damage area divided by thickness) for the CF/Epoxy composite panels. 213
Figure 5-33: Optical microscopy images of a 2.3 mm thick CF/Epoxy composite panel after (a) one and (b) three impacts at 5 J. (Showing a cross-section cut from the panel after grinding and polishing.) 214
Figure 5-34: Optical microscopy images of a 4.6 mm thick CF/Epoxy composite panel after (a) one and (b) three impacts at 5 J. (Showing a cross-section cut from the panel after grinding and polishing.) 214
Figure 5-35: Optical microscopy images of a 2.3 mm thick CF/Epoxy composite panel after (a) one and (b + c) three impacts at 15 J (showing panels with DAs of (b) 1013 mm^2 and (c) 1454 mm^2). (Showing a cross-section cut from the panel after grinding and polishing.) Magnified image showing fibre fracture in (c) has a scale bar of 200 µm. 216
Figure 5-36: Optical microscopy images of a 4.6 mm thick CF/Epoxy composite panel after (a) one and (b) three impacts at 15 J. (Showing a cross-section cut from the panel after grinding and polishing.) 217

Figure 6-1: C-scan damage maps obtained from the CF/PPS replicate composite panels with impact energies of 2, 5, 7.5, 10 and 12.5 J. 223
Figure 6-2: Rear surface of the CF/PPS panel impacted at 12.5 J, showing severe damage, including fibre fracture. 224
Figure 6-3: (a) Load versus time traces and (b) load versus displacement traces for the CF/PPS composite panels impacted at 2, 5, 7.5, 10 and 12.5 J. 225
Figure 6-4: (a) Load versus time traces and (b) load versus displacement traces for the CF/PPS composite panels and 2.3 mm thick CF/Epoxy composite panels impacted at 2, 5 and 10 J. 227
Figure 6-5: Energy versus time traces for impacts at 2, 5, 7.5, 10 and 12.5 J on CF/PPS composite panels. 228
Figure 6-6: Indentation cross-section in a CF/PPS composite panel after an impact of 2, 5, 7.5 and 10 J. 229
Figure 6-7: (a) Indentation depth versus impact energy and (b) delamination damage area versus impact energy for the CF/PPS composite panels and the 2.3 mm thick CF/Epoxy composite panels. 232
Figure 6-8: The indentation depth versus the delamination damage area for the CF/PPS composite panels and the 2.3 mm thick CF/Epoxy composite panels. 233
Figure 6-9: Optical microscopy images of a CF/PPS composite panel after impact at (a) 5 J, (b) 7.5 J and (c) 10 J. (Showing cross-sections cut from the panel after grinding and polishing.) Exploded view images have scale bars of (a) 100 μm and (c) 200 μm. 235
Figure 6-10: Optical microscopy images of (a) CF/Epoxy and (b) CF/PPS composite panels after impact at 5 J. (Images from Figure 4-13(a) and Figure 6-9(a), repeated here to allow easy comparison.) .. 237
Figure 7-1: Diagram showing the position of a 200 mm x 100 mm panel for (a) a first impact and (b) a second impact (after 180° rotation). The clamp locations are shown by the black and red circles (for first and second impacts, respectively) and the impact points (located 75 mm from the edge of the rear guide pin) are shown by the black and red crosses (again for first and second impacts, respectively). The dashed rectangle shows the position of the window cut-out beneath the panel. The arrow indicates the 0° direction. 241

Figure 7-2: Diagram showing the impact locations and clamp locations for first (black) and second (red) impacts on the (a) 160, (b) 180 and (c) 200 mm long panels. The arrows indicate the 0° direction.. 242
Figure 7-3: C-scan damage maps obtained from the 160, 180 and 200 mm long CF/Epoxy composite panels after one impact, and then a second impact, separated from the first by 10, 30 and 50 mm, respectively, at an energy of 15 J..... 244
Figure 7-4: C-scan damage maps obtained from the 160, 180 and 200 mm long CF/Epoxy composite panels after one impact, and then a second impact, separated from the first by 10, 30 and 50 mm, respectively, at an energy of 20 J..... 245
Figure 7-5: C-scan damage maps obtained from the 160, 180 and 200 mm long CF/Epoxy composite panels after one impact, and then a second impact, separated from the first by 10, 30 and 50 mm, respectively, at an energy of 25 J..... 246
Figure 7-6: (a) Load versus time traces and (b) load versus displacement traces for first and second impacts at 15 J separated by 10 mm on 160 mm long CF/Epoxy composite panels..... 249
Figure 7-7: (a) Load versus time traces and (b) load versus displacement traces for first and second impacts at 15 J separated by 30 mm on 180 mm long CF/Epoxy composite panels..... 250
Figure 7-8: (a) Load versus time traces and (b) load versus displacement traces for first and second impacts at 15 J separated by 50 mm on 200 mm long CF/Epoxy composite panels..... 251
Figure 7-9: Photographs of the edge of the CF/Epoxy composite panel after CAI testing at the location of failure for (a) 15 J - 30 mm and (b) 25 J - 30 mm cases, showing propagation of delaminations to the edge of the panel at the 0/90° and 90/0° ply boundaries..... 252
Figure 7-10: Load versus displacement graphs from compressive loading of the CF/Epoxy composite panels impacted twice at 15, 20 and 25 J, with impacts separated by (a) 10, (b) 30 and (c) 50 mm. For the panels with a separation distance of 50 mm, impact energies of 10, 30 and 35 J are also included. 254
Figure 7-11: Load versus displacement graphs from compressive loading of the CF/Epoxy composite panels impacted twice at (a) 15, (b) 20 and (c) 25 J, with impacts separated by 10, 30 and 50 mm. 257
Figure 7-12: The compressive strength (i.e. CAI strength) plotted against the delamination damage area for the CF/Epoxy panels impacted twice at 15, 20 and 25 J, with impacts separated by 10, 30 and 50 mm..... 258

Figure 8-1: Graphs showing (a) load versus time and (b) load versus displacement traces for the two pristine panels after one and then two impacts at 7.5 J in the same location (adapted from [294]). . 265
Figure 8-2: C-scan images of two pristine panels after one and two impacts at 7.5 J. 266
Figure 8-3: Graphs showing (a) load versus time and (b) load versus displacement traces for a 55 mm diameter patch-only repair, a 65 mm diameter patch-only repair and a pristine panel, all impacted at 7.5 J (adapted from [294]). 267
Figure 8-4: C-scan images of (a) the pristine panel, (b) the 55 mm diameter patch-only repair and (c) the 65 mm diameter patch-only repair after impact at 7.5 J, (adapted from [294]). 268
Figure 8-5: Graphs showing (a) load versus time and (b) load versus displacement traces for a 55 mm diameter patch + plug repair, a 65 mm diameter patch + plug repair and a pristine panel, all impacted at 7.5 J (adapted from [294]). 270
Figure 8-6: C-scan images of (a) the pristine panel, (b) the 55 mm diameter patch + plug repair and (c) the 65 mm diameter patch + plug repair. The C-scans were taken from the top (impacted) face and show the delamination damage in the patch, (adapted from [294]). 271
Figure 8-7: C-scan images of the plug and surrounding parent panel for (a) the 55 mm diameter patch + plug repair and (b) the 65 mm diameter patch + plug repair. The C-scans were taken from the rear (non-impacted) face and show the delamination damage in the plug, (adapted from [294]). 272
Figure 8-8: Graphs showing (a) load versus time and (b) load versus displacement traces for a 2.3 mm thick patch-only repair, a 4.6 mm thick patch-only repair and a pristine panel, all impacted at 7.5 J. All patches are 65 mm in diameter (adapted from [294]). 274
Figure 8-9: C-scan images of (a) + (b) the 2.3 mm thick patch-only repairs and (c) + (d) the 4.6 mm thick patch-only repairs after impact at 7.5 J. All patches are 65 mm in diameter, (adapted from [294]). 275
Figure 8-10: Graphs showing (a) load versus time and (b) load versus displacement traces for a 2.3 mm thick patch-only repair, a 4.6 mm thick patch-only repair, a (2.3 mm thick) patch + plug repair and a pristine panel, all impacted at 7.5 J. All patches are 65 mm in diameter (adapted from [294]). 277
Figure 8-11: C-scan images from (a) the pristine panel, (b) the 65 mm diameter 2.3 mm thick patch-only repair, (c) the 65 mm diameter 4.6 mm thick patch-only repair and (d) the 65 mm diameter patch + plug repair, (adapted from [294]). 278

Figure 8-12: Series of high-speed photographic images showing the indentation process for an impact of 7.5 J on a 65 mm diameter patch + plug repair (inter-frame time is 0.7 ms). The first image (top left) is captured just after the impact event and total contact time is approximately 3.5 ms, with the last image (bottom right) showing the start of the rebounding of the impactor. The hemispherical stainless-steel impactor has a diameter of 16 mm. 279
Figure 8-13: Images taken using a high-speed camera of a 65 mm diameter patch + plug repair (a) before impact and (b) after impact, showing an indentation in the centre of the patch. 280
Figure 8-14: The indentation depth versus repair thickness for the thin patch-only, thick patch-only and (thin) patch + plug repaired CF/Epoxy composite panels after impact at 7.5 J. 281
Figure 8-15: The indentation depth versus the delamination damage area within only the patch for the thin patch-only, thick patch-only and patch + plug repaired CF/Epoxy composite panels after impact at 7.5 J. 282
Figure 8-16: The indentation depth versus the delamination damage area within the patch (for the patch-only repairs) or within the patch and the plug combined (for the patch + plug repairs) for the thin patch-only, thick patch-only and patch + plug repaired CF/Epoxy composite panels after impact at 7.5 J. 282
Figure 8-17: Graphs showing (a) load versus time and (b) load versus displacement traces for a 55 mm diameter patch + plug repair and a 65 mm diameter patch + plug repair which both showed delamination damage, a 65 mm diameter patch + plug repair which showed no delamination damage and a pristine panel, all impacted at 7.5 J (adapted from [294]). 284
Figure 8-18: Diagram showing (a) a patch-only repair and (b) a patch + plug repair and the area viewed under the microscope in each case. 286
Figure 8-19: Optical microscope images of (a) a patch-only repair and (b) a patch + plug repair after impact at 7.5 J. Both images are at the same scale (scale bar is 5 mm for both). 286
Figure 8-20: (a) Optical microscope and (b) SEM images of a patch-only repair after impact at 7.5 J. Note, these images are not at the same scale (optical scale bar is 5 mm and SEM scale bar is 500 μm). 289
Figure 8-21: (a) Optical microscope and (b) SEM images of a patch + plug repair after impact at 7.5 J. Both images are at approximately the same scale (optical scale bar is 5 mm and SEM scale bar is 2 mm). 290

Figure 8-22: (a) Optical microscope and (b) SEM images of a patch + plug repair after impact at 7.5 J. Note, these images are not at the same scale (optical scale bar is 500 μm and SEM scale bar is 50 μm). 291
Figure 8-23: (a) Optical microscope and (b) SEM images of intralaminar damage in a patch-only repair. Note, these images are not at the same scale (optical scale bars are 200 μm and 20 um and SEM scale bars are 50 μm and 10 μm). 292
Figure 8-24: SEM image of fibre fracture and matrix damage in a patch + plug repair after impact at 7.5 J. (Scale bar is 2 μm). 293
Figure A-1: Pull-out rig before the cartridges were inserted into place. 345
Figure A-2: Solidworks model of a single hot plate showing the thermocouple holes and channels, cartridge holes and bolt holes. 346
Figure A-3: Pull-out rig in position on the support plate on an Instron Universal Testing Machine. The grips and CFRP samples are not shown in this image. 348
Figure B-1: C-scan damage maps obtained from the CF/Epoxy composite panels with a thickness of 2.3 mm with impact energies of 5, 10 and 15 J. 349
Figure B-2: C-scan damage maps obtained from the CF/Epoxy composite panels with a thickness of 4.6 mm with impact energies of 5, 10, 15 and 20 J. 350
Figure C-1: C-scan damage maps obtained from the CF/Epoxy replicate composite panels with a thickness of 2.3 mm after one, two and three impacts at 15 J. 351
Figure C-2: (a) Load versus time traces and (b) load versus displacement traces for a first impact at 15 J on two 2.3 mm thick CF/Epoxy composite panels. 353
Figure C-3: (a) Load versus time traces and (b) load versus displacement traces for a second impact at 15 J on two 2.3 mm thick CF/Epoxy composite panels. 354
Figure C-4: (a) Load versus time traces and (b) load versus displacement traces for a third impact at 15 J on two 2.3 mm thick CF/Epoxy composite panels. 356
Figure D-1: (a) Load versus time traces and (b) load versus displacement traces for first, second and third impacts at 2 J on 2.3 mm and 4.6 mm thick CF/Epoxy composite panels. 358
Figure E-1: C-scan damage maps obtained from the CF/Epoxy composite panels with a thickness of 4.6 mm after two and three impacts at impact energies of 10 J and 20 J. 359

Figure F-1: C-scan damage maps obtained from the CF/PPS replicate composite panels with impact energies of 2, 5, 7.5, 10 and 12.5 J. 360
Figure G-1: C-scan damage maps obtained from the 160 and 180 mm long CF/Epoxy composite panels after one impact, and then a second impact, separated from the first by 10 and 30 mm, respectively, at an energy of 3 J. 362
Figure G-2: C-scan damage maps obtained from the 160 and 180 mm long CF/Epoxy composite panels after one impact, and then a second impact, separated from the first by 10 and 30 mm, respectively, at an energy of 6 J. 363
Figure G-3: C-scan damage maps obtained from the 160 and 180 mm long CF/Epoxy composite panels after one impact, and then a second impact, separated from the first by 10 and 30 mm, respectively, at an energy of 9 J. 364
Figure G-4: C-scan damage maps obtained from the 200 mm long CF/Epoxy composite panels after one impact, and then a second impact, separated from the first by 50 mm, at impact energies of 10, 30 and 35 J. 365

List of Tables

Table 2-1: Test conditions in ply-ply friction studies [176,186,230–234,245]..... 98

Table 2-2: Test conditions in tool-ply friction studies [232–236,239,241–243,246,247]..... 100

Table 2-3: Effect of increase in process parameters on the ply-ply and tool-ply shear stress and μ. 104

Table 2-4: Effect of an increase in certain processing parameters on a selection of mechanical and physical properties. 122

Table 3-1: Materials properties for MTC510 UD pre-preg, supplied by SHD Composites Ltd, UK [284]. 125

Table 3-2: Materials properties for MTFA-500 film adhesive, supplied by SHD Composites Ltd, UK. 127

Table 3-3: Materials properties for TC1100 woven pre-preg, supplied by Toray Advanced Composites, The Netherlands [287]..... 129

Table 4-1: The values of the constants in Equations (4.1) and (4.2) and the approximate initiation energies required for indentation and delamination. 163

Table 7-1: Summary of the impact energies used for each of the three lengths of panel. 240

Nomenclature

A	Delamination damage footprint area
A_i	Instantaneous contact area
C'	Constant equal to $k_{delamination}$. $(U_{threshold} - U_{yield})$
d	Indentation depth
D	Patch diameter
F	Pull-out force
H	Hersey number
$k_{delamination}$	Constant of proportionality between A and $(U_{impactor} – U_{threshold})$
$k_{1indentation}$	First-order parameter for the second-order polynomial fit between d and $(U_{impactor} - U_{yield})$
$k_{2indentation}$	Second-order parameter for the second-order polynomial fit between d and $(U_{impactor} - U_{yield})$
N	Normal load
P	Normal pressure
t	Panel thickness
T_{deg}	Degradation temperature
T_g	Glass transition temperature
T_m	Melting temperature
U	Speed
$U_{impactor}$	Initial impact energy of the impactor
$U_{threshold}$	Threshold energy for delamination
U_{yield}	Impact energy for yielding
w_k	Kink band width

β	Kink band angle of inclination
γ	Shear angle
η	Resin viscosity
μ	Friction coefficient
μ_{pp}	Ply-ply friction coefficient
μ_{tp}	Tool-ply friction coefficient
τ	Shear stress

Abbreviations

ASTM	American Society for Testing and Materials
BVID	Barely visible impact damage
CAI	Compression-after-impact
CF	Carbon fibre
CFRP	Carbon fibre-reinforced polymer
CPT	Cured ply thickness
CT	Computed tomography
DA	Delamination damage area
DMA	Dynamic mechanical analysis
FRP	Fibre-reinforced polymer
FRTP	Fibre-reinforced thermoplastic
GF	Glass fibre
GFRP	Glass fibre-reinforced polymer
HDPE	High-density polyethylene
ILSS	Interlaminar shear strength
IR	InfraRed
NDT	Non-destructive testing
PA6	Polyamide 6 (Nylon 6)
PA66	Polyamide 66 (Nylon 66)
PC	Polycarbonate
PEEK	Poly(ether-ether ketone)
PEI	Polyetherimide
PP	Polypropylene
PPS	Polyphenylene sulphide
PU	Polyurethane
QIT	Quasi-isotropic

SCF	Stress concentration factor
SEM	Scanning electron microscopy
TP	Thermoplastic
UD	Unidirectional
VF	Fibre volume fraction

Chapter 1 Introduction

1.1 Background

The aerospace and automotive industries are significant contributors to worldwide greenhouse gas emissions [1,2] and the issue of climate change has led to a drive towards improving energy efficiency and reducing emissions. In the aerospace industry, the cost savings associated with improved fuel efficiency act as an incentive for this development. In the automotive industry, regulations establishing limits on the emissions produced by new vehicles help ensure targets are reached [2]. A significant contributor to this reduction in emissions is the development and application of lightweight materials which give the required strength for structural integrity and safety. Fibre-reinforced polymers (FRPs) are known for their high strength-to-weight ratio and good fatigue resistance. Therefore, they have replaced metals in certain applications and are now widely used in aerospace structures and increasingly used in the automotive industry [3–7]. For example, composites comprise 53% [8] and 50% [9] of the total structural weight of the Airbus A350-900 XWB and Boeing 787 Dreamliner, respectively. The Boeing 787 is therefore 20% lighter than other aircraft of a similar configuration, leading to a 10-12% improvement in fuel efficiency [10]. Adopting these lightweight materials in vehicles is a solution for improving vehicle efficiency across the transport industry. As an important type of composite materials, fibre-reinforced thermoplastics (FRTPs) which have excellent formability and recyclability, are also finding more and more applications. This thesis focuses on continuous FRPs due to their superior mechanical properties compared to short or discontinuous FRPs [11].[1]

However, the damage resistance of these FRPs is not well understood, particularly compared to current knowledge of metal damage resistance. FRPs are thought to be particularly susceptible to low-velocity impact damage. This can be caused by tool drop, collision of service vehicles and aircraft

[1] The majority of this paragraph comes from the paper: ‘A review on stamp forming of continuous fibre-reinforced thermoplastics’ [16].

or runway debris. This type of damage is difficult to detect, hence it is referred to as barely visible impact damage (BVID) and special equipment and methods are required to identify and map the damage area. Although this damage may not cause immediate failure, it can weaken the structure significantly [12–15]. Furthermore, if left unrepaired, this damage may be increased in extent by fatigue stresses, or even further impacts. If the strength falls below the working load of the component, catastrophic failure could occur. Therefore, the effect of the damage on the structural integrity must be understood and corresponding action, such as repairing the structure, should be undertaken.

This thesis therefore explores the damage behaviour of certain FRPs under low-velocity impact conditions and also studies a possible method to repair FRP components which have sustained impact damage.

1.2 Aims and Objectives

In this PhD project, the main aim is to explore the relationship between the permanent external deformation (i.e. indentation) and the intralaminar and interlaminar (i.e. delamination) damage in carbon fibre composite material caused by an impact event. This could lead to improvements in the efficiency and cost of servicing aircraft and potentially even help improve safety. To achieve the proposed objective, the following tasks were undertaken:

- To conduct a thorough literature review of past and current research work into impact testing of FRP composites.
- To manufacture FRP composite panels for impact testing.
- To conduct experimental impact testing of FRP composites.
- To assess the level of external and internal damage in FRP composites after an impact event.
- To assess the effect of multiple impacts in the same location and in different locations and to investigate the effect of the separation distance between the impacts on the resulting structural integrity of the structure.
- To assess the external and internal damage in repaired FRP composites after an impact event.

1.3 Structure of the Thesis

The chapters in this thesis are outlined as follows:

Chapter 1 introduces the field of research studied in this thesis by discussing the background, aims and objectives and overall structure.

Chapter 2 presents a detailed literature review into the main topics of research in this thesis. These topics include: the different forms of damage caused during impact, the effect of different variables on the impact behaviour and the resultant damage, non-destructive testing (NDT) techniques used to survey impact damage, repair of damaged composites and the performance of such repairs, and finally stamp forming of continuous FRTPs.[2]

Chapter 3 details the materials and experimental methods used in the current research. The specific carbon fibre-reinforced polymer (CFRP) used during testing and the relevant manufacturing processes are explained. Descriptions of the drop-weight tower used to perform the impacts, the ultrasonic C-scanner used to inspect the damaged panels and the other methods used to analyse the panels after impact are given here.

Chapter 4 investigates the relationship between the extent of indentation and the impact damage caused during low-velocity impact of carbon fibre/epoxy (CF/Epoxy). The effect of different impact energies and thicknesses of material is considered. The delamination damage maps, load versus time and load versus displacement traces, indentation depth measurements and optical microscope images are all examined and discussed.

---

[2] This PhD project originally involved the study of stamp forming of FRTPs, hence, a detailed literature review was completed and published on this subject [16]. Similarly, in Appendix A, the design of a pull-out rig is outlined which was intended to be used as part of this stamp forming project.

Chapter 5 examines the extent of indentation and the impact damage caused during multiple low-velocity impacts in the same location on CF/Epoxy. The effect of impact energy, thickness of material and number of impacts is considered. The delamination damage maps, load versus time and load versus displacement traces, indentation depth measurements and optical microscope images are all examined and discussed.

Chapter 6 explores the relationship between the extent of indentation and the impact damage caused during low-velocity impact of carbon fibre/polyphenylene sulphide (CF/PPS). The effect of different impact energies is considered and the delamination damage maps, load versus time and load versus displacement traces, indentation depth measurements and optical microscope images are all examined and discussed. A comparison of the impact behaviour of woven CF/PPS and unidirectional (UD) CF/Epoxy is included.

Chapter 7 investigates the impact damage caused during two low-velocity impacts in different locations on the same CF/Epoxy panel. The effect of different impact energies and separation distances between the impacts is assessed. The delamination damage maps, load versus time and load versus displacement traces and compression-after-impact (CAI) data are all examined and discussed.

Chapter 8 surveys the performance of repaired CF/Epoxy under low-velocity impact. The effect of repair type (patch-only versus patch + plug), patch diameter and patch thickness are considered. In particular, the indentation depth measurements and optical microscope images are examined, analysed and discussed.

Chapter 9 summarises the conclusions from the studies undertaken in this thesis.

Chapter 10 suggests further work which could be undertaken to develop and continue the research undertaken in this thesis.

Chapter 2 Literature review

2.1 Introduction

In this chapter, past and current research work into the behaviour of continuous fibre-reinforced polymers (FRPs), particularly carbon fibre-reinforced polymer (CFRP), is explored and summarised. Firstly, continuous FRPs, the particular type of composite materials of interest in this thesis, are introduced. This is followed by an investigation into the behaviour of these composites under a variety of impact conditions. Non-destructive testing (NDT) techniques used to measure the extent of impact damage are also surveyed. Repair of composites which have been subjected to impact is also considered and examined in detail. Finally, a detailed literature review into stamp forming of continuous fibre-reinforced thermoplastics (FRTPs) is also included.

2.2 Continuous FRPs

The majority of this section comes from the paper: 'A review on stamp forming of continuous fibre-reinforced thermoplastics' [16].

Continuous FRPs are formed of multiple plies of FRP pre-preg. Each ply is formed of high modulus fibres, often made from carbon or glass, within either a partially-cured thermoset matrix, such as epoxy, or a thermoplastic (TP) matrix, such as poly(ether-ether ketone) (PEEK) or polyphenylene sulphide (PPS). The fibres, also known as the reinforcement, provide much of the strength and stiffness whereas the matrix holds the fibres together and transfers the load, as well as contributing to the toughness [17]. The fibres can either all be aligned in the same direction (unidirectional (UD)), see macro-scale schematic in Figure 2-1(a), or woven together to form a fabric, see macro-scale schematic in Figure 2-1(b). Note that the UD schematic shows two plies whereas the woven schematic only depicts one. The meso- and micro-scale schematics in Figure 2-1 demonstrate the fibre structure when viewed at shorter length scales.

When laid on top of each other and consolidated into a single sheet, these plies (both UD and woven) form a laminate. For a thermoset matrix composite, the material is typically laid-up, vacuum bagged and placed in an autoclave where the raised temperature causes the material to undergo a curing process. For a TP matrix composite, a variety of forming methods may be used and these are discussed in detail in Section 2.5.1.1. For TP matrix composites an alternative to pre-preg is commingled fabric, in which carbon or glass fibres are mingled into bundles along with fibres made of polymer. Commingled fabrics can be designed to be highly drapeable and thus suitable for forming. When heat is applied the thermoplastic yarn melts and, after pressure application and cooling, a rigid composite is formed [18].

Thermoset matrix FRPs are widely used in aerospace but thermoplastic matrix FRPs, a.k.a. FRTPs, have replaced thermoset matrix FRPs in some applications. In contrast to their thermosetting counterparts, FRTPs can melt and therefore be formed under high temperatures, without needing to undergo a time-consuming cure cycle. This gives potential regarding large-scale, fast and economical production processes and has led to increased interest in FRTPs as an alternative to commonly used thermoset matrix composites. Further advantages of TP matrices include improved impact resistance [19] and the potential for recycling or remoulding [20].

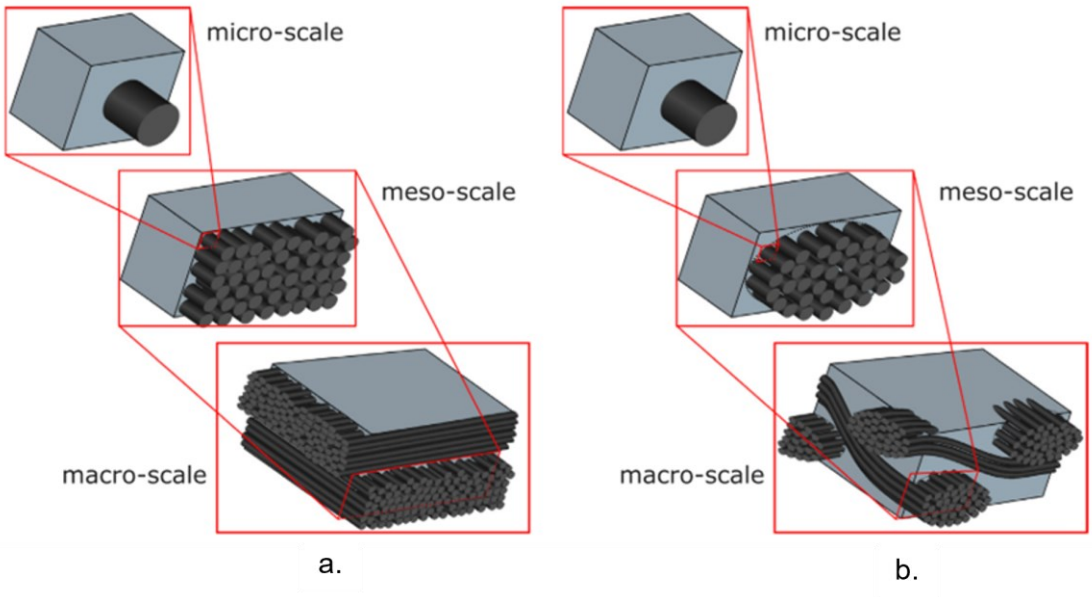


Figure 2-1: Multi-scale structures of (a) unidirectional (UD) and (b) woven composite [21].

2.3 Impact performance of FRPs

2.3.1 Introduction

FRPs are known to be particularly sensitive to impact damage and their damage resistance is not well understood. In an aerospace environment, impact can occur in a variety of ways, including through tool drop during servicing, collision of service vehicles and aircraft, and through runway debris thrown up by the wheels upon take-off or landing. The type of damage formed by these impacts is often not easily visible to the naked eye, hence it is referred to as barely visible impact damage (BVID). Therefore, special equipment and methods are required to identify and map the damage area. Although this damage may not cause immediate failure, it can weaken the structure significantly [12–15].

Damage tolerance refers to the ability of a material or structure to survive a certain amount of damage without suffering an excessive reduction in residual strength, for a stipulated period of time [22–26]. The application a composite material is being used in determines the type of damage tolerance required by the material. If the composite is part of a primary structure in which a high residual strength and/or stiffness is required, then a suitable material should absorb most of the impact energy through elastic-plastic deformations and little energy through damage propagation [27]. However, if the composite is part of a secondary structure in which a high penetration resistance is required, then a suitable material should absorb a large amount of energy through both elastic-plastic deformations and damage initiation and propagation, as residual strength is less important for this application.

If left unnoticed and unrepaired, impact damage may be increased in extent through fatigue or further impacts. If the strength falls below the working load of the component, catastrophic failure could occur. Therefore, the effect of the damage on the structural integrity must be understood and corresponding action, such as repairing the structure (see Section 2.4), should be undertaken.

This review section starts by investigating the types of damage caused by impact on CFRP (i.e. intralaminar and interlaminar damage). Then, the effect of certain variables on the resulting damage is explored, including the effects of impact velocity, impactor hardness, impactor shape, material structure

(i.e. matrix type and reinforcement geometry) and the number of impacts. Finally, a number of NDT techniques are surveyed in relation to their ability to examine damage within CFRP.

Note, this section is all about continuous FRPs. Most studies analysed have used CFRP, however, some have used glass fibre-reinforced polymer (GFRP).

2.3.2 Impact damage

Impact damage is generally categorised based on the specific area of the laminate in which the damage occurs. Damage which forms within the plies that form the laminate is known as intralaminar damage, whereas damage which forms between the plies is known as interlaminar or delamination damage. This section provides a detailed description of these two damage systems.

2.3.2.1 Intralaminar failure

Intralaminar failure takes place within the individual plies which form a laminate and consists of two main types: matrix cracking and fibre fracture.

Matrix cracking can form due to matrix tensile failure, matrix compressive failure or fibre-matrix shearing failure [28,29], see Figure 2-2, and initiates before the laminate has a significant loss of residual strength [30]. The interfibre crack formed runs parallel to the fibres. Matrix cracking can initiate other more harmful forms of damage, such as delamination damage, see Section 2.3.2.2. As well as initiating more harmful damage, matrix cracks can initiate new matrix cracks in an adjacent ply [30], effectively causing propagation of a continuous crack (formed of both intralaminar cracks and delaminations) through the thickness of the material.

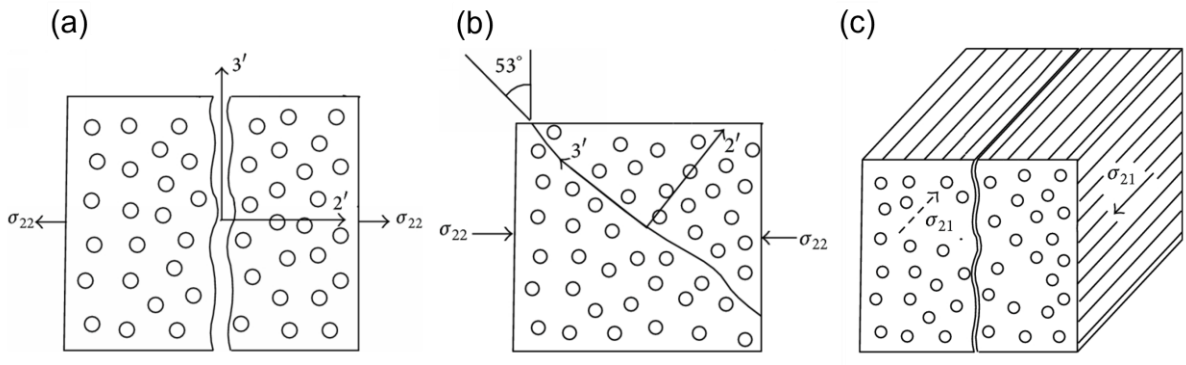


Figure 2-2: Matrix cracking in composite laminates under: (a) tensile, (b) compressive and (c) shear loading [28].

Fibre fracture can occur due to fibre tensile damage or fibre compressive damage [28]. The stress concentrations formed from isolated fibre fractures form another mechanism through which matrix cracks can initiate [28]. Under compressive loads, fibres can fail by microbuckling. Once the compressive strain in the fibres reaches a critical value, the fibres break at two points and form a kink band [31], see Figure 2-3. The width of the kink band, w_k, is usually 10-15 fibre diameters and the angle of inclination, β, is approximately 5-15° [31]. A microscope image of a kink band can be seen in Figure 2-4 in the following section.

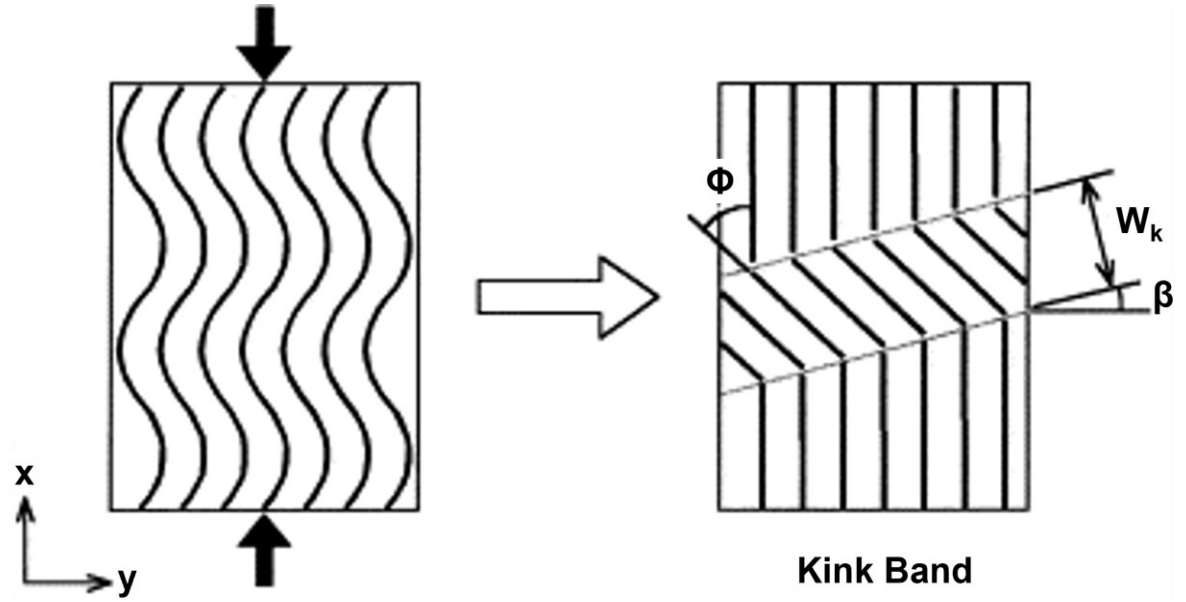


Figure 2-3: Diagram showing microbuckling of fibres and kink band geometry [31].

2.3.2.2 Interlaminar failure

Interlaminar failure, also known as delamination damage, takes place between the individual plies which make up a laminate. The two plies de-bond and a crack propagates between them, forming a gap. These resin-rich interlaminar planes have the lowest resistance to failure of the whole material due to the lack of fibres. Therefore, their resistance to crack propagation is largely dictated by the toughness of the matrix [32].

Delamination damage occurs preferentially at ply boundaries where the fibre direction in adjacent plies is different [19,33]. Upon impact, compressive stress waves are generated and move through the laminate [34]. Upon reaching the rear layer, they are reflected and form tensile waves which act upon neighbouring ply interfaces. The stiffness values in a particular direction at these interfaces change dramatically from one ply to the next. This can generate high interfacial stresses between plies which initiates delaminations through the relatively weak matrix which is relied upon to transfer the load between plies [35]. The delaminations then usually propagate in a direction dictated by the ply orientation below the delamination [19,33]. Between neighbouring plies with the same orientation, known as blocked plies, delamination is not usually seen [33]. Delaminations can also be initiated by the stress concentration around the tip of an intralaminar crack interacting with the high interlaminar stresses at a ply interface [30,36]. Alternatively, a critical number or density of matrix cracks can initiate a delamination [37]. Figure 2-4 shows a delamination which appears to have been initiated by the intralaminar crack in the ply above. Also, a kink band can be seen in the ply beneath the delamination.

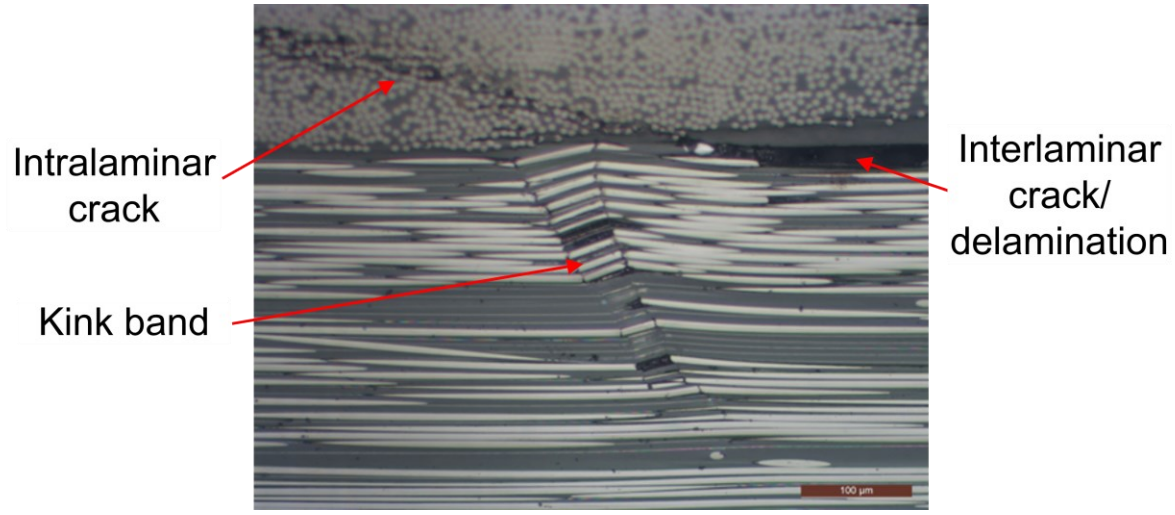


Figure 2-4: Intralaminar and interlaminar damage in an impacted UD CF/Epoxy composite panel.

Delaminations not only affect the damage behaviour of the composite during impact but also the post-impact residual strength [35]. Compressive strength is particularly affected by the presence of delaminations, hence after impact the compression-after-impact (CAI) strength is commonly tested. The mechanism causing this reduction in compressive strength is out-of-plane buckling of plies or groups of plies [38–40]. Although samples with a larger delamination generally exhibit a lower buckling load and failure load [38,40], this is not the only important factor.

For the simplified example of only a single delamination, the groups of plies above and below the delamination are known as sub-laminates. Once a compressive load which is high enough to cause buckling of one of the sub-laminates is reached, the remaining plies (or sub-laminate) are subject to a bending force caused by the asymmetric compressive load. This increases the stresses in the remaining plies and leads to a lower overall failure load. The degree to which the failure load is reduced can be related to the initial buckling of the panel. Depending on the delamination geometry, three characteristic buckling modes can be defined [38,40,41]. When a sub-laminate is relatively thin (compared to the other sub-laminate for a single delamination case) and the delamination area is large, the stiffness of the thinner sub-laminate is lower compared to the sub-laminate on the other side of the delamination. This causes the local mode of delamination induced buckling [38,40–42], see Figure 2-5(a), in which the thinner sub-laminate buckles out of plane. When the delamination is smaller in size, deeper within the composite and the thickness of both sub-laminates is comparable, the global mode

of delamination induced buckling occurs [38,40,41], see Figure 2-5(b). Both sub-laminates buckle in the same out of plane direction with the same magnitude of displacement. This can also be considered as buckling of both the delaminated layer and the overall plate. The mixed mode of delamination induced buckling occurs when both local and global buckling occur in the sub-laminates on either side of the delamination [41], see Figure 2-5(c).

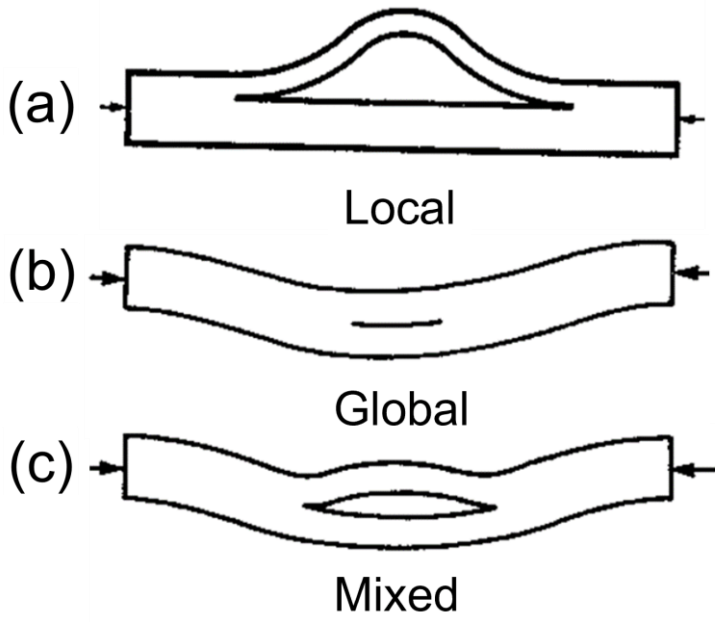


Figure 2-5: Modes of delamination induced buckling – (a) local, (b) global and (c) mixed (adapted from [41]*).*

Samples with delaminations near the surface and that therefore buckle in the local mode, show a lower buckling load than those with delaminations closer to the centre [40]. As the delamination moves closer to the centre the mode changes to a mixed and then a global mode [40]. However, a greater failure load is shown by the samples buckling in the local mode rather than those exhibiting the global mode [38]. Furthermore, the shape and orientation of a delamination in relation to the load direction must also be considered [40].

2.3.2.3 Impact damage summary

Clearly a variety of different types of damage can form during an impact event. These damage forms can interact, affecting the final damage pattern found in the material after impact. These complex

interactions contribute to the difficulty in predicting the overall damage pattern which will be formed in a given impact.

The specific types of damage formed in CFRPs are dependent on many factors of the impact event, including impact energy, impact speed, impactor hardness, impactor shape, matrix type and fibre layout. These factors are investigated in the following sections.

2.3.3 Effect of impact velocity

Vaidya [43] defined an upper boundary for low-velocity impact as 10 $m.s^{-1}$, with intermediate-velocity impact as 10 $m.s^{-1}$ to 50 $m.s^{-1}$, high-velocity impact as 50 $m.s^{-1}$ to 1000 $m.s^{-1}$ and hyper-velocity impact as >2-5 $km.s^{-1}$. The upper boundary of 10 $m.s^{-1}$ for low-velocity impact is based upon how a target responds during an impact.

Under low-velocity impact the geometry of the target determines the impact response and the elastic energy absorbing capability [44–46]. Under this condition, the contact time between impactor and target is relatively long, allowing response from the entire target structure and enabling energy to be stored at points well away from the impact location, see Figure 2-6(a). The target absorbs the impact energy through processes such as elastic deformation, damage formation and vibration. When the target reaches maximum displacement, the impactor velocity is zero and the elastic energy stored in the target propels the impactor to rebound. The energy absorbed due to vibration is usually negligible, therefore, the final absorbed energy is generally attributed to damage formation [44].

In contrast, high-velocity impact loading causes a localised response in the target, dissipating energy over a comparatively smaller region around the point of impact [44,47], see Figure 2-6(b). The contact time between projectile and target is relatively short and the momentum of the projectile may not be enough to accelerate the whole target. Therefore, the damage induced is less affected by the size of the target [44,45].

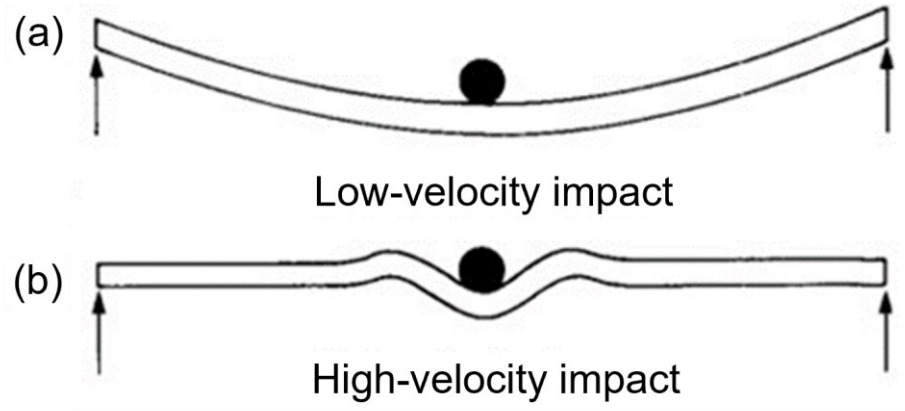


Figure 2-6: Schematic representation of the impact response under (a) low-velocity and (b) high-velocity impact loading [44].

Cantwell and Morton [44] impacted a beam with low-velocity impacts and found that increasing the beam length improves the energy absorbing ability of the target and increases the energy required for damage initiation and perforation. Furthermore, increasing the beam length led to a change in the initial failure mode from top surface splitting (initiated by the contact stress field) to lower surface matrix cracking (initiated by the flexural response of the beam). When impacting the beam using high-velocity impacts, the size of the damage zone and the perforation energy were approximately constant with increases in beam length due to the localised response. Therefore, high-velocity impact usually imparts greater levels of damage and causes a greater reduction in residual tensile strength compared to low-velocity impact [44,46].

For the same impact energy, high-velocity impacts generate greater delamination damage areas than low-velocity impacts and result in poorer post-impact properties [19,44,45]. This is highlighted in Figure 2-7 which shows a comparison of the C-scans of samples impacted by Liu et al. [19] at (a) a low-velocity of 2.56 $m.s^{-1}$ and (b) a high-velocity of 54.4 $m.s^{-1}$. The impacted material has less time to absorb the impact energy, therefore, the deformation is initially more localised around the impact zone, as mentioned earlier. This increases the curvature of the material near the impact site which generates larger delaminations [19]. This may also explain why damage is first detected at a lower impact energy for high-velocity impact [44]. Furthermore, the interlaminar and matrix fracture toughnesses are sensitive to the strain rate. The larger strain rate imposed during high-velocity impacts

reduces the fracture toughness values, allowing delaminations and matrix damage to initiate and propagate more easily [19]. Although matrix damage can occur under low-velocity impact, it is much more localised than the delamination damage, occurring directly beneath the impactor [19]. Fibre damage is also possible provided the impact energy is high enough [48]. Fibre and matrix damage release more energy than delamination damage [48], hence these forms of damage are more apparent for higher velocity impact as more energy is dissipated [44]. Liu et al. [19] also observed a lower maximum out-of-plane displacement for high-velocity impacts.

However, Robinson and Davies [49] observed that the level of damage is only affected by the magnitude of the impact energy, not by impactor mass or velocity separately. Ghaseminejhad and Parvizi-Majidi [27] also observed little effect of impact velocity on damage performance, although a large enough range of velocities (1.59-3.39 $m.s^{-1}$) may not have been used to see any significant variations.

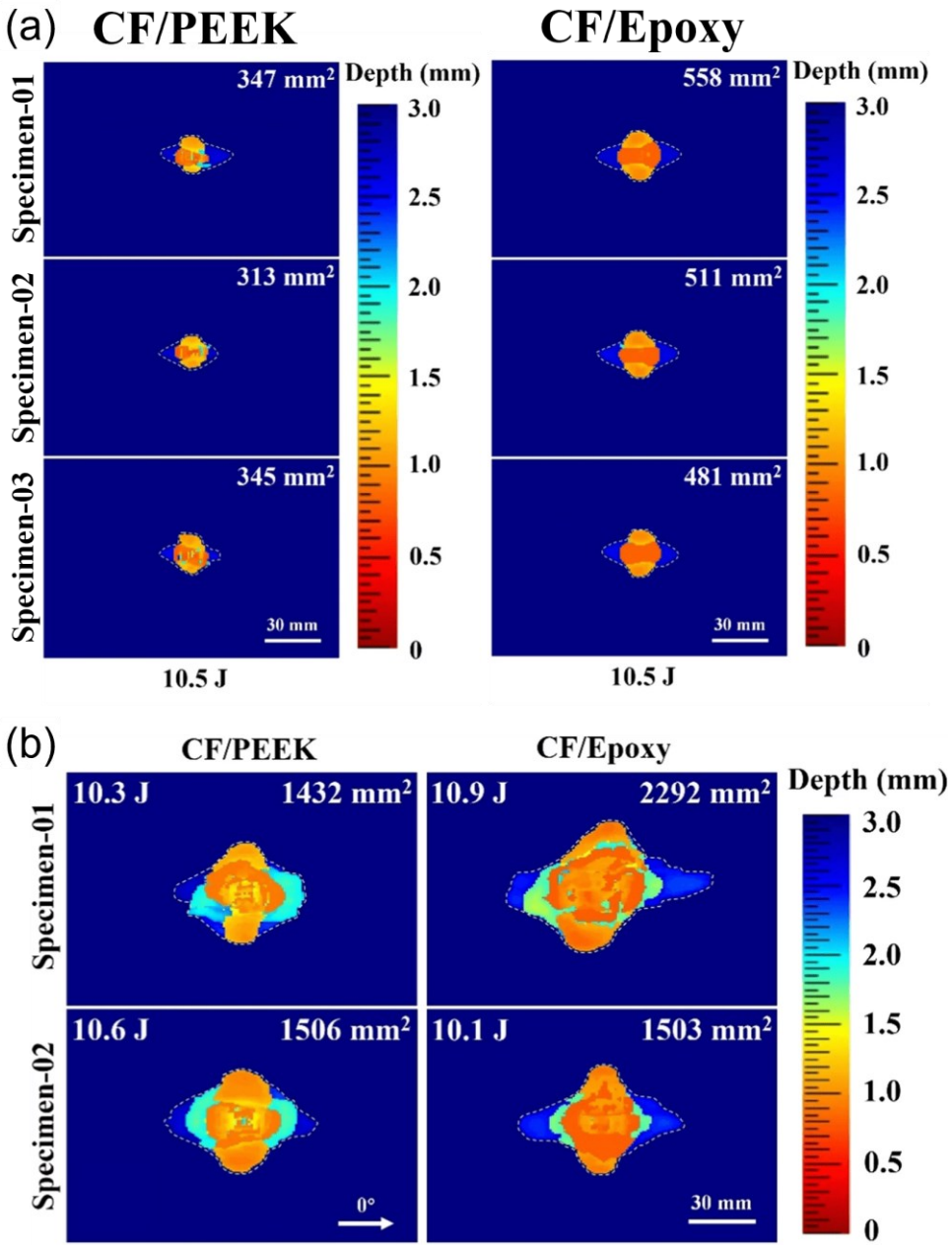


Figure 2-7: C-scans of CF/PEEK and CF/Epoxy samples after impact at (a) low-velocity (2.56 m.s^{-1}) and (b) high-velocity (54.4 m.s^{-1}) [19].

2.3.4 Effect of impactor hardness

The hardness of a projectile or impactor affects the way a structure behaves during an impact event, as well as affecting the level of damage sustained. Researchers have come up with differing definitions to characterise hard or soft impacts. Yankelevsky [50] defined soft impacts as those in which the

projectile or impactor deforms considerably more than the target during impact and hard impacts as those in which the projectile or impactor deforms significantly less than the target. Hou and Ruiz [51] considered a hard projectile as a rigid non-deformable mass which forms a local indentation in the target sample, the depth of which may be calculated using a Hertzian contact approach. However, Koechlin and Potapov [52] claim that the velocity of the impactor must also be considered. Instead, they defined a soft impact as one in which the projectile is damaged and the target is not, with a hard impact involving penetration of the target.

CFRPs are more vulnerable to impact from hard projectiles compared to soft projectiles [34,53]. Harder projectiles undergo less deformation and implement a higher contact pressure on the CFRP [34,53], leading to greater damage. Note, this is assuming the projectile has a high enough strength that it does not shatter upon impact. Soft projectiles made from gelatine have been shown to give a good representation of the pressure loading caused during bird impact upon an aeronautical structure [54]. At velocities of interest, gelatine projectiles behave like a fluid and can flow over the impacted surface, distributing pressure over a larger area. Calculating the pressure distribution and its variation with time is much more challenging for soft projectiles compared to hard projectiles as these quantities depend on the target deflection and the deformation of the projectile [51,54]. Hard and soft projectiles have been used to investigate impact caused by runway debris and bird strikes, respectively.

Liu et al. [53] demonstrated that gelatine and high-density polyethylene (HDPE) projectiles gave similar values of out-of-plane displacement (HDPE gave a slightly larger value) but HDPE projectiles imparted greater damage. For impact velocities and energies of 61 $m.s^{-1}$ (37 J) for the gelatine and 58 $m.s^{-1}$ (34 J) for the HDPE, the gelatine caused no visible damage whereas the HDPE caused fracture and delamination damage, as shown by the post-impact C-scans in Figure 2-8. This is attributed to the greater contact pressures caused by the HDPE projectile, in particular near the edge of the contact area. As the gelatine projectile deforms upon impact, a greater contact area leads to a reduction in the average contact pressure during impact. Similar conclusions were obtained by Liu et al. [34] who tested gelatine and aluminium-alloy projectiles on CF/PEEK and CF/Epoxy targets. Gelatine projectiles caused no damage in CF/PEEK samples at any of the tested impact velocities and only caused damage in CF/Epoxy samples at the highest tested impact velocity of 100 $m.s^{-1}$. In contrast, aluminium-alloy

projectiles caused damage to both CF/PEEK and CF/Epoxy samples at all tested impact velocities. The damage ranged from minor at ~30 $m.s^{-1}$ to major penetration at ~70 $m.s^{-1}$. This greater damage severity when impacted with aluminium-alloy projectiles is again due to the larger contact pressures sustained and their localisation.

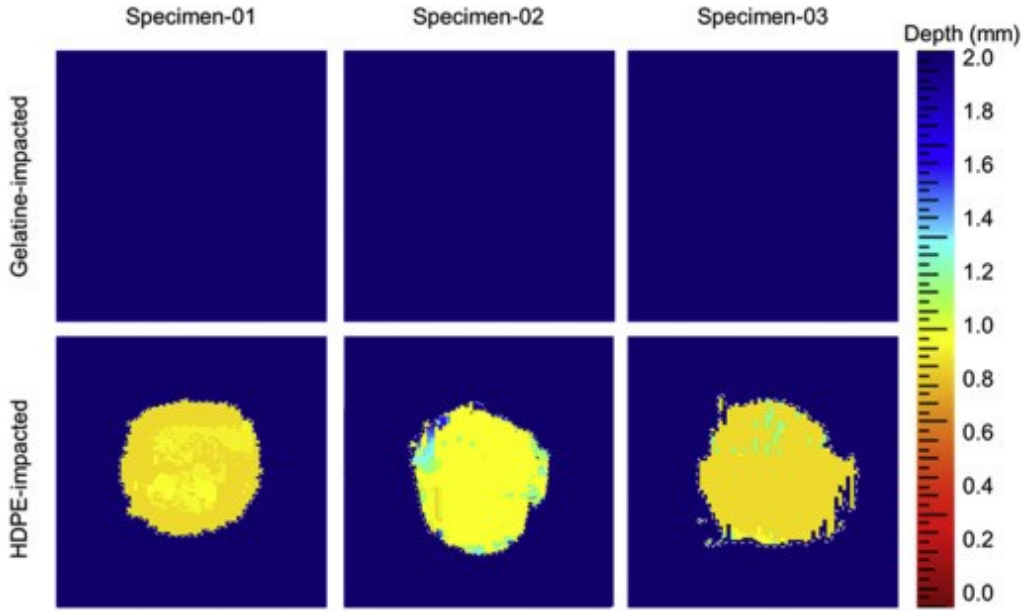


Figure 2-8: Ultrasonic scanning images of gelatine-impacted and HDPE-impacted CF/PEEK samples [53].

As an example of a more intermediate test between hard and soft impacts, Hall [55] investigated the effect of adhering different thicknesses of rubber to the end of a flat-ended impactor on the damage sustained. Adding rubber reduced the delamination damage area compared to the impactor with no rubber. Furthermore, the greater the thickness of rubber, the lower the damage area. The rubber deformed, absorbing some of the impact energy, and increased the maximum displacement of the target, leaving less energy available for initiation and propagation of delaminations.

2.3.5 Effect of impactor geometry

Studies have compared the damage level inflicted by different shapes of impactor (mainly conical, hemispherical and flat-ended) [13,55–62]. Generally, conical impactors create the smallest damage area, followed by hemispherical impactors and then flat-ended impactors, see Figure 2-9. This may be summarised as, in general, the blunter the impactor, the greater the delamination damage caused by

the impact. Alternatively, Mahesh et al. [59] summarised that the contact area of the impactor with the laminate was directly proportional to the damage area. With sharper impactors, the target can bend more around the impactor and absorb more energy [55]. However, with blunter impactors, the target deforms less and therefore more energy is absorbed through initiation and propagation of delaminations, leading to larger damage areas.

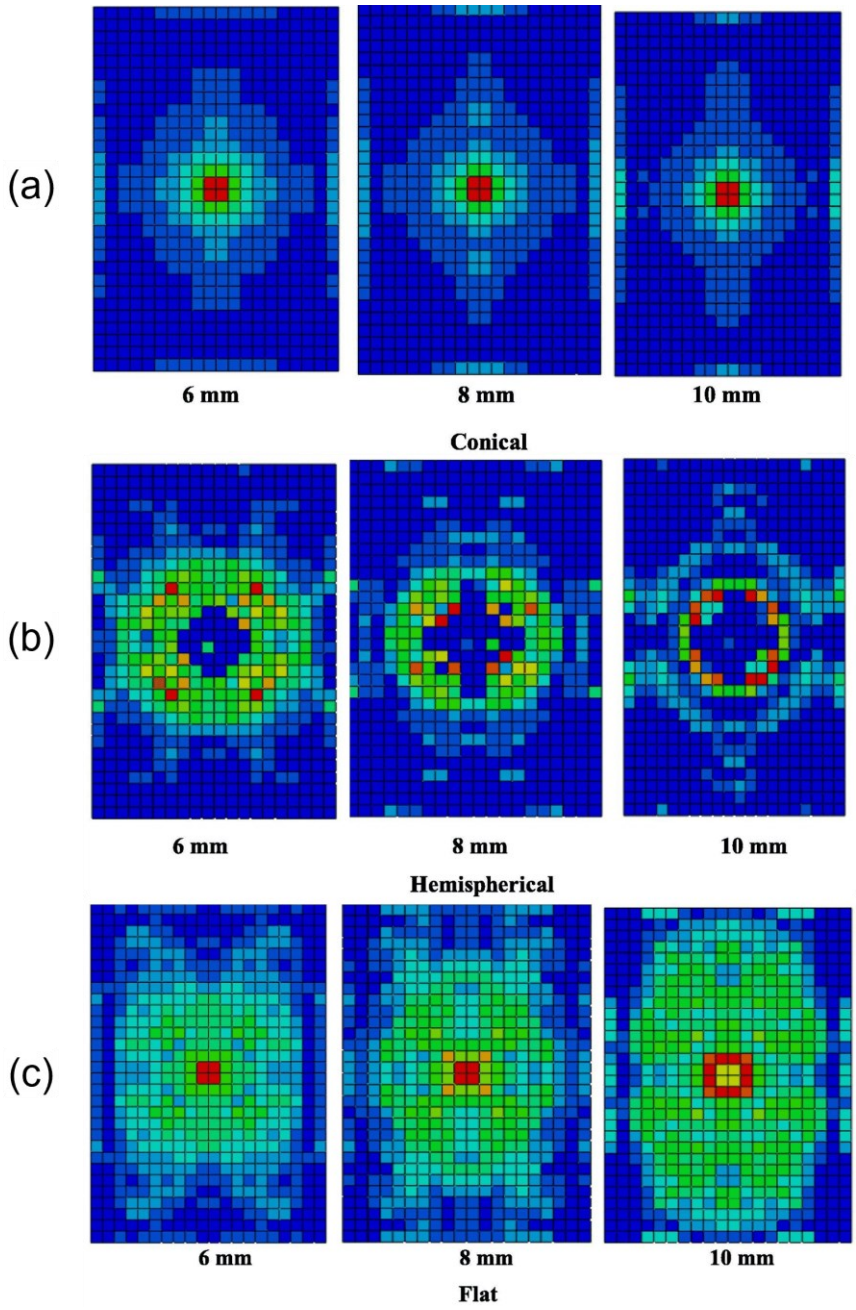


Figure 2-9: Damage in jute/epoxy laminates of thicknesses 6 mm, 8 mm and 10 mm after impact at 8 m.s^{-1} using (a) a conical, (b) a hemispherical and (c) a flat-ended impactor [59].

Conical impactors cause the greatest amount of fibre breakage, resulting in a localised damage area and the largest indentation and penetration depth. They also lead to the greatest amount of energy absorption (due to local penetration) whereas hemispherical impactors produce a larger peak force and shorter contact duration [13,56,59,61]. Flat-ended impactors provide a further increase in peak force and decrease in contact duration [55,61]. As impactor sharpness increases, the kinetic energy loss reduces, allowing sharper and narrower projectiles to penetrate the laminate more efficiently, with less energy lost due to initiation and propagation of delaminations. This is attributed to a change in mechanism as, with increasing projectile sharpness, penetration changes from crushing and tensile failure of the fibres to a cleaner shear or piercing failure. Fracture of the fibres also occurs earlier during penetration as projectile nose sharpness increases [57].

Conical impactors give a smaller damage threshold load than hemispherical impactors [13,56,61,62], with a further increase in damage threshold load shown by flat-ended impactors [55,58,61,63]. Ding et al. [63] observed this when comparing a hemispherical and a flat-ended impactor. The flat-ended impactor caused a larger delamination area than the hemispherical impactor at impact energies above 20 J, see Figure 2-10, in agreement with the studies discussed previously [13,55–62]. However, at 20 J and below no delamination damage was formed by the flat-ended impactor, whereas the hemispherical impactor caused delamination damage at all tested energies, see Figure 2-10. The large difference in the damage initiation loads for the two impactors (~5 kN for the hemispherical impactor and ~12 kN for the flat-ended impactor) is thought to be due to the deeper indentation that the hemispherical impactor forms on the surface which plays a significant role in the initiation of damage in the laminate. Similarly, Hall [55] compared a hemispherical and a flat-ended impactor and only observed delamination at the highest tested energy of 30 J by the flat-ended impactor. In contrast, the hemispherical impactor caused delamination at 7.5 J and 15 J. Therefore, the general judgement of “the blunter the impactor, the greater the delamination damage” may only be valid above certain impact energies which cause the damage initiation load to be reached.

However, Liu et al [64] compared hemispherical and flat-ended impactors on CF/Epoxy at 15 J using the same drop-weight set up as Ding et al. [63]. Similar delamination damage areas were obtained for both impactors, although the flat-ended impactor saw two separate delamination areas with a central

zone showing no damage (this phenomenon has been observed in other studies [55,61,63]). This is the location directly beneath the flat-ended impactor during impact. The similar damage areas for the hemispherical and flat-ended impactors could be explained by the relatively low impact energy of 15 J which was used. Only one impact energy was tested so 15 J may have been only just above the initiation energy for a flat-ended impact on the sample. Furthermore, Liu et al. used 3 mm thick CF/Epoxy and Ding et al. used 4.6 mm thick CF/Epoxy. This difference in material thickness is a likely cause of the lower initiation load observed by Liu et al.

Most research into impactor geometry has focused on only conical, hemispherical and flat-ended impactors. Although these cover some of the potential impactor shapes within a composite's working environment, there are many other impactor shapes which may behave differently. For example, runway debris comes in an almost infinite number of shapes and sizes. Furthermore, the direction in which the debris strikes a composite airframe will also affect the impact damage caused. Of course, it is not possible or reasonable to test so many different impactor shapes, particularly given engineers inspecting the damage will not know what the exact shape of the debris was that caused the impact - this may have to be interpreted from the shape of the external indentation damage. Therefore, a key impactor shape which does not appear to have been widely tested is an edge or line impactor. This could have a hemispherical cross-section and be extended along one axis, or could be similar to a conical impactor but again be extended along one axis. This is important to test as it may cause some penetration, but is not so penetrative as just a spike or conical impactor given it is longer along one axis. Furthermore, impact by edges could occur in a wide variety of scenarios, including tool drop, vehicle collisions (e.g. from aircraft stairs) and impact from elongated sharp runway debris.

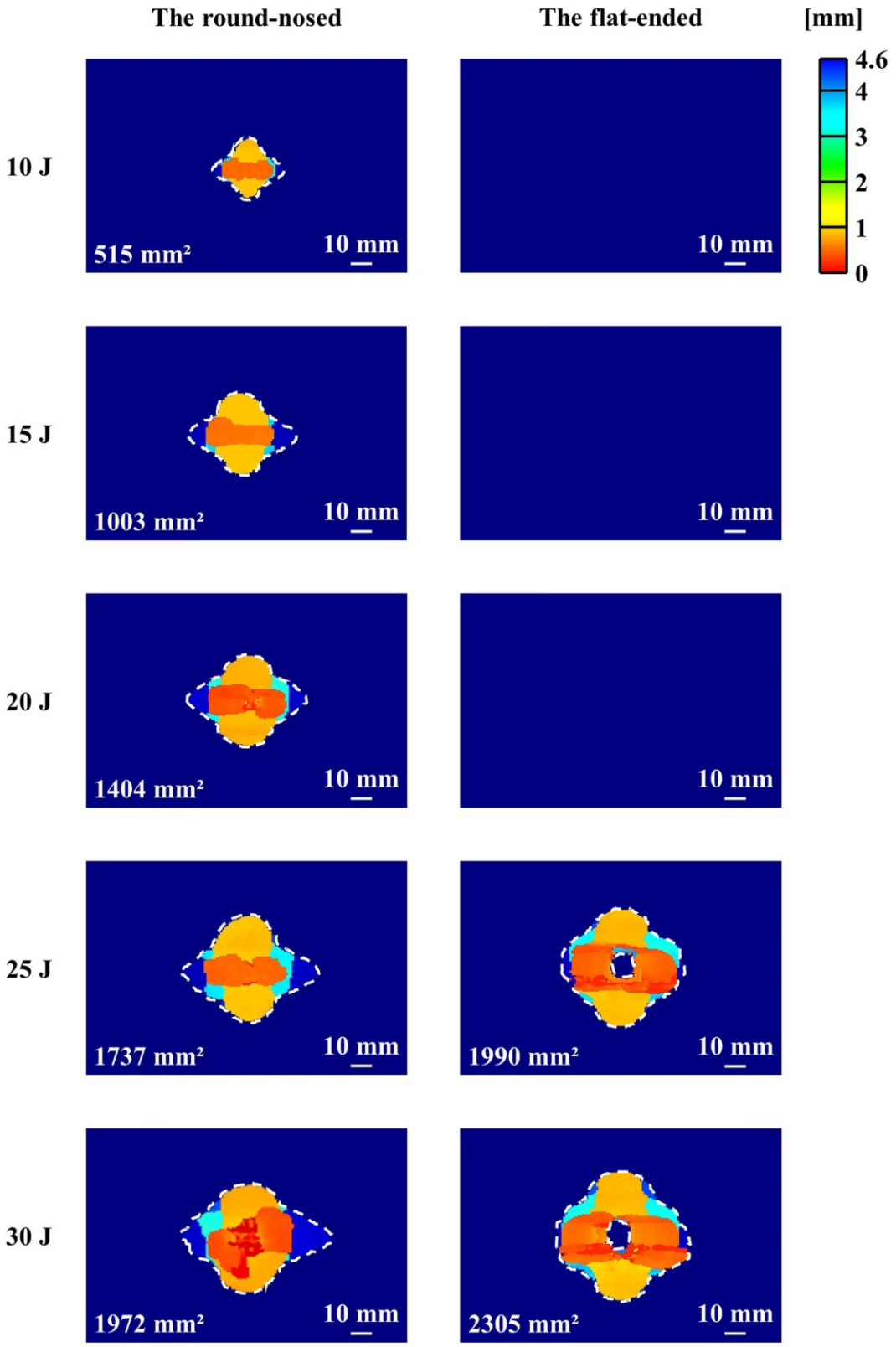


Figure 2-10: C-scan maps obtained from the round-nosed and flat-ended impact tests performed at impact energies of 10, 15, 20, 25 and 30 J, respectively. (The footprint of the delamination area is highlighted by white dashed lines and the area is given in the bottom left of each map) [63].

2.3.6 Effect of matrix type

Thermoplastic matrix composites generally show superior impact resistance compared to thermoset matrix composites [19,34,65–69]. Previous studies by numerous researchers [19,34,65–68] have demonstrated the increased damage area in CF/Epoxy (a thermoset matrix) compared to in CF/PEEK (a thermoplastic matrix) after impact at the same impact energies, see Figure 2-7 and Figure 2-11. Liu et al. [19] also observed that CF/PEEK required a higher load and impact energy to initiate damage than CF/Epoxy. Liu et al. [34] noted that CF/PEEK showed a reduced maximum out-of-plane displacement compared to CF/Epoxy, as greater damage leads to a larger reduction in stiffness of the sample.

A smaller delamination damage area leads to CF/PEEK having a greater CAI residual strength than CF/Epoxy [65–67,70,71]. This is assisted by the increased resistance to delamination growth in CF/PEEK (a greater propagation energy is required for delamination). Significantly greater threshold energies are required for initial reductions in compressive strength [66,71]. Vieille et al. [65,70] observed fibre-bridging in the CF/PEEK samples but not in the CF/Epoxy samples. This contributes to the higher interlaminar fracture toughness in modes I, II and III for the thermoplastic materials. In contrast, undamaged CF/PEEK has a lower compressive strength than CF/Epoxy due to the lower modulus of PEEK [67]. However, Vieille et al. [65,70] observed that the relative difference in delamination damage area decreased with increasing impact energy, see Figure 2-11, making the CAI residual strength become similar for all materials tested (PPS, PEEK and epoxy matrices) at these higher impact energies. In highly ductile thermoplastic laminates, plastic deformation occurs alongside micro-buckling, causing plastic buckling. This can delay the onset and propagation of transverse cracks under compressive loading (the matrix toughness should offset the effect of local buckling). However, larger permanent indentation is observed in thermoplastic samples compared to thermoset samples and this facilitates local buckling which, at high impact energy, becomes a primary compressive failure mode. This could explain why the higher toughness values of thermoplastic composites may not give a significantly higher CAI residual strength. Bajurko [72] also made similar observations, with the tested thermoplastic matrix material (note that the name of the specific type of thermoplastic was not given)

exhibiting a CAI strength which was 27%, 8.8% and 6.8% higher than the epoxy matrix material at impact energies of ~30 J, ~50 J and ~63 J, respectively. Although Wagner et al. [73] found that using a PEEK matrix did not give an improved impact performance compared to using an epoxy matrix, this may have been due to the relatively high impact speeds and energies used (between 43.37 and 100.30 $m.s^{-1}$, corresponding to 51.37 and 276.65 J) compared to most of the other studies in the literature.

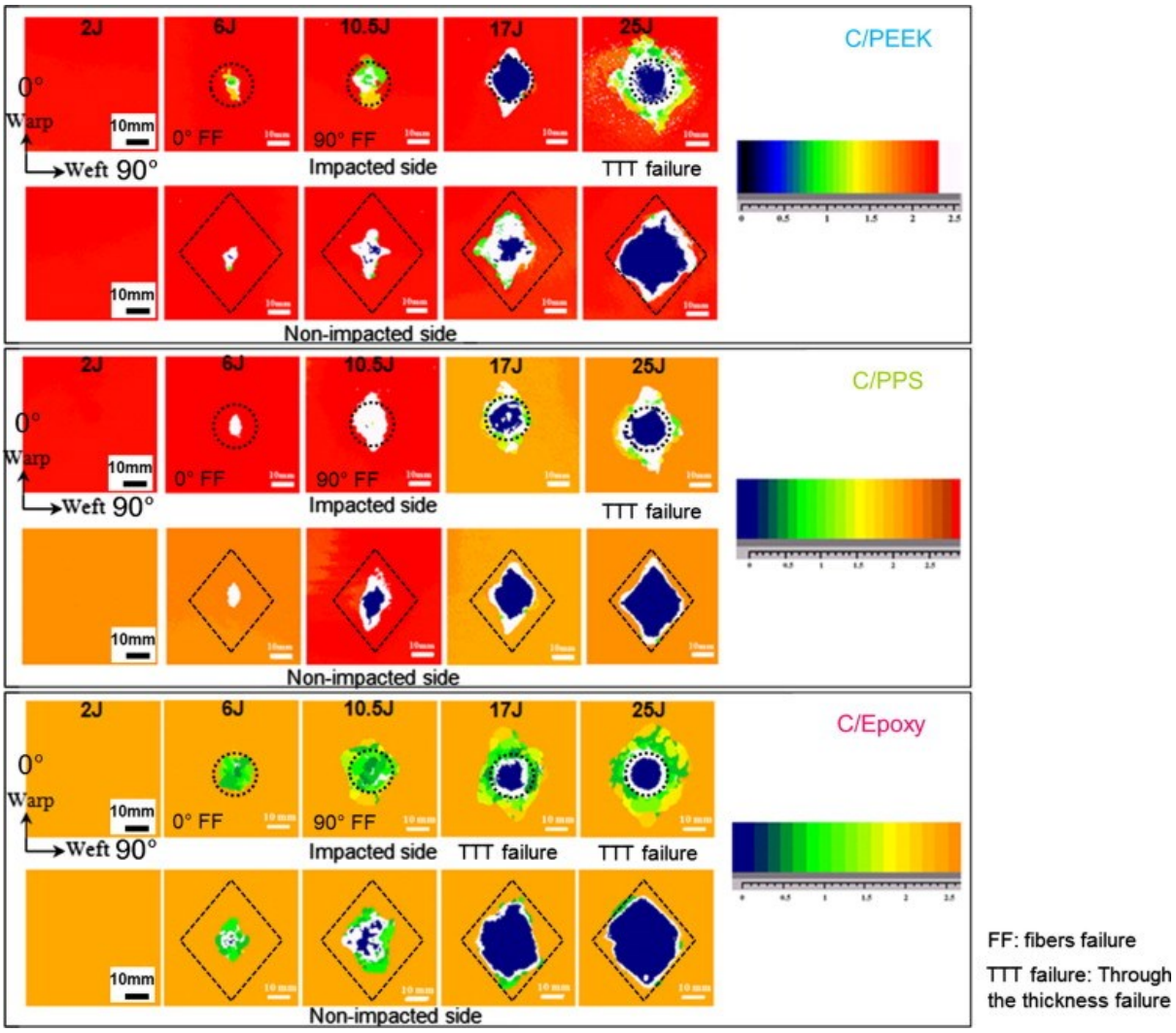


Figure 2-11: C-scan inspection of CF/PEEK, CF/PPS and CF/Epoxy samples after impact at 2, 6, 10.5, 17 and 25 J [65].

Studies have also found that the residual tensile strength is similar for both CF/PEEK and CF/Epoxy [66,67]. It appears that the lower damage area in the CF/PEEK is offset by the material's increased notch sensitivity as the ability of PEEK to deform plastically means there is much less matrix

cracking due to the restricted crack blunting mechanisms. The strain rate sensitivity may also have an effect as Liu et al. [19] found that the delamination damage area increased by a greater percentage for the CF/PEEK upon changing from low-velocity to high-velocity impact, indicating that CF/PEEK is more sensitive to strain rate effects.

The difference in impact resistance between different thermoplastic matrix materials has also been compared, in particular CF/PEEK and CF/PPS. Previous studies have demonstrated that CF/PEEK shows a smaller damage area after impact than CF/PPS when impacted at the same energies [27,69,74]. This leads to a higher CAI strength in the CF/PEEK [27,74]. CF/PEEK has a higher strength, ductility, strain-to-failure and interlaminar fracture toughness in both mode I and mode II, leading to a lower level of crack densities forming, greater resistance to delaminations and a greater residual strength [27,74]. Ghaseminejhad and Parvizi-Majidi [27] also noted that for increasing energy levels the damage area in CF/PEEK increased by a greater amount than in CF/PPS. Furthermore, although both materials exhibited similar damage initiation energy values, CF/PPS demonstrated a significantly higher perforation energy. A threshold point was also observed, beyond which the damage area decreased with further increases in impact energy, in contrast to the increase in damage area with increasing energy at energy levels below the threshold point. CF/PPS exhibited a slightly larger threshold energy. The smaller delamination area is explained by more fibre breakage taking place, forming a denser damage zone. Therefore, the residual compressive strength continued to decrease with increasing impact energy until the perforation energy. CF/PEEK showed a gradual decrease in residual strength and strain with increasing impact energy which indicates a ductile and damage tolerant material. In contrast, CF/PPS showed a sharp fall in residual strength and strain with increasing impact energy which is characteristic of a brittle and less damage tolerant material. In contrast, Vieille et al. [65] observed CF/PEEK delaminating to a greater extent at increasing impact energies compared to CF/PPS, see Figure 2-11.

Leicy and Hogg [69] compared the impact resistance of amorphous and crystalline CF/PEEK (8% and 35% degree of crystallinity) and CF/PPS (5% and 50% crystallinity). Crystalline laminates absorbed more energy than amorphous laminates, with the amorphous CF/PPS showing more extensive damage than crystalline CF/PEEK and the crystalline CF/PPS showing even more severe

cracking. Furthermore, amorphous laminates required a greater impact energy than crystalline laminates for cracking to be initiated. Therefore, it is important to consider the degree of crystallinity of a thermoplastic when using it in an impact resistant structure. The level of crystallinity in the samples used by Vieille et al. [65] may be a potential reason for their contrasting results compared to other studies.

This section has demonstrated that a detailed understanding of the damage behaviour of a certain matrix when incorporated into a composite is desired to allow for their use in applications which are susceptible to impact damage. For example, areas of the underside of an aircraft are susceptible to runway debris, while other locations may be subject to lower velocity impact through tool drop.

2.3.7 Effect of reinforcement geometry and lay-up

Laminates formed from woven fabrics generally exhibit greater impact damage resistance than laminates formed from UD reinforcement [22–24,51,75–77]. The smaller damage area formed in woven laminates compared to UD laminates is partly due to the architecture of the woven fabric. This hinders the spread of damage through the structure by obstructing the propagation of delaminations and shear cracks [24,51,75]. The woven architecture further helps prevent the characteristic cone of damage forming through the laminate, as is commonly seen in UD laminates [22]. Also, delamination usually forms more readily between plies with a different fibre orientation [78]. The plies in woven laminates are often all laid up in the same direction, hence the stress between the woven plies will be lower. The smaller damage areas in the woven laminates lead to a higher CAI residual strength compared to UD laminates [24,75,76]. This is particularly notable given that undamaged woven laminates generally show a lower compressive strength than equivalent UD laminates due to the reduced fibre volume fraction in the direction of loading [23,76]. However, Curtis and Bishop [76] noted that, in some cases, the residual tensile strength of woven laminates was lower than equivalent UD laminates, depending on the direction of plies in the laminate. Curtis and Bishop [76] tested mixed laminates formed of both woven and UD layers. These laminates showed a reduced damage area and an improved CAI residual strength in comparison to purely UD laminates.

Kim et al. [24] found that 18 layer thick cross-ply laminates (formed from plies oriented at 0° and 90°) showed a slightly larger damage area than 16 layer thick cross-ply laminates. Caminero et al. performed two studies [79,80] and also found that delaminations propagated over a larger area in thicker laminates (ranging between 8 and 24 plies), see Figure 2-12. However, the delaminations were more localised in the thinner laminates. For thinner laminates, impact damage was formed through the entire thickness whereas damage was only detected in the upper plies of the thicker laminates. The increased thickness of the thicker laminates increased the interlaminar stress, causing more severe delamination damage. Furthermore, thicker plies were less resistant to matrix cracking, therefore, delaminations initiated and propagated more easily in the thicker laminate. However, the larger bending stiffness of thicker laminates did result in a greater CAI residual strength for the same impact energy compared to thinner laminates [80].

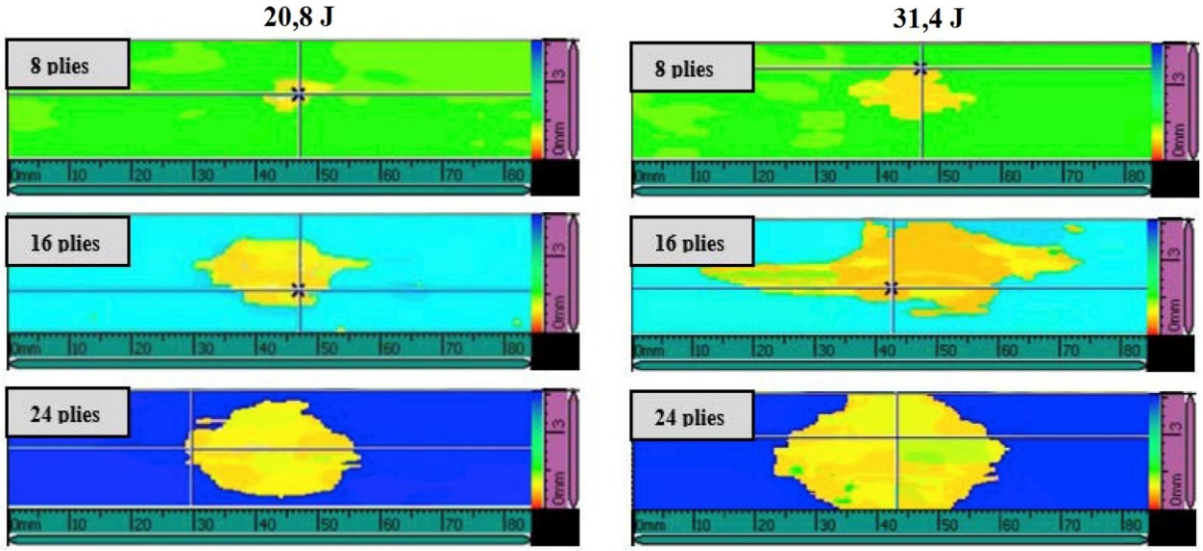


Figure 2-12: Ultrasonic C-scanning images of the damage area of $[0/90]_{ns}$ cross-ply CF/Epoxy laminates showing the effect of impact energy and thickness on the impact damage area [79].

Caminero et al. [79,80] tested quasi-isotropic (QIT), angle-ply (formed from plies oriented at ±45°) and cross-ply laminates and found that the greater the difference in fibre orientation between adjacent plies, the greater the delamination area. Therefore, the cross-ply and angle-ply laminates exhibited a larger delamination area than the QIT laminates, see Figure 2-13. Although, in the C-scans in Figure 2-13 from Caminero et al. [79], the cross-ply seems to be similar to the QIT, with the angle-ply showing significantly less delamination area. The difference in areas between the cross-ply and

angle-ply can be attributed to the difference in bending stiffness of the two laminates. Caminero et al. [80] found that angle-ply laminates (formed from plies oriented at ±45°) showed a higher CAI strength than cross-ply laminates as the off-axis plies provided lateral support to the inner plies, delaying the onset of buckling. The 90° plies in the cross-ply laminates make the central sublaminate less stiff and more unstable, leading to failure at a lower load. Sanchez-Saez et al. [75] found that, while a QIT laminate exhibited a lower CAI residual strength than a cross-ply laminate, the QIT laminate demonstrated a lower loss of normalised strength (defined as the ratio between the average strengths of damaged sample and unimpacted sample), with the cross-ply laminates showing the greater loss of normalised strength. The relatively low loss of normalised strength shown by the QIT laminate may be due to the ±45° surface plies which protected the load-bearing 0° plies from impact damage.

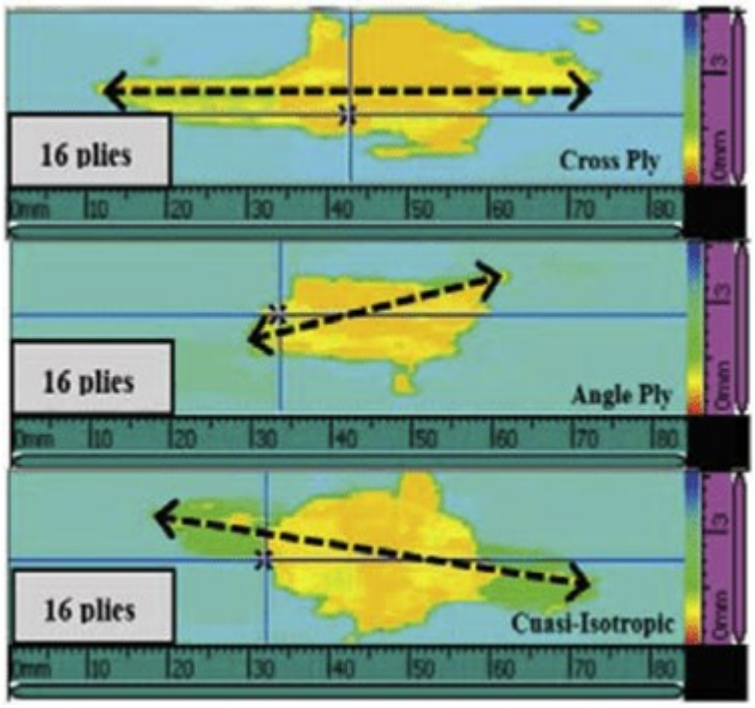


Figure 2-13: Ultrasonic C-scanning images of the damage area of $[0/90]_{4s}$, $[\pm45]_{4s}$ and $[0/90/\pm45]_{2s}$ CF/Epoxy laminates subjected to an impact of energy 31.4 J [79].

Caminero et al. [79,80] also investigated the effect of changing the distribution of plies through the laminate. Using distributed plies ($[0/90]_{4s}$) compared to blocked plies ($[0_4/90_4]_s$) gave a better impact response, with the blocked ply laminates exhibiting an increased interlaminar shear stress due to the heightened difference in bending stiffness between ply groups. This led to excessive matrix cracking

which initiated delaminations. Furthermore, using blocked plies reduces the number of interlayers where delamination can take place. Therefore, larger delaminations were formed at the remaining interfaces. However, the lack of delaminations between plies with the same orientation led to an improvement in CAI strength compared to the distributed ply laminate as the thickness of the blocked plies delayed the buckling of the total laminate. Sebaey et al. [81] also found that clustering plies led to a larger delamination damage area but could improve the CAI residual strength by up to 30%.

2.3.8 Effect of multiple impacts

The impact energy used when subjecting laminates to repeated impacts appears to be a key factor in determining the impact behaviour and evolution of damage. Amaro et al [82] concluded that a single impact at a larger impact energy promotes more damage than multiple smaller impacts totalling the same energy. The results of Found and Howard [83] support this observation as for impact energies of 0.54 J and 0.73 J, damage area quadrupled after 100 impacts for 0.54 J but only 33 impacts were required at 0.73 J. At 0.93 J, critical damage was achieved with only two impacts. However, Appleby-Thomas et al. [84] found that the delamination damage area and CAI residual strength varied linearly with cumulative impact energy. This study used relatively high impact energies of above 72 J and impact velocities between 81 and 268 $m.s^{-1}$ which may account for some of the differences compared to the low-velocity impact studies mentioned previously.

Comparatively low energies may cause damage upon a first impact but may not cause significant further damage when impacted multiple times [85]. Contrastingly, comparatively high energies appear to cause further damage for each additional impact [14,85]. This also causes an increase in impact duration, maximum displacement and permanent indentation, as well as a decrease in the CAI residual strength due to the increased damage area [14]. Which energies are considered low (i.e. beneath the threshold for damage propagation) and high (i.e. above threshold for damage propagation) will depend upon multiple variables, including the material being used. Amouzou et al. [85] found that a 10 J impact was low enough not to significantly propagate damage through multiple impacts in CF/Epoxy, however, Amaro et al. [83] observed damage propagation after subsequent impacts in Glass/Epoxy after impacts at only 6 J. Furthermore, Found and Howard [83] found that repeated

impacts as low as 0.54 J continued to increase damage area in CF/Epoxy. This may be due to the lower thickness of material used compared to the study of Amouzou et al. (0.8 mm versus 3.6 mm) or the different clamping conditions used (annular rings of 100 mm diameter versus 76 mm diameter).

Tuo et al. [14] found that the rate at which the delamination area increased (and CAI residual strength decreased) for each subsequent impact reduced significantly for the third impact, see Figure 2-14. However, this again appears to be a function of the impact energy used as Found and Howard [83] found that for impact energies of 0.54 J and 0.73 J, the rate of increase of damage was similar for the first few impacts and then decreased as the number of impacts increased. Using a larger impact energy also means a larger delamination damage area is created initially, therefore, with only limited space on the sample (for a given sample size), there is less space available for the damage zone to increase. For example, the first 30 J impact investigated by Tuo et al. (on a 150 mm x 100 mm sample) gave a delamination area of 966 mm^2 whereas the first 0.54 J impact investigated by Found and Howard (on a 100 mm diameter circular sample) gave a delamination area of ~30 mm^2. There was more space for expansion for the lower energy impacts which means the rate of increase was not initially affected by sample size.

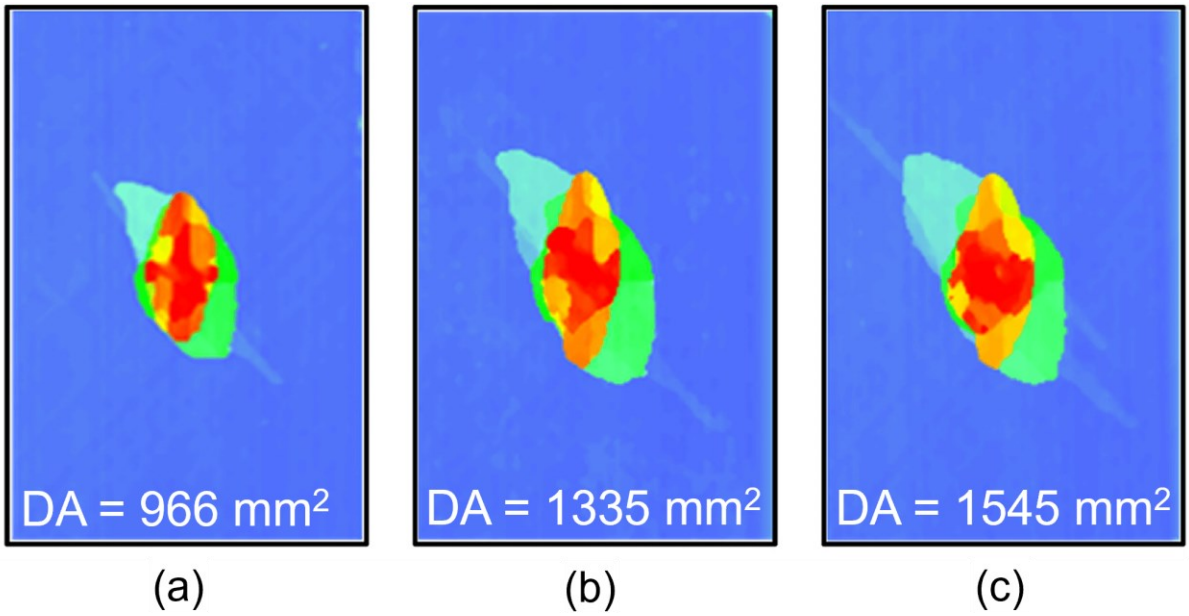


Figure 2-14: Delamination shapes and delamination areas (DA) in CF/Epoxy after (a) one, (b) two and (c) three impacts at 30 J [14].

Zhou et al. [86] performed two sequential impacts in different locations and observed that, for impacts where the second impact zone joined together with the impact zone created by the first impact, the amplitude of the fluctuations on the rising part of the load versus time trace (including any load drops) for the second impact decreased with a decrease of impact distance for the same impact energy (i.e. the curve became smoother). The area of delamination damage which overlapped also increased with a decrease in impact distance. Also, the initiation load drop for a second impact was lower when the damage zones joined, however, the load drop for the second impact did approach the load drop for the first impact with increasing impact distance. Furthermore, if the two impact zones combined, the second impact had a larger maximum displacement due to the decrease in bending stiffness. Zhou et al. also noted that the indentation depth of the second impact was greater if the two damage zones joined but was similar if the two damage zones were separate. Nevertheless, experimental testing of multiple impacts in different locations has not been widely reported in the literature, so further investigation is suggested.

2.3.9 Surface indentation

Most of this section comes from the following paper: 'The relationship between the extent of indentation and impact damage in carbon-fibre reinforced-plastic composites after a low-velocity impact' [87].

Impact on a CFRP structure is usually accompanied by some form of permanent indentation at the point of contact between the impactor and the CFRP. Therefore, relatively small permanent indentations on a composite surface could be an indicator of major internal damage and/or the precursor to major internal damage developing later in the service-life of the CFRP component.

Permanent surface indentations after impact loading of a range of very different materials have interested researchers for at least the last 75 years. Hutchings [88] has quoted the work of Tabor who showed that the process of indentation during impact requires yielding and plastic flow of the impacted material to occur and that the volume of the remaining permanent indentation was directly related to the difference between the impact energy and the rebound energy of the impacting body, assuming that the impactor did not deform in the impact event. Tabor studied mostly metals and clearly showed

that there was a threshold for these indentation processes determined by the plastic behaviour of the metal.

For composite materials, Wardle and Lagace [89] were some of the first researchers to link the indentation damage to the interlaminar delamination and intralaminar (e.g. matrix cracking and fibre debonding and fracture) damage and demonstrated that they were physically related. Shi et al. [90] showed that it was the absorption during the impact event of the initial impact energy which was key in determining these various damage processes. In particular, Wagih et al. [91] showed clearly that indentation in the composite material is often a pre-requisite for intralaminar and interlaminar delamination damage. Wardle and Lagace [89] found that for plate and shell structures, with thicknesses less than 2.4 mm, no correlation was found between the indentation depth and internal damage that occurred. However, Komorowski et al. [92] reported a clear correlation between the indentation depth and the area of the interlaminar delamination damage for CFRP panels ranging from 8 to 48 plies in thickness. Notwithstanding, Talreja and Phan [93] have suggested that the indentation depth may be affected by the strength and toughness of only the surface ply of the impacted CFRP. Thus, they considered that the claim that the entire indentation depth was associated with the impact-induced damage within the CFRP was not substantiated. Indeed, the suggestion that the indentation depth may be correlated with interlaminar or intralaminar cracks within the CFRP laminate, and is indicative of the incident impact energy, has to date not been completely supported by analysis or experiments [93]. Further, Vieille et al. [70] observed a higher extent of permanent indentation in thermoplastic-matrix CFRPs (i.e. CF/PEEK and CF/PPS) compared to a thermosetting-matrix CFRP (i.e. CF/Epoxy). On the other hand, Leicy and Hogg [69] observed only a relatively small indentation depth, on the impacted face, for the thermoplastic-matrix CFRPs after a low-velocity impact, leading to a dome forming on the rear tensile surface at higher impact energies. Cracking initiated earlier on the rear tensile surface for thermoset-matrix CFRPs and no indentation was observed on the impacted front face. Leicy and Hogg [69] suggested that the initial indentation seen in the thermoplastic-matrix CFRPs could modify the local stresses under the impactor, allowing damage to develop in a more stable manner, compared to the thermoset-matrix CFRPs. Hence, thermoplastic matrices were deemed to be better than thermosetting matrices for energy absorption after total penetration. Shuck, as cited by

Talreja and Phan [93], tested woven CF/Epoxy composites with thicknesses of 10, 13 or 16 plies at impact energies below 15 J. As would be expected, the indentation depth increased with an increasing impact energy. Furthermore, 10 ply panels gave a greater indentation depth compared to the 13 and 16 ply panels for the same impact energy. Similarly, Panettieri et al. [94] investigated the indentation depth in QIT lay-up CF/Epoxy panels of different thicknesses. For a laminate of 16 plies, the maximum indentation depth was approximately 0.25 mm at an impact energy of 19.3 J. Whereas, for a 24 ply laminate, a maximum indentation depth of approximately 0.15 mm was measured at an impact energy of 30.5 J. Therefore, from the limited research that has been undertaken into the extent of the indentation depth in impacted composite panels, it appears that thinner panels may sustain a larger indentation depth than thicker panels for a given impact energy but no overall link between the extent of the indentation depth and the extent of interlaminar delamination damage has been established. Clearly further research into this would be of interest to help understand the relationship between visible surface indentation and internal damage.

The phenomenon responsible for this permanent deformation behaviour is not fully known but multiple potential causes have been suggested. For example, Bouvet et al. [95] have suggested that impact debris accumulating in the intralaminar matrix cracks could prevent the interlaminar delaminations from closing and thus contribute to the extent of the permanent indentation. Other suggestions proposed by Bouvet et al. [95] include the compaction of the matrix polymer, the friction of the delaminated surfaces and the initiation and development of the intralaminar damage modes of matrix cracking and fibre debonding.

When impacted multiple times in the same location, Tuo et al. [14] found that the indentation depth continued to increase. Interestingly, the indentation depth increased by a greater amount between a second and third impact than between a first and second impact.

2.3.10 Non-destructive testing (NDT) techniques for damage detection

A variety of NDT techniques are widely utilised to inspect composite components for damage and give an accurate indication of the size of the damage. Using these results, decisions can be made regarding whether to repair the component or, if the damage is severe, replace the entire component. In this section, three NDT techniques are discussed in detail: ultrasonic C-scanning, X-ray Computed Tomography (CT) and thermography.

2.3.10.1 Ultrasonic C-scanning

Ultrasonic C-scanning is a widely used NDT technique which uses high-frequency ultrasonic waves (typically ranging from 0.5 to 20 MHz [96]) to detect flaws in a material through volumetric examination. Interfaces separating regions of differing acoustic impedance reflect ultrasonic waves [97], therefore, when ultrasonic waves travel through the material, defects (such as delaminations) cause a reflection. A transducer receives the reflection from the defect (as well as reflections from the front and rear surfaces of the material) and, based on the travel time and amplitude of the reflection, the location and size of the defect can be evaluated [96]. Results from ultrasonic C-scanning can be viewed as an A-, B-, C- or L-scan (linear scan), see Figure 2-15. The A-scan is a waveform showing the amplitude of the ultrasound signal as a function of either time or distance [98]. The C-scan uses a data gate to form a 2-D representation of the A-scan data. This is usually presented as a colour map, showing the size of defects through the thickness of the material, with different colours corresponding to different depths.

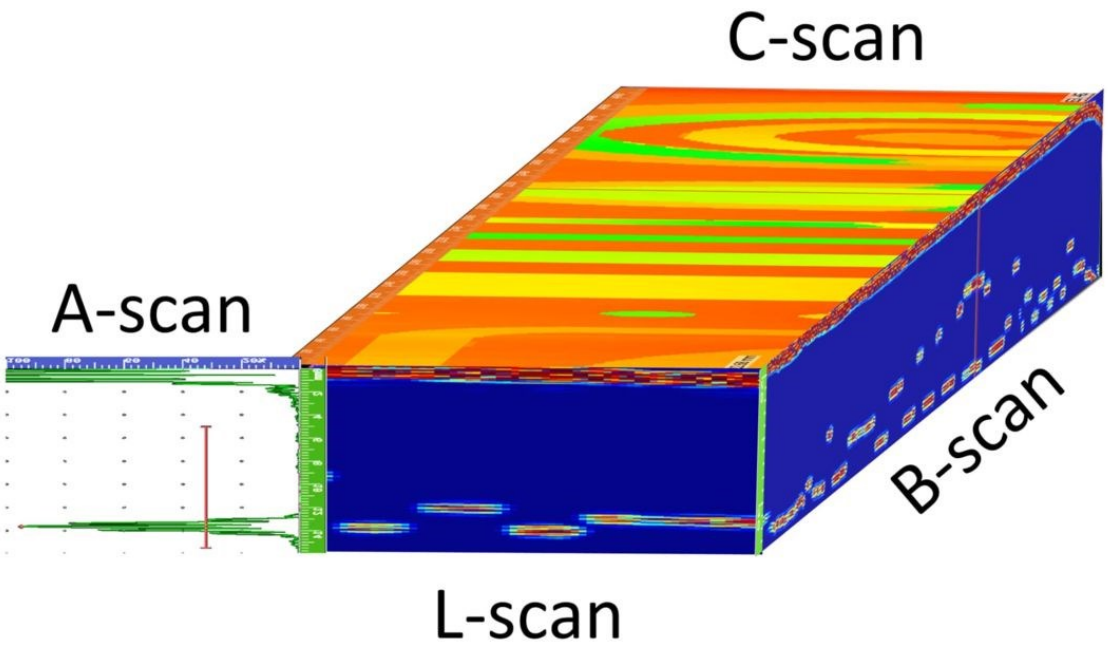


Figure 2-15: Diagram showing volumetric examination through A-scan, B-scan, C-scan and L-scan [98].

Ultrasonic C-scanning allows precise measurements of defect size and depth to be obtained [99] and can be done at a relatively high speed while still producing scans of a good resolution [100]. Furthermore, this NDT method can be used in the field through portable devices [100]. Also, access is only needed to one side of the component to use this method.

However, ultrasonic testing devices can be fairly difficult and time consuming to set up initially [99,100]. A suitable frequency must be chosen as using too low a frequency leads to poor spatial resolution, however, using too high a frequency leads to excessive signal attenuation [101]. Also, trained operators are needed to use these devices to scan parts accurately [100]. Curved samples can be more difficult to examine using this method [97], however, scanners of different shapes exist to assist with this, for example, Sonatest's WheelProbes. C-scanning cannot usually detect small voids or intralaminar cracking, however, if voids appear in large numbers or a void is larger than the wavelength being used, then the voids can be detected [97].

2.3.10.2 X-ray Computed Tomography (CT)

During X-ray CT, multiple radiographs or projections of the target sample are taken using different angles of illumination. These radiographs are then combined through computational reconstruction to form a 3-D image. The contrast in the image is due to differences in the attenuation of X-rays by the matrix, fibres and damage [102–104].

X-ray CT gives a detailed 3-D image of the structure and interior damage [100,104,105]. This allows precise visual analysis of the nucleation and evolution of damage taking place within a material. Compared to ultrasonic C-scanning, X-ray CT allows a much more detailed image to be obtained [103], see Figure 2-16. In the example shown in Figure 2-16, the ultrasonic C-scan gives a pixel size of 1 mm whereas the X-ray CT gives a pixel size of 17 µm.

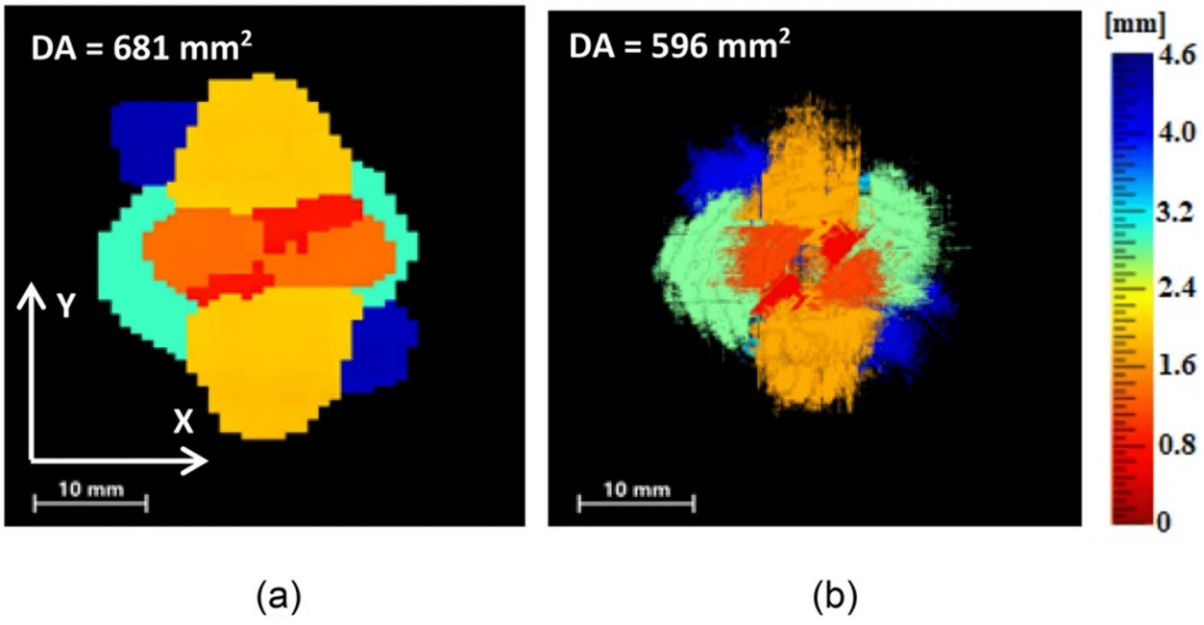


Figure 2-16: Typical damage maps in an impacted CF/Epoxy panel from (a) an ultrasonic C-scan inspection technique and (b) an X-ray CT technique. Delaminations are colour-coded from the top (red) surface to the bottom (black) as indicated by the damage depth colour bar [103].

Although X-ray CT is classed as an NDT technique, this method does require the damaged area to be extracted from the structure [105]. Furthermore, only relatively small samples up to a few centimetres in length are able to be scanned due to limitations imposed by the size of the instrument chamber [105]. Therefore, large components, particularly those with a large length-to-thickness ratio,

are difficult to inspect using this method [102–104]. This is unsuitable for the medium and large panels used in many composite-utilising structures, e.g. aircraft. X-ray CT scanners are very expensive [105] and this cost is added to by the specialized hardware and software needed for the reconstruction and evaluation [104]. The extensive data acquisition process means this method is very time consuming [102–105]. These issues contribute to the unsuitability of this method for use in the field [105].

2.3.10.3 Thermography

Thermography is an NDT technique which uses InfraRed (IR) radiation to detect defects and damage in a component by measuring temperature gradients. Generally, the surface of a component is heated using an external heat source and the thermal response is observed over time by capturing the IR radiation [4,99,101]. Upon heating, thermal waves propagate through the material and upon reaching a different medium (i.e. a defect), a thermal gradient is generated. The emissivity coefficients of the two mediums differ, which is picked up by IR sensors. The measured emissivity coefficient is converted to temperature, allowing the thermal gradients to be viewed and defects detected [99].

The relatively low thermal conductivity of composite structures makes them ideal for use with thermography [4]. Thermography allows large and complex surfaces to be evaluated rapidly [4,97,100]. Also, the monitoring equipment does not have to be too close to the scanning surface, allowing monitoring to take place without significantly affecting other work taking place around the component [97]. Furthermore, access to only one side is needed. This method gives a good estimation of defect dimensions, although it does not directly determine the defect depth [99].

However, thermography requires expensive equipment, as well as highly trained operators which adds further to the high cost of this technique [100]. Additionally, this technique may not be very accurate if the defects being investigated are too far below the surface of the part being analysed as it may not be possible to analyse the full thickness of the component, particularly in thicker samples. Generally, defects with a diameter smaller than their depth below the surface will not be picked up using this method [100]. Therefore, thin components are more suitable for this method of inspection. This method may also be susceptible to ambient effects, such as draughts [97].

2.3.10.4 Other

Other NDT techniques exist for detecting delaminations in carbon fibre composites, including shearography, eddy current and acoustic emission techniques. These techniques are not detailed here but are widely discussed in the literature. Gholizadeh [100] provides a comparison of a wide variety of NDT methods.

2.3.11 Impact summary

The effect of changing just a single variable of the impact event can have a significant effect on the final damage level in the material, highlighting the high sensitivity of CFRPs to impact damage. Therefore, an accurate estimate of each identified variable must be used in order to predict an accurate damage level for a given impact event. Other variables not investigated in this review section which may also need to be considered include the effect of preloading [54,106,107] and the effect of the presence of holes within the panel [108].

Limited research has investigated the external (i.e. indentation) damage present after low-velocity impacts. Although there appears to be some agreement on the effect of matrix type and material thickness on the resulting indentation, the number of studies supporting such statements is minimal and few studies have suggested detailed relationships. Furthermore, experimental testing of multiple impacts in different locations has not been widely reported in the literature so more research is required to improve understanding of a relatively common scenario.

2.4 Repair of FRPs

Given the relatively high cost of FRPs, replacement of a damaged component is not ideal. Instead, a variety of repair methods can be used to restore the strength of the composite structure. These methods are detailed and compared in the following review section.

2.4.1 Repair techniques

Repair of composite structures is desirable compared to replacement due to the lower costs involved and the reduction in waste material. However, a detailed understanding of repair behaviour is difficult to obtain due to the complex interactions which take place between repair patches, adhesive and the parent material. Therefore, research into the behaviour of composite repairs under the loads experienced during service must be undertaken to ensure the safety of repairs on commercial aircraft.

A variety of repair methods are used to restore the strength of composite structures [109], some of which are shown in Figure 2-17. The choice of repair method depends on factors including structural dimensions, accessibility, the repair equipment available and the repair longevity required. This section mainly focuses only on hard patch scarf and patch repairs. However, bonded-bolted and resin injection repairs are also briefly investigated as potential repair methods.

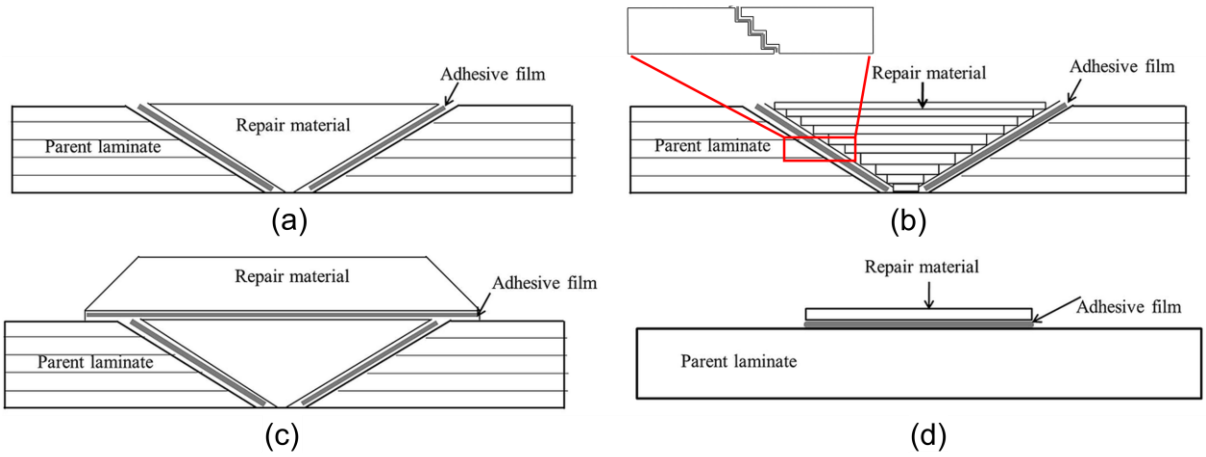


Figure 2-17: Composite repair configurations utilising bonded joints – (a) scarf repair, (b) stepped scarf repair, (c) scarf doubler bonded repair and (d) patch repair (adapted from [109]*).*

2.4.1.1 Scarf repair

In the scarf repair procedure, a disc containing the damage is cut out of the material and the edge of the repair hole is either tapered or stepped to form a slanted surface to which the repair patch can be adhered. The repair patch is in the form of a wide frustum and has a taper angle corresponding to that

of the edge of the machined hole. The patch is held in place using adhesive. This forms either a tapered (Figure 2-17(a)) or a stepped (Figure 2-17(b)) repair.

Scarf repairs can provide benefits compared to other repair methods. These include improved stress transfer mechanisms, higher joint efficiencies, higher strength restoration and better aerodynamic performance (due to the flush surface) [4,5,110–115]. This section will highlight the different varieties of scarf repairs available as well as the manufacturing processes required to form them.

2.4.1.1.1 Effect of scarf repair type

Tapered scarf repairs are those in which a continuous slanted surface is manufactured on the edge of the repair hole at the chosen scarf angle and a corresponding surface is manufactured on the patch, see Figure 2-17(a). This repair procedure is the hard-patch approach to tapered scarf repairs. An alternative soft-patch approach involves placing layers of pre-preg into the machined hole and curing both the pre-preg and adhesive together (some methods do not require use of an adhesive [116]). This method has been shown to improve compressive failure load (compared to an unrepaired panel) by up to 100% [117]. Although the hard-patch approach can be more time consuming, advantages include being able to match the patch and parent laminate properties and only needing to choose a cure temperature based on the adhesive and not the pre-preg [118]. Furthermore, the integrity of the patch can be guaranteed before it is adhered to the repair surface [119].

A variant of the tapered scarf repair is the stepped scarf repair, in which the flat slanted surface is replaced by a series of steps, usually one for each ply in the laminate, see Figure 2-17(b). Although manufacture of a stepped repair is easier than that of a scarf repair [120–123], high stress concentrations found around the corners of the steps can have a detrimental effect on the overall strength of the repair [121–123]. However, Wang et al. [121] found that stepped joints on coupons with sharp corners were stronger than the joints with rounded corners. This is explained by the round cornered joints having a shorter bond length compared to the sharp cornered joints which reduces the adhesive area and increases the stress in the adhesive. Bendemra et al. [123] showed that the higher stress concentrations can be mitigated by using overplies (discussed further in Section 2.4.1.1.4),

shown in Figure 2-17(c), and changing certain design parameters. To improve the failure load, the number of steps on the patch should be equal to the number of plies being repaired [124]. Using fewer steps would lead to a less effective repair.

2.4.1.1.2 Effect of scarf angle

A key design parameter for a scarf repair is the scarf angle. This is the angle between the bottom face of the composite and the scarf repair surface. Studies have indicated that a lower scarf angle leads to a stronger scarf repair [111,112,122,125–130]. Kumar et al. [126] found that shallower scarf angles gave joints with a higher tensile strength and Li et al. [112] confirmed that an increase in scarf angle leads to a decrease in ultimate failure load. Pinto et al. [111] used numerical modelling to show that a reduction in scarf angle leads to an exponential increase in strength improvement, a conclusion also supported by modelling from Campilho et al. [128]. This strength improvement can be attributed to the longer bond lengths and larger bond areas present in lower scarf angle joints and repairs [128,129]. A larger bond area lowers the stress in the bond [125]. The peel stress is particularly decreased, with most of the bond load in the form of shear stress. Shear stress is more evenly distributed in the bond, hence the ultimate failure load is improved. Although Hoshi et al. [129] observed a decrease in total delamination with increasing scarf angle for impact directly on the scarf joint, an increase in total debonding length of the adhesive layer took place, leading to a decrease in residual strength. Models established by Darwish and Shivakumar [130] indicate an optimum scarf angle of around 2.5-3°.

Harman and Wang [131] found that by using shallower scarf angles in more highly loaded areas and higher angles in more lightly loaded areas, a more even stress distribution within the joint could be achieved (provided the repair laminate has an identical layup to the parent laminate). Although designing and using optimum taper profiles may be possible, manufacturing these optimum joints would be very complicated and difficult to achieve.

2.4.1.1.3 Effect of layer orientation

Another important factor is the orientation and arrangement of layers within the scarf repair. The stacking sequence within the patch affects the impact properties of the repair and the patch rotation

angle has an even greater effect [132]. Even a small discrepancy in patch rotation angle compared to the parent laminate can lead to large differences in impact performance. When designed and implemented correctly, a scarf repair which matches the original ply by ply structure of the parent laminate can provide impressive stiffness restoration by reducing the stress discontinuities in the repair [5]. Local stiffness variations, caused by changes in the orientation of plies, allow stress and strain concentrations to form in the adhesive [115,133], so careful design is required to mitigate the effects of these on the overall repair strength. Breitzman et al. [134] found that optimising the stacking sequence in the scarf patch can reduce stress in the adhesive and provide a strength restoration of up to 85%.

2.4.1.1.4 Effect of overplies

The repair strength of scarf patches can be further improved through the use of an overply, also called a doubler [123,135], see Figure 2-17(c). A laminate just a few plies thick, or even a single ply [134], when adhered across the top of the scarf repair, can increase the flexural stiffness and lead to significant reductions in peak stresses within the repair [134,136,137]. The impact performance can also be improved, as well as the extra environmental resistance leading to a more durable repair. Bendemra et al. [123] found that the addition of an overply reduces the peak stresses by increasing the stiffness and protecting the joint tips. Furthermore, increasing the thickness of the overply reduces the peak shear and peel stresses, with a greater decrease in tapered scarf joints compared to in stepped scarf joints. The over-ply lap length had less of an effect for the stepped-lap joints, with a critical lap length of 5 mm identified. Larger lap lengths had little effect on the peak stresses. The overply stacking sequence also showed little effect on the peak adhesive stresses.

Pinto et al. [111] also found that the strength of a scarf repair can be improved by using overplies. If overplies are used on both sides of the repair the strength can be improved from 50% to 70% that of the undamaged laminate. Using overplies on one side of the repair is not as effective but still increases the strength restoration compared to using no overplies.

2.4.1.1.5 Manufacture

Achieving the required accuracy of the scarf repair surface can be problematic. Conventional machining techniques, such as high speed, diamond-coated cutters and water jets [138], struggle to achieve the complex features of a scarf joint and the forces and heat generated during the machining can cause further damage [4]. Performing scarf repairs with the required shallow angles on thin sections of composite material is particularly difficult given the deflections caused [122,131,139], although extra support can mitigate these to an extent. Also, significant quantities of undamaged material are removed (in addition to damaged material) when preparing a scarf repair [110,136]. This is exacerbated by thick structures as scarf lengths between 20 and 100 times the structure's thickness are common [110].

Wang and Gunnion [110] investigated optimum shapes for scarf repairs using numerical modelling and found that, for low scarf angles, a concentric ellipse with aspect ratio similar to the biaxial stress ratio is optimum. This is beneficial compared to a standard scarf repair as the level of material removal can be reduced. Similarly, Holtmannspötter et al. [140] suggests that the repair area can be reduced by producing scarf steps in the fibre direction only, see Figure 2-18. This can reduce the repair area by up to half by eliminating the ineffective bond area which is perpendicular to the fibre direction. By taking into account the loads the structure is under and incorporating these into the scarf design, the repair area could be reduced further. Although a smaller repair reduces the required manufacturing time, using larger patches was found to give higher strength restorations compared to smaller patches [124].

Li et al. [141] reduced the area of a single-sided scarf repair (Figure 2-19(a)) by using a double-sided scarf repair (Figure 2-19(b)). The damage area after impact was found to be lower for the double-sided repair, indicating that this could have a better impact resistance than the single-sided scarf repair. Furthermore, the double-sided repair also exhibited a higher CAI strength compared to the single-sided repair and pristine laminate, although the CAI modulus remained similar.

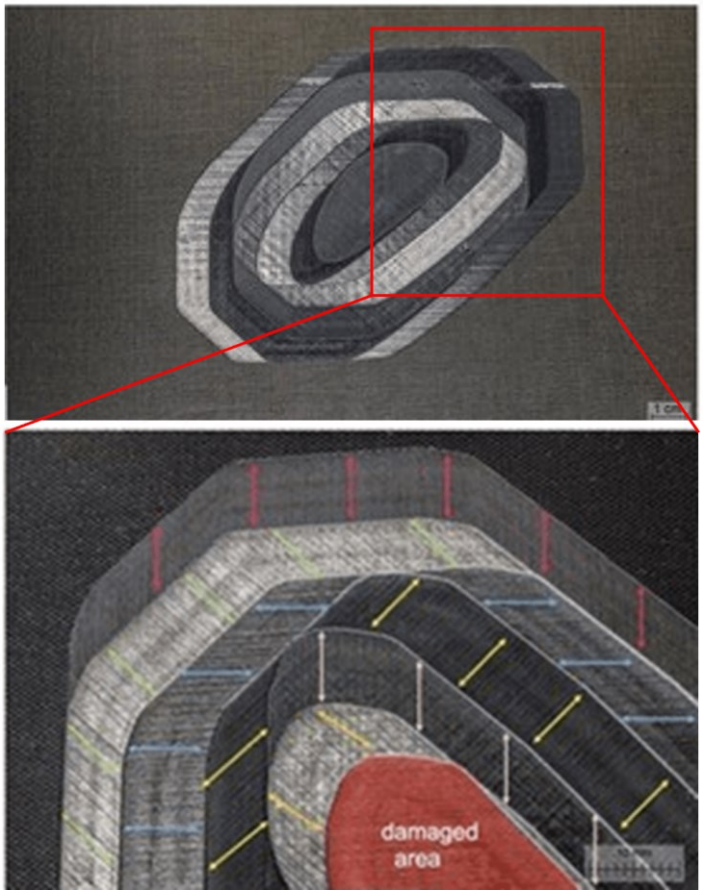


Figure 2-18: A compact scarf repair with steps in the fibre direction only [140].

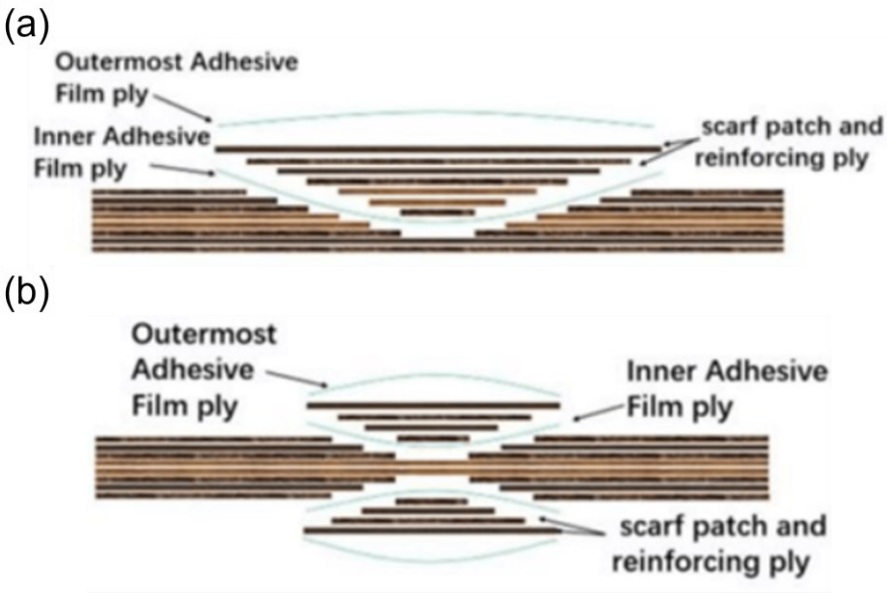


Figure 2-19: Repair geometry used by Li et al. [141] *for (a) a single-sided scarf repair and (b) a double-sided scarf repair.*

2.4.1.1.6 Effect of impact location

A scarf repair's susceptibility to impact is dependent on whereabouts on the repair an impactor hits. Impact at the centre of the repair patch can actually result in a lower damage area than for a pristine laminate [142]. The majority of damage occurs in the patch and adhesive [143] and the adhesive layer reduces damages in the bondline and in material adjacent to the patch [142]. Damage initiates later in the parent laminate and terminates earlier compared to that in the patch [143]. This shows that the adhesive can provide some damage protection for the parent laminate. In contrast, impact directly onto the bondline causes a much larger damage area and consequently a large reduction in strength [142].

2.4.1.2 Patch repair

In the patch repair procedure, a patch of composite material is adhesively bonded over the damaged area of composite. In some cases, the damage is cut out of the material and may be replaced with a plug of pristine material prior to patch adhesion. The adhesively bonded patch allows the applied load to be transferred around the damage, thus reducing the stress concentration at the edges of the damage or the hole [5,144]. These are known as hard patch repairs. Alternatively, soft patch repairs, which involve curing pre-preg material directly onto the structure, can implement slightly better properties compared to hard patches [116]. However, they are significantly more complex to manufacture and their quality cannot be consistently guaranteed. Patch repairs can be divided into single-sided and double-sided, depending on whether one or two patches (on opposite sides of the material) are used.

2.4.1.2.1 Single-sided

In a single-sided patch repair, a patch is bonded onto only one side of the hole or damage area. Soutis et al. [145] found that using an externally bonded patch can restore around 80% of the compressive strength of a sample. Park et al. [146] found that filling the damage hole with adhesive and then bonding an external patch across the top of the hole can achieve an even greater recovery of compressive strength of 91% that of the pristine laminate.

Plugs, attached to the material by adhesive, can be used to fill in the hole and these are particularly advantageous under compression [145]. They can reduce the stress concentrations at the

edge of the hole, as well as increasing the local stiffness in the area underneath the patch or patches. Therefore, plugs can improve the performance of a repair [145,147]. However, Finn et al. [148] mentions that using a plug does not necessarily improve the compressive strength because damage initiation could occur between the plug and the laminate.

2.4.1.2.2 Double-sided

In a double-sided patch repair, a patch is bonded onto both sides of the hole or damage area. Using double-sided repairs can allow the repaired material to support higher loads and undergo lower displacements due to the higher stiffness, thus reducing the level of damage caused during impact [144,149]. The higher stiffness caused by the double-sided patch causes a change in damage mechanisms which also leads to a higher impact fatigue life [144]. Caminero et al. [7] found that double-sided repairs were able to restore a greater amount of the pristine laminate's strength than single-sided repairs. The lower failure load exhibited by the single-sided repairs is due to the lower capability of only a single patch to reduce the stress concentration. Kashfuddoja and Ramji [150] observed that double-side repairs can reduce the stress concentration factor (SCF) by up to 80% compared to the unrepaired material.

2.4.1.2.3 Effect of patch properties

Many factors must be considered during the design of the repair patch in order to achieve a high quality repair. In this section, the size, thickness, stiffness, shape and orientation of the repair patch are discussed.

Larger patches can transfer higher loads due to the greater area of overlap and subsequently can reduce stress concentrations [150]. Furthermore, the larger bond area reduces the stress in the adhesive, therefore, a greater load is required to cause debonding [151]. Tie et al. [152] studied the effect of both the shape and the size of the patch on the repair performance of single-sided joints. The greatest repair performance was found for the circular patch. This is explained by the stress being evenly distributed around the whole area of the repair, rather than concentrated at sharp corners (as in other shapes). The optimum size of the circular patch was found to have a diameter five times that of

the damage hole. Other studies have found different optimum patch sizes ranging from two to four times that of the hole diameter [153–156], although this may be due to the different hole sizes used in the studies (between 6 and 30 mm). For smaller patches, the narrow overlap means that a high stress concentration forms more easily, leading to adhesive shear failure under tensile load, see Figure 2-20(a), (b) and (c), detachment of the patch from the laminate and a low failure load. Wider patches give a larger overlap region, allowing the stress to be transferred through the adhesive more evenly and with lower stress concentrations. This reduces the shear failure area under tensile load, see Figure 2-20(d), and makes the failure process slower and more stable, allowing a higher ultimate strength to be reached [153]. However, the stresses are mainly carried by the thin regions at the patch and hole edges, therefore above a certain diameter, increasingly large patches no longer improve the ultimate strength [153]. The differing test conditions used by the studies may have led to differing results. Only Tie et al. [152] found an optimum patch size under impact conditions, whereas Hu and Soutis [156] used compressive loading and the remainder used tensile loading. Also, the impact was offset from the patch. Therefore, impact directly onto the patch may give further different results.

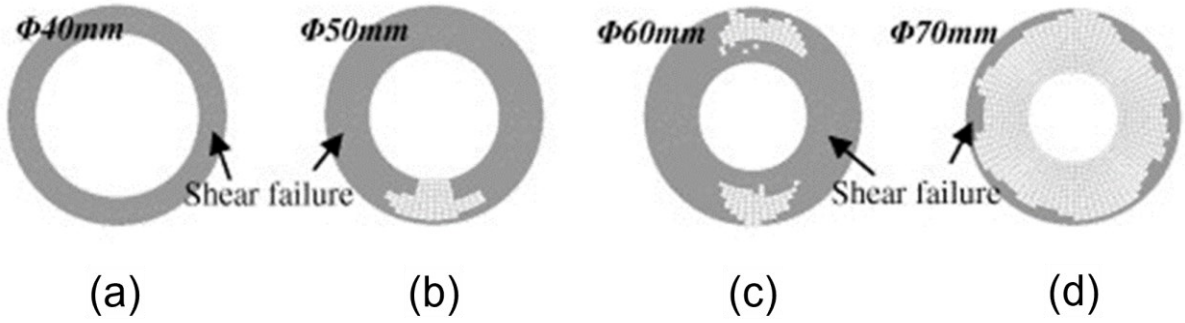


Figure 2-20: Final failure pictures of adhesive in a patch repair showing shear failure of adhesive in patches of (a) 40 mm, (b) 50 mm, (c) 60 mm and (d) 70 mm in diameter [153].

The thickness and stiffness of the patch is also a vital design choice. This has been investigated under impact, tensile and compressive testing [151,154,157]. Although having a greater number of layers in the patch reduces the impact damage caused, too many layers can cause singularities to be introduced in the structure [157]. With increasing patch thickness, through-thickness peel stresses increase and play an increasingly important role. Given the relatively poor through-thickness tensile strengths of composite laminates, the thickness of the patch can limit the joint strength [157]. Campilho

et al. [154] found that patch thickness had little effect on the tensile strength for single-sided repairs, but with double-sided repairs a very slight increase in strength with patch thickness was observed. This indicates that tensile strength may not be strongly influenced by patch thickness. Deng et al. [151] found that, under compression, although thicker patches could reduce the lateral flexibility and stresses induced from buckling, they led to increased stresses in the adhesive and therefore, earlier damage initiation. Therefore, patch thickness only affected the buckling strength up to a certain degree as failure could occur through patch debonding or parent laminate failure prior to buckling. Furthermore, patches which are too thick or are oversized often add unnecessary weight to the structure and can cause high peel and shear stress concentrations in the over-lap [145,156]. The resulting high shear stresses within the adhesive cause significant detachment of the patch from the parent laminate before final failure, leading to a lower ultimate strength [153]. This can be mitigated to an extent by tapering the patch at the edges to reduce the peel and shear stresses [158]. Increasing the thickness of the adhesive towards the edge of the patch also causes the local stresses and shear strains to be reduced and an improvement in the failure load [159].

In contrast, a patch which has too low a thickness or stiffness can divert load around the repair which can over-stress the surrounding structure [144]. Patches which are too thin are poor at preventing crack propagation around the hole so often large areas of damage occur in the patch. Therefore, it appears that both patches which are either too thick or too thin (or too soft or too rigid) have a detrimental effect of the strength of the repair [153,160]. An optimum thickness and stiffness should instead be used for the patch. Hu and Soutis [156] recommend an optimum patch-membrane stiffness equal to half that of the parent stiffness. Similarly, Liu and Wang [153] recommend an optimum patch thickness of 60% that of the parent material.

Fibre orientation also affects the stiffness of the patch. Bhatia et al. [139] observed that the compressive strength of patch repaired laminates was improved by using a greater number of 0° plies in the patch. However, Cheng et al. [160] demonstrated that only the fibre orientation in the layer of the patch adjacent to the adhesive was found to have a significant effect on the repair strength. The highest strength under tensile load was measured for the 0º fibre orientation, with reductions in strength for 90º and 45º.

2.4.1.3 Bonded and bolted repair

In the mixed bonded-bolted repair procedure, a combined joint of adhesive and bolts are used. Purely bonded joints are not permitted in some aerospace structures for which a load needs to be transferred [161]. The regulations require a second load path in case of adhesive failure, therefore, bolts are inserted through the bond. This is due to the uncertainty regarding the strength of adhesive bonds. The only accurate method for testing bond strength is by breaking the bond [162]. Although testing bonds through the use of test samples and coupons can give an indication of bond strength, the results may not give a true representation of the actual strength of a bond in an application.

The combined bonded-bolted joint is not thought to be any stronger than a bonded joint acting alone, provided that the bonded joint has been properly designed [163]. This is because the load path through the adhesive bond is significantly stiffer than that through the bolts. Once adhesive failure has occurred, the bolts will suddenly be subjected to the entire load, often causing brittle failure [164]. However, in terms of repair, the combined joint can be useful as it can prevent the spreading of damage [163]. In structures under light loading, bolts are unlikely to ever experience any load. In more heavily loaded structures however, bolts can arrest cracks which, in a purely bonded joint, could spread catastrophically [163,164]. Hence, they can improve the strength and lifetime of the joint. Furthermore, the presence of bolts can reduce some out of plane peel stresses in bonds, thus improving the joint strength [164].

Li et al. [165] investigated a variant on the bonded-bolted joint by adhesively bonding steel screws in holes within a delaminated region of a CFRP sample. This is known as a through-thickness reinforcement repair. The unrepaired delaminated sample had a compression strength of 68% that of the pristine sample. By using eight screws in a ring shape, as shown in Figure 2-21(a), the compressive strength was restored to 93% that of the pristine material. Using more screws in multiple ring layouts (see Figure 2-21(b) and (c)) was found not to improve the compression strength further. This is due to these layouts employing pins further from the centre of the sample. The centre is where the forces driving buckling would have their maximum. Furthermore, drilling more holes for more screws increases

the damage in the sample so can be more detrimental to buckling strength than the improvement given by the screws.

This through-thickness reinforcement repair technique could be suitable for depot-level repairs given the availability of drilling machines. If a suitable portable drilling machine is developed, the technique could be extended to rapid on-the-spot field repairs.

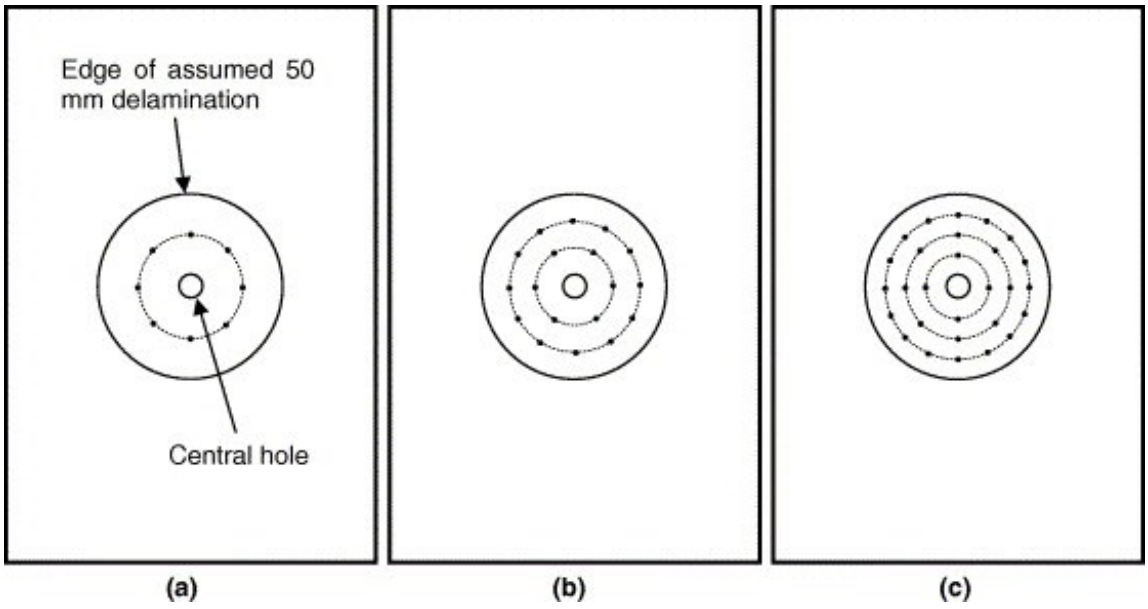


Figure 2-21: Through-thickness reinforcement technique pinning patterns: (a) 8 pins in one ring, (b) 18 pins in two rings and (c) 28 pins in three rings. Pins have equal circumferential spacing in each ring and the rings divide the distance uniformly between the edge of the central hole and that of the assumed 50 mm diameter delamination [165].

2.4.1.4 Resin injection repair

In the resin injection repair procedure, a low viscosity adhesive is injected into the damaged composite. The adhesive flows into the delaminations and matrix cracks prior to curing, allowing delaminations to be re-bonded and fibres to realign. This allows potential restoration of load paths [166]. A diagram of one version of this method is shown in Figure 2-22. Injection repair can be used to repair narrow and small composite parts, allowing a restoration of strength without a significant increase in weight [122].

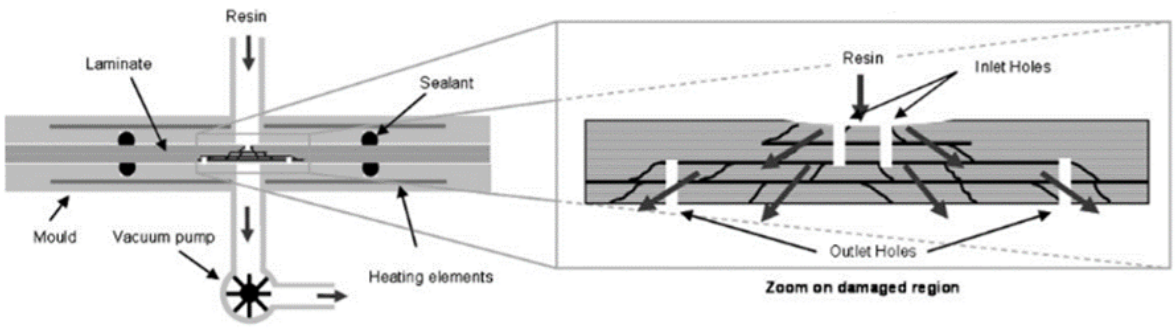


Figure 2-22: Diagram of resin injection repair method, showing resin infiltration through the delaminations [167].

Injection repair has been found to restore over 90% of the compressive strength of a material [122,166–169]. In some cases, full restoration of the pristine compressive strength was achieved [122,168]. However, tensile strength cannot be significantly restored by this method as broken fibres are not replaced during the repair procedure [122,166,169].

2.4.2 Other Parameters

Certain critical parameters of repairs have not been surveyed in detail in this review, such as surface preparation and adhesive properties. However, many relevant papers in the literature explore adhesive joints and cover these topics, for example [170]. The fatigue properties of repairs have also not been investigated in detail in this review. Adhesive bonded repairs have however been shown to exhibit good fatigue resistance [114,171–173].

2.4.3 Repair summary

Overall, scarf repairs can be preferable to external patch repair because they do not create an extra bending moment and stress concentration in the adhesive [125]. Furthermore, they can provide high repair efficiencies and strength restoration as well as good aerodynamic properties. However, patch repairs are easier to manufacture and can also provide high strength restoration. Aerodynamic properties are not usually considered too important, with the strength of the repair and manufacturability more critical. The optimum choice of repair is dependent on how critical the damaged part is and how accessible it is. Furthermore, the design of the chosen repair often has to include a compromise

between repair strength and manufacturability (e.g. smaller scarf angles lead to an increase in repair strength but are more complex to manufacture and lead to more pristine material removal). The available literature has proven that both scarf and patch repairs are capable of high strength restoration under certain circumstances.

Limited research has investigated the impact performance of repairs, particularly patch repairs. If a CFRP panel has previously sustained impact damage due to its location on the aircraft, once it has been repaired it seems logical to assume the panel may be susceptible to the same impact again. Therefore, the effect of damage caused by an impact on a repair needs to be investigated further.

2.5 Stamp forming of FRTPs

This literature review comes from the following paper: 'A review on stamp forming of continuous fibre-reinforced thermoplastics' [16].

2.5.1 Introduction

Continuous fibre-reinforced thermoplastics (FRTPs) are replacing metals in certain applications in the aerospace industry due to their superior properties e.g., high strength-to-weight ratio and good fatigue resistance. Adopting these lightweight materials in vehicles is a solution for improving vehicle efficiency across the transport industry. Among various manufacturing techniques for FRTP parts, stamp forming is one of the most advantageous when small structures and mass production are targeted. However, a significant barrier for this technique is the quality control of manufacturing. The current section reviews the development of stamp forming technology, benefits of using such technology and the typical quality issues in stamp forming of FRTP parts. First, advantages of stamp forming, compared to other thermoforming techniques, are discussed, followed by a review of the historical development of the process. Second, deformation mechanisms of FRTPs during stamp forming are examined, with particular focuses on the frictional behaviour and testing thereof. Third, the main defects associated with stamp forming are considered, alongside suggestions towards reducing their presence. Finally, an extensive survey of the effect of process parameters on the mechanical properties of formed parts is

included, with generally expected trends highlighted and methodologies for finding optimum conditions presented. Based on the thorough review of state-of-the-art stamp forming, future trends and research gaps to be tackled for widening the applicability of FRTP stamp forming are suggested.

2.5.1.1 Stamp forming vs. other thermoforming methods for FRTPs

The most common forming method for FRTPs involves pre-preg (material containing fibres pre-impregnated with resin) being placed into a mould by hand and then processed in an autoclave. This conventional method of lay-up followed by autoclave processing is time-consuming, energy-intensive and expensive [174,175] so is not appropriate for high volume production. Other thermoforming methods which do not require hand lay-up are detailed below.

Stamp forming allows relatively complex shapes to be formed comparatively quickly from pre-consolidated composite laminates. A general stamp forming process using a matched metal die set is shown in Figure 2-23. Stamp forming involves heating a material (usually to above the matrix melting temperature, T_m, in the case of FRTPs) (Figure 2-23(a)) before transferring the material to a matched metal die or mould set (Figure 2-23(b)). The two halves of the mould are brought together and the heated material is deformed into the shape of the mould (Figure 2-23(c)). After a given holding time, the mould sections move apart and the formed part is removed (Figure 2-23(d)).

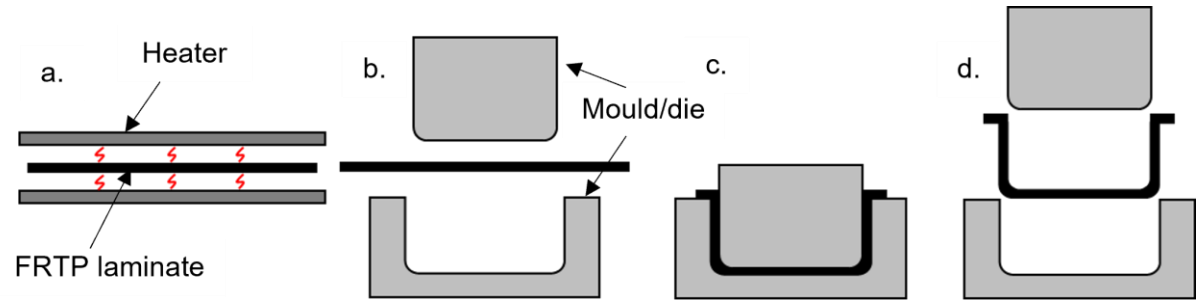


Figure 2-23: Typical stamp forming process for FRTPs, showing stages: (a) heating, (b) transfer, (c) forming, (d) removal.

In rubber forming, the laminate is formed between a pair of dies made from different materials. One is rigid (usually made of metal, as in the stamp forming process) and the other is made of rubber [176]. The laminate is heated to above T_m, transferred to the tool and pressed into shape when the dies

close. This process can be considered similar to the stamp forming process, but with one die made from rubber instead of metal.

In double-diaphragm forming, flexible diaphragms surround the laminate on each side and are clamped on top of a mould [176]. A similar single-diaphragm forming process uses only one diaphragm; however, this makes forming double curvature shapes difficult [177]. The diaphragm forming assembly is usually placed into an autoclave, the area between the diaphragms is put under vacuum and the material is heated to above T_m [178]. Air pressure is applied to one side which forces the diaphragms and laminate into the shape of the mould. The laminate can slide between the diaphragms and the subsequent interfacial shear stresses create tensile stresses within the laminate [179]. This means out-of-plane wrinkling is restricted due to the presence of the diaphragms [180]. Therefore, high quality parts can be produced.

Hydroforming is similar to double-diaphragm forming in that a fluid is used to deform a diaphragm. However, in this method, a pressurised hydraulic fluid, rather than pressurised air, behind a rubber diaphragm is used to form the laminate against a mould [179]. These systems have been known to generate pressures of up to 10,000 psi and have been widely utilised in the sheet metal forming industry.

Although the rubber die used in rubber forming can give a more even pressure distribution across the part compared to the metal die used in stamp forming, complex details are difficult to produce and there are limitations on the forming temperature which can be used to allow a suitable working life for the die [177,179]. In addition, the low thermal diffusivity of the rubber die leads to reduced cooling rates and increased cycle times, making this method less suitable for large volume manufacturing [177]. While diaphragm forming can restrict wrinkle formation and give high quality parts, the relatively long cycle times and common use of an autoclave make this method expensive and inappropriate for large volume manufacturing [177]. Furthermore, degradation of the diaphragm material at high temperatures limits which materials can be formed through this method [176]. The high pressures which can be achieved by the hydraulic fluid in hydroforming give the potential to form undercuts, however, the thickness of the diaphragm can limit the size of cavities which can be formed while still achieving good

definition of features on the mould [179]. Stamp forming can achieve fast cycle times of one minute or less [181], leading to high productivity. Other advantages of stamp forming include that close tolerances can be achieved and high consolidation pressures can be applied during forming [179]. However, there are also some disadvantages including potential thickness mismatch and non-uniform pressure distribution, as well as a high initial tool fabrication cost [179]. Furthermore, stamp forming requires pre-consolidated laminates and the time required for preparing these from pre-preg (using an autoclave or hot pressing) may be significant. Overall, stamp forming is considered the most appropriate thermoforming method for large scale and economical manufacture of components at a high productivity rate.

2.5.1.2 A brief history of stamp forming for FRTPs

Stamp forming of FRTPs is similar to the process used in stamp forming of sheet metals [182]. Investigations into stamp forming of FRTPs began in the 1980s, with studies using existing sheet metal forming equipment to shape continuous FRTPs [179]. Later, researchers such as Bigg et al. [183] investigated the solid-state stamping (i.e. forming temperature below T_m but above the matrix glass transition temperature, T_g) of a variety of GF/TPs into trapezoidal and hemispherical parts. Following this, Zahlan et al. [184] formed CF/PEEK into top hat shapes while Hou et al. [185] and Scherer et al. [186] formed CF/polypropylene (CF/PP) into right angle shapes, with the forming temperatures above T_m. Most research focuses on forming at temperatures above T_m and this is the temperature region which is focused on in this review. Hemispheres (Figure 2-24(a)) and right angle V-bends (Figure 2-24(b)) have commonly been used in forming studies over the years [181,182,187–198]. In recent years, more complex shapes have been formed, including double-domes, U-shapes, variant-cross-sectional-beams, wing fixed leading edge stiffeners (Figure 2-24(c)) and boxes with multiple steps (Figure 2-24(d)) [199–219]. Figure 2-25 summarises the development of different shapes which have been formed through stamp forming since the 1980s. Advancements in the stamp forming process have allowed increasingly complex geometries to be formed, especially during the past decade. Although a mixture of components with flat and curved faces have been successfully formed using stamp forming, each different shape brings slightly different challenges. Therefore, stamp forming processes for a new

shape must be carefully designed to reduce defect formation for successful forming of a high quality final part.

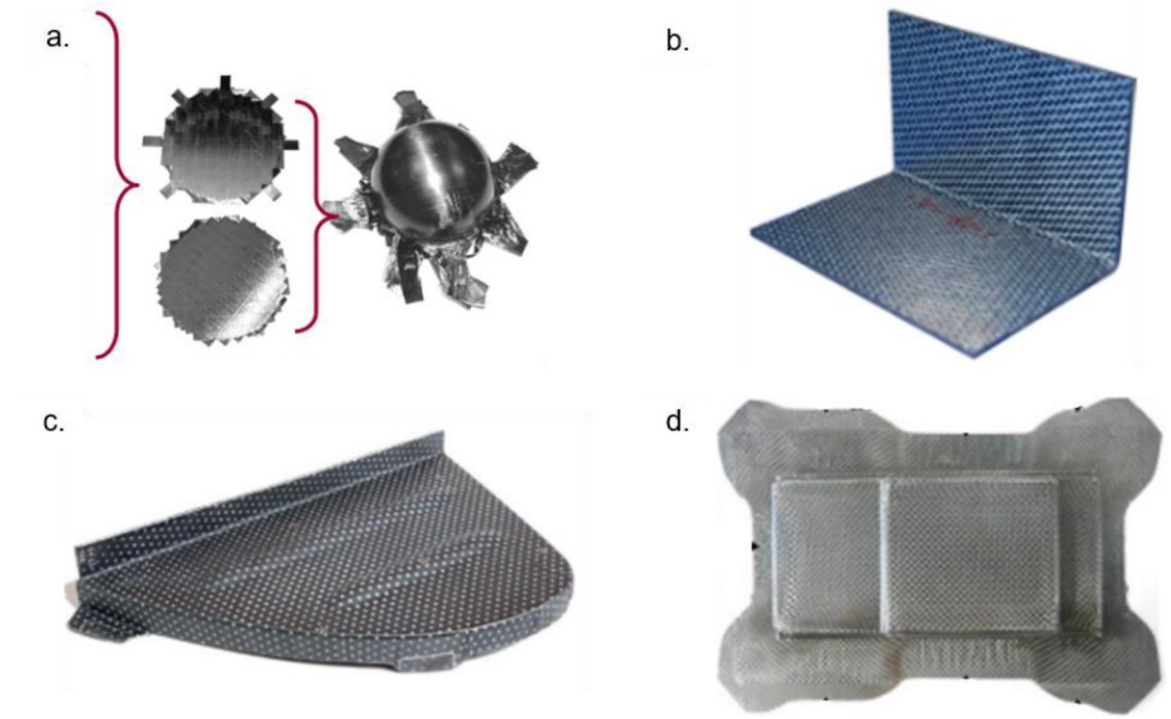


Figure 2-24: Example shapes formed by stamp forming: (a) hemisphere, (b) V-shape, (c) wing fixed leading edge stiffener, (d) square cup with two steps [181,191,211,215].

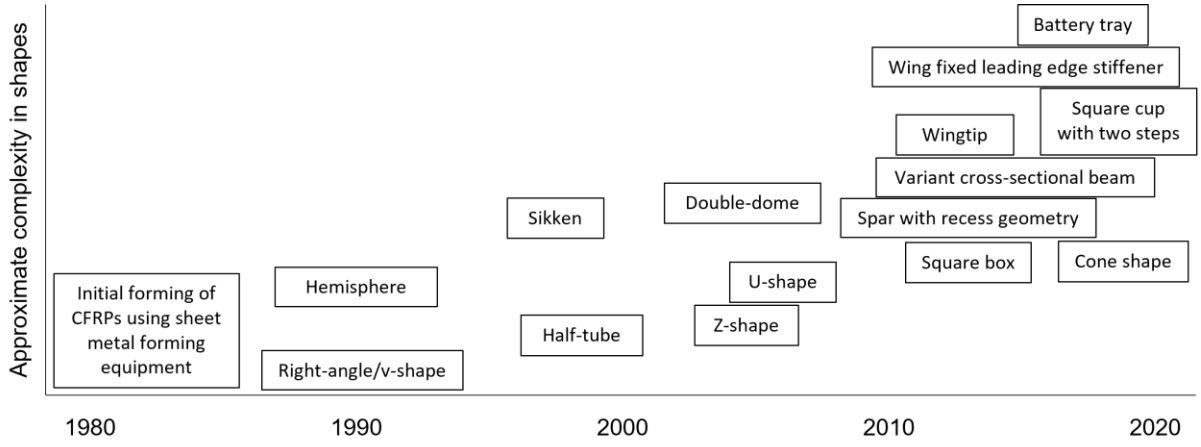


Figure 2-25: Development of FRTP shapes/components formed by stamp forming and their approximate complexities [179,185,199–201,203,204,207–209,211,213–216].

2.5.2 Mechanisms for stamp forming of FRTPs

2.5.2.1 Deformation mechanisms

The four main deformation mechanisms of FRTPs during forming are: resin percolation, transverse flow, inter-ply slip and intra-ply shear [178,220,221]. These mechanisms are shown in Figure 2-26, alongside the deformation modes they are required for. The deformation modes increase in complexity moving down Figure 2-26 and each one requires not just the deformation mechanism in the same row as it, but also all of the previous deformation mechanisms in the rows above.

Resin percolation is the flow of resin through the fibre network [220], both along and across the fibre direction [221,222], as shown in the first row of Figure 2-26. This is required to achieve good consolidation through resin redistribution and the formation of resin-rich interlayers between plies [178]. Resin percolation is mainly dependent on the matrix viscosity, although the lay-up is also important as using different ply orientations will reduce through-thickness permeability (i.e. the ease with which resin can percolate through the fibre structure) compared to having all plies oriented in the same direction [178]. Permeability is higher along the fibre direction compared to the through-thickness direction [178] and is increased for larger diameter fibres due to the larger holes formed between the fibres [222].

Transverse flow occurs when the applied normal pressure forces UD fibres to move in a sideways direction from the centre of the mould [220] or from positions of greater laminate thickness, to which the pressure is applied first [178], to accommodate local pressure variations [221], as shown in the second row of Figure 2-26. This occurs due to the uneven pressure distribution which is caused by an uneven laminate surface. Under high pressures, resin flow can also occur along the fibre direction and bleed out of the laminate [178]. This combined with transverse flow can lead to thinning of the plies [178]. Transverse flow is much more significant during forming of UD FRTPs because, in woven FRTPs, transverse flow is restricted by the warp/weft structure [220]. The extent of the mechanism is described by the transverse viscosity [220]. To characterise the transverse flow during forming, parallel-plate “squeeze flow” apparatus can be used [220].

Inter-ply slip involves plies sliding over each other in order to conform to a curved surface [220], as shown in the third row of Figure 2-26. The fibres within each ply are assumed to be inextensible, hence the plies must move relative to each other to allow for the different path length of each ply around the curve. For example, when forming a laminate into a bend shape, the inner plies of the bend will be under compression and the outer plies will be under tension. To prevent fibre buckling, inter-ply slip allows the plies to slide over each other and reduce the high compressive stresses in the inner plies.

Damage can be controlled in the outer plies as the tensile stresses are also reduced, which will decrease the chance of crack formation. Rotational slip can also occur between the plies when forming doubly-curved surfaces [220] as many parts with complex curvatures require a change in initial fibre direction between adjacent plies [221]. If the stress within each ply is high enough, the shear yield strength (i.e. the stress which must be exceeded for ply slippage to occur) of the resin-rich interlayers can be exceeded, allowing inter-ply slip to take place [176]. The shear yield strength of the interlayer decreases with increasing temperature and, when a certain high temperature above T_m is reached, the thermoplastic matrix can act as a lubricant between the plies and decrease the inter-ply friction [176], facilitating inter-ply slip. The shear stress required for inter-ply slip is dependent on factors including temperature and normal force and is investigated in detail in Section 2.5.2.2.1, in which studies characterising ply-ply friction are discussed.

Intra-ply shear occurs within the plane of each ply and allows the material to conform to complex curvature geometries [221]. Fibres are nearly inextensible, therefore, tensile deformations in the fibre direction cannot occur [178,222] for UD FRTPs. Unlike UD FRTPs, woven fabrics can undergo some extension due to their initially crimped nature. For UD FRTPs, intra-ply shear occurs through individual fibres moving relative to each other [222]. As shown in the fourth row of Figure 2-26, for a UD FRTP ply, axial (in 1-3 plane), transverse (in 2-3 plane) and intra-ply shear (in 1-2 plane) can take place [222]. For woven FRTPs, intra-ply shear often occurs through the trellis effect, in which the angle between the two sets of tows in the material changes [220]. This is quantified by the shear angle, γ, which is defined in the fourth row of Figure 2-26 [223]. Intra-ply shear in woven FRTPs can be limited when the locking angle (i.e. the angle beyond which the tows cannot rotate any further [220]) of the woven material is reached and further increases in shear strain are not possible [221]. The intra-ply shear behaviour for

both cross-plied UD and woven FRTPs can be characterised by bias extension or picture frame tests [224–226]. Haanappel et al. [227] also proposed a torsion bar test to characterise axial or longitudinal shear in UD FRTPs.

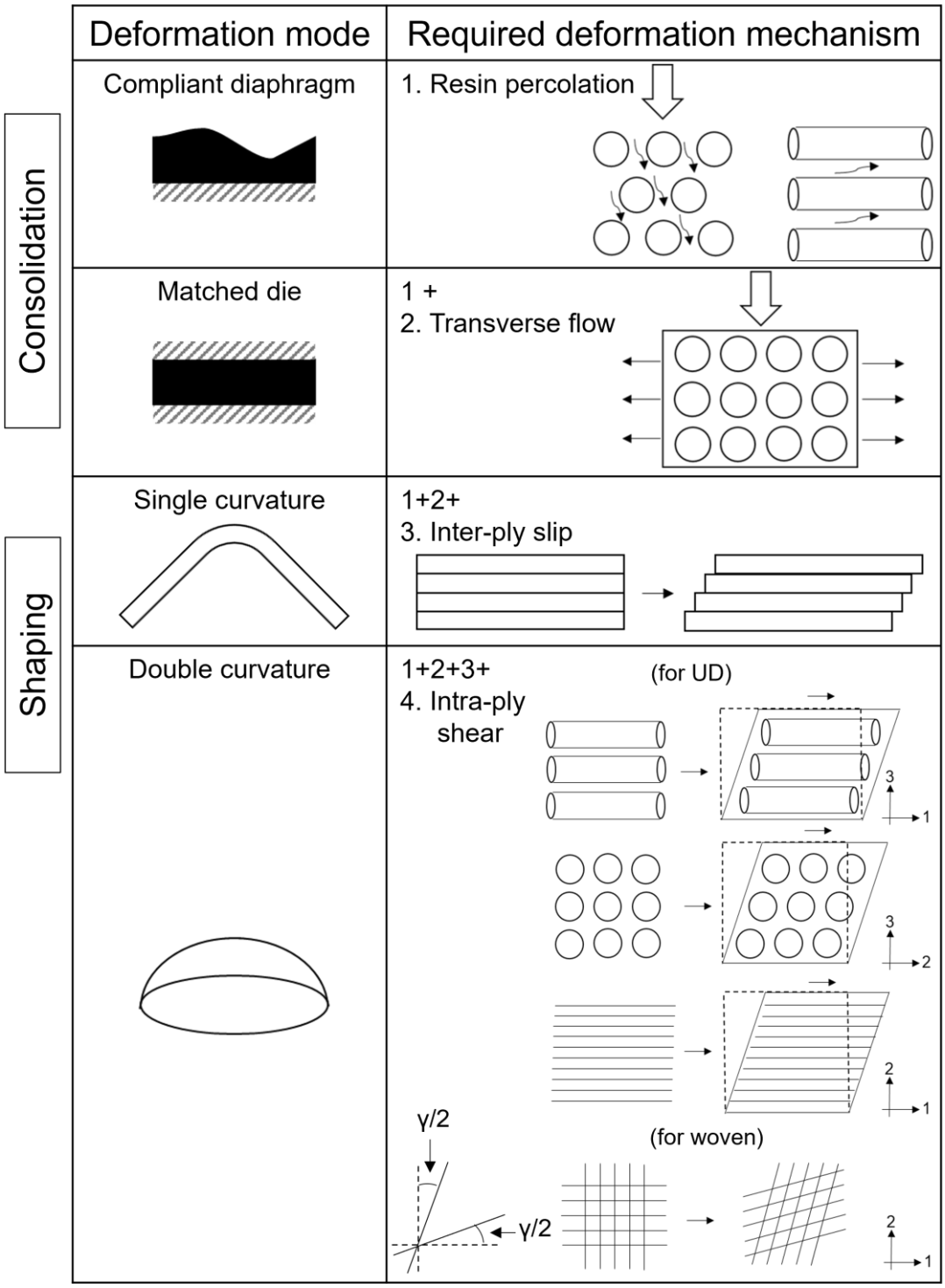


Figure 2-26: Deformation mechanisms required for different deformation modes (adapted from [178]*).*

2.5.2.2 Friction

Given the requirement for plies to be able to slide over each other during forming and the subsequent importance of inter-ply slip on the deformation process, a clear understanding of inter-ply frictional behaviour is required. Frictional forces present both between plies (known as inter-ply or ply-ply friction) and at the tool-ply interface affect the subsequent deformation. Therefore, the frictional properties at the ply-ply and tool-ply interfaces need to be characterised to give suitable forming conditions and predictable behaviours, so that the formation of defects such as wrinkles can be avoided. This section provides a comprehensive review of studies from the literature which have investigated the frictional behaviour of FRTPs through a variety of experimental set-ups.

One example of a set-up which can be used to measure inter-ply friction is shown in Figure 2-27(a), in which the plies are sandwiched between two metal plates. One ply is pulled out from between two other fixed plies which are under a normal load and have been heated to a certain temperature. A similar set-up which can be used to measure tool-ply friction is shown in Figure 2-27(b), in which the fixed plies are removed and one or multiple plies are pulled out from between the metal plates. The pull-out fixture is usually set up on a universal testing machine which provides the pull-out force. Alternative set-ups to measure the friction include a pull-through test arrangement on a universal testing machine [228] or using a sled and plane in accordance with ASTM Standard D1894 [229], which was originally designed to measure the frictional behaviour of plastic films.

A load cell in the testing machine measures the pulling force with increase in displacement throughout the pull-out tests. Figure 2-28 shows a typical relationship between pull-out force and displacement during a test [230–234]. The pull-out force, F, increases in a relatively linear fashion up until a yield point and then decreases, initially sharply, to reach an approximately steady-state value. The shear stress, τ, can be calculated by taking into account the change of contact area during a test. This is shown in Equation (2.1), in which A_i is the instantaneous contact area and F is divided by a factor of two due to there being two contacting surfaces present in the set-up described in Figure 2-27 [233]. In ply-ply friction tests, the yield point is related to the shear stress required to initiate ply slippage [230]. In tool-ply friction tests, the yield point has been related to the stress required to break the bond

formed between the composite and tool surface during heating prior to the start of slipping [235]. However, Ten Thije et al. [236] observed that the peak friction occurred when the composite is already moving compared to the tool. Therefore, the peak friction may not be identified as a static friction property, but instead as a running-in phenomenon which is not yet fully understood. The friction coefficient, μ, can be calculated using Equation (2.2), in which N is the normal load, P is the normal pressure and the factor of two is due to there being two contacting surfaces present in the set-up described in Figure 2-27 [233]. For an experimental set-up with only one frictional surface, the factor of two is removed from Equations (2.1) and (2.2).

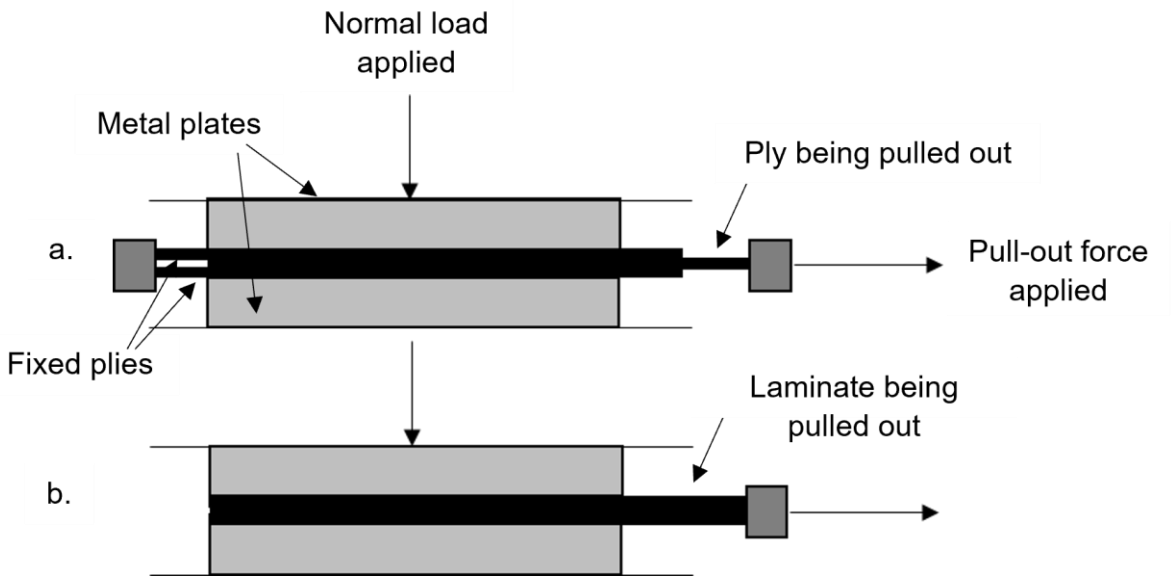


Figure 2-27: Example pull-out experiment set-up to measure (a) inter-ply and (b) tool-ply friction.

The trends for μ and τ with increase in displacement and pressure follow a similar general shape to that for F [232]. As displacement increases, A_i decreases and N is constant, therefore, P also increases. Hence, increasing displacement is comparable to increasing P. However, in [232], the approximately steady state region for τ has a slightly positive gradient with increasing P whereas for μ, there appears to be a slightly negative gradient. This is in accordance with Equation (2.2). Different values for μ can be defined, depending on the part of the pull-out curve the force is taken from. The static coefficient of friction corresponds to the initial peak of the pull-out curve and the dynamic coefficient of friction corresponds to the approximately steady-state pull-out force [233]. Changes in test conditions affect the yield and steady-state shear stresses and the static and dynamic friction

coefficients. The subsequent results can be used to determine appropriate forming parameters, such as a suitable temperature for inter-ply slip to occur.

$$\tau = \frac{F/2}{A_i} \tag{2.1}$$

$$\frac{F}{2} = \mu N \therefore \mu = \frac{F}{2N} = \frac{\frac{F}{2A_i}}{\frac{N}{A_i}} = \frac{\tau}{P} \tag{2.2}$$

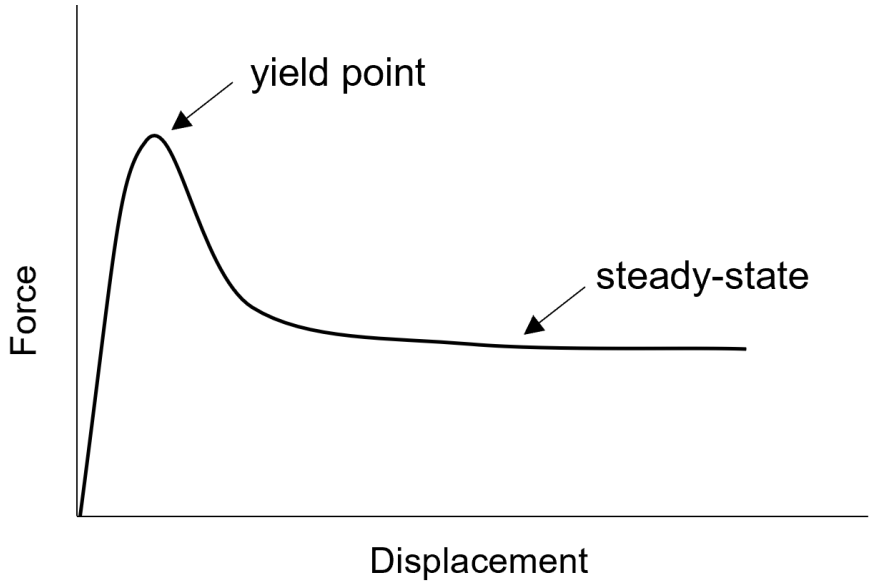


Figure 2-28: Typical force-displacement curve for a pull-out test.

The friction coefficient, μ, can be related to the Hersey number, H. The Stribeck curve in Figure 2-29 demonstrates the variation of μ with H and highlights the different forms of lubrication which can be present. Contacting surfaces are assumed to be fully separated by a fluid film for hydrodynamic lubrication whereas elasto-hydrodynamic lubrication allows for surface deformation [233]. H is a function of resin viscosity, η, speed, U, and normal load, N, as described in Equation (2.3) [237]. N was originally defined as the normal force per unit width when analysing friction in bearings [237] and this

makes H dimensionless. However, studies have since used N (total normal force) [207,233,238–240] or P as the denominator [211,236,241–244]. η is highly temperature dependent, which means μ is related to temperature as well as speed and normal pressure. The complex relationship between μ and various test conditions indicates the need to perform tests on specific materials to establish a clear understanding of frictional behaviour to allow for accurate modelling and successful forming.

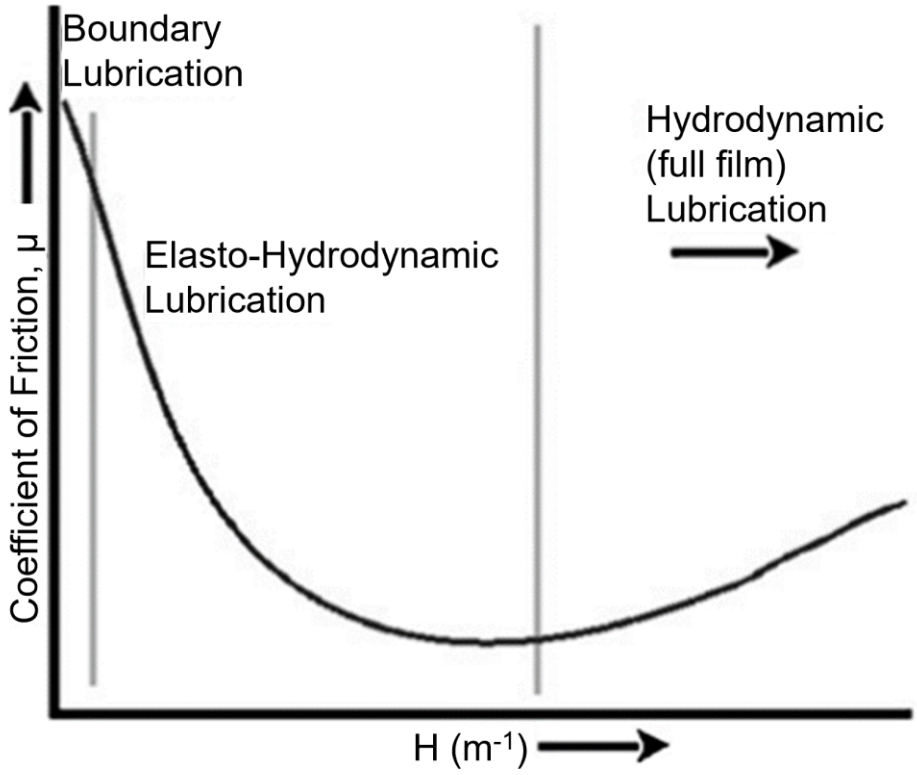


Figure 2-29: Stribeck curve [71].

$$H = \frac{\eta \cdot U}{N} \tag{2.3}$$

2.5.2.2.1 Ply-ply friction

The ply-ply (or inter-ply) friction behaviour needs to be characterised so that appropriate processing parameters can be chosen for inter-ply slip to occur during forming, which will allow the material to conform to the shape of the mould with fewer defects. As well as changing processing parameters,

using a thicker resin-rich interlayer can also reduce the shear yield strength [176]. The tests described in the literature have been undertaken on FRTPs at temperatures around or above T_m. The studies investigating inter-ply frictional behaviours are listed in Table 2-1, with details of the materials used and variables studied. A summary of the trends observed when changing four key parameters (temperature, pressure, pull-out speed and ply orientation) will be given in the following paragraphs.

Table 2-1: Test conditions in ply-ply friction studies [176,186,230–234,245].

Authors	Material	Temperatures (ºC)	Pressures (MPa)	Speeds (mm/min)	Orientations of adjacent plies (°)
Morris et al. 1994 [230]	CF/PEEK UD	324-354	0.62-1	0.762-762	0/0, 0/45, 0/90
Scherer et al. 1990/1991 [186,245]	CF/PP UD	180	Slight	~1-23	0/0, 0/45, 0/90, +45/-45, 45/90, 45/45, 90/90
Lebrun et al. 2004 [232]	GF/PP woven	Preheat: 170-200 Testing: 135-200	0.069-0.28	5-35	N/A
Vanclooster et al. 2008 [231]	GF/PP woven	175-205	0.016-0.063	12.5-400	N/A
Fetfatsidis et al. 2013 [233]	GF/PP woven	Tool: 85 Fabric: 180	0.11-1.033	120-4998	N/A
Bersee et al. 1991 [176]	GF/PEI* woven	250-325	1.3-2.0	-	N/A
Akkerman et al. 2010 [234]	GF/PPS + CF/PPS woven	310	0.01-0.05	20-500	N/A

*polyetherimide (PEI)

The yield and steady-state shear stresses decreased with an increase in temperature [176,230–232]. At temperatures above T_m, the resin-rich layer enhances slippage between the plies [230] as the viscosity decreases [176], giving a lower shear stress. At lower temperatures, the viscosity of the matrix increases, giving a more pronounced yield stress [231].

The yield shear stress slightly increased with increasing normal pressure [176]. However, a large normal pressure increase was required to give only a relatively small increase in yield shear stress (i.e. the increase in normal pressure was much larger than the increase in yield shear stress). This led to the ply-ply friction coefficient, μpp, decreasing as normal pressure increased [231–234], as described by Equation (2). An increased normal pressure may cause increased thinning of the inter-ply resin-rich layer, leading to increased frictional contact between plies [230]. In fabrics, higher normal pressures can increase interlaminar penetration and reduce the thickness of the resin interlayer [231]. This interlaminar penetration can cause interlocking between rovings oriented perpendicular to the direction of slip [232].

Higher yield and steady-state shear stresses were observed for slip between adjacent plies with the same orientation [186,230], as fibres can penetrate from one layer into another when a higher normal pressure is applied [186]. This is because commingling of fibres can occur when adjacent plies have the same orientation and this leads to a lack of a resin-rich layer between the fibres, which can result in a higher inter-ply shear stress as the surface is no longer planar [230]. In contrast, for adjacent plies with different orientations, fibre penetration is much less likely to be possible [186].

Higher yield and steady-state shear stresses were also observed with increasing pull-out speed [230–234,245]. Lebrun et al. [232] found that the pull-out speed had a much greater effect on μ_{pp} and the interlaminar shear stress than the temperature, with the effect becoming more pronounced at higher normal pressures. The decrease in μ_{pp} with increasing pressure was also more pronounced for higher speeds [232]. Additionally, the shear stresses became more rate-dependent at higher temperatures [230].

In summary, inter-ply shear stress increases with:

- a decrease in temperature,
- an increase in pressure,
- an increase in speed,
- the use of adjacent plies with the same orientation.

2.5.2.2.2 Tool-ply friction

The tool-ply friction needs to be characterised so that the forces acting on the material during deformation can be correctly predicted, allowing accurate modelling and simulation of the forming process. Studies investigating tool-ply frictional behaviour are listed in Table 2-2, which details the materials used and variables studied. Most tests were undertaken above T_m, although some tests were undertaken at room temperature or at intermediate temperatures. For a non-isothermal test, a low tool temperature may lead to fast cooling of the laminate, meaning that the test does not entirely take place above T_m. This can affect the type of lubrication present.

Table 2-2: Test conditions in tool-ply friction studies [232–236,239,241–243,246,247].

Authors	Material	Temperatures (ºC)	Pressures (MPa) or Loads (N)	Speeds (mm/min)	Orientations between fibres and pulling direction (°)
Murtagh et al. 1995 [235]	CF/PEEK UD	Isothermal: 25-405	100-750 N	< 15–120	0, 90
Sachs et al. 2011 [242]	CF/PEEK UD	Isothermal: 400-420	0.01-0.05 MPa	20-500	N/A
Chow 2002 [246]	GF/PP woven	Tool: Room-120 Fabric: 100-200	1500-4000 N	1000-2500	0/90, 30/60, 45/45, 90/0 (Warp/Weft)
Gorczyca et al. 2004 [239]	GF/PP woven	Tool: 21-140 Fabric: 160-200	218-4000 N	100.2-4998	0/90, 30/60, 45/45, 60/30, 90/0
Lebrun et al. 2004 [232]	GF/PP woven	Tool: 135-200 Fabric: 170-200	0.069 MPa	20	N/A
Akkerman et al. 2007 [247]	GF/PP woven	Isothermal: 180-220	400-1200 N	20-500	N/A
Ten Thije et al. 2011 [236]	GF/PP woven	Isothermal: 180-220	0.02105-0.06316 MPa	20-500	N/A
Fetfatsidis et al. 2013 [233]	GF/PP woven	Tool: 85 Fabric: 180	0.11-1.033 MPa	120-4998	N/A

Sachs et al. 2014 [243]	GF/PP woven	Isothermal: 23-220 (23 for dry, above 180 for wet)	0.01-0.1 MPa	20-1000	N/A
Akkerman et al. 2010 [234]	GF/PPS and CF/PPS woven	Isothermal: 290-310	0.01-0.05 MPa	20-500	0/90, 90/0
Lee et al. 2017 [241]	CF/PU* woven	Isothermal: 110-190	1-5 MPa	600	N/A

*polyurethane (PU)

Some studies observed an increase in tool-ply friction coefficient, μ_{tp}, with an increase in temperature [232,235,241]. However, other studies observed the opposite trend of a decrease in μ_{tp} with increasing temperature [232,236,239,243,246,247], or indeed no significant effect of temperature on friction [242]. The differing results may be due to the different apparatus set-ups and processing parameters used. Lebrun et al. [232] obtained contrasting trends depending on whether the tool temperature was below or above T_m, however, other studies [235,236] obtained contrasting trends, despite both using temperatures above T_m. The temperatures being below or above T_m could have a significant effect on μ_{tp} due to the effect of the presence of liquid on the type of lubrication present. Also, the pressure and speed affect the type of lubrication present which in turn affects μ_{tp} [236]. For temperatures above T_m, the increased temperature may cause a greater contact area between the composite and tool due to softening of the matrix or may reduce the thickness of the resin layer, thus increasing μ_{tp} [235]. Additionally, as matrix viscosity decreases, more fibres are able to penetrate the resin-rich surface layer which increases the Coulomb friction between the tool and the fibres [232]. Alternatively, a higher tool temperature allows a fluid film to remain on the fabric surface for longer, acting as a lubricant and reducing μ_{tp} at higher temperatures [239]. Furthermore, the increased temperature reduces the matrix viscosity [236] which can improve lubrication and lower μ_{tp}. For temperatures below T_m, fibres cannot penetrate the resin-rich layer so the increase in μ_{tp} with reducing tool temperature may be due to solidification of the matrix and subsequent Coulomb friction between matrix and tool [232]. A cooler tool increases the rate of matrix solidification, leading to an overall increase in μ_{tp} [246]. Lebrun et al. [232] noted that tool-ply shear stress was higher than inter-ply shear stress at higher temperatures, but a transition occurred as temperature dropped, with the tool-ply shear stress becoming lower than the inter-ply shear stress at lower temperatures. The lower tool-ply shear

stress compared to inter-ply shear stress at lower temperatures can reduce the chance of fibre breakage during the latter part of the forming process [232]. Based on existing studies, factors such as viscosity, fibre penetration, resin layer thickness and lubrication type appear to dictate the dependence of friction on temperature, but how these factors interact to give a predictable value of μ_{tp} is still not clear. The variability in results from different studies complicates obtaining a consistent understanding of the effect of temperature on tool-ply friction.

A decrease in μ_{tp} was observed for increasing normal loads [232–236,239,241,243,246]. An increased normal load may lead to more resin being squeezed from the centre of the laminate out to the surfaces, increasing the lubrication and decreasing μ_{tp} [239]. The trend observed is consistent with that expected for friction occurring in the hydrodynamic region of the Stribeck curve [233], see Figure 2-29 (and Equation (3)), in which it is assumed that the sliding surfaces are completely separated by a fluid film. Additionally, Sachs et al. [242] noted that an increase in pressure made the steady-state friction more velocity dependent and the peak friction less velocity dependent.

A decrease in μ_{tp} for UD ply orientation increasing from 0 to 90° or warp yarn increasing from 0 to 45° from the sliding direction has been observed [234,235,246]. However, some studies concluded that fabric or fibre orientation had no significant influence on μ_{tp} [234,239]. Resin flow across the fibres may be easier than resin flow along the fibre direction, leading to an improvement in lubrication [235]. Also, some materials had more surface warp yarns than weft yarns, resulting in a lower μ_{tp} for sliding in the weft dominant direction [246].

An increase in μ_{tp} was observed for increasing pull-out speeds [233–236,239,242,243,246,247]. The results follow the trend shown in the Stribeck curve developed by Ten Thije et al. [236], in which μ_{tp} increases with increasing slipping speed. The trend may also be described by a power-law viscosity model which is able to describe the resin viscosity [239]. The model indicates that, for low speeds, shear stress increases with speed and at high speeds, the shear stress levels off with further increases in speed. The levelling off of μ_{tp} at higher speeds may be due to shear thinning, where resin viscosity decreases at higher speeds, or an increase in thickness of the resin layer due to a layer of transferred polymer building up on the tool surface [235]. Ten Thije et al. [236] observed that

the peak friction force was more pronounced at higher speeds. Following the peak, the initially randomly oriented polymers became more oriented as the test progressed, thus μ_{tp} was reduced [236].

In summary, μ_{tp} increases with:

- an increase or decrease in temperature (different conclusions have been obtained),
- a decrease in pressure,
- an increase in speed,
- a decrease in angle between fibre/warp direction and sliding direction.

2.5.2.2.3 Friction summary

A summary of the trends seen in the literature between test conditions and shear stress and μ is shown in Table 2-3. Clearly, the effect of temperature on the tool-ply friction is not universally understood, despite being widely studied. Furthermore, little investigation has taken place regarding the effect of ply orientation on the inter-ply friction of woven composites. The ply-ply and tool-ply friction characteristics of a wide range of materials have not been investigated, with the focus concentrated mainly on woven GF/PP. Wider studies on high performance materials, such as UD and woven CF/PEEK and CF/PPS, are recommended to obtain a consistent understanding of frictional behaviour under a larger range of conditions, given their potential applications in aerospace and automotive industries. Multiple studies are necessary for a detailed understanding of material behaviour due to differences between experimental set-ups across studies. Although the trends from the literature may apply to other materials, the friction characteristics should be investigated prior to stamp forming for each material being used, particularly given the variability in certain conclusions from different studies. Results from these studies can then be used to choose suitable processing parameters for stamp forming, which can be optimised to give good formability and final part quality.

Table 2-3: Effect of increase in process parameters on the ply-ply and tool-ply shear stress and μ.

	Shear stress		**μ**	
	Ply-ply	**Tool-ply**	**μ_{pp}**	**μ_{tp}**
Temperature	-	+ or -	-	+ or -
Pressure	+	+	-	-
Speed	+	+	+	+
Angle between fibre/warp direction and sliding direction	-	- or unchanged	-	- or unchanged

*+ indicates increase, - indicates decrease

2.5.2.3 Consolidation

Several properties constitute the consolidation quality of a material, including void content and interlaminar bond strength [175]. Consolidation quality changes during material processing and is strongly affected by the thermal and pressure history of the component, such as the pre-consolidation quality of the blank prior to stamp forming [175]. Deconsolidation often occurs when pre-consolidated laminates are heated towards T_m, particularly if little pressure is applied, which can reduce through-thickness heat transfer and increase the required heating time [175,217]. Reasons for deconsolidation include the expansion of dissolved moisture and gas within the matrix and the release of stresses induced during laminate manufacture [206,248]. Therefore, deconsolidation may be reduced through drying of the blanks prior to heating [248].

Once plies have been able to slide against one another to form the required shape, strong bonding between layers is required to achieve good final part quality. The main mechanisms which determine reconsolidation are void collapse and interlaminar bonding [249]. Resin percolation and transverse flow assist these processes [230]. Interlaminar bonding occurs when the molecular chains of the matrix at the ply interface diffuse into the adjacent ply [250]. Over a long enough time, full interpenetration of the chains occurs, meaning the interface is indistinguishable from the bulk polymer. This is called autohesion or self-diffusion. Higher temperatures increase the rate at which this autohesive bond strength reaches the cohesive strength of the bulk polymer [250]. However, autohesive

bond formation can only occur if the plies are in intimate contact. Low tow thickness variations within plies are required to achieve good interlaminar bonding at short holding times [249,250]. Short holding times do not allow enough time for the matrix to redistribute and a uniform pressure distribution to be achieved [249]. However, increasing the consolidation pressure can allow blanks with greater thickness variations to be used and still form parts with an acceptable degree of consolidation. Alternatively, the holding time and pressure required for consolidation can be reduced by using pre-preg with a resin-rich surface which enhances matrix redistribution and interlaminar bonding.

2.5.3 Challenges and defects

Stamp forming is a complex process and it is a challenge to form defect-free parts. Through understanding the formation mechanisms of defects, the processing parameters can be optimised to reduce the forming defects and improve the final part quality. Common defects include geometric inaccuracies, such as spring-forward, cracks, delaminations, wrinkles and voids. In this section, the latter two defects are discussed in detail.

2.5.3.1 Wrinkles

This section gives an overview of wrinkle formation during forming and discusses methods to reduce or eliminate wrinkles. Wrinkles can cause fibre breakage, leading to poor quality final parts. The geometric inaccuracies created might also make parts unsuitable, particularly if a tight tolerance is required. More detailed reviews regarding wrinkles are available in the literature. Gereke et al. [251] conducted a review on forming of the textile reinforcement prior to resin infusion, with much focus on wrinkle formation. Boisse et al. [252] gave a review on bending properties and wrinkling of pre-preg during draping simulations.

Out-of-plane buckling and, therefore, wrinkles can occur when fibres are under an in-plane compressive loading condition during deformation [179]. If less energy is required to cause out-of-plane buckling than in-plane deformation, a wrinkle can form [223]. Forming double-curved parts gives a particularly high risk of wrinkle formation [214]. Figure 2-30 shows the global laminate deformations observed by Haanappel [253] while forming UD quasi-isotropic laminates into double curvature shapes.

If the deformation mode involves only intra-ply shear with some inter-ply slippage, wrinkles will not form (option 1). If this deformation mode presents too much resistance, then a fold can form (option 2). For a material with an adequately low bending stiffness, multiple smaller wrinkles can initially form (option 3), which will then undergo straightening (option 1) or folding (option 2).

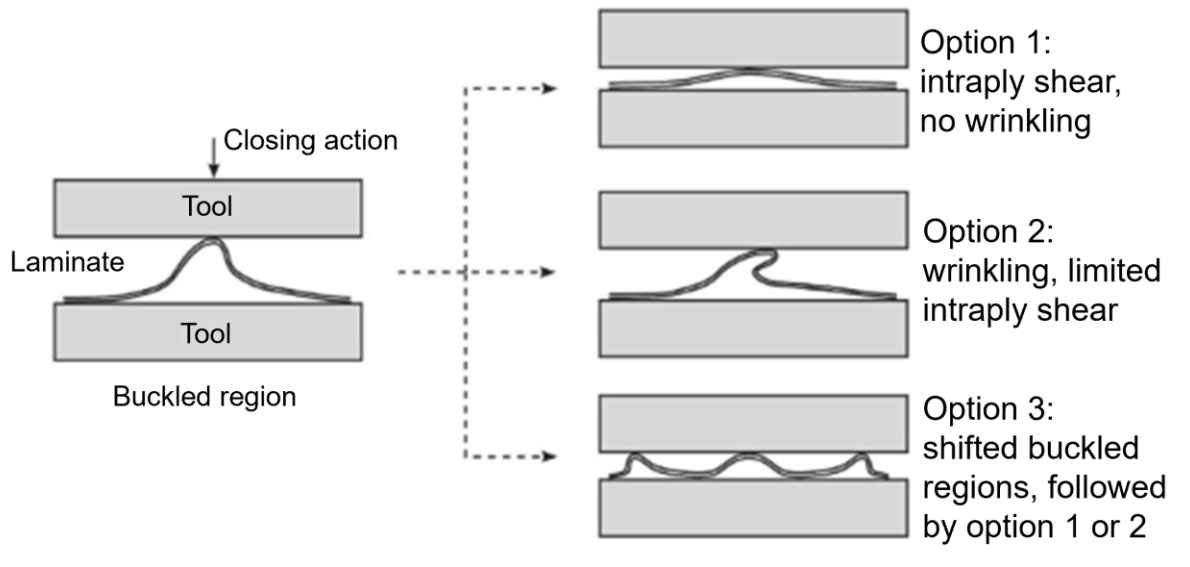


Figure 2-30: Laminate deformation behaviours when double curvature leads to excess material during forming [253].

In textile fabrics, large in-plane shear strains can also lead to wrinkling, particularly if the shear angle, γ, reaches or exceeds the locking angle [223] (i.e. the angle following which the yarns become in contact with neighbouring yarns and start to laterally compact [254]). In-plane shear stiffness increases at larger shear angles required to form doubly curved parts due to lateral contact between adjacent yarns, increasing the chance of wrinkling [223]. Wrinkles can form when γ exceeds the locking angle because the bending strain energy due to wrinkling is smaller compared to the in-plane shear strain energy (i.e. wrinkle formation has a lower energy dissipation compared to further in-plane deformation) [223]. By forming the wrinkle, the fabric length is increased which reduces the strain energy due to compression. Therefore, out-of-plane wrinkle formation is energetically preferable compared to further in-plane deformation. Furthermore, the formation of wrinkles can also lead to a decrease in the shear angles [223]. However, wrinkling can be mitigated by applying in-plane tension to the material, allowing continued in-plane shear deformation beyond the locking angle without

wrinkling. Harrison et al. [226] used biaxial bias extension tests to characterise the onset of wrinkling in woven fabrics and observed that, under increased in-plane tension, γ at onset of wrinkling increased. Therefore, comparing γ to the locking angle cannot be used to predict wrinkle formation alone. Other factors such as tension implemented by blank holders, in-plane shear and bending energies must be taken into account [223,251,255].

Wrinkle shape is highly dependent on bending stiffness, with higher bending stiffness giving larger wrinkles [223,251,256]. In this way, wrinkle shape is also dependent on temperature as the bending stiffness decreases with increasing temperature. Therefore, the number of wrinkles increases with increasing temperature [256], while their size reduces. The bending properties of the material can be characterised through tests such as the Peirce cantilever, Kawabata bending and three-point bending tests [252]. During cantilever tests conducted on pre-preg in a thermal environmental chamber, the deflection increases with an increase in temperature, confirming a decrease in bending stiffness with increasing temperature, until a point at which the resin is fully melted [256]. At this point the deflection reaches an upper limit, where the fabric (fibre only rather than fibre and matrix) is entirely responsible for the bending stiffness. An accurate value of bending stiffness should be predicted and taken into account, in order to ensure that wrinkles do not extend beyond the excess area and into the final part area, as has occurred in the parts in Figure 2-31 [256].

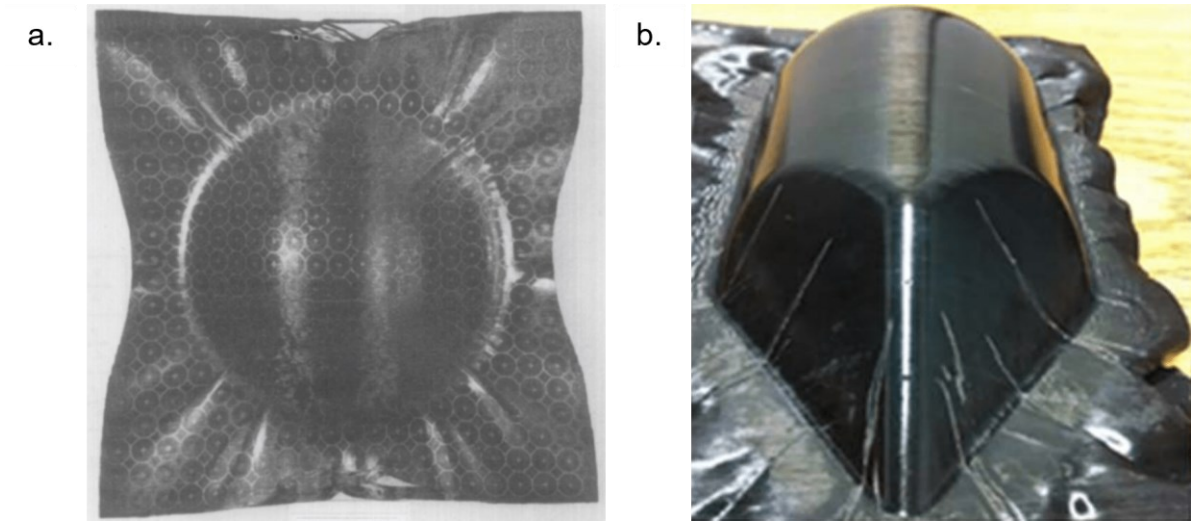


Figure 2-31: Wrinkles in final formed parts: (a) hemisphere and (b) shape containing cylindrical portion, quarter sphere and flat faces [218,257].

Wrinkling can be reduced by applying in-plane tension to the laminate through constraints such as blank holders [223,251]. This helps prevent the material being under an in-plane compressive stress so reduces the chance of buckling. The buckling and hence the wrinkling behaviour is also affected by the blank shape [258]. Too much excess material forming the flange area can hinder stretching in other parts of the material during deformation, leading to reduced formability [213]. Behrens et al. [214] reduced wrinkling-induced fibre fracture while forming a battery tray with step-geometry and tunnel-geometry by inducing local fibre shear and yarn straightening. Reducing the clamping width near the tunnel area induced yarn straightening in the load direction and local intra-ply fibre shear transverse to the load direction. This kept surplus material out of the tool, which prevented wrinkle formation. Furthermore, fibre fracture was also prevented in part of the mould by using a 45/45º instead of a 0/90º fibre orientation. This choice of material avoided fibres orthogonal to the wrinkle.

Haanappel et al. [211] compared wrinkling during forming of UD CF/PEEK and woven GF/PPS. Although both materials showed similar frictional behaviour, the UD material showed a greater resistance to intra-ply shear. Therefore, the part formed from UD material showed many wrinkles whereas the woven material showed a smooth deformation behaviour. To avoid wrinkle formation when forming a part with double curvature, laminates with more than two unique fibre orientations (such as quasi-isotropic UD laminates) must allow both inter-ply and intra-ply deformation [211,258]. If only two unique fibre orientations are present, intra-ply shear can occur without evoking inter-ply slip if the frictional rigidity is greater than the intra-ply shear rigidity [253,258]. Overall, for forming complex double curved shapes, woven fabrics can more easily form high quality parts than UD material [211,228].

2.5.3.2 Voids

Void content has been shown to be directly related to the mechanical properties of formed FRTPs. Liu et al. [259] have written a literature review covering void formation and the effect on mechanical performance in thermoset matrix composites. Some concepts detailed in Liu et al. [259] can also apply for thermoplastic matrix composites.

2.5.3.2.1 Formation mechanisms

Voids can form through a number of different mechanisms. One of the most dominant mechanisms is fibre-matrix and interlayer debonding during heating [215], which leads to increasing void formation within the laminate as temperature increases [201], see Figure 2-32. This debonding is one of the main contributors to deconsolidation, as explained in Section 2.5.2.3. The change in void content can be used as an indication of the degree of thermal deconsolidation [260] and a severe increase in void content can lead to complete delamination of plies [175]. A high processing temperature can reduce the number and size of voids seen in the final part due to the improvement in matrix fluidity, see Figure 2-33(a-b). This can enhance matrix migration and result in void elimination, a more even matrix distribution and improved force transfer and interlayer adhesion [261]. However, at higher temperatures, thermal degradation of the matrix can increase the size of voids [261]. In particular, bar-shaped voids increase in size due to the depletion of interlayer resins [261], see Figure 2-33(b-c).

Due to shrinkage of the matrix during cooling, the holding pressure can decline which allows pear-shaped voids to form in resin-rich regions and bar-shaped voids to form in the interlayer due to a lack of resin [261], see Figure 2-33(d-f). In addition, voids can also form if air is not fully evacuated from between plies when using unconsolidated material, such as commingled fabrics [262]. Air evacuation can be more difficult when a greater number of plies are used, but this can be mitigated by using a higher temperature which therefore gives a lower matrix viscosity [262]. Moreover, when commingled fibre bundles within a ply are not completely parallel, large regions of resin are required to fill the gaps between the bundles [263]. A lack of matrix in these regions increases the chance of void formation.

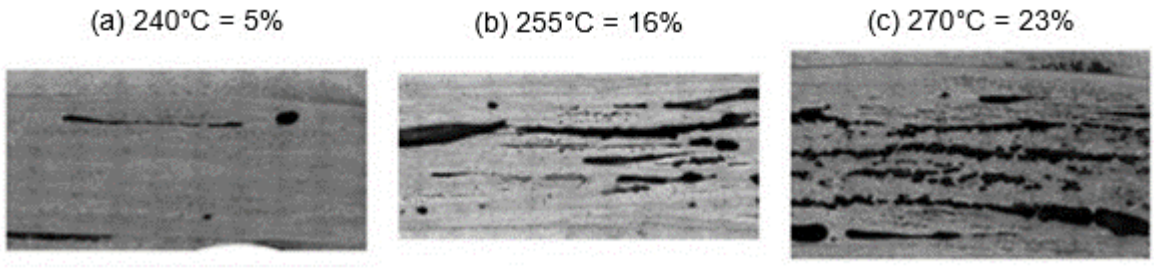


Figure 2-32: Void content in GF/PA6 after preheating to: (a) 240 °C, (b) 255 °C and (c) 270 °C [201]

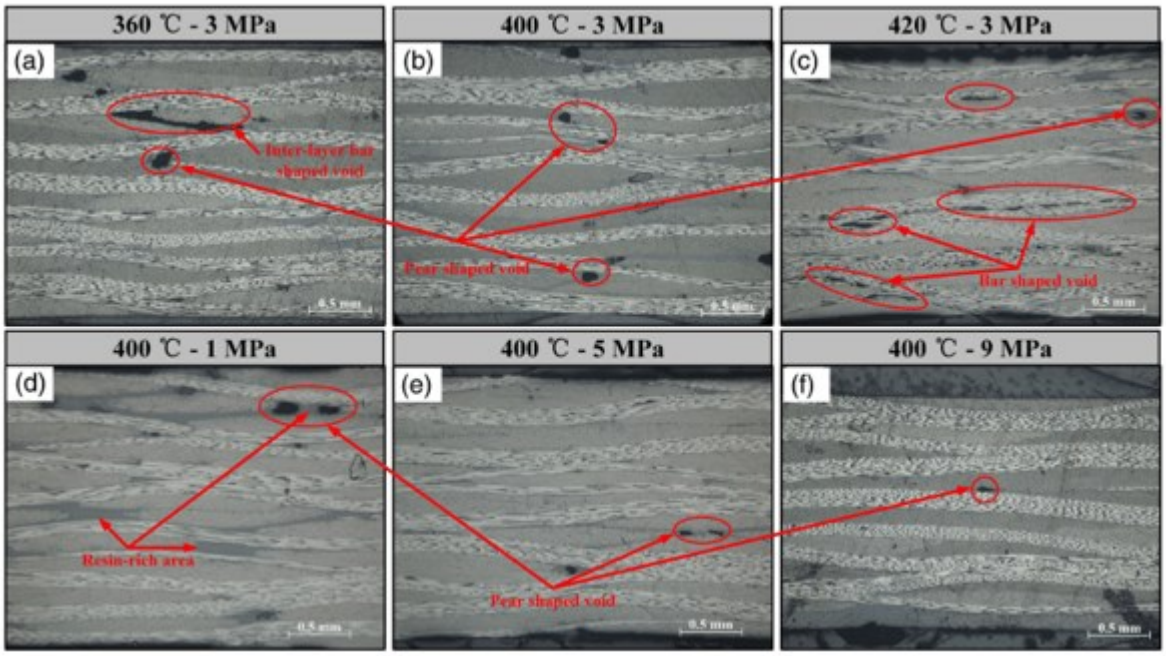


Figure 2-33: Microscopic images of woven CF/PEEK laminates fabricated at: (a) 360°C and 3 MPa, (b) 400°C and 3 MPa, (c) 420°C and 3 MPa, (d) 400°C and 1 MPa, (e) 400°C and 5 MPa and (f) 400°C and 9 MPa [261].

2.5.3.2.2 Distribution

The distribution of voids changes from being present in both the matrix and fibre-rich regions to being concentrated in fibre-rich regions under higher loading rates and pressures [262]. Fibres within the bundles are compacted together under high pressure, meaning the matrix has more difficulty impregnating the centre of the fibre bundles, leading to voids within the bundles [261]. Jiang et al. [264] found that voids were initially concentrated in the interlaminar region and under increasing pressure void growth occurred along the fibre direction. The overall elongation of the voids slightly increased and the void size, calculated from the average value of the equivalent diameter for each void, slightly decreased, due to the increase in the number of small voids. For longer dwell times, many of the large voids were broken and turned into smaller ones, see Figure 2-34. The elongation and flatness of the voids also reduces, with voids becoming more spherical and the equivalent diameter reducing.

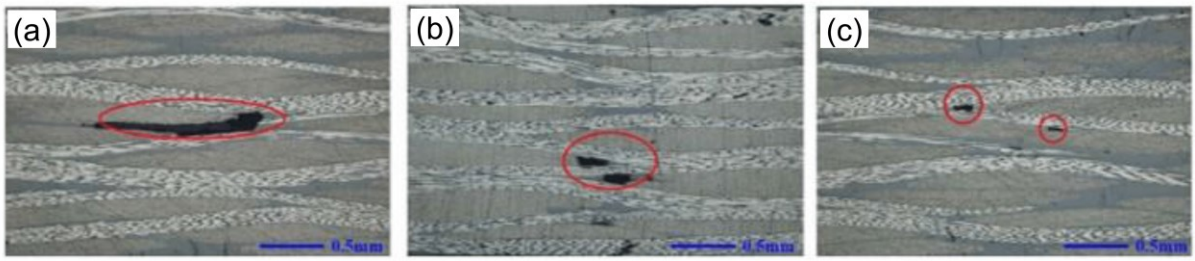


Figure 2-34: Optical microscopy photographs of the cross section of woven CF/polycarbonate (CF/PC) laminates manufactured at 255 °C and 1 MPa with different dwell times: (a) 5 minutes, (b) 10 minutes and (c) 20 minutes [264].

2.5.3.2.3 Effect on mechanical properties

In general, an increase in void content leads to a reduction in mechanical properties [18,201,261–264]. In particular, matrix-dominated properties such as the flexural strength and modulus and the interlaminar shear strength (ILSS) are strongly affected by void content [262,264]. Subsequently, mechanical properties can be approximated by measuring the void content [262]. Linear relations can be formed between mechanical properties (such as flexural strength and modulus) and void content which allow mechanical properties for components with complex shapes to be approximated [262]. It is difficult to cut samples of standard dimensions from complex components which have limited flat surfaces, so by measuring the void content, material properties which would otherwise be difficult to measure, can be determined.

Reasons for the deterioration in mechanical properties with an increase in void content include the facts that voids can result in stress concentrations and weaken fibre-matrix and interlaminar bonding. Also, increased void size and content reduces the fracture surface area, which reduces the fracture toughness [263]. Void content changes depending on the processing parameters used and the trends relating void content and mechanical properties to processing parameters are discussed in detail in Section 2.5.4.

2.5.3.2.4 Void reduction

Intuitively, a high enough pressure must be applied while the matrix is in the molten state to suppress void formation and expansion. Void collapse is an important mechanism to allow good consolidation

during stamp forming [249], see Section 2.5.2.3. Void reduction strategies are implemented through the determination of optimum forming conditions which can reduce the void content to a level which gives acceptable mechanical properties. Figure 2-33 highlights the effect of varying processing parameters (in this case temperature and pressure) on void content and distribution. The effect of the choice of process parameters on final part quality is discussed in detail in Section 2.5.4.

2.5.4 Effect of process parameters on stamp formed parts

In order to find optimum processing conditions for forming high quality parts, an understanding of the effects of different processing parameters on the final part quality is required. To choose specific values for forming parameters, some testing specific to the chosen material or mould shape may be required. For materials which have not previously been studied in detail, preliminary tests to characterise properties such as matrix degradation temperature, T_{deg}, are required. This section presents and compares the findings from forming studies in the literature and allows trends for different parameters to be compared between studies. The current understanding of the effect of processing parameters is summarised. Results from these studies can be used to give an indication of the optimum forming conditions which give the highest quality parts.

2.5.4.1 Temperature

Stamping temperature (also known as forming temperature) is dependent on both the laminate and tool temperatures. Cooling of the laminate occurs during transfer from heating source to mould as the large surface area to thickness ratio leads to significant heat loss due to convection [214]. This is followed by cooling of the laminate through conduction upon contact with the cooler mould. Thicker laminates remain at a higher temperature for longer due to their higher thermal capacity, leading to a higher stamping temperature [221]. The change in temperature during forming means that the matrix viscosity also changes, which in turn affects the fibre motion [215] and inter-ply friction. Inter-ply slip is particularly temperature dependent (see Section 2.5.2.2.1). Hence, stamping temperature has an important effect

on both the formability and the post-form mechanical properties. Therefore, temperature may be considered the most important processing parameter.

Figure 2-35 shows the forming temperatures of the matrix materials used by the studies analysed in this section and indicates that most stamp forming studies are conducted at temperatures between T_m and T_{deg}. T_{deg} corresponds to the onset of degradation, which is often defined as the temperature at which 5% or 10% weight loss takes place [265,266]. Therefore, some degradation does occur prior to this "onset" T_{deg}. However, the matrix may degrade at a different temperature when combined with the fibres, with degradation usually initiating at the fibre/matrix boundary. For example, Zheng et al. [261] observed degradation in woven CF/PEEK at 420 °C, significantly lower than the "onset" T_{deg} of the pure polymer.

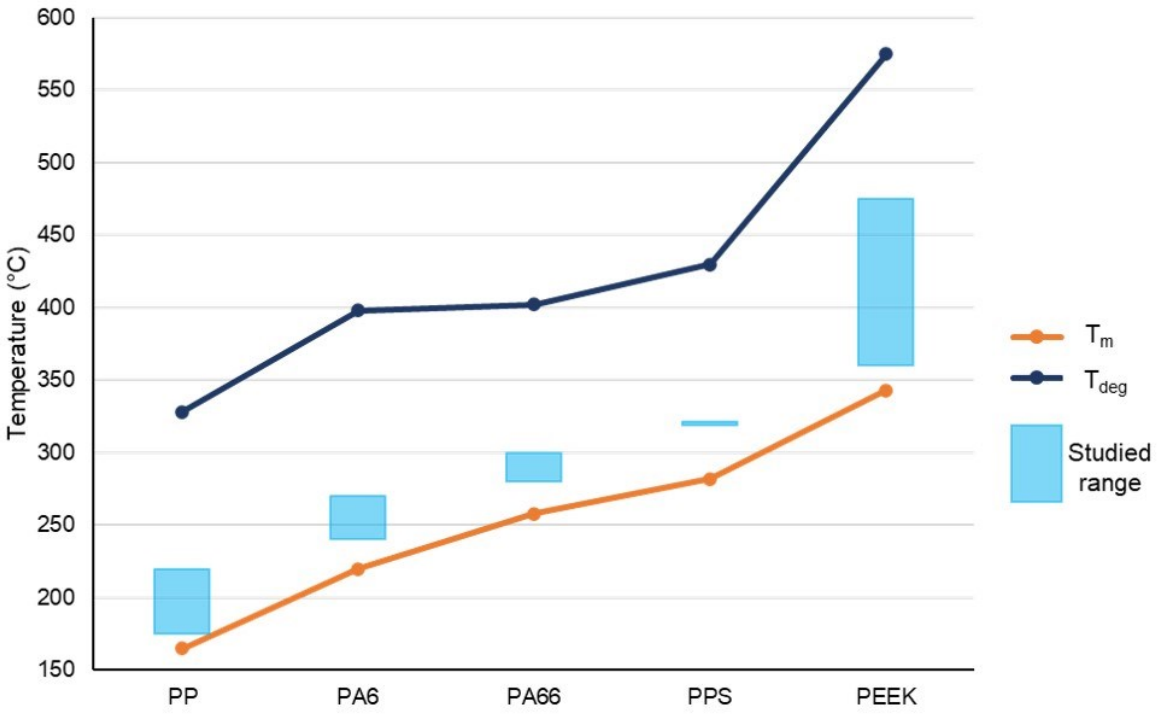


Figure 2-35: Studied forming temperatures for different thermoplastic matrices in relation to their melting (T_m) and degradation temperatures (T_{deg}) [191,197,201,217,261,262,265–272].

Studies in the literature indicate that the tensile, flexural and interlaminar shear strengths (ILSS) of post-form materials increase with increasing forming temperature prior to the onset of matrix degradation [197,261,262,267–269]. There is evidence that flexural modulus may also increase with

forming temperature [201,262]. The general trend for tensile strength, ILSS, flexural strength and flexural modulus with variation in temperature is shown in Figure 2-36(a).

Higher forming temperatures reduce damage and defect formation and improve consolidation between plies, leading to improvements in mechanical properties. In particular, higher forming temperatures result in lower resin viscosity, which can enhance air evacuation from the laminate [262] and give a more even distribution of resin [261], giving a lower void content and stronger inter-ply adhesion. A higher temperature increases the speed of autohesive bond development between plies, as outlined in Section 2.5.2.3.

However, higher forming temperatures can increase the spring-forward effect [191,192,197] and compromise the geometric accuracy of the final part. This is because the larger temperature drop during cooling results in greater anisotropic shrinkage strains [191]. Nevertheless, the shape distortions are mitigated by changes in the mould shape (i.e. mould compensation) or in other processing parameters, such as holding time.

Overall, a higher forming temperature is often beneficial provided that matrix degradation is avoided and that the material does not become too flexible to handle [199]. Therefore, an optimum temperature significantly below T_{deg} but above T_m is preferred.

2.5.4.2 Speed

Stamping speed is the speed of the die during forming and can refer to the (initial) closing speed or the compression speed (also called the final closing speed). Initial closing speed is the speed of the die prior to material deformation and compression speed is the speed of the die during material deformation [199,262]. Changing the initial closing speed affects the amount of heat lost from the laminate due to convective cooling prior to material deformation. The compression speed can affect the viscous forces in the matrix during forming, leading to differing behaviour and damage formation in the laminate [200]. The intra- and inter-ply viscous forces and inter-ply friction forces (see Section 2.5.2.2.1) are reduced by using a lower stamping speed, which improves the formability. High stamping speeds can cause severe thinning of the sides of a bend due to resin migration to the outer bend region [273] as well as

increasing the damage in the material, such as cracks [195], fibre buckling [178], wrinkling [274] and delamination [198]. In commingled fabrics, high stamping speeds can cause increased tearing and splitting between yarns [275]. However, if using a constant speed for the whole process, the speed must be considered alongside the temperature as using a slower speed to reduce wrinkle formation may actually have the opposite effect due to excessive laminate cooling taking place prior to the final shape being achieved. Hence, stamping speed appears to have a significant effect on the formability, with less of an effect on post-form mechanical properties, unless damage is formed. In this case, poor formability can highly affect post-form mechanical properties.

Trudel-Boucher et al. [262] used a higher initial closing speed until just before the die contacted the material (commingled GF/PP in this study), at which point a slower compression speed was used to force the material into the mould. The use of different speeds reduced the level of material cooling during mould closure and allowed greater accuracy in controlling the displacement of the tool [262]. This study varied loading rate as the equipment used did not allow the pressure to be controlled for constant forming speeds. The effects of loading rate (i.e. the time taken to attain the chosen stamping pressure) and stamping speed (compression speed) are related, but loading rate only refers to the final part of the process, occurring after the main deformation stage. For forming above T_m, flexural strength and modulus increased with loading rate before becoming approximately constant [262]. These properties may decrease slightly at higher loading rates. In contrast, when forming in the solid state (below T_m), Zheng et al. [198] observed that an increase in stamping speed decreased the flexural strength due to increased damage formation [198]. For forming above T_m, void content reduced with increasing loading rate before plateauing [262], demonstrating that a critical loading rate is required to ensure that, prior to the matrix being cooled significantly, sufficient pressure is applied to evacuate the air and wet the fibres. Upon cooling to a certain temperature, the viscosity will increase to a level at which full fibre wetting is impossible. Whether this trend is the same for pre-consolidated laminates (in contrast to the commingled material investigated in [262]) has not been widely investigated and is unclear. The low void content present in pre-consolidated material prior to heating may make this parameter less important. Furthermore, loading rate relates to the rate at which pressure was applied after the shape had been achieved, so may not give the same trends as stamping speed, which relates

to deformation speed. Also, stamping speed affects both void content and formability, but which of these has a greater influence on post-form mechanical properties requires further investigation.

Other processing parameters are partly dependent on the forming speed. A faster speed can lead to a higher pressure [221]. The inertia of the die causes greater compression of the blank due to the higher pressure exerted [185] and, hence, causes a reduced thickness [186]. A faster closing speed leads to an increase in stamping temperature [199,221,276] as there is less time for the sample to lose heat prior to mould closure. Too slow a stamping speed can lead to the laminate temperature decreasing below that required for inter-ply slip to occur [185,273], severely reducing the formability and compromising the final part quality through fibre buckling and breakage [276]. The general trend for flexural strength and modulus with variation in speed (for forming above T_m) is shown in Figure 2-36(b), in which an optimum speed which is fast enough to not allow too much cooling to reduce formability significantly, but slow enough not to create too high viscous and friction forces in the laminate, gives the best mechanical properties.

Overall, a forming speed which is sufficiently slow for excessive resin migration and fibre rupture to be avoided but fast enough to not allow the sample to cool below a workable temperature is preferred. Furthermore, higher speeds increase inter-ply friction, see Section 2.5.2.2.1, so a low enough speed to reduce wrinkle formation is also required. Few studies have investigated the effect of forming speed on the mechanical properties of the final part, in particular when using a pre-consolidated laminate as the blank material instead of commingled fabrics, so further detailed study of this is recommended to assist in obtaining optimum stamping speeds. Although a faster forming speed will give a small increase in process cycle time, the holding time is much longer than the stamping time. Therefore, stamping time is not as critical as holding time for overall process cycle time.

2.5.4.3 Pressure

During heating, the sheet thickness increases when the matrix becomes molten because of thermal expansion, phase transformation and, in the case of woven fabrics, due to the fibre waviness increasing [215]. This causes de-bonding at the fibre-matrix and layer-layer interfaces, see Section 2.5.2.3. Therefore, in addition to forcing the material into the mould, a compression load is required to compress

the plies and enhance the consolidation quality, see Section 2.5.2.3. Hence, pressure has a great effect on the post-form mechanical properties, in addition to its effect on formability. In particular, the void content is highly dependent on the holding pressure (also known as stamping pressure). The pressure acting on the material during deformation must also be considered due to the increase in inter-ply shear stress caused by higher normal pressures, see Section 2.5.2.2.1.

Studies in the literature indicate that post-form flexural strength and ILSS may increase with holding pressure up to a certain level and then decrease or plateau with further pressure increases [261–263,267,277]. Mode I fracture toughness follows the same trend, but mode II fracture toughness continues to improve at higher pressures [263]. The in-plane shear modulus and elongation at failure also increase [262,277]. However, the effects on ILSS are particularly unclear. Dai et al. [267] saw an increase then decrease with pressure increasing up to 3 MPa whereas Zheng et al. [261] saw a slight increase between 1 and 3 MPa, but the change was within the experimental error range. Overall, Zheng et al. [261] observed no significant change with pressure increase up to 9 MPa as void decrease and reduction in interlayer adhesion combined to give an almost unchanged ILSS. Load holding enhances material strength compared to position holding [213,215]. Maintaining the pressure as the sheet shrinks gives a good quality bond strength between fibres and matrix. The general trend for flexural strength, ILSS and Mode I fracture toughness with variation in pressure is shown in Figure 2-36(c).

A higher holding pressure promotes re-compaction of the network of fibres and migration of the molten resin into the fibre bundles [261]. This can improve inter-ply and fibre-matrix bonding so may explain the resulting increase in flexural strength and modulus. However, when the pressure is too high, resin overflow occurs along with excessive fibre compression [261,267]. Consequently, it becomes more difficult for resin to flow into the bundles, reducing overall fibre impregnation and hence reducing the capacity for force transmission between fibres and matrix. This can ultimately compromise the mechanical properties.

Overall, an optimum holding pressure must be chosen to give a high level of consolidation while avoiding resin overflow and excessive fibre compression to achieve the optimum mechanical properties. Furthermore, higher normal pressures increase the inter-ply shear stress, see Section 2.5.2.2.1, so

using a low enough pressure during the deformation stage to reduce wrinkle formation must also be considered for good formability. The relationship between ILSS and holding pressure is not clearly understood, so further studies in this area are recommended.

2.5.4.4 Holding time

After the die is closed, the part is usually held in the mould to allow further cooling and consolidation to take place before removal. If the part is removed prior to the completion of matrix solidification, elastic strains in the fibres cannot be arrested [221]. The resulting distortions and shrinkage can give final part shapes which are different to those intended by the mould design. The continued application of pressure while the matrix is still molten allows more time for matrix migration which can improve consolidation quality and reduce void content. This is particularly important for parts formed at relatively lower temperatures and pressures as they require a longer time to achieve good consolidation [181]. Hence, holding time has a significant effect on the post-form mechanical properties and the geometric accuracy of the component.

In general, an increase in holding time appears to improve the ILSS and flexural properties [262,264,267,269]. However, at long holding times no further changes occur. At short holding times, a reduction in flexural strength and modulus may occur if the holding time is less than the solidification time of the matrix [262]. Furthermore, almost identical ILSS values can be obtained for samples moulded at a high temperature with a shorter holding time and those moulded at a lower temperature with a longer holding time [267]. In contrast to samples made from commingled fibres, holding time appears to have little effect on the shear strength of pre-preg due to the strong fibre-matrix interaction already present [269]. Therefore, holding time may be less important for pre-consolidated material. The general trend for flexural strength and modulus and ILSS with variation in holding time is shown in Figure 2-36(d).

A reduction in the geometric inaccuracy can be observed with increasing holding time [185,221]. The elastic fibre deformation is not completely prevented if the matrix has not fully solidified. This leads to a distorted cross-section which reduces the final part angle [221]. A solidified matrix can

reduce movement of the bent fibres, allowing uniform cross-sections and, hence, uniform parts to be achieved [185].

Overall, too short a holding time can lead to high void contents but too long a holding time can lead to a long processing time. A balance between achieving a low void content and attaining an economical processing time is required to establish an optimum holding time for a given material. A shorter holding time has the benefit of speeding up the manufacturing process and reducing costs as holding time makes up the largest portion of total processing time.

2.5.4.5 Cooling rate

The cooling rate experienced by the deformed laminate is dependent on the mould temperature. A higher mould temperature gives a lower cooling rate. Cooling rate is likely to have an effect on the microstructure of the material, particularly the degree of crystallinity which tends to decrease with a higher cooling rate. This will, in turn, affect the mechanical properties and the amount of volumetric shrinkage. Furthermore, cooling rate is not uniform throughout the material, with greater cooling rates being experienced by surface layers. This reduces the time available for consolidation in these regions which can increase void content [249]. Hence, cooling rate has a great influence on the post-form mechanical properties. In particular, the flexural strength and modulus and fracture toughness are particularly sensitive to cooling rate.

The flexural strength and ILSS generally improve with a decrease in cooling rate [217,269,278–280], as do the elastic and flexural modulus [279–281]. The longitudinal flexural strength is more sensitive to cooling rate than the fibre-dominated longitudinal tensile strength and modulus, given the high dependency on fibre-matrix bonding and matrix strength during bending [279]. Fracture toughness increases with an increase in cooling rate [281,282]. The general trend for flexural strength and modulus, ILSS and elastic modulus with variation in cooling rate is shown in Figure 2-36(e). Note that fracture toughness shows the opposite trend to these properties with variation in cooling rate.

The higher degree of crystallinity obtained due to a decreased cooling rate leads to the improvement in strength and modulus [217,280]. Furthermore, a lower cooling rate allows the part to

stay molten for longer so gives a more uniform consolidation pressure over the part [217]. This also gives more time for the applied pressure to force the resin into the fibre bundles. Therefore, more entanglement occurs between the molecular chains and the fibres, improving the interfacial bond strength [280]. Slow cooling forms more closely packed crystalline lamellae in the fibre-matrix interphase region, imparting strong fibre-matrix interfacial bonds which undergo debonding in a relatively brittle manner [278,279]. The stress transfer between fibre and matrix is increased by the thicker crystalline region around the fibre [283]. Faster cooling forms more amorphous regions of polymer which form a much weaker fibre-matrix interfacial bond and undergo ductile failure [278,279]. Although the improvement in fracture toughness is due to extensive matrix plasticity, the increased matrix ductility may not lead to as great an increase in fracture toughness as might be expected, because of premature interface debonding resulting from the reduced fibre-matrix interfacial strength [282].

Overall, lower cooling rates tend to give superior flexural and shear properties, although, the fracture toughness can be reduced. However, lower cooling rates lead to increased processing times and hence make manufacturing more expensive. An optimum compromise must be made based on the required material properties and application to give an appropriate cooling rate for processing.

2.5.4.6 Effect of process parameters summary

A summary of the effect of an increase in certain processing parameters on a selection of post-form mechanical and physical properties is shown in Table 2-4. Figure 2-36 demonstrates visually the general trends of increasing certain processing parameters on a selection of mechanical properties. It should also be noted that some of these independent trends are actually highly inter-dependent on other processing parameters. For example, the applied pressure will affect the required holding time and using too low a pressure may change the indicated holding time trend. Furthermore, these trends assume a certain temperature is reached, e.g. for temperatures significantly below T_m, stamp forming cannot take place and the effect of these parameters becomes irrelevant.

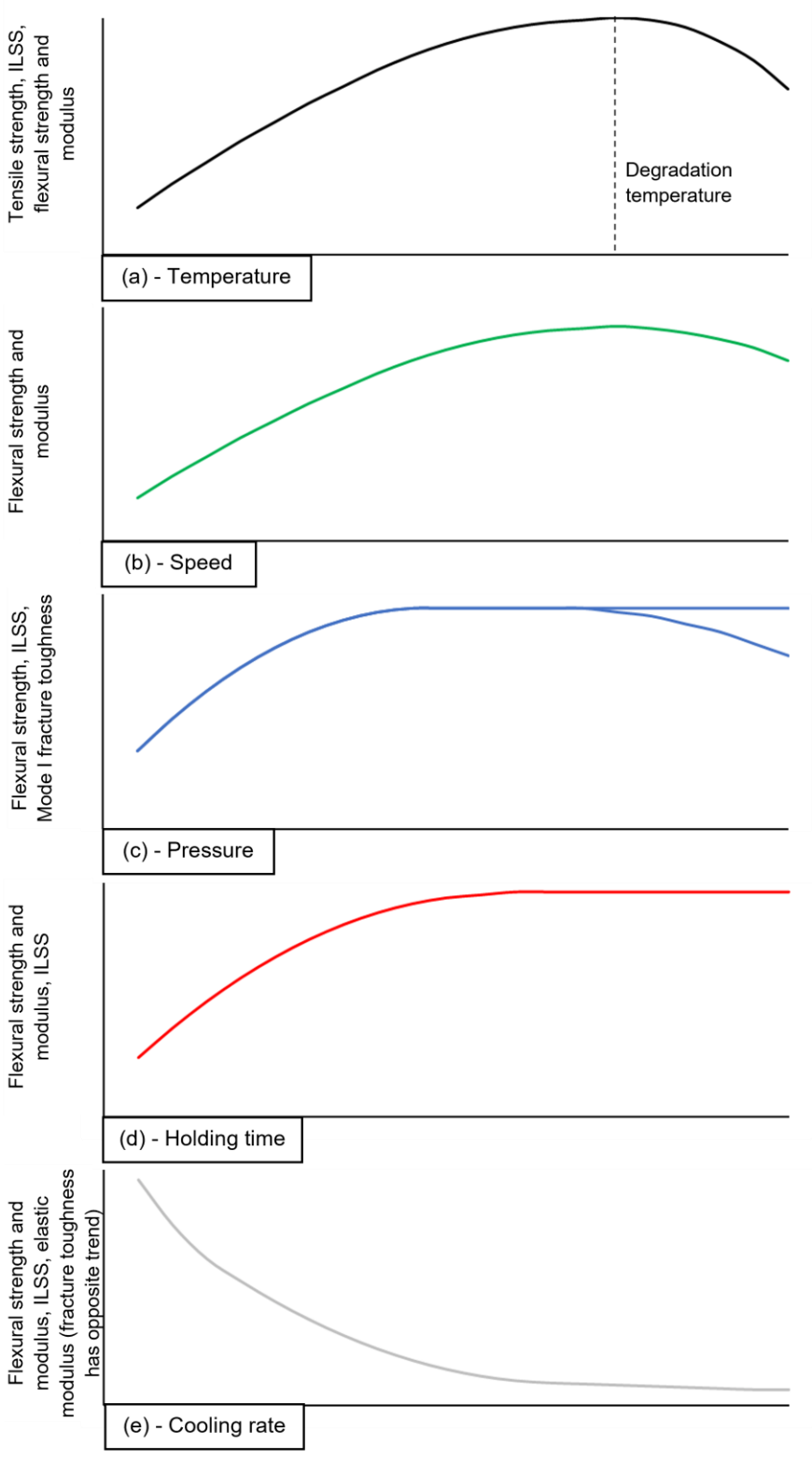


Figure 2-36: General trends of the effect of an increase in a certain processing parameter on some post-form material properties. Increase in: (a) - temperature, (b) - speed, (c) - pressure, (d) - holding time, (e) - cooling rate [197,201,217,261–264,267–269,277–281].

Table 2-4: Effect of an increase in certain processing parameters on a selection of mechanical and physical properties.

	Tensile strength	Flexural strength and modulus	ILSS	Fracture toughness	Void content
Temperature	+	+	+	+	-
Speed		+			-
Pressure	+	+	+ or unchanged	+	-
Holding time		+	+		-
Cooling rate	-	-	-	+	+

*+ indicates increase, - indicates decrease

2.5.5 Forming summary

This review section provides an extensive survey of current fibre-reinforced thermoplastic (FRTP) stamp forming technology. A comprehensive analysis of the deformation mechanisms, the frictional behaviour and the formation of defects in FRTPs during stamp forming, as well as the effect of different processing parameters on mechanical properties of as-formed parts, has been conducted. Major forming defects, including wrinkles and voids, have been discussed. Void content has a large influence on resulting mechanical properties so must be minimised as part of optimising the process parameters. Wrinkling remains a challenge during stamp forming but can be minimised through a detailed knowledge of material behaviour and the use of computational modelling and simulations. The main findings of this review are summarised below.

It is concluded that inter-ply shear stress increases with a decrease in temperature, an increase in pressure or speed, or having adjacent plies with the same orientation. Further friction studies on high performance FRTPs, such as CF/PEEK and CF/PPS, are recommended, particularly at a wider range of test temperatures. These materials offer significant potential in aerospace and automotive applications. Therefore, a detailed understanding of their behaviours during stamp forming can pave the way to high quality and economical production of parts.

Higher temperatures can lower the probability of wrinkle formation and give better mechanical properties through reducing voids and improving consolidation. However, the temperature must remain below the temperature for the onset of matrix degradation (T_{deg}). Higher forming speeds can increase the chance of wrinkle formation, but may prevent excessive laminate cooling prior to the completion of forming. Higher pressures increase the inter-ply friction but improve post-form mechanical properties through improved consolidation and void reduction, although excessive pressure must be avoided to prevent resin overflow and excessive fibre compression. Longer holding times lower the void content but increase the cycle time and cost of the manufacturing process. Higher cooling rates can improve toughness but reduce other post-form material properties, allowing a suitable cooling rate to be chosen based on the required mechanical properties for a specific application. Determining the optimum processing parameters which give the most desirable post-form mechanical properties and processing time for a particular material and part requires a systematic study of the material and a thorough understanding of the aforementioned factors. Relatively few studies have directly investigated the effect of forming speed on the post-form mechanical properties, so more detailed study of this is also recommended.

With further developments in understanding of FRTP material behaviour under stamp forming conditions, the manufacture of increasingly complex shapes at reasonable costs is possible. This will increase the number of applications for FRTP parts in the transport industry, allowing improved efficiencies and emissions targets to be reached. Investigating more extensive material constituents, such as new thermoplastic matrices, may push the current boundaries for structural performance, manufacturability and cost to new levels.

Chapter 3 Materials and experimental procedures

3.1 Introduction

The research presented in this thesis involved the testing of carbon fibre-reinforced polymer (CFRP) composite materials. This chapter explains the methods through which the materials were manufactured and the test panels produced, as well as the testing and inspection methods employed during the research.

3.2 Materials and manufacturing processes

3.2.1 Thermoset matrix material (i.e. CF/Epoxy)

3.2.1.1 Pristine panels

The thermoset matrix panels used in the studies throughout this thesis were formed from unidirectional (UD) CF/Epoxy pre-preg (MTC510-UD300-HS-33%RW) supplied by SHD Composites Ltd, UK. This pre-preg is composed of an epoxy matrix (MTC510) and T700 carbon fibres at a fibre volume fraction of 60%. Table 3-1 gives the measured and theoretical properties of the pre-preg. This data was supplied by SHD Composites Ltd, UK. To form the panels, the pre-preg was cut and assembled in quasi-isotropic (QIT) lay-ups of $[45/-45/0/90]_s$ and $[45_2/-45_2/0_2/90_2]_s$, i.e. the same lay-up but with two blocked plies in each direction in the case of the thicker panels. Flat laminates approximately were formed from the pre-preg using an autoclave. A constant pressure of 6 bar was used throughout the curing cycle, with a 2 °C/min temperature ramp up to 110 °C, at which point a 120 minute dwell time was used. The glass transition temperature of the cured CFRP was 133 °C.

Table 3-1: Materials properties for MTC510 UD pre-preg, supplied by SHD Composites Ltd, UK [284].

Test	Property	Result		Test Method
Fibre volume fraction (VF)	Measured	60.20	%	N/A
	Theoretical	57.71	%	
Cured ply thickness (CPT)	Measured	0.286	mm	N/A
	Theoretical	0.289	mm	
Tension 0°	Tensile strength	2282	MPa	BS EN ISO 527-5
	Tensile modulus	119.3	GPa	
	Poisson's ratio	0.34		
Tension 90°	Tensile strength	54	MPa	BS EN ISO 527-5
	Tensile modulus	8.2	GPa	
	Poisson's ratio	0.01		
Compression 0°	Compressive strength	1067	MPa	EN 2850 Type B
	Compressive modulus	113.6	GPa	
Compression 90°	Compressive strength	200	MPa	EN 2850 Type B
	Compressive modulus	9.3	GPa	
In-plane shear ±45°	In-plane shear strength	99	MPa	ASTM D3518
	In-plane shear modulus	3.6	GPa	
Interlaminar shear strength	Interlaminar shear strength	84.8	MPa	BS EN ISO 14130
Dynamic mechanical analysis (DMA)	T_g onset	123	°C	Modified ASTM D7028 (Single cantilever)
	Peak tan delta	133	°C	

Using a cut-off saw, the laminates were cut into panels of four different sizes: 150 mm x 100 mm, 160 mm x 100 mm, 180 mm x 100 mm and 200 mm x 100 mm. Most panels were cut to a size of 150 mm x 100 mm, see Figure 3-1, to adhere to ASTM Standard D7136 [285]. The three sizes of longer panel were only used in the study presented in Chapter 7. The 0° plies were aligned with the longer

edge of the panels which had a thickness, t, of either 2.3 mm or 4.6 mm – in the case of the 150 mm x 100 mm panels – or only 4.6 mm – in the case of all three panels with length greater than 150 mm.

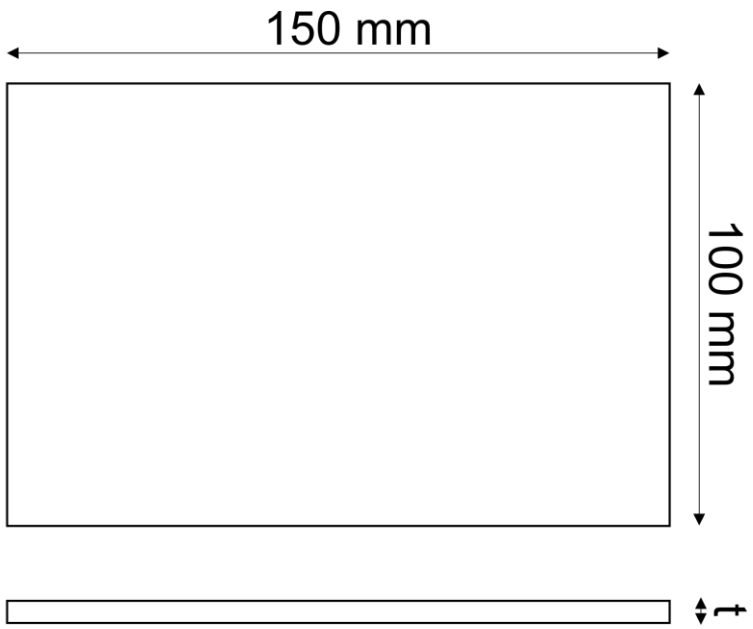


Figure 3-1: Diagram of a pristine CF/Epoxy panel.

3.2.1.2 Repaired panels

Patch repairs were manufactured by Polar Manufacturing Ltd, UK. A 40 mm diameter disc was removed from the centre of a pristine panel in two stages: roughing and finishing. Initially a 2 mm diameter carbide corn-cutter was used (roughing) followed by a 2 mm diameter carbide 3-flute end mill (finishing). This hole represents the area of damage which would be caused by an impact at 7.5 J and was kept constant for all patch-repaired panels. Furthermore, this area of damage is large enough to cause a considerable change in the response of the panel, yet is small enough not to be affected by edge effects. A circular patch of diameter, D, (either 55 mm or 65 mm) and formed of QIT CF/Epoxy with lay-ups $[45/-45/0/90]_s$ or $[45_2/-45_2/0_2/90_2]_s$ (thicknesses of 2.3 mm and 4.6 mm, respectively) was then adhered over the hole using a single layer of MTFA-500 toughened epoxy-film adhesive of nominal thickness 0.25 mm, supplied by SHD Composites Ltd, UK, which was then cured. Table 3-2 gives some of the properties of the film adhesive. This data was supplied by SHD Composites Ltd, UK. A constant pressure of 6 bar was used throughout, with a 3 °C/min temperature ramp up to 130 °C, at which point a 90 min dwell

time was used. Prior to bonding, the surfaces of the parent panel and patch were prepared using 50 grit sanding paper and then cleaned with acetone. Figure 3-2 shows a schematic of the final repair configuration and Figure 3-3 shows an image of repaired panel with a 65 mm diameter patch.

Table 3-2: Materials properties for MTFA-500 film adhesive, supplied by SHD Composites Ltd, UK.

Test	Property	Result		Test Method
Climbing drum peel	Peel strength (T)	437	N	ASTM D3165
	Peel strength (L)	538	N	ASTM D1781
Dynamic mechanical analysis (DMA)	T_g – storage modulus onset	141	°C	AITM 1-0003 Issue 3
	T_g – tan delta peak	150	°C	

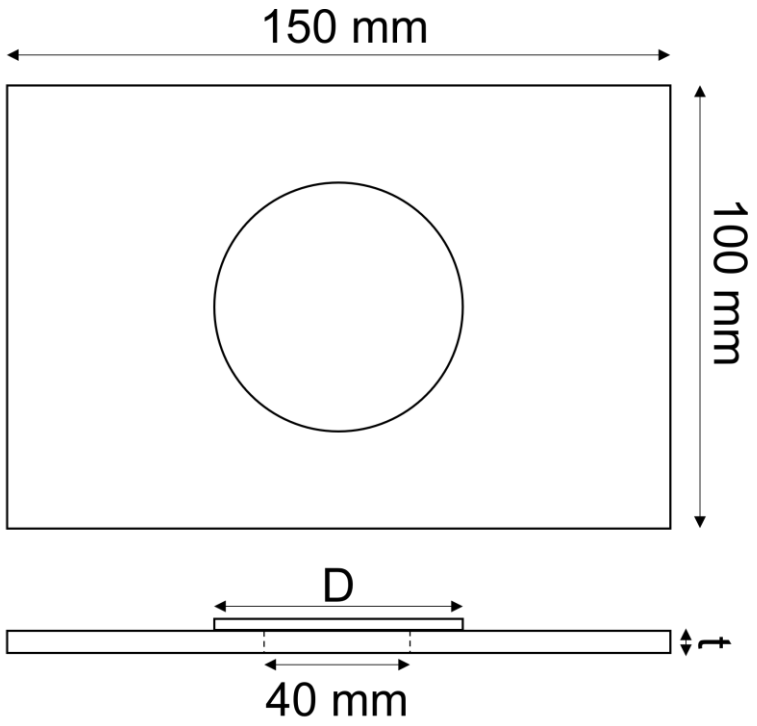


Figure 3-2: Diagram of a repaired CF/Epoxy panel.

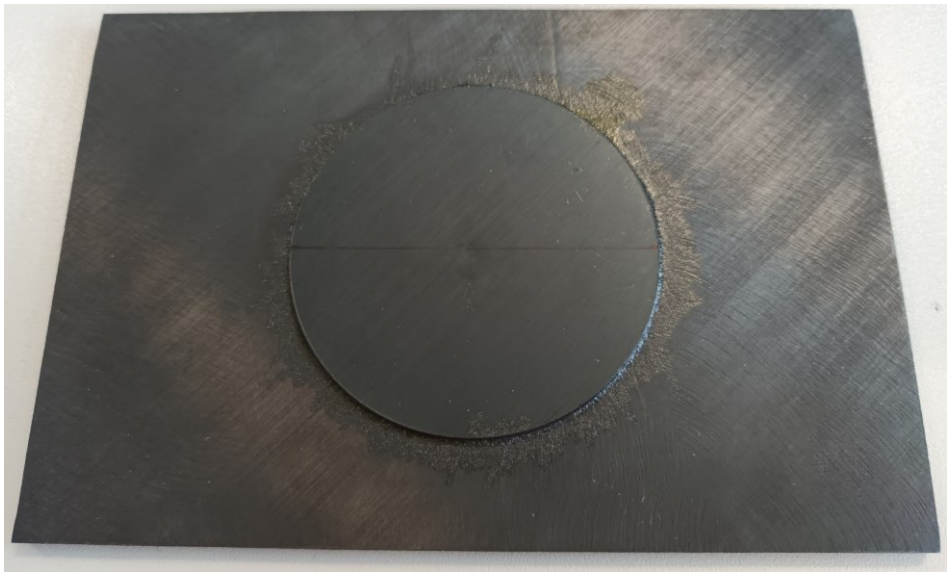


Figure 3-3: Repaired panel with a 65 mm diameter patch and no plug.

For patch + plug repairs, the same procedure was followed, but with the addition of a push-fit plug with an identical lay-up to the parent laminate being placed into the 40 mm hole prior to curing the adhesive. The plug was orientated to match the orientation of plies within the parent panel. During the heating and curing process, the adhesive was able to flow into the gap between the plug and parent laminate, thus holding the plug in place beneath the patch. This would help to prevent plug dislodgement during the impact tests.

3.2.2 Thermoplastic matrix material (i.e. CF/PPS)

The thermoplastic matrix panels used in this thesis were formed from 5 harness satin woven CF/PPS pre-preg supplied by Toray Advanced Composites, The Netherlands. This pre-preg is composed of a Polyphenylene sulphide (PPS) matrix (TC1100) and T300JB carbon fibres at a fibre volume fraction of 50%. Table 3-3 gives the measured and theoretical properties of the pre-preg. This data was supplied by Toray Advanced Composites, The Netherlands. Satin weaves have fewer intersections of warp and weft and an improved drapability compared to plain weaves [286].

Table 3-3: Materials properties for TC1100 woven pre-preg, supplied by Toray Advanced Composites, The Netherlands [287].

Test	Property	Result		Test Method
Fibre volume fraction (VF)	Measured	50	%	N/A
Tension 0°	Tensile strength	752	MPa	EN 2597 Type B
	Tensile modulus	58.0	GPa	
Tension 90°	Tensile strength	785	MPa	EN 2597 Type B
	Tensile modulus	56.0	GPa	
Compression 0°	Compressive strength	619	MPa	EN 2850 Type B
	Compressive modulus	53.0	GPa	
Compression 90°	Compressive strength	609	MPa	EN 2850 Type B
	Compressive modulus	53.0	GPa	
In-plane shear ±45°	In-plane shear strength	130	MPa	AITM 1-0002
	In-plane shear modulus	3.9	GPa	
Flexural 90°	Flexural strength 90°	842	MPa	EN 2562 A
	Flexural modulus 90°	45.0	GPa	

To form the panels, the pre-preg was cut into 158 mm x 108 mm pieces and eight plies were assembled with identical orientation of the warp parallel to the longer edge, see Figure 3-4. Flat laminates were formed from the pre-preg using a specially designed stainless-steel mould[3], see Figure 3-5, which was manufactured in-house, in a LP_M4SH50 Manual Hot Press, supplied by MSE Teknoloji Ltd., Türkiye, see Figure 3-6. Teflon sheets were placed on the top and bottom surfaces of the group of 8 plies, see Figure 3-7 and release agent was applied to prevent the laminate sticking to the mould. An initial pressure of 10 bar was applied during the initial temperature ramp up to 320 °C which was

[3]The mould was designed using preliminary tests done on an 82 mm x 82 mm mould of the same style.

reached after 45 minutes. The pressure was then increased to 27.6 bar for the rest of the cycle, in line with the recommended manufacturing parameters [288], and a 20 minute dwell time at 310 ºC was used. Following this, the heating in the hot plates was turned off and the mould was allowed to air cool until a temperature of 200 °C had been reached. At this point, water cooling of the hot plates was used to reduce the laminate temperature to 60 °C in approximately 10 minutes. Once this temperature had been reached, the pressure was removed and the mould was removed from the hot press. A graph showing how temperature and pressure varied during the forming process is shown in Figure 3-8.

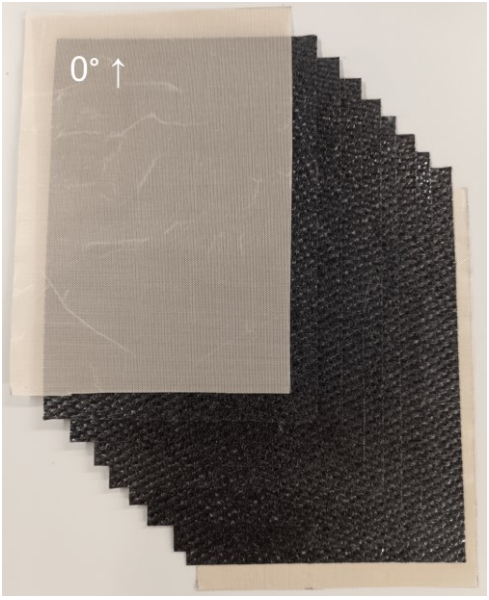


Figure 3-4: CF/PPS pre-preg and Teflon sheeting before forming into a laminate.

The formed 160 mm x 110 mm laminate had a thickness of 2 mm and was then trimmed using the cutting method described in Section 3.3.4.1 into a panel of size 150 mm x 100 mm, in accordance with ASTM Standard D7136 [285]. An optical microscope image of a pristine panel after forming is shown in Figure 3-9. The low void content highlights that a high enough temperature was used during the forming process to provide sufficient matrix fluidity for void elimination and matrix distribution. However, a low enough temperature was still used to prevent thermal degradation increasing the size of the voids.

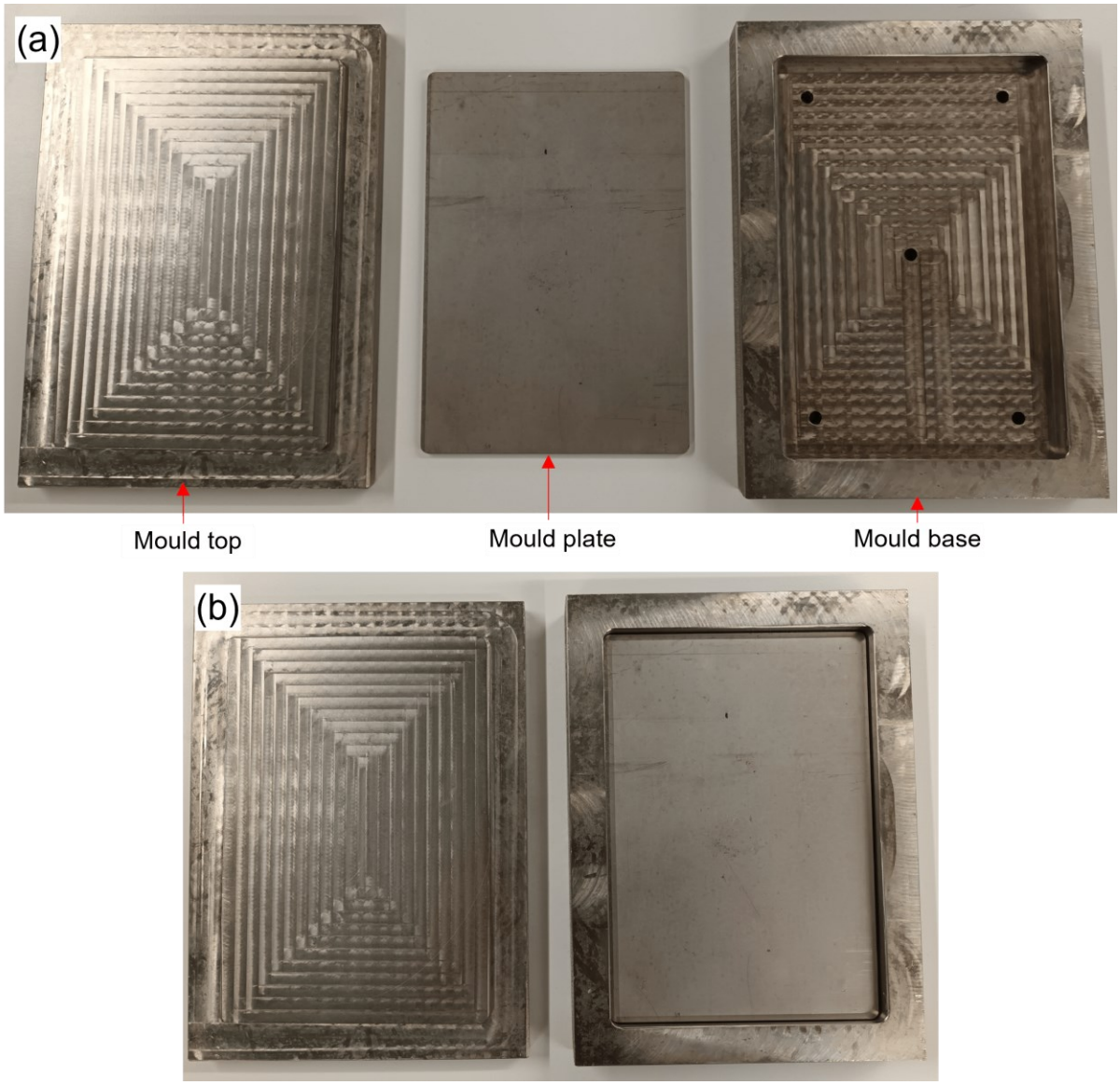


Figure 3-5: Stainless-steel mould (a) with all three parts laid out - base, plate and top and (b) with plate inside the base, ready for pre-preg to be placed inside.



Figure 3-6: LP_M4SH50 manual hot press with attached cooling unit.

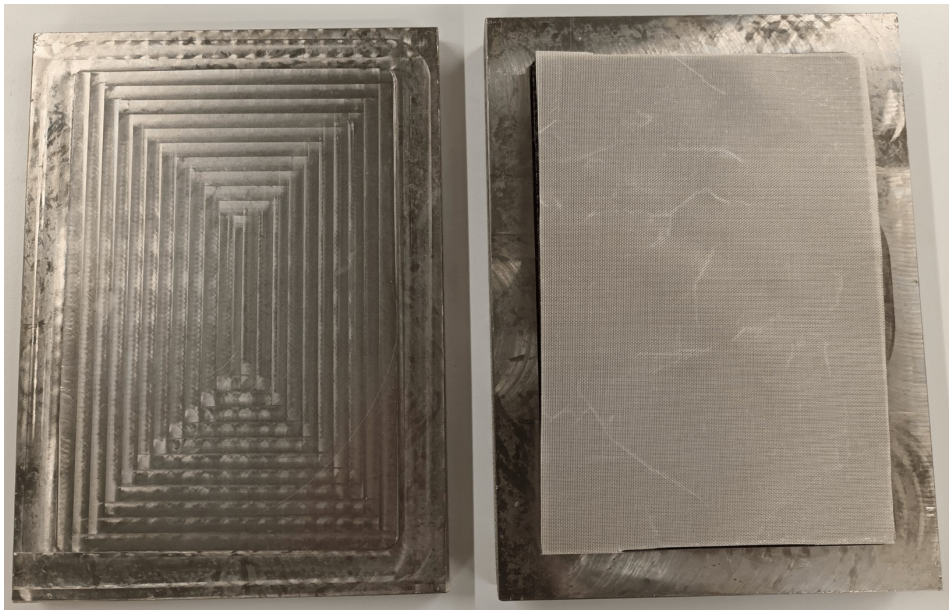


Figure 3-7: Stainless-steel mould with CF/PPS pre-preg and teflon sheets positioned inside for forming.

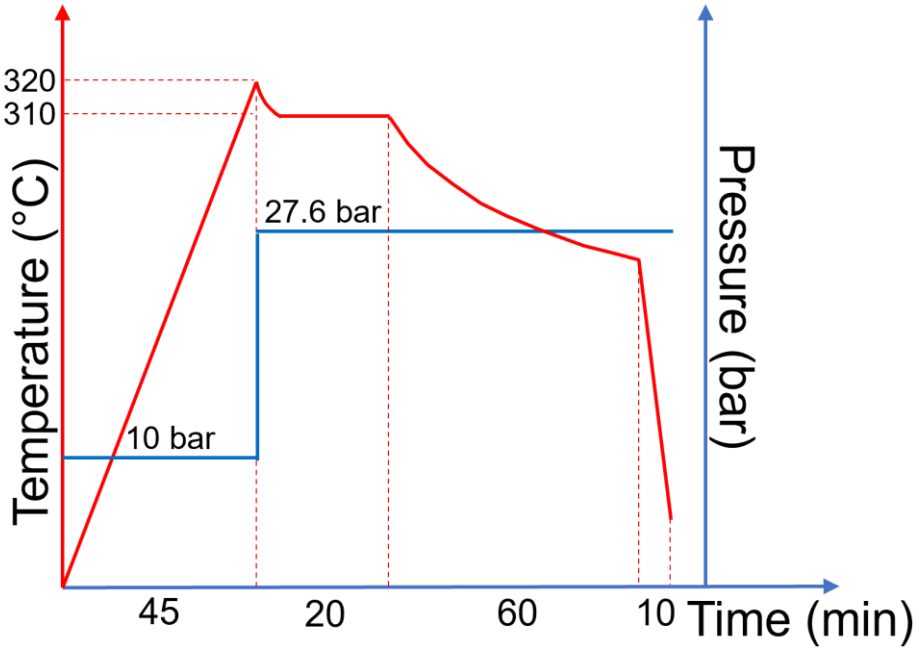


Figure 3-8: Graph showing the temperature and pressure of the CF/PPS pre-preg during forming into a laminate using the manual hot press.

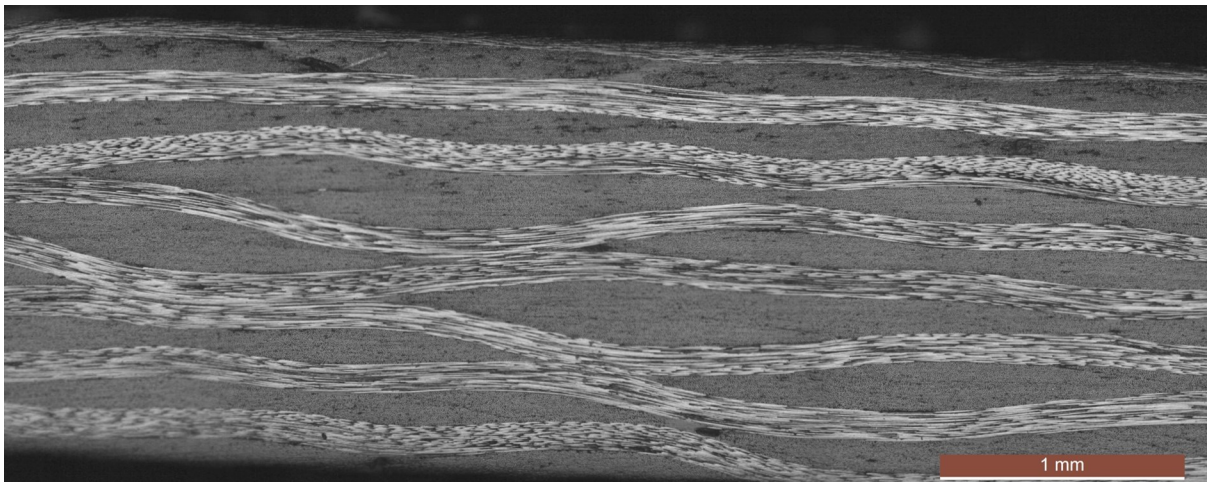


Figure 3-9: Optical microscope image of a pristine CF/PPS panel.

3.3 Overview of experiments

3.3.1 Low-velocity drop-weight testing

3.3.1.1 Drop-weight tower

Low-velocity drop-weight testing was undertaken in accordance with ASTM Standard D7136 [285] using an Instron CEAST 9340 drop-weight tower, shown in Figure 3-10, fitted with a hemispherical stainless-steel impactor of diameter of 16 mm. CFRP panels were clamped onto a steel picture frame using four rubber-tipped toggle clamps which prevented slippage of the panel during the impact test, see Figure 3-10(b) and (c). Three guide pins allowed the panel to be aligned in the centre of the impact zone, above a window cut-out of 125 mm x 75 mm. The impactor had an overall mass of 5.27 kg and was dropped from varying heights to give impact energies between 2 J and 35 J, with corresponding impact velocities between of 0.87 $m.s^{-1}$ and 3.65 $m.s^{-1}$, respectively. A load cell located in the forward section of the impactor measured the resulting load versus time data, with a sampling frequency of 500 kHz. Multiple impacts were prevented by an anti-rebound system, which was able to catch the impactor after the first impact.

The drop-weight tower was connected to a PC equipped with a CEAST DAS 64K data acquisition system, through which the tower was controlled and the data collected. Before the impact test, information regarding certain test parameters, such as the overall mass of the drop-weight, chosen impact energy and panel thickness, were entered into the CeastVIEW software. From this information, the software calculated the required impact velocity and corresponding drop height, before moving the impactor to the correct height above the panel. No software filtering was applied to the load versus time data that was gathered and the displacement was determined by integration of the load versus time trace assuming Newton's second law. Duplicate experimental tests were undertaken and there was good agreement from these replicate tests.

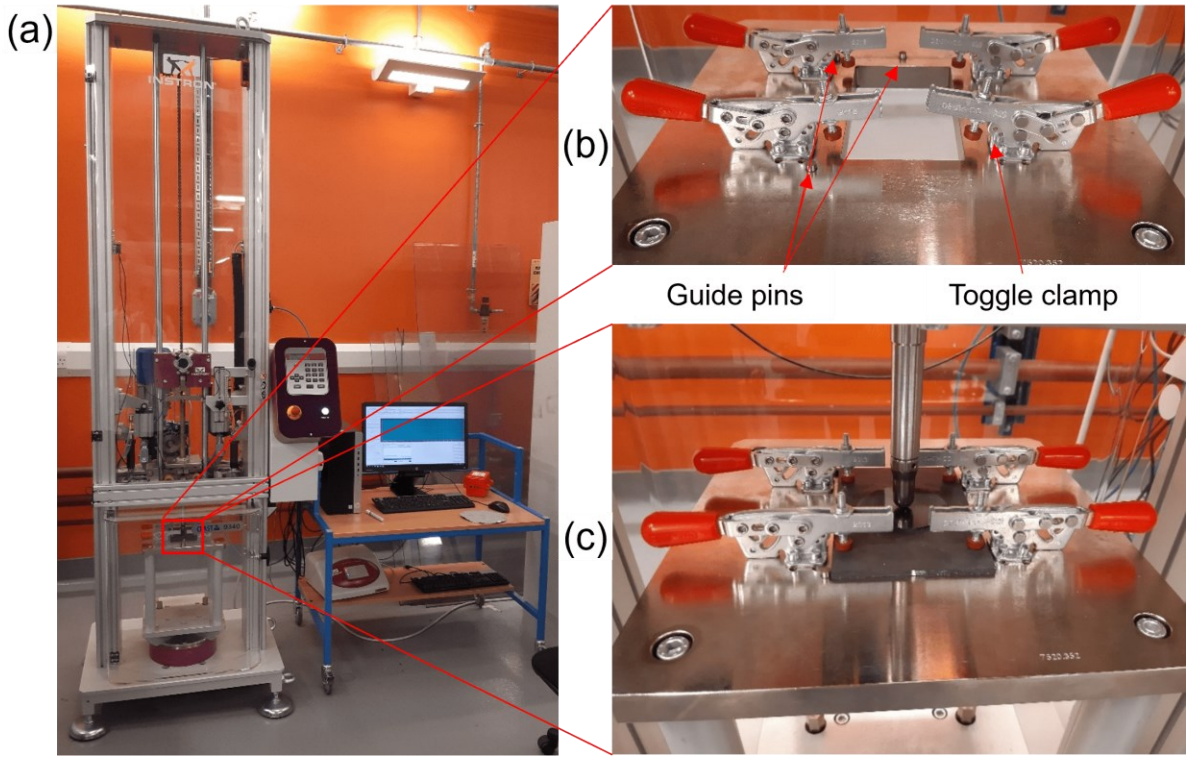


Figure 3-10: (a) Drop-weight tower and PC, (b) window cut-out in impact zone and (c) hemispherical impactor and clamped repaired panel.

3.3.1.2 High-speed cameras

For some impacts, two Photron high-speed cameras were used to capture the impact. The cameras were set up in a master-slave configuration and were triggered at the same time. One camera viewed the panel from above at an angle of around 25° to the horizontal and the other was set to view in the plane of the panel, see Figure 3-11. A frame rate of 10000 frames per second was used for all panels. LED lights were used throughout to light up the panel.

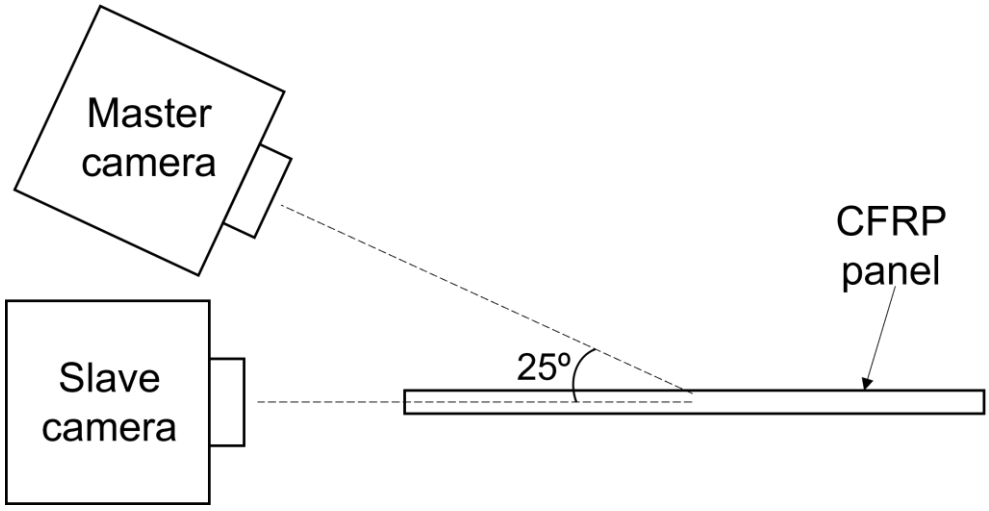


Figure 3-11: Diagram showing the setup of the two high-speed cameras used to record impacts on the CFRP panels.

3.3.2 Ultrasonic C-scanning

Both inter- and intralaminar damage can be formed during impact and various techniques can be used to evaluate these forms of damage. Although optical microscopy gives a detailed image of both types of damage, sectioning of the material is required, meaning that the material can no longer be used as part of a structure. In contrast, non-destructive testing (NDT) techniques can show accurate depictions of the damage within a material without causing further damage. Hence, they are desired when inspecting structures which are in use or required for use in the future.

Ultrasonic C-scanning, a non-destructive method of determining the level of delamination damage within the composite material, was utilised to examine damage in the composite panels. Scanning was undertaken both before and after the impact tests to allow damage accumulated during manufacturing, transport and storage to be identified separately to damage caused by the impact test.

Scanning was undertaken using a portable ‘Prisma 16:64 TOFD’ ultrasonic C-scan device with a phased-array probe of scanning frequency 5 MHz, supplied by Sonatest Ltd., UK. This phased-array probe was attached to a 16 /mm encoder which measured the position of the probe along the scan axis. A water spray or ultrasonic gel was applied to the impacted surface of the panel to act as a contact agent to improve the transmission of the ultrasonic waves from the transducer probe into the composite

and to reduce surface noise. These devices are shown in Figure 3-12. Prior to scanning, a configuration was set up on the device based on the material being used and the thickness of the material. A suitable gate setting was chosen to cover the positive waves reflected from the internal damage or the rear surface of the panel. The ultrasonic waves are reflected back to the transducer upon interacting with any delamination damage in the panel, and the position and size of the interlaminar damage can be determined from the total travel time (which gives the location of the delamination) and amplitude received by the transducer (which gives the size of the delamination), respectively. The C-scans taken in the lab were processed using UTstudio+ 4.2.4 software, through which surface noise could be filtered out through alterations to the gate settings, leaving high-quality images of only the delamination damage area.

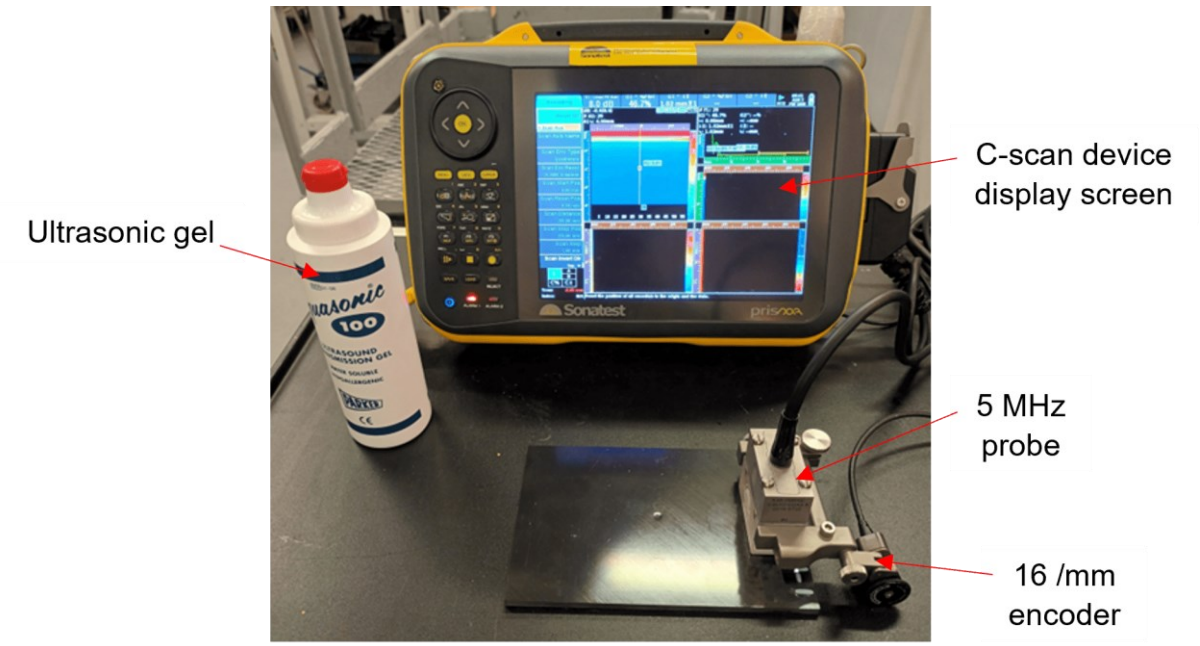


Figure 3-12: The equipment used for C-scanning the CFRP panels.

To scan the entire surface of a panel, the surface was divided into up to three strips and a scan was taken along each strip. These strips were stitched together to produce an overall C-scan damage map for a panel. The resulting C-scan damage maps show the damage area as a function of depth through the panel thickness, with different colours corresponding to different depths throughout the material. The total damage area was calculated by counting the number of pixels that were not dark blue in colour, since dark blue corresponds to areas of the laminate free from interlaminar damage.

3.3.3 Indentation depth measurement

Indentation measurements were taken following each impact using two different methods. A photograph of a typical indentation caused by the striking of the impactor on the CFRP panel is shown in Figure 3-13. Firstly, a handheld digital depth gauge was used to measure the indent depth immediately after, 24 hours after and 48 hours after impact. The depth reduction over time due to relaxation was minimal (no more than 20 microns) and the permanent indentation values taken after 48 hours are used in the analysis for all panels. For each measurement value, the indentation depth was measured eight times. Each time the gauge was rotated by 45° in order to account for any surface defect which could have raised the gauge and given an inaccurate depth reading. An average was taken to give the measurement value.



Figure 3-13: Photograph of a CF/Epoxy composite panel 150 mm x 100 mm in size with a thickness of 4.6 mm after an impact of 7.5 J showing a typical surface indentation [87].

Secondly, an Olympus Lext OLS5000 Confocal Laser Scanning Microscope was used to give a 3D surface scan of the centre of each panel, either 12 mm x 12 mm or 18 mm x 18 mm in size, from which an accurate value of the surface indentation could be identified (after removing any effects from any tilting of the panel). Figure 3-14 shows that the results from the Confocal microscope aligned closely with measurements from the handheld depth gauge, justifying that the handheld gauge could give

accurate indentation depth readings in a quick, easy and cheap process. Data from the Confocal microscope also allowed depth plots of entire indentations to be produced, as well as cross sections.

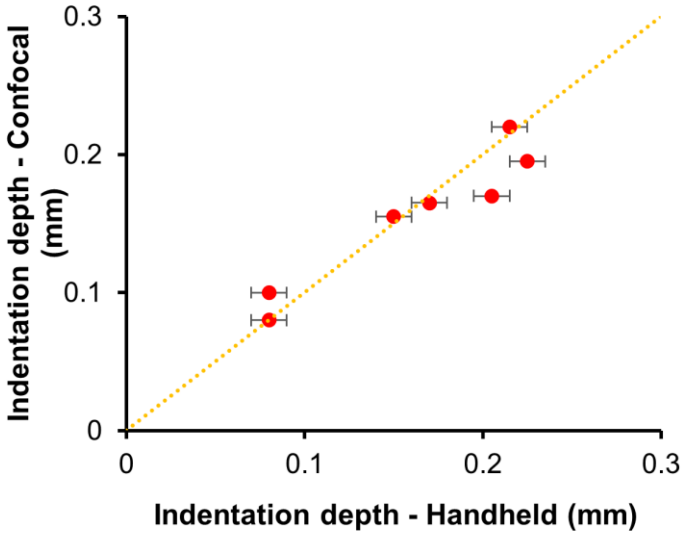


Figure 3-14: The indentation depth in CF/Epoxy composite panels impacted once, measured using the Confocal laser scanning microscope versus using the handheld gauge [87].

3.3.4 Compression-after-impact (CAI) testing

Compression-after-impact (CAI) was undertaken in accordance with ASTM Standard D7137 [289] using a 250 kN Instron Universal Testing Machine, see Figure 3-15. The machine was controlled by a connected PC with accompanying Instron Bluehill Universal software, through which the experimental data was also recorded. The impacted composite panel was held in a CAI test rig, see Figure 3-15, which is specifically designed to suppress global buckling behaviour by supporting the edges of the panel and induce failure by causing delamination to spread. This rig and the associated standard requires panels of dimension 150 mm x 100 mm for testing. Therefore, prior to testing, the 160, 180 and 200 mm long panels were cut to approximately 152 mm in length (keeping the damage centred around the middle of the panel) and ground down to an even 150 mm across the entire length using the methods described in Section 3.3.4.1, ensuring that the edge of the panel was completely flat. Not having a flat edge could cause stress concentrations in the panels, leading to failure occurring away from the delamination damage zone.

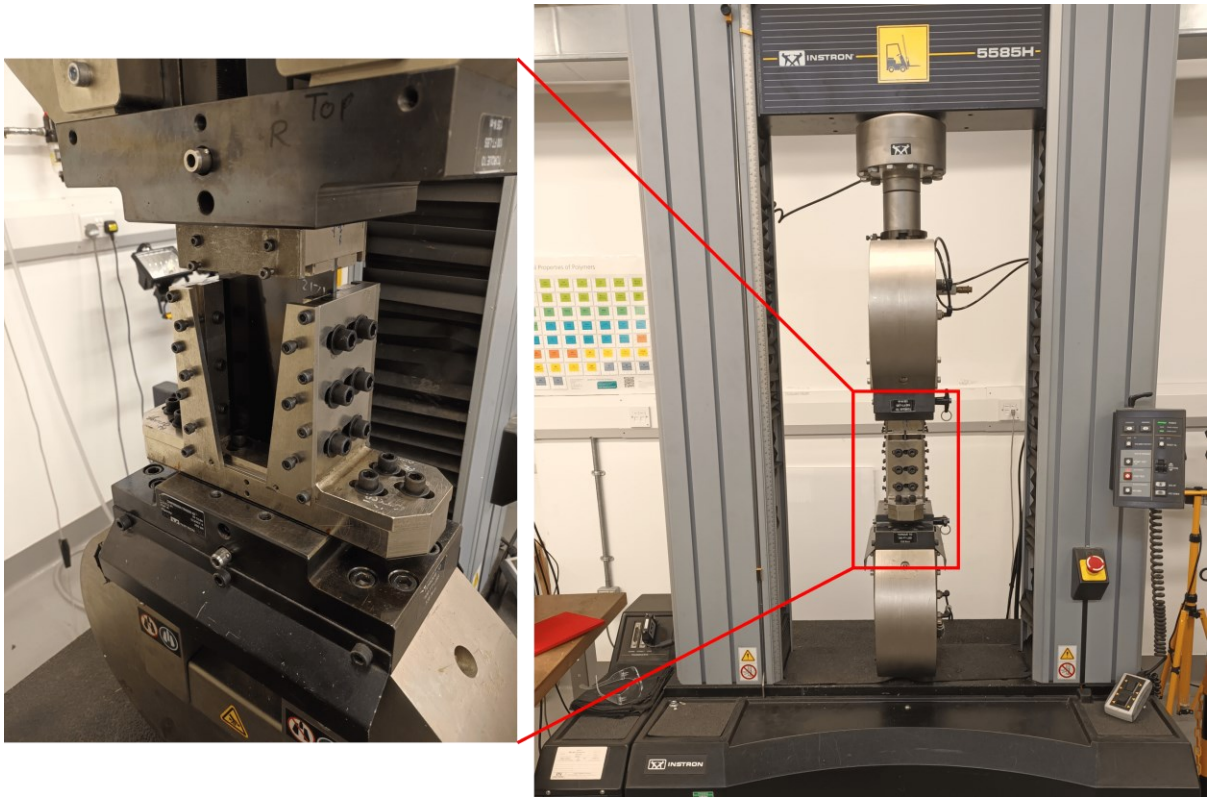


Figure 3-15: CAI testing set-up, showing the CAI test rig in a 250 kN Instron Universal Testing Machine.

Once installed in the rig, the panels were tested in compression with a constant displacement rate of 1.25 mm/min. The load, displacement and time were recorded. Once failure occurred (i.e. once a significant drop in load was detected), the machine stopped automatically to prevent further damage occurring in the panel. From the acquired data, load versus displacement graphs were plotted, allowing the residual compressive strengths (or CAI strengths) to be compared.

3.3.4 Microscopy

3.3.4.1 Preparation

Prior to being viewed under a microscope, the impacted panels were sectioned using a Brillant 220 cutting machine, see Figure 3-16, using a diamond blade rotating at 3,000 rpm. Support plates were used on either side of the blade to reduce blade deflection during the cutting process. The panels were secured to a bi-axis plate and lined up with the diamond blade, ensuring the cut was directly through the indentation and parallel to the shorter (i.e. 100 mm) edges. During cutting, a feed rate of 0.1 mm

per second ensured no additional damage was induced in the panel during the cutting process. This method was also used to trim the formed CF/PPS panels by removing 5 mm of material from each edge.

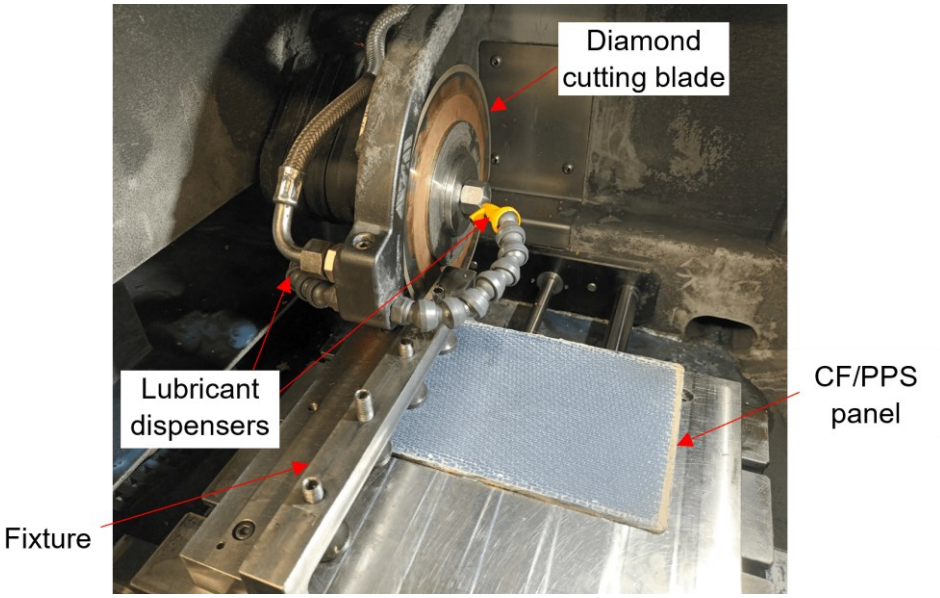


Figure 3-16: Photograph of the inside of the Brillant 220 cutting machine showing the general set-up used for cutting the panels with the diamond blade.

After sectioning, initially some samples were set in an epoxy filler to improve ease of sample preparation (i.e. grinding and polishing) and supporting in the microscopes. Later samples were not set in epoxy as the epoxy had filled some of the delaminations, making them less distinct compared to the rest of the sample and therefore more difficult to view. It was still possible to prepare the samples without the surrounding epoxy support while still maintaining a flat polished face for viewing under the microscope, therefore this method was preferred.

Once sectioned, the samples were prepared to improve their image under the microscope. Grinding was undertaken using a grinding wheel and silicon carbide grinding paper, see Figure 3-17, of increasing grades from P180 to P4000. Water was used for lubrication and cooling throughout. Polishing was then undertaken using polishing cloths magnetically attached to the grinding wheel, see Figure 3-17. Diamond suspensions of 6 µm, 3 µm, 1 µm and 0.25 µm were used alongside polishing

lubricant to give the polished finish. The grinding and polishing procedure allows for brighter and more detailed microscope images to be taken.

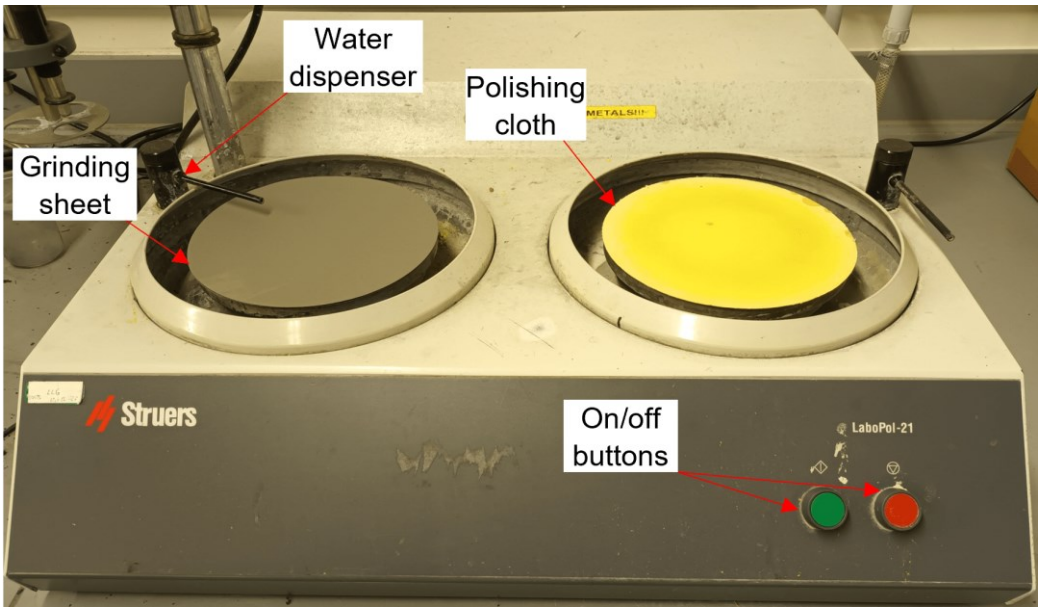


Figure 3-17: Grinding wheels set up for grinding (left) and polishing (right).

3.3.4.2 Optical microscopy

An optical microscope was used to inspect the samples after impact and C-scanning to give further information about the type and location of damage. After being suitably ground and polished the samples were viewed using a Zeiss Axio Scope.A1 optical microscope, see Figure 3-18 which also allowed images to be taken of the samples. Optical microscopy gave high-quality images, clearly showing intralaminar and interlaminar damage in the samples.

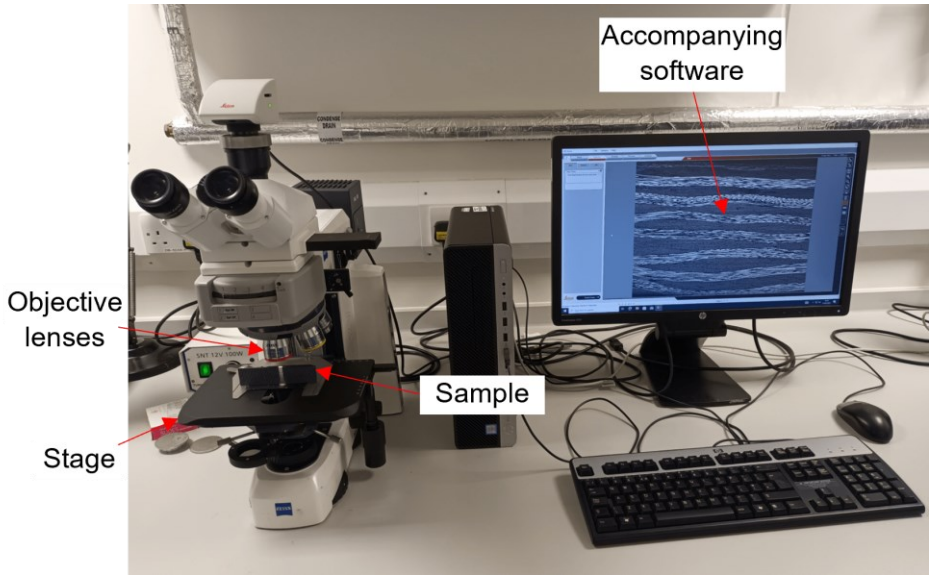


Figure 3-18: Zeiss Axio Scope.A1 optical microscope set-up with accompanying PC.

3.3.4.3 Scanning electron microscopy (SEM)

Scanning electron microscopy (SEM) was initially used to inspect impacted samples to provide further detailed information about the type and location of damage within. Prior to viewing in the TESCAN MIRA SEM, the sample was attached to a metal mount and silver conductive paint was applied in a line from the sample surface down to the mount. This provides a conductive patch between the sample surface and the mount and is necessary given the low electrical conductivity of the CF/Epoxy being viewed. Finally, a chromium sputter coating was applied to the sample using a Quorum Q150T ES Plus turbomolecular pumped coater. This is a thin layer (approximately 15 nm in thickness) of conducting material which helps prevent charging of the sample (which would otherwise occur due to the accumulation of static electric charges on the sample surface). When viewing the samples using the SEM, a beam current between 3 and 4 nA was used.

A comparison of optical microscopy versus SEM for viewing damage in CF/Epoxy is included in Chapter 8. Optical microscopy was used instead of SEM for the majority of study in this thesis as high-quality images showing the relevant damage in the samples could be achieved more easily and with less preparation. Furthermore, optical microscopy provided large enough magnifications for the

damage investigations undertaken and the greater magnifications which could be achieved using SEM were deemed unnecessary.

3.3.5 Pull-out testing

A machine was designed in order to test the inter-ply friction between layers of CF/PPS. This data was to be used for modelling stamp forming processes prior to forming trials. A pull-out rig was designed and manufactured but the planned experiments were not performed. The design process and details of this pull-out rig are outlined in Appendix A.

Chapter 4 Study on the internal and external damage formed in CFRP thermoset laminates under low-velocity impact conditions

The majority of this chapter comes from the following paper: 'The relationship between the extent of indentation and impact damage in carbon-fibre reinforced-plastic composites after a low-velocity impact' [87].

4.1 Introduction

The current chapter presents the results from an experimental study into the behaviour of unidirectional (UD) CF/Epoxy composite under low-velocity impact. In this chapter, only single impacts are investigated. Low-velocity drop-weight testing with a rigid hemispherical impactor was used to perform the impacts and ultrasonic C-scanning was used to examine the internal delamination damage formed during the impacts. The depth of the surface indentations formed during impact was also determined and studied to see how the depth related to the delamination damage area. Finally, optical microscopy was used to investigate the intralaminar and interlaminar damage within the panels.

The studies revealed that the formation of a surface indentation can be related to the onset of yielding/plasticity in the matrix and matrix cracking of the carbon fibre-reinforced polymer (CFRP) and the extent of associated interlaminar delaminations that result. The indentation depth has been shown to be related to the delamination damage area for the low-velocity impact energies of 2 to 20 J by a second-order polynomial relationship.

4.2 Test specification and methods

4.2.1 Materials

The CF/Epoxy panels used in the study presented in this chapter were manufactured following the method described in Section 3.2.1.1. The panels had thicknesses of 2.3 mm and 4.6 mm and quasi-isotropic (QIT) lay-ups of $[45/-45/0/90]_s$ and $[45_2/-45_2/0_2/90_2]_s$, respectively. Each panel was cut to a size of 150 mm x 100 mm and the 0° plies were aligned with the longer edge of the panels.

4.2.2 Experimental methods

Low-velocity drop-weight testing was undertaken following the method outlined in Section 3.3.1. The 16 mm diameter round-nosed impactor had an overall mass of 5.27 kg and was dropped from varying heights to give impact energies of 2, 5, 10, 15 or 20 J, with corresponding impact velocities of 0.87, 1.38, 1.95, 2.39 or 2.76 $m.s^{-1}$, respectively. For some impacts, two Photron slow motion cameras were used to capture the impact. One camera viewed the panel from above at an angle of around 25° to the horizontal and the other was set to view in the plane of the panel, see Figure 3-11.

Ultrasonic C-scanning (a non-destructive testing (NDT) method) was undertaken to view the delamination damage within each panel after impact following the method described in Section 3.3.2. Indentation depth was measured using the two methods described in Section 3.3.3. Measurement of the indentation depth using the handheld digital depth gauge could be completed quickly and easily and gave accurate values of the indentation depth. Measurement of the indentation depth using the Confocal microscope provided not only a very accurate value of indentation depth, but also data showing the cross-section of the indent. This allowed comparison of the indent shape in different panels as well as comparison of just the indentation depth. Optical microscopy was undertaken to view the intralaminar and interlaminar (i.e. delamination) damage within each panel following the method described in Section 3.3.4. Samples were cut, ground and polished before being viewed using the optical microscope.

4.3 Experimental results and discussion

4.3.1 Delamination (i.e. interlaminar) damage

Figure 4-1 and Figure 4-2 show the C-scan damage maps for two repeat tests after impacts at 2, 5, 10, 15 and 20 J for the two thicknesses, i.e. 2.3 and 4.6 mm, of CF/Epoxy panels, with the corresponding scales showing the depth of each delamination beneath the impacted surface. Note that 20 J impact tests were not performed on the 2.3 mm thick CF/Epoxy panels since the damage severity would have been too great, potentially causing damage to the drop-weight tower. In such figures, the damage area (DA) is indicated and was calculated by counting the number of pixels that were not dark blue in colour, since dark blue corresponds to areas of the laminate free from delaminations. The results from the replicate tests demonstrate the high level of reproducibility achieved in the present study. As expected, the extent of delamination increases as the impact energy is increased. The delaminations propagate at ply boundaries where the fibre direction in adjacent plies differs [19,33], i.e. not between blocked plies. This is because the dramatic change in stiffness in a particular direction from one ply to the next at the ply boundaries generates high interfacial stresses, leading to delamination [35]. The direction of delamination propagation is usually dictated by the orientation of the ply directly beneath the delamination [33]. This explains the direction of the characteristic peanut-shaped delamination footprints.

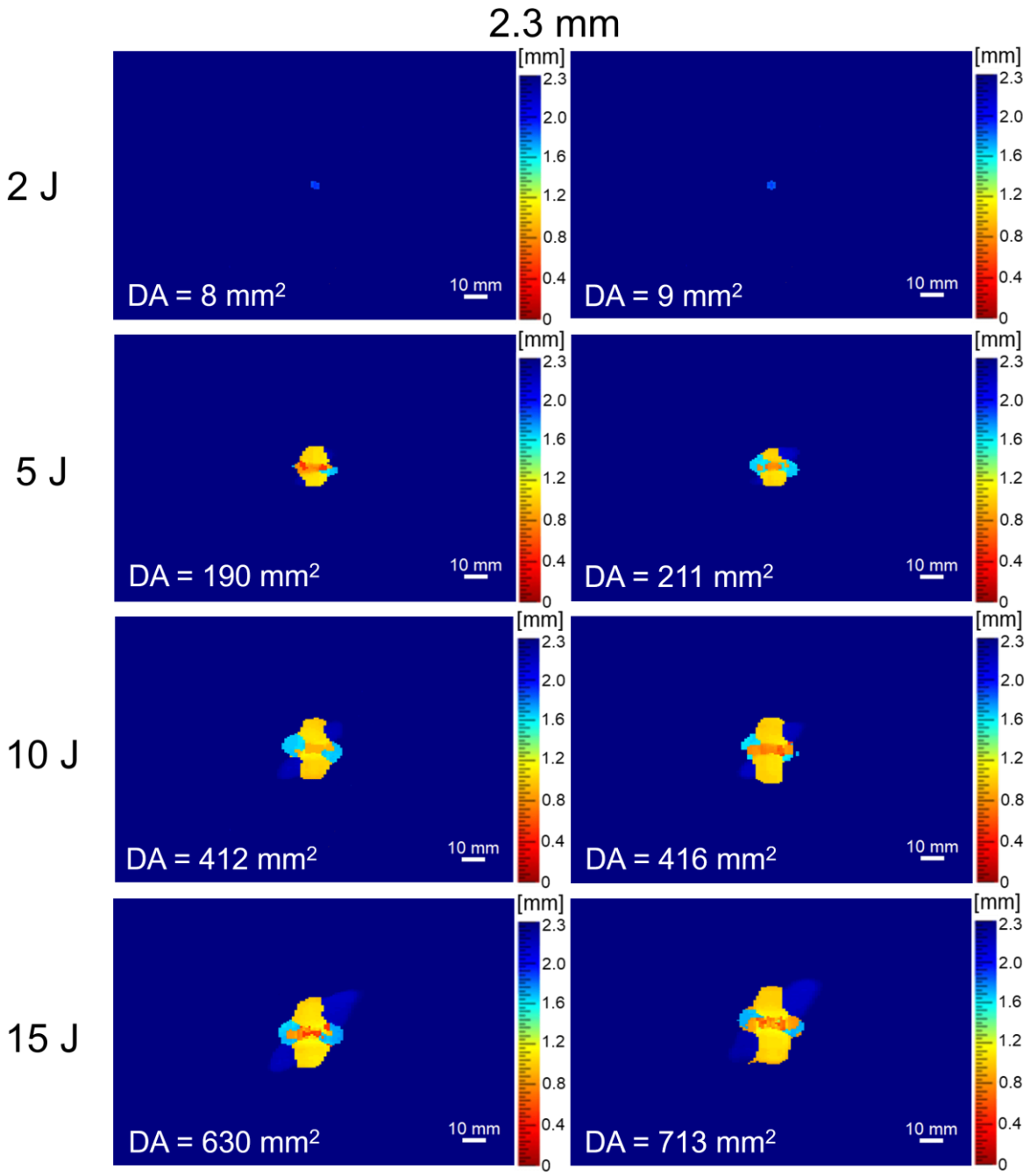


Figure 4-1: C-scan damage maps obtained from the CF/Epoxy replicate composite panels with a thickness of 2.3 mm with impact energies of 2, 5, 10 and 15 J. The right-hand side scale indicates the location of the interlaminar delamination as a function of the depth through the thickness of the panel (0 to 2.3 mm), where the dark red colour represents the front (impacted) face and the dark blue colour represents the rear (non-impacted) face of the composite panel. The footprint of the delamination damage area (DA) detected is given in the bottom left-hand corner for each panel and was determined by counting the pixels which had a colour which was not dark blue. The bottom right of each damage map shows a 10 mm scale bar [87].

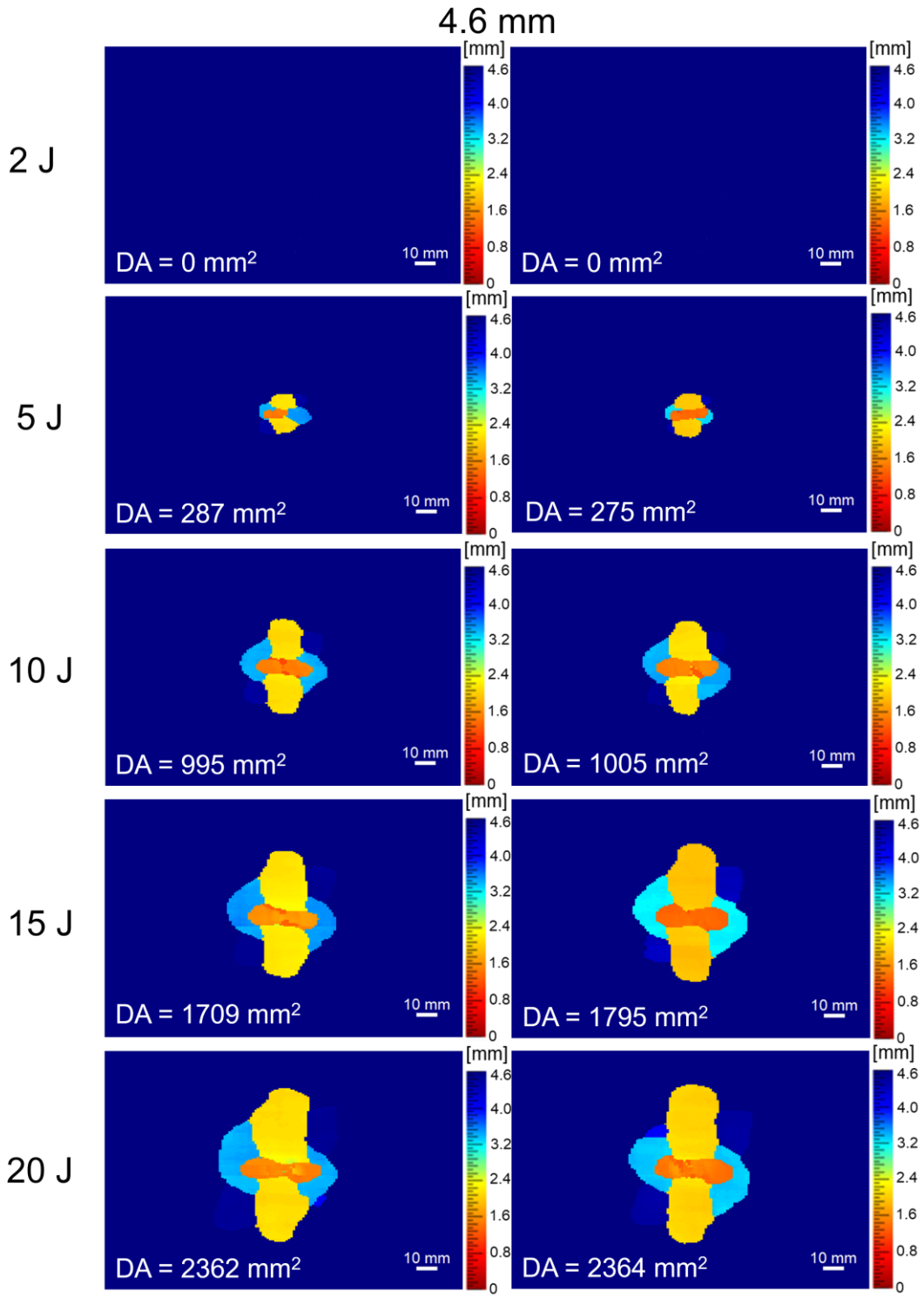


Figure 4-2: C-scan damage maps obtained from the CF/Epoxy replicate composite panels with a thickness of 4.6 mm with impact energies of 2, 5, 10, 15 and 20 J. The right-hand side scale indicates the location of the interlaminar delamination as a function of the depth through the thickness of the panel (0 to 4.6 mm). The footprint of the delamination damage area (DA) detected is given in the bottom left-hand corner for each panel. The bottom right of each damage map shows a 10 mm scale bar [87].

Figure 4-3 compares the C-scan damage maps obtained in the 2.3 mm and 4.6 mm material at a given impact energy. Note that just the first scan is shown for each thickness and was arbitrarily chosen. The difference in the delamination damage area for the 2.3 mm and 4.6 mm panels can be clearly seen. For the same impact energy, the 4.6 mm panels exhibit a greater delamination area than the 2.3 mm panels. The difference in delamination area increases with increasing impact energy. This can be explained as intralaminar cracks and delaminations tend to form a conical shape through the thickness of the material, with wider delaminations at the base [46]. Hence, in a thicker panel a greater area of delamination damage is formed in the rear of the panel, leading to a larger total damage area. The CFRP test panels impacted at 2 J show very little delamination damage in the case of the 2.3 mm thickness panel and in the case of the 4.6 mm panels no delamination damage at all is detected. This suggests that the threshold energy for damage to occur for the 2.3 mm thick test panels is just below 2 J and the threshold energy for the 4.6 mm thick panels is between 2 and 5 J. The delaminations visible in the 2.3 mm thickness panels are close to the rear surface. This observation suggests that, at very low impact energies, the impactor may not be able to initiate matrix cracks in the front face. However, instead, for the 2.3 mm thick panels, delamination occurs near the rear surface due to bending and the resulting higher tensile and shear stresses across the ply interfaces near the rear impacted surface. For the 4.6 mm thick panels, at an impact energy of 2 J, the bending deformation would be less marked and hence delaminations at the rear ply interfaces do not occur.

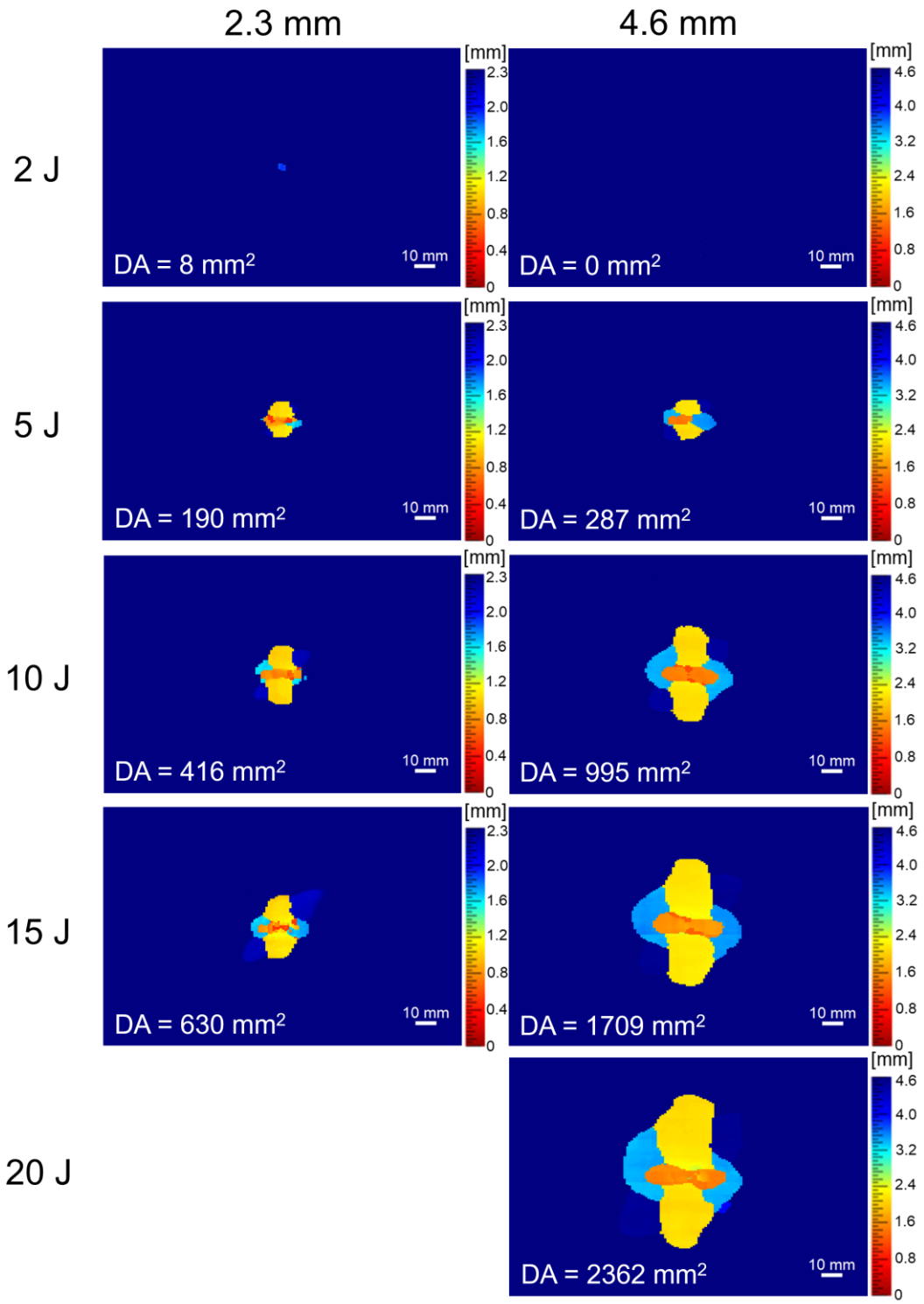


Figure 4-3: Comparison of the C-scan damage maps obtained from the impacted CF/Epoxy composite panels with a thickness of 2.3 or 4.6 mm. The right-hand side scale indicates the location of the interlaminar delamination as a function of the depth through the thickness of the panel. The footprint of the delamination damage area (DA) detected is given in the bottom left-hand corner for each panel. The bottom right of each damage map shows a 10 mm scale bar [87].

4.3.2 Load versus time and load versus displacement results

Load versus time and load versus displacement traces are shown in Figure 4-4 for impacts at 2, 5, 10, 15 and 20 J on both thicknesses of CFRP. The small sinusoidal oscillations on the rising section of the traces are indicative of mass-spring oscillations and have been observed by other researchers [290–292]. Clear load drops, which are seen for most of the composite panels, show the load and time at which damage initiated in the panels during the impact event. The load versus time traces, shown in Figure 4-4(a), for the 2 and 5 J impact energy cases for the 2.3 mm thickness panels, do not show a clear load drop, despite damage clearly having occurred, as shown by subsequent C-scans, see Figure 4-3. In this figure there may be seen to be some very slight delamination damage observed at the 2 J impact for the panel of 2.3 mm thickness near the rear surface of the panel but no damage was observed for the 2 J impact for the thicker panel of 4.6 mm in thickness. Thus, at these relatively low impact energies, and for the more flexible 2.3 mm thick panel, the load drop which is indicative of the damage threshold is less noticeable in Figure 4-4(a). The results shown in Figure 4-4(b) for the load versus displacement traces clearly demonstrate the different stiffnesses of the two thicknesses of CFRP panel.

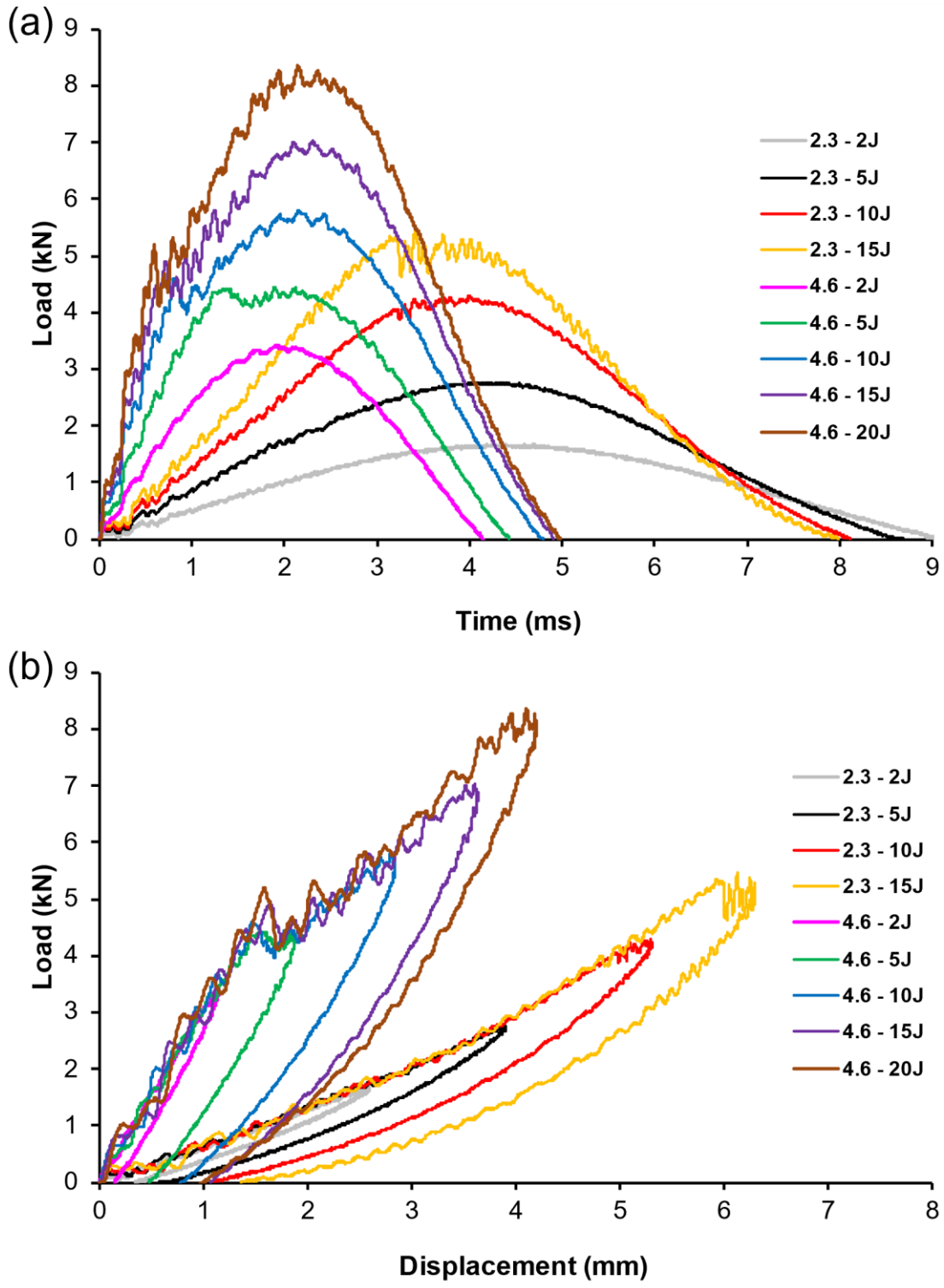


Figure 4-4: (a) Load versus time traces and (b) load versus displacement traces for 2.3 mm and 4.6 mm thick CF/Epoxy composite panels impacted at 2, 5, 10, 15 and 20 J [87].

Some impact events were also recorded using two high-speed cameras at a frame rate of 10000 frames per second. Filming the impact event at high-speed allows detailed analysis of the indentation process, helping to reveal the stages in the formation of the indent. Figure 4-5 and Figure 4-6 show a sequence of high-speed images which clearly illustrate the indentation process for impacts of 15 J on 2.3 mm and 4.6 mm thick CFRP composite panels, with an inter-frame time of 1.6 ms and 1 ms, respectively. The first image (frame 1 - top left) is captured just before the impact event and the total contact times are approximately 8 ms and 5 ms, respectively, with the last image (frame 6 - bottom right) showing the start of the rebounding of the impactor. Figure 4-5 and Figure 4-6 clearly show that the impactor indents the front surface and that there is a clear contact area for frames 2, 3, 4 and 5. The deformation beneath the impactor exhibits both viscoelastic and plastic behaviour. This indentation damage is also accompanied by intralaminar damage, involving matrix cracking within the ply and fibre debonding and fracture and, in addition, delamination between the differently orientated plies, see Figure 4-3 and as discussed above. After the impact event, a residual permanent indentation, see Figure 3-13, is left in the panel from this plasticity, intralaminar and interlaminar damage.

When watching the high-speed images as a video a ‘judder’ is seen at the point of damage initiation within the panel and the impactor depresses further into the material without the panel deforming significantly. This occurs between the second and third frames for 2.3 mm panel and between the first and second frames for the 4.6 mm panel, so is not seen on these image sequences. This is followed by relatively smooth deformation up until maximum displacement is reached.

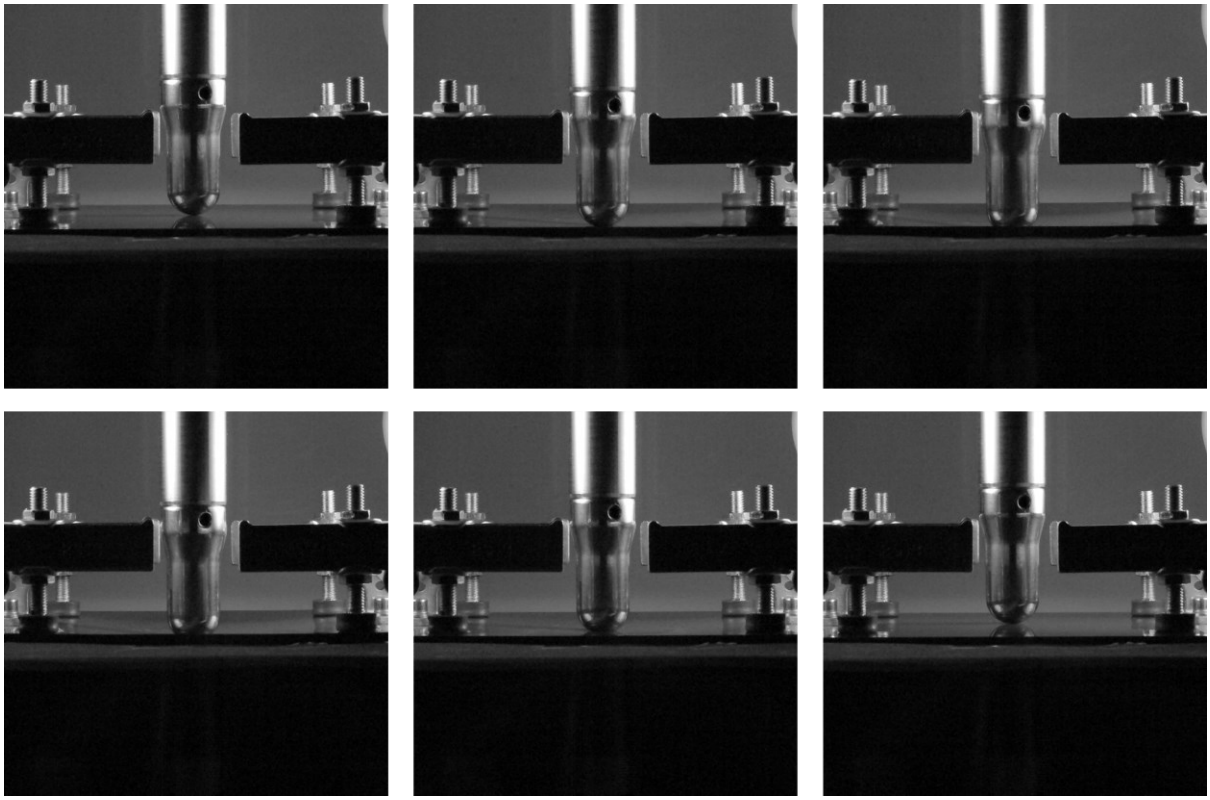


Figure 4-5: Series of high-speed photographic images showing the indentation process for an impact of 15 J on a 2.3 mm thick CF/Epoxy composite panel (inter-frame time is 1.6 ms). The first image (top left) is captured just before the impact event and the total contact time is approximately 8 ms, with the last image (bottom right) showing the start of the rebounding of the impactor. The hemispherical stainless-steel impactor has a diameter of 16 mm.

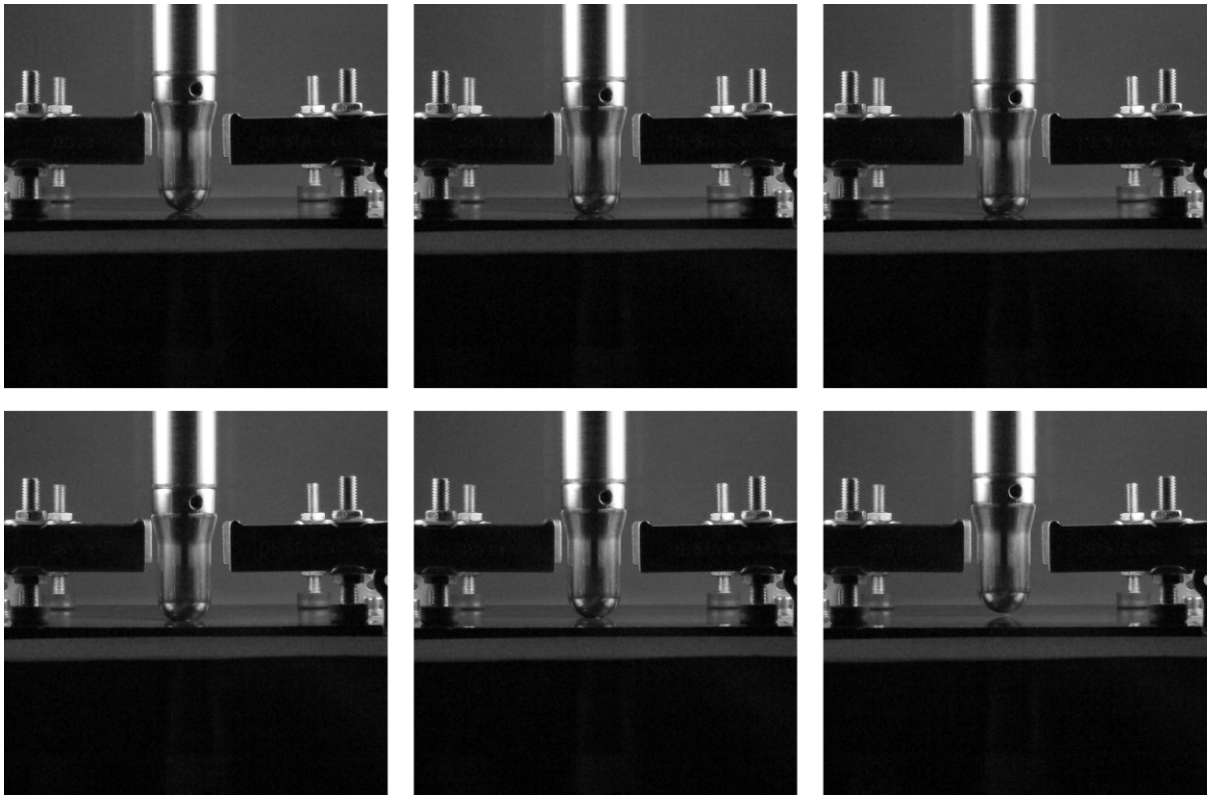


Figure 4-6: Series of high-speed photographic images showing the indentation process for an impact of 15 J on a 4.6 mm thick CF/Epoxy composite panel (inter-frame time is 1 ms). The first image (top left) is captured just before the impact event and the total contact time is approximately 5 ms, with the last image (bottom right) showing the start of the rebounding of the impactor. The hemispherical stainless-steel impactor has a diameter of 16 mm [87].

Energy versus time graphs are shown in Figure 4-7 for all the impact energies for tests on both thicknesses of CFRP composite panel. The energy shown is the energy stored or absorbed by the panel during the impact event. The graphs show an increasing amount of energy transferred to the panel by the impactor up until the peak. After the peak some energy is transferred back to the impactor and this rebound energy is shown by the difference between the peak energy and the final energy. Figure 4-7 shows that the rebound energy increases for relatively high impact energies for both thicknesses. At low impact energies, the panel is more able to absorb the energy of the impact event locally with less rebound energy provided back to the impactor. As the impact energy increases, the whole test panel deforms and acts like a spring, storing elastic strain-energy which is then available to rebound the impactor. Of course, some of this energy is lost in intralaminar damage around the

impactor, delamination between the plies and friction, vibration and acoustic losses, particularly around the supports.

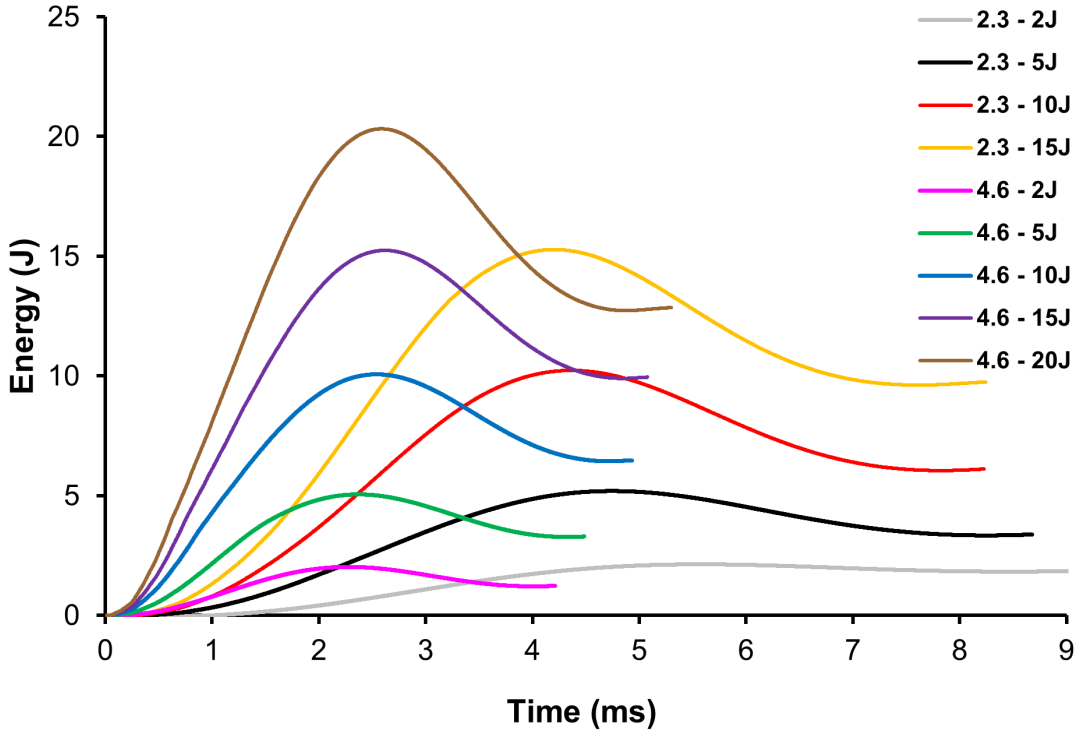


Figure 4-7: Energy versus time traces for 2.3 mm and 4.6 mm thick CF/Epoxy composite panels for impact energies of 2, 5, 10, 15 and 20 J [87].

4.3.3 Indentation depth studies

Figure 4-8 shows cross-sections of the resulting indentations after 2, 5, 10, 15 and 20 J impact energies for each thickness of CF/Epoxy composite, taken from the Confocal microscopy measurements. An impact at 20 J was not performed on the 2.3 mm material, as discussed above. From these cross-sections, an indentation depth was calculated and compared with the indentation depth measurements taken from using the handheld digital gauge and, as shown previously in Figure 3-14, the two different methods of measuring the indentation depth are in excellent agreement. These results, given in Figure 4-8, generally show that a section through the permanent indentation profile has a central depression, with gently shelving sides, and this shape deepens with impact energy.

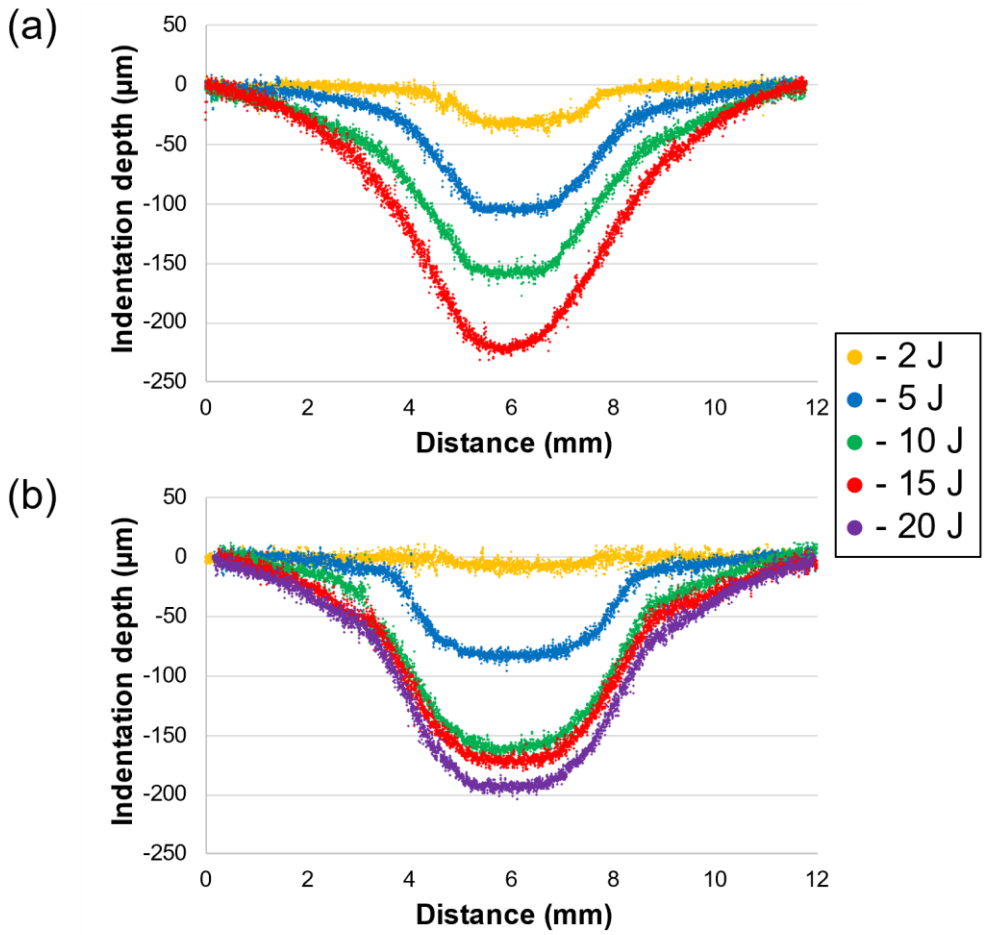


Figure 4-8: Typical indentation cross-section in (a) 2.3 mm thick and (b) 4.6 mm thick CF/Epoxy composite panels after an impact of 2, 5, 10, 15 and 20 J [87].

Figure 4-9 presents the indentation depths measured for different impact energies, and also the associated delamination damage areas versus the impact energy, for both the 2.3 mm thick (Figure 4-9(a)) and the 4.6 mm thick (Figure 4-9(b)) panels. In most cases, a third replicate result, in addition to the duplicate results presented in Figure 4-1 and Figure 4-2, is also included to improve the confidence in these data. The C-scan maps for these data points are included in Appendix B. As may be seen, the data points for the plots of damage area versus impact energy for both the 2.3 and 4.6 mm thick panels lie on an approximately linear relationship, whilst those for the plots of indentation depth versus impact energy do not. This aspect is discussed in detail below.

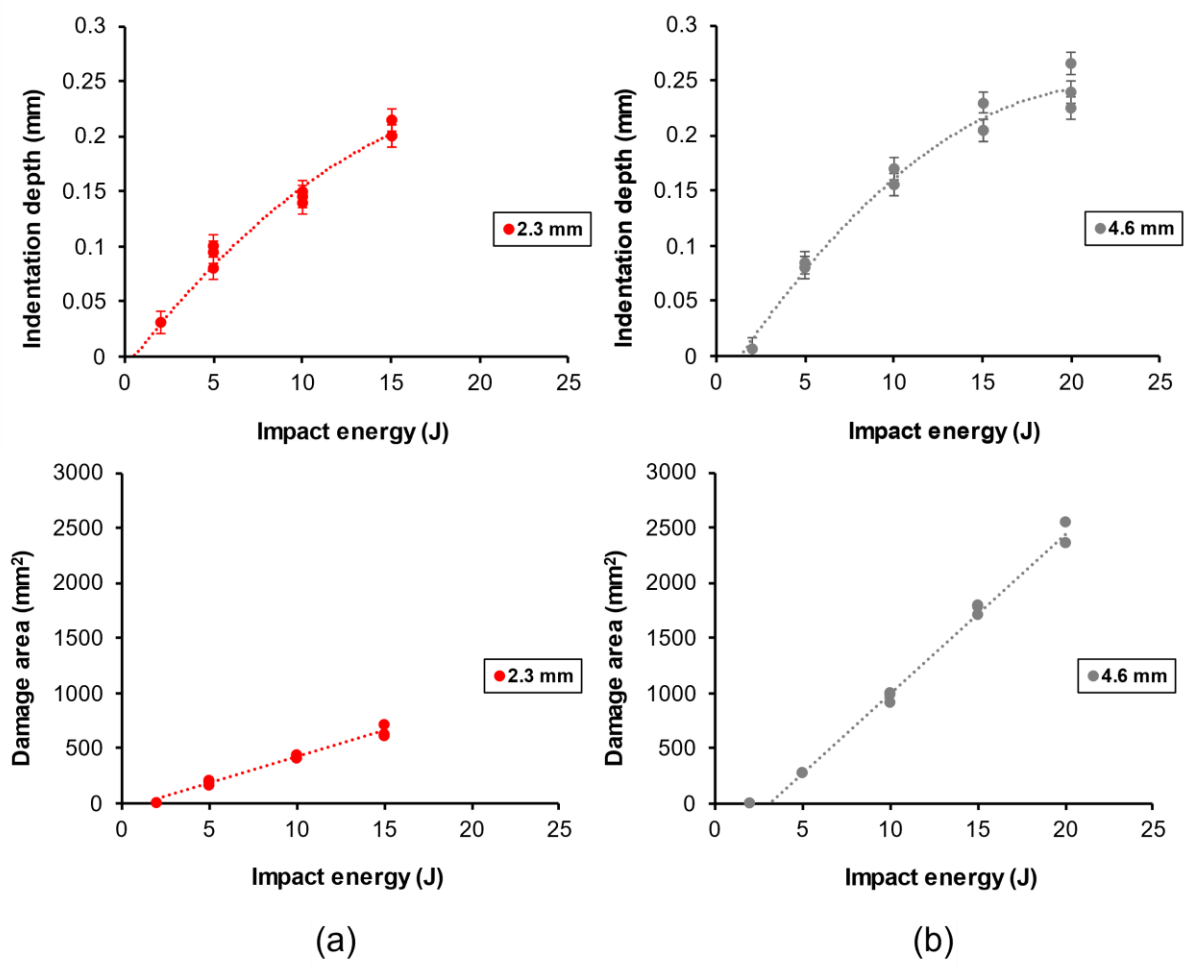


Figure 4-9: The indentation depth versus impact energy, and delamination damage area versus impact energy, for the CF/Epoxy composite panels of (a) thickness 2.3 mm and (b) thickness 4.6 mm, for the two replicate cases presented in Figure 4-1 and Figure 4-2 and, in some cases, for a third replicate test [87].

The results for the indentation depth versus the impact energy, and versus the associated damage area, for the two different thicknesses of panel, are compared in Figure 4-10. It is shown in Figure 4-10(a) that there is little effect of the thickness of the panel on the indentation depth incurred from the impact event. Thus, for an impact event at the same impact energy, the CF/Epoxy composite panels of a thickness of 4.6 mm show a similar indentation depth to the panels of a thickness of 2.3 mm. This observation is in contrast to that from the work of Shuck, as cited by Talreja and Phan [93], and of Panettieri [94]. These authors found that thinner CFRP composites showed a larger indentation depth.

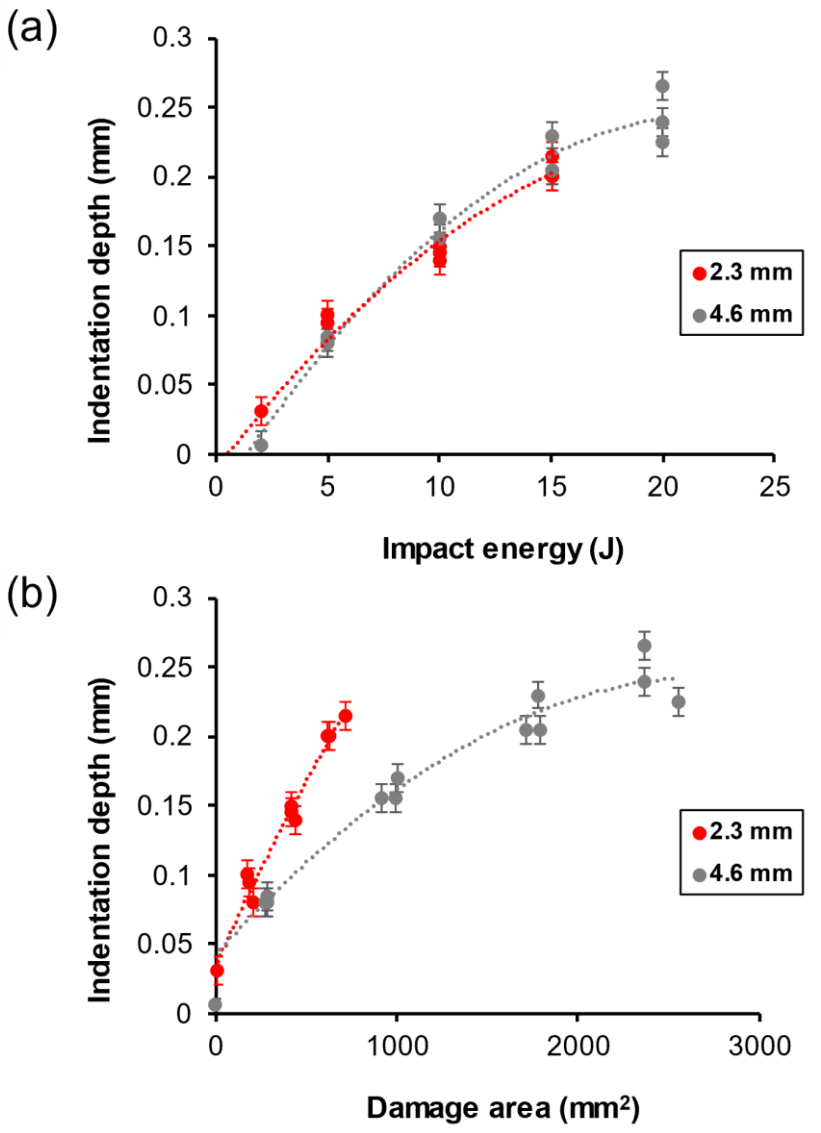


Figure 4-10: The indentation depth versus (a) the impact energy and (b) the interlaminar damage area for the 2.3 mm and 4.6 mm thick CF/Epoxy composite panels [87].

On the other hand, the relationship between the indentation depth and the damage area, for a given impact energy, as shown in Figure 4-10(b), reveals a very significant effect of the panel thickness, with the thicker 4.6 mm panel suffering more damage for a given indentation depth when the impact energy is greater than about 5 J. This arises, of course, from the results shown in Figure 4-3, Figure 4-8 and Figure 4-9. Thus, whilst the indentation depths are similar in value for a given impact energy in the two panels, see Figure 4-10(a), the corresponding damage areas are significantly greater for the 4.6 mm panel at an impact energy of about 5 J and above, see Figure 4-10(b). Interestingly, for both

thicknesses of panel, Figure 4-10(b) reveals that an indentation may occur in a panel with little, or no, accompanying damage area. For example, at an impact energy of 2 J both panel thicknesses exhibit a clearly visible indentation after the impact event, see Figure 4-8 and Figure 4-10(b), whilst the associated damage area for the 2.3 mm panel is very localised at about 8 mm^2 and there is no damage area observed at all for the 4.6 mm panel. These observations strongly suggest that the indentation damage is initiated before any delamination damage develops.

Finally, Figure 4-11 shows that all the relationships between the indentation depth and the damage area for both thicknesses of panel from Figure 4-10(b) can be unified to give a 'master' relationship, which is not linear, by plotting the indentation depth versus the associated damage area normalised with respect to the panel thickness. By normalising the damage area by dividing by the panel thickness, almost all the resulting data points for impact energies of 2, 5, 10 and 15 J converge onto an approximately unique 'master' line, see Figure 4-11. Several interesting points arise from Figure 4-11. Firstly, from the impact tests on both composite panels, of thickness 2.3 mm and the 4.6 mm, at impact energies above about 15 J it appears that the increase in indentation depth does not keep rising at the same rate as that of the damage area as a function of the impact energy. Secondly, the unique relationship in Figure 4-11 demonstrates that there is no need to have separate relationships for each thickness of composite when comparing the measured indentation depth against the corresponding delamination damage area. Thirdly, by assuming this unique 'master' relationship is indeed valid for all appropriate thicknesses of this lay-up within a range of at least 2.3 to 4.6 mm based on the current tests, one can (a) measure the indentation depth, (b) then read off the corresponding normalised damage area, and (c) then, from a knowledge of the chosen composite's thickness, the approximate damage area can be calculated. Fourthly, it may be noted that to take into account varying lay-ups of the same composite material, and hence differing numbers of interfaces where delamination can occur, normalisation by the bending stiffness could be used. For example, in the present study, for the 4.6 mm thickness laminate, blocking of two plies for each fibre orientation were employed to reduce the number of interfaces where delamination occurs, so that the delaminations are more clearly visible with the ultrasonic C-scan technique. It should be pointed out that a $[45/-45/0/90]_{2s}$ layup could be used which would have the same thickness, i.e. 4.6 mm, but double the number of ply interfaces, i.e. twelve rather

than six, and all these interfaces could be potential locations for delamination initiation. However, given that alternative lay-ups were not tested in the present study, the simpler normalisation method based only on the thickness was used.

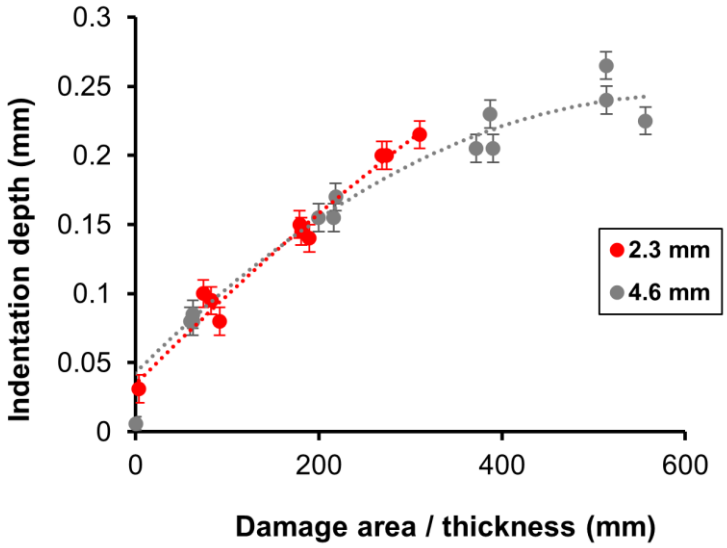


Figure 4-11: The indentation depth versus normalised interlaminar damage area (i.e. damage area divided by thickness) for the CF/Epoxy composite panels [87].

With the results above in mind, a possible explanation of why the indentation depth is related to the delamination area as shown in Figure 4-10(b) and Figure 4-11 may follow from earlier research by Tabor [88]. He suggested that, as the initial impact energy for the impactor is increased, there is indeed a relationship between the resulting depth of indentation, d, and the initial impact energy of the impactor, $U_{impactor}$, but only once the impact energy for yielding of the material, and hence the associated permanent indentation, U_{yield}, has been exceeded. He assumed a linear relationship but in the analysis below, to provide a more general representation of the experimental data, a second-order polynomial relationship is employed. Thus, we have:

$$d = k_{1\,indentation} \cdot (U_{impactor} - U_{yield}) + k_{2\,indentation} \cdot (U_{impactor} - U_{yield})^2 \quad (4.1)$$

with the threshold condition:

$$d = 0 \quad \text{for } U_{impactor} < U_{yield}$$

Where $k_{1indentation}$ and $k_{2indentation}$ are first-order and second-order parameters for the second-order polynomial fit. Now, from research by Liu et al. [293], an approximately linear relationship exists between the footprint area, A, of the delamination damage and the impact energy, $U_{impactor}$, once the threshold energy for delamination, $U_{threshold}$, which is related to the threshold load, is exceeded. This observation is in agreement with the results shown in Figure 4-9 (see lower graphs). Thus:

$$A = k_{delamination} \cdot (U_{impactor} - U_{threshold}) \quad (4.2)$$

with the threshold condition:

$A = 0$ for $U_{impactor} < U_{threshold}$

and where $k_{delamination}$ is a constant of proportionality.

These equations are fitted to the data points given in Figure 4-9 and Figure 4-10 using the constants given in Table 4-1. As may be seen, these simple relationships are in good agreement with the experimentally measured results. The polynomial relationship was adopted with a threshold as this could be fitted to the experimental data well and the parameters were relatively easy to determine. A power-law relationship would be more physical and would probably also need a threshold condition to be introduced.

Table 4-1: The values of the constants in Equations (4.1) and (4.2) and the approximate initiation energies required for indentation and delamination.

	2.3 mm	**4.6 mm**
$k_{1\ indentation}$ (mm/J)	0.0209	0.0251
$k_{2\ indentation}$ (mm/J)	-0.0004	-0.0006
$k_{delamination}$ (mm^2/J)	47.8	144.5
U_{yield} (J)	~0.5	~1.4
$U_{threshold}$ (J)	~1.3	~3.1

Combining Equations (4.1) and (4.2) to eliminate the initial impact energy, it can be shown that the indentation depth versus delamination footprint area will also be a second-order polynomial of the form:

$$d = \left(\frac{k_{1\ indentation}}{k_{delamination}}\right).(A + C') + \left(\frac{k_{2\ indentation}}{k^2_{delamination}}\right).(A + C')^2 \quad (4.3)$$

which can be expanded to give:

$$d = \left(\frac{k_{1\ indentation}}{k_{delamination}}\right).A + \left(\frac{k_{2\ indentation}}{k^2_{delamination}}\right).A^2 + \left(\frac{2k_{2\ indentation}}{k^2_{delamination}}\right).A.C' + \left(\frac{k_{2\ indentation}}{k^2_{delamination}}\right).C'^2 + \left(\frac{k_{1\ indentation}}{k_{delamination}}\right).C' \quad (4.4)$$

Here the constant C' ($C' = k_{delamination} . (U_{threshold} - U_{yield})$) is a positive quantity since yielding, which gives rise to the indentation, has been found to occur at a slightly lower impact energy than the threshold impact energy for delamination, as noted above. Indeed, it is suggested that, at least in the present tests, indentation is a prerequisite for delamination damage. (Since, the indentation process provides for shear and tensile loading of the ply interface and so indentation occurs at a lower impact energy than for delamination.) Therefore, a second-order polynomial relationship between indentation depth, d, and delamination footprint area, A, is to be expected, with a positive intercept on the vertical indentation depth axis, as is indeed apparent in Figure 4-11. The positive intercept, on the vertical axis of indentation depth versus delamination footprint area curve, is given by the term:

$$\left(\frac{k_{2\ indentation}}{k^2_{delamination}}\right).C'^2 + \left(\frac{k_{1\ indentation}}{k_{delamination}}\right).C' \quad (4.5)$$

which is greater than zero, if $C' > 0$ (or $U_{threshold} > U_{yield}$) as is usually the case, with the indentation damage occurring at a slightly lower impact energy than the delamination damage. As may be seen from Figure 4-11, the experimental results are in good agreement with the fit provide by the above equations, using the values of the various parameters in these equations as given in Table 4-1.

It is expected that similar relationships to those identified in the present study between indentation depth and delamination damage area would be obtained for other composite laminates, for both thermoset and thermoplastic matrices. Similar relationships may also be obtained for other types of continuous-fibre composites, e.g. woven fibre composites. However, in order to use this method for

a given composite material, a unique ‘master’ curve of indentation depth versus normalised damage area must firstly be established through impact testing for the specific composite of interest.

4.3.4 Optical microscopy studies

Firstly, it should be noted that the full delamination lengths seen in the optical microscope images were similar in value to the delamination lengths detected by the ultrasonic C-scans. However, the full delamination lengths are not shown for the optical microscope images in order to show the intralaminar cracking in detail.

Figure 4-12 shows a central cross-section, cut directly beneath the indentation along a line parallel to the 100 mm edge, from a 4.6 mm thick composite panel that had been subjected to a 15 J impact. The various types of microstructural damage sustained during the impact are highlighted. The intralaminar damage mainly consists of matrix cracks which are initiated at the impact site and then radiate outwards. These cracks propagate through the plies of the composite until they reach an interlaminar delamination, which occurs where adjacent plies have differing orientations. At this point, the intralaminar cracks can initiate a further delamination which propagates in a direction away from the impact site. This interlaminar delamination damage is the type of damage that is detected in the ultrasonic C-scans. Fibre debonding and fracture are other forms of intralaminar damage which take place and these are visible in Figure 4-12 as a kink band. Fracturing the fibres can significantly reduce the residual stiffness of the composite. Finally, the resulting indentation is clearly visible on the top surface of the panel in the lower micrograph in Figure 4-12.

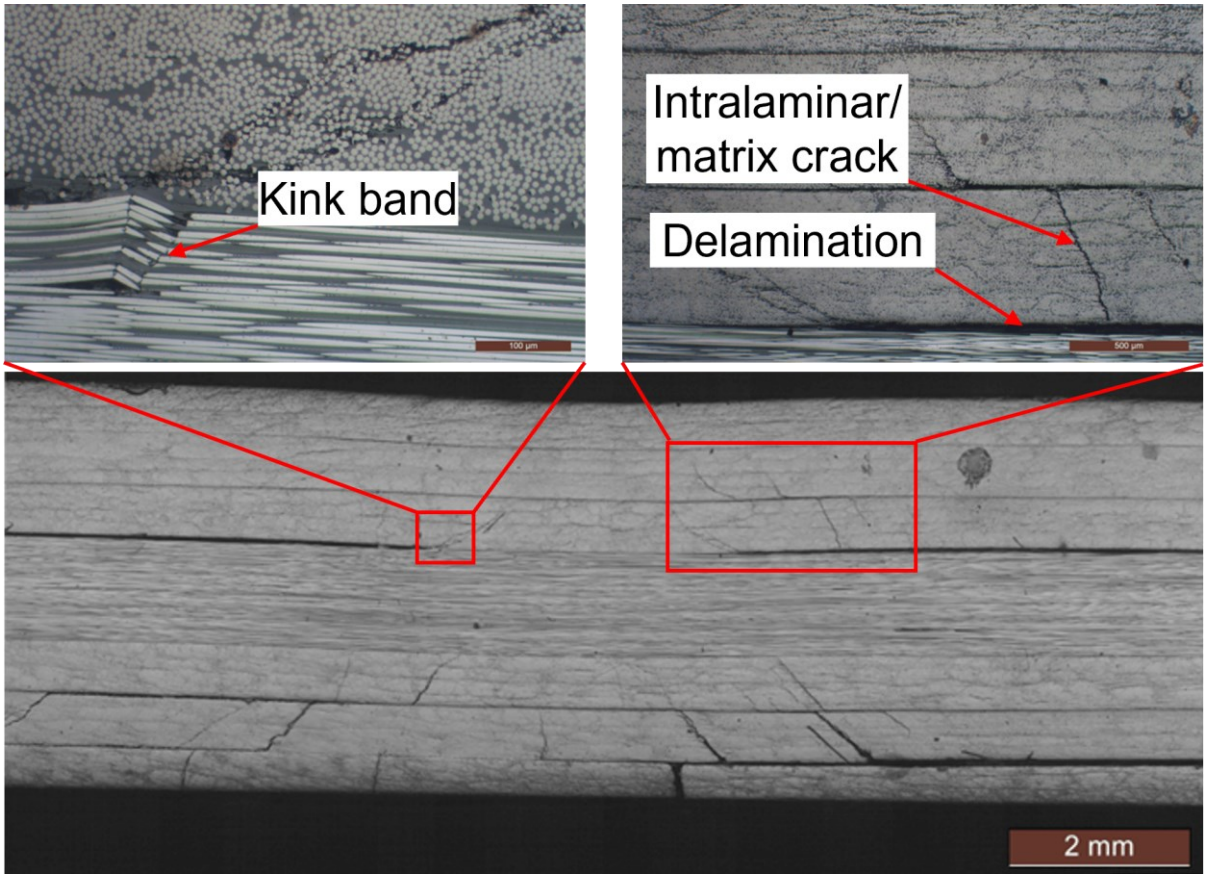


Figure 4-12: Optical microscopy images of a 4.6 mm thick CF/Epoxy composite panel after an impact of 15 J. (Showing a cross-section cut from the panel after grinding and polishing. The scale bars in the upper-left and upper-right micrographs represent 100 µm and 500 µm, respectively.) [87].

Figure 4-13 and Figure 4-14 compare cross-sections of composite panels with thicknesses of 2.3 mm and 4.6 mm after impact at 5 J and 15 J, respectively. These micrographs highlight the conical-shaped intralaminar cracking zone which occurs through the thickness of the composite panel during the impact event. Thus, leading to the increased delamination area in the 4.6 mm composite panels compared to the 2.3 mm panels. For the panels impacted at 15 J, it is interesting that, although more delamination damage is seen in the 4.6 mm panel, a greater severity of intralaminar damage is seen in the 2.3 mm panel as the deflection of the panel is greater during the impact event, see Figure 4-4(b).

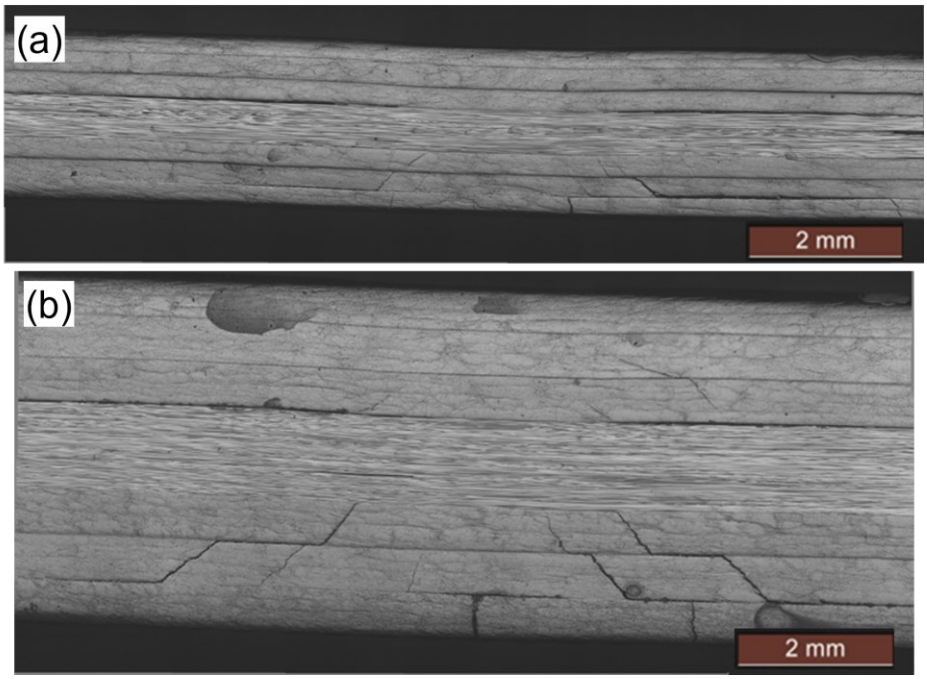


Figure 4-13: Optical microscopy images of (a) a 2.3 mm and (b) a 4.6 mm thick CF/Epoxy composite panel after an impact at 5 J. (Showing a cross-section cut from the panel after grinding and polishing.)

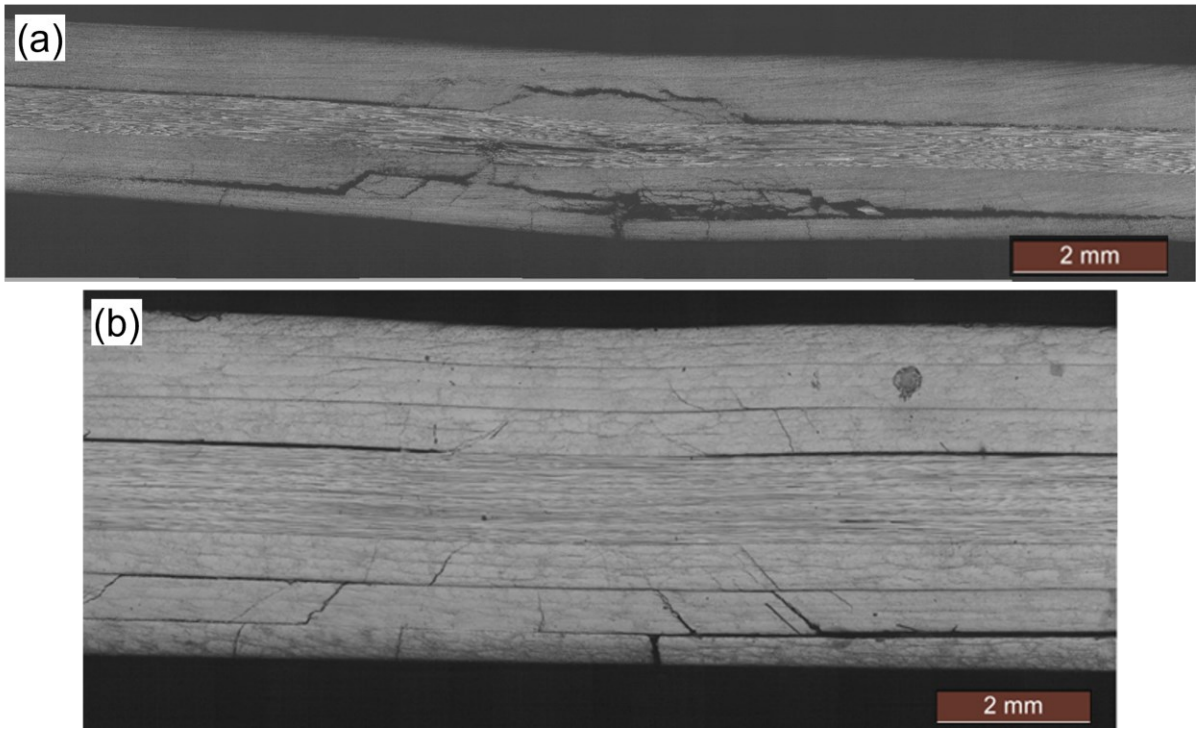


Figure 4-14: Optical microscopy images of (a) a 2.3 mm and (b) a 4.6 mm thick CF/Epoxy composite panel after an impact at 15 J. (Showing a cross-section cut from the panel after grinding and polishing.) [87].

4.4 Summary

The relationship between the extent of indentation and the resulting impact damage in CF/Epoxy composite has been investigated. Two lay-ups of $[45/-45/0/90]_s$ and $[45_2/-45_2/0_2/90_2]_s$ were tested with corresponding thicknesses of 2.3 mm and 4.6 mm. Low-velocity impacts of 2, 5, 10, 15 and 20 J were undertaken using a drop-weight tower and a hemispherical stainless-steel impactor of diameter 16 mm. The resulting damage formation and surface indentation depth have been investigated using ultrasonic C-scanning, a digital depth gauge and optical microscopy.

The impact testing revealed that a larger delamination damage area is formed in the 4.6 mm thick panels than in the 2.3 mm thick panels when impacted at the same energy. This is due to the delamination and intralaminar damage spreading out like a cone from the impact site. Also, for the same impact energy, the 4.6 mm thick panels exhibit a higher peak load and a lower maximum displacement.

The deformation caused by a surface indentation exhibits both viscoelastic and plastic behaviour and is accompanied by intralaminar damage, involving matrix cracking within the ply and fibre debonding and fracture, and interlaminar damage, i.e. delaminations, between the differently orientated plies. The indentation occurs in the impact test at a slightly lower impact energy than that required for interlaminar delamination damage to initiate and develop. At higher impact energies there is a saturation effect where it becomes more difficult for the indentation to increase in depth. Therefore, the indentation depth has been shown to be related to the delamination damage area for the low-velocity impact energies of 2 to 20 J by a second-order polynomial relationship. This highlights that measuring the indentation depth has the potential to be used as a quick and cheap alternative to employing expensive ultrasonic C-scan or X-ray Computed Tomography equipment for estimating the extent of internal delamination damage.

Therefore, the present study has identified a relationship between indentation depth and delamination damage for UD CF/Epoxy after impact by a 16 mm diameter rigid hemispherical impactor.

Chapter 5 Study on the internal and external damage formed in CFRP thermoset laminates after multiple impacts in the same location

5.1 Introduction

The current chapter presents the results from an experimental study into the impact behaviour of unidirectional (UD) CF/Epoxy composite under low-velocity impact. In this chapter, repeated impacts on the same panel and in the same location are investigated. Low-velocity drop-weight testing with a rigid hemispherical impactor was used to perform the impacts and ultrasonic C-scanning was used to examine the internal delamination damage formed during the impacts. The depth of the surface indentations formed during impact was also determined and analysed to investigate how the depth related to the delamination damage area. Finally, optical microscopy was also used to investigate the intralaminar and interlaminar damage within the panels.

The studies revealed that subsequent impacts increase the delamination damage area by propagating existing delaminations. Also, the indentation depth slightly increases for each subsequent impact and, for low-velocity impact energies of 2 to 20 J, follows a second-order polynomial relationship with delamination damage area.

5.2 Test specification and methods

5.2.1 Materials

The CF/Epoxy panels used in the study presented in this chapter were manufactured following the method described in Section 3.2.1.1. The panels had thicknesses of 2.3 mm and 4.6 mm and quasi-isotropic (QIT) lay-ups of $[45/-45/0/90]_s$ and $[45_2/-45_2/0_2/90_2]_s$, respectively. Each panel was cut to a size of 150 mm x 100 mm and the 0° plies were aligned with the longer edge of the panels.

5.2.2 Experimental methods

Low-velocity drop-weight testing was undertaken following the method outlined in Section 3.3.1. The 16 mm diameter round-nosed impactor had an overall mass of 5.27 kg and was dropped from varying heights to give impact energies of 2, 5, 10, 15 or 20 J, with corresponding impact velocities of 0.87, 1.38, 1.95, 2.39 or 2.76 $m.s^{-1}$, respectively. For some impacts, two Photron slow motion cameras were used to capture the impact. One camera viewed the panel from above at an angle of around 25° to the horizontal and the other was set to view in the plane of the panel, see Figure 3-11.

Ultrasonic C-scanning (a non-destructive testing (NDT) method) was undertaken to view the delamination damage within each panel after impact following the method described in Section 3.3.2. Indentation depth was measured using the two methods described in Section 3.3.3. Measurement of the indentation depth using the handheld digital depth gauge could be completed quickly and easily and gave accurate values of the indentation depth, see Figure 3-14. Measurement of the indentation depth using the Confocal microscope provided not only a very accurate value of indentation depth, but also data showing the cross-section of the indent. This allowed comparison of the indent shape in different panels as well as comparison of just the indentation depth. Optical microscopy was undertaken to view the intralaminar and interlaminar (i.e. delamination) damage within each panel following the method described in Section 3.3.4. Samples were cut, ground and polished before being viewed using the optical microscope.

5.3 Experimental results and discussion

5.3.1 Delamination damage

Figure 5-1 and Figure 5-2 show the C-scan damage maps for two repeat tests, each of two impacts at 2, 5, 10, 15 and 20 J for the two thicknesses (i.e. 2.3 and 4.6 mm) of CF/Epoxy panels, respectively. The corresponding coloured scales show the depth of each delamination beneath the impacted surface. Note that 20 J impact tests were not performed on the 2.3 mm thick CF/Epoxy panels since the damage severity would have been too great, potentially causing damage to the drop-weight tower. The results

from the replicate tests highlight the high level of reproducibility achieved in the present study. As expected and as seen in the C-scans taken after a single impact (see Figure 4-3), the extent of delamination increases as the impact energy is increased. Furthermore, impacting the panel for a second time has caused the area of delamination to increase. The second impact has propagated the existing delaminations at ply boundaries where the fibre direction in adjacent plies differs. The large change in stiffness in a particular direction between adjacent plies causes high interfacial stresses, leading to the damage propagation [19,33,35]. Propagation of existing delaminations by subsequent impacts has also been observed by other research studies [14,85]. Although the overall size of the delaminations is increased, the characteristic peanut-shape of each is maintained. As seen for the C-scans taken after a single impact, no delaminations are visible between blocked plies after a second impact. Also, there is still no sign of delamination damage in the 4.6 mm thick panel after two impacts at 2 J.

Figure 5-3 compares the C-scan damage maps obtained in the 2.3 mm and 4.6 mm material after two impacts at a given impact energy. Note that just the first scan is shown for each thickness and was arbitrarily chosen. As seen in the C-scans taken after a single impact (see Figure 4-3), for the same impact energy the 4.6 mm panels exhibit a greater delamination area than the 2.3 mm panels. This is because the intralaminar cracks and delaminations usually form a conical shape through the thickness of the panel, with wider delaminations near the rear surface [46]. Therefore, in a thicker panel larger delaminations are formed in the rear of the panel which leads to a larger overall damage area. The difference in delamination area between the two thicknesses of panel increases with increasing impact energy. This could be explained by the 4.6 mm thick panels having a greater delamination edge length after the first impact, therefore there is a greater crack length to be propagated by a second impact.

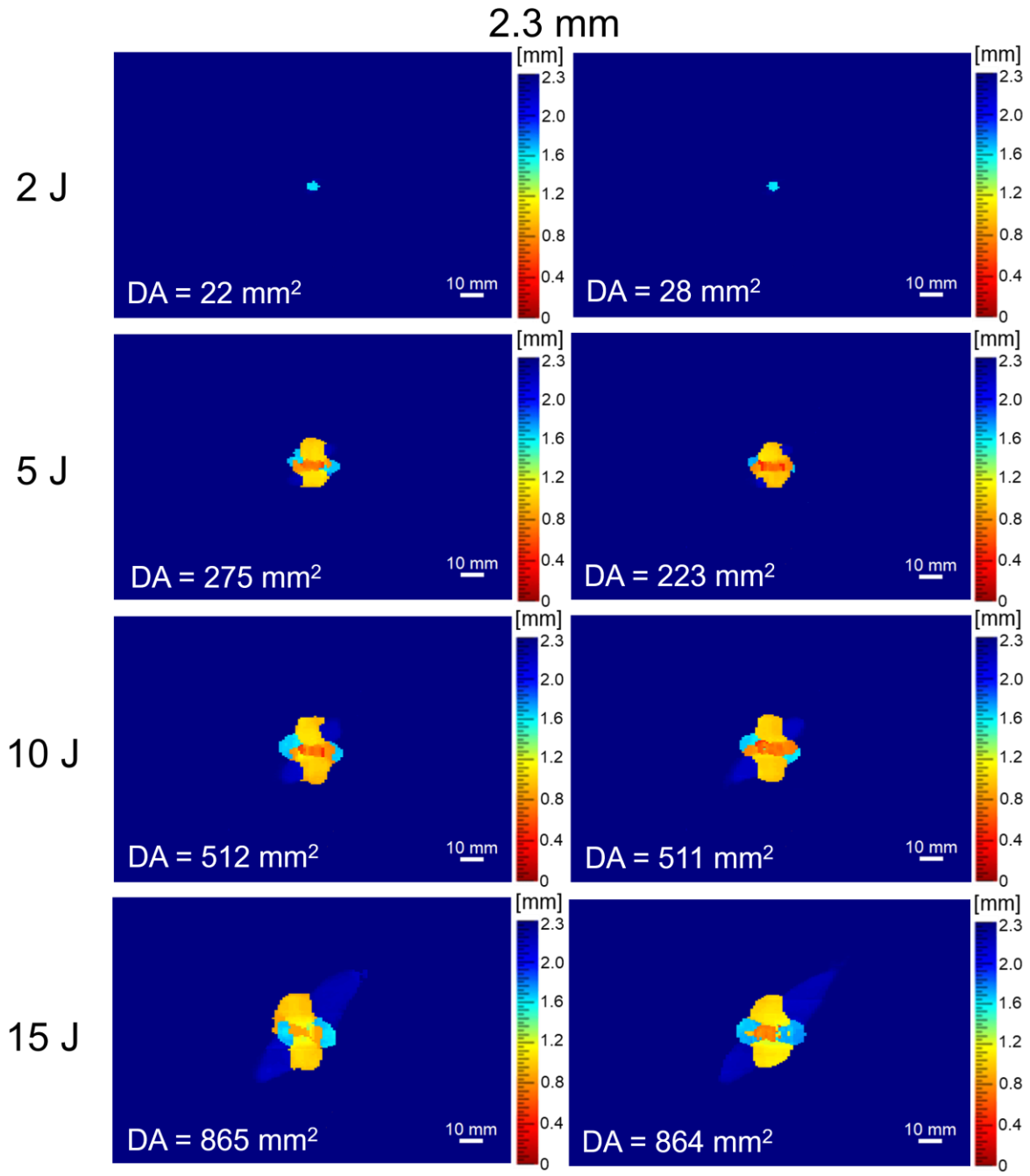


Figure 5-1: C-scan damage maps obtained from the CF/Epoxy replicate composite panels with a thickness of 2.3 mm after two impacts at impact energies of 2, 5, 10 and 15 J. The right-hand side scale indicates the location of the interlaminar delamination as a function of the depth through the thickness of the panel (0 to 2.3 mm), where the dark red colour represents the front (impacted) face and the dark blue colour represents the rear (non-impacted) face of the composite panel. The footprint of the delamination damage area (DA) detected is given in the bottom left-hand corner for each panel and was determined by counting the pixels which had a colour which was not dark blue. The bottom right of each damage map shows a 10 mm scale bar.

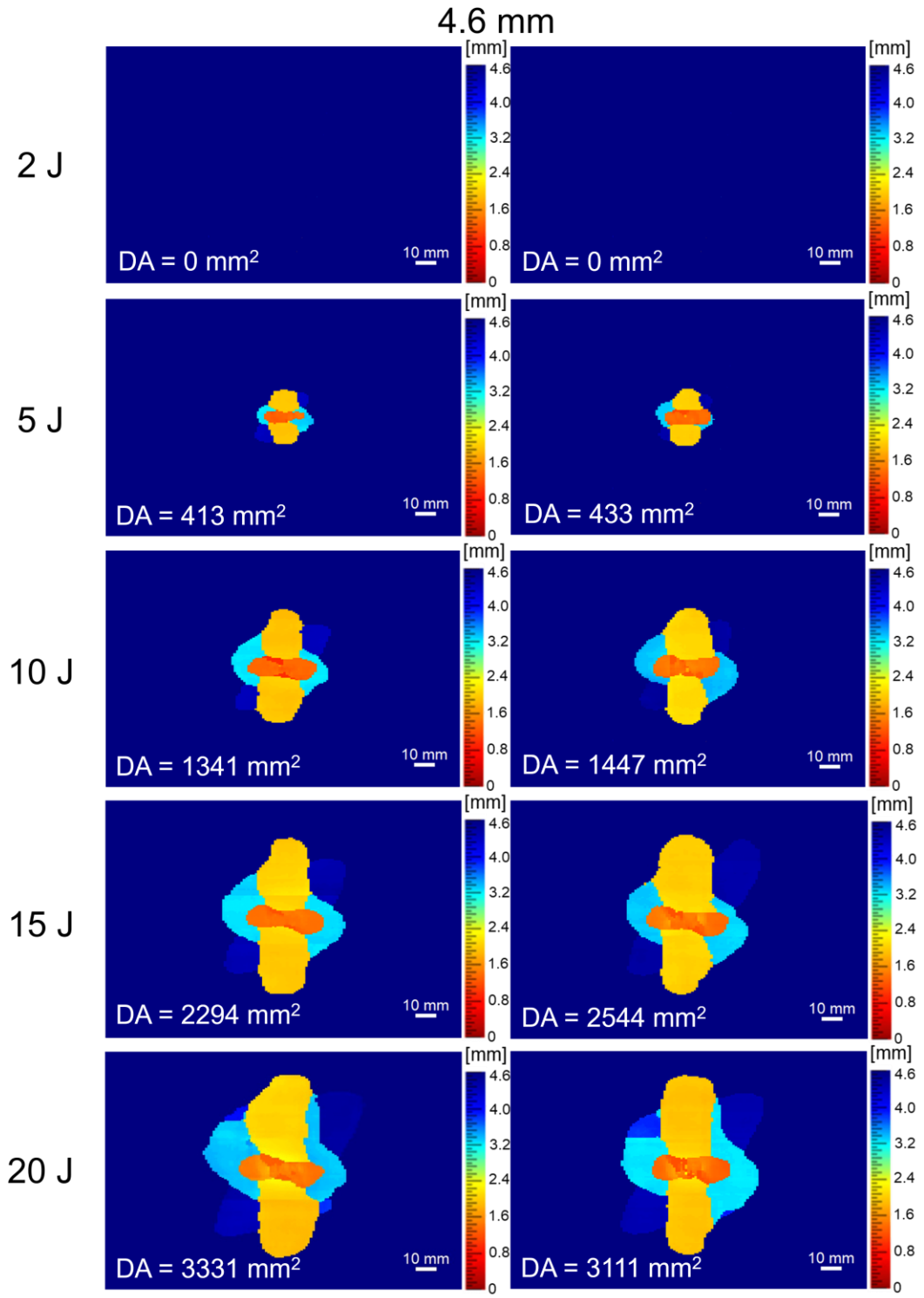


Figure 5-2: C-scan damage maps obtained from the CF/Epoxy replicate composite panels with a thickness of 4.6 mm after two impacts at impact energies of 2, 5, 10, 15 and 20 J. The right-hand side scale indicates the location of the interlaminar delamination as a function of the depth through the thickness of the panel (0 to 4.6 mm). The footprint of the delamination damage area (DA) detected is given in the bottom left-hand corner for each panel. The bottom right of each damage map shows a 10 mm scale bar.

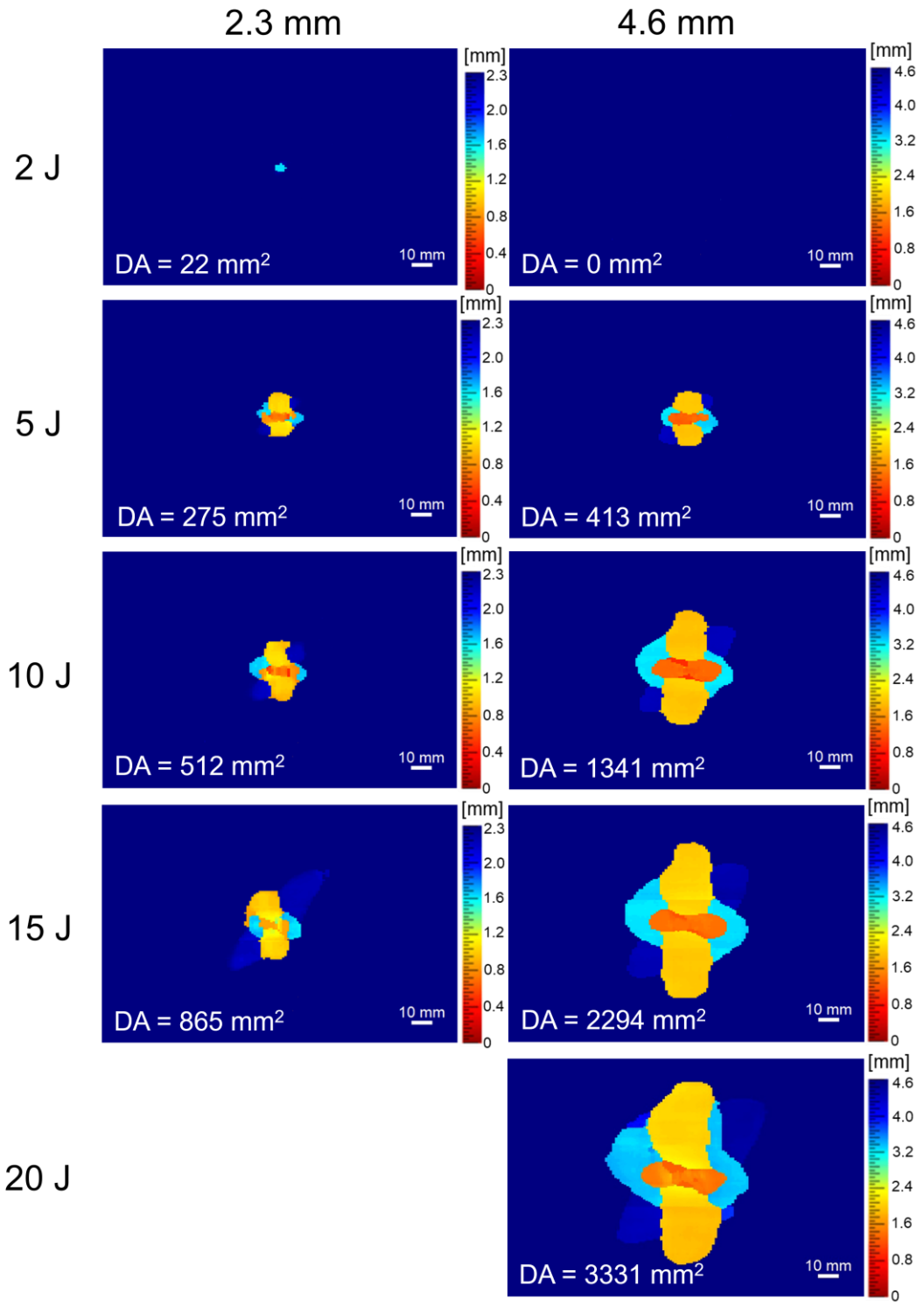


Figure 5-3: Comparison of the C-scan damage maps obtained from the impacted CF/Epoxy composite panels with a thickness of 2.3 or 4.6 mm after two impacts. The right-hand side scale indicates the location of the interlaminar delamination as a function of the depth through the thickness of the panel. The footprint of the delamination damage area (DA) detected is given in the bottom left-hand corner for each panel. The bottom right of each damage map shows a 10 mm scale bar.

Figure 5-4 and Figure 5-5 show the C-scan damage maps for two repeat tests of three impacts at 2, 5, 10, 15 and 20 J for the two thicknesses (i.e. 2.3 and 4.6 mm) of CF/Epoxy panels, respectively. The results from the replicate tests highlight the high level of reproducibility achieved in the present study, although the delamination damage areas for the 2.3 mm thick panels impacted at 15 J do differ considerably. This large difference is examined further in Appendix C. As seen in the C-scans taken after both one and two impacts (see Figure 4-3 and Figure 5-3), the extent of delamination increases as the impact energy is increased. Also, impacting the panel for a third time has caused the area of delamination to increase further by propagating the existing delaminations at ply boundaries where the fibre direction in adjacent plies differs. Again, no delaminations appear to have been created between blocked plies by a third impact. Despite the increase in size, the characteristic peanut-shape of these delaminations is maintained.

However, one notable change is the rear-most delamination in the 2.3 mm thick panels impacted at 15 J. After three impacts, this delamination significantly lengthens. This lengthening corresponds to the rear-most blocked ply coming away from the rear surface of the panel. This is further shown in Figure 5-6 in which the rear surface of the panel with a damage area 1454 mm^2 is shown and has a strip of the rear-most ply (at an orientation of 45°) almost completely detached. This highlights that at relatively large impact energies, relatively thin composite materials may struggle to sustain the damage caused by multiple impacts and start to lose structural integrity. Another observation is that three impacts at 2 J have still not led to the initiation of delamination damage in the 4.6 mm thick panel.

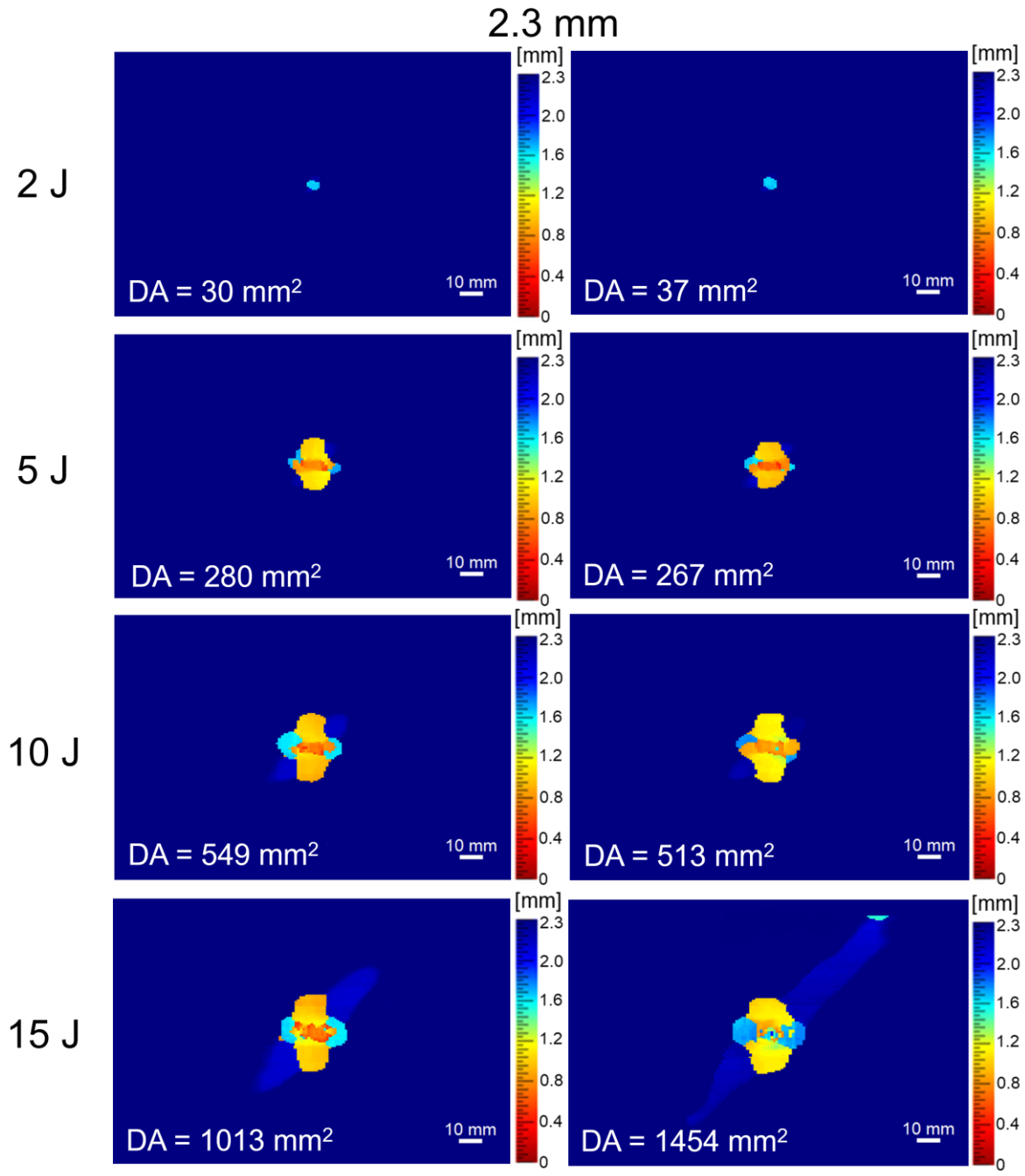


Figure 5-4: C-scan damage maps obtained from the CF/Epoxy replicate composite panels with a thickness of 2.3 mm after three impacts at impact energies of 2, 5, 10 and 15 J. The right-hand side scale indicates the location of the interlaminar delamination as a function of the depth through the thickness of the panel (0 to 2.3 mm). The footprint of the delamination damage area (DA) detected is given in the bottom left-hand corner for each panel. The bottom right of each damage map shows a 10 mm scale bar.

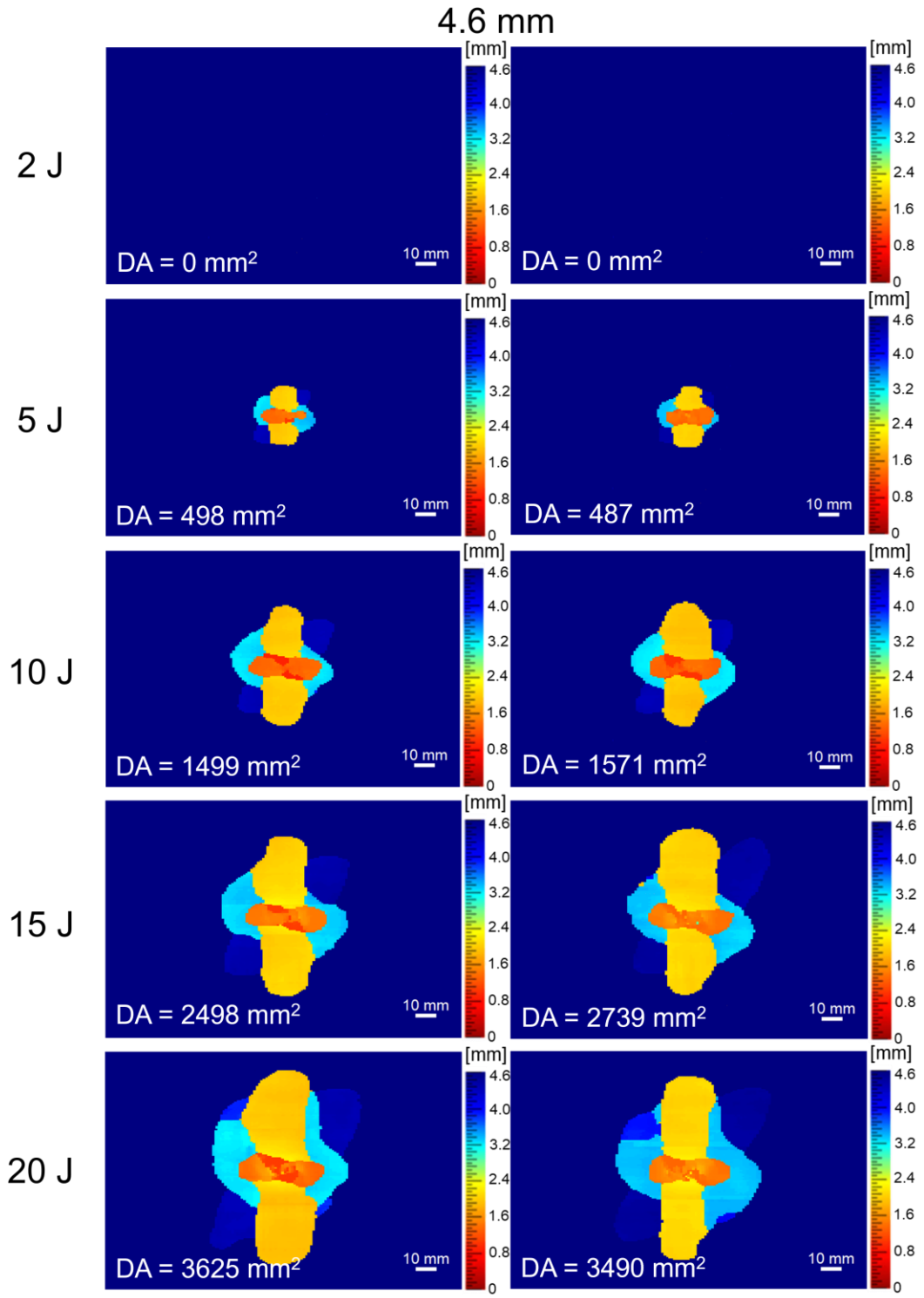


Figure 5-5: C-scan damage maps obtained from the CF/Epoxy replicate composite panels with a thickness of 4.6 mm after three impacts at impact energies of 2, 5, 10, 15 and 20 J. The right-hand side scale indicates the location of the interlaminar delamination as a function of the depth through the thickness of the panel (0 to 4.6 mm). The footprint of the delamination damage area (DA) detected is given in the bottom left-hand corner for each panel. The bottom right of each damage map shows a 10 mm scale bar.

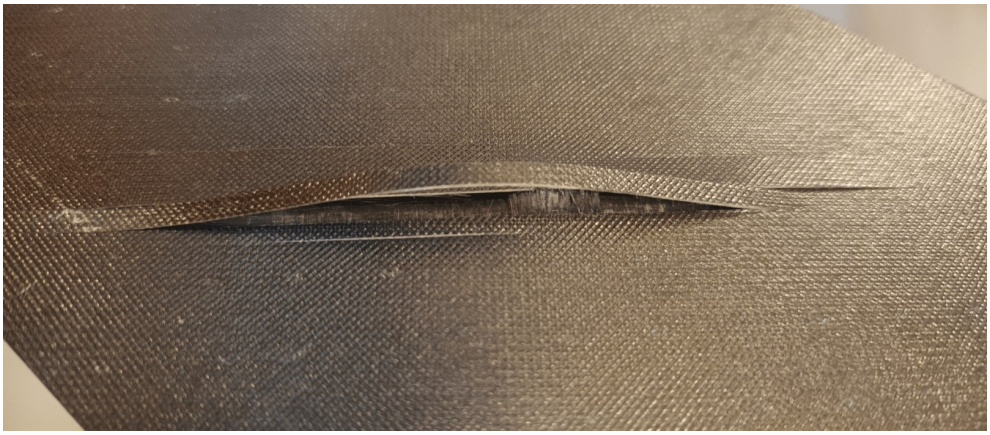


Figure 5-6: Image of the rear surface of a 2.3 mm thick CF/Epoxy panel after three impacts at 15 J. The delamination damage area shown by this panel was 1454 mm^2.

Figure 5-7 compares the C-scan damage maps obtained in the 2.3 mm and 4.6 mm material after three impacts at a given impact energy. Note that just the first scan is shown for each thickness and was arbitrarily chosen. As seen in the C-scans taken after both one and two impacts (see Figure 4-3 and Figure 5-3), for the same impact energy the 4.6 mm panels exhibit a greater delamination area than the 2.3 mm panels. The difference in delamination area increases with increasing impact energy. It is useful to also note that every impact energy which was high enough to cause delamination damage during a first impact also propagated the delaminations during subsequent impacts. Only 2 J impacts on 4.6 mm thick material caused no delamination damage during any of the three impacts.

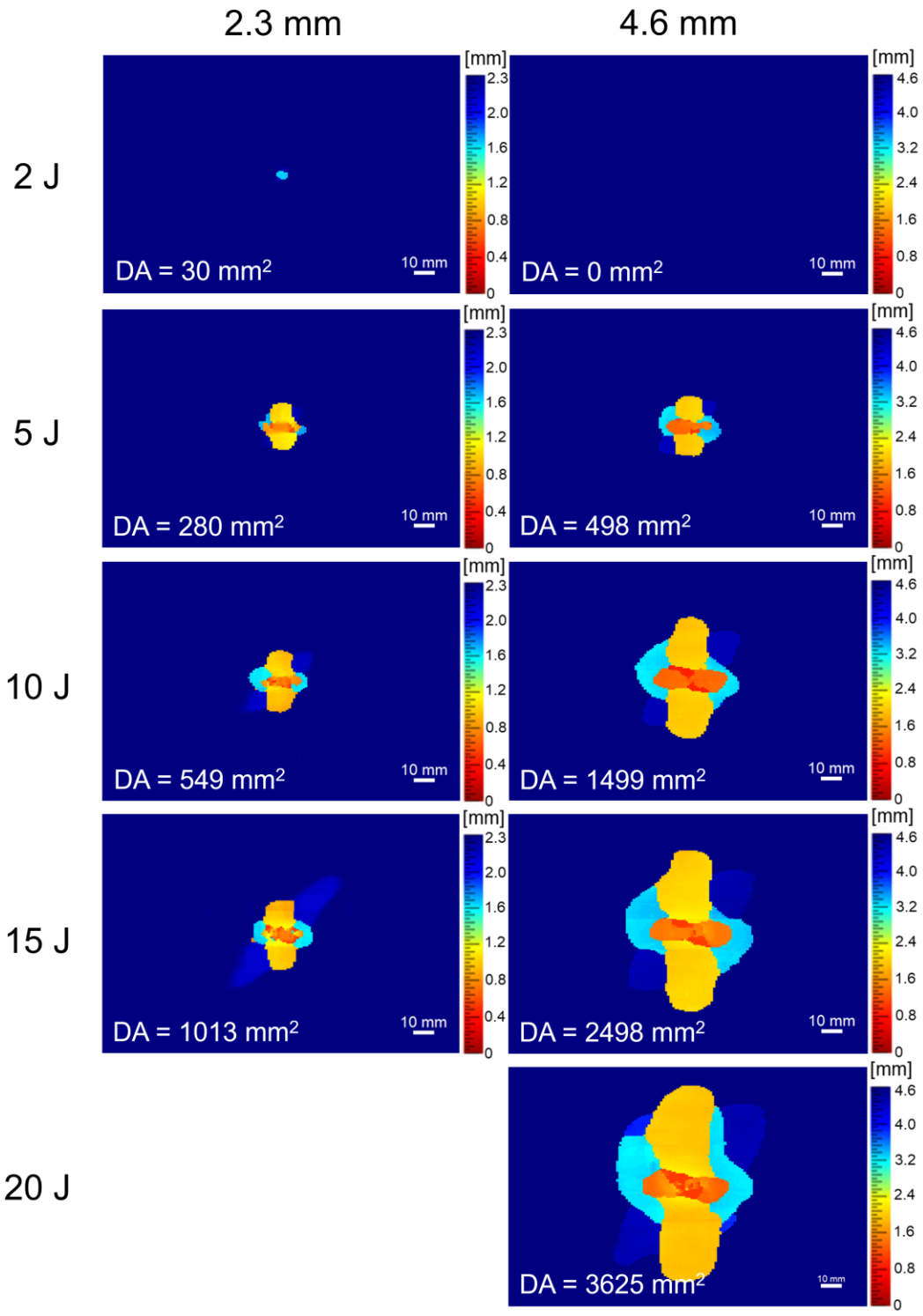


Figure 5-7: Comparison of the C-scan damage maps obtained from the impacted CF/Epoxy composite panels with a thickness of 2.3 or 4.6 mm after three impacts. The right-hand side scale indicates the location of the interlaminar delamination as a function of the depth through the thickness of the panel. The footprint of the delamination damage area (DA) detected is given in the bottom left-hand corner for each panel. The bottom right of each damage map shows a 10 mm scale bar.

Figure 5-8, Figure 5-9, Figure 5-10 and Figure 5-11 show C-scan damage maps for both thicknesses of panel after one, two and three impacts at 5, 10, 15 and 20 J, respectively. These C-scans were chosen so that the same panel is shown for each impact scenario and for all three impacts. For 15 J, the panel showing a lower level of delamination damage after three impacts was chosen. Note that 2 J impacts are not included here due to the very small level of damage created compared to impacts at 5 J and above. The percentage increase in delamination damage area between the first and second impact, and the second and third impact is highlighted for comparison. For all tested impact energies there is a greater increase in damage area caused by a second impact compared to a third impact for both thicknesses of panel. This has also been noted in research performed at similar impact velocities by Tuo et al. [14]. Lack of space for delamination damage to propagate on the panel (due to the size of the panels being tested) may be a factor, particularly for the 4.6 mm thick panels, although the 2.3 mm panels still show a significantly lower damage increase despite the edge of the damage zone being relatively far from the panel edge. Another factor is the reduction in bending stiffness caused by the presence of the increasingly large delaminations which allows a greater proportion of the impact energy to be stored through elastic deformation by the panel during the impact. Hence, there is less energy available to propagate the delaminations for a third impact compared to a second impact. This is discussed further in relation to the load versus time and load versus displacement traces in Section 5.3.2.

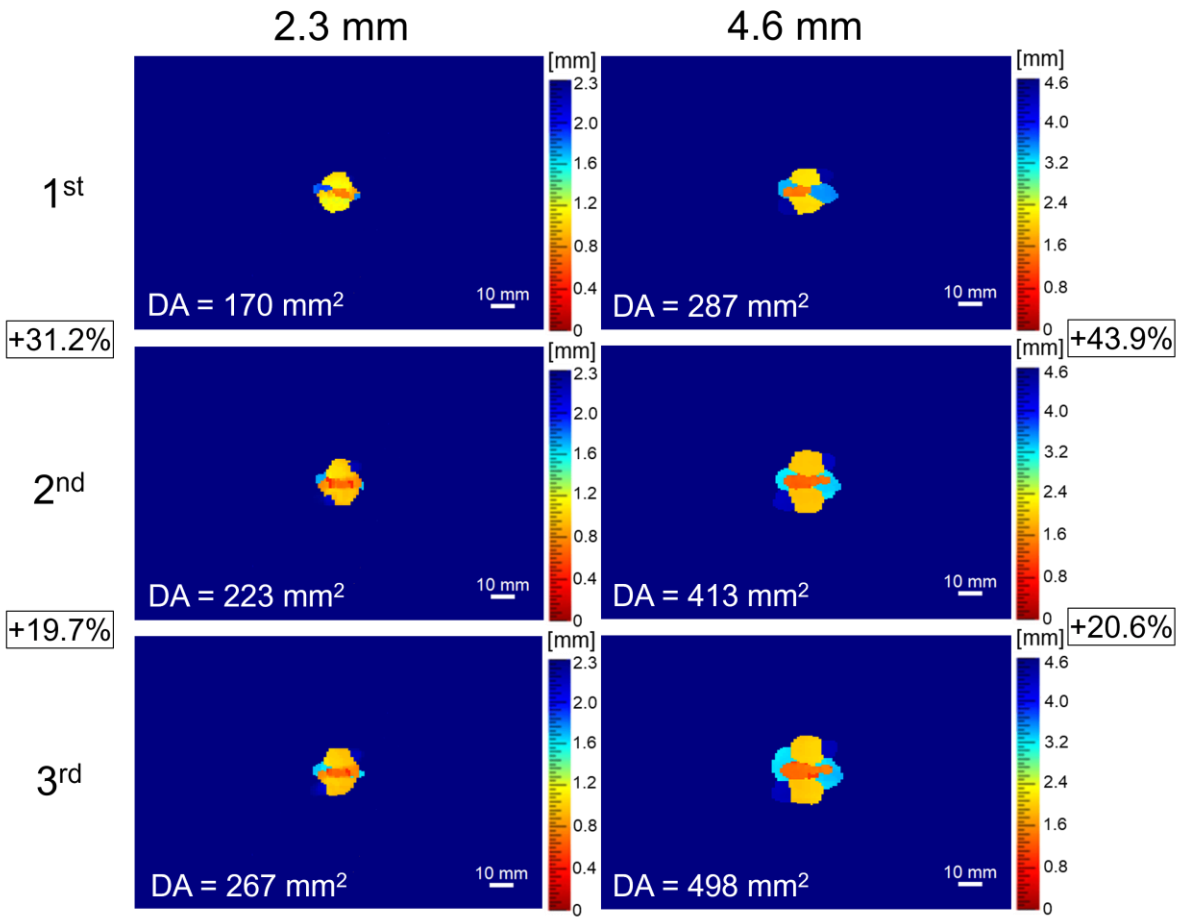


Figure 5-8: C-scan damage maps for 2.3 mm and 4.6 mm thick CF/Epoxy composite panels after one, two and three impacts at 5 J. The increase in delamination damage area (DA) between impacts is shown.

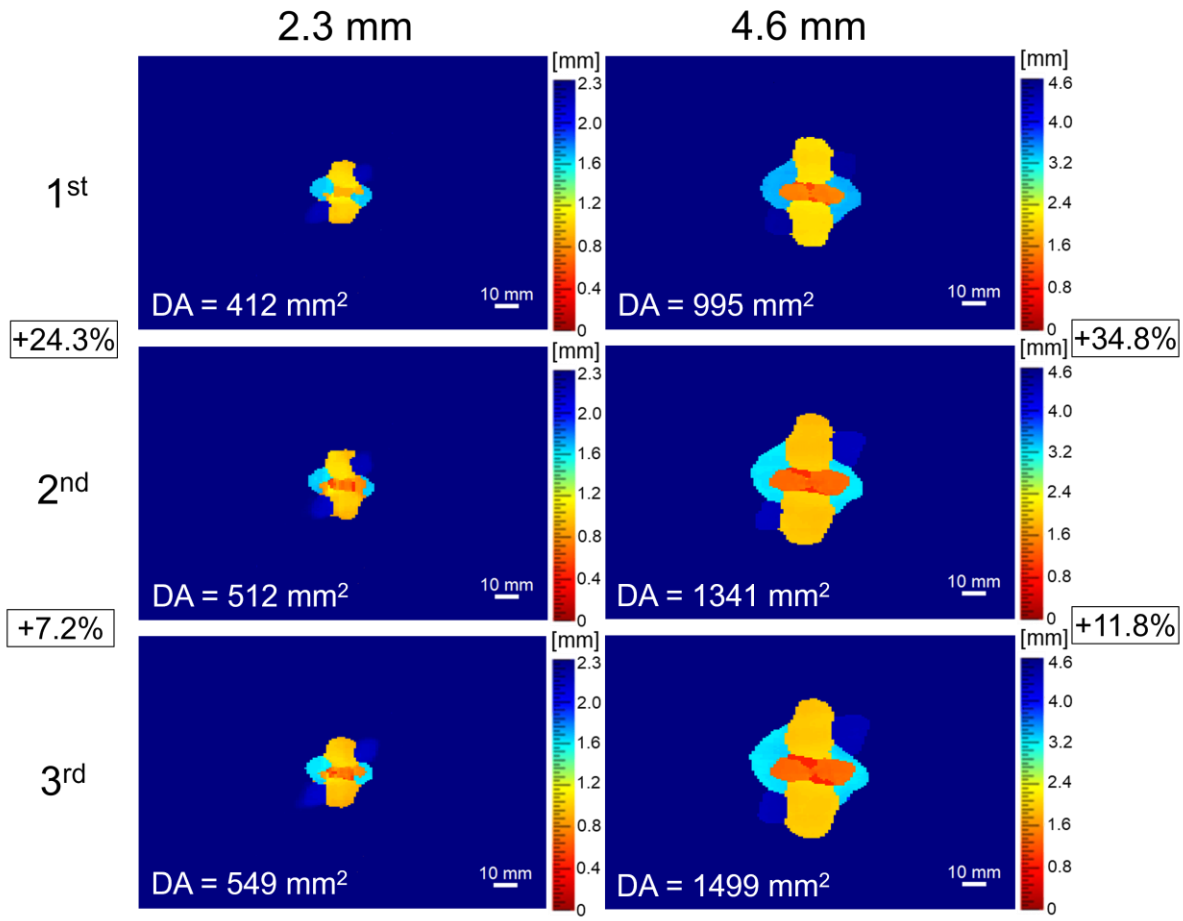


Figure 5-9: C-scan damage maps for 2.3 mm and 4.6 mm thick CF/Epoxy composite panels after one, two and three impacts at 10 J. The increase in delamination damage area (DA) between impacts is shown.

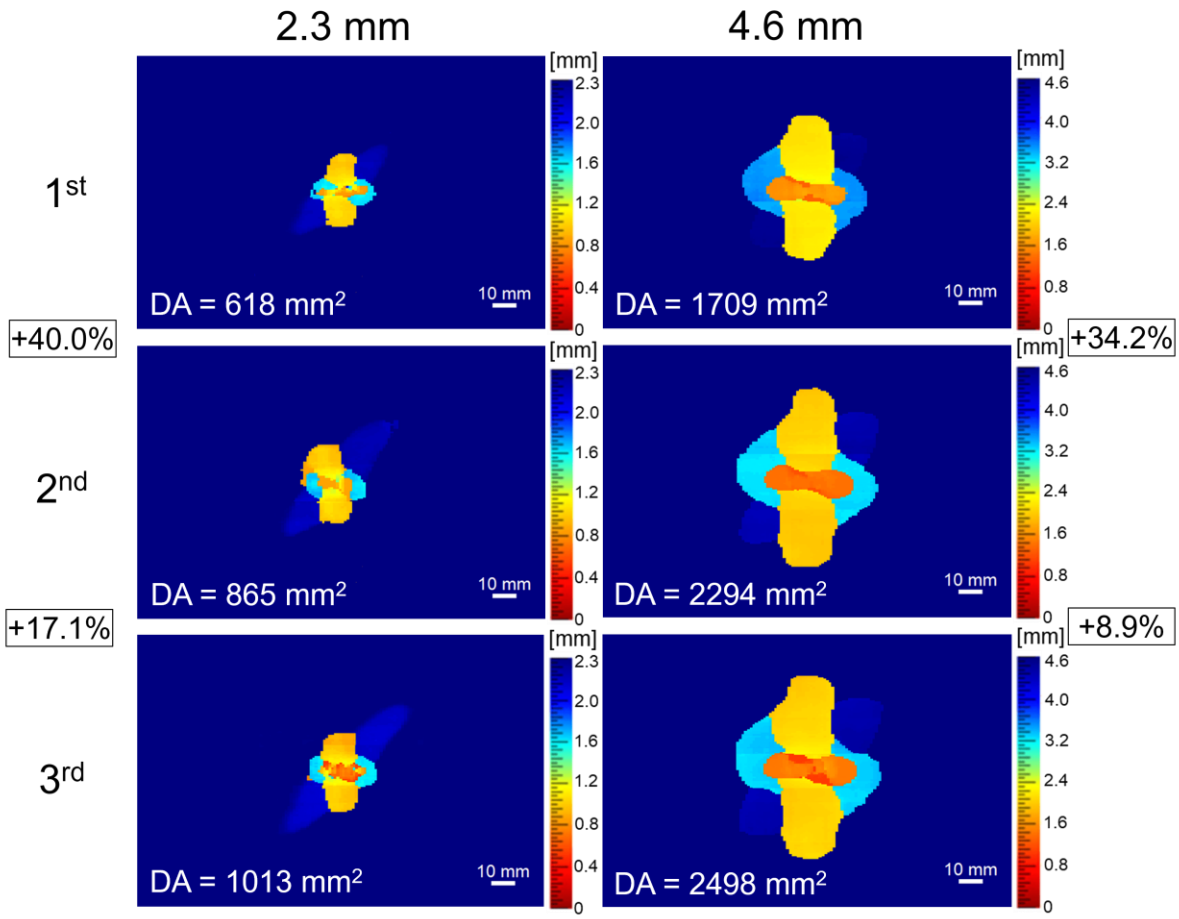


Figure 5-10: C-scan damage maps for 2.3 mm and 4.6 mm thick CF/Epoxy composite panels after one, two and three impacts at 15 J. The increase in delamination damage area (DA) between impacts is shown.

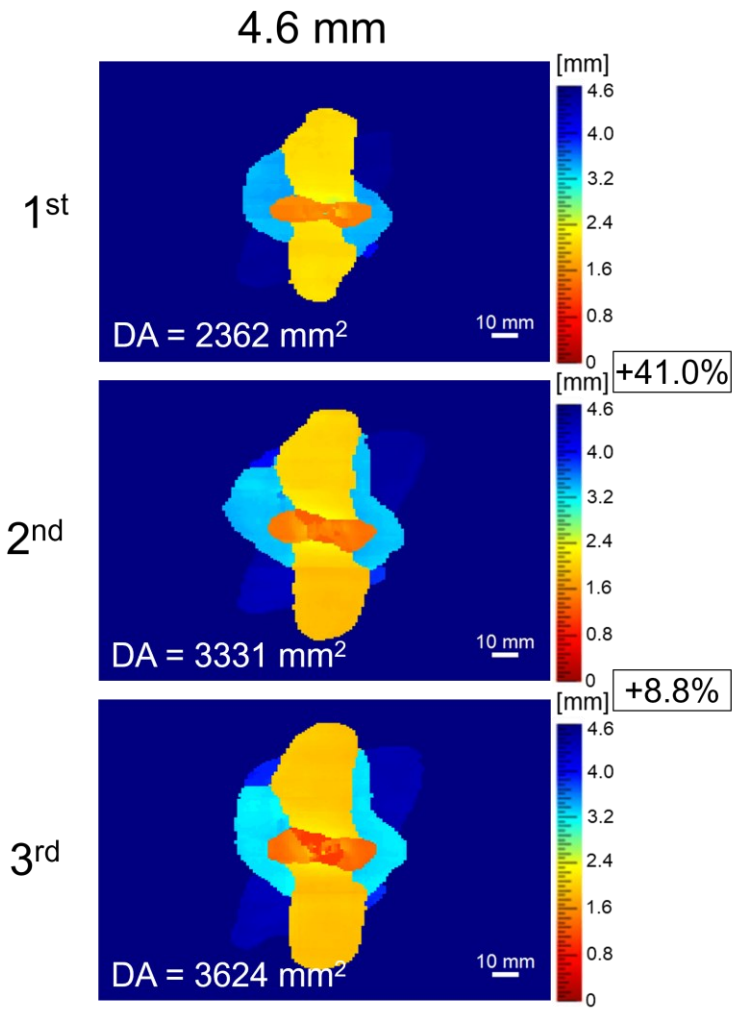


Figure 5-11: C-scan damage maps for a 4.6 mm thick CF/Epoxy composite panel after one, two and three impacts at 20 J. The increase in delamination damage area (DA) between impacts is shown.

Figure 5-12 summarises the delamination damage area versus the accumulated impact energy for each panel and again highlights the lower increase in damage caused by a third impact compared to a second impact (also noted in research performed at similar impact velocities by Tuo et al. [14]). Note that the 2 J data has not been included due to the damage being significantly smaller than scale being used on the damage area axis. For lower impact energies (0.54-1.71 J), Found and Howard [83] found that the rate of increase of damage was similar for the first few impacts and then decreased as the number of impacts increased. The damage in the panels impacted at 5 J does increase by similar amounts for a second and third impact, although slightly less for the third impact in both cases. Higher

impact energies cause greater deviations from this trend, with significantly lower increases in delamination damage area between the second and third impacts.

Figure 5-12 also reveals that a single impact at a larger energy creates a greater damage area than multiple lower energy impacts totalling the same accumulated energy. This supports the observations of Amaro et al. [82] and Found and Howard [83], who also conducted low-velocity impact studies, while being in contrast to the high-velocity results of Appleby-Thomas et al. [84] who found that delamination damage area varied linearly with cumulative impact energy. The different deformation behaviours of the panels under low- and high-velocity impacts is likely the cause of this discrepancy. Under low-velocity impact, the target geometry determines the impact response and ability to store elastic energy [44–46] whereas high-velocity impact loading causes a localised response and shorter impact duration, resulting in energy dissipation over a comparatively smaller region around the impact zone [44,45,47]. Therefore, the reduction in stiffness caused by the damage from previous impacts will affect the impact response under low-velocity impact more than for high-velocity impact. Under high-velocity impact, less energy is absorbed elastically so more is available to be absorbed through damage. Hence, a greater percentage of the impact energy is used to create damage under high-velocity impact and the variation of damage with impact energy is more linear for high-velocity. The effect of previous damage on the impact response and resulting damage formation is discussed in detail in Section 5.3.2. It is useful to also note that every impact energy which was high enough to cause delamination damage during a first impact also propagated the delaminations during subsequent impacts. Only 2 J impacts on 4.6 mm thick material caused no delamination damage during any of the three impacts.

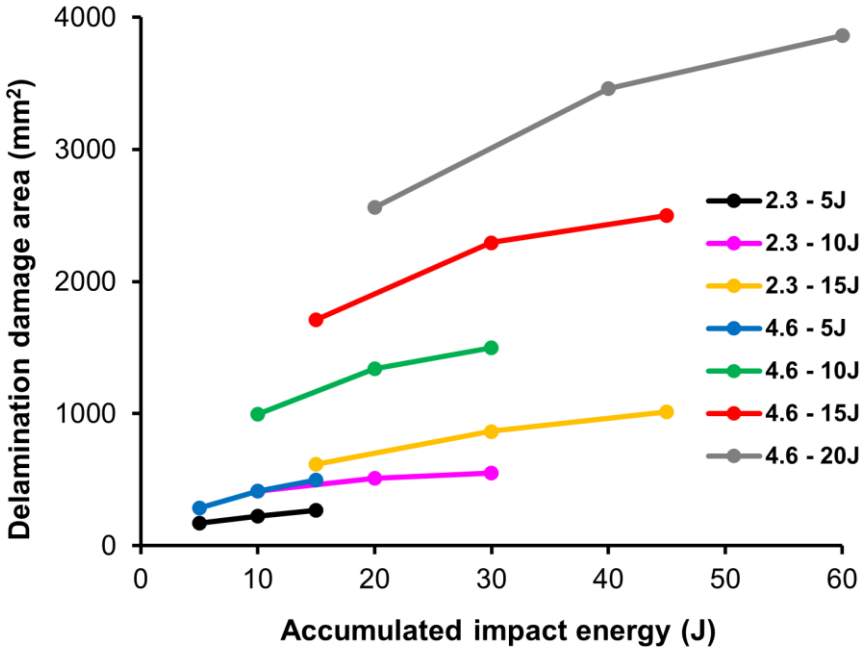


Figure 5-12: Graph of delamination damage area versus accumulated impact energy for first, second and third impacts at 5, 10, 15 and 20 J on 2.3 mm and 4.6 mm thick CF/Epoxy composite panels.

5.3.2 Load versus time and load versus displacement results

Load versus time and load versus displacement traces are shown in Figure 5-13 for first, second and third impacts at 5 J on both thicknesses of CF/Epoxy panel. (The load versus time and load versus displacement graphs for first, second and third impacts at 2 J are not included and analysed here due to the lack of any clear damage initiation load drops. These graphs are instead included in Appendix D.) The small sinusoidal oscillations on the rising section of the traces are indicative of mass-spring oscillations and have been observed by other researchers [290–292]. For the first impact, a clear load drop is visible for the 4.6 mm thick panel. This load drop indicates the load, time and displacement at which damage initiated in the panel during the impact event. On the other hand, the load versus time trace for the 2.3 mm thick panel does not show a clear load drop, despite the subsequent C-scan clearly showing damage in the panel, see Figure 4-1. For a second and third impact, no load drop is visible for either thickness of CF/Epoxy and the load versus time traces are indicative of a uniform elastic response. This suggests that minimal further damage initiation processes were started during subsequent impacts and instead, delamination damage formed during the first impact was propagated.

The load versus displacement traces in Figure 5-13(b) clearly demonstrate the difference in stiffness between the two thicknesses of panel. Furthermore, for both thicknesses of panel, the stiffness is significantly decreased after a single impact. This is due to the intralaminar and delamination damage causing a reduction in bending stiffness and increase in maximum displacement. A very slight further reduction in stiffness and increase in maximum displacement can also be seen after a second impact (i.e. from the third load versus displacement trace). Both of these reductions in stiffness are comparatively larger for the 4.6 mm panel. This is because the 4.6 mm thick panel suffers a greater delamination damage area and a greater increase in delamination area than the 2.3 mm panel. Hence, the stiffness of the 2.3 mm thick panel is less affected. The increase in maximum displacement The peak load is higher for the second and third impacts compared to the first impact for both thicknesses of panel, with the third impact achieving the highest peak load for the 4.6 mm panel. The 4.6 mm thick material also exhibits a higher peak load than the 2.3 mm thick material. Following the first impact, the panel exhibits a slightly reduced bending stiffness and the effective damage threshold has been raised. Therefore, during the impact event, more energy can be stored through elastic deformation of the panel, resulting in a higher peak load and maximum displacement [294]. The minimal increase in peak load for the 2.3 mm panels between the second and third impact highlights the comparatively smaller increase in damage area for subsequent impacts compared to the larger increases in peak load and damage area observed for the 4.6 mm panels. The slight increase in impact duration for subsequent impacts, again due to the panel becoming softer, has also been noted in studies by other researchers [83,85,108,294]. The similarity in peak load for the second and third impact on the 2.3 mm panel, yet the slightly longer impact duration for the third impact may indicate that damage propagates later in the impact event than for the second impact for this thickness of panel.

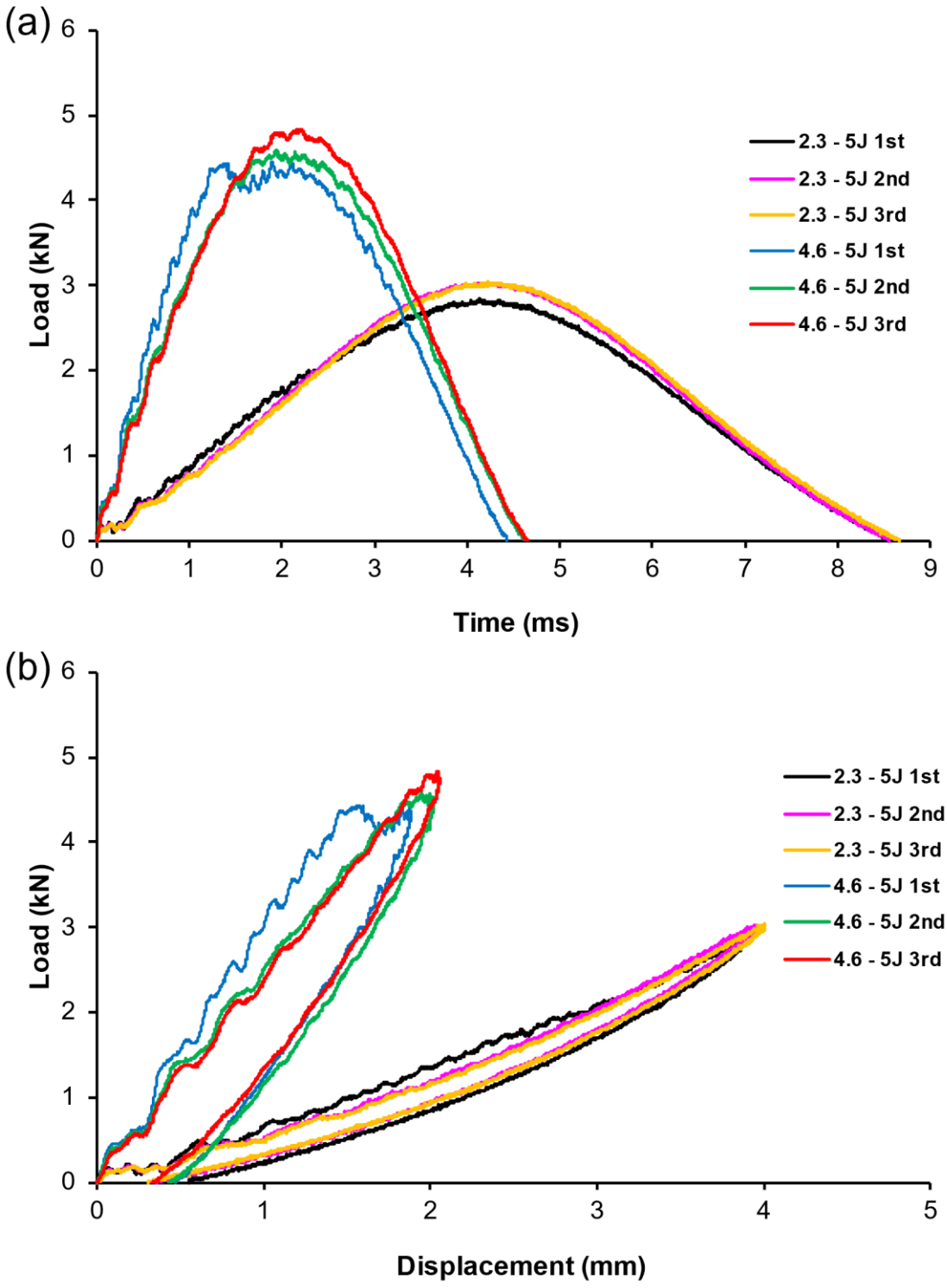


Figure 5-13: (a) Load versus time traces and (b) load versus displacement traces for first, second and third impacts at 5 J on 2.3 mm and 4.6 mm thick CF/Epoxy composite panels.

Load versus time and load versus displacement traces are shown in Figure 5-14 for first, second and third impacts at 10 J on both thicknesses of CF/Epoxy panel. For a first impact, a clear load drop is visible for the 4.6 mm thick panel and a relatively small load drop is visible for the 2.3 mm thick panel. The load drop occurs at a lower load for the 2.3 mm thick panel than for the 4.6 mm thick panel, albeit relatively close to the peak load, and also at a greater displacement. For a second and third impact, no load drop is visible for the 4.6 mm thick panels. However, a load drop is visible for the 2.3 mm thick panels for a second impact and occurs at approximately the peak load. This load drop is larger than the load drop seen for the 2.3 mm thick panels for a first impact and may indicate some new damage initiation taking place (in addition to the damage propagation observed from the C-scan for this impact, see Figure 5-9). No load drop was visible for the 2.3 mm thick panels for a third impact.

The load versus displacement traces in Figure 5-14(b) clearly demonstrate the difference in stiffness between the two thicknesses of panel. Furthermore, for both thicknesses of panel, the stiffness is significantly decreased after a single impact and a small further reduction in stiffness and increase in maximum displacement takes place after a second impact (i.e. from the third load versus displacement trace). The peak load is higher for the second and third impacts compared to the first impact for both thicknesses of panel, with the third impact achieving the highest peak load. Also, the 4.6 mm thick material exhibits a higher peak load than the 2.3 mm thick material. The 2.3 mm panel shows a smaller increase in peak load for subsequent impacts which corresponds to the smaller increase in damage areas.

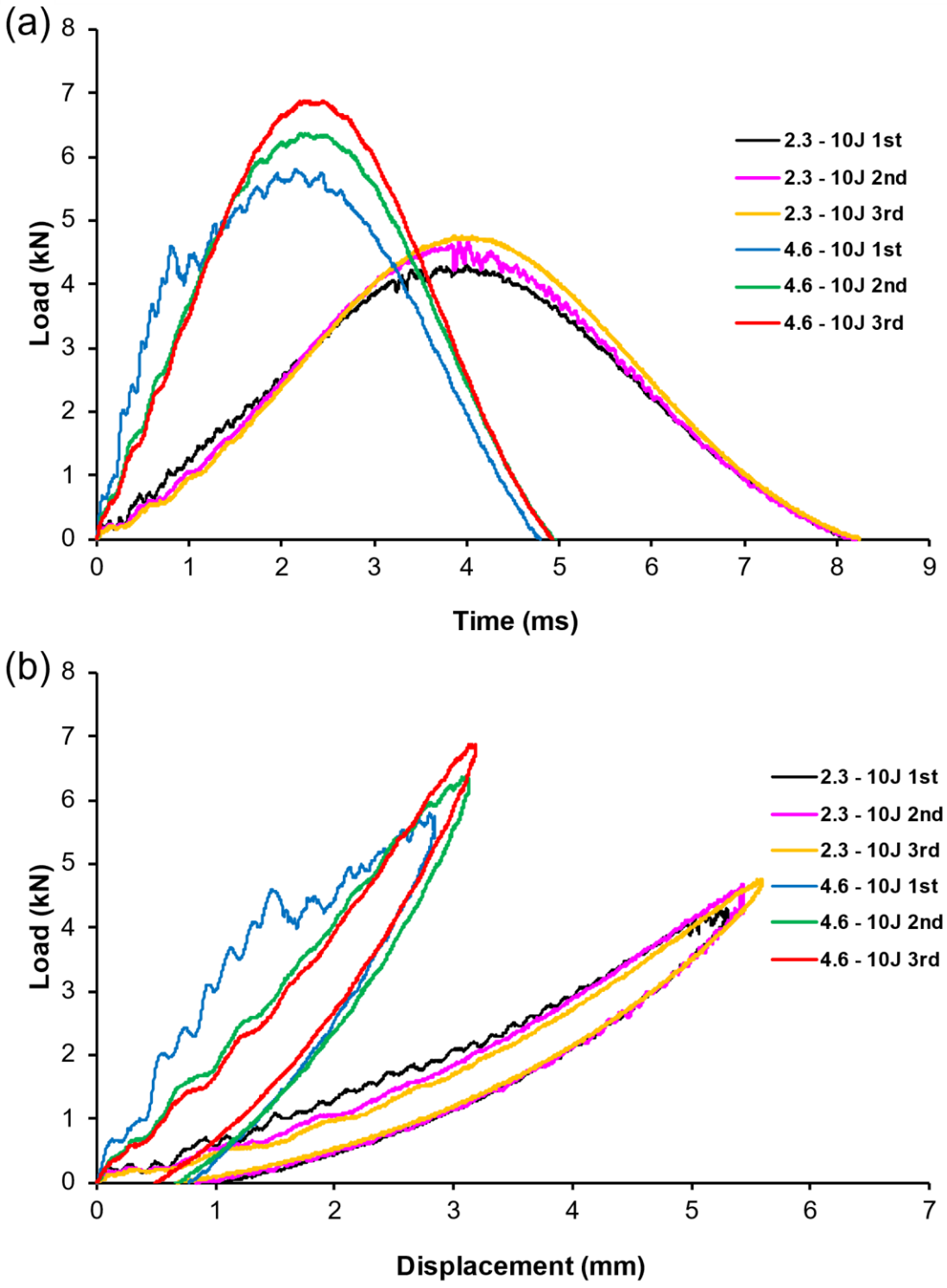


Figure 5-14: (a) Load versus time traces and (b) load versus displacement traces for first, second and third impacts at 10 J on 2.3 mm and 4.6 mm thick CF/Epoxy composite panels.

Load versus time and load versus displacement traces are shown in Figure 5-15 for first, second and third impacts at 15 J on both thicknesses of CF/Epoxy panel. The data for the 2.3 mm thick panel which showed a delamination damage area of 1013 mm^2 after three impacts is used in Figure 5-15. The 2.3 mm thick panel which showed a significantly greater damage area of 1454 mm^2 after three impacts exhibited a different load versus time behaviour. This is discussed further in Appendix C. For a first impact, clear load drops are visible for both thicknesses of panel. The initial load drop occurs at a lower load for the 2.3 mm thick panel than for the 4.6 mm thick panel and also at a greater displacement, as seen for the 10 J impacts. Interestingly, the 2.3 mm thick panel also exhibits a second, much larger load drop, close to the peak load, indicating some further damage initiation. For a second and third impact, no load drop is visible for either thickness of CF/Epoxy.

The load versus displacement traces in Figure 5-15(b) clearly demonstrate the difference in stiffness between the two thicknesses of panel and also highlight the reduction in stiffness for each subsequent impact. These reductions in stiffness are accompanied by an increase in maximum displacement. Again, the peak load is higher for the second and third impacts compared to the first impact for both thicknesses of panel, with the third impact achieving the highest peak load. The increase in peak load between the second and third impacts is greater for the 4.6 mm thick panel than for the 2.3 mm thick panel, in which the peak loads are very similar for the second and third impacts. The damage area increases significantly between the second and third impacts for 2.3 mm thick panel so it would be expected for peak load to increase by a greater amount, however the impact duration has slightly lengthened which is as expected. The 4.6 mm thick material exhibits a higher peak load than the 2.3 mm thick material.

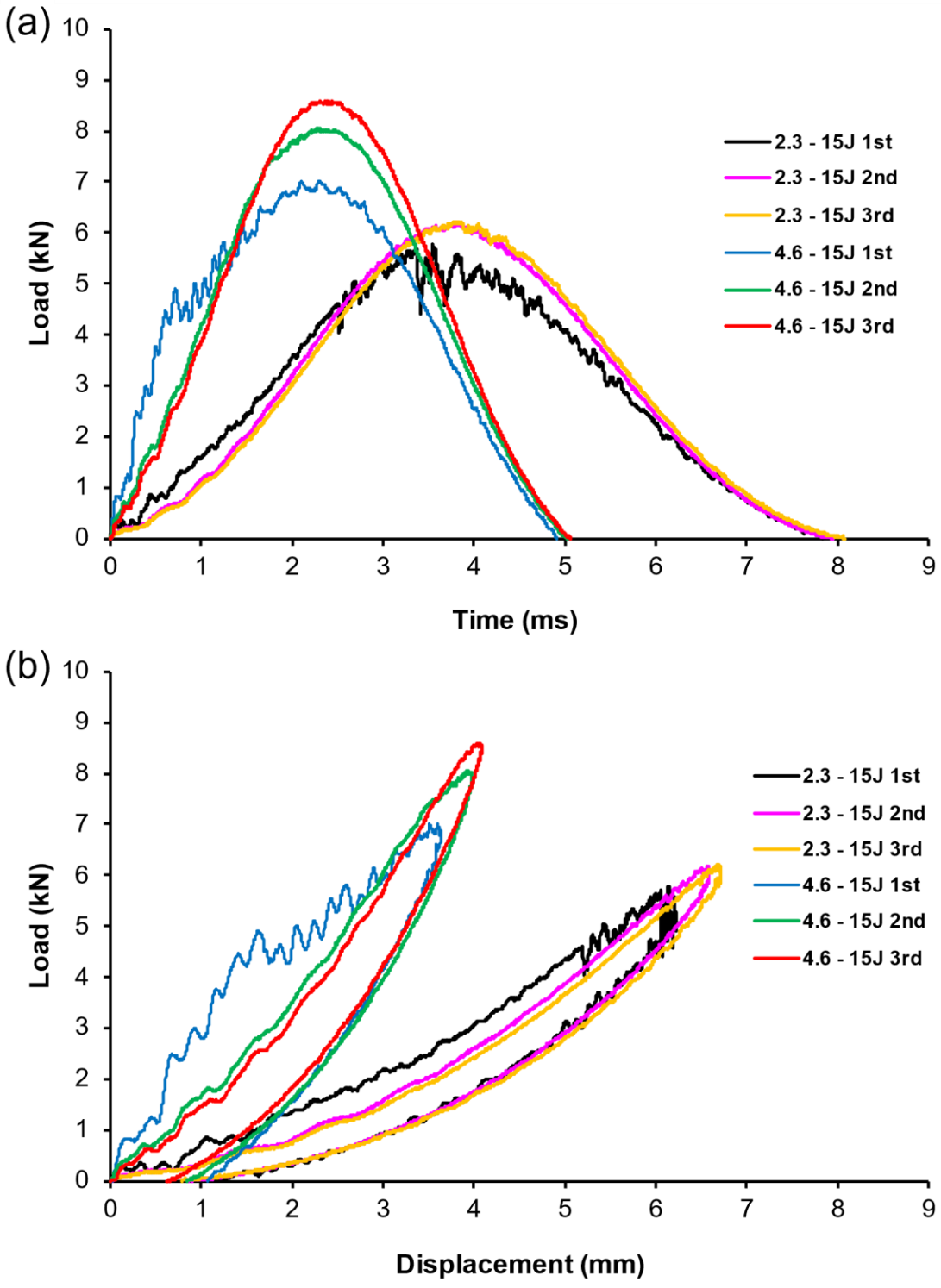


Figure 5-15: (a) Load versus time traces and (b) load versus displacement traces for first, second and third impacts at 15 J on 2.3 mm and 4.6 mm thick CF/Epoxy composite panels.

Load versus time and load versus displacement traces are shown in Figure 5-16 for first, second and third impacts at 20 J on a 4.6 mm thick CF/Epoxy panel. Note that 20 J impact tests were not performed on the 2.3 mm thick CF/Epoxy panels since the damage severity would have been too great. For the first impact, a clear load drop is visible, just as for the other tested impact energies. For the second impact, a small load drop is visible near to the peak load, which may indicate a small amount of new damage initiation. No load drop is visible for the third impact.

The load versus displacement traces in Figure 5-16(b) indicate that the stiffness is significantly decreased after a single impact and a further reduction in stiffness and increase in maximum displacement takes place for a second impact (i.e. from the third load versus displacement trace). Also, the peak load is higher for the second and third impacts compared to the first impact, with the third impact achieving the highest peak load.

Overall, for subsequent impacts, the load versus time and load versus displacement traces suggest that minimal further damage initiation processes took place and instead, delamination damage initiated during the first impact was propagated. The peak load increased more for the 4.6 mm panels than for the 2.3 mm panels and all load versus time and load versus displacement graphs show an increase in impact duration and maximum displacement with subsequent impacts, in accordance with studies in the literature [14,82,83,85]. The maximum displacement increased by a similar amount for both thicknesses of panel and the impact duration increased by slightly more for 4.6 mm panels for subsequent impacts. The presence of delamination damage causes a reduction in bending stiffness, allowing more impact energy to be stored through elastic deformation for a given impact energy. Hence, a higher peak load and maximum displacement are seen for subsequent impacts.

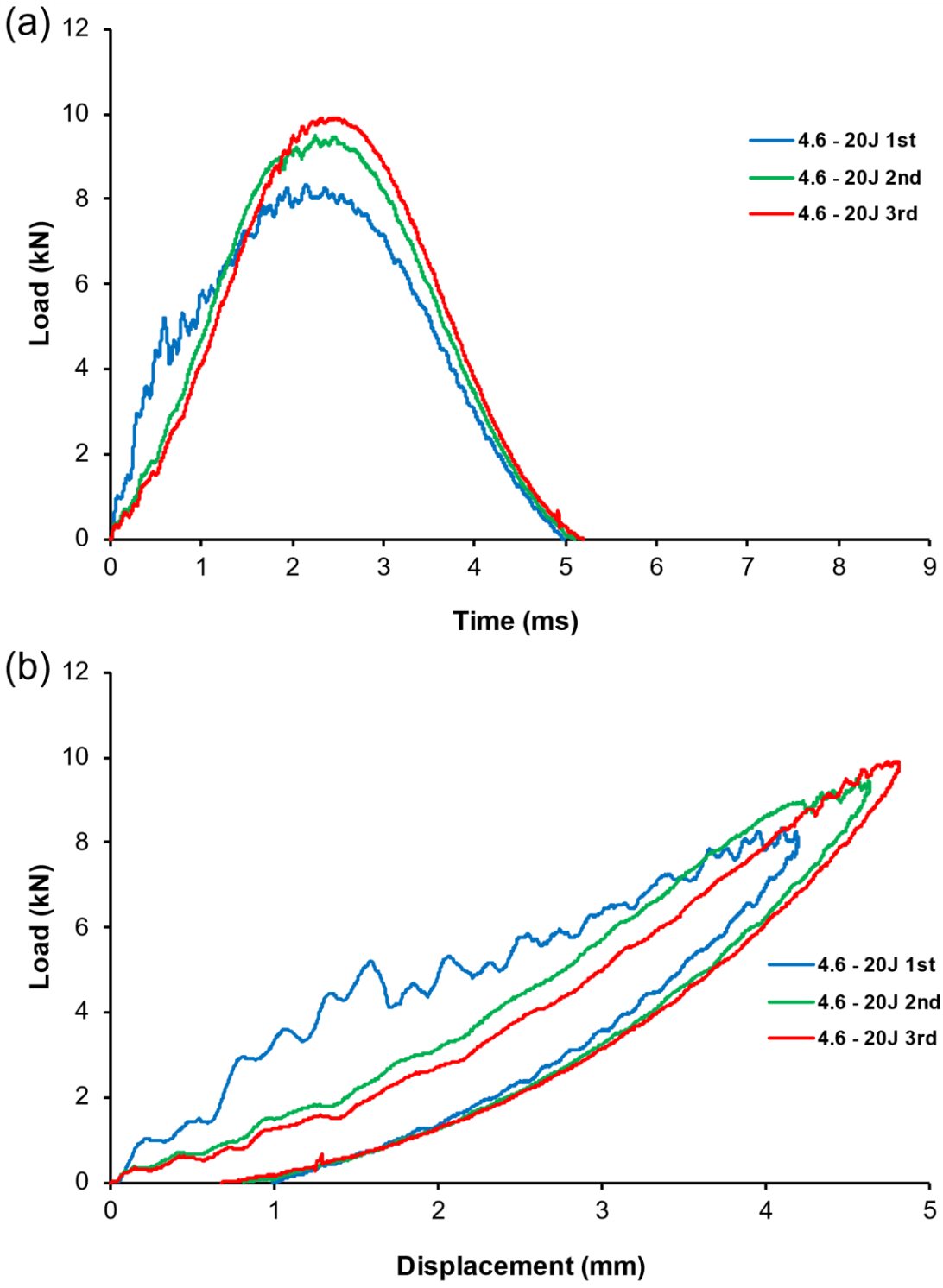


Figure 5-16: (a) Load versus time traces and (b) load versus displacement traces for first, second and third impacts at 20 J on 4.6 mm thick CF/Epoxy composite panels.

Figure 5-17 and Figure 5-18 show high-speed photographic image sequences, taken at a frame rate of 10000 frames per second, of the second impacts at 15 J on 2.3 and 4.6 mm thick CF/Epoxy panels, respectively. The total contact times are 8 ms and 5 ms, respectively. The 2.3 mm thick panel has a longer contact time and shows a significantly greater displacement compared to the 4.6 mm panel. These observations are confirmed by the load versus time and load versus displacement traces shown in Figure 5-15.

As well as showing the process of indentation, filming the impacts at high-speed allows the deformation behaviour of panels during first and second impacts to be compared. By comparing Figure 4-5 and Figure 4-6 to Figure 5-17 and Figure 5-18 some differences between the first and second impacts are highlighted. The displacement appears to increase slightly more quickly for a second impact (in the third images of the second impact sequences the impactor has depressed further into the panel). This is because the panel has become softer with the presence of delaminations so deforms more easily, whereas during a first impact, the panel deforms relatively slower due to the increased stiffness from the lack of damage. During a second impact, the impactor fits into the indent created by the first impact and stays in contact until the last frame. While pushing the panel to a greater displacement, the impactor causes further viscoelastic and plastic behaviour and slightly extends the depth of the formed indentation. In addition, the delaminations from the first impact are propagated.

In the slow-motion video of the first impacts a ‘judder’ is seen at the point of damage initiation within the panel and the impactor depresses further into the material without the panel deforming significantly. This is followed by relatively smooth deformation up until maximum displacement is reached. For the second impacts, no ‘judder’ is observed and a seemingly elastic sequence takes place. This is because the sudden initiation of delaminations does not take place during a second impact, as shown by the load versus time and load versus displacement traces in Figure 5-13, Figure 5-14, Figure 5-15 and Figure 5-16.

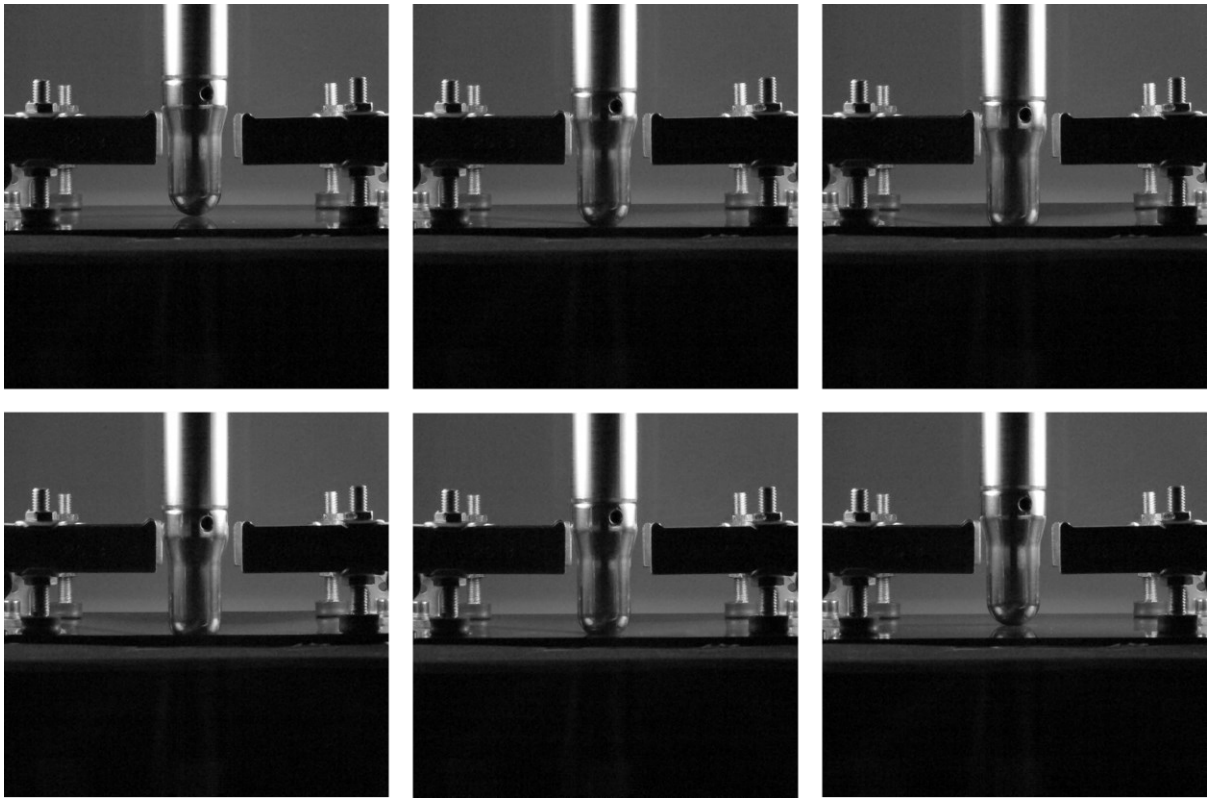


Figure 5-17: Series of high-speed photographic images showing the indentation process for an impact of 15 J on a previously impacted 2.3 mm thick CF/Epoxy composite panel (inter-frame time is 1.6 ms). The first image (top left) is captured just after the impact event and total contact time is approximately 8 ms, with the last image (bottom right) showing the start of the rebounding of the impactor. The hemispherical stainless-steel impactor has a diameter of 16 mm.

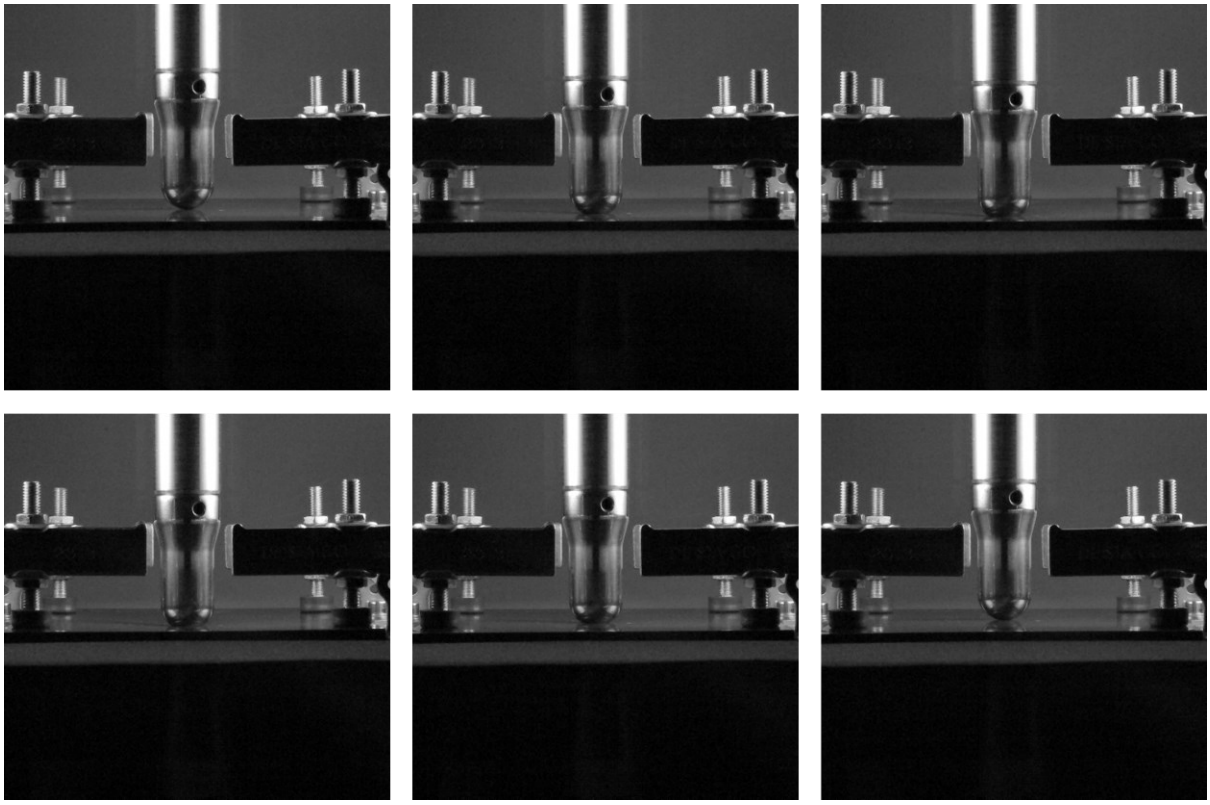


Figure 5-18: Series of high-speed photographic images showing the indentation process for an impact of 15 J on a previously impacted 4.6 mm thick CF/Epoxy composite panel (inter-frame time is 1 ms). The first image (top left) is captured just after the impact event and total contact time is approximately 5 ms, with the last image (bottom right) showing the start of the rebounding of the impactor. The hemispherical stainless-steel impactor has a diameter of 16 mm.

Energy versus time graphs are shown in Figure 5-19, Figure 5-20, Figure 5-21, Figure 5-22 and Figure 5-23 for first, second and third impacts at 2, 5, 10, 15 and 20 J, respectively, on both thicknesses of CF/Epoxy panel. The energy shown is the energy stored or absorbed by the panel during the impact event. The graphs show an increasing amount of energy transferred to the panel by the impactor up until the peak. After the peak some energy is transferred back to the impactor and this rebound energy is shown by the difference between the peak energy and the final energy. The panel impacted at 15 J which showed a delamination damage area of 1013 mm^2 after three impacts is used in Figure 5-22. Note also that 20 J impact tests were not performed on the 2.3 mm thick CF/Epoxy panels since the damage severity would have been too great. Figure 5-24 shows graphically how the percentage of energy rebounded changes with impact energy for first, second and third impacts at 2, 5, 10, 15 and 20 J. For all the panels which showed delamination damage, the amount of energy

absorbed by the panel decreases for subsequent impacts and the rebound energy increases. These changes in absorbed and rebound energies between subsequent impacts become more apparent as the impact energy increases for the 4.6 mm thick panels. In contrast, when the delamination damage area stays constant for the three impacts, for instance the 4.6 mm panel impacted at 2 J, the amount of energy absorbed stays relatively constant for each subsequent impact. Subsequent impacts cause a lower percentage increase in damage area, see Figure 5-8, Figure 5-9, Figure 5-10 and Figure 5-11, therefore less energy is absorbed through damage formation. In turn, more energy is available to deform the panel, which is also less stiff due to the presence of the larger delaminations. Therefore, the panels deform further, see Figure 5-13(b), Figure 5-14(b), Figure 5-15(b) and Figure 5-16(b), allowing more energy to be stored as elastic strain-energy, which in turn is available to rebound the impactor. The same is true when the impact energy increases – a greater deformation occurs and a higher percentage of energy is rebounded. In contrast, at lower impact energies the panel absorbs the impact energy locally, a lower maximum displacement is reached and therefore less rebound energy is provided back to the impactor. This is particularly apparent for the 2.3 mm thick panel impacted at 2 J, in which around 90% of the impact energy is absorbed. Some of the impact energy is also lost due to friction, vibration and acoustic losses, particularly around the supports of the drop-weight machine. The 2.3 mm panel impacted at 15 J absorbed a larger than expected percentage of the impact energy on the first impact as a second load drop near the peak load led to a lower maximum displacement being achieved displacement, see Figure 5-15. Hence, less energy was stored as elastic strain-energy and was therefore available to rebound the impactor.

The percentage of energy rebounded versus impact energy line is likely not linear between 2 and 5 J for the 2.3 mm panel. Also, a drop in rebound energy is likely at the energy at which delaminations initiate in the 4.6 mm panel. Hence, the linear extrapolations on Figure 5-24 are dashed between 2 and 5 J to act as a guide rather than an accurate description of the variation of percentage of energy rebounded with impact energy.

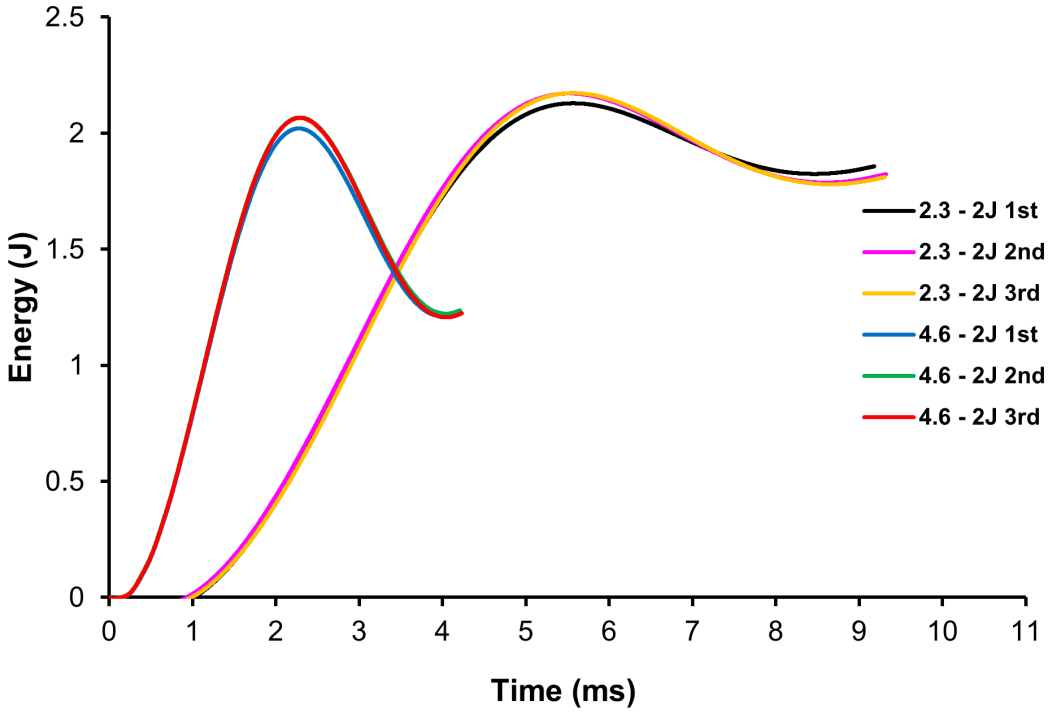


Figure 5-19: Energy versus time traces for first, second and third impacts at 2 J on 2.3 mm and 4.6 mm thick CF/Epoxy composite panels.

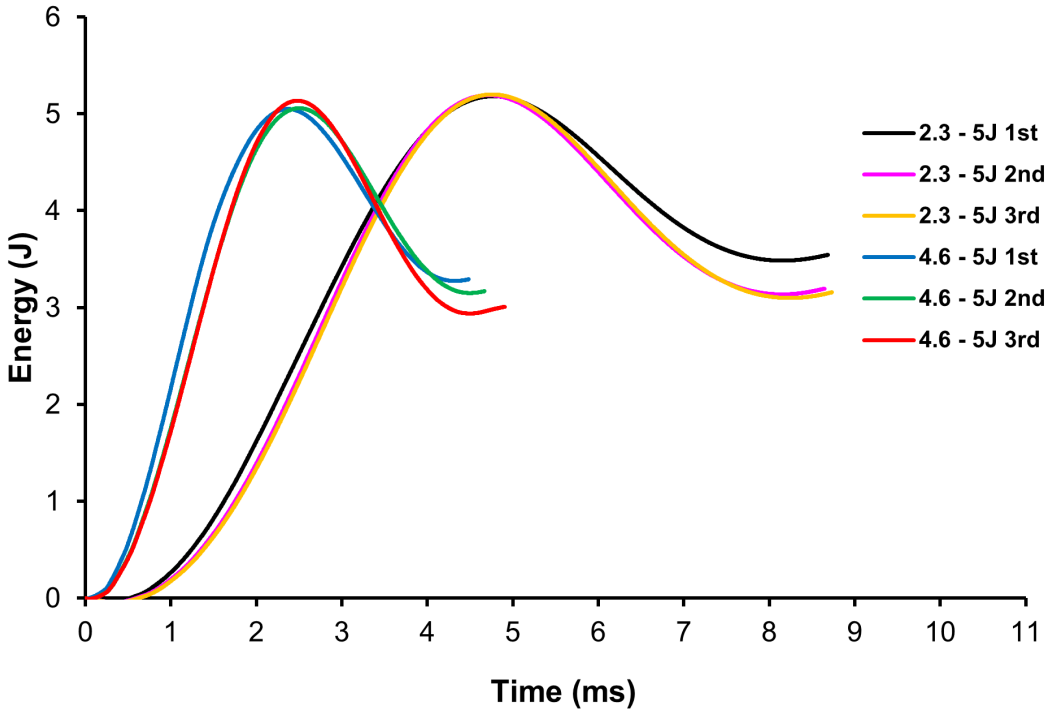


Figure 5-20: Energy versus time traces for first, second and third impacts at 5 J on 2.3 mm and 4.6 mm thick CF/Epoxy composite panels.

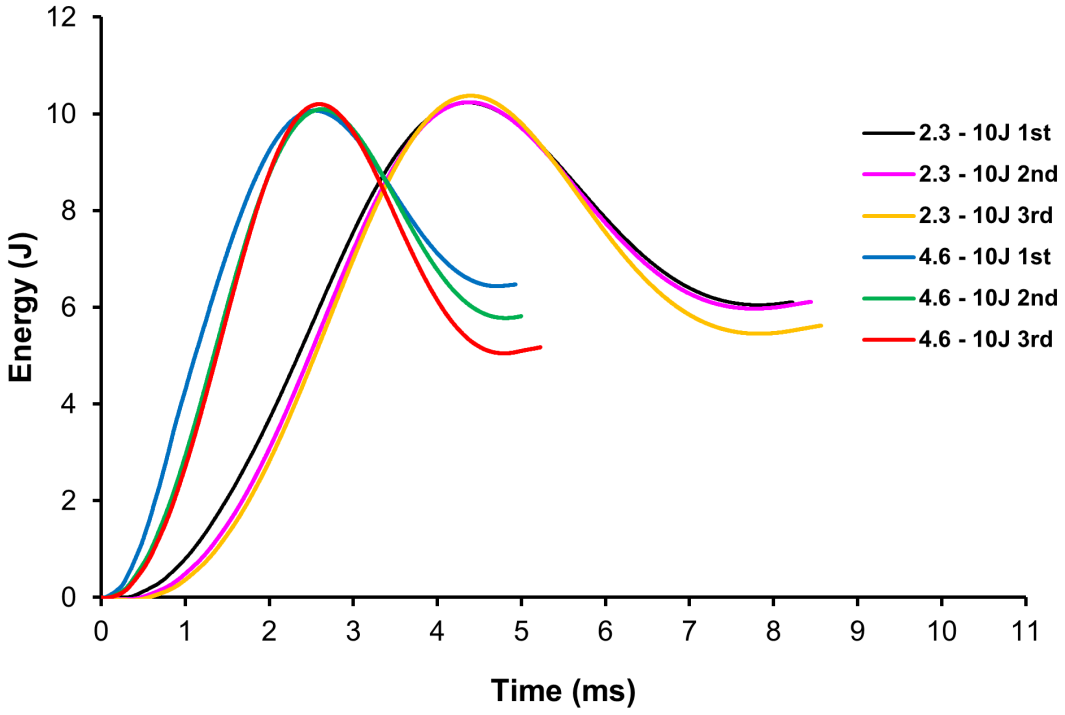


Figure 5-21: Energy versus time traces for first, second and third impacts at 10 J on 2.3 mm and 4.6 mm thick CF/Epoxy composite panels.

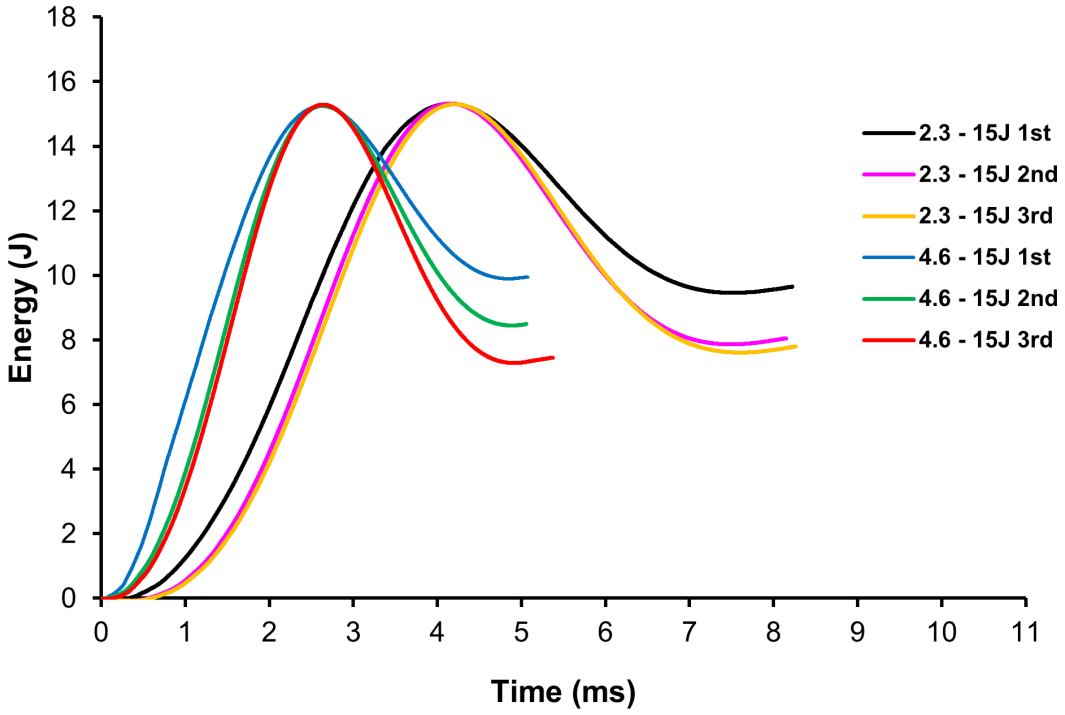


Figure 5-22: Energy versus time traces for first, second and third impacts at 15 J on 2.3 mm and 4.6 mm thick CF/Epoxy composite panels.

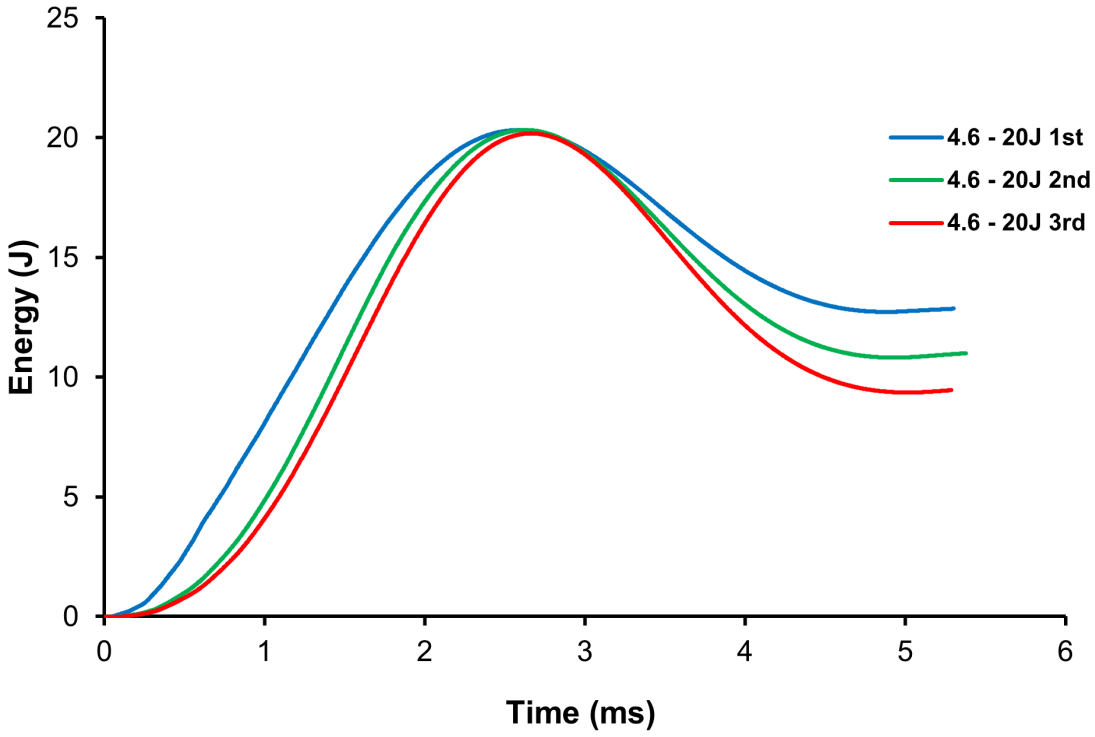


Figure 5-23: Energy versus time traces for first, second and third impacts at 20 J on 4.6 mm thick CF/Epoxy composite panels.

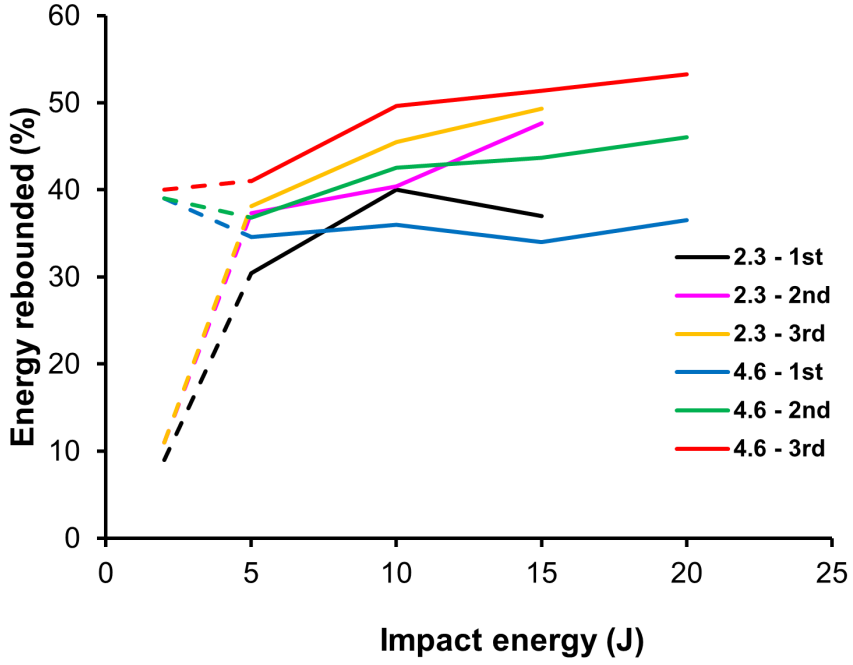


Figure 5-24: Graph of percentage of impact energy rebounded versus the impact energy for first, second and third impacts at 2, 5, 10, 15 and 20 J on 2.3 mm and 4.6 mm thick CF/Epoxy composite panels.

5.3.3 Indentation depth studies

Figure 5-25, Figure 5-26 and Figure 5-27 show cross-sections of the resulting indentation after one, two and three impacts at 5, 10 and 15 J, respectively, on both thicknesses of CF/Epoxy panel, taken from the Confocal microscopy measurements. Note that no cross-section data was obtained for second and third impacts at 20 J. As explained in Chapter 4, from these cross-sections an indentation depth was calculated and compared with the indentation depth measurements taken from using the handheld digital gauge. Again, the two different methods of measuring the indentation depth are in excellent agreement, see Figure 5-28. The results given in Figure 5-25, Figure 5-26 and Figure 5-27 generally show that a section through the permanent indentation profile continues to have a similar shape for subsequent impacts. The central depression deepens with both impact energy and number of impacts and hence the sides of the indentation steepen. A smaller increase in the indentation depth is seen between the second and third impacts compared to between the first and second impacts as the material has less ability to accommodate further plastic deformation. The smaller increases in indentation depth are likely from a mixture of further plastic deformation and increase in depth due to delamination propagation.

The increase in indentation depth for successive impacts is not taken into account in the load-displacement graphs of Figure 5-13, Figure 5-14, Figure 5-15 and Figure 5-16. Rather than measuring the displacement of the rear of the panel, the displacement of the top of the impactor head is being measured. Therefore, the maximum displacement being measured is in fact the maximum displacement of the rear of the panel plus the increase in indentation depth caused by that impact. However, the increase in indentation depth for successive impacts is smaller than the increase in maximum displacement (of the impactor head) for successive impacts. For example, first, second and third impacts at 15 J on a 4.6 mm panel lead to indentation depths of approximately 0.17, 0.21 and 0.25 mm, respectively. The corresponding maximum displacements, as measured at the impactor head, are 3.63, 3.98 and 4.08 mm. Clearly the increase in maximum displacement is greater than the increase in indentation depth. Therefore, even after correction, the results still show that the maximum displacement of the panel increases for subsequent impacts.

Both thicknesses of CF/Epoxy panel show similar indentation depths for a single impact at the same energy. For subsequent impacts, the 2.3 mm panel starts to show a lower indentation depth than the 4.6 mm panel. However, one 2.3 mm thick panel impacted multiple times at 15 J showed severe damage within indentation, as shown by the rough and disjointed surface in Figure 5-27(a). Cracking around some sections of the surface ply beneath the impactor was severe, causing sections within the indentation to rise up from the surface, hence the disjointed indentation cross sections. The other 2.3 mm thick panel impacted multiple times did not show such severe damage and instead showed the same standard indentation shape as the rest of the panels. Figure 5-27(a) shows all three indentation profiles for the panel with subsequent delamination damage areas of 280, 549 and 1454 mm^2 (for first, second and third impacts) and the indentation profile for only the third impact case for the panel with a final delamination damage area of 1013 mm^2. The different behaviour of these two 2.3 mm panels under 15 J impact is examined further in Appendix C.

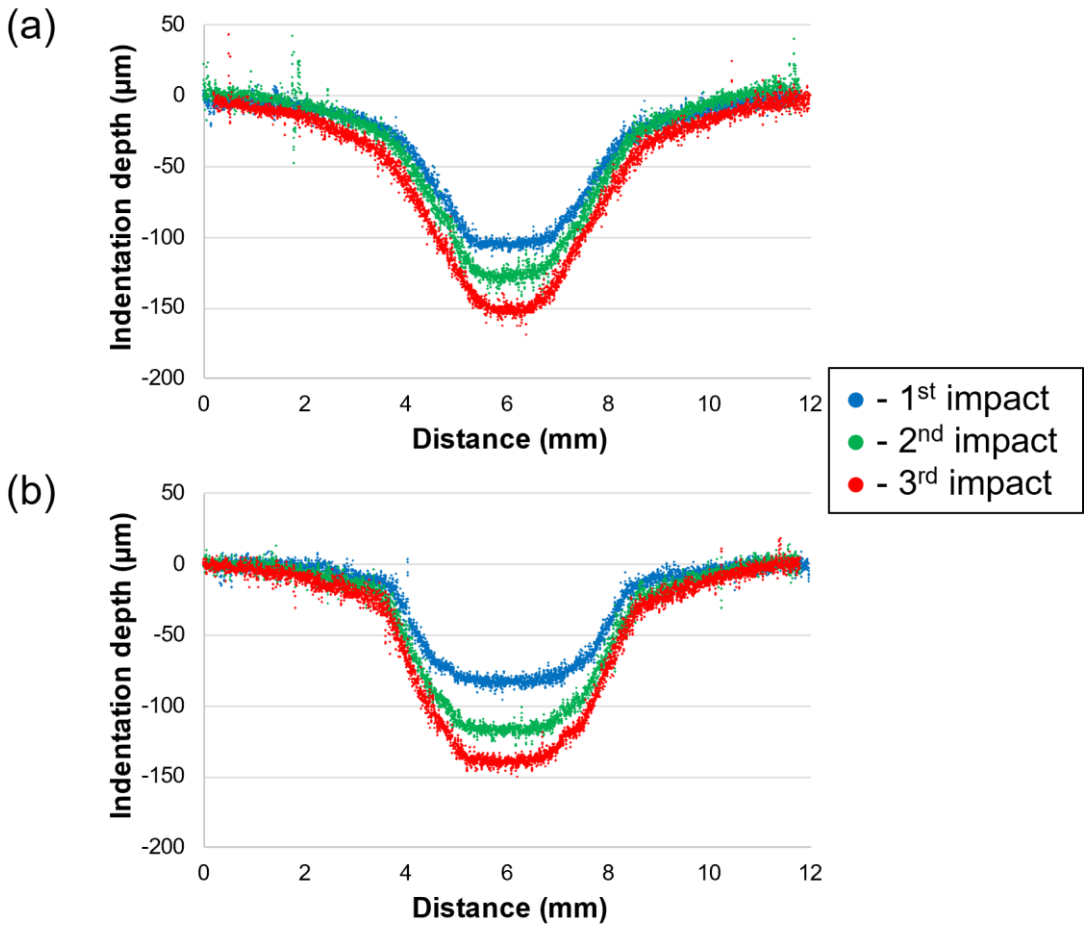


Figure 5-25: Indentation cross-section in (a) 2.3 mm thick and (b) 4.6 mm thick CF/Epoxy composite panels after one, two and three impacts at 5 J.

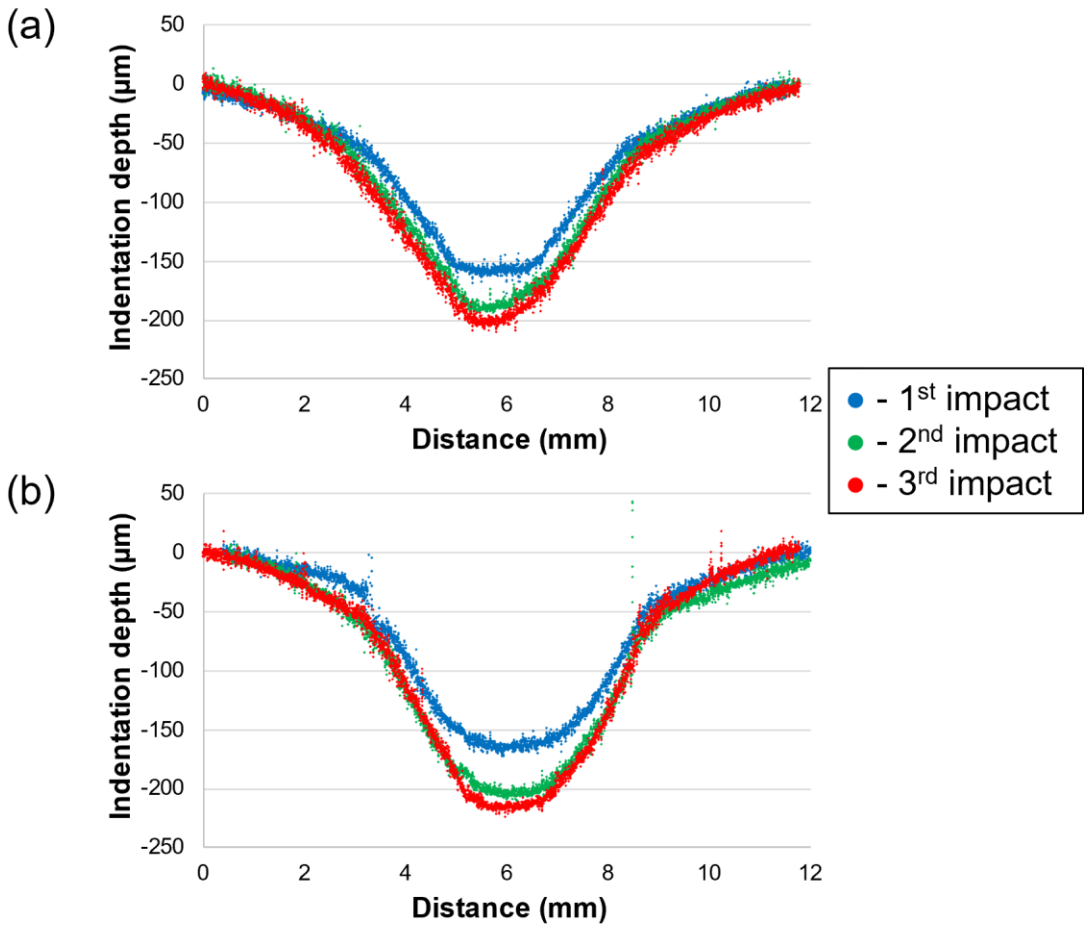


Figure 5-26: Indentation cross-section in (a) 2.3 mm thick and (b) 4.6 mm thick CF/Epoxy composite panels after one, two and three impacts at 10 J.

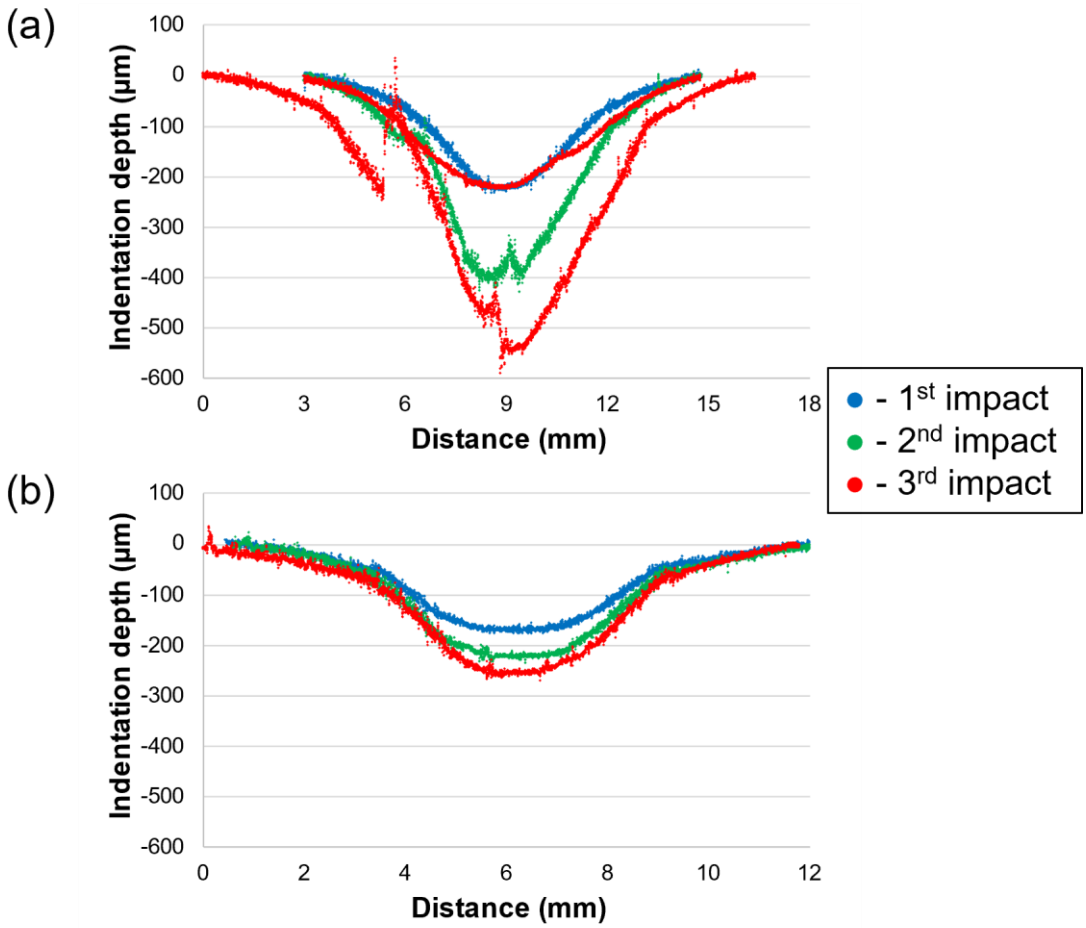


Figure 5-27: Indentation cross-section in (a) 2.3 mm thick and (b) 4.6 mm thick CF/Epoxy composite panels after one, two and three impacts at 15 J. Cross-sections from two panels are shown for the 2.3 mm thick third impact case.

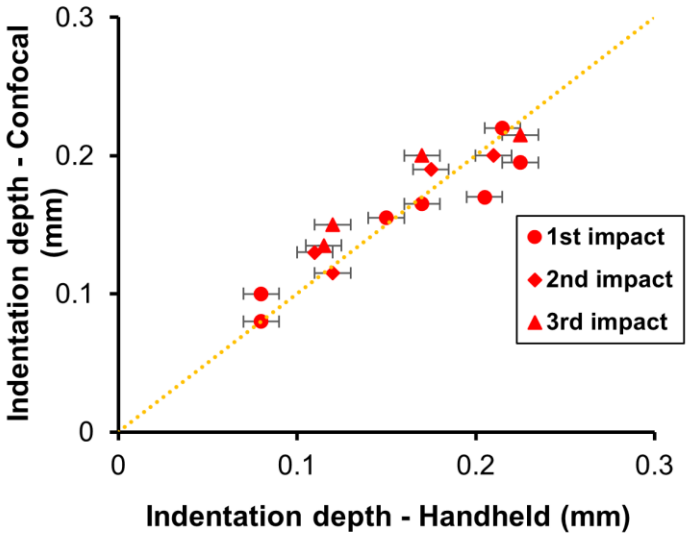


Figure 5-28: The indentation depth in the CF/Epoxy composite panel measured using the Confocal laser scanning microscope versus using the handheld gauge, including measurements taken after first, second and third impacts.

Figure 5-29 presents a summary of the cross-sections of the resulting indentation after one, two and three impacts at 5, 10 and 15 J on both thicknesses of CF/Epoxy panel. The depth scales are kept consistent for each thickness of panel.

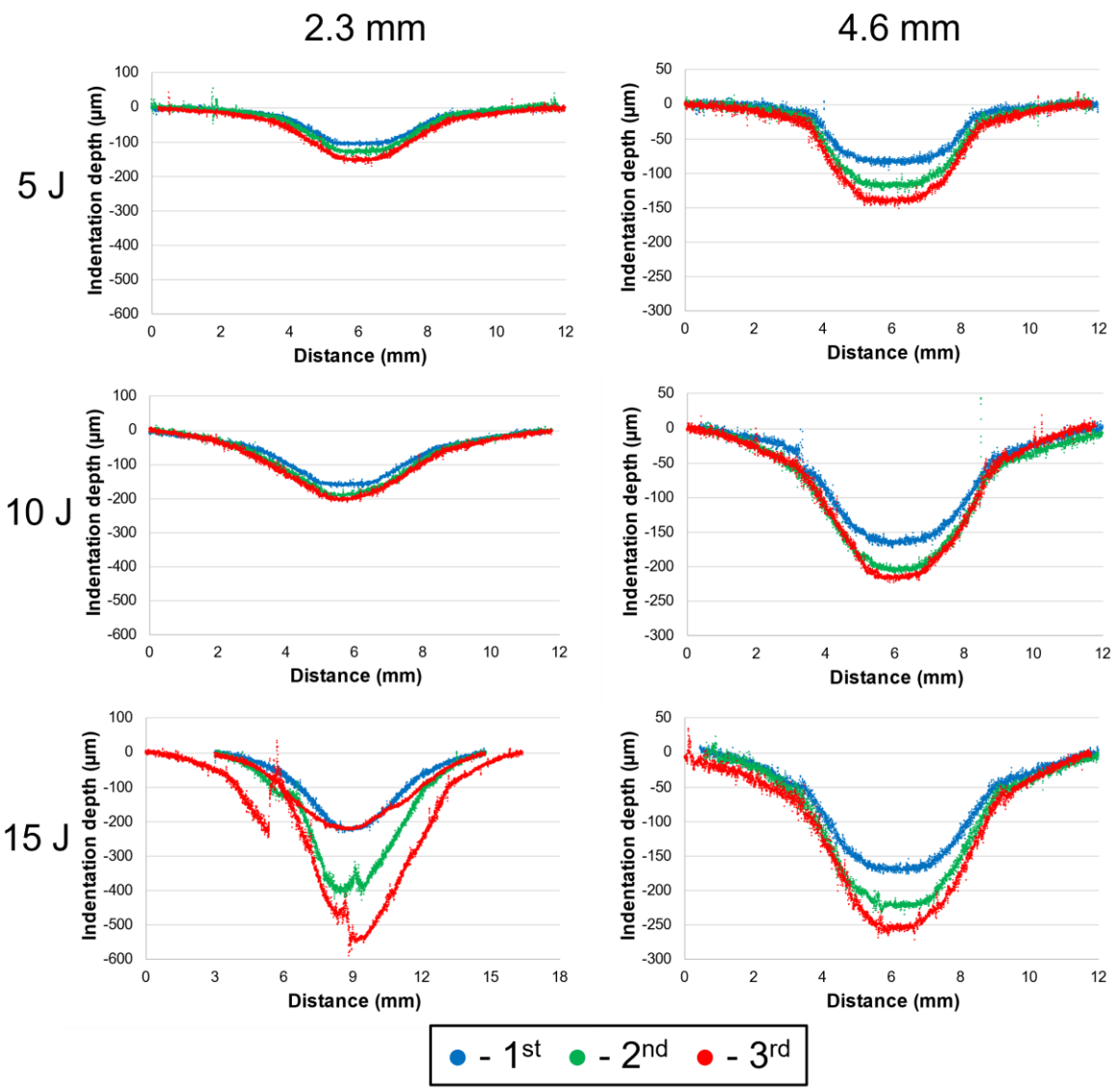


Figure 5-29: Summary of indentation cross-sections in 2.3 mm and 4.6 mm thick CF/Epoxy composite panels after one, two and three impacts at 5, 10 and 15 J. Cross-sections from two panels are shown for the 2.3 mm thick third impact case.

Figure 5-30 plots the indentation depths measured for different impact energies, and the associated delamination damage areas versus the impact energy for both 2.3 mm and 4.6 mm thick panels after (a) two and (b) three impacts. In some cases, a third replicate result, in addition to the duplicate results presented in Figure 5-1, Figure 5-2, Figure 5-4 and Figure 5-5, is also included to improve the confidence in these data. The C-scan maps for these data points are included in Appendix E. The 2.3 mm panel which exhibited damage areas of 549 and 1454 mm^2 after two and three impacts is included on the graphs (the corresponding data point is shown in brackets on the indentation depth

versus impact energy graphs) but was not included when calculating the second-order polynomial fits. As for the single impact cases in Figure 4-9, the damage area demonstrates an approximately linear relationship with the impact energy for both thicknesses of panel for both the second and third impact cases. Furthermore, for a given impact energy, the corresponding damage areas are substantially greater for the 4.6 mm thick panels for impact energies of 5 J and above, as seen in the C-scans in Figure 5-3 and Figure 5-6.

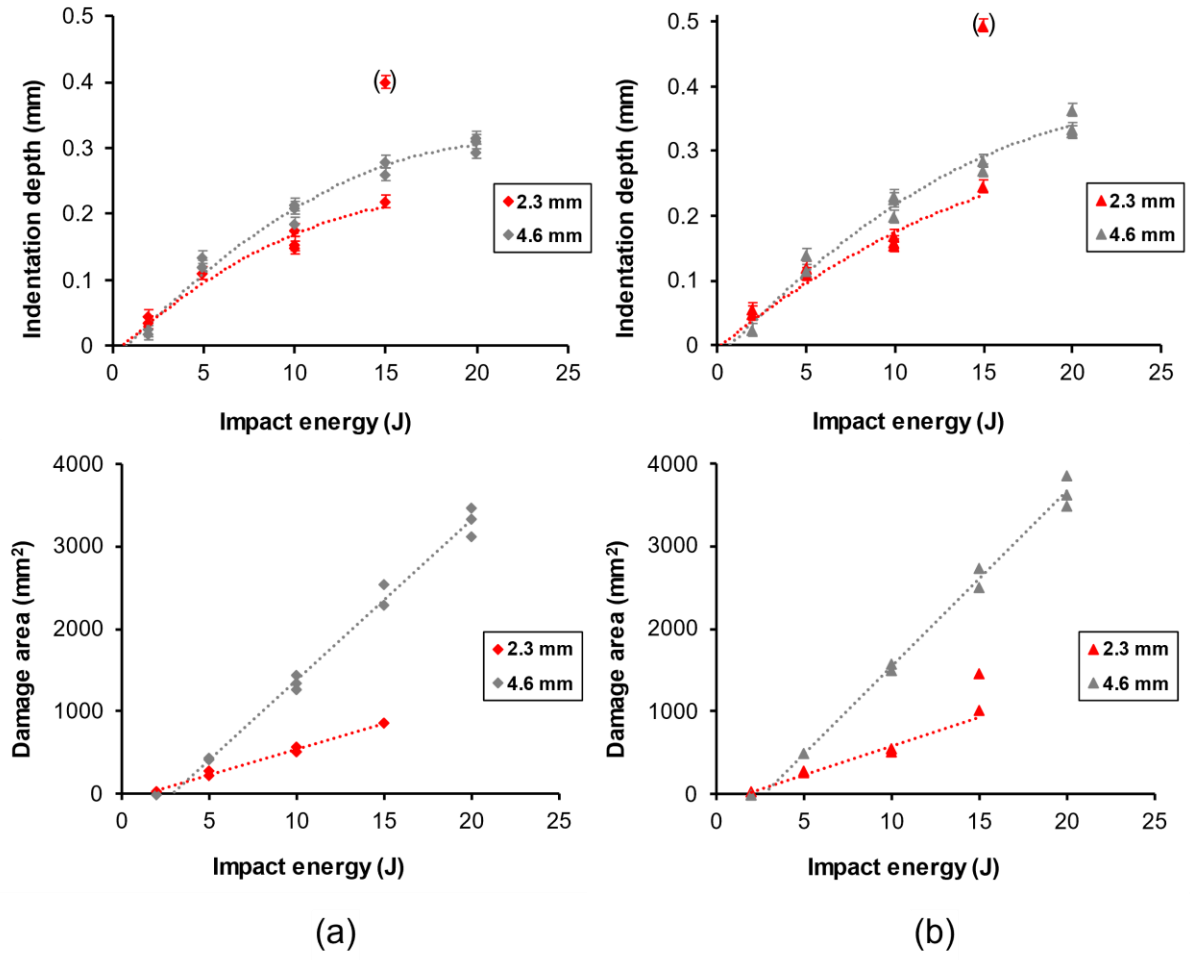


Figure 5-30: The indentation depth versus impact energy, and delamination damage area versus impact energy, for the 2.3 mm and 4.6 mm thick CF/Epoxy composite panels after (a) two impacts and (b) three impacts.

Contrastingly, the results for indentation depth versus impact energy, after a second and third impact do not have a linear relationship. Although for the single impact case the panel thickness had little effect on the resulting indentation depth, Figure 5-30 highlights that this is not the case for the second and third impact cases, where the 2.3 mm thick panels show a slightly smaller indentation depth

compared to the 4.6 mm thick panels. The work of Shuck, as cited by Talreja and Phan [93], and of Panettieri [94] indicated that thinner carbon fibre-reinforced polymer (CFRP) composites showed a larger indentation depth after a single impact. Therefore, it might have been expected that the opposite results (i.e. the 2.3 mm thick panels having a larger indentation depth) would have occurred after multiple impacts. However, the larger amount of material beneath the impactor in the 4.6 mm panel may have been able to accommodate more plastic deformation. Also, the 4.6 mm panels showed a greater delamination area increase for subsequent impacts. There is a higher probability of more debris being present within the longer delaminations and preventing the cracks closing, which may have contributed to the slightly higher indentation depths. Furthermore, Tuo et al. [14] found that the indentation depth increased more between a second and third impact than between a first and second impact. However, this was at an impact energy of 30 J, so the more severe damage created at a higher impact energy could be a cause of this (i.e. the relationships shown here are only accurate for the tested impact energies). For the 4.6 mm panels impacted at 2 J the indentation depth increases slightly after each impact, however, no delamination damage was observed after any of the three repeated impacts. This supports the conclusions obtained from Section 4.3.3 that the indentation depth initiates before any delamination damage develops.

Figure 5-31 plots the indentation depth versus the delamination damage area for both thicknesses of panel after (a) two and (b) three impacts and reveals that the relationship between indentation depth and delamination damage area is also not linear. Furthermore, Figure 5-31 highlights that panel thickness has a very substantial effect, with the 4.6 mm panel suffering a greater delamination damage for a given indentation depth for indentation depths above about 0.1 mm. Below this depth, the 2.3 mm panel shows more damage for a given indentation depth. This is largely because, until an indentation depth of just below 0.1 mm, the 4.6 mm panels do not show any delamination damage (based on the second-order polynomial relationships drawn). Once delaminations are present, damage area increases much more rapidly with indentation depth for the 4.6 mm panels. Multiple impacts at 2 J did not initiate any delamination damage in the 4.6 mm panels (see Figure 5-2 and Figure 5-5), and, according to the relationships shown in Figure 5-31, an indentation depth of around 0.09 mm would correspond to the formation (or first presence) of delamination damage. From Figure 5-30, this

corresponds to a repeated impact energy of around 4 J. This is similar to what the analysis from Chapter 4 suggests, in which an approximately 0.04 mm indentation is required for delamination initiation for a single impact, see Figure 4-10(b), which again corresponds to an impact energy of around 4 J, see Figure 4-10(a).

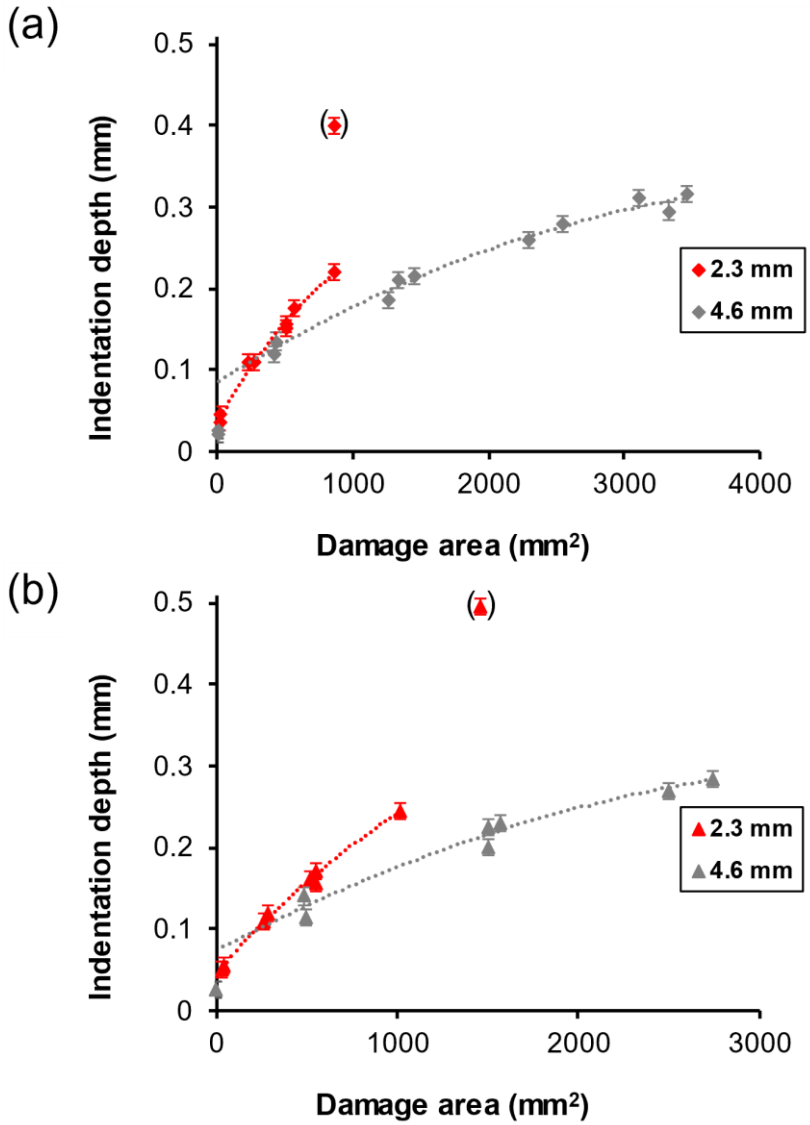


Figure 5-31: The indentation depth versus the delamination damage area for the 2.3 mm and 4.6 mm thick CF/Epoxy composite panels after (a) two impacts and (b) three impacts.

Figure 5-32 demonstrates that all the relationships between indentation depth and delamination damage area, for both thicknesses of panel and for all three impacts at the same repeated energy, can be unified to give a non-linear 'master' relationship by plotting the indentation depth versus the

associated delamination damage area normalised with respect to the panel thickness. By dividing the damage area divided by the panel thickness, almost all the resulting data points converge onto an approximately unique ‘master’ line. This highlights that the ‘master’ relationship concept first explained in Section 4.3.3 still holds if a panel has been impacted multiple times at the same impact energy (albeit a slightly different relationship given there is more data). Therefore, there is no need to have separate relationships for each thickness of composite when comparing the measured indentation depth against the corresponding delamination damage area, even when a panel has been impacted multiple times.

For multiple impacts, the increase in indentation depth does not keep rising at the same rate as that of the damage area, just as for a single impact the rate of depth increase is different to the rate of impact energy increase. By assuming this ‘master’ relationship is valid for all appropriate thicknesses of this lay-up within a range of at least 2.3 to 4.6 mm based on the current research, one can follow the same three steps explained in Section 4.3.3. These are (a) measuring the indentation depth, (b) reading off the corresponding damage area and (c) from a knowledge of the chosen composite’s thickness, calculating the approximate delamination damage area. As mentioned in Chapter 4, to take into account varying lay-ups of the same CF/Epoxy material and the resulting differing numbers of interfaces where delamination could occur, normalisation by the bending stiffness could alternatively be used. However, the simpler normalisation method based only on the thickness of the material was used given that alternative lay-ups were not tested in the current study.

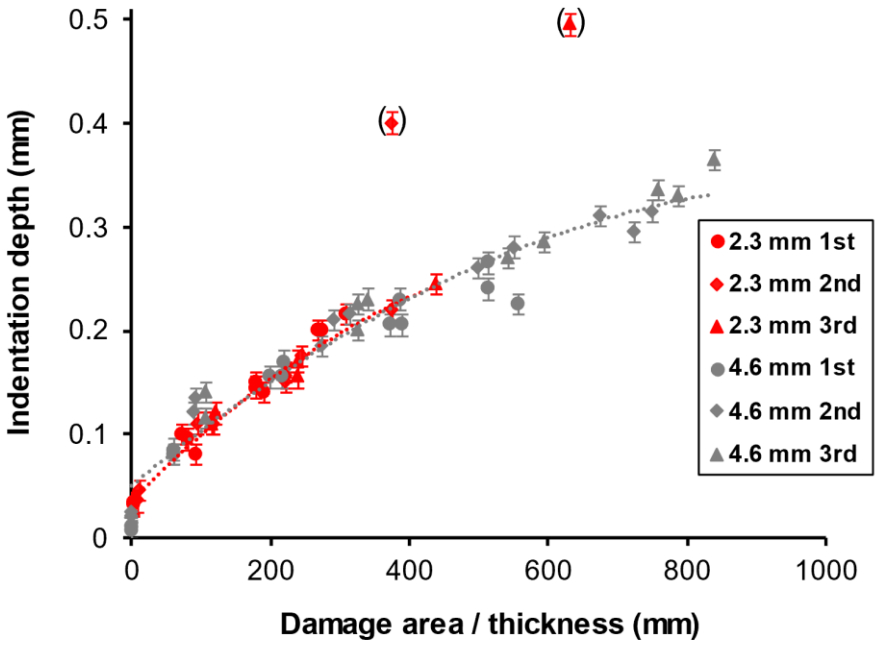


Figure 5-32: The indentation depth versus normalised interlaminar damage area (i.e. damage area divided by thickness) for the CF/Epoxy composite panels.

5.3.4 Optical microscopy studies

Figure 5-33 and Figure 5-34 show central cross-sections, cut directly beneath the indentation along a line parallel to the 100 mm edge, from 2.3 and 4.6 mm panels, respectively, after (a) one impact and (b) three impacts at 5 J. Note that the scale in all these images is the same (i.e. the 2 mm scale bars are the same size). These micrographs highlight the conical-shaped intralaminar cracking zone which occurs through the thickness of the composite panel during the impact event. Comparing the micrographs in Figure 5-33 and Figure 5-34, the conical-shaped intralaminar cracking zones appear to be a similar size after both a single impact and after three impacts. The total amount of intralaminar cracking is not significantly different after three impacts compared to after a single impact either. In contrast, the delamination cracks are both longer and wider in both thicknesses of CF/Epoxy panel after three impacts. The full delamination lengths observed in the optical microscope images agree with the delamination lengths detected by the ultrasonic C-scans. Only a portion of the delamination length around the central impact zone is shown in the optical microscope images below in order to show the intralaminar cracking in detail. These observations suggest that subsequent impacts do not generally

initiate new intralaminar or interlaminar damage, but instead mainly propagate existing delamination cracks.

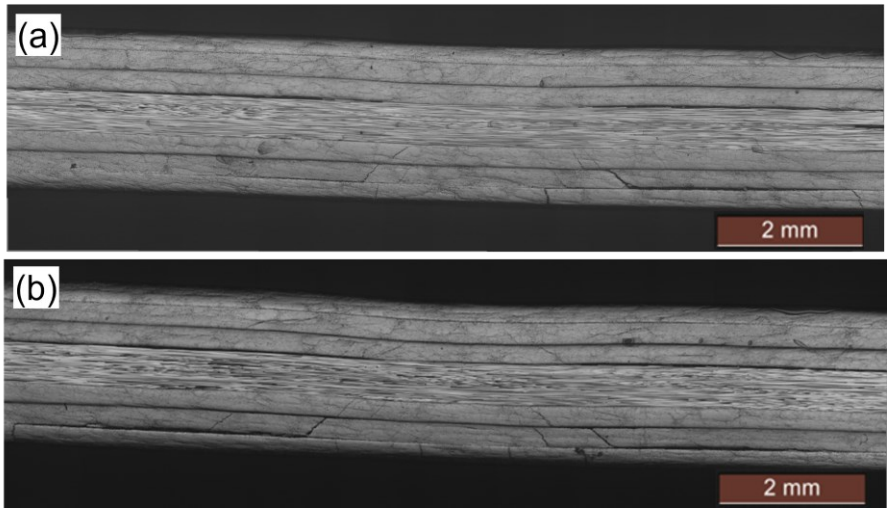


Figure 5-33: Optical microscopy images of a 2.3 mm thick CF/Epoxy composite panel after (a) one and (b) three impacts at 5 J. (Showing a cross-section cut from the panel after grinding and polishing.)

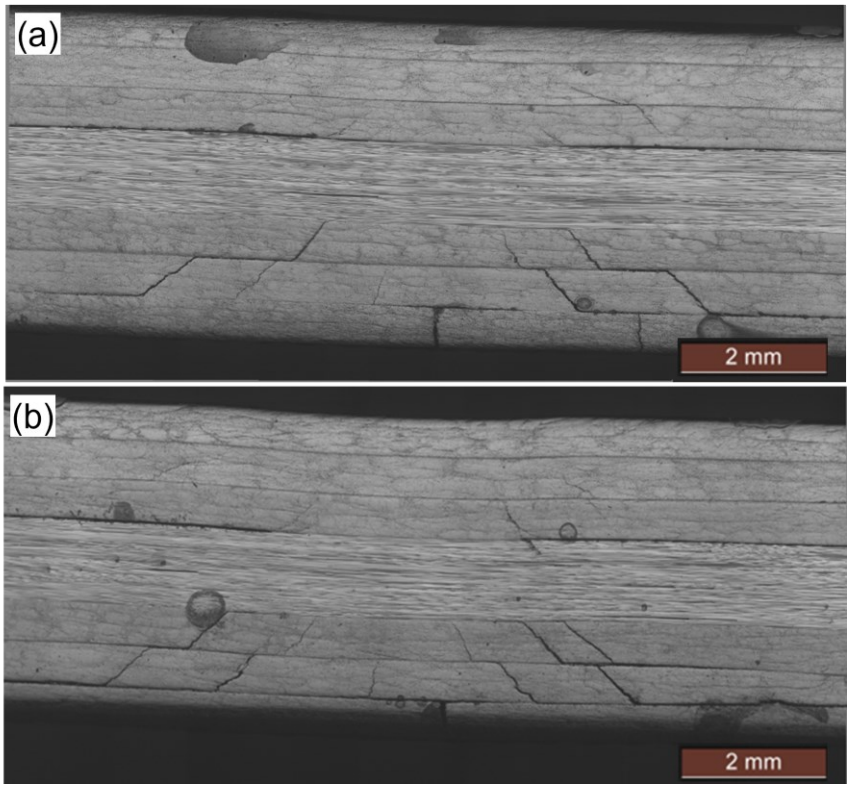


Figure 5-34: Optical microscopy images of a 4.6 mm thick CF/Epoxy composite panel after (a) one and (b) three impacts at 5 J. (Showing a cross-section cut from the panel after grinding and polishing.)

Figure 5-35 and Figure 5-36 show central cross-sections, cut directly beneath the indentation along a line parallel to the 100 mm edge, from 2.3 and 4.6 mm panels, respectively, after (a) one impact and (b) (+ (c) for the 2.3 mm panel) three impacts at 15 J. Note that the scale in all these images is the same (i.e. the 2 mm scale bars are the same size). Figure 5-35(b) and (c) shows the panels with delamination damage areas of 1013 mm^2 and 1454 mm^2, respectively, as shown in Figure 5-4. Although more delamination damage is seen in the 4.6 mm panel after both a single and three impacts, a greater severity of intralaminar damage is seen in the 2.3 mm panel. This is because the deflection of the 2.3 mm panel is greater during the impact event which causes higher stresses within the individual plies, leading to severe matrix cracking and fibre fracture. For the 2.3 mm thick panel, a conical-shaped intralaminar cracking zone is visible after a single impact, however after three impacts this is less apparent, with the intralaminar and delamination damage being so severe that the rear-most ply/plies have become detached from the panel around the central impact zone, see Figure 5-6. Comparing both of the 2.3 mm panels impacted 3 times at 15 J in Figure 5-35(b) and (c), the delamination damage is similar in both panels, although the width of the delaminations does vary. The intralaminar damage is slightly different however, with the lower delamination area panel (Figure 5-35(b)) showing a larger density of intralaminar cracks and the larger delamination area panel (Figure 5-35(c)) showing more severe cracking (i.e. the cracks have caused more permanent deformations). At the centre of Figure 5-35(c), fibre fracture in the two central plies is highlighted. This could explain the change in indentation profile and the greater increase in delamination seen in this panel, due to the reduction in strength caused by the fibre fracture. Some fibre fracture is visible in Figure 5-35(b) but only across one of the two central blocked plies. The different behaviour seen in the two panels shown in Figure 5-35(b) and (c) is explored further in Appendix C.

Comparing the micrographs in Figure 5-36, the conical-shaped intralaminar cracking zone appears to be a similar size after both a single impact and three impacts. The total amount of intralaminar cracking is not significantly different after three impacts compared to after a single impact, although the intralaminar cracks, particularly in the top half of the panel, are wider and more clearly visible after three impacts. In contrast, the delamination cracks have increased in length and in the top half of the panel are slightly wider. As with the 2.3 mm thick panels, these observations suggest that

subsequent impacts do not generally initiate new intralaminar or interlaminar damage, but instead mainly propagate existing cracks. It should also be noted that all these optical images confirm that no delaminations were formed between plies of the same orientation (i.e. blocked plies).

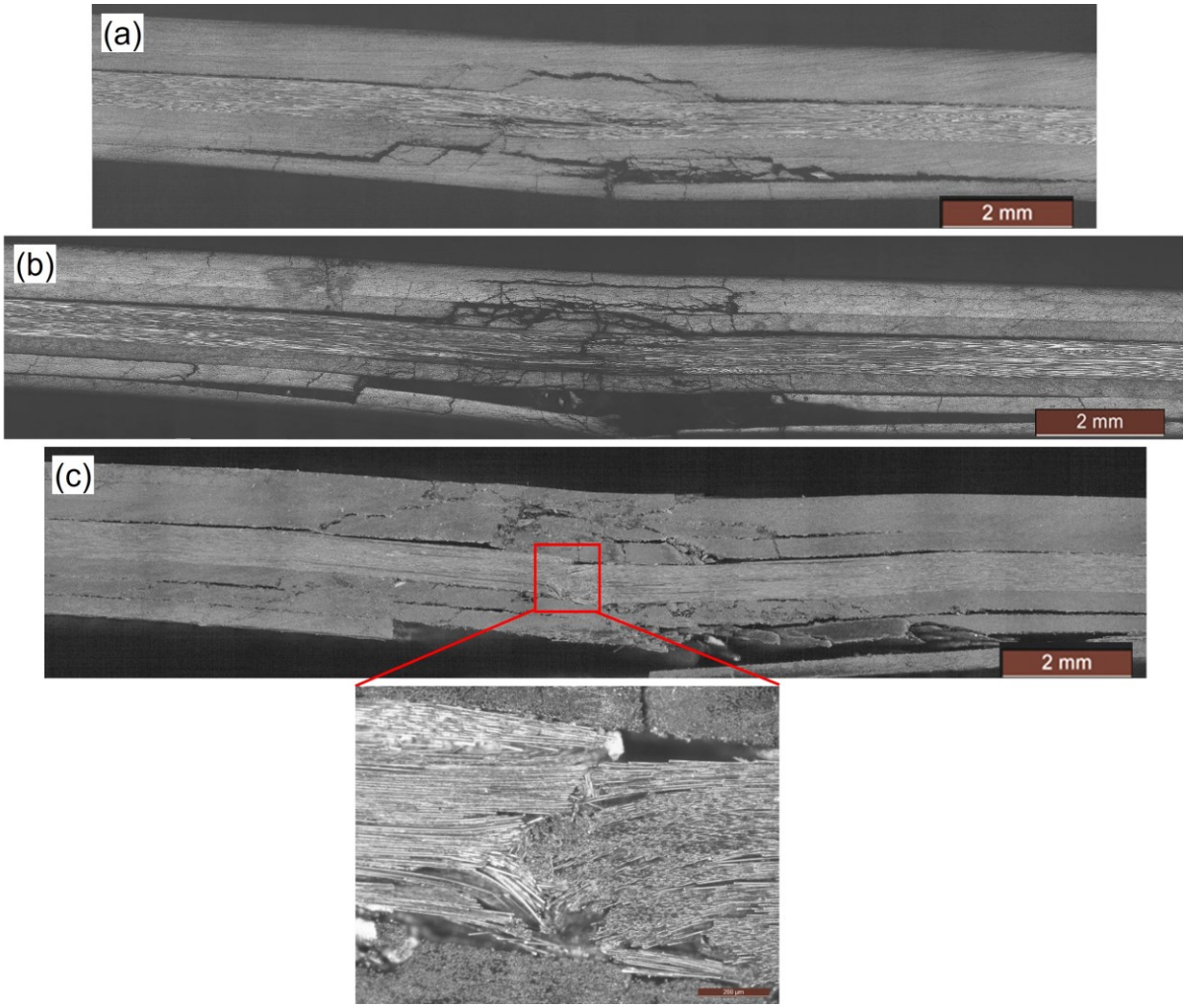


Figure 5-35: Optical microscopy images of a 2.3 mm thick CF/Epoxy composite panel after (a) one and (b + c) three impacts at 15 J (showing panels with DAs of (b) 1013 mm^2 and (c) 1454 mm^2). (Showing a cross-section cut from the panel after grinding and polishing.) Magnified image showing fibre fracture in (c) has a scale bar of 200 µm.

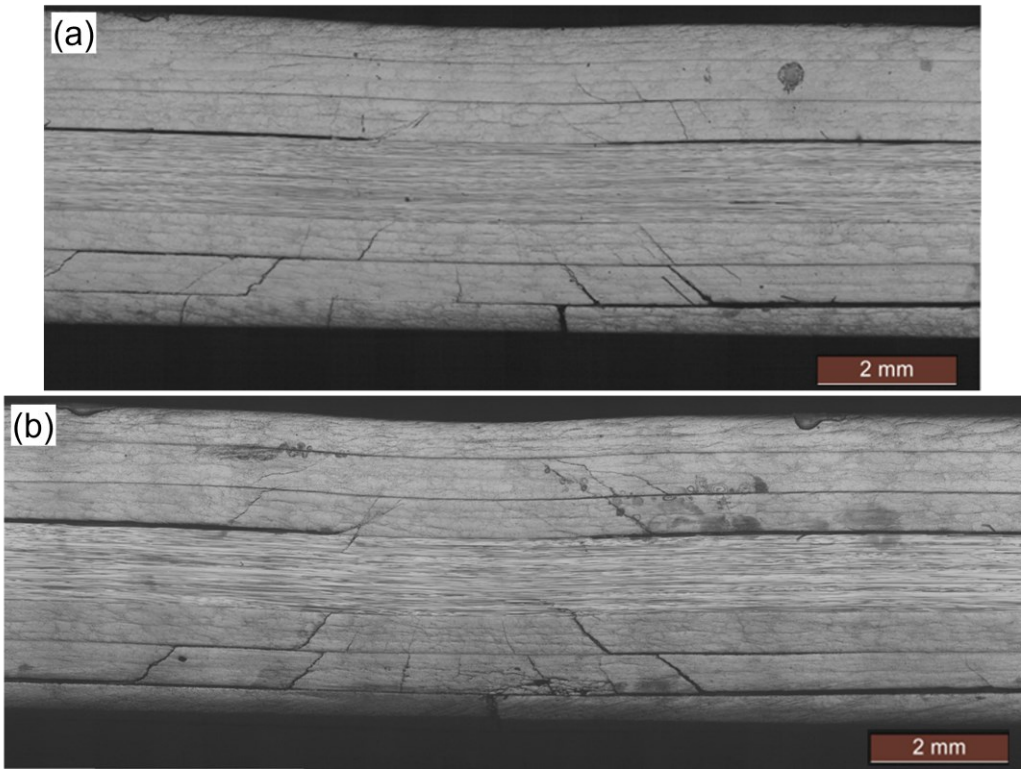


Figure 5-36: Optical microscopy images of a 4.6 mm thick CF/Epoxy composite panel after (a) one and (b) three impacts at 15 J. (Showing a cross-section cut from the panel after grinding and polishing.)

5.4 Summary

The effect of multiple impacts at the same impact energy and in the same location on the impact response of a CF/Epoxy composite has been investigated. Two lay-ups of $[45/-45/0/90]_s$ and $[45_2/-45_2/0_2/90_2]_s$ were tested with corresponding thicknesses of 2.3 mm and 4.6 mm. Low-velocity impacts of 2, 5, 10, 15 and 20 J were undertaken using a drop-weight tower and a hemispherical stainless-steel impactor of diameter 16 mm. The resulting damage formation and surface indentation depth have been investigated using ultrasonic C-scanning, a digital depth gauge and optical microscopy.

The impact testing revealed that the increase in delamination area caused by subsequent impacts is mainly due to propagation of the existing delaminations. Furthermore, a greater increase in damage area is caused by a second impact compared to a third impact, mainly due to the reduction in bending stiffness caused by the presence of the delaminations and therefore the greater proportion of the impact energy stored through elastic deformation by the panel rather than being used to propagate

the delaminations. This also leads to an increase in both the maximum displacement and the rebound energy for subsequent impacts.

The indentation depth continues to slightly increase for each subsequent impact due to viscoelastic and plastic behaviour around the impactor and delamination propagation. The depth also follows a second-order polynomial relationship with delamination damage area for the tested low-velocity impact energies between 2 J and 20 J. As for the single impact cases discussed in Chapter 4, a unique 'master' relationship between indentation depth and the normalised delamination damage area (i.e. the damage area divided by the panel thickness) has been found. Consequently, measuring the indentation depth still has the potential to be used as a quick and cheap alternative to employing expensive ultrasonic C-scan or X-ray Computed Tomography equipment for estimating the extent of internal delamination damage, even if a location has been impacted multiple times.

Therefore, the present study has identified the effects of multiple impacts in the same location on the impact behaviour of CF/Epoxy and revealed the relationship between indentation depth and delamination damage.

Chapter 6 Study on the internal and external damage formed in CFRP thermoplastic laminates under low-velocity impact conditions

6.1 Introduction

The current chapter presents the results from an experimental study into the behaviour of woven carbon fibre/polyphenylene sulphide (CF/PPS) composite under low-velocity impact. Low-velocity drop-weight testing with a rigid hemispherical impactor was used to perform the impacts and ultrasonic C-scanning was used to examine the internal delamination damage formed during the impacts. The depth of the surface indentations formed during impact was also determined and studied to see how the depth related to the delamination damage area. Finally, optical microscopy was used to investigate the intralaminar and interlaminar damage within the panels. The results for the CF/PPS material are compared against those for the 2.3 mm thick CF/Epoxy material analysed in Chapter 4.

The studies revealed that the depth of a surface indentation can be related to the delamination damage area by a second-order polynomial. Also, woven CF/PPS exhibits a higher indentation depth than 2.3 mm thick CF/Epoxy for low-velocity impact energies of 2 to 12.5 J, however, the resulting delamination damage area is lower.

6.2 Test specification and methods

6.2.1 Materials

The CF/PPS panels used in the study presented in this chapter were manufactured following the method described in Section 3.2.2. The panels had a thickness of 2 mm and each ply was orientated identically. Each panel was cut to a size of 150 mm x 100 mm and the 0° direction (warp) was aligned with the longer edge of the panels.

6.2.2 Experimental methods

Low-velocity drop-weight testing was undertaken following the method outlined in Section 3.3.1. The 16 mm diameter round-nosed impactor had an overall mass of 5.27 kg and was dropped from varying heights to give impact energies between 2 J and 12.5 J, with corresponding impact velocities between 0.87 $m.s^{-1}$ and 2.18 $m.s^{-1}$, respectively.

Ultrasonic C-scanning (a non-destructive testing (NDT) method) was undertaken to view the delamination damage within each panel after impact following the method described in Section 3.3.2. Indentation depth was measured using the two methods described in Section 3.3.3. Measurement of the indentation depth using the handheld digital depth gauge could be completed quickly and easily and gave accurate values of the indentation depth. Measurement of the indentation depth using the Confocal microscope provided not only a very accurate value of indentation depth, but also data showing the cross-section of the indent. This allowed comparison of the indent shape in different panels as well as comparison of just the indentation depth. Optical microscopy was undertaken to view the intralaminar and interlaminar (i.e. delamination) damage within each panel following the method described in Section 3.3.4. Samples were cut, ground and polished before being viewed using the optical microscope.

6.3 Experimental results and discussion

6.3.1 Delamination damage

Figure 6-1 shows the C-scan damage maps for the CF/PPS panels after impacts at 2, 5, 7.5, 10 and 12.5 J. The scales to the right-hand side of the damage maps show the depth of the damage beneath the impacted surface. Further C-scan damage maps of CF/PPS panels impacted at 2.15, 5.15 and 10.15 J are shown in Appendix F. As expected, the extent of the damage generally increases as the impact energy is increased. However, the damage areas measured for the 7.5 J and 10 J impacts are very similar. One factor contributing to this is the larger void content seen in the panel impacted at 7.5 J, explored later in Section 6.3.4, which likely led to a decrease in damage resistance. Note that no

voids were detected by the C-scans. The majority of damage appears to occur in the panels at a depth of around 1.2 mm or below. Therefore, the C-scans signify that the location of the first delamination from the top is between the fifth and sixth plies of the laminate. This delamination is in irregular shapes or even disjointed, which may be because the layers are not as flat as in unidirectional (UD) laminates. The undulations in each ply make it more difficult for a delamination to progress smoothly along the ply boundary (i.e. stable crack propagation) and also create a large fracture surface area [23,65]. Also, in UD laminates with different ply orientations, the stiffness changes dramatically between plies due to the different fibre orientation, allowing delaminations to form more readily [78]. Delamination is further investigated later in Section 6.3.4.

As impact energy increases, the dark blue area near the centre of the damage zone becomes more prominent. This could indicate that increased penetration is causing the permanent indentation depth to approach the thickness of the material and a transition to perforation behaviour is starting. Note, penetration has been defined as the entrance of the impactor into the panel without a complete passage through the thickness, whereas perforation refers to the complete piercing of the panel by the impactor [27]. When the impactor starts to penetrate the uppermost layers of the laminate, shear failures occur. When the impactor then reaches the delaminated layers further from the surface, these can slide over each other and eventually fail due to the tensile load subjected on them [34]. Therefore, at higher impact energies where the impactor is able to penetrate multiple layers, fibre fracture can be seen on the plies close to the rear surface and this indicates a transition to perforation behaviour. This is highlighted in Figure 6-2 which shows significant fibre fracture on the rear surface of the CF/PPS panel impacted at 12.5 J.

The woven CF/PPS material demonstrates a lower delamination damage for a given impact energy (up to 10 J) compared to the 2.3 mm thick UD CF/Epoxy, see Figure 4-1. Both the thermoplastic matrix and the woven fabric architecture contribute to the lower damage areas seen in the CF/PPS. Firstly, and in general, thermoplastic matrix composites show superior impact resistance compared to thermoset matrix composites [19,34,65–69]. One contribution to this is the higher toughness of the thermoplastic itself. However, using a tougher matrix has been proven not to increase the mode I and II fracture toughness of the composite by as much as the comparative fracture toughness of the resins

alone [65]. Nevertheless, the higher in-plane shear strength of the CF/PPS, see Table 3-1 and Table 3-3, does contribute to the reduction in damage area. Secondly, the woven architecture of the plies hinders shear crack and delamination propagation [65,75]. The undulating yarns cause crack deviation, allowing multiple crack fronts to form, leading to higher fracture toughness values and a lower delamination damage area [23]. Furthermore, cracks following the undulating yarn pattern form a larger fracture surface area [65]. The presence of resin-rich regions within the woven architecture where plastic deformation can develop also contributes to an increased fracture toughness [65]. The conclusion that woven laminates show a lower delamination damage area for a given impact energy is supported by other studies in the literature [23,24,51,75]. Interestingly, both materials showed a similar damage area when impacted at 2 J, suggesting that a similar energy is needed to initiate delamination damage in both materials. This point is analysed in more detail in Section 6.3.3.

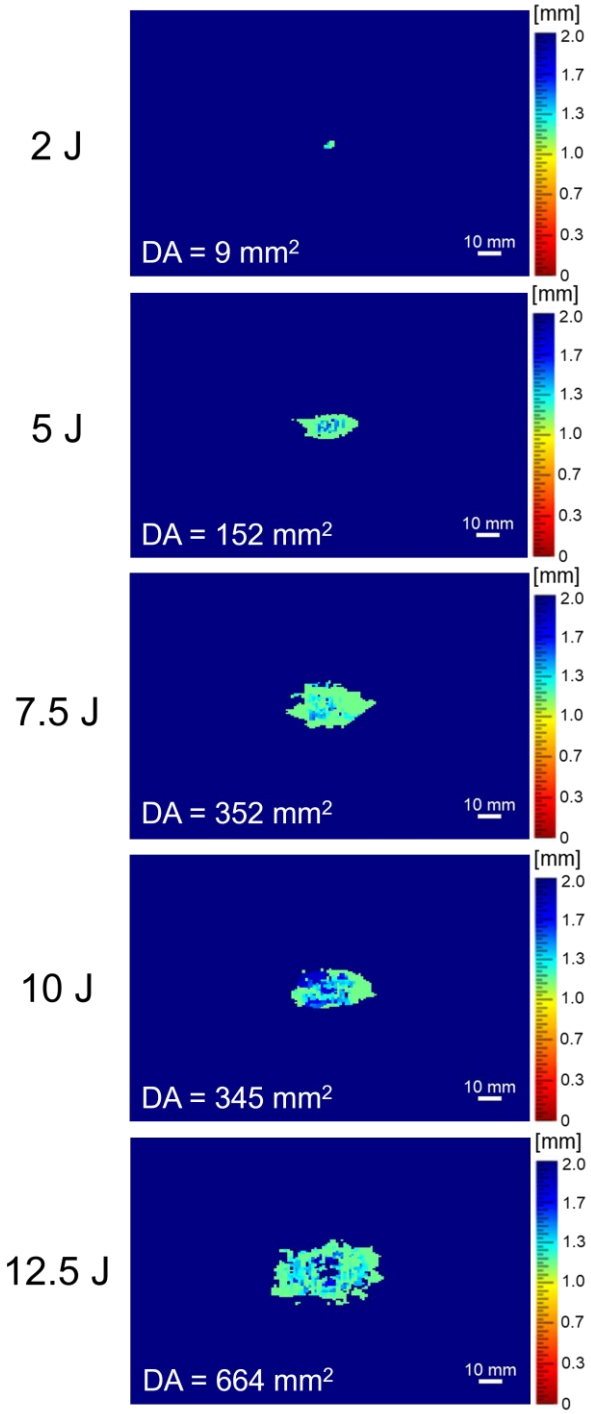


Figure 6-1: C-scan damage maps obtained from the CF/PPS replicate composite panels with impact energies of 2, 5, 7.5, 10 and 12.5 J. The right-hand side scale indicates the location of the interlaminar delamination as a function of the depth through the thickness of the panel (0 to 2.0 mm), where the dark red colour represents the front (impacted) face and the dark blue colour represents the rear (non-impacted) face of the composite panel. The footprint of the delamination damage area (DA) detected is given in the bottom left-hand corner for each panel and was determined by counting the pixels which had a colour which was not dark blue. The bottom right of each damage map shows a 10 mm scale bar.



Figure 6-2: Rear surface of the CF/PPS panel impacted at 12.5 J, showing severe damage, including fibre fracture.

6.3.2 Load versus time and load versus displacement results

Figure 6-3 shows (a) load versus time and (b) load versus displacement traces for the CF/PPS panels impacted at 2, 5, 7.5, 10 and 12.5 J. The small sinusoidal oscillations on the rising section of the traces are indicative of mass-spring oscillations and have been observed by other researchers [290–292]. Load drops are seen for all of the panels impacted at energies of 5 J and above and these indicate the load, time and displacement at which damage initiated in the panels during the impact event. The panel impacted at 12.5 J suffered a particularly large load drop at 2.8 kN. This is due to the impact causing severe fibre fracture on the rear surface and a deep permanent indentation. Fibre fracture causes a large loss in load-carrying capacity, hence, a considerably larger maximum displacement was seen for the panel impacted at 12.5 J compared to the panel impacted at 10 J.

The load versus time trace for the 2 J impact energy case does not show a clear load drop. The C-scan for the 2 J impact energy case shown in Figure 6-1 shows that only some very slight damage formed during the impact event which explains why any potential load drop is much less noticeable than for the higher impact energies which resulted in much larger damage areas forming. Larger and higher frequency oscillations occur following a load drop for higher energy impacts. These larger oscillations seen at higher impact energies are an indication that more severe damage is being formed in the laminates [14]. One specific mechanism causing these jumps in load can be explained by unstable crack propagation. The woven structure causes the multiple crack fronts to jump forward, before being arrested at the next yarn undulation [23,65]. This process is repeated as the crack propagates.

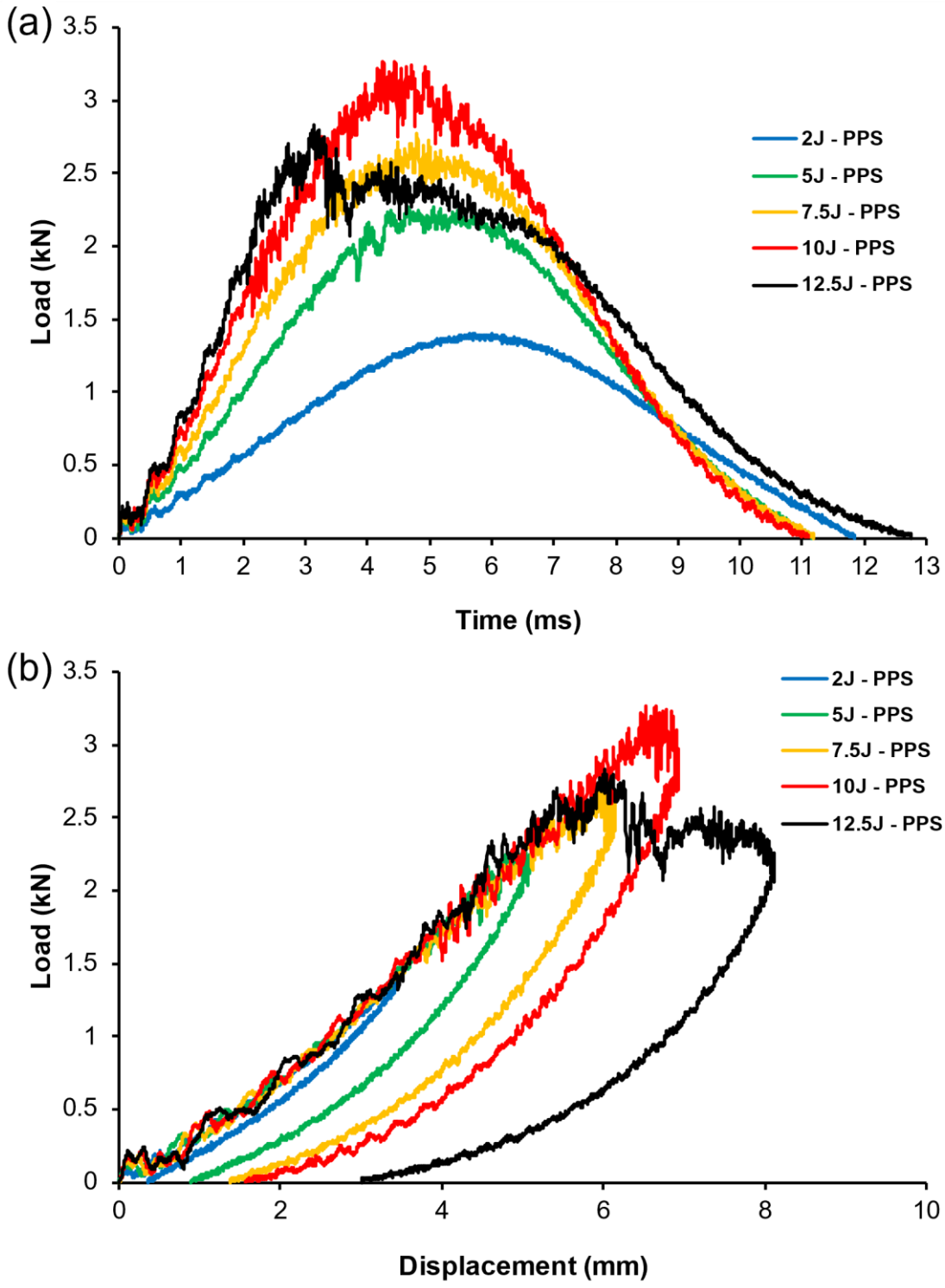


Figure 6-3: (a) Load versus time traces and (b) load versus displacement traces for the CF/PPS composite panels impacted at 2, 5, 7.5, 10 and 12.5 J.

Figure 6-4 shows (a) load versus time and (b) load versus displacement traces for the CF/PPS panels and the 2.3 mm thick CF/Epoxy panels impacted at 2, 5 and 10 J. Although both types of panel show no clear load drop when impacted at 2 J, when impacted at 5 J a differing behaviour is observed in each. The CF/Epoxy does not show a clear load drop whereas the CF/PPS panel does show a clear load drop. At an impact energy of 10 J, both types of panel show a load drop, however the locations of the load drop vary significantly. While the CF/Epoxy panel displays a load drop close to the point at which the peak load is reached, the CF/PPS panel suffers a load drop at approximately halfway up the curve towards the peak load. Therefore, the results indicate that the UD CF/Epoxy exhibits a higher damage threshold than the woven CF/PPS and can sustain higher loads before sustaining damage. However, when impact does occur, the delamination damage area is higher in the CF/Epoxy.

Furthermore, more oscillations are observed in CF/PPS than CF/Epoxy, which may indicate that the damage being formed in the CF/PPS is more severe [14], even though the area of the damage footprint is lower, see Section 6.3.1. This is investigated further in Section 6.3.4. Furthermore, the UD structure of the CF/Epoxy is less likely to undergo unstable crack propagation than the woven CF/PPS, as discussed previously. The variation in structure also contributes to the woven CF/PPS being significantly less stiff. Although, the larger thickness of the CF/Epoxy panels is also a contributing factor. The impact duration decreases for both materials with increasing impact energy, however the 10 J impact on CF/PPS has only a slightly smaller impact duration than that for the 5 J impact. The higher severity of damage formed during the 10 J impact could be a cause of this.

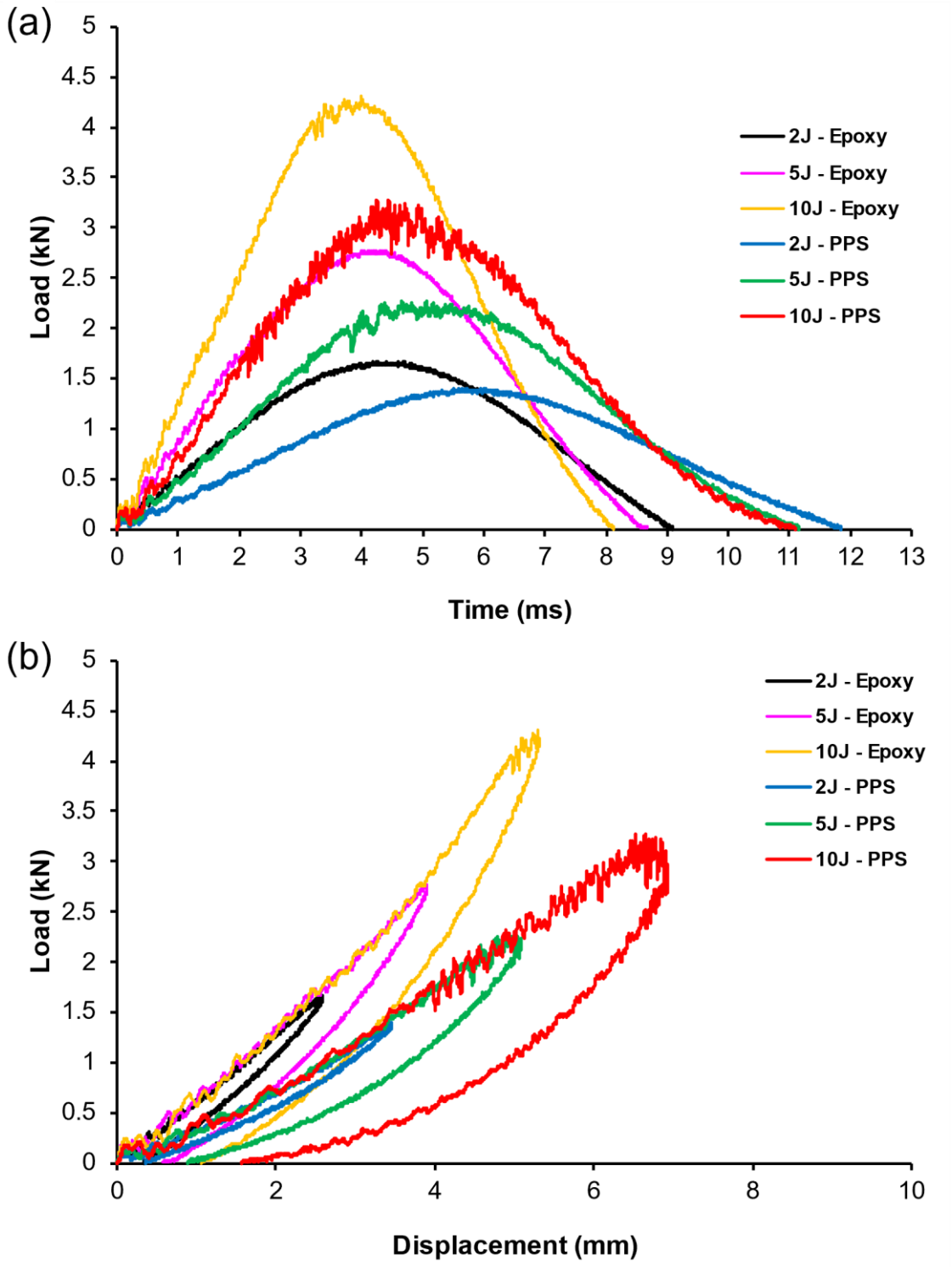


Figure 6-4: (a) Load versus time traces and (b) load versus displacement traces for the CF/PPS composite panels and 2.3 mm thick CF/Epoxy composite panels impacted at 2, 5 and 10 J.

Figure 6-5 shows an energy versus time graph for the CF/PPS panels impacted at 2, 5, 7.5, 10 and 12.5 J. The energy shown is the energy stored or absorbed by the panel during the impact event. The graphs show an increasing amount of energy transferred to the panel by the impactor up until the peak. After the peak some energy is transferred back to the impactor and this rebound energy is shown by the difference between the peak energy and the final energy. Figure 6-5 clearly shows that a much larger percentage of impact energy was absorbed for the impact at 12.5 J than for any other impact which caused significant damage. This is again due to the deep permanent indentation and resulting fibre fracture which this impact caused. Fibre fracture causes energy to be absorbed through processes such as interface debonding and fibre pull-out and causes a large loss in load-carrying capacity. This reduces the amount of elastic strain-energy stored in the panel and therefore reduces the amount of rebound energy transferred back to the impactor.

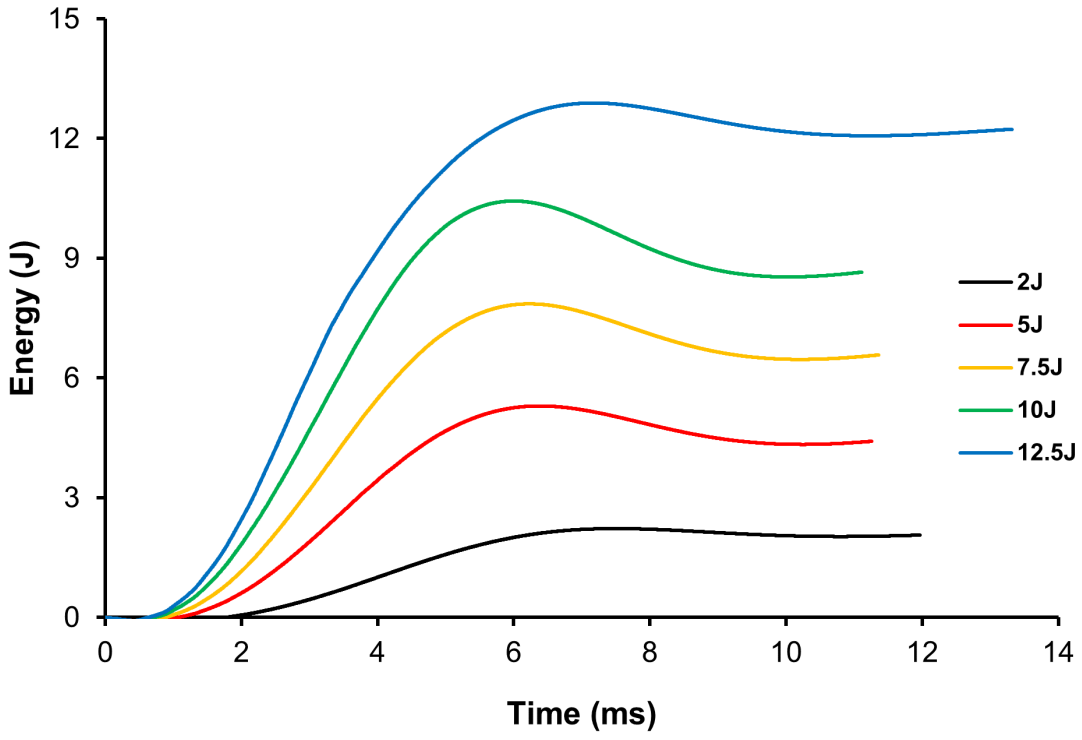


Figure 6-5: Energy versus time traces for impacts at 2, 5, 7.5, 10 and 12.5 J on CF/PPS composite panels.

6.3.3 Indentation depth studies

Figure 6-6 shows cross-sections of the resulting indentations after 2, 5, 7.5 and 10 J energy impacts on the CF/PPS composite, taken from the Confocal microscopy measurements. The indentation cross-section for the panel impacted at 12.5 J is not included as this panel had significant rear surface damage so could not be positioned on the flat platform of the Confocal microscope. These results generally show that a cross-section through the permanent indentation profile has a central depression, with gently sloping sides and this shape deepens with impact energy. The surface roughness seen in Figure 6-6 is due to the imprint left by the Teflon sheeting which was used during manufacture, see Section 3.2.2.

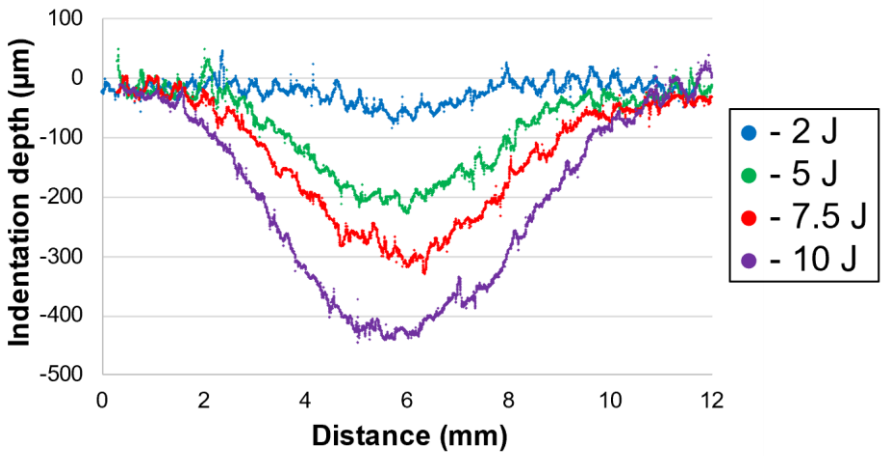


Figure 6-6: Indentation cross-section in a CF/PPS composite panel after an impact of 2, 5, 7.5 and 10 J.

Figure 6-7 presents (a) the resultant indentation depth versus the impact energy and (b) the associated delamination damage area versus the impact energy for both the CF/PPS composite panels and, as a comparison, the 2.3 mm thick CF/Epoxy composite panels which were previously analysed in Chapter 4. The tests at impact energies of 2.15, 5.15 and 10.15 J are also included to provide more confidence in the data. Firstly, CF/PPS suffers a significantly higher indentation depth compared to CF/Epoxy when impacted at the same energy, a conclusion which has also been observed by Vieille et al. [65]. This is in part due to the comparative ease with which the PPS matrix yields underneath the impactor compared to the epoxy. Also, the resin-rich regions in the woven structure undergo matrix plasticization and crushing, leading to the larger permanent indentation [65]. The undulations in the

woven structure may make it more difficult for cracks to close up again after delamination formation and this is exacerbated by the presence of debris within the cracks, leading to further increases in permanent indentation.

The indentation depth initially has an approximately linear relationship with impact energy for the CF/PPS panels. At approximately 10 J, this linear relationship ends and much greater indentation depth values are measured for further increases in impact energy. This is due to fibre fracture in the rear plies having taken place in the two panels impacted above 10 J, showing a transition towards perforation behaviour. This relationship has also been observed for woven composites by Vieille et al. [65]. Once fibre fracture has occurred in the rear plies it becomes easier for the impactor to penetrate into the panel surface as there is less resistance from the material beneath the impactor.

In contrast, the increase in indentation depth for the CF/Epoxy panels continues to reduce at higher impact energies up to 15 J without any transition to perforation behaviour, see Section 4.3.3, so the points follow a second-order polynomial relationship. Also, it must be remembered that the CF/PPS panels are 0.3 mm thinner (only 87% of the thickness of the CF/Epoxy), therefore there is less material beneath the impactor to provide resistance to indentation. Shuck, as cited by Talreja and Phan [93] and Panettieri et al. [94] both observed that thinner material exhibited a larger indentation depth, however the differences in thickness tested in those studies were significantly greater than the 15% difference present in this study. Also, little difference was observed between panels of different thicknesses in the study from Chapter 4 of this thesis. These factors indicate that the different matrix and different reinforcement geometries are likely more significant contributors to the difference in indentation depths between the two materials.

The data points for the plot of damage area versus impact energy lie on an approximately linear line for both the CF/PPS panels (up to an energy of 10 J) and the CF/Epoxy panels. Note the data points for the two ‘nearly perforated’ CF/PPS panels (i.e. the panels showing fibre fracture in the rear plies) are shown in brackets and have not been used for drawing this linear line. In general, the CF/PPS exhibits a lower damage area than CF/Epoxy, see Section 6.3.1. This supports the observations seen in the literature in which thermoplastic matrices and woven laminates reduce the delamination damage

area, see Sections 2.3.6 and 2.3.7. There is much more scatter in the CF/PPS results and a second-order polynomial fit could alternatively have been used. Also, there is a large difference in damage area for the two 'nearly perforated' panels. Ghaseminejhad and Parvizi-Majidi [27] noted that CF/PPS shows a threshold point, beyond which the damage area decreases with further increases in impact energy. The panel impacted at 10.15 J shows a significantly lower damage area than the panel impacted at 10 J, which may indicate that this threshold point is around 10 J. However, the panel impacted at 12.5 J shows the largest damage area of all the panels. The differences in damage area may be due to more fibre breakage taking place in the panel impacted at 10.15 J, leading to a denser damage zone. Repeating the cases shown in the chapter would improve confidence in the data and help to understand the damage behaviour at higher impact energies.

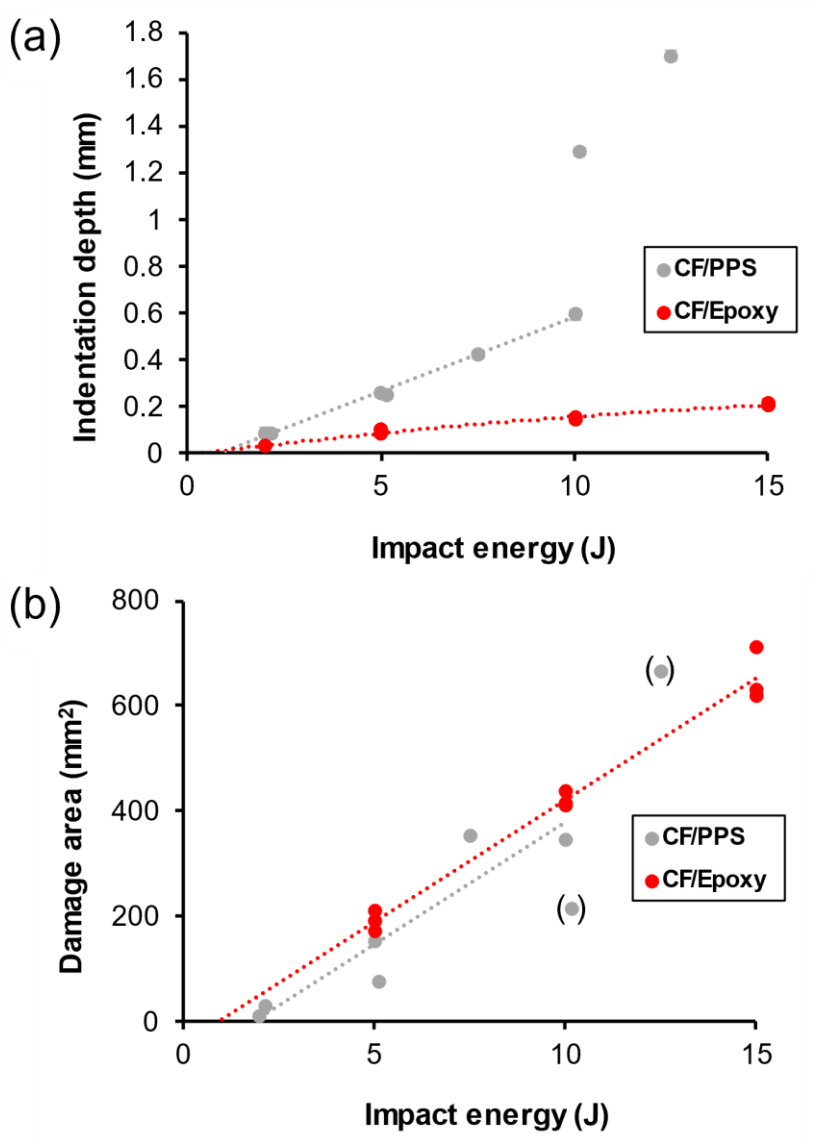


Figure 6-7: (a) Indentation depth versus impact energy and (b) delamination damage area versus impact energy for the CF/PPS composite panels and the 2.3 mm thick CF/Epoxy composite panels.

Figure 6-8 relates the indentation depth to the delamination damage area for the CF/PPS panels and the 2.3 mm CF/Epoxy panels. Note the data points for the two 'nearly perforated' CF/PPS panels are shown in brackets and have not been used when fitting the curves. Clearly for a similar damage area the CF/PPS shows a greater indentation depth than the CF/Epoxy. Although at an impact energy of 2 J both materials show an almost identical damage area, the CF/PPS has an indentation depth of more than double the indentation depth shown by the CF/Epoxy. Nevertheless, both of these materials indicate that the indentation damage is initiated before the establishment of any delamination

damage, supporting the theory established in Chapter 4. Furthermore, the permanent indentation depth in CF/PPS is related to the damage area by a second-order polynomial, as was the case for the CF/Epoxy. Although, given the scatter, a linear fit could also have been used. Therefore, from a measurement of the surface indentation depth, an estimate for the internal damage area can be gained.

However, this is only valid up until the transition to perforation behaviour. This transition can be identified from the visible impacted surface as the permanent indentation zone is uneven, rather than showing a relatively smooth hemispherical indentation where the surface conforms to the impactor head. Once significant fibre failure occurs in the rear plies the indentation depth cannot be related to the damage area. This is demonstrated by the panels impacted at 10.15 J and 12.5 J which showed very different delamination damage areas of 214 mm^2 and 664 mm^2, indicated on Figure 6-8 by the data points in brackets.

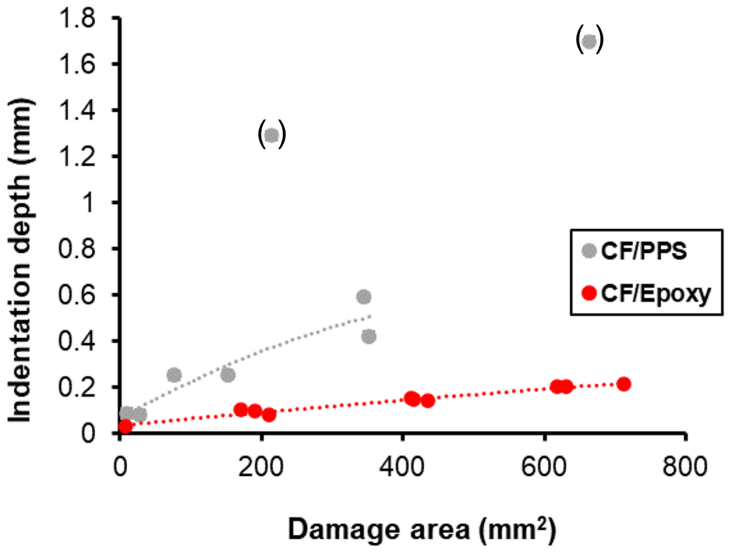


Figure 6-8: The indentation depth versus the delamination damage area for the CF/PPS composite panels and the 2.3 mm thick CF/Epoxy composite panels.

6.3.4 Optical microscopy studies

The optical microscopy images shown in Figure 6-9 highlight the increasing severity of damage seen in the CF/PPS panels with increasing impact energy from 5 to 10 J. In the panel impacted at 5 J, a large number of intralaminar cracks have been formed around the damage zone, particularly in the top half

of the panel. However, only some of these appear to have initiated delaminations. Some fibre fracture has been caused near the surface of the panel (see exploded image of Figure 6-9(a)) due to the compressive forces on the fibre yarns causing kinking. For the 7.5 J impact, the intralaminar cracks are more centred beneath from the impact zone. However, a greater severity of both intralaminar cracks and delamination is visible directly beneath the impact zone in the lower half of the panel. For the 10 J impact, very few intralaminar cracks have formed outside of the immediate impact zone. Furthermore, the severity of damage has again increased and intralaminar and delamination damage are visible throughout the entire panel thickness beneath the impact zone. Interestingly, vertical intralaminar cracks have formed in the top half of the panel impacted at 10 J and diagonal ones have formed in the bottom half. The vertical intralaminar cracks spread through multiple plies and are formed of both matrix cracking between the warp fibres and fibre fracture of the weft fibres (see exploded images of Figure 6-9(c). (Weft fibres are the horizontal fibres in the microscope images.) The fibre fractures indicate that the weft fibres failed under tensile load, directly beneath the impactor head. The depression of weft fibres in the plies in this location due to the permanent indentation which has extended through the entire thickness of the panel is a likely cause of this. The tensile force on the weft fibres as they conformed to the shape of the impactor head helps offset the compressive forces from the bending of the panel which may have caused crushing. Delaminations can clearly be seen in the bottom half of the panel propagating out from the impact zone, although some appear to be disjointed due to the woven structure. This supports the findings of the C-scans in Section 6.3.1.

For impacts of 7.5 J and above, the fibres in the rear-most ply have suffered tensile failure and become disconnected. For the 10 J this has happened for the two rear-most plies. This is because when the impactor has enough energy to start to penetrate the uppermost layers of the laminate, shear failures occur (shown here by the intralaminar cracks) and the impactor still has enough energy to cause the delaminated layers in the bottom half of the panel to slide over each other, leading to the rear plies failing due to the resulting tensile load placed on them [34]. Furthermore, the outer plies are subjected to flexural loading, causing a higher stress in the yarns. Fibre breakages are more likely to occur in a woven structure due to fibre crimping [65].

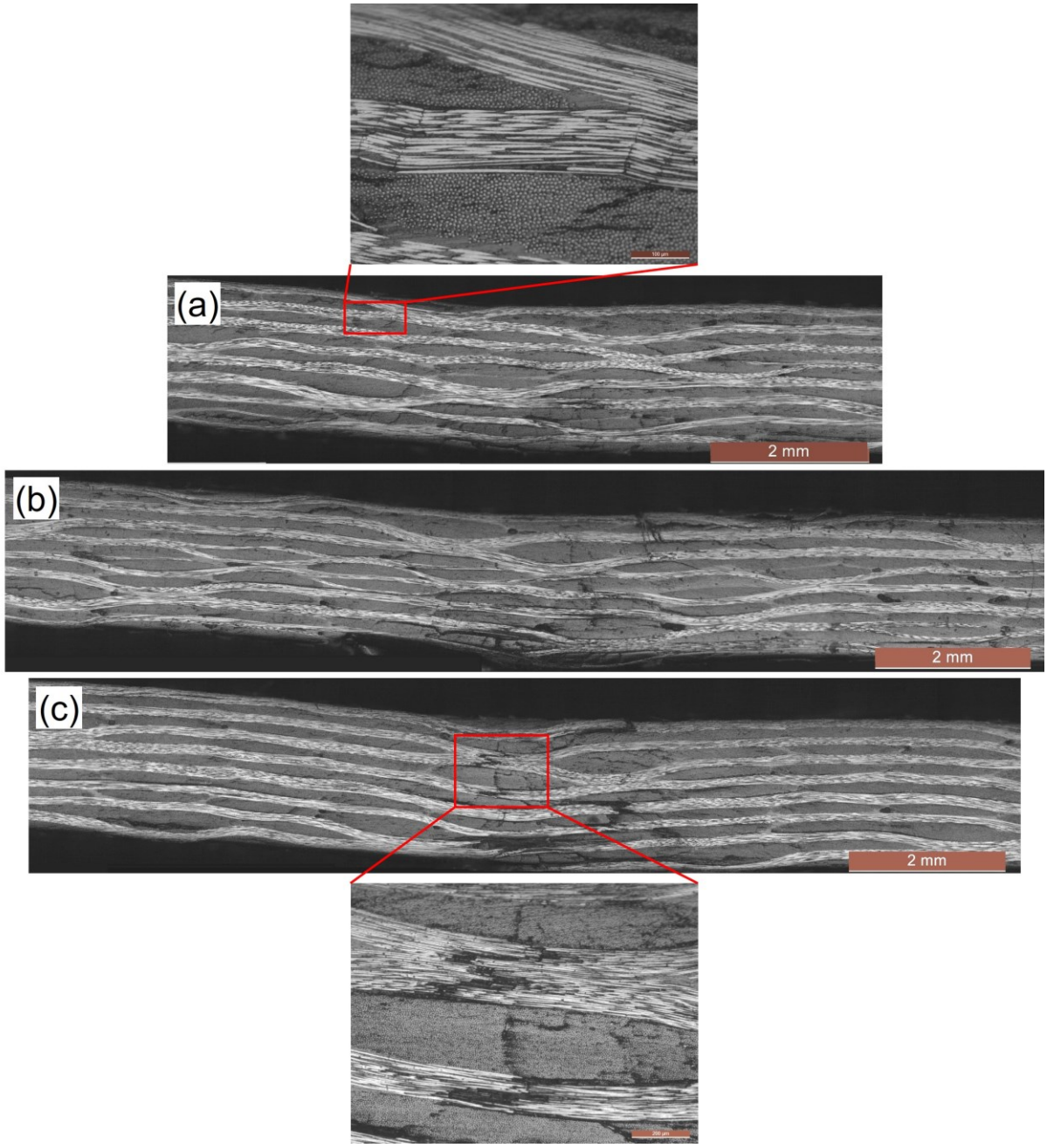


Figure 6-9: Optical microscopy images of a CF/PPS composite panel after impact at (a) 5 J, (b) 7.5 J and (c) 10 J. (Showing cross-sections cut from the panel after grinding and polishing.) Exploded view images have scale bars of (a) 100 µm and (c) 200 µm.

The panel impacted at 7.5 J shows a significantly higher quantity of voids than the other panels. For this panel, pear-shaped voids have formed in resin-rich regions, possibly due to shrinkage of the matrix during cooling if the holding pressure was not maintained. This could explain the larger than

expected delamination area seen for this panel, see Section 6.3.1, as the voids may have weakened the panel and increased the ease with which delaminations could propagate during the impact event.

Figure 6-10 compares optical microscopy images of the CF/Epoxy and CF/PPS panels after impact at 5 J. The CF/Epoxy shows a conical intralaminar damage zone, increasing in diameter through the panel thickness, whereas the CF/PPS does not show this as clearly. In fact, diagonal intralaminar cracks are seen further from the impact zone in the top half of the CF/PPS panel than in the bottom half for the 5 J impact. This may be because the CF/PPS shows a higher permanent indentation and therefore the impactor penetrates further into the panel. This causes the cracking as the top-most plies are pulled towards the centre more so therefore more intralaminar damage is created near the top of the CF/PPS panel. Also, the woven architecture limits shear crack and delamination propagation, narrowing the zone of delamination [22,23].

The delaminations are also clearer in the CF/Epoxy panel. Apart from the delaminations stretching for a longer distance in the CF/Epoxy, this may be because the undulations of the fibre yarns in CF/PPS mean the delaminations are not continuous, instead starting and stopping multiple times along a single ply boundary. This is related to the unstable crack propagation seen in woven composites. Although longer delaminations are seen in CF/Epoxy, the damage is more severe in CF/PPS. Much more intralaminar cracking and some fibre fracture are seen near the rear of the panel for CF/PPS. One contribution to this may be the T300 carbon fibres used in the CF/PPS, which have a lower tensile strength than the T700 fibres present in the CF/Epoxy.

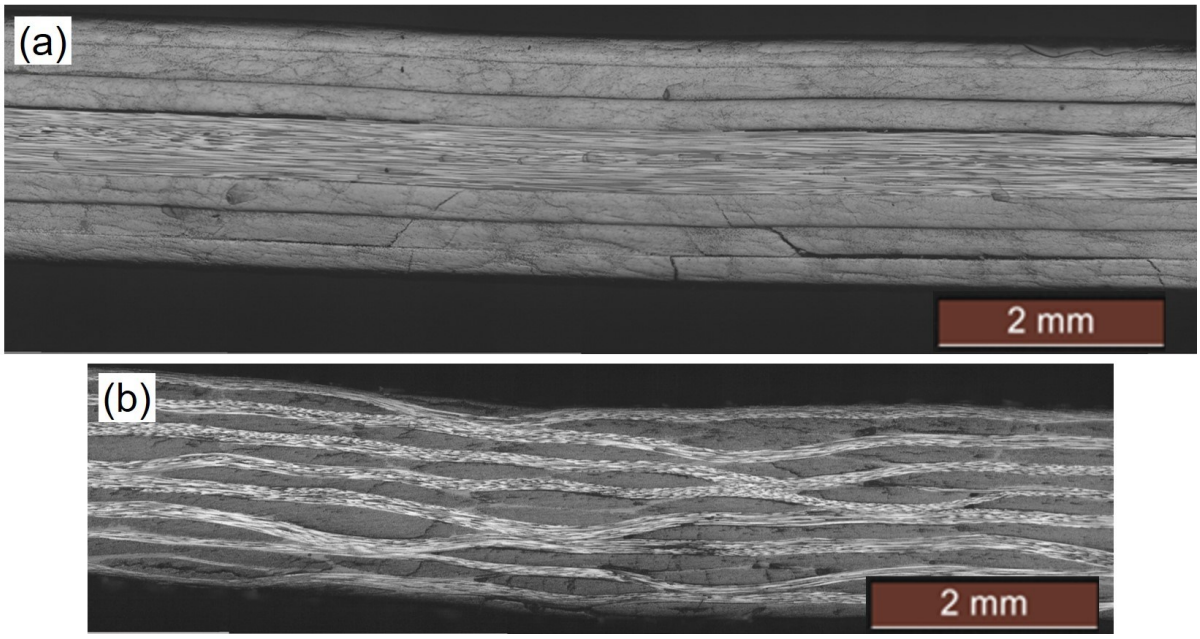


Figure 6-10: Optical microscopy images of (a) CF/Epoxy and (b) CF/PPS composite panels after impact at 5 J. (Images from Figure 4-13(a) and Figure 6-9(a), repeated here to allow easy comparison.)

6.4 Summary

The relationship between the extent of indentation and the resulting impact damage in 2 mm thick woven CF/PPS composite has been investigated and compared to that in 2.3 mm thick UD CF/Epoxy (tested in Chapter 4). Low-velocity impacts of 2, 5, 7.5, 10 and 12.5 J were undertaken using a drop-weight tower and a hemispherical stainless-steel impactor of diameter 16 mm. The resulting damage formation and surface indentation depth have been investigated using ultrasonic C-scanning, a digital depth gauge and optical microscopy.

The impact testing revealed that a smaller delamination damage area is formed in the CF/PPS panels than in the CF/Epoxy panels when impacted at the same impact energy. This is due to both the different matrices and the different fibre architectures. Thermoplastics usually provide a tougher matrix than thermosets, leading to a lower damage area in the CF/PPS. The woven fibres present in the CF/PPS deflect cracks and hinder shear crack and delamination propagation, increasing the fracture toughness and reducing the delamination damage area. Also, for the same impact energy, the CF/Epoxy panels exhibit a higher peak load and a lower maximum displacement.

The permanent surface indentation formed in the CF/PPS is accompanied by both intralaminar damage, including matrix cracking within the ply and fibre fracture, and interlaminar (i.e. delamination) damage between plies. Indentation depth initially has a linear relationship with impact energy, however at higher impact energies the panel shows a transition to perforation behaviour where large increases are seen in indentation depth due to fibre failure in the rear plies of the panel. Although the indentation depth has been shown to be related to the delamination damage area in the CF/PPS panels for the low-velocity impact energies of 2 to 10 J by a second-order polynomial relationship, this is only valid up until the transition to perforation behaviour. This transition can be identified from the visible surface as the permanent indentation zone has an uneven surface rather than a surface conforming to the hemispherical impactor. This highlights that, until the transition to perforation behaviour, measuring the indentation depth has the potential to be used as a quick, easy and cheap alternative to employing expensive NDT equipment for estimating the extent of internal delamination damage.

Therefore, the present study has identified a relationship between indentation depth and delamination damage for woven CF/PPS after impact by a 16 mm diameter rigid hemispherical impactor.

Throughout this chapter, it must be remembered that the thickness, reinforcement architecture and matrix are all different for the two materials being compared, i.e. CF/PPS and CF/Epoxy. Therefore, the differences in impact resistance cannot be attributed to only a single variable.

Chapter 7 Study on the damage formed in CFRP thermoset laminates and the residual compressive strength after multiple impacts in different locations

7.1 Introduction

The current chapter presents the results from an experimental study into the behaviour of unidirectional (UD) CF/Epoxy composite under low-velocity impact. Low-velocity drop-weight testing with a rigid hemispherical impactor was used to perform the impacts and ultrasonic C-scanning was used to examine the internal delamination damage formed during the impacts. Compression-after-impact (CAI) testing was undertaken using a rig which suppresses global buckling behaviour in the panel. Each panel was subjected to two impacts in different locations and the effect of the distance between the impacts and the impact energy on both the resulting delamination damage footprint and the residual CAI strength is examined in this chapter.

The studies revealed that the distance separating the two impacts has a large effect on both the delamination damage formed and the subsequent CAI strength. In general, although the area of the delamination damage footprint increases with separation distance, the CAI strength also increases.

7.2 Test specification and methods

7.2.1 Materials

The CF/Epoxy panels used in the study presented in this chapter were manufactured following the method described in Section 3.2.1.1. Each panel had a thickness of 4.6 mm and a quasi-isotropic (QIT) lay-up of $[45_2/-45_2/0_2/90_2]_s$. The panels were cut to three different sizes: 160 mm x 100 mm, 180 mm x 100 mm and 200 mm x 100 mm and the 0° plies were aligned with the longer edge of the panels.

7.2.2 Experimental methods

Low-velocity drop-weight testing was undertaken following the method outlined in Section 3.3.1. The 16 mm diameter round-nosed impactor had an overall mass of 5.27 kg and was dropped from varying heights to give impact energies of 3, 6, 9, 10, 15, 20, 25, 30 and 35 J, with corresponding impact velocities of 1.07, 1.51, 1.85, 1.95, 2.39, 2.76, 3.08, 3.38, 3.65 $m.s^{-1}$, respectively. The impact energies tested on each of the three lengths of panel are shown in Table 7-1. The energy levels and panel lengths used were decided upon by analysing the delamination diameters given by previous impacts on 150 mm x 100 mm panels. By measuring the distance from the 100 mm long edge to the far side of the delamination area, an appropriate panel length could be calculated to give two completely separate delamination areas after two impacts at a given impact energy. Alternatively, extrapolation was used between the previously tested energy levels to calculate a required energy level to give two completely separate delamination zones for a given panel length. The energy levels were chosen to give a range of completely separate and combined damage zones in the panels. For the 200 mm panels, higher energies of 25, 30 and 35 J were also used to provide more overlap between the delamination areas and ensure more of the individual delaminations combined. To allow comparison between the three lengths of panel (i.e. the three impact separation distances) the impacts at 15, 20 and 25 J are analysed in this chapter.

Table 7-1: Summary of the impact energies used for each of the three lengths of panel.

Panel length (mm)	Distance between impacts (mm)	Impact energies tested (J)
160	10	3, 6, 9, 15, 20, 25
180	30	3, 6, 9, 15, 20, 25
200	50	10, 15, 20, 25, 30, 35

In order to impact the same panel in two different locations, once the first impact had been completed the panel was removed from the drop-weight tower, rotated by 180° and inserted back into the drop-weight tower for the second impact. This is demonstrated in Figure 7-1, in which the black

cross shows the position of the first impact and the red cross shows the position of the second impact on a 200 mm length panel (i.e. impact separation distance of 50 mm). The black and red circles show the positions of the clamps for a first and second impact, respectively. The position of the rear guide pin, see Figure 3-10(b), ensures there is a distance of 75 mm from the rear edge of the panel to the impact location. Therefore, using panels of length 160, 180 and 200 mm resulted in impacts separated by 10, 30 and 50 mm, respectively. Figure 7-2 highlights the impact locations and clamp locations for (a) 160, (b) 180 and (c) 200 mm long panels. During the course of this chapter, the panels will be referred to by the distance separating the two impacts. Therefore, a separation distance of 10 mm refers to the 160 mm panel, 30 mm refers to the 180 mm panel and 50 mm refers to the 200 mm panel.

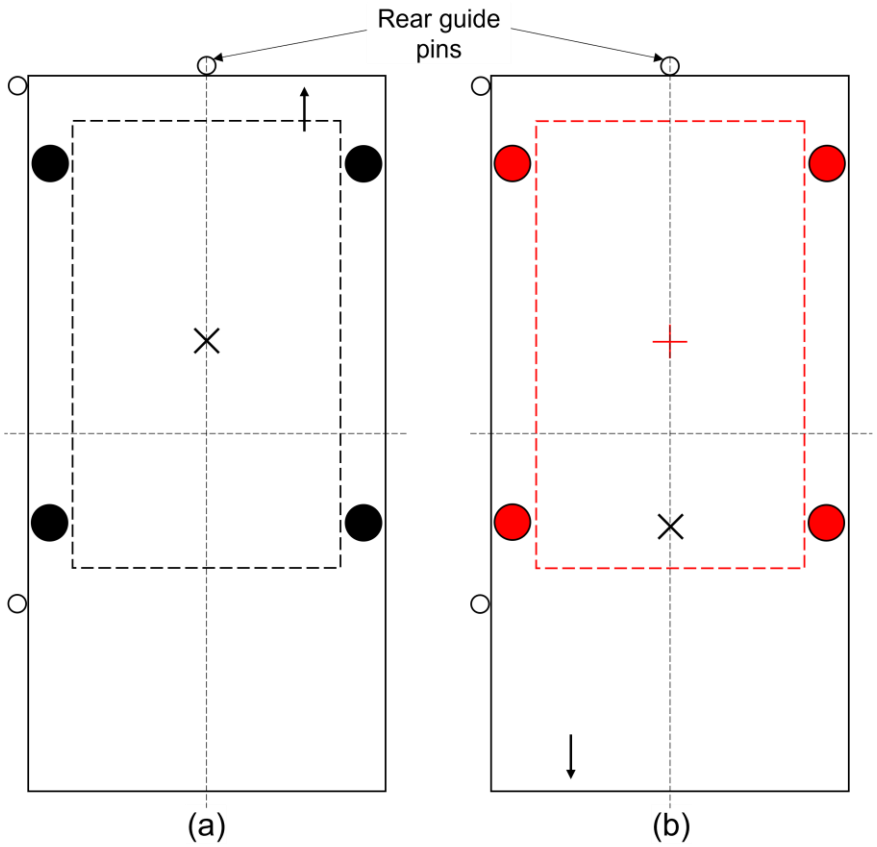


Figure 7-1: Diagram showing the position of a 200 mm x 100 mm panel for (a) a first impact and (b) a second impact (after 180° rotation). The clamp locations are shown by the black and red circles (for first and second impacts, respectively) and the impact points (located 75 mm from the edge of the rear guide pin) are shown by the black and red crosses (again for first and second impacts, respectively). The dashed rectangle shows the position of the window cut-out beneath the panel. The arrow indicates the 0° direction.

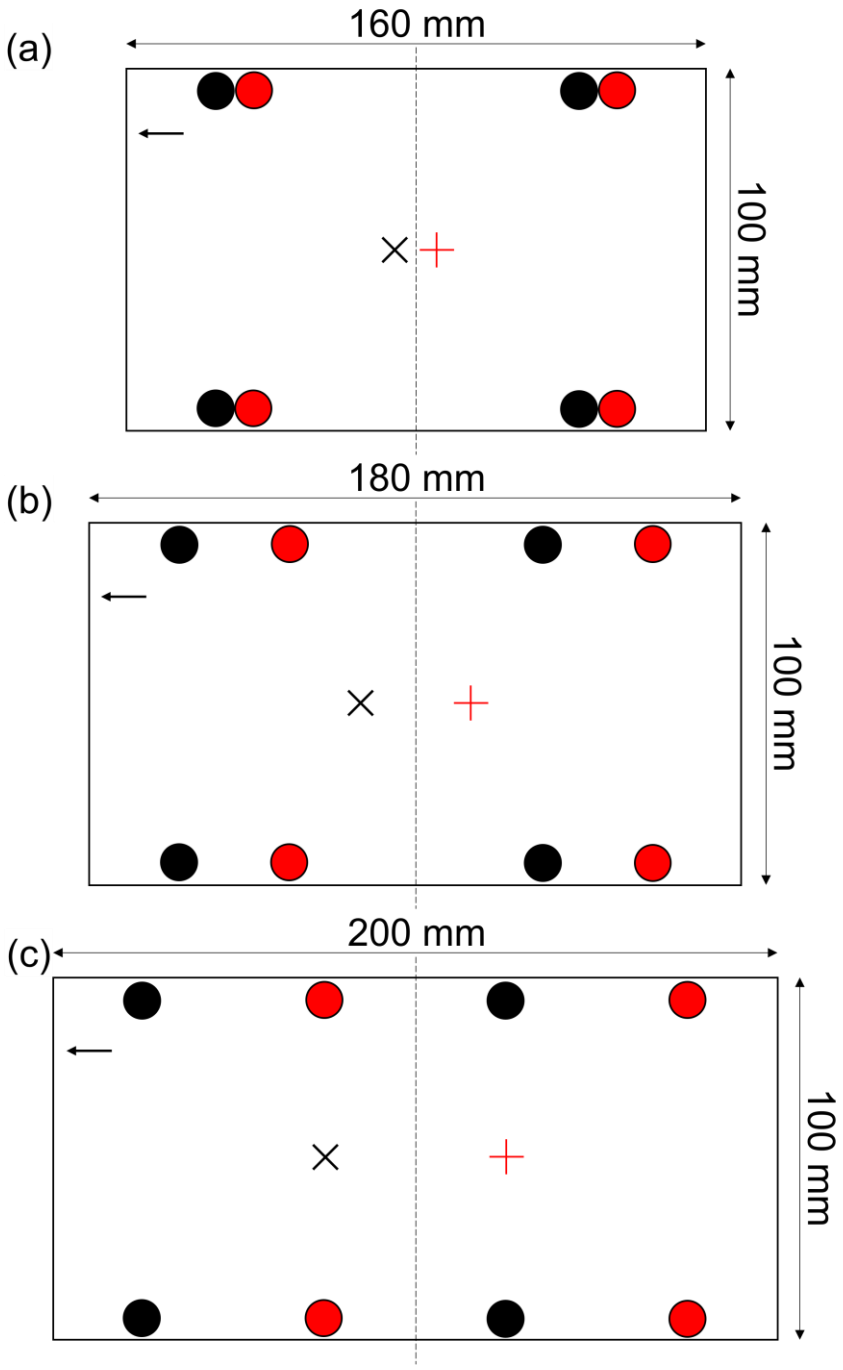


Figure 7-2: Diagram showing the impact locations and clamp locations for first (black) and second (red) impacts on the (a) 160, (b) 180 and (c) 200 mm long panels. The arrows indicate the 0° direction.

Ultrasonic C-scanning (a non-destructive testing (NDT) method) was undertaken to view the delamination damage within each panel after impact following the method described in Section 3.3.2. CAI testing was undertaken following the method described in Section 3.3.4 to allow comparison between the residual compressive strengths of the panels.

7.3 Experimental results and discussion

7.3.1 Delamination damage

Figure 7-3, Figure 7-4 and Figure 7-5 show the C-scan damage maps after a first and second impact, both at 15, 20 and 25 J, respectively, on the same panel, with the two impacts separated by 10, 30 and 50 mm. For all the C-scans shown, the right-hand side scale indicates the location of the interlaminar delamination as a function of the depth through the thickness of the panel (0 to 4.6 mm), where the dark red colour represents the front (impacted) face and the dark blue colour represents the rear (non-impacted) face of the composite panel. The footprint of the delamination damage area (DA) detected is given in the bottom left-hand corner for each panel and was determined by counting the pixels which had a colour which was not dark blue. The bottom right of each damage map shows a 10 mm scale bar. Firstly, from a comparison of the C-scans after only the first impact, the delamination damage area increases with an increase in impact energy. This is to be expected and has also been highlighted in the previous chapters of this thesis. However, the differing lengths of the panels does appear to have slightly affected the impact response, with the damage area increasing for a single impact at the same impact energy with increasing length of the panel. A potential reason for this could be the increased amount of material along one edge of the panel increasing the stiffness along that edge and increasing the constraint, which therefore affects the dynamic response of the panel and subsequent damage formation. The extra material may also be excited into oscillation during the impact which could drive delamination damage formation due to the increased localised bending. This phenomenon could be investigated further using high-speed cameras to compare the deformation behaviour of the three lengths of panel.

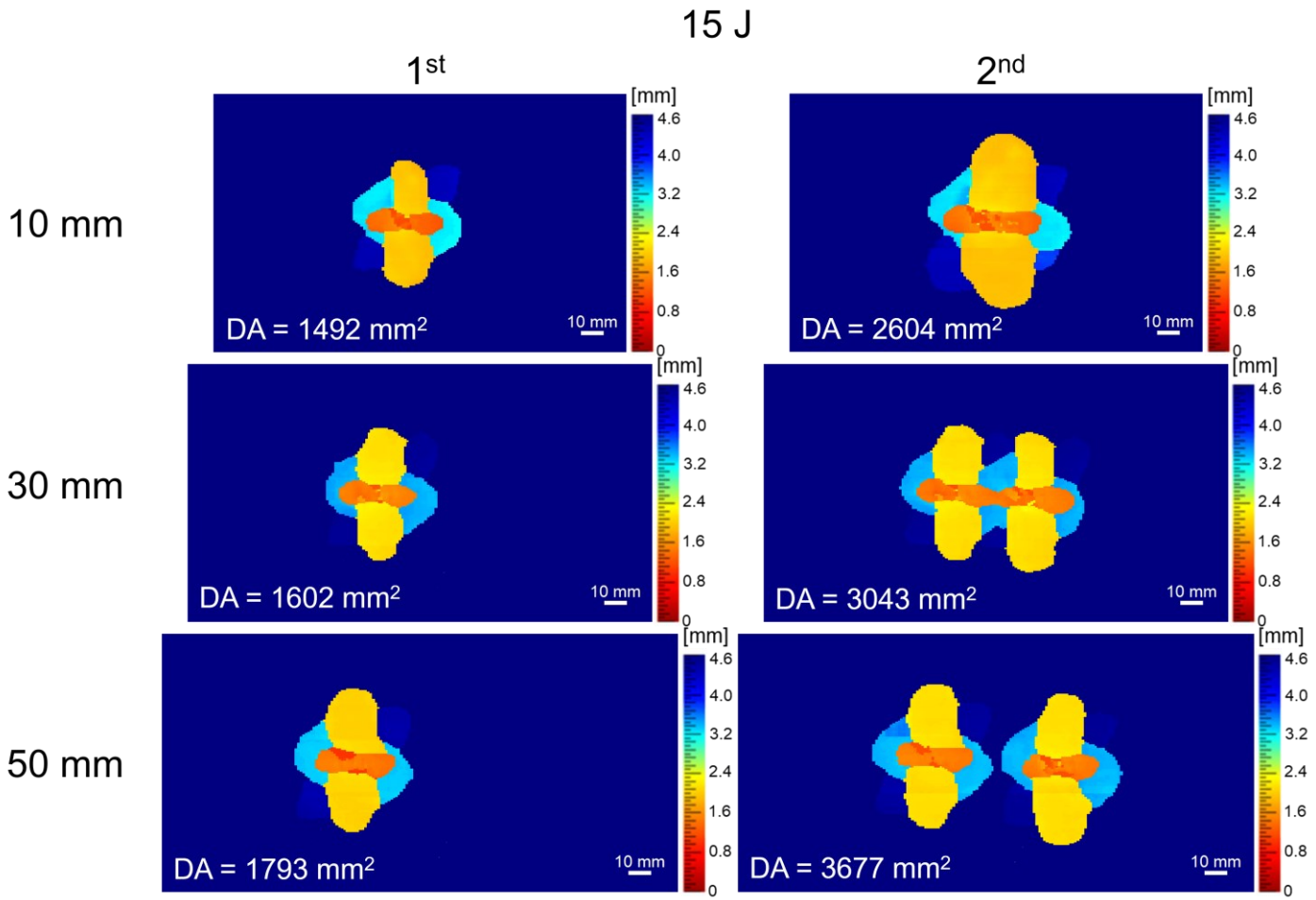


Figure 7-3: C-scan damage maps obtained from the 160, 180 and 200 mm long CF/Epoxy composite panels after one impact, and then a second impact, separated from the first by 10, 30 and 50 mm, respectively, at an energy of 15 J.

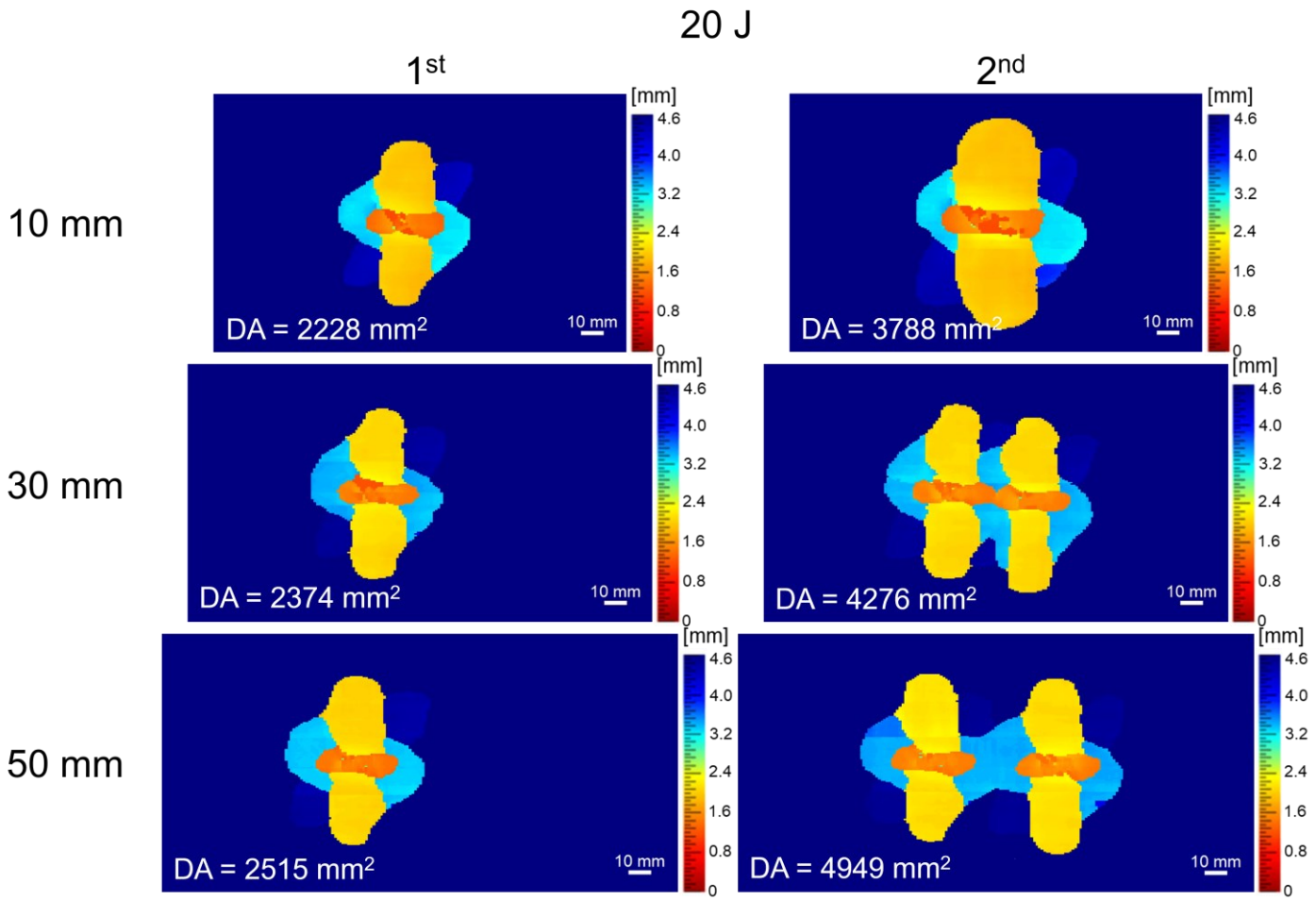


Figure 7-4: C-scan damage maps obtained from the 160, 180 and 200 mm long CF/Epoxy composite panels after one impact, and then a second impact, separated from the first by 10, 30 and 50 mm, respectively, at an energy of 20 J.

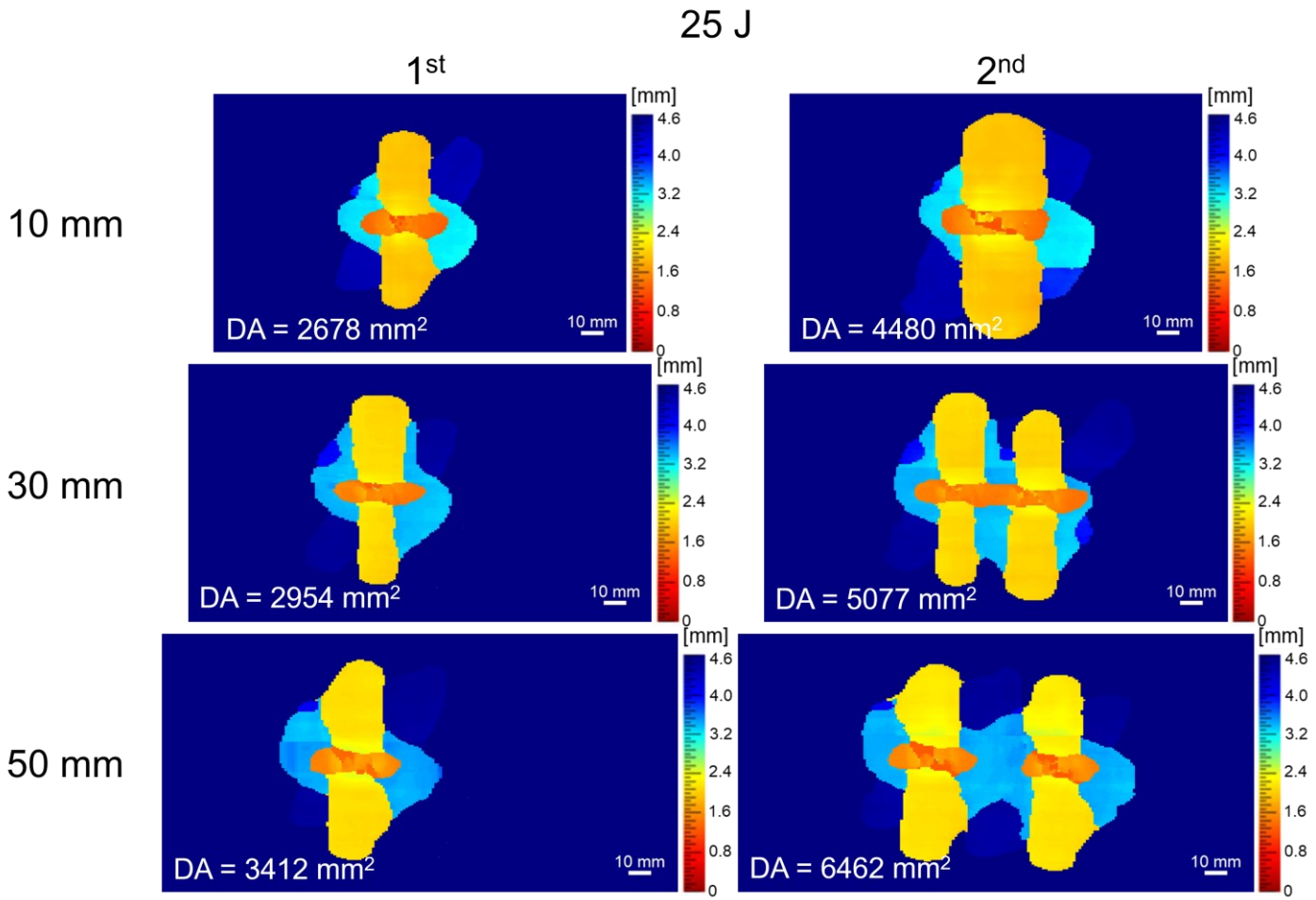


Figure 7-5: C-scan damage maps obtained from the 160, 180 and 200 mm long CF/Epoxy composite panels after one impact, and then a second impact, separated from the first by 10, 30 and 50 mm, respectively, at an energy of 25 J.

Secondly, from a comparison of the panels after the second impact, the distance between the impacts clearly has a large effect on both the shape and the size of the resulting delamination footprints. For all three impact energies, the impacts separated by 10 mm have created a damage zone which is a very similar shape to that created after a single impact. A distance of only 10 mm from the original impact site means that the second impact takes place on top of all the existing delaminations. Therefore, the panel has a reduced bending stiffness and deforms more under impact, meaning more impact energy is absorbed through elastic deformation. New intralaminar cracks and delaminations are not initiated and instead the panel appears to propagate the existing delaminations within the panel. This is similar to the behaviour for a second impact in the same location which was analysed in Chapter 5. Contrastingly, when the impacts are separated by 30 and 50 mm, two damage zones clearly radiate from the two impact points. For an energy of 15 J and an impact separation distance of 50 mm, these damage zones do not combine and are separated by a zone of delamination-free material, see Figure 7-3. However, at higher energy levels the delaminations of the two damage zones start to combine. This is further shown in Appendix G - Figure G-2 and Figure G-3, where separate damage zones occur at a smaller separation distance (i.e. 30 mm) if the impact energy is low enough (i.e. 6 and 9 J).

For a certain energy level, the larger the separation distance between the two impacts, the larger the footprint of the resulting delamination damage area. At a distance between 10 and 30 mm, the single damage zone transitions into two damage zones, each centred on a single impact point. Once the two damage zones are far enough apart that they no longer combine, the total size of the delamination damage area reaches its maximum and stays approximately constant for further increases in separation distance.

7.3.2 Load versus time and load versus displacement results

Load versus time and load versus displacement traces are shown in Figure 7-6, Figure 7-7 and Figure 7-8 for first and second impacts at 15 J for separation distances of 10, 30 and 50 mm, respectively. The small sinusoidal oscillations on the rising section of the traces are indicative of mass-spring oscillations and have been observed by other researchers [290–292]. For a first impact, all three separation distances (i.e. all three panel lengths) show a clear load drop, indicating the initiation of damage in the

panels. This occurs at around 5 kN for impact energies of 15 J. The 10 mm separation case exhibits a slightly higher load throughout the impact and a slightly smaller maximum displacement than the 30 and 50 mm (i.e. 180 and 200 mm) panels. These small differences are likely due to the differing dynamic responses of the different length panels.

For a second impact, a large difference in impact response is shown by the 10 mm separation panels. No initiation load drop occurs for these panels whereas the 30 and 50 mm panels both show another load drop for the second impact. This was also the case for impacts at 20 and 25 J. Note, the graphs for these energies are not shown due to their similarity to the 15 J graphs. For a separation distance of 10 mm, the second impact occurs on top of existing delaminations and only 10 mm from the centre of the damage caused by the first impact, therefore, propagation of the existing delaminations occurs as there is no delamination-free material beneath the impactor in which new delaminations can be initiated. The presence of the existing delaminations causes a reduction in bending stiffness of the panel and an increase in the maximum displacement, as shown by the load versus displacement trace in Figure 7-6(b). Therefore, more energy can be stored through elastic deformation, meaning less energy is available to propagate the existing delaminations. This contributes to the lower damage footprint formed when the separation distance is only 10 mm. When the separation distance is 30 or 50 mm, a slightly lower stiffness and larger maximum displacement is seen for the second impact as the panel has been slightly weakened by the presence of the existing delaminations. These differences are not large as the existing damage is not in the centre of the impact zone and there is still enough delamination-free material for a second damage zone to form. However, the differences do increase with increasing impact energy as the damage zones interact more and the impact response is therefore more affected by the presence of the larger delaminations from the previous impact.

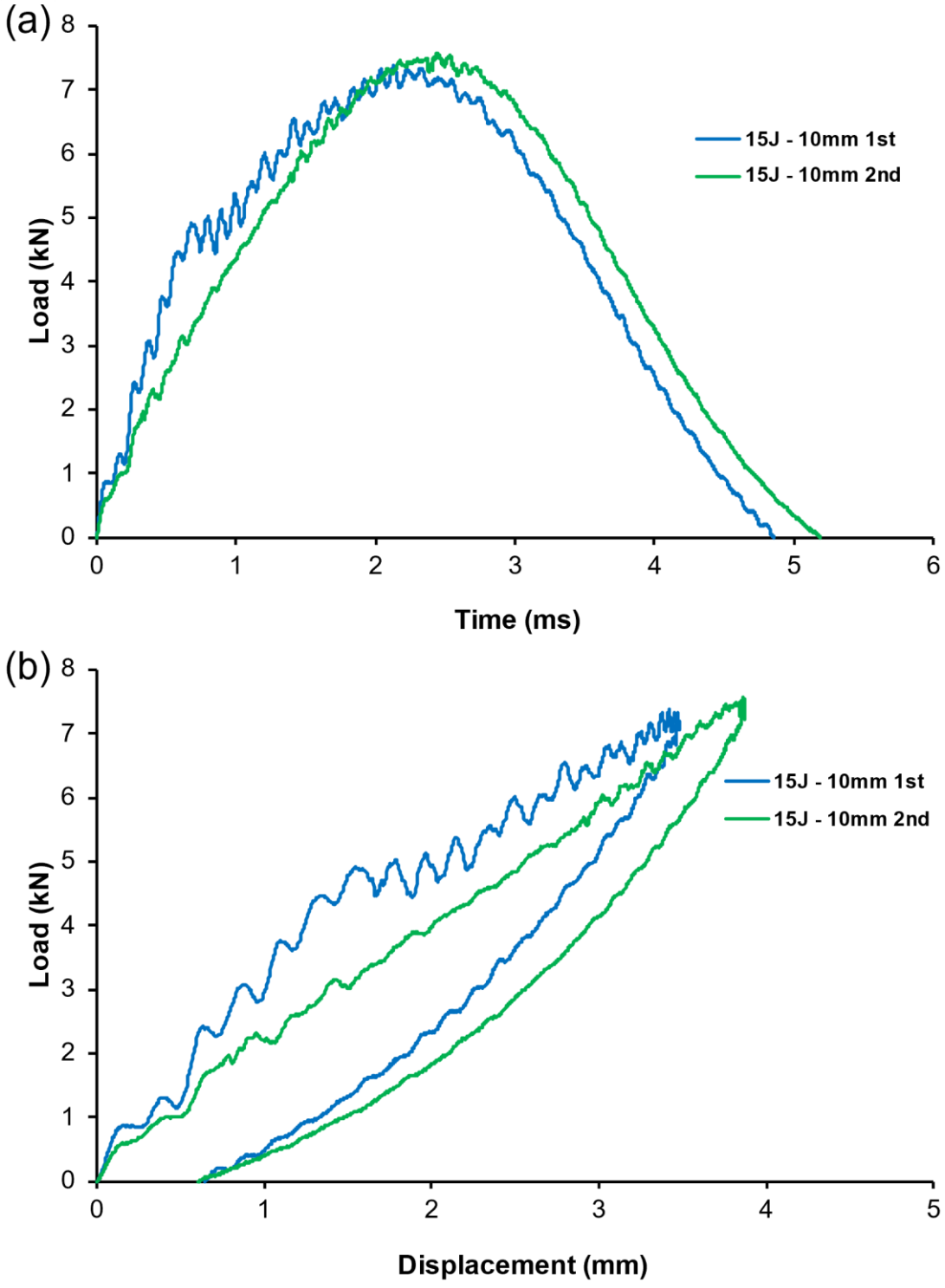


Figure 7-6: (a) Load versus time traces and (b) load versus displacement traces for first and second impacts at 15 J separated by 10 mm on 160 mm long CF/Epoxy composite panels.

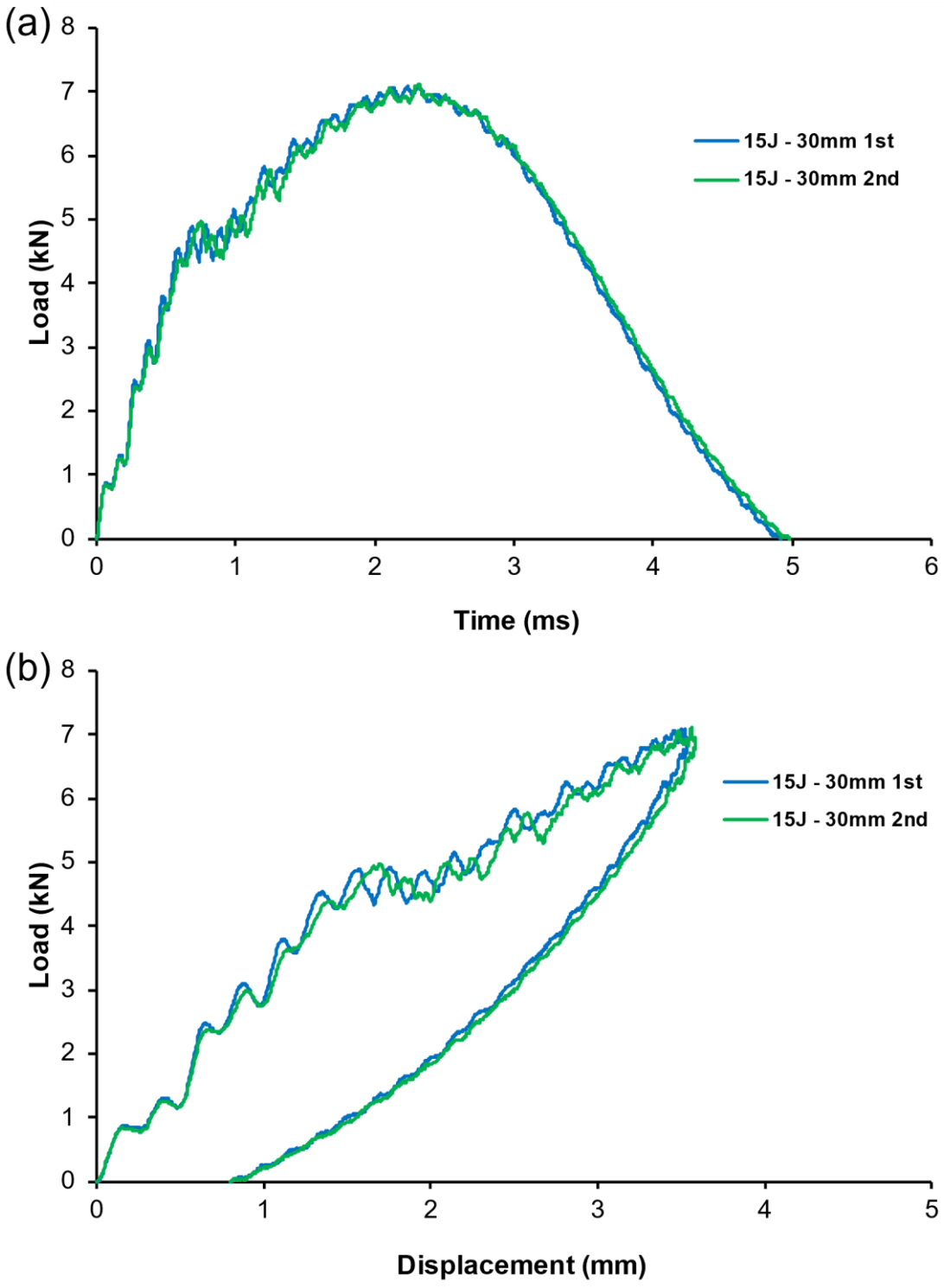


Figure 7-7: (a) Load versus time traces and (b) load versus displacement traces for first and second impacts at 15 J separated by 30 mm on 180 mm long CF/Epoxy composite panels.

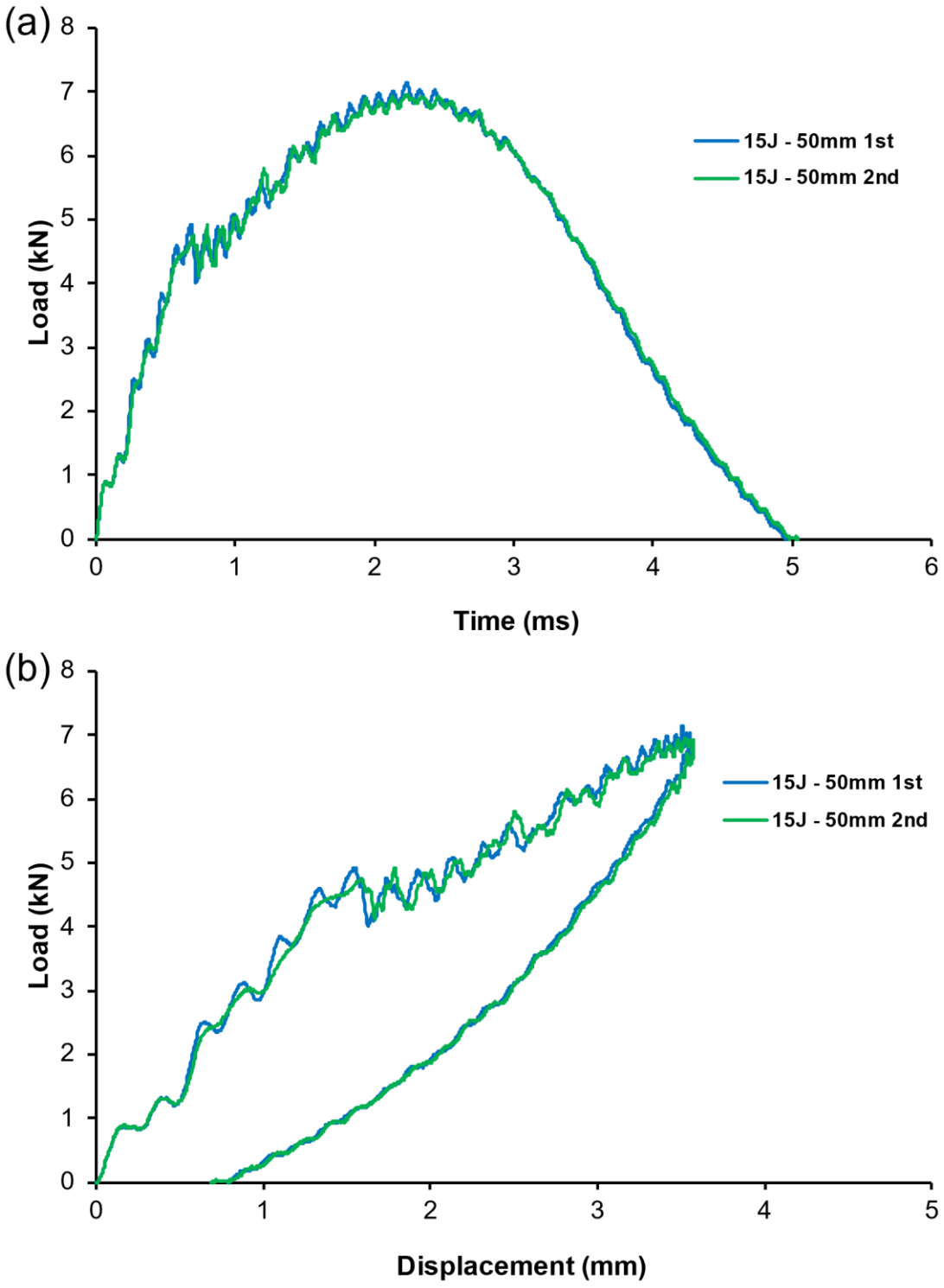


Figure 7-8: (a) Load versus time traces and (b) load versus displacement traces for first and second impacts at 15 J separated by 50 mm on 200 mm long CF/Epoxy composite panels.

7.3.3 Compression-after-impact (CAI) results

Of the eighteen panels tested, all panels impacted at 10 J and above provided a valid test result, with failure occurring either across the centre of the panel (in the 10 mm separation case) or across one of the damage zones (in the 30 and 50 mm separation cases). Note that the compressive load was applied to the 100 mm long edge closest to the damage area from the first impact (i.e. the left-hand side of the C-scans in Figure 7-3, Figure 7-4 and Figure 7-5) while all other edges were held by the CAI rig. The panels appear to have mainly failed due to mixed mode buckling-induced delamination propagation which has led to compressive failure, see Figure 7-9. The delaminations between the 0° and 90° plies appear to have propagated in a transverse direction towards the edge of the panel in most cases, see Figure 7-9, pushing the 0° plies, and the plies closer to the surface, away from the centre of the panel. This is explained in more detail later. The transverse propagation of delaminations under compressive loading has also been observed by other researchers [71,295].

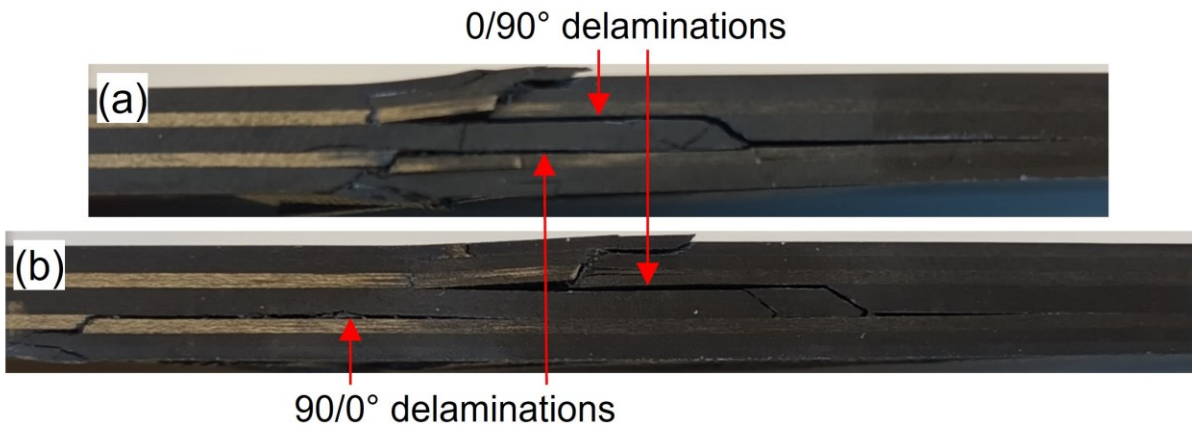


Figure 7-9: Photographs of the edge of the CF/Epoxy composite panel after CAI testing at the location of failure for (a) 15 J - 30 mm and (b) 25 J - 30 mm cases, showing propagation of delaminations to the edge of the panel at the 0/90° and 90/0° ply boundaries.

7.3.3.1 Effect of impact energy

The compressive loading response of the CF/Epoxy panels impacted twice at 15, 20 and 25 J is shown in Figure 7-10 for impact separation distances of (a) 10, (b) 30 and (c) 50 mm. Impact energies of 10, 30 and 35 J are also included for the 50 mm separation case. The C-scans for these cases are shown

in Appendix G - Figure G-4. In general, the CAI strength (i.e. the residual compressive strength) decreases with increasing impact energy. A larger impact energy causes a larger delamination footprint and longer delaminations. As discussed in Section 2.3.2.2, this increases the ease with which buckling can take place and causes a reduction in compressive strength [38,40].

The trend is not quite so clear for a separation distance of 30 mm, for which the 20 J and 25 J impacts have very similar CAI strengths. The lack of repeated data for the tests performed in this section means confidence in the trends shown cannot be considered high. Repeat tests for the cases analysed in this section would help to confirm the trends seen and provide possible explanations for any variation from the trends.

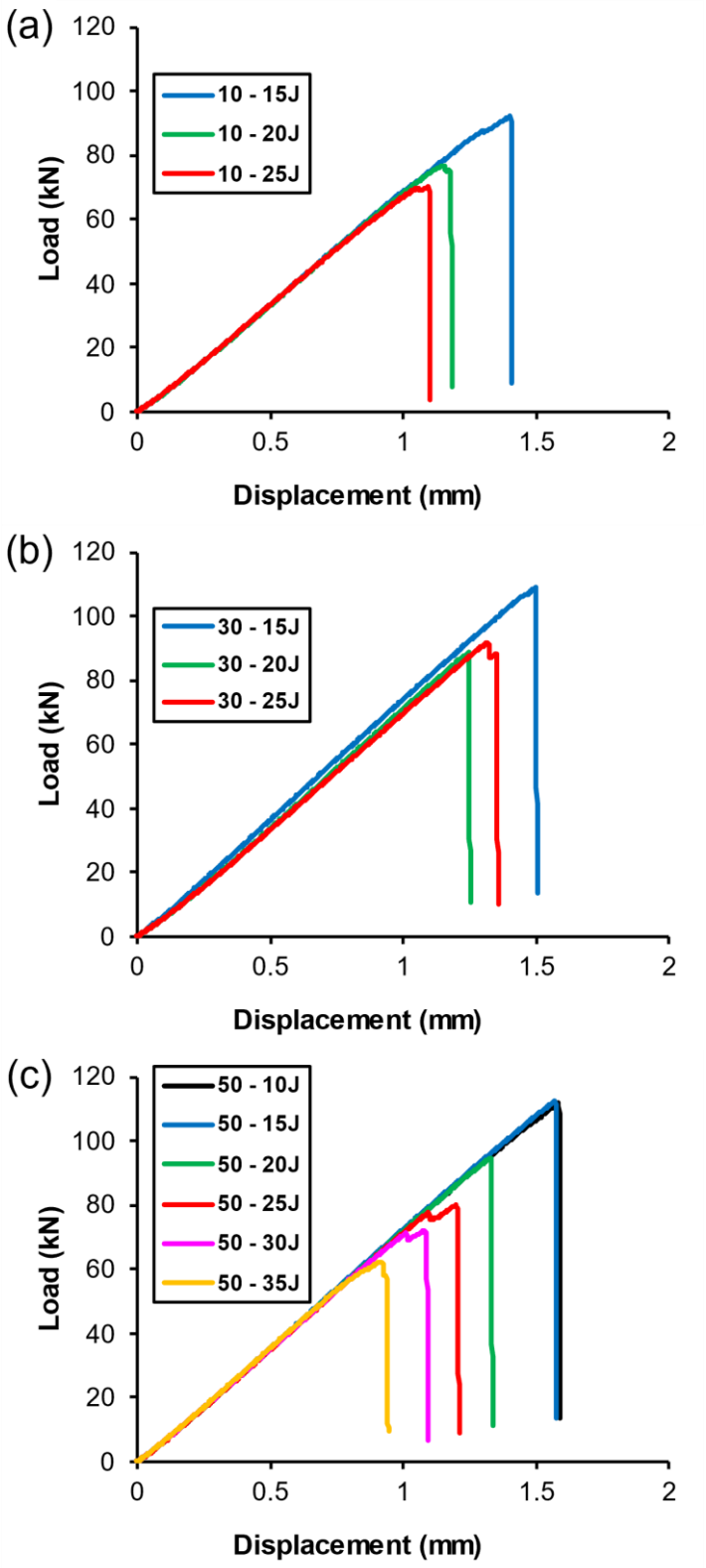


Figure 7-10: Load versus displacement graphs from compressive loading of the CF/Epoxy composite panels impacted twice at 15, 20 and 25 J, with impacts separated by (a) 10, (b) 30 and (c) 50 mm. For the panels with a separation distance of 50 mm, impact energies of 10, 30 and 35 J are also included.

7.3.3.2 Effect of separation distance

The compressive loading data from Figure 7-10 is shown again in Figure 7-11, but to allow the effect of separation distance to be analysed, the data is grouped by impact energy. In general, the larger the separation distance, the higher the CAI strength. Initially, this may seem surprising as a larger delamination footprint area is leading to a higher compressive strength. However, considering the size and shape of the delaminations which have the greatest effect on the buckling behaviour provides some answers. As mentioned earlier, mixed mode buckling has occurred with delaminations propagating to the panel edges, most commonly between the 0° and 90° plies. The 0° plies carry the greatest share of the load, hence they are most prone to buckling [40]. As the 0° plies above and below the 0/90° and 90/0° ply boundary delaminations, respectively, try to undergo buckling behaviour during compressive loading, they are constrained by the delamination-free material around them. As the compressive load increases, the buckling behaviour causes the delaminations to spread towards the edges of the panel, in a direction transverse to the loading direction, leading to compressive failure [71,295].

When the impacts are close enough to each other (e.g. for a 10 mm separation distance), two separate damage zones do not form. Therefore, the length of the upper 0/90° delamination (i.e. the lighter orange delamination at a depth of around 1.8 mm) is highest for the 10 mm case, as there are not two separate delaminations on this ply boundary, see Figure 7-3, Figure 7-4 and Figure 7-5. As a result, buckling and delamination propagation will occur preferentially for this case, instead of for the 30 and 50 mm cases, where the two separate upper 0/90° ply boundary delaminations are both shorter in length and separated by a region of the ply boundary which is free from delamination. This contributes to the higher CAI strength for the 30 and 50 mm cases.

Furthermore, when the two impacts are close enough not to form two separate damage zones (e.g. for a 10 mm separation distance), a much greater propagation of the existing delaminations occurs during the second impact. This causes delamination propagation along not just the length, but the width of the panel as well. For example, for an impact energy of 15 J, the width of the delamination (i.e. the distance the delamination covers along the width of the panel) at the upper 0/90° ply boundary reduces from around 70 mm when the impacts are separated by 10 mm, to around 55 mm when the impacts

are separated by 30 and 50 mm. This reduces the width of material free from delamination at the edge of this damage zone, meaning there is less resistance to the buckling behaviour as the delamination spreads across the width, leading to a reduced CAI strength. The same can be said for the lower 90/0° ply boundary delamination. This delamination has been widened by the second impact for a separation distance of 10 mm, whereas for a 30 and 50 mm separation the delamination width is approximately equal to that after a single impact given the limited propagation of the existing delaminations that takes place during the second impact. Given that delaminations spread transversely during compressive loading [71,295] and the compressive failure occurred across a single impact zone rather than in the middle of the two impact zones for the 30 and 50 mm cases, the delamination width at each impact zone rather than in the centre of the panel is more critical for determining the CAI strength.

For the 15 J - 50 mm case, the two damage zones are completely separated by delamination-free material. This reduces the total length of the lower 90/0° ply boundary delamination and improves resistance to buckling, which contributes to the larger CAI strength in the 50 mm case than in the 30 mm case (when the damage zones combine). However, at 20 and 25 J the damage zones start to combine for both 50 mm cases, but the trend in CAI strength is different, with the 20 J - 50 mm and the 25 J - 30 mm cases having the highest CAI strengths, respectively. The complicated nature of having two damage zones combining will likely lead to more variability for the 30 and 50 mm cases, leading to the requirement to test repeat cases before being able to have good confidence in the data gained.

This analysis highlights that it is a combination of delamination size, shape and location (both through the thickness and along the panel) which determines the CAI strength. A second impact which is close enough to the first to cause significant delamination propagation is more detrimental to the residual CAI strength than an impact which initiates a new damage zone, even though a larger damage footprint results from the second scenario.

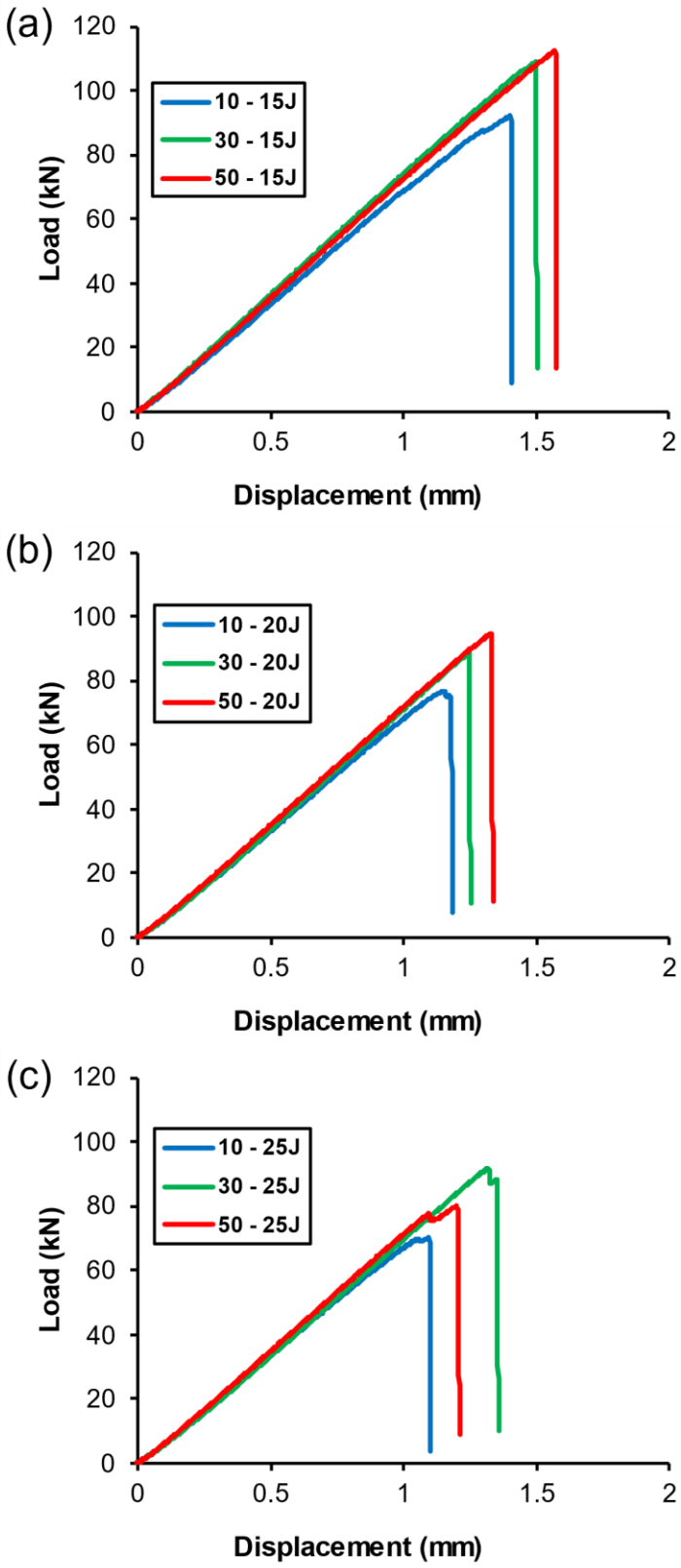


Figure 7-11: Load versus displacement graphs from compressive loading of the CF/Epoxy composite panels impacted twice at (a) 15, (b) 20 and (c) 25 J, with impacts separated by 10, 30 and 50 mm.

7.3.3.3 CAI summary

The findings from the CAI tests are summarised in Figure 7-12. A larger impact energy leads to a lower CAI strength as larger delaminations increase the ease with which buckling occurs and also mean there is less delamination-free material to resist the propagation of delaminations. A larger separation distance increases the CAI strength as, for very low separation distances, more delamination propagation takes place during the second impact so the length and width of the delaminations is greater, aiding buckling and meaning less pristine material is available to resist delamination propagation towards the edges of the panel. This relationship tails off and will likely plateau at a maximum CAI strength as the two damage zones become completely separate and move further apart. The data point for the 25 J - 30 mm case highlights that a higher than expected CAI strength was measured for this scenario in the current testing. Repeat tests for the cases analysed in this section would help to confirm the trends seen and provide physical explanations for any deviations from the trends.

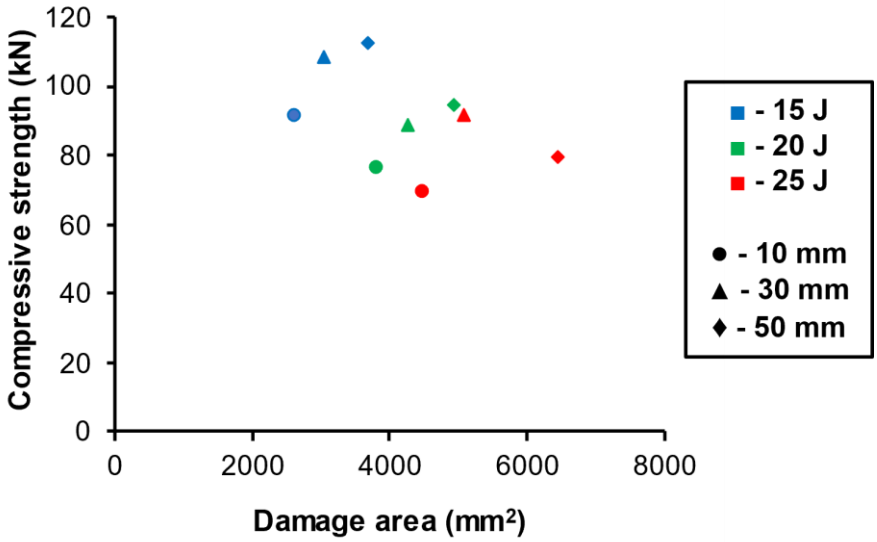


Figure 7-12: The compressive strength (i.e. CAI strength) plotted against the delamination damage area for the CF/Epoxy panels impacted twice at 15, 20 and 25 J, with impacts separated by 10, 30 and 50 mm.

7.4 Summary

The effect of the separation distance between two impacts on the resulting delamination damage and the residual CAI strength in 4.6 mm thick CF/Epoxy composite has been investigated. Repeated low-velocity impacts separated by 10, 30 and 50 mm were undertaken using a drop-weight tower and a hemispherical stainless-steel impactor of diameter 16 mm. The resulting delamination damage has been investigated using ultrasonic C-scanning and the residual CAI strength has been tested using a CAI test rig which is designed to suppress global buckling behaviour.

The impact testing revealed that a second impact within a small distance of the first impact does not initiate new delaminations but instead propagates existing damage. In the panels tested, this was only the case for a separation distance of 10 mm. At larger separation distances (i.e. 30 and 50 mm), a new damage zone starts to initiate in the panel which, depending on the impact energy, may combine with the first damage zone. This causes an increase in the area of the delamination damage footprint with separation distance, up until the point at which the damage zones become completely separate. For the CF/Epoxy panels tested, the separation distance at which new damage starts to be initiated during a second impact is between 10 and 30 mm and this transition can be identified from a load versus time curve by the presence of an initiation load drop.

Despite the delamination damage footprint increasing with impact separation distance, the CAI strength was also found to increase with separation distance. This is attributed to the increased propagation of existing delaminations that takes place at a smaller separation distance, leading to longer and wider delaminations which aide buckling and reduce resistance to delamination propagation. This relationship tails off at higher separation distances and is expected to plateau as the two damage zones become completely separate and move further apart. Also, the CAI strength decreased with an increase in impact energy due to the longer delamination lengths increasing susceptibility to buckling and reducing resistance to delamination propagation.

Therefore, the present study has identified the effects of multiple impacts in different locations on the delamination damage formed in CF/Epoxy and revealed the relationship between impact separation distance and residual CAI strength.

Chapter 8 Study on the impact behaviour of patch-repaired CFRP thermoset laminates

Part of this chapter presents results and analysis from the following paper: 'The effectiveness of patch repairs to restore the impact properties of carbon-fibre reinforced-plastic composites' [294].

Section 8.3.1 initially summarises the main results of the paper to provide a background (this work was undertaken as a group[4]) and Sections 8.3.2 and 8.3.3 present work I have done independently based on the repaired panels used for the study in that paper.

8.1 Introduction

The current chapter presents the results from an experimental study into the behaviour of repaired unidirectional (UD) CF/Epoxy composite under low-velocity impact. Low-velocity drop-weight testing with a rigid hemispherical impactor was used to perform impacts on two different types of repair: patch-only and patch + plug repairs. Ultrasonic C-scanning was used to examine the internal delamination damage formed during the impacts. The depth of the surface indentations formed on the repair patch during impact was also determined and studied to see how the depth related to the thickness of the repair and the delamination damage area within. Finally, optical microscopy and scanning electron microscopy (SEM) were used to investigate in detail the intralaminar and interlaminar damage within the repairs.

The studies revealed that using a 4.6 mm thick patch instead of a 2.3 mm thick patch reduces the delamination damage area in the patch. Addition of a plug beneath the repair patch significantly

[4] I contributed much of the experimental drop-weight tests, C-scans, impact data analysis and C-scan processing to the joint work summarised in Section 8.3.1. Independent research which only I have worked on follows this summary.

reduces this damage area. This observation is supported by analysis of optical microscope and SEM images. From a comparison of images from the two microscopic techniques, it was decided that the optical microscope provides more appropriate images for viewing intralaminar and interlaminar damage in CF/Epoxy. Indentation depth reduces with increasing thickness of the repair and larger indentation depths correspond to larger delamination damage areas.

8.2 Test specification and methods

8.2.1 Materials

The CF/Epoxy panels used in the study presented in this chapter were manufactured following the method described in Section 3.2.1.1. The panels had a thickness of 4.6 mm and a quasi-isotropic (QIT) lay-up of $[45_2/-45_2/0_2/90_2]_s$. Each panel was cut to a size of 150 mm x 100 mm and the 0° plies were aligned with the longer edge of the panels.

The patch-repaired panels were manufactured following the method described in Section 3.2.1.2 and a diagram of a repaired panel is shown in Figure 3-2. The 40 mm damage hole which was cut out of the parent panel was chosen because it is the approximate diameter of delamination damage formed by a 7.5 J drop-weight impact. This area of damage is large enough to cause a considerable change in the response of the panel, yet is small enough not to be affected by edge effects. This diameter was kept constant for all tests performed. The repair patches were formed of QIT CF/Epoxy with lay-ups of $[45/-45/0/90]_s$ or $[45_2/-45_2/0_2/90_2]_s$, giving thicknesses of 2.3 and 4.6 mm, respectively, and were cut into discs of diameter, D, 55 mm or 65 mm. In some cases, a plug with the same QIT lay-up as the parent panel was inserted into the 40 mm damage hole to form a patch + plug repair.

8.2.2 Experimental methods

Low-velocity drop-weight testing was undertaken following the method outlined in Section 3.3.1. The 16 mm diameter round-nosed impactor had an overall mass of 5.27 kg and was dropped from a height of 145 mm to give an impact energy of 7.5 J. This gave a corresponding impact velocity of 1.69 $m.s^{-1}$. For some impacts, two Photron slow motion cameras were used to capture the impact. One camera

viewed the panels from above at an angle of around 25° to the horizontal and the other was set to view in the plane of the panel, see Figure 3-11.

Ultrasonic C-scanning (a non-destructive testing (NDT) technique) was undertaken to view the delamination damage within each repair after impact following the method described in Section 3.3.2. Indentation depth was measured using a handheld digital depth gauge, a method described in detail in Section 3.3.3. This method could be completed quickly and easily and gave accurate values of the indentation depth. Microscopy was undertaken to view the intralaminar and interlaminar (i.e. delamination) damage within each repair following the methods described in Section 3.3.4. Samples were cut, ground and polished before being viewed using the optical microscope and SEM.

8.3 Experimental results and discussion

8.3.1 Summary of previous work

This section summarises the main results published in the paper: 'The effectiveness of patch repairs to restore the impact properties of carbon-fibre reinforced-plastic composites' [294]. For a more detailed discussion of the experimental results, see the full paper.

8.3.1.1 Effect of patch diameter

Firstly, impact tests were performed on pristine CF/Epoxy panels at an impact energy of 7.5 J. Figure 8-1 shows (a) load versus time and (b) load versus displacement traces for a first and second impact in the same location (the centre of the panel) for two repeat tests on separate panels, labelled Test 1 and Test 2. Note, only Test 1 uses data published in [294]. The repeat tests shown in Figure 8-1 show the high reproducibility which was achieved by using the testing setup. Figure 8-1 shows that, for a single impact at 7.5 J, there are small sinusoidal oscillations on the rising sections of the load versus time and load versus displacement curves. These oscillations are indicative of mass-spring oscillations and have been observed by other researchers [290–292]. A local peak in the load of approximately 4.7 kN is achieved at a time of approximately 1 ms. This is followed by a noticeable drop in the load, corresponding to the initiation of damage within the panel. Following this, the oscillations observable in

the traces have a greater amplitude up to the peak load of approximately 5 kN, which occurs at a time of approximately 2 ms and gives a maximum displacement of the panel of approximately 2.4 mm. The load traces for the second impacts do not show a load drop which indicates that new damage processes are not initiated by a subsequent impact and instead existing damage is propagated, see Chapter 5. During a second impact, a higher peak load and maximum displacement is achieved as more energy is stored through elastic deformation and less energy is dissipated by damage formation. Furthermore, the panel has a lower stiffness due to the presence of delaminations.

Figure 8-2 shows C-scan images of both pristine panels after each had been subjected to one and then two impacts, both at 7.5 J. The coloured scales to the right-hand side of the damage maps show the depth of the delaminations beneath the impacted surface, ranging from 0 to 4.6 mm. Note, only the C-scans at the top of Figure 8-2 were published in [294]. The C-scans for a first impact on both panels show high reproducibility and, in both cases, the approximate diameter of the delamination damage was 40 mm. Therefore, for making the repair, it was decided to cut out a 40 mm diameter hole in the centre of the parent panel as this represents the approximate extent of the delamination damage formed by an impact of energy 7.5 J. Furthermore, a 40 mm damage hole allows an appreciable change in the impact response of the panel at 7.5 J to be measured but is not large enough for edge effects to be observed once patch repairs are performed on the panel and impact tested. The performance of these patch repairs is discussed in the following sub-sections. A second impact on the pristine panel increases the delamination damage area by approximately 50%.

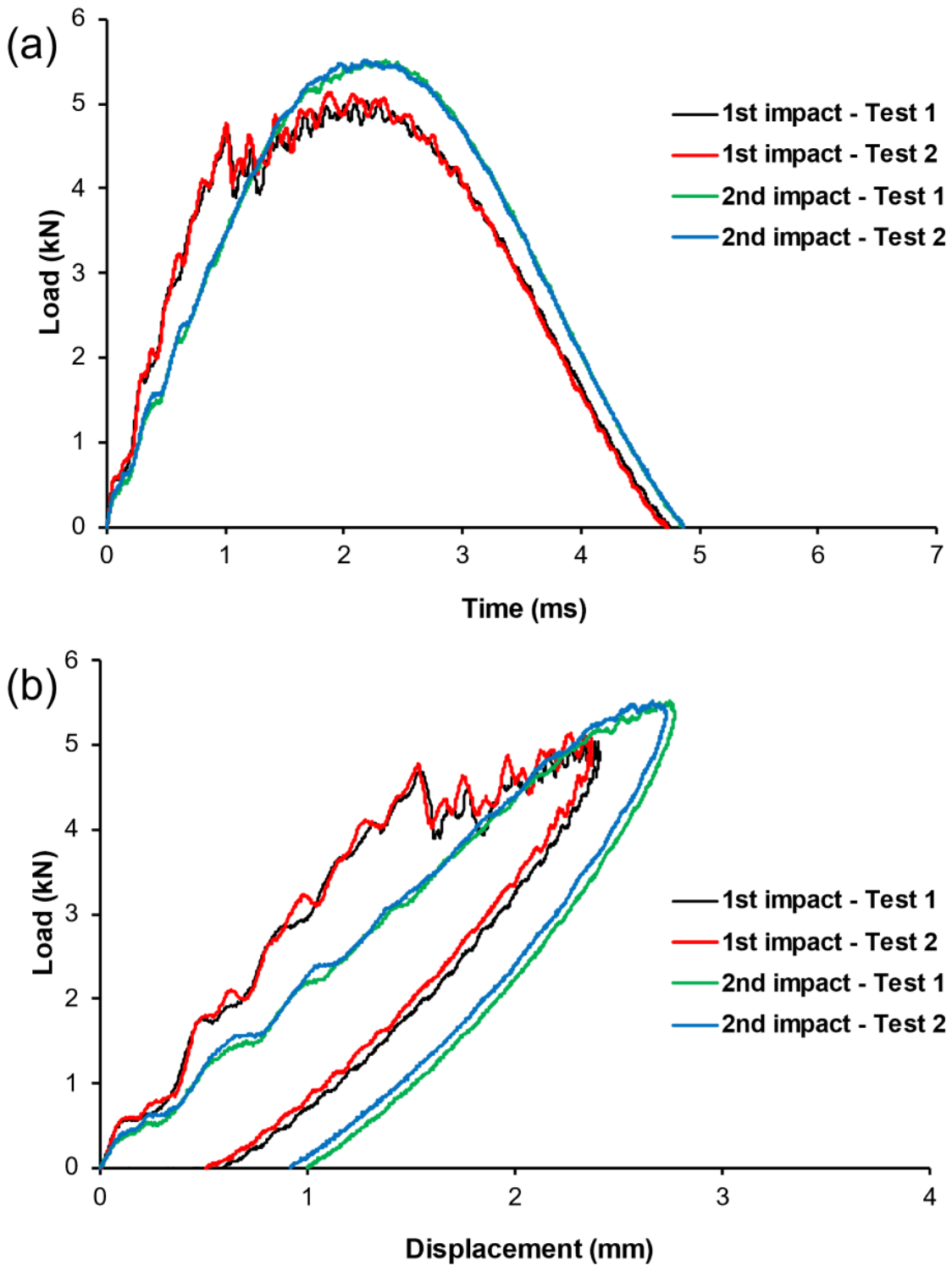


Figure 8-1: Graphs showing (a) load versus time and (b) load versus displacement traces for the two pristine panels after one and then two impacts at 7.5 J in the same location (adapted from [294]*).*

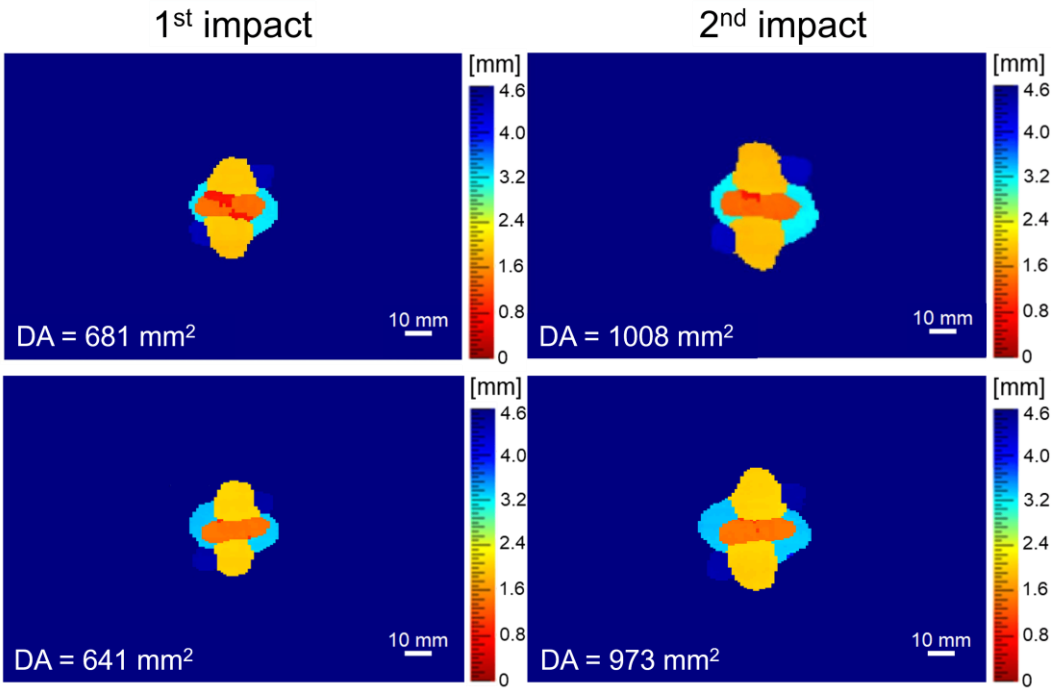


Figure 8-2: C-scan images of two pristine panels after one and two impacts at 7.5 J. The right-hand side scale indicates the location of the interlaminar delamination as a function of the depth through the thickness of the panel (0 to 4.6 mm), where the dark red colour represents the front (impacted) face and the dark blue colour represents the rear (non-impacted) face of the composite panel. The footprint of the delamination damage area (DA) detected is given in the bottom left-hand corner for each panel and was determined by counting the pixels which had a colour which was not dark blue. The bottom right of each damage map shows a 10 mm scale bar. The C-scans at the top were used in [294] *and below are the results from a repeat test.*

8.3.1.1.1 Patch only (No plug)

To investigate the performance of patch-only repairs, two different patch diameters of 55 and 65 mm were impacted at 7.5 J. The patches had a thickness of 2.3 mm, half of the thickness of the parent panel (4.6 mm). Figure 8-3 shows (a) load versus time and (b) load versus displacement traces for the two different diameters of patch-only repair, compared to a pristine panel. The two patch repairs demonstrate a similar impact response to each other, with damage initiation loads of approximately 1.7 kN at a time of approximately 0.6 ms. These are significantly lower than the damage initiation load shown by the pristine panel and they occur earlier in the impact.

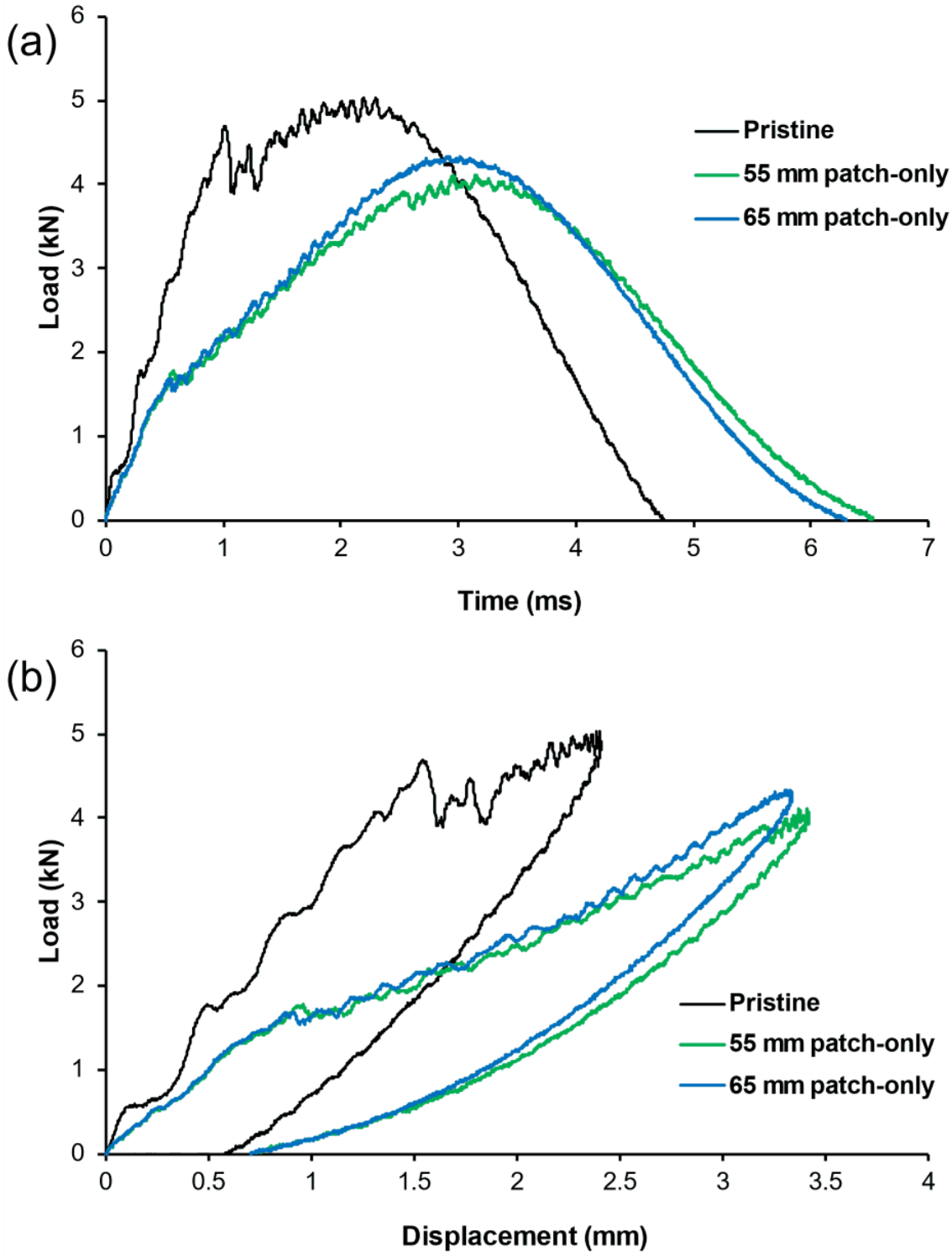


Figure 8-3: Graphs showing (a) load versus time and (b) load versus displacement traces for a 55 mm diameter patch-only repair, a 65 mm diameter patch-only repair and a pristine panel, all impacted at 7.5 J (adapted from [294]*).*

Figure 8-4 shows C-scan images of (a) the pristine panel, (b) the 55 mm diameter patch-only repair and (c) the 65 mm diameter patch-only repair after impact at 7.5 J. There is significantly more damage in the patch-only repaired cases compared to in the pristine panel. The delaminations in the patch extend slightly further than the white-dashed line, which indicates the location of the damage hole beneath the patch. This is more apparent in the 55 mm diameter patch than in the 65 mm diameter patch, where the delamination damage area for the 55 mm patch is 1365 mm^2 compared to 1252 mm^2 in the 65 mm patch. The patch area on the outside of the white-dashed line is bonded to the parent panel and this helps support the repair patch. The larger bonded area for the 65 mm patch slightly reduces the maximum displacement, leading to a reduction in delamination area. C-scans were also taken from the rear face of the parent panels after impact and these showed that no delamination damage had taken place in the parent panel.

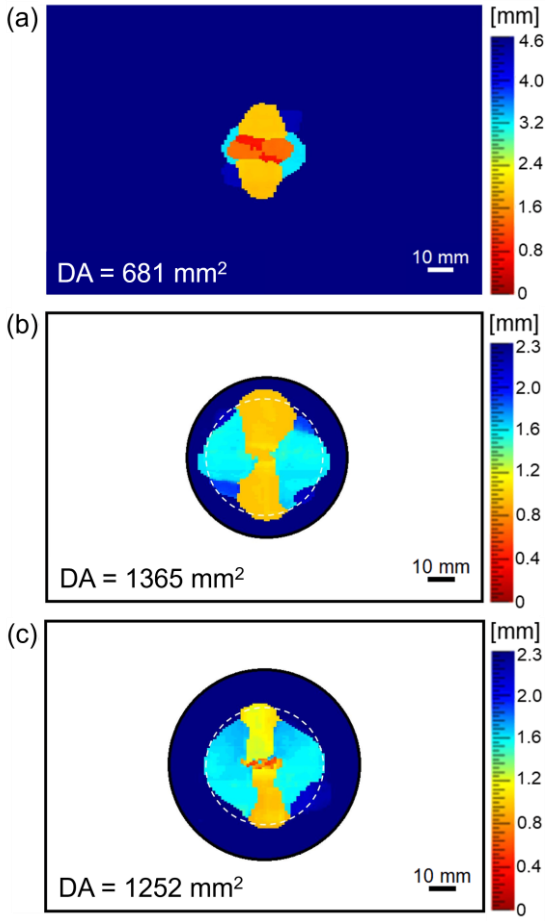


Figure 8-4: C-scan images of (a) the pristine panel, (b) the 55 mm diameter patch-only repair and (c) the 65 mm diameter patch-only repair after impact at 7.5 J, (adapted from [294]*).*

8.3.1.1.2 Patch + plug

To investigate the performance of patch + plug repairs, two different patch diameters of 55 and 65 mm with a plug beneath were impacted at 7.5 J. The patches had a thickness of 2.3 mm and the plugs had a thickness of 4.6 mm, the same thickness as the parent panel. Figure 8-5 shows (a) load versus time and (b) load versus displacement traces for the two different patch + plug repairs, compared to a pristine panel. The two patch + plug repairs demonstrate a similar impact response to each other, with the smaller patch showing a damage initiation load of approximately 7.5 kN and the larger patch showing a slightly higher initiation load of approximately 7.9 kN, both at a time of approximately 1.2 ms. These initiation loads are significantly higher than that of the pristine panel and both occur slightly later during the impact. These initiation loads are also the peak loads demonstrated by the patch + plug repairs during the impact. Patch + plug repairs demonstrate a more sudden drop in load following damage initiation than the pristine panels, which may be due to the overall increased stiffness of the panel (demonstrated by the higher initial gradient of the traces) or potentially due to damage occurring around the plug. Also, compared to the patch-only repairs, the maximum displacement during impact is reduced by almost half.

Figure 8-6 shows C-scan images of (a) the pristine panel, (b) the 55 mm diameter patch + plug repair and (c) the 65 mm diameter patch + plug repair after impact at 7.5 J. There is significantly less damage in the patch + plug repaired cases compared to in the pristine panel and in the patch-only repairs. Figure 8-7 shows C-scan images of the rear face of (a) the 55 mm patch + plug repair and (b) the 65 mm patch + plug repair after impact at 7.5 J. The C-scans show that delamination damage occurred in the plug but not in the parent panel. Although the delamination damage area in the plugs is larger than in the patch, it is still smaller than the damage area in the pristine panel. Clearly, addition of a plug is beneficial by reducing the delamination damage formed in the patch and increasing the load achieved before damage initiation. Without the plug present to support the patch, deformation occurs more easily in the patch and damage is initiated at a lower load. Furthermore, the lower maximum displacement shown by the patch + plug repair also contributes to the reduction in delamination damage area as the stresses in the plies are lower.

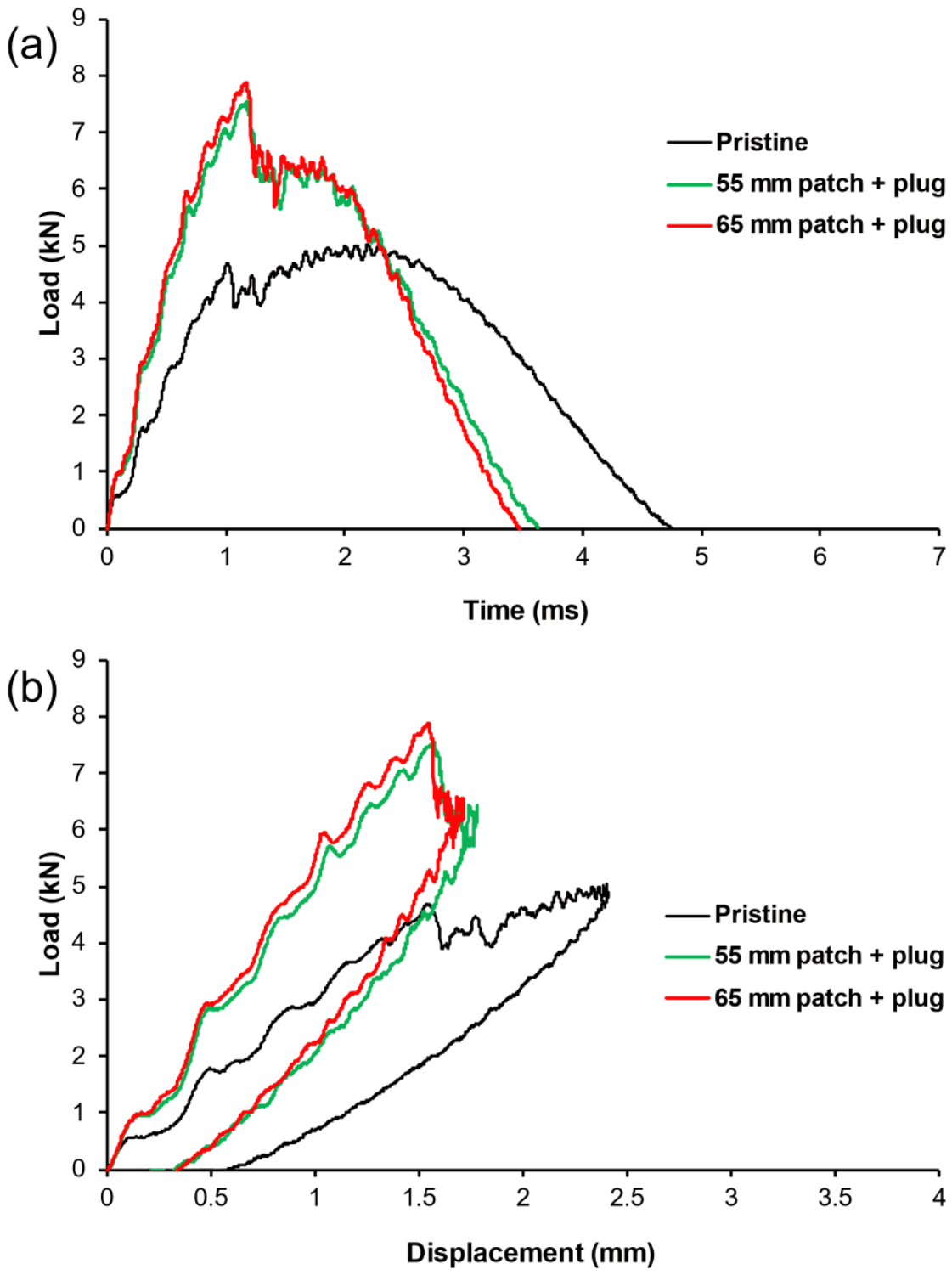


Figure 8-5: Graphs showing (a) load versus time and (b) load versus displacement traces for a 55 mm diameter patch + plug repair, a 65 mm diameter patch + plug repair and a pristine panel, all impacted at 7.5 J (adapted from [294]*).*

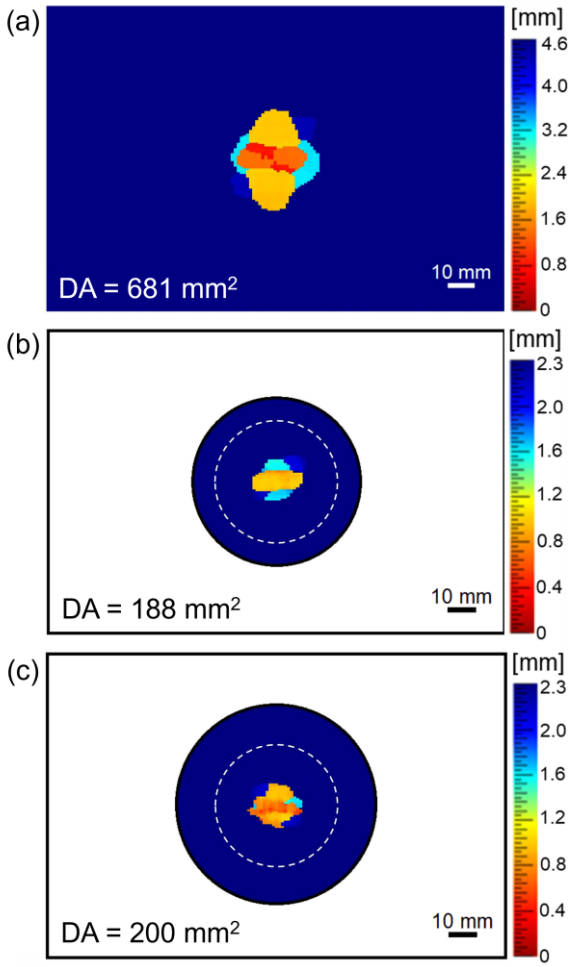


Figure 8-6: C-scan images of (a) the pristine panel, (b) the 55 mm diameter patch + plug repair and (c) the 65 mm diameter patch + plug repair. The C-scans were taken from the top (impacted) face and show the delamination damage in the patch, (adapted from [294]*).*

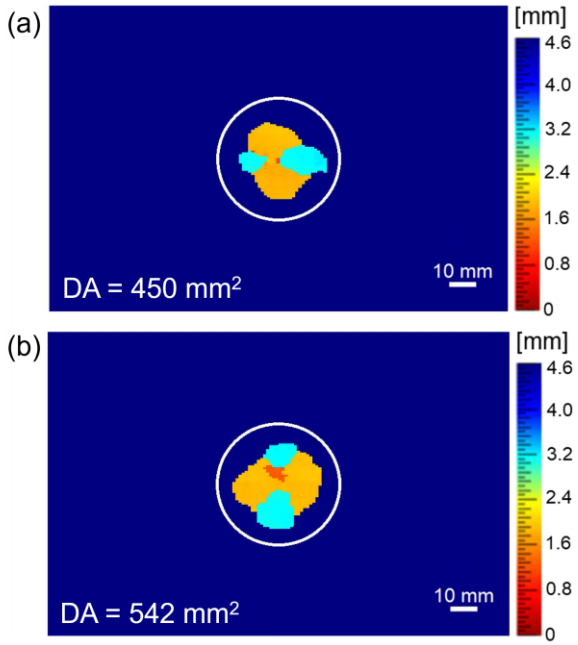


Figure 8-7: C-scan images of the plug and surrounding parent panel for (a) the 55 mm diameter patch + plug repair and (b) the 65 mm diameter patch + plug repair. The C-scans were taken from the rear (non-impacted) face and show the delamination damage in the plug, (adapted from [294]*).*

8.3.1.2 Effect of patch thickness

To investigate the effect of patch thickness, two different patch thicknesses of 2.3 and 4.6 mm were impacted at 7.5 J. Both patches had a diameter of 65 mm and neither repair had a plug inserted into the damage hole. Figure 8-8 shows (a) load versus time and (b) load versus displacement traces for the two repairs of different patch thickness, compared to a pristine panel. The thick patch-only repair exhibits a similarly shaped loading response to the pristine panel and a slightly higher stiffness. In contrast, the thin patch-only repair has a much less distinct initiation load drop, a lower stiffness and a peak load approximately 1 kN lower than the pristine panel and the thick patch-only repair. The thick patch-only repair demonstrates a damage initiation load of approximately 5.2 kN at a time of approximately 0.7 ms and the thin patch-only repair shows a lower initiation load of approximately 1.7 kN at a time of approximately 0.6 ms. The thin patch deforms more easily due to the reduced stiffness compared to the thicker patch and pristine panel and the localised strain gradients in the patch cause damage to initiate more readily at a lower initiation load. The thicker patch provides additional material

and the corresponding increase in stiffness raises the initiation load. This increase in stiffness may be responsible for the large load drop after damage initiation experienced by the thicker patch.

A repeat test was performed on another identical repair for each case at 7.5 J. Figure 8-9 shows C-scan images of (a) + (b) the thin patch-only repairs and (c) + (d) the thick patch-only repairs after impact at 7.5 J. In all cases, the delamination damage area extends slightly further than the white-dashed line, which indicates the location of the damage hole beneath the patch. Although the damage area in each repair is greater than that recorded in the pristine panel, the thick patch-only repair exhibits a damage area of around 300 mm^2 less than in the thin patch-only repair due to the increased stiffness. This is in contrast to the trend seen in Chapter 4 in which, when 2.3 mm and 4.6 mm pristine panels were impacted, the larger damage area was seen in the thicker panel. This difference may be due to the constraint provided by the geometry of the patch which affects the deformation and the resulting delamination damage. C-scans were also taken from the rear face of the parent panels after impact and these showed that no delamination damage had taken place in the parent panel.

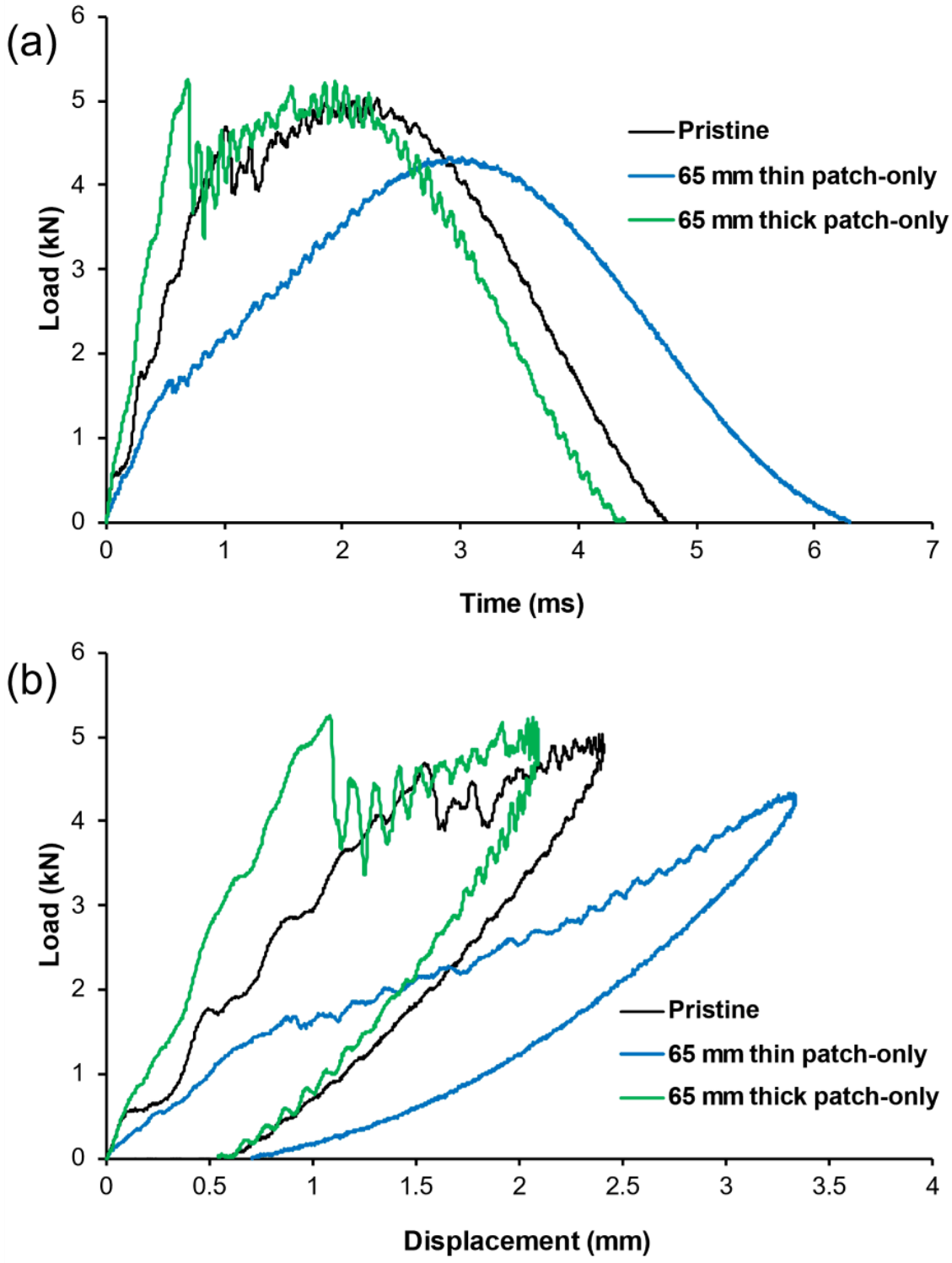


Figure 8-8: Graphs showing (a) load versus time and (b) load versus displacement traces for a 2.3 mm thick patch-only repair, a 4.6 mm thick patch-only repair and a pristine panel, all impacted at 7.5 J. All patches are 65 mm in diameter (adapted from [294]*).*

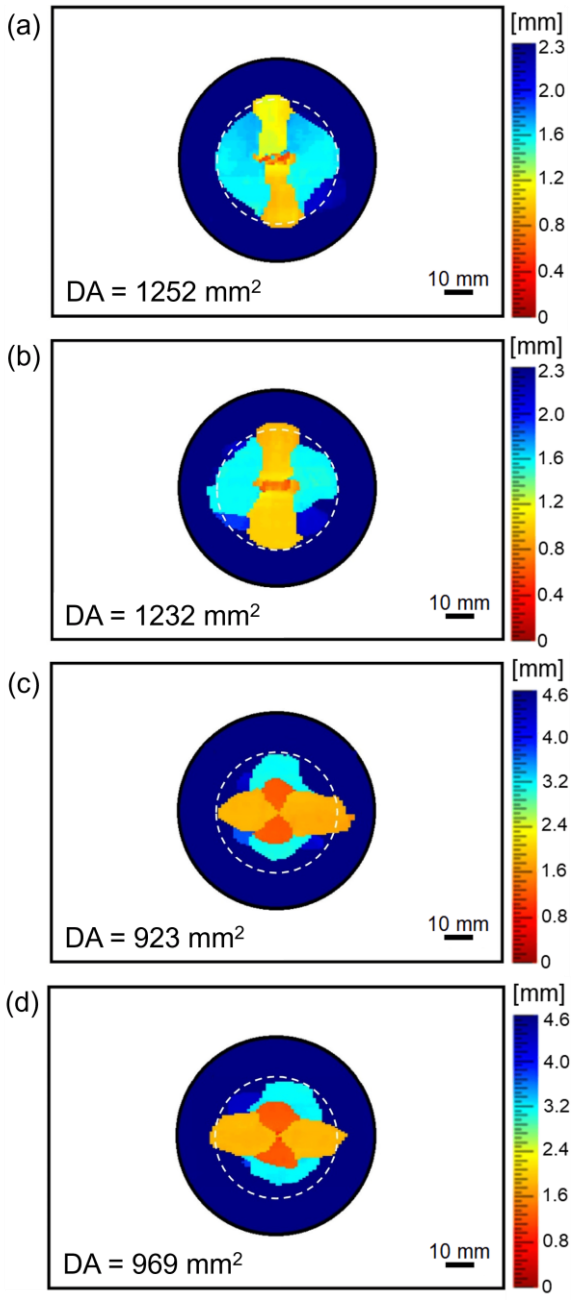


Figure 8-9: C-scan images of (a) + (b) the 2.3 mm thick patch-only repairs and (c) + (d) the 4.6 mm thick patch-only repairs after impact at 7.5 J. All patches are 65 mm in diameter, (adapted from [294]*).*

8.3.1.3 Summary

Figure 8-10 shows (a) load versus time and (b) load versus displacement traces for each of the repair cases tested in this chapter, as well as for a pristine panel. All tests have used an impact energy of 7.5 J. The thin patch-only repair exhibits a lower initiation load than the pristine panel and the thick patch-

only repair exhibits a higher initiation load than the pristine panel. The addition of a plug beneath the thin patch results in an even higher initiation load than in the thick patch-only repair.

Figure 8-11 shows C-scan images from (a) the pristine panel, (b) the 65 mm diameter thin patch-only repair, (c) the 65 mm diameter thick patch-only repair and (d) the 65 mm diameter patch + plug repair. The patch-only repairs exhibit a greater delamination damage area than the pristine panel, with the thin patch-only repair showing a larger damage area than the thick patch-only repair. The addition of a plug beneath the thin patch reduces the damage area in the patch dramatically to less than that seen in the pristine panel. Likewise, the damage formed in the plug is also less than that formed in the pristine panel. The total combined damage area in the patch and the plug is only slightly more than the damage area in the pristine panel. However, Figure 8-2 shows that if no repair is performed after an initial 7.5 J impact and the damaged panel is then impacted in the same location for a second time, the delamination damage area increases further by approximately 50%. Therefore, performing a patch + plug repair successfully reduces the amount of impact damage in the panel after a further impact.

Overall, the patch + plug repair exhibited the best impact performance and even showed a lower damage area than the pristine panel. Alternatively, using a thicker patch with no plug does give an improved peak load and lower maximum displacement compared to the pristine panel. Furthermore, this repair is easier and quicker to manufacture than the patch + plug repair as the initial damage would not necessarily need to be removed before the patch is adhered. However, replacing the damaged material with a plug would be beneficial.

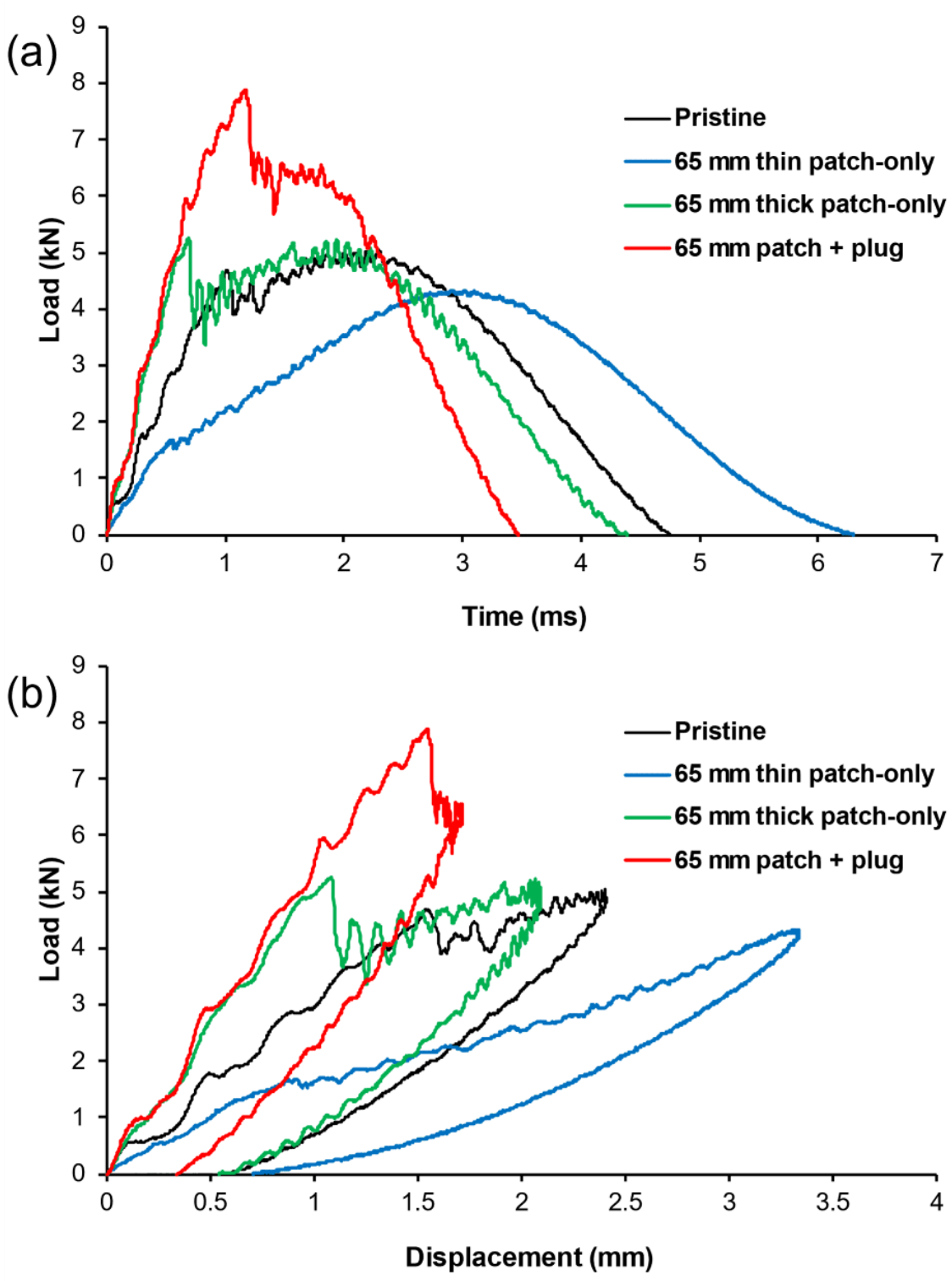


Figure 8-10: Graphs showing (a) load versus time and (b) load versus displacement traces for a 2.3 mm thick patch-only repair, a 4.6 mm thick patch-only repair, a (2.3 mm thick) patch + plug repair and a pristine panel, all impacted at 7.5 J. All patches are 65 mm in diameter (adapted from [294]*).*

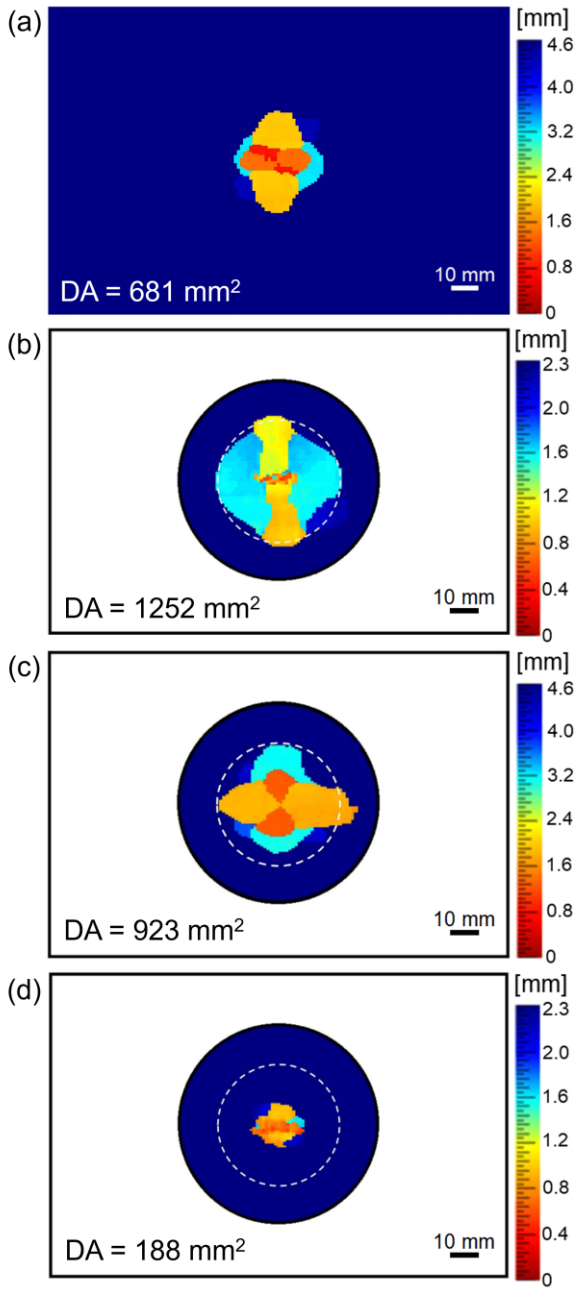


Figure 8-11: C-scan images from (a) the pristine panel, (b) the 65 mm diameter 2.3 mm thick patch-only repair, (c) the 65 mm diameter 4.6 mm thick patch-only repair and (d) the 65 mm diameter patch + plug repair, (adapted from [294]*).*

8.3.2 Indentation

Just as for the pristine panels, the repairs also showed a permanent indentation after impact. Figure 8-12 shows a sequence of high-speed images, taken at a frame rate of 10000 frames per second, which clearly indicate the indentation process on a 65 mm diameter patch + plug repair, with an inter-frame time of 0.7 ms. The first image (frame 1 - top left) is captured just before the impact event and the total contact time is approximately 3.5 ms, with the last image (frame 6 - bottom right) showing the start of the rebounding of the impactor. Figure 8-12 shows that the impactor indents the top surface of the patch and that there is a clear contact area for frames 2, 3, 4 and 5. Following the impact event, a residual permanent indentation, see Figure 8-13, is left due to plasticity, intralaminar and interlaminar damage.

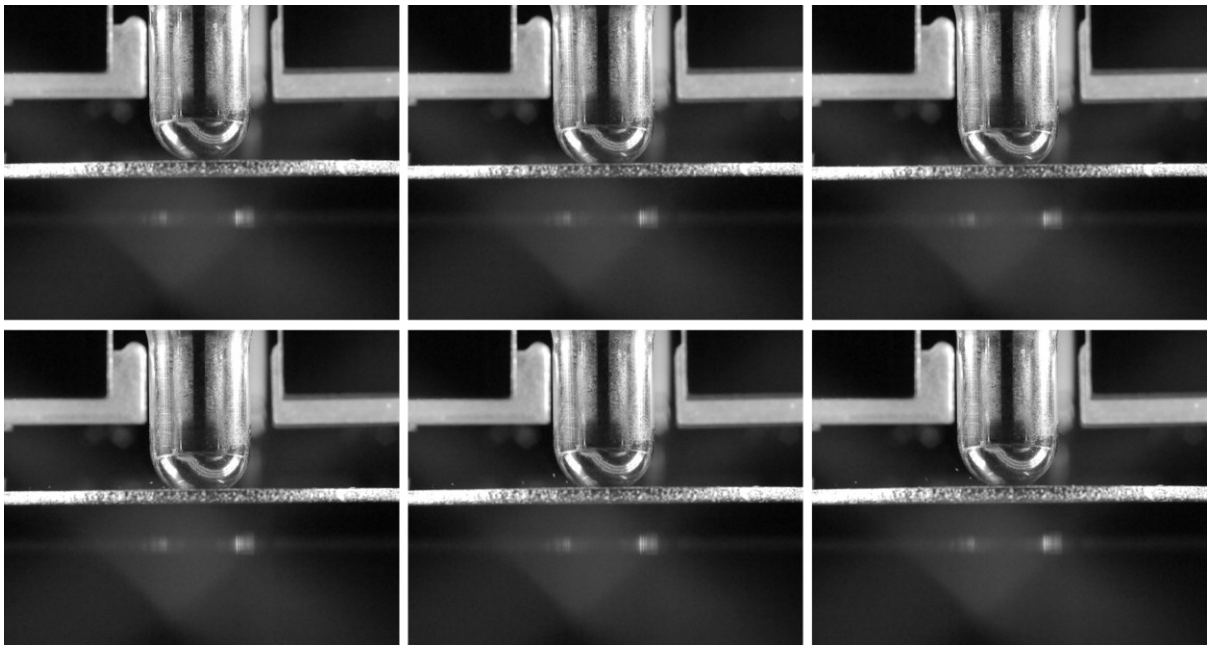


Figure 8-12: Series of high-speed photographic images showing the indentation process for an impact of 7.5 J on a 65 mm diameter patch + plug repair (inter-frame time is 0.7 ms). The first image (top left) is captured just after the impact event and total contact time is approximately 3.5 ms, with the last image (bottom right) showing the start of the rebounding of the impactor. The hemispherical stainless-steel impactor has a diameter of 16 mm.

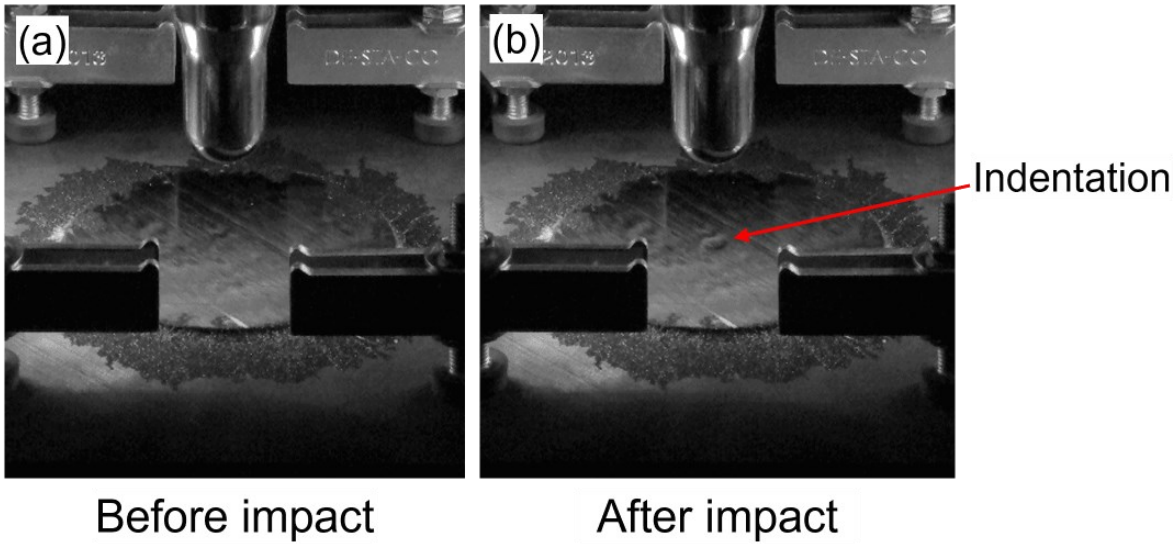


Figure 8-13: Images taken using a high-speed camera of a 65 mm diameter patch + plug repair (a) before impact and (b) after impact, showing an indentation in the centre of the patch.

Figure 8-14 shows a graph of indentation depth versus repair thickness for the three different varieties of repair tested. Clearly repair thickness has a very significant effect on the resulting indentation depth. The indentation depth decreases with an increased thickness of material beneath the impactor in an approximately linear relationship. The addition of a plug helps support the patch from underneath and reduce the deformation around the impactor during the impact event, inhibiting delamination propagation and leading to a lower indentation. The thick patch has a greater stiffness than the thin patch so also deforms less during the impact event, contributing to the slightly lower indentation. Note that the patch + plug repair with the lowest indentation depth did not show any delamination damage area.

These results are in disagreement with the results gained in Chapter 4 where similar indentation depths were measured for both 2.3 mm and 4.6 mm thick pristine panel. However, the variation in the indentation depths in that chapter is only slightly lower than the variation in indentation depths between the thin patch-only and thick patch-only seen in the current study. Also, from Figure 4-10(a), the indentation depth on a pristine panel for both thicknesses at 7.5 J is predicted to be around 0.12 mm – similar to the thick patch-only repair but slightly less than for the thin patch-only repair. The thicker patch provides more resistance beneath the impactor and increases the stiffness of material around the

impactor, allowing less deformation and therefore less plastic behaviour and delamination formation to take place. Hence, a lower indentation depth is produced in the 4.6 mm thick patch. Furthermore, addition of a plug causes further resistance due to the even greater thickness of CF/Epoxy (and adhesive) resisting deformation from the impactor, significantly reducing indentation depth. The change in geometry is also relevant because the CF/Epoxy parent panel deforms similarly for each type of repair, with the local deformation of the repair causing the majority of the differences in impact response. A patch will deform differently to a pristine panel, therefore the indentation depth in a repaired panel will be different to that in a pristine panel.

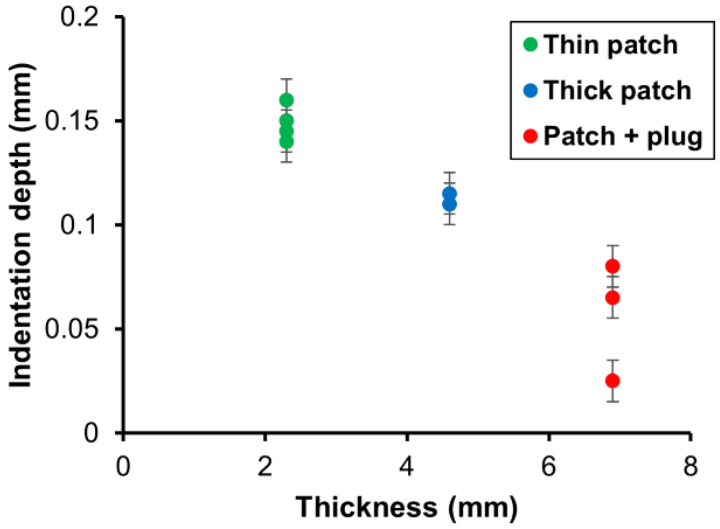


Figure 8-14: The indentation depth versus repair thickness for the thin patch-only, thick patch-only and (thin) patch + plug repaired CF/Epoxy composite panels after impact at 7.5 J.

Figure 8-15 shows a graph of indentation depth versus the delamination damage area within only the patch for the three varieties of repair tested. Clearly a larger indentation depth indicates a larger delamination damage area in the patch. This agrees with the trend presented in Chapter 4 for pristine panels. This may be explained by a larger indentation depth being formed by a greater local deformation of the repair. The larger localised strain gradients cause a greater severity of intralaminar damage, leading to a greater area of delaminations being produced. The same trend is demonstrated in Figure 8-16 which shows the indentation depth versus the combined delamination damage area in both the patch and the plug for the three varieties of repair tested. Note, for patch-only repairs the combined

damage area is the same as the damage area in the patch. Also, Figure 8-15 and Figure 8-16 reveal that an indentation may form in a patch + plug repair when no delamination damage is present. This suggests that indentation damage initiates during the impact event prior to the formation of any delamination damage. Again, this supports the conclusions gained in Chapter 4.

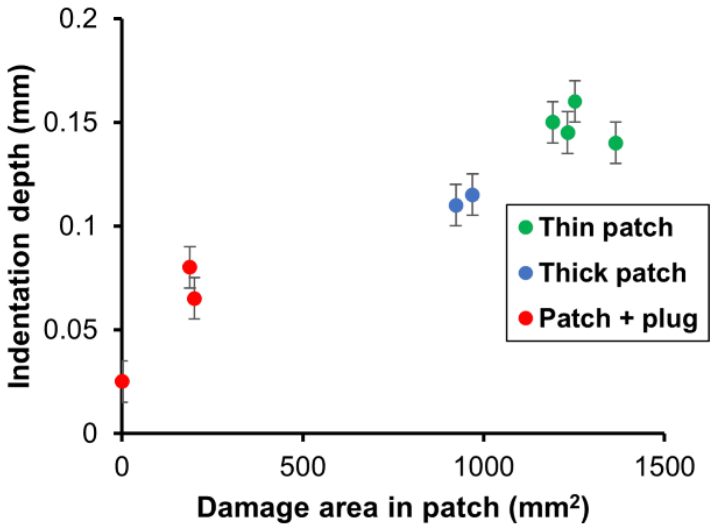


Figure 8-15: The indentation depth versus the delamination damage area within only the patch for the thin patch-only, thick patch-only and patch + plug repaired CF/Epoxy composite panels after impact at 7.5 J.

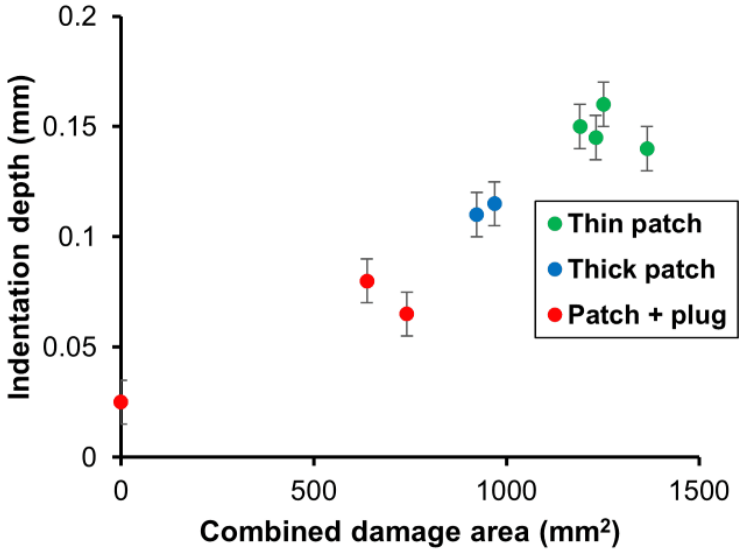


Figure 8-16: The indentation depth versus the delamination damage area within the patch (for the patch-only repairs) or within the patch and the plug combined (for the patch + plug repairs) for the thin patch-only, thick patch-only and patch + plug repaired CF/Epoxy composite panels after impact at 7.5 J.

One patch + plug repair impacted at 7.5 J showed no delamination damage in either the 65 mm diameter patch or in the plug and only showed an indentation depth of around 20 μm. This is in contrast to the two other patch + plug repairs, one with a 55 mm diameter patch and the other with a 65 mm diameter patch, which showed combined damage areas of 638 mm^2 and 742 mm^2 and indentation depths of 80 μm and 70 μm, respectively. The different behaviour of this delamination-free 65 mm diameter patch + plug repair is investigated using Figure 8-17, which shows (a) load versus time and (b) load versus displacement traces for the three patch + plug repairs, compared to a pristine panel. The two repairs which showed damage had damage initiation loads of approximately 7.6 kN (for the 55 mm diameter patch) and 7.9 kN (for the 65 mm diameter patch). In contrast, the undamaged repair reached a slightly higher peak load of approximately 8.2 kN and a higher displacement without showing a load drop. This peak load is less than 5% higher than the damage initiation load of the other patch + plug repairs. Also, both 65 mm diameter repairs acted similarly up until the onset of damage in the damaged repair. Therefore, it is reasonable to expect that the undamaged repair would indeed have shown damage had it reached only a slightly higher load (i.e. been impacted at only a slightly higher energy).

The reason for the two 65 mm diameter repairs not behaving identically is likely due to small manufacturing differences in the repairs. The repair which exhibited no damage was manufactured as part of a second batch of repairs, whereas the other patch + plug repairs were made as part of the first batch. Therefore, it is likely that a different machinist or a slightly different set-up was used during repair manufacture. This could have led to the diameter of the machined plug varying and therefore more or less adhesive being present around the edge of the hole in one repair compared to the other. This would have led to changes in the repair strength and damage initiation load.

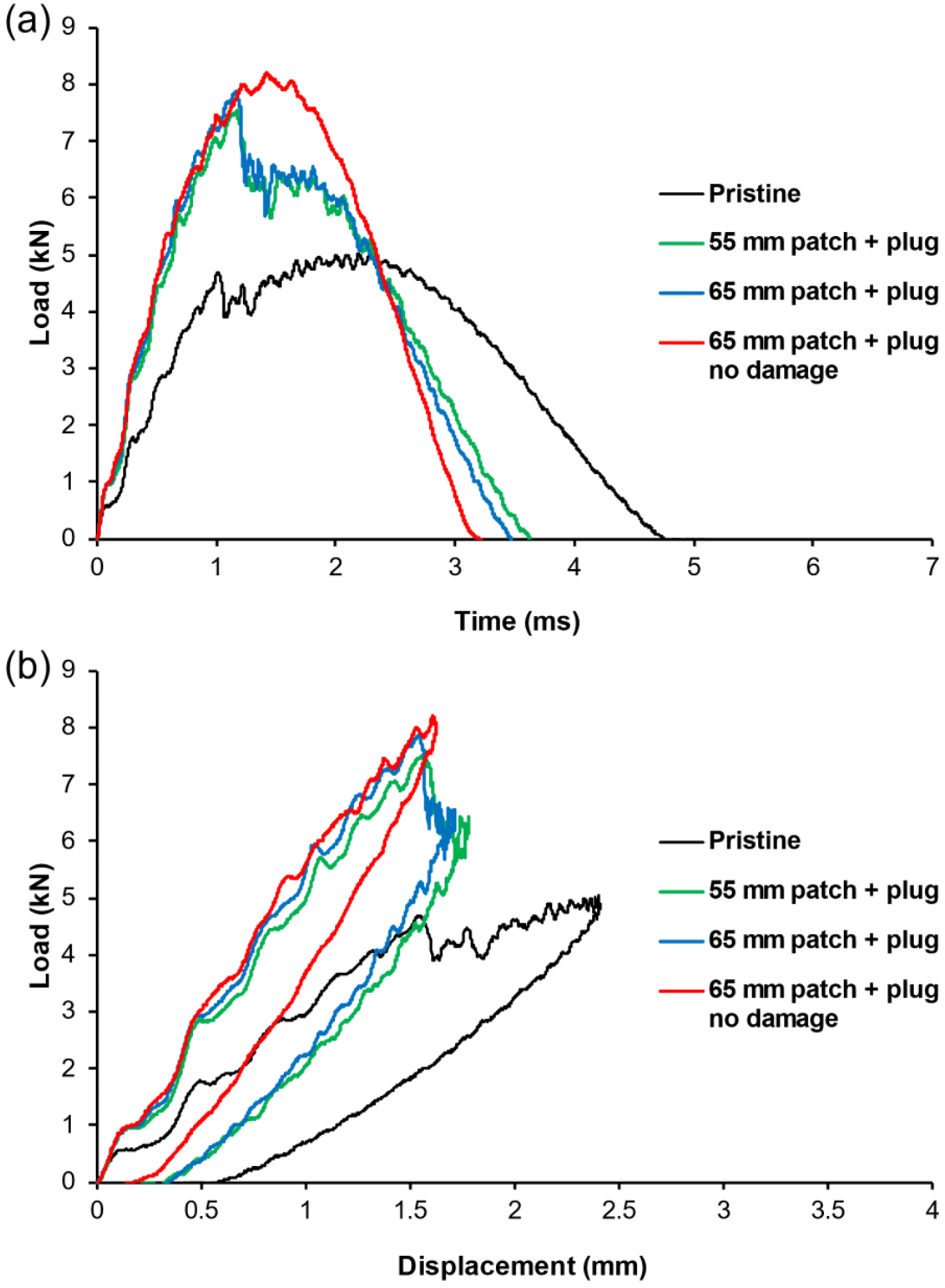


Figure 8-17: Graphs showing (a) load versus time and (b) load versus displacement traces for a 55 mm diameter patch + plug repair and a 65 mm diameter patch + plug repair which both showed delamination damage, a 65 mm diameter patch + plug repair which showed no delamination damage and a pristine panel, all impacted at 7.5 J (adapted from [294]*).*

8.3.3 Microscopy

Both optical microscopy and SEM were used to investigate the internal damage in the impacted repaired panels. A comparison of the images gained from the two techniques follows, along with analysis of the damage within the repairs which were viewed under the microscopes.

8.3.3.1 Patch-only repair versus patch + plug repair

Figure 8-18 shows a diagram of the area viewed under the microscopes with reference to the rest of the panel cross-section for (a) the patch-only and (b) the patch + plug repairs. Figure 8-19 shows optical microscope images of (a) a patch-only repair and (b) a patch + plug repair after impact at 7.5 J. Both images are at approximately the same scale (i.e. the 5 mm scale bars are approximately the same size). The notches in the centre of the patch and the plug were made during manufacture of the repair to aid with patch and plug orientation. This was only done for the first batch of repairs and for later batches any notch on the surface was removed. The full delamination diameters in the patches shown in the microscopy images are approximately the same as those shown on the C-scans in Figure 8-4 and Figure 8-6. As described in Section 8.3.1.1.2, the delamination damage within the patch is significantly lower in the patch + plug repair compared to in the patch-only repair, hence the length of delaminations seen in the microscope images is also reduced. Figure 8-19 also highlights that the delaminations are slightly wider in the patch-only repair.

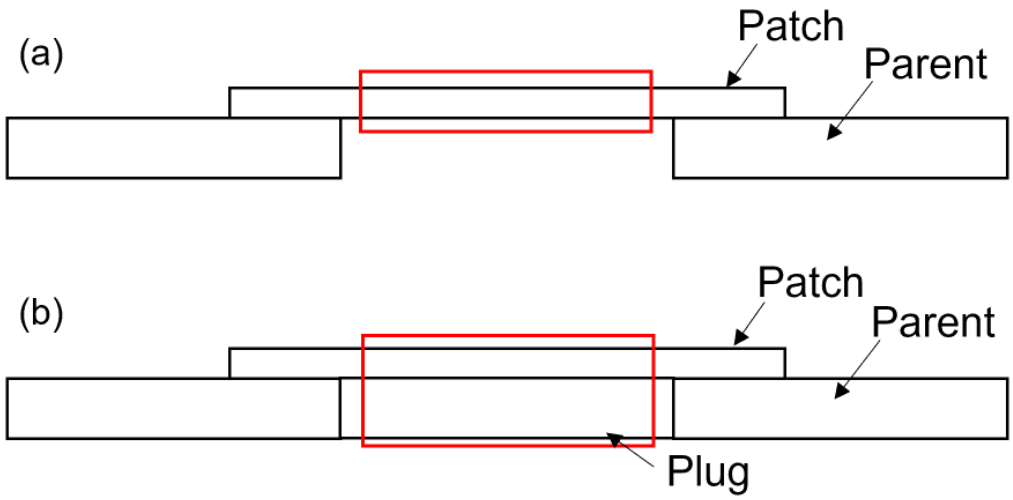


Figure 8-18: Diagram showing (a) a patch-only repair and (b) a patch + plug repair and the area viewed under the microscope in each case.

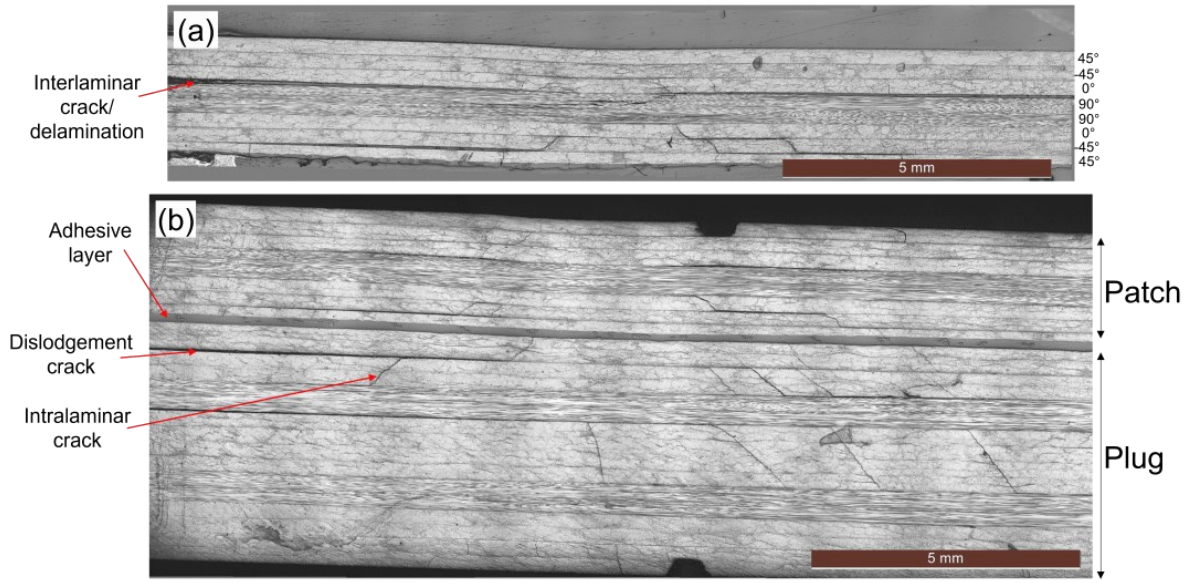


Figure 8-19: Optical microscope images of (a) a patch-only repair and (b) a patch + plug repair after impact at 7.5 J. Both images are at the same scale (scale bar is 5 mm for both).

On the other hand, the level of intralaminar cracking in the patch is similar for the two repairs. In the patch + plug repair a cone of intralaminar cracks can be seen extending through the entire thickness of the patch and the plug. Interestingly, as these intralaminar cracks spread further into the repair, fewer delaminations appear to be initiated by them. The lack of delaminations near the rear surface of the repair plug can also be seen on the C-scans, see Figure 8-7, in which the final

delamination (coloured orange) occurs around 1.7 mm from the rear surface. This is just visible on the right-hand side of Figure 8-19, six plies from the bottom. Deformation and cracking in the adhesive layer surrounding the circumference of the repair plug may mean that the rear section of the plug isn't deformed as much and therefore under as much stress, leading to the lower density of cracking and lack of delaminations.

However, it is important to note that the plug shown in Figure 8-19(b) did show a very small dislodgement upon impact, so isn't the same repair as the one shown in the C-scans, load versus time and load versus displacement traces above. The patch + plug repairs which didn't show dislodgement were not sectioned as they will be used for future compression-after-impact (CAI) testing. The slight dislodgement meant the panel could not be C-scanned from the rear side due to the protrusion of the plug. However, the C-scan of the patch in this repair was comparable to the C-scan of the same repair when no dislodgement took place, see Figure 8-6. A large dislodgement crack (a delamination which has been propagated and widened by the dislodgement) can be seen two plies beneath the adhesive layer on the left-hand side of the repair plug, along with another widened delamination crack four plies further down. The dislodgement has reduced the intralaminar cracking beneath the dislodgement cracks in the plug on the left-hand side (compared to the right-hand side). This has therefore prevented delaminations forming nearer the bottom surface of the patch. If the plug was dislodged before the intralaminar cracks reached the lower ply boundaries, bending of the plug would be lower so it would be more difficult for delaminations to initiate due to the lower stresses between plies. Therefore, dislodgement doesn't appear to affect the damage level within the patch, however it does affect the damage level on the side of the plug where dislodgement occurs.

Although plug dislodgement absorbs a significant amount of the impact energy and prevents intralaminar cracking and delaminations forming in certain parts of the plug, it increases the delamination length in other parts (i.e. dislodgement cracks). It is likely that this dislodgement severely weakens the repair as the plug no longer provides the same support to the patch. If the dislodged repair was subjected to another subsequent impact, the patch + plug repair would likely behave very differently. A much larger delamination damage area would probably be seen in the patch due to the reduced support from underneath.

Another interesting point to consider is how a patch + plug repair would behave if the impact was not in the centre of the patch. This would cause increased deformation on one side of the repair, increasing the chances of dislodgement occurring on that side. To make a patch + plug repair more resistant to dislodgement, another patch could be added on the rear side of the panel, effectively creating a double-sided patch repair with a plug inside.

8.3.3.2 Optical microscopy versus Scanning electron microscopy (SEM)

Figure 8-20 shows (a) an optical microscope and (b) an SEM image of a patch-only repair after impact at 7.5 J. Note, these images are not at the same scale. Software on the optical microscope makes it fairly easy to stitch images together, allowing one continuous image of a long thin sample to be produced. However, this was not possible using the SEM. Furthermore, the damage (both intralaminar and interlaminar) is very clear in the optical microscope image where it is visible as a dark grey or black line. In contrast, in the SEM image damage is visible as bright lines in some cases, but in other cases the damage can hardly be seen. The bright round patches of material on the surface seen in the SEM image are likely formed of silver conductive paint which has been transferred onto the surface of the sample during preparation.

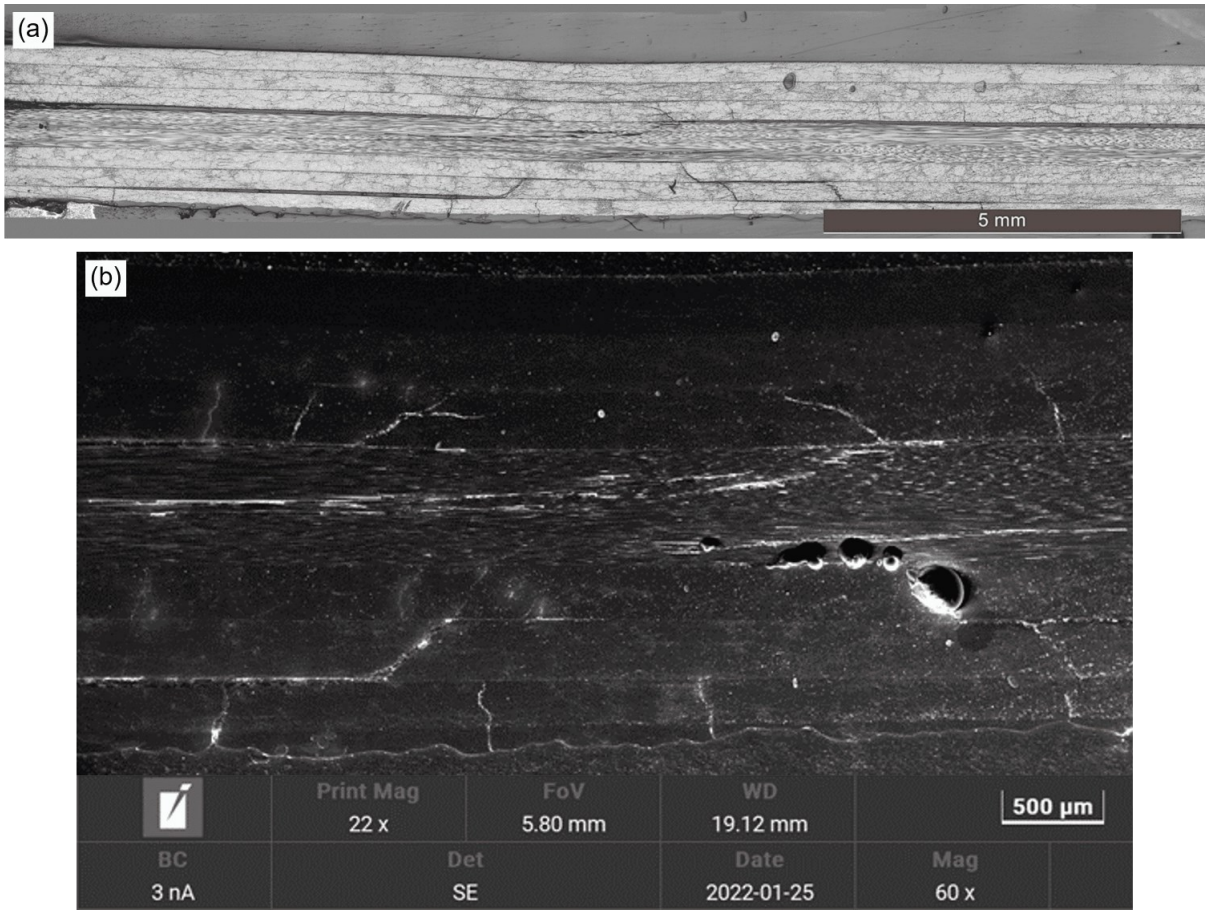


Figure 8-20: (a) Optical microscope and (b) SEM images of a patch-only repair after impact at 7.5 J. Note, these images are not at the same scale (optical scale bar is 5 mm and SEM scale bar is 500 µm).

Figure 8-21 shows (a) an optical microscope and (b) an SEM image of a patch + plug repair after impact at 7.5 J. Both images are at approximately the same scale. Similarly, Figure 8-22 shows the same repair with images taken at a greater magnification on both microscopes to provide greater detail of the intralaminar and interlaminar (i.e. delamination) damage within the repair. Note, these images are not at the same scale. The optical microscope images provide excellent quality images of both intralaminar and interlaminar damage. Although the SEM image in Figure 8-21(b) does highlight most of the interlaminar and intralaminar damage, the intralaminar cracks are not as clear and the overall level of detail is not as high at this magnification as for the optical microscope. Furthermore, in Figure 8-22(b) it is very difficult to make out the intralaminar cracks and delaminations.

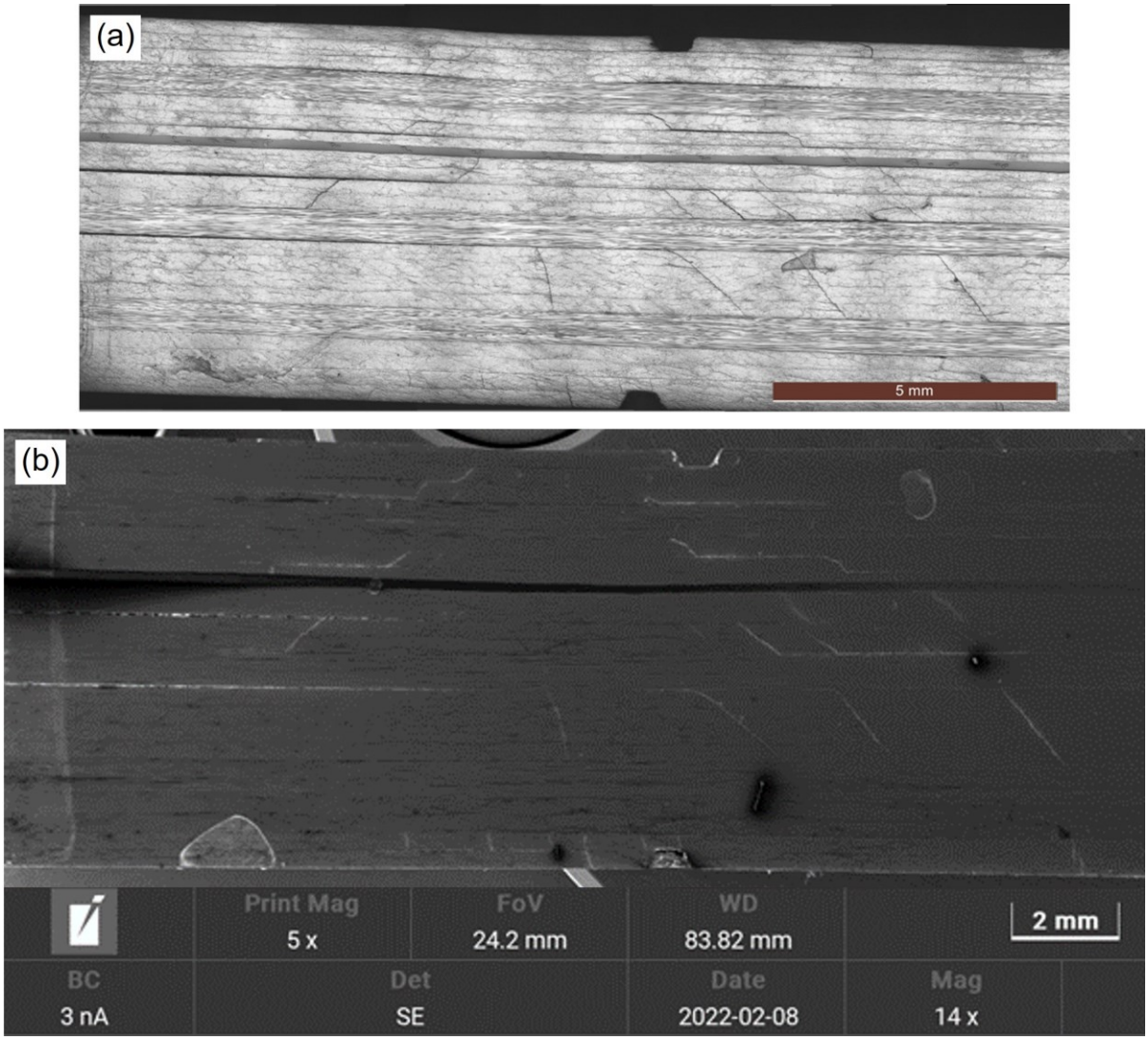


Figure 8-21: (a) Optical microscope and (b) SEM images of a patch + plug repair after impact at 7.5 J. Both images are at approximately the same scale (optical scale bar is 5 mm and SEM scale bar is 2 mm).

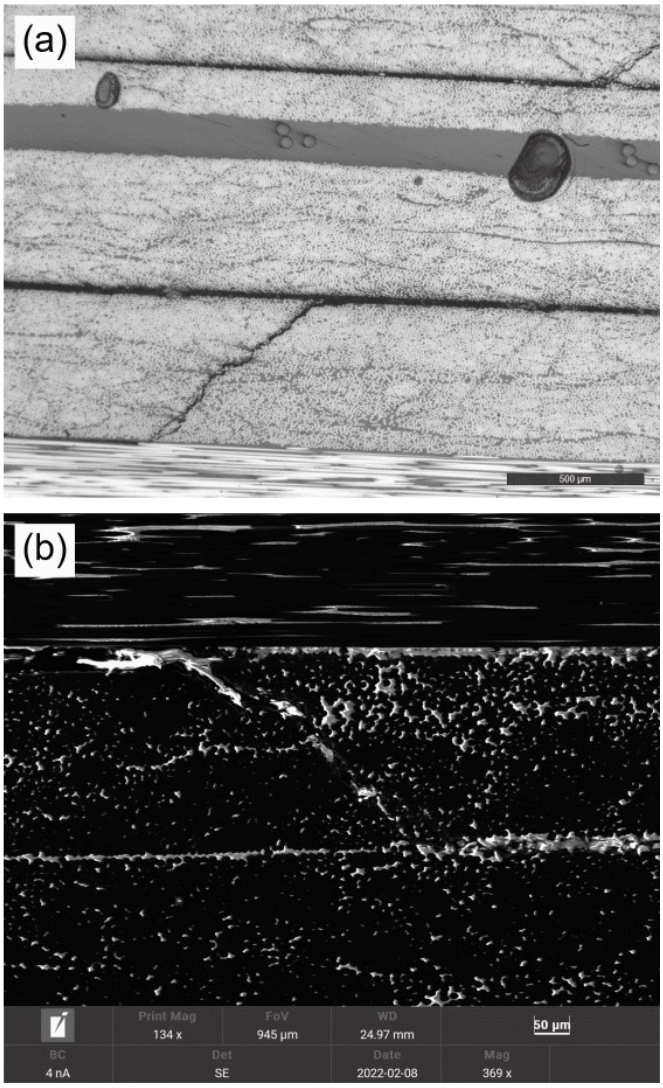


Figure 8-22: (a) Optical microscope and (b) SEM images of a patch + plug repair after impact at 7.5 J. Note, these images are not at the same scale (optical scale bar is 500 µm and SEM scale bar is 50 µm).

Figure 8-23 shows (a) an optical microscope and (b) an SEM image of intralaminar damage in a patch-only repair. The regions near the start of the intralaminar cracks are viewed at a greater magnification on the right-hand side of the figure. The optical microscope images provide a good contrast between fibres and matrix which allows easy identification of the types of intralaminar damage present (i.e. both matrix cracking and fibre fracture). Although the SEM images show an intralaminar matrix crack, it is difficult to make out both the damage and the rest of the material and therefore distinguish between fibres and matrix. However, Figure 8-24 shows another SEM image of a patch +

plug repair at a much greater magnification. This shows fibre fracture in great detail and some matrix damage can also be seen.

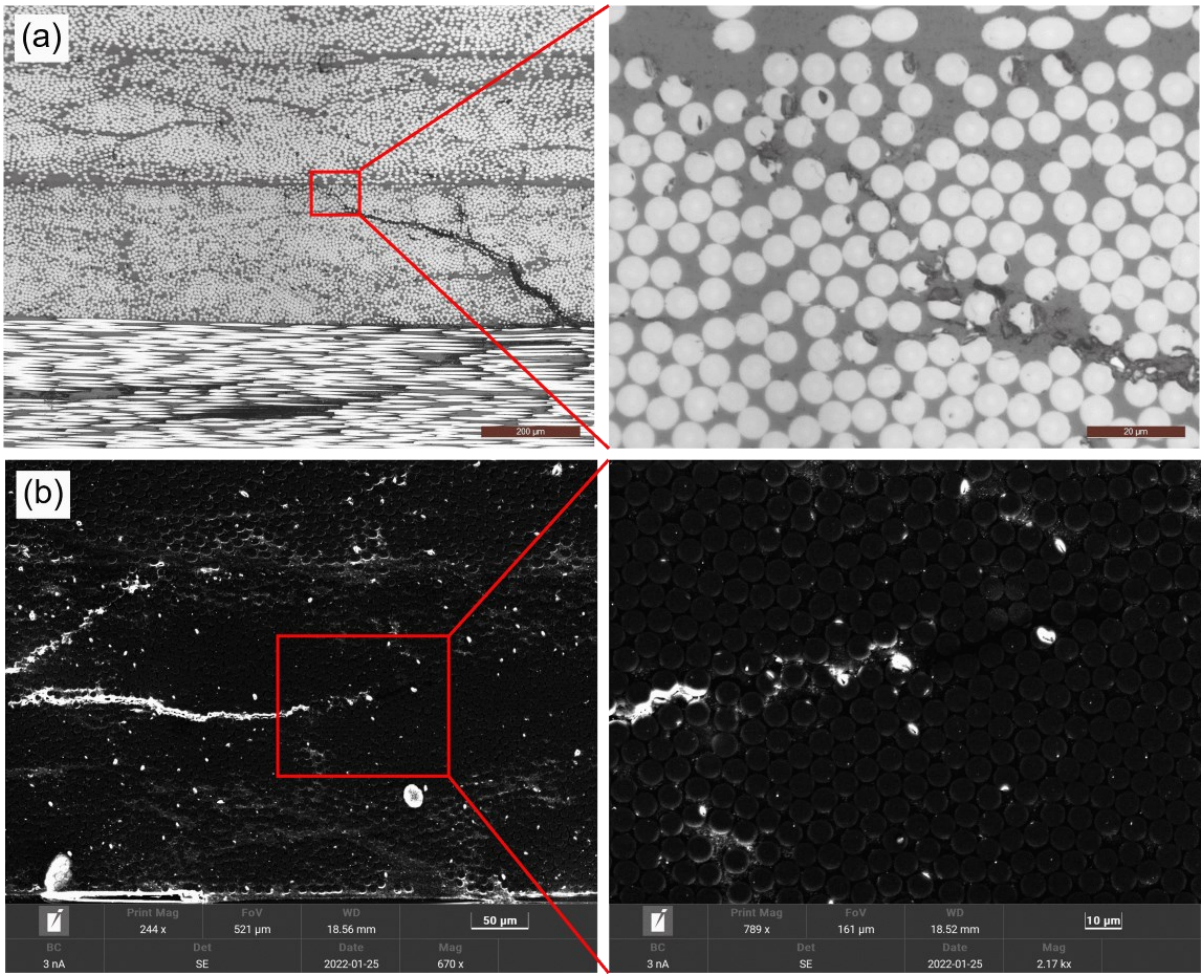


Figure 8-23: (a) Optical microscope and (b) SEM images of intralaminar damage in a patch-only repair. Note, these images are not at the same scale (optical scale bars are 200 µm and 20 um and SEM scale bars are 50 µm and 10 µm).

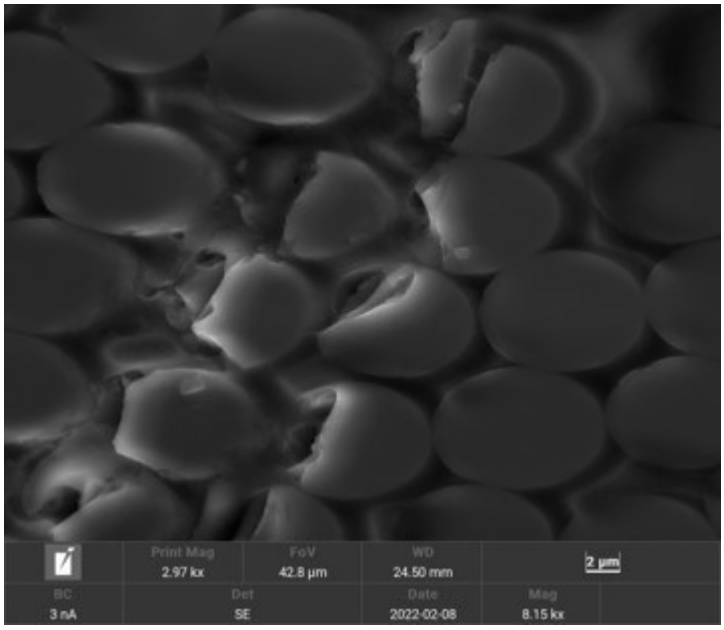


Figure 8-24: SEM image of fibre fracture and matrix damage in a patch + plug repair after impact at 7.5 J. (Scale bar is 2 µm).

In summary, SEM is useful for providing good quality highly detailed images of fibre fracture and other damage at very large magnifications, see Figure 8-24, and can provide more detailed images than the optical microscope. This is particularly useful as it is difficult to adjust the focus of the optical microscope correctly across the entire view area at high magnifications if the sample isn't perfectly flat. However, investigating the damage at such high magnifications isn't necessary for the current research. It has been shown by comparing the images from the two microscopy techniques at the magnifications needed to view intralaminar and interlaminar (i.e. delamination) damage in CF/Epoxy that the optical microscope provides more appropriate images. Therefore, optical microscopy was used in the earlier chapters in this thesis. Note, the results presented in this chapter were achieved prior to the results from the preceding chapters.

8.4 Summary

The present study has shown that an impact of 7.5 J on a pristine panel creates a delamination diameter of approximately 40 mm. Therefore, for the repair panels tested, a damage hole of diameter 40 mm was used beneath the patches. If the damaged pristine panel is impacted in the same location a second

time, the delamination damage area increases by approximately 50%. However, if the damaged panel is repaired using either a thick patch-only or patch + plug repair, the overall delamination damage footprint sustained after a subsequent impact is lower.

2.3 mm thick patch-only repairs show a much larger damage area than the pristine panel and a much lower damage initiation load, with a 55 mm diameter patch showing a higher delamination area than a 65 mm diameter patch. Addition of a plug dramatically reduces the damage area in the patch and increases the damage initiation load. Damage forms in the plug but this damage is also less than in the pristine panel. A 4.6 mm thick patch-only repair demonstrates a smaller damage area compared to the 2.3 mm thick patch-only repair while also increasing the damage initiation load.

Indentation depth reduces with increasing thickness of the repair and a larger indentation depth corresponds to a larger delamination damage area. Optical microscope and SEM images showed intralaminar and interlaminar (i.e. delamination) damage within the repairs, however optical microscopy images were better for viewing these types of damage across a whole cross-section of CF/Epoxy. Therefore, optical microscopy was chosen for use during future research due to the relative ease of use, slightly less time-consuming sample preparation and, most importantly, the more appropriate images for viewing damage in this material.

Therefore, the present study has identified that a patch + plug repair will provide the highest impact resistance of the tested repair types. However, if ease of manufacture is a priority, the thick patch-only repair also provides a reduction in delamination damage area after impact.

Chapter 9 Conclusions

9.1 Introduction

From the research presented in this thesis, a number of conclusions can be drawn regarding the performance of pristine and repaired carbon fibre-reinforced polymer (CFRP) panels under low-velocity impact conditions. This section highlights and summarises the main outcomes from each chapter.

9.2 Study on the internal and external damage formed in CFRP thermoset laminates under low-velocity impact conditions

This section comes from the following paper: 'The relationship between the extent of indentation and impact damage in carbon-fibre reinforced-plastic composites after a low-velocity impact' [87].

The present study has shown that:

- For composite panels of 4.6 mm in thickness there is a larger delamination damage area observed than for a panel of 2.3 mm in thickness, when impacted at the same impact energy. This is due to the delamination and intralaminar damage spreading out like a cone from the impact site. It is suggested that the matrix cracking and other types of intralaminar damage in the ply are strongly linked to the shear and tensile loading of the ply interface beneath the ply, leading to interlaminar, i.e. delamination, damage occurring at this lower ply interface. For these reasons, with a thicker panel the extent of the delamination increases away from the impacted face, with a larger extent of the delaminations near the rear face.
- The deformation that results from any indentation in the surface of the composite panel caused by the impactor exhibits both viscoelastic and plastic behaviour. The reduction in the depth of the indentation that occurs over time due to relaxation of the composite is minimal, i.e. no more

than 20 μm, and after 48 hours a steady-state permanent indentation is recorded. These are the depth values used in the present section for subsequent analysis.

- This indentation damage is also accompanied by intralaminar damage, involving matrix cracking within the ply and fibre debonding and fracture, and interlaminar damage, i.e. delaminations, between the differently orientated plies.
- The indentation depth has been shown to be related to the delamination damage area for the low-velocity impact energies of 2 to 20 J by a second-order polynomial relationship. This arises because the indentation depth has a second-order polynomial relationship with the impact energy but the delamination footprint area has a linear relationship with the impact energy. The indentation occurs in the impact test at a slightly lower impact energy than that required for interlaminar delamination damage to initiate and develop. At higher impact energies there is a saturation effect where it becomes more difficult for the indentation to increase in depth and hence the nonlinear second-order relationship is observed. These observations strongly suggest that the indentation damage is initiated before any delamination damage develops.
- For the 2.3 and 4.6 mm thick composite panels, there is a unique ‘master’ relationship between the indentation depth and the normalised interlaminar delamination damage area, i.e. the damage area divided by the panel thickness, for impact energies up to 15 J.
- Measuring the indentation depth has the potential to be used as a quick and cheap alternative to employing expensive ultrasonic C-scan or X-ray Computed Tomography (CT) equipment for estimating the extent of internal interlaminar delamination damage.

9.3 Study on the internal and external damage formed in CFRP thermoset laminates after multiple impacts in the same location

The present study has shown that:

- Subsequent impacts in the same location on 2.3 mm and 4.6 mm thick composite panels increase the delamination damage area in the panel by propagating existing delaminations. A lack of load drops on load versus time and load versus displacement graphs indicates that new damage is not usually formed. Similarly, optical microscopy suggests that the conical intralaminar cracking zone is created only during the first impact and is hardly affected by subsequent impacts. Instead, delaminations are lengthened and widened.
- The 4.6 mm panels exhibit a greater delamination area than the 2.3 mm panels for the same impact scenario and the difference in delamination area between the two thicknesses increases with both impact energy and number of subsequent impacts. This is due to the cone-shaped damage zone through the thickness of the panel.
- A greater increase in damage area is observed for a second impact compared to a third impact. Although lack of space for delamination damage to propagate on the panel (due to the size of the panel) may be a factor, the reduction in bending stiffness caused by the presence of intralaminar and delamination damage allows a greater proportion of the impact energy to be stored through elastic deformation by the panel during the impact. This means less energy is available to propagate the delaminations.
- After an initial impact, the indentation depth continues to slightly increase for each subsequent impact due to viscoelastic and plastic behaviour around the impactor and delamination propagation.
- As for single impacts, the indentation depth continues to follow a second-order polynomial relationship with delamination damage area for the tested low-velocity impact energies of 2 to 20 J. Again, this arises because the indentation depth continues to exhibit a second-order polynomial relationship with the impact energy but the delamination damage area still exhibits a linear relationship with the impact energy. The saturation effect where it becomes more difficult for the indentation to increase in depth for higher impact energies is also seen for multiple impacts, and hence the nonlinear second-order relationship is observed.
- Multiple impacts at an energy below that required to initiate delamination damage continue to slightly increase the indentation depth due to viscoelastic and plastic behaviour.

- Again, after multiple impacts, there continues to be a unique ‘master’ relationship between indentation depth and the normalised delamination damage area (i.e. the damage area divided by the panel thickness) for the 2.3 mm and 4.6 mm thick composite panels.
- After multiple impacts in the same location, measuring the indentation depth still has the potential to be used as a quick and cheap alternative to employing expensive ultrasonic C-scan or X-ray CT equipment for estimating the amount of internal interlaminar delamination damage.

9.4 Study on the internal and external damage formed in CFRP thermoplastic laminates under low-velocity impact conditions

The present study has shown that:

- For woven CF/PPS panels of 2 mm in thickness there is a smaller delamination damage area observed than for UD CF/Epoxy panels of 2.3 mm in thickness when impacted at the same impact energy. Both the different matrix materials and the different fibre architectures contribute to this variation in damage area. In particular, the woven fibres in the CF/PPS increase the fracture toughness of the composite by deflecting cracks and hindering shear crack and delamination propagation. This combined with the usually tougher thermoplastic matrix leads to the lower delamination damage area. In addition, the CF/Epoxy panels exhibit a higher peak load and a lower maximum displacement than the CF/PPS panels when impacted at the same energy.
- The permanent surface indentation formed in the CF/PPS by the impactor is accompanied by both intralaminar damage, including matrix cracking and fibre fracture, and interlaminar (i.e. delamination) damage between plies. As was the case for the CF/Epoxy material, the surface indentation occurs at a slightly lower impact energy in the CF/PPS than that required for interlaminar delamination damage to initiate in the panel.

- The indentation depth has been shown to be related to the delamination damage area in the CF/PPS panels for the low-velocity impact energies of 2 to 10 J by a second-order polynomial relationship. However, this is only valid up until the transition to perforation behaviour.
- For woven CF/PPS (in addition to UD CF/Epoxy), until the transition to perforation behaviour, measuring the indentation depth has the potential to be used as a quick, easy and cheap alternative to employing expensive non-destructive testing (NDT) equipment for estimating the scope of internal delamination damage.

9.5 Study on the damage formed in CFRP thermoset laminates and the residual compressive strength after multiple impacts in different locations

The present study has shown that:

- A second impact separated from the first by a relatively small distance (10 mm in this study) does not initiate new delaminations, instead propagating existing delaminations created by the first impact. A lack of load drops on load versus time and load versus displacement graphs indicates that new damage is not usually formed. Instead, existing delaminations are lengthened and widened.
- In contrast, a second impact separated from the first by a large enough distance (30 and 50 mm in this study) does create new delaminations in a separate damage zone. This is indicated by a load drop on the load versus time and load versus displacement graphs. Depending on the impact energy and separation distance, this damage zone may combine with the damage zone from the first impact. Based on the distances tested in this study, the distance at which damage initiation starts to occur rather than just propagation is between 10 and 30 mm for the CF/Epoxy panels.
- For increasing separation distances, the delamination damage footprint increases until the damage zones become completely separate.

- Larger impact energies cause a larger delamination footprint. This in turn leads to a lower compression-after-impact (CAI) strength due to the increased size of the delaminations which aides buckling and reduces resistance to delamination propagation.
- The CAI strength was found to increase with impact separation distance, despite the delamination damage footprint also increasing. For a smaller separation distance (i.e. 10 mm) delamination propagation takes place during a second impact, leading to longer and wider delaminations which aide buckling and reduce resistance to delamination propagation. As the impacts move further apart, this relationship tails off due to the separate damage zones which are created.

9.6 Study on the impact behaviour of patch-repaired CFRP thermoset laminates

The present study has shown that:

- For a 4.6 mm thick pristine panel, the delamination damage area increases by approximately 50% when impacted for a second time at 7.5 J. However, by repairing the panel, the damage sustained upon a second impact can be reduced by using a thick patch-only or a patch + plug repair.
- For a 2.3 mm thick patch-only repair, the delamination damage area sustained from impact is greater than the entire delamination damage area within the pristine panel after two impacts. Changing the diameter of the patch slightly affects the delamination area, with a 55 mm diameter patch exhibiting a higher damage area than a 65 mm diameter patch.
- Addition of a plug beneath the 2.3 mm patch significantly reduces the damage area and increases the damage initiation load. The plug supports the patch during impact, reducing the local deformation and therefore reducing the inter-ply stresses.
- Using a 4.6 mm patch-only repair reduces the delamination area and increases the damage initiation load in comparison to the 2.3 mm patch-only repair but is not as effective as the patch

+ plug repair. However, for cases where only one side of the CFRP panel can be accessed (i.e. a patch + plug repair cannot be implemented), this repair would provide a suitable alternative.

- Indentation depth reduces with increasing thickness of the repair and a larger indentation depth corresponds to a larger delamination damage area. Although thickness doesn't appear to have a significant influence on indentation depth for pristine panels, see Chapter 4, the constraint provided on the patches means the localised deformation is more important for the repairs. Therefore, the relative stiffness (i.e. thickness) of the repair has more of an effect on the indentation.
- Optical microscope and SEM images showed intralaminar and interlaminar (i.e. delamination) damage within the repairs, however optical microscopy provided better images of these types of damage across a whole cross-section of CF/Epoxy. Good detail of fibre fracture and matrix cracking could also be obtained at relatively high magnifications using the optical microscope.

9.7 Summary

To summarise, the work in this thesis highlights the relationship between the permanent indentation depth and the internal delamination damage formed during single and multiple impacts on pristine and repaired CFRP panels. It is suggested that measurement of this indentation depth may be a useful tool for estimating the extent of delamination damage in lieu of expensive and time-consuming NDT techniques. The work also demonstrates that the distance between two impacts can have a large effect on the residual strength of a structure.

Chapter 10 Future work

10.1 Introduction

To extend the investigations in this thesis, further work is suggested to improve understanding of the concepts discussed. Given the complicated nature of the damage response of carbon fibre-reinforced polymer (CFRP) and the influence of so many variables on the final damage level, thorough investigations with a deep understanding are required before applying new findings to real life situations. Therefore, and first of all, to improve confidence in the proposed conclusions, further repeat tests should be completed on identical panels.

10.2 Measuring indentation depth in alternative CFRP materials after low-velocity impact

As mentioned in Chapter 4, the relationship between indentation depth and (normalised) delamination damage area obtained is only valid for the particular type of unidirectional (UD) CF/Epoxy tested. This includes only being valid between a thickness of 2.3 and 4.6 mm and for the quasi-isotropic (QIT) lay-ups tested. Firstly, further testing of this same pre-preg material would be of interest to extend knowledge of the effects of using different lay-ups on the resulting delamination damage area and indentation depth. Furthermore, normalisation of the delamination damage area using the panel stiffness, instead of the panel thickness, could also be investigated. Varying the lay-up could also widen the number of thicknesses tested.

Secondly, the investigation could be further expanded to include other CFRP materials with differing matrices and reinforcement, as has been done in Chapter 6 with the impact testing of woven CF/PPS. If only one of the matrix or reinforcement is changed at a time, the effects of either the matrix material or the fibre architecture on the relationship between the indentation depth and delamination damage area could be isolated and more easily compared.

Finally, the indentation depth after multiple impacts in the same location could also be studied for the different materials, following the same methods as in Chapter 5 of this thesis. However, this could be further extended by not just repeating impacts at the same energy, but by varying the impact energy on subsequent impacts. The effect of a low-energy impact followed by a high-energy impact could be compared to the effect of a high-energy impact followed by a low-energy impact. It could then be decided whether the measurement of indentations still provides an accurate estimate of the damage area when the impact energies for multiple impacts have been varied.

10.3 Effects of impactor shape and size on the resulting indentation shape and depth

The indentation shape and depth formed are highly dependent on the impactor shape. Obviously, a hemispherical impactor would not cause the same indentation shape as a conical or flat impactor. Furthermore, hemispherical impactors do not initiate damage in the same way as other impactor shapes due to the difference in deformation which result, in particular the deformation close to the impactor. Therefore, testing using different impactor shapes is essential to make the theory gained in this thesis more applicable to real life scenarios. While a hemispherical impactor may accurately model impact from a hailstone or a spanner dropped lengthways, it does not accurately model impact from some runway debris (e.g. stones with sharp edges) or a spanner dropped on its flat face. Therefore, impact using flat-ended, conical and ogival impactors would help extend the number of real life scenarios tested. Additionally, the effect of impactor size is likely an important factor for investigation. For example, the diameter of a hemispherical impactor will likely affect the indentation depth and profile and change the impact energy required to initiate delamination.

Although different shaped and sized impactors have been used for studies in the literature, see Section 2.3.5, there has been little investigation into the indent shape and depth caused, with most of the focus on the resulting damage area. By relating the indentation depth to the resulting delamination area for the different impactors, a deeper understanding of the effect of the indentation on the initiation and propagation of delaminations within the CFRP could be obtained.

10.4 Effects of high-velocity impact on the indentation depth in CFRP materials

As mentioned in Section 2.3.3, CFRP materials show a large difference in behaviour depending on if they are subject to low-velocity or high-velocity impact, including the amount of delamination damage suffered. Therefore, it may be expected that the indentation depth will also be highly affected by the speed of impact. The effects of impact speed on the relationship between indentation depth and delamination damage area would be useful to understand to extend knowledge and ensure that, if indentation depth was being used to estimate damage area, any signs of the speed of impact were taken note of and adjustments to the indentation depth versus damage area relationship were made.

For suitably high velocities, perforation occurs so the indentation depth cannot be measured. Therefore, low-enough velocities would need to be used during testing to establish a relationship. Furthermore, testing using a different impactor mass but remaining in the low-velocity regime may also be relevant if this has a significant effect on the resulting indentation depth.

10.5 Multiple impacts of different energies in different locations

The investigation of Chapter 7 could be extended by having two impacts of differing impact energies on the same panel, rather than repeating the same energy level. This may provide a more realistic scenario and would provide a more thorough understanding of the impact response when previous impact damage is near to the impact zone. Furthermore, a greater number of impact separation distances could be tested to allow investigation of the transition from a single damage zone (created from two impacts close together) to two separate damage zones.

Also, the investigation could be made more realistic by impacting larger panels which are a similar size to structures on an aircraft. Although smaller test panels often provide a good indication of

impact behaviour, they have different boundary conditions to aircraft panels which is likely to significantly affect the deformation and damage response of the CFRP composite.

10.6 Impact testing of formed CFRP components

Not many CFRP aircraft components are flat panels, therefore the behaviour of formed components compared to flat panels should be considered. Once formed into shapes it would be interesting to see both the damage caused by the impact and the shape of indentation which resulted, and indeed if curvature made a difference to the delamination area. Depending on the component, it may be difficult to relate the indentation depth to the damage area, particularly if impact has occurred on a corner. Furthermore, viewing the resulting delamination may be difficult, given impact has not occurred on a flat surface and therefore non-destructive testing (NDT) methods are more difficult to use in this scenario.

10.7 Testing of scarf repairs with similar dimensions to the patch repairs

Impact testing of alternative repair methods, in particular the scarf repair, with similar dimensions to the patch repairs tested in Chapter 8 would provide a very useful comparison. Testing would help to prove whether the significantly more complex manufacturing process of scarf repairs leads to a significant improvement in impact performance. To understand how the delamination damage area in both types of repair affects the residual strength of the panel, CAI testing could also be undertaken.

List of references

1. Mahashabde A, Wolfe P, Ashok A, Dorbian C, He Q, Fan A, et al. Assessing the environmental impacts of aircraft noise and emissions. *Progress in Aerospace Sciences.* 2011;47(1):15–52. Available from: http://dx.doi.org/10.1016/j.paerosci.2010.04.003

2. European Union. *setting CO2 emission performance standards for new passenger cars and for new light commercial vehicles, and repealing Regulations (EC) No 443/2009 and (EU) No 510/2011*. European Union. 2019.

3. Soutis C. Carbon fiber reinforced plastics in aircraft construction. *Materials Science and Engineering A.* 2005;412(1–2):171–6. Available from: https://doi.org/10.1016/j.msea.2005.08.064

4. Katnam KB, Da Silva LFM, Young TM. Bonded repair of composite aircraft structures: A review of scientific challenges and opportunities. *Progress in Aerospace Sciences.* 2013;61:26–42. Available from: http://dx.doi.org/10.1016/j.paerosci.2013.03.003

5. Caminero MA, Pavlopoulou S, Lopez-Pedrosa M, Nicolaisson BG, Pinna C, Soutis C. Analysis of adhesively bonded repairs in composites: Damage detection and prognosis. *Compos Struct.* 2013;95:500–17. Available from: http://dx.doi.org/10.1016/j.compstruct.2012.07.028

6. Balaganesan G, Chandra Khan V. Energy absorption of repaired composite laminates subjected to impact loading. *Compos B Eng.* 2016;98:39–48. Available from: http://dx.doi.org/10.1016/j.compositesb.2016.04.083

7. Caminero MA, Lopez-Pedrosa M, Pinna C, Soutis C. Damage monitoring and analysis of composite laminates with an open hole and adhesively bonded repairs using digital image correlation. *Compos B Eng.* 2013;53:76–91. Available from: http://dx.doi.org/10.1016/j.compositesb.2013.04.050

8. Hellard G. Composites in Airbus: a long story of innovations and experiences. *In: Airbus Global Investor Forum.* Seville; 2008.

9. Boeing. *Advanced Composite Use*. Available from: https://www.boeing.com/commercial/787/by-design/#/advanced-composite-use [Accessed 6th May 2021].

10. Marino M, Sabatini R. Advanced Lightweight Aircraft Design Configurations for Green Operations. *In: Practical Responses to Climate Change Conference (PRCC) 2014, 25-27 November 2014.* Melbourne, Australia; 2014. Available from: http://dx.doi.org/10.13140/2.1.4231.8405

11. Such M, Ward C, Potter K. Aligned Discontinuous Fibre Composites: A Short History. *Journal of Multifunctional Composites.* 2014;2(3):155–68. Available from: http://dx.doi.org/10.12783/issn.2168-4286/2/3/4

12. Liu H, Falzon BG, Tan W. Predicting the Compression-After-Impact (CAI) strength of damage-tolerant hybrid unidirectional/woven carbon-fibre reinforced composite laminates. *Compos Part A Appl Sci Manuf.* 2018;105:189–202. Available from: https://doi.org/10.1016/j.compositesa.2017.11.021

13. Mitrevski T, Marshall IH, Thomson R. The influence of impactor shape on the damage to composite laminates. *Compos Struct.* 2006;76(1–2):116–22. Available from: https://doi.org/10.1016/j.compstruct.2006.06.017

14. Tuo H, Lu Z, Ma X, Zhang C, Chen S. An experimental and numerical investigation on low-velocity impact damage and compression-after-impact behavior of composite laminates. *Compos B Eng.* 2019;167:329–41. Available from: https://doi.org/10.1016/j.compositesb.2018.12.043

15. Rivallant S, Bouvet C, Abi Abdallah E, Broll B, Barrau JJ. Experimental analysis of CFRP laminates subjected to compression after impact: The role of impact-induced cracks in failure.

Compos Struct. 2014;111:147–57. Available from: http://dx.doi.org/10.1016/j.compstruct.2013.12.012

16. Brooks RA, Wang H, Ding Z, Xu J, Song Q, Liu H, et al. A review on stamp forming of continuous fibre-reinforced thermoplastics. *International Journal of Lightweight Materials and Manufacture.* 2022;5(3):411–30. Available from: https://doi.org/10.1016/j.ijlmm.2022.05.001

17. Matthews FL, Rawlings RD. *Composite Materials: Engineering and Science*. Cambridge: Woodhead Publishing Ltd; 1999.

18. Ye L, Friedrich K, Kästel J, Mai YW. Consolidation of unidirectional CF/PEEK composites from commingled yarn prepreg. *Compos Sci Technol.* 1995;54(4):349–58. Available from: https://doi.org/10.1016/0266-3538(95)00061-5

19. Liu H, Liu J, Ding Y, Zheng J, Kong X, Zhou J, et al. The behaviour of thermoplastic and thermoset carbon fibre composites subjected to low-velocity and high-velocity impact. *J Mater Sci.* 2020;55:15741–68. Available from: https://doi.org/10.1007/s10853-020-05133-0

20. Witik RA, Teuscher R, Michaud V, Ludwig C, Månson JAE. Carbon fibre reinforced composite waste: An environmental assessment of recycling, energy recovery and landfilling. *Compos Part A Appl Sci Manuf.* 2013;49:89–99. Available from: http://dx.doi.org/10.1016/j.compositesa.2013.02.009

21. Bussetta P, Correia N. Numerical forming of continuous fibre reinforced composite material: A review. *Compos Part A Appl Sci Manuf.* 2018;113:12–31. Available from: https://doi.org/10.1016/j.compositesa.2018.07.010

22. Bibo GA, Hogg PJ. The role of reinforcement architecture on impact damage mechanisms and post-impact compression behaviour. *J Mater Sci.* 1996;31(5):1115–37. Available from: https://doi.org/10.1007/BF00353091

23. Kim JK, Sham ML. Impact and delamination failure of woven-fabric composites. *Compos Sci Technol.* 2000;60(5):745–61. Available from: http://dx.doi.org/10.1016/S0266-3538(99)00166-9

24. Kim JK, Leung LM, Lee SWR, Hirai Y. Impact Performance of a Woven Fabric CFRP Laminate. *Polymers and Polymer Composites.* 1996;4(8):549–61. Available from: https://doi.org/10.1177/147823919600400803

25. Baker AA, Jones R, Callinan RJ. Damage tolerance of graphite/epoxy composites. *Compos Struct.* 1985;4(1):15–44. Available from: https://doi.org/10.1016/0263-8223(85)90018-2

26. Kim JK, MacKay DB, Mai YW. Drop-weight impact damage tolerance of CFRP with rubber-modified epoxy matrix. *Composites.* 1993;24(6):485–94. Available from: https://doi.org/10.1016/0010-4361(93)90018-4

27. Ghaseminejhad MN, Parvizi-Majidi A. Impact behaviour and damage tolerance of woven carbon fibre-reinforced thermoplastic composites. *Constr Build Mater.* 1990;4(4):194–207. Available from: https://doi.org/10.1016/0950-0618(90)90040-8

28. Zhao L, Qin T, Zhang J, Chen Y. 3D gradual material degradation model for progressive damage analyses of unidirectional composite materials. *Math Probl Eng.* 2015;2015:145629. Available from: http://dx.doi.org/10.1155/2015/145629

29. Chowdhury NT, Wang J, Chiu WK, Yan W. Matrix failure in composite laminates under tensile loading. *Compos Struct.* 2016;135:61–73. Available from: http://dx.doi.org/10.1016/j.compstruct.2015.09.022

30. Kashtalyan M, Soutis C. Analysis of composite laminates with intra- and interlaminar damage. *Progress in Aerospace Sciences.* 2005;41(2):152–73. Available from: https://doi.org/10.1016/j.paerosci.2005.03.004

31. Berbinau P, Soutis C, Guz IA. Compressive failure of 0° unidirectional carbon-fibre-reinforced plastic (CFRP) laminates by fibre microbuckling. *Compos Sci Technol.* 1999;59(9):1451–5. Available from: https://doi.org/10.1016/S0266-3538(98)00181-X

32. Hashemi S, Kinloch AJ, Williams JG. The analysis of interlaminar fracture in uniaxial fibre-polymer composites. *Proceedings of the Royal Society of London A Mathematical and Physical Sciences.* 1990;427(1872):173–99. Available from: https://doi.org/10.1098/rspa.1990.0007

33. Liu H, Falzon BG, Tan W. Experimental and numerical studies on the impact response of damage-tolerant hybrid unidirectional/woven carbon-fibre reinforced composite laminates. *Compos B Eng.* 2018;136:101–18. Available from: https://doi.org/10.1016/j.compositesb.2017.10.016

34. Liu J, Liu H, Kaboglu C, Kong X, Ding Y, Chai H, et al. The Impact Performance of Woven-Fabric Thermoplastic and Thermoset Composites Subjected to High-Velocity Soft- and Hard-Impact Loading. *Applied Composite Materials.* 2019;26(5–6):1389–410. Available from: https://doi.org/10.1007/s10443-019-09786-2

35. Wisnom MR. The role of delamination in failure of fibre-reinforced composites. *Philosophical Transactions of the Royal Society A: Mathematical, Physical and Engineering Sciences.* 2012;370(1965):1850–70. Available from: https://doi.org/10.1098/rsta.2011.0441

36. Goyal VK, Jaunky NR, Johnson ER, Ambur DR. Intralaminar and interlaminar progressive failure analyses of composite panels with circular cutouts. *Compos Struct.* 2004;64(1):91–105. Available from: https://doi.org/10.1016/S0263-8223(03)00217-4

37. Choi HY, Wu HT, Chang F. A New Approach toward Understanding Damage Mechanisms and Mechanics of Laminated Composites Due to Low-Velocity Impact: Part II—Analysis. *J Compos Mater.* 1991;25(8):1012–38. Available from: https://doi.org/10.1177/002199839102500804

38. Short GJ, Guild FJ, Pavier MJ. The effect of delamination geometry on the compressive failure of composite laminates. *Compos Sci Technol.* 2001;61(14):2075–86.

39. Pavier MJ, Clarke MP. Experimental techniques for the investigation of the effects of impact damage on carbon-fibre composites. *Compos Sci Technol.* 1995;55(2):157–69. Available from: https://doi.org/10.1016/0266-3538(95)00097-6

40. Sekine H, Hu N, Kouchakzadeh MA. Buckling Analysis of Elliptically Delaminated Composite Laminates with Consideration of Partial Closure of Delamination. *J Compos Mater.* 2000;34(7):551–74. Available from: https://doi.org/10.1177/002199830003400702

41. Kardomateas GA, Schmueser DW. Buckling and Postbuckling of Delaminated Composites Under Compressive Loads Including Transverse Shear Effects. *AIAA Journal.* 1988;26(3):337–43. Available from: https://doi.org/10.2514/3.9894

42. Bolotin V V. Delaminations in composite structures: Its origin, buckling, growth and stability. *Compos B Eng.* 1996;27(2):129–45. Available from: https://doi.org/10.1016/1359-8368(95)00035-6

43. Vaidya UK. Impact Response of Laminated and Sandwich Composites. In: Abrate S, (ed.) *Impact Engineering of Composite Structures*. Vienna, Austria: Springer; 2011. p. 97–191.

44. Cantwell WJ, Morton J. Comparison of the low and high velocity impact response of CFRP. *Composites.* 1989;20(6):545–51. Available from: https://doi.org/10.1016/0010-4361(89)90913-0

45. Cantwell WJ, Morton J. The influence of varying projectile mass on the impact response of CFRP. *Compos Struct.* 1989;13(2):101–14. Available from: https://doi.org/10.1016/0263-8223(89)90048-2

46. Cantwell WJ, Morton J. Impact perforation of carbon fibre reinforced plastic. *Compos Sci Technol.* 1990;38(2):119–41. Available from: https://doi.org/10.1016/0266-3538(90)90002-M

47. Cantwell WJ, Morton J. The impact resistance of composite materials - a review. *Composites.* 1991;22(5):347–62. Available from: https://doi.org/10.1016/0010-4361(91)90549-V

48. Tuo H, Lu Z, Ma X, Xing J, Zhang C. Damage and failure mechanism of thin composite laminates under low-velocity impact and compression-after-impact loading conditions. *Compos B Eng.* 2019;163:642–54. Available from: https://doi.org/10.1016/j.compositesb.2019.01.006

49. Robinson P, Davies GAO. Impactor mass and specimen geometry effects in low velocity impact of laminated composites. *Int J Impact Eng.* 1992;12(2):189–207. Available from: https://doi.org/10.1016/0734-743X(92)90408-L

50. Yankelevsky DZ. Local response of concrete slabs to low velocity missile impact. *Int J Impact Eng.* 1997;19(4):331–43. Available from: https://doi.org/10.1016/S0734-743X(96)00041-3

51. Hou JP, Ruiz C. Soft body impact on laminated composite materials. *Compos Part A Appl Sci Manuf.* 2007;38:505–15. Available from: https://doi.org/10.1016/J.COMPOSITESA.2006.02.018

52. Kœchlin P, Potapov S. Classification of soft and hard impacts-Application to aircraft crash. *Nuclear Engineering and Design.* 2009;239(4):613–8. Available from: https://doi.org/10.1016/j.nucengdes.2008.10.016

53. Liu H, Liu J, Kaboglu C, Chai H, Kong X, Blackman BRK, et al. Experimental investigations on the effects of projectile hardness on the impact response of fibre-reinforced composite laminates. *International Journal of Lightweight Materials and Manufacture.* 2020;3(2):77–87. Available from: https://doi.org/10.1016/j.ijlmm.2019.10.001

54. Heimbs S, Bergmann T. High-velocity impact behaviour of prestressed composite plates under bird strike loading. *International Journal of Aerospace Engineering.* 2012;2012:372167. Available from: https://doi.org/10.1155/2012/372167

55. Hall ZEC. *Impact Testing of Pristine and Repaired Carbon Fibre Reinforced Polymer Composite Materials for Aircraft Structures.* PhD thesis. Imperial College London; 2023.

56. Mitrevski T, Marshall IH, Thomson R, Jones R, Whittingham B. The effect of impactor shape on the impact response of composite laminates. *Compos Struct.* 2005;67(2):139–48. Available from: https://doi.org/10.1016/j.compstruct.2004.09.007

57. Appleby-Thomas GJ, Wood DC, Hameed A, Leighs JA. On the ballistic response of an aerospace-grade composite panel to non-spheroidised fragment simulants. *Compos Struct.* 2015;119:90–8. Available from: http://dx.doi.org/10.1016/j.compstruct.2014.08.016

58. Sevkat E, Liaw B, Delale F. Drop-weight impact response of hybrid composites impacted by impactor of various geometries. *Mater Des.* 2013;52:67–77. Available from: http://dx.doi.org/10.1016/j.matdes.2013.05.016

59. Mahesh V, Joladarashi S, Kulkarni SM. Influence of laminate thickness and impactor shape on low velocity impact response of jute-epoxy composite: FE study. *Mater Today Proc.* 2020;28(2):545–50. Available from: https://doi.org/10.1016/j.matpr.2019.12.216

60. Elaldi F, Baykan B, Akto C. Experimental analysis for the effect of impactor geometry on carbon reinforced composite materials. *Polymers and Polymer Composites.* 2017;25(9):677–82. Available from: https://doi.org/10.1177/096739111702500905

61. Kazemianfar B, Esmaeeli M, Nami MR. Response of 3D woven composites under low velocity impact with different impactor geometries. *Aerosp Sci Technol.* 2020;102:105849. Available from: https://doi.org/10.1016/j.ast.2020.105849

62. Dhakal HN, Zhang ZY, Bennett N, Reis PNB. Low-velocity impact response of non-woven hemp fibre reinforced unsaturated polyester composites: Influence of impactor geometry and impact velocity. *Compos Struct.* 2012;94(9):2756–63. Available from: http://dx.doi.org/10.1016/j.compstruct.2012.04.004

63. Ding Y, Liu J, Hall ZEC, Brooks RA, Liu H, Kinloch AJ, et al. Damage and energy absorption behaviour of composite laminates under impact loading using different impactor geometries. *Compos Struct.* 2023;321:117259. Available from: https://doi.org/10.1016/j.compstruct.2023.117259

64. Liu H, Liu J, Ding Y, Zhou J, Kong X, Blackman BRK, et al. Effects of Impactor Geometry on the Low-Velocity Impact Behaviour of Fibre-Reinforced Composites: An Experimental and

Theoretical Investigation. *Applied Composite Materials.* 2020;27:522–53. Available from: https://doi.org/10.1007/s10443-020-09812-8

65. Vieille B, Casado VM, Bouvet C. About the impact behavior of woven-ply carbon fiber-reinforced thermoplastic- and thermosetting-composites: A comparative study. *Compos Struct.* 2013;101:9–21. Available from: http://dx.doi.org/10.1016/j.compstruct.2013.01.025

66. Dorey G, Bishop SM, Curtis PT. On the impact performance of carbon fibre laminates with epoxy and PEEK matrices. *Compos Sci Technol.* 1985;23(3):221–37. Available from: https://doi.org/10.1016/0266-3538(85)90019-3

67. Bishop SM. The mechanical performance and impact behaviour of carbon-fibre reinforced PEEK. *Compos Struct.* 1985;3(3–4):295–318. Available from: https://doi.org/10.1016/0263-8223(85)90059-5

68. Lu T, Chen X, Wang H, Zhang L, Zhou Y. Comparison of low-velocity impact damage in thermoplastic and thermoset composites by non-destructive three-dimensional X-ray microscope. *Polym Test.* 2020;91:106730. Available from: https://doi.org/10.1016/j.polymertesting.2020.106730

69. Leicy D, Hogg PJ. The Effect of Crystallinity on the Impact Properties of Advanced Thermoplastic Composites. In: Bunsell AR. (ed.) *Developments in the Science and Technology of Composite Materials.* Dordrecht, The Netherlands: Springer; 1989. p. 809–15.

70. Vieille B, Casado VM, Bouvet C. Influence of matrix toughness and ductility on the compression-after-impact behavior of woven-ply thermoplastic- and thermosetting-composites: A comparative study. *Compos Struct.* 2014;110:207–18. Available from: http://dx.doi.org/10.1016/j.compstruct.2013.12.008

71. Ishikawa T, Sugimoto S, Matsushima M, Hayashi Y. Some experimental findings in compression-after-impact (CAI) tests of CF/PEEK (APC-2) and conventional CF/epoxy flat

plates. *Compos Sci Technol.* 1995;55(4):349–63. Available from: https://doi.org/10.1016/0266-3538(95)00079-8

72. Bajurko P. Comparison of damage resistance of thermoplastic and thermoset carbon fibre-reinforced composites. *Journal of Thermoplastic Composite Materials.* 2021;34(3):303–15. Available from: https://doi.org/10.1177/0892705719844550

73. Wagner T, Heimbs S, Franke F, Burger U, Middendorf P. Experimental and numerical assessment of aerospace grade composites based on high-velocity impact experiments. *Compos Struct.* 2018;204:142–52. Available from: https://doi.org/10.1016/j.compstruct.2018.07.019

74. Ivanov SG, Beyens D, Gorbatikh L, Lomov S V. Damage development in woven carbon fibre thermoplastic laminates with PPS and PEEK matrices: A comparative study. *J Compos Mater.* 2017;51(5):637–47. Available from: https://doi.org/10.1177/0021998316653460

75. Sanchez-Saez S, Barbero E, Zaera R, Navarro C. Compression after impact of thin composite laminates. *Compos Sci Technol.* 2005;65(13):1911–9. Available from: https://doi.org/10.1016/j.compscitech.2005.04.009

76. Curtis PT, Bishop SM. An assessment of the potential of woven carbon fibre-reinforced plastics for high performance applications. *Composites.* 1984;15(4):259–65. Available from: https://doi.org/10.1016/0010-4361(84)90706-7

77. López-Puente J, Zaera R, Navarro C. The effect of low temperatures on the intermediate and high velocity impact response of CFRPs. *Compos B Eng.* 2002;33(8):559–66. Available from: https://doi.org/10.1016/S1359-8368(02)00065-3

78. Abrate S. Impact on laminated composites: Recent advances. *Appl Mech Rev.* 1994;47(11):517–44. Available from: https://doi.org/10.1115/1.3111065

79. Caminero MA, García-Moreno I, Rodríguez GP. Damage resistance of carbon fibre reinforced epoxy laminates subjected to low velocity impact: Effects of laminate thickness and ply-stacking

sequence. *Polym Test.* 2017;63:530–41. Available from: https://doi.org/10.1016/j.polymertesting.2017.09.016

80. Caminero MA, García-Moreno I, Rodríguez GP. Experimental study of the influence of thickness and ply-stacking sequence on the compression after impact strength of carbon fibre reinforced epoxy laminates. *Polym Test.* 2018;66:360–70. Available from: https://doi.org/10.1016/j.polymertesting.2018.02.009

81. Sebaey TA, González E V., Lopes CS, Blanco N, Costa J. Damage resistance and damage tolerance of dispersed CFRP laminates: Effect of ply clustering. *Compos Struct.* 2013;106:96–103. Available from: http://dx.doi.org/10.1016/j.compstruct.2013.05.052

82. Amaro AM, Reis PNB, De Moura MFSF, Neto MA. Influence of multi-impacts on GFRP composites laminates. *Compos B Eng.* 2013;52:93–9. Available from: http://dx.doi.org/10.1016/j.compositesb.2013.03.041

83. Found MS, Howard IC. Single and multiple impact behaviour of a CFRP laminate. *Compos Struct.* 1995;32(1–4):159–63. Available from: https://doi.org/10.1016/0263-8223(95)00024-0

84. Appleby-Thomas GJ, Hazell PJ, Dahini G. On the response of two commercially-important CFRP structures to multiple ice impacts. *Compos Struct.* 2011;93(10):2619–27. Available from: http://dx.doi.org/10.1016/j.compstruct.2011.04.029

85. Ezéckiel Amouzou AS, Sicot O, Chettah A, Aivazzadeh S. Experimental characterization of composite laminates under low-velocity multi-impact loading. *J Compos Mater.* 2019;53(17):2391–405. Available from: https://doi.org/10.1177/0021998319827351

86. Zhou J, Liao B, Shi Y, Ning L, Zuo Y, Jia L. Experimental investigation of the double impact position effect on the mechanical behavior of low-velocity impact in CFRP laminates. *Compos B Eng.* 2020;193:108020. Available from: https://doi.org/10.1016/j.compositesb.2020.108020

87. Brooks RA, Liu J, Hall ZEC, Joesbury AM, Harper LT, Liu H, et al. The Relationship Between the Extent of Indentation and Impact Damage in Carbon-Fibre Reinforced-Plastic Composites

after a Low-Velocity Impact. *Applied Composite Materials.* 2024; Available from: https://doi.org/10.1007/s10443-024-10223-2

88. Hutchings IM. The contributions of David Tabor to the science of indentation hardness. *J Mater Res.* 2009;24(3):581–9. Available from: https://doi.org/10.1557/jmr.2009.0085

89. Wardle BL, Lagace PA. On the Use of Dent Depth as an Impact Damage Metric for Thin Composite Structures. *Journal of Reinforced Plastics and Composites.* 1997;16(12):1093–110. Available from: https://doi.org/10.1177/073168449701601202

90. Shi Y, Swait T, Soutis C. Modelling damage evolution in composite laminates subjected to low velocity impact. *Compos Struct.* 2012;94(9):2902–13. Available from: https://doi.org/10.1016/j.compstruct.2012.03.039

91. Wagih A, Maimí P, Blanco N, Costa J. A quasi-static indentation test to elucidate the sequence of damage events in low velocity impacts on composite laminates. *Compos Part A Appl Sci Manuf.* 2016;82:180–9. Available from: https://doi.org/10.1016/j.compositesa.2015.11.041

92. Komorowski JP, Simpson DL, Gould RW. A technique for rapid impact damage detection with implication for composite aircraft structures. *Composites.* 1990;21(2):169–73. Available from: https://doi.org/10.1016/0010-4361(90)90009-L

93. Talreja R, Phan N. Assessment of damage tolerance approaches for composite aircraft with focus on barely visible impact damage. *Compos Struct.* 2019;219:1–7. Available from: https://doi.org/10.1016/j.compstruct.2019.03.052

94. Panettieri E, Fanteria D, Montemurro M, Froustey C. Low-velocity impact tests on carbon/epoxy composite laminates: A benchmark study. *Compos B Eng.* 2016;107:9–21. Available from: http://dx.doi.org/10.1016/j.compositesb.2016.09.057

95. Bouvet C, Rivallant S, Barrau JJ. Low velocity impact modeling in composite laminates capturing permanent indentation. *Compos Sci Technol.* 2012;72(16):1977–88. Available from: http://dx.doi.org/10.1016/j.compscitech.2012.08.019

96. Sonatest. *Ultrasonic Non-Destructive Examination*. Available from: https://sonatest.com/technology/ultrasonic-non-destructive-testing [Accessed 3rd February 2024].

97. Scott IG, Scala CM. A review of non-destructive testing of composite materials. *NDT International.* 1982;15(2):75–86. Available from: https://doi.org/10.1016/0308-9126(82)90001-3

98. Sonatest. *What is Linear Scanning*. Available from: https://archive.sonatest.com/resources/educational-notes/what-linear-scanning [Accessed 3rd February 2024].

99. Garnier C, Pastor ML, Eyma F, Lorrain B. The detection of aeronautical defects in situ on composite structures using Non Destructive Testing. *Compos Struct.* 2011;93(5):1328–36. Available from: http://dx.doi.org/10.1016/j.compstruct.2010.10.017

100. Gholizadeh S. A review of non-destructive testing methods of composite materials. *Procedia Structural Integrity.* 2016;1:50–7. Available from: http://dx.doi.org/10.1016/j.prostr.2016.02.008

101. Kersemans M, Verboven E, Segers J, Hedayatrasa S, Paepegem W Van. Non-Destructive Testing of Composites by Ultrasound, Local Defect Resonance and Thermography. *In: The 18th International Conference on Experimental Mechanics, 1-5 July 2018.* Brussels, Belgium; 2018. p. 554. Available from: https://doi.org/10.3390/ICEM18-05464

102. Garcea SC, Wang Y, Withers PJ. X-ray computed tomography of polymer composites. *Compos Sci Technol.* 2018;156:305–19. Available from: https://doi.org/10.1016/j.compscitech.2017.10.023

103. Evans EE, Brooks RA, Liu J, Hall ZEC, Liu H, Lowe TJE, et al. Comparison of X-ray Computed Tomography and Ultrasonic C-Scan Techniques and Numerical Modelling of Impact Damage in a CFRP Composite Laminate. *Applied Composite Materials.* 2023;31:249–64. Available from: https://doi.org/10.1007/s10443-023-10171-3

104. Rus J, Gustschin A, Mooshofer H, Grager JC, Bente K, Gaal M, et al. Qualitative comparison of non-destructive methods for inspection of carbon fiber-reinforced polymer laminates. *J Compos Mater.* 2020;54(27):4325–37. Available from: https://doi.org/10.1177/0021998320931162

105. Pelivanov I, Ambroziński Ł, Khomenko A, Koricho EG, Cloud GL, Haq M, et al. High resolution imaging of impacted CFRP composites with a fiber-optic laser-ultrasound scanner. *Photoacoustics.* 2016;4(2):55–64. Available from: https://doi.org/10.1016/j.pacs.2016.05.002

106. Saghafi H, Minak G, Zucchelli A. Effect of preload on the impact response of curved composite panels. *Compos B Eng.* 2014;60:74–81. Available from: http://dx.doi.org/10.1016/j.compositesb.2013.12.026

107. Whittingham B, Marshall IH, Mitrevski T, Jones R. The response of composite structures with pre-stress subject to low velocity impact damage. *Compos Struct.* 2004;66(1–4):685–98. Available from: https://doi.org/10.1016/j.compstruct.2004.06.015

108. Amaro AM, Reis PNB, de Moura MFSF, Neto MA. Multi-impact response of composite laminates with open holes. *Polym Compos.* 2018;39(7):2490–8. Available from: https://doi.org/10.1002/pc.24235

109. Budhe S, Banea MD, de Barros S. Bonded repair of composite structures in aerospace application: a review on environmental issues. *Applied Adhesion Science.* 2018;6(3). Available from: https://doi.org/10.1186/s40563-018-0104-5

110. Wang CH, Gunnion AJ. Optimum shapes of scarf repairs. *Compos Part A Appl Sci Manuf.* 2009;40(9):1407–18. Available from: http://dx.doi.org/10.1016/j.compositesa.2009.02.009

111. Pinto AMG, Campilho RDSG, De Moura MFSF, Mendes IR. Numerical evaluation of three-dimensional scarf repairs in carbon-epoxy structures. *Int J Adhes Adhes.* 2010;30(5):329–37. Available from: http://dx.doi.org/10.1016/j.ijadhadh.2009.11.001

112. Li J, Yan Y, Zhang T, Liang Z. Experimental study of adhesively bonded CFRP joints subjected to tensile loads. *Int J Adhes Adhes.* 2015;57:95–104. Available from: http://dx.doi.org/10.1016/j.ijadhadh.2014.11.001

113. Herszberg I, Feih S, Gunnion AJ, Li HCH. Impact damage tolerance of tension loaded bonded scarf repairs to CFRP laminates. *In: Proceedings 16th International Conference on Composite Materials.* Kyoto, Japan; 2007.

114. Archer E, McIlhagger A. Repair of damaged aerospace composite structures. In: Irving PE, Soutis C. (eds.) *Polymer Composites in the Aerospace Industry*. Elsevier Ltd; 2015. p. 393–412.

115. Wang CH, Gunnion A. *Design Methodology for Scarf Repairs to Composite Structures*. Australian Government Department of Defence. 2006.

116. Cheng P, Gong X, Hearn D, Aivazzadeh S. Tensile behaviour of patch-repaired CFRP laminates. *Compos Struct.* 2011;93(2):582–9. Available from: http://dx.doi.org/10.1016/j.compstruct.2010.08.021

117. Found MS, Friend MJ. Evaluation of CFRP panels with scarf repair patches. *Compos Struct.* 1995;32(1–4):115–22. Available from: https://doi.org/10.1016/0263-8223(95)00045-3

118. Whittingham B, Baker AA, Harman A, Bitton D. Micrographic studies on adhesively bonded scarf repairs to thick composite aircraft structure. *Compos Part A Appl Sci Manuf.* 2009;40(9):1419–32. Available from: http://dx.doi.org/10.1016/j.compositesa.2008.12.011

119. Savage G, Oxley M. Repair of composite structures on Formula 1 race cars. *Eng Fail Anal.* 2010;17(1):70–82. Available from: http://dx.doi.org/10.1016/j.engfailanal.2008.11.006

120. Liu B, Han Q, Zhong X, Lu Z. The impact damage and residual load capacity of composite stepped bonding repairs and joints. *Compos B Eng.* 2019;158:339–51. Available from: https://doi.org/10.1016/j.compositesb.2018.09.096

121. Wang CH, Venugopal V, Peng L. Stepped flush repairs for primary composite structures. *Journal of Adhesion.* 2015;91(1–2):95–112. Available from: https://doi.org/10.1080/00218464.2014.896212

122. Santhanakrishnan Balakrishnan V, Seidlitz H. Potential repair techniques for automotive composites: A review. *Compos B Eng.* 2018;145:28–38. Available from: https://doi.org/10.1016/j.compositesb.2018.03.016

123. Bendemra H, Compston P, Crothers PJ. Optimisation study of tapered scarf and stepped-lap joints in composite repair patches. *Compos Struct.* 2015;130:1–8. Available from: http://dx.doi.org/10.1016/j.compstruct.2015.04.016

124. Psarras S, Loutas T, Papanaoum M. Investigating the Effect of Stepped Scarf Repair Ratio in Repaired CFRP Laminates under Compressive Loading. *Journal of Composites Science.* 2020;4(153). Available from: https://doi.org/10.3390/jcs4040153

125. Yoo JS, Truong VH, Park MY, Choi JH, Kweon JH. Parametric study on static and fatigue strength recovery of scarf-patch-repaired composite laminates. *Compos Struct.* 2016;140:417–32. Available from: http://dx.doi.org/10.1016/j.compstruct.2015.12.041

126. Kumar SB, Sridhar I, Sivashanker S, Osiyemi SO, Bag A. Tensile failure of adhesively bonded CFRP composite scarf joints. *Materials Science and Engineering B.* 2006;132(1–2):113–20. Available from: https://doi.org/10.1016/j.mseb.2006.02.046

127. Tzetzis D, Hogg PJ. Experimental and finite element analysis on the performance of vacuum-assisted resin infused single scarf repairs. *Mater Des.* 2008;29(2):436–49. Available from: https://doi.org/10.1016/j.matdes.2007.01.002

128. Campilho RDSG, De Moura MFSF, Domingues JJMS. Stress and failure analyses of scarf repaired CFRP laminates using a cohesive damage model. *J Adhes Sci Technol.* 2007;21(9):855–70. Available from: https://doi.org/10.1163/156856107781061477

129. Hoshi H, Nakano K, Iwahori Y. Study on repair of CFRP laminates for aircraft structures. *In: Proceedings 16th International Conference on Composite Materials.* Kyoto, Japan; 2007.

130. Darwish FH, Shivakumar KN. Experimental and analytical modeling of scarf repaired composite panels. *Mechanics of Advanced Materials and Structures.* 2014;21(3):207–12. Available from: https://doi.org/10.1080/15376494.2013.834096

131. Harman AB, Wang CH. Improved design methods for scarf repairs to highly strained composite aircraft structure. *Compos Struct.* 2006;75(1–4):132–44. Available from: https://doi.org/10.1016/j.compstruct.2006.04.091

132. Cheng X, Du X, Zhang J, Zhang J, Guo X, Bao J. Effects of stacking sequence and rotation angle of patch on low velocity impact performance of scarf repaired laminates. *Compos B Eng.* 2018;133:78–85. Available from: https://doi.org/10.1016/j.compositesb.2017.09.020

133. Wang CH, Gunnion AJ. On the design methodology of scarf repairs to composite laminates. *Compos Sci Technol.* 2008;68(1):35–46. Available from: https://doi.org/10.1016/j.compscitech.2007.05.045

134. Breitzman TD, Iarve E V., Cook BM, Schoeppner GA, Lipton RP. Optimization of a composite scarf repair patch under tensile loading. *Compos Part A Appl Sci Manuf.* 2009;40(12):1921–30. Available from: http://dx.doi.org/10.1016/j.compositesa.2009.04.033

135. Li HCH, Mitrevski T, Herszberg I. Impact on bonded repairs to CFRP laminates under load. *In: ICAS-Secretariat - 25th Congress of the International Council of the Aeronautical Sciences, 3-8th September 2006.* Hamburg, Germany; 2006. p. 2581–8.

136. Gunnion AJ, Herszberg I. Parametric study of scarf joints in composite structures. *Compos Struct.* 2006;75(1–4):364–76. Available from: https://doi.org/10.1016/j.compstruct.2006.04.053

137. Préau M, Hubert P. Processing of co-bonded scarf repairs: Void reduction strategies and influence on strength recovery. *Compos Part A Appl Sci Manuf.* 2016;84:236–45. Available from: https://doi.org/10.1016/j.compositesa.2016.01.016

138. Hanser S, Ferrer G, Dupoy S. A350 XWB composite bonded repair. *Airbus - Flight Airworthiness Support Technology*. March 2018. p. 10-17. Available from: https://www.airbus.com/content/dam/corporate-topics/publications/fast/airbus-fast61-april2018.pdf [Accessed 14th November 2020].

139. Bhatia GS, Andrew JJ, Arockiarajan A. Experimental investigation on compressive behaviour of different patch–parent layup configurations for repaired carbon/epoxy composites. *J Compos Mater.* 2019;53(23):3269–79. Available from: https://doi.org/10.1177%2F0021998318822706

140. Holtmannspötter J, Czarnecki J V., Feucht F, Wetzel M, Gudladt HJ, Hofmann T, et al. On the fabrication and automation of reliable bonded composite repairs. *Journal of Adhesion.* 2015;91(1–2):39–70. Available from: https://doi.org/10.1080/00218464.2014.896211

141. Li N, Sun L, Chen D. An Experimental Study on the Low Velocity Impact Response of Repaired Carbon Fibre/Benzoxazine Composites. *Fibers and Polymers.* 2019;20(1):129–37. Available from: https://doi.org/10.1007/s12221-019-8423-0

142. Shufeng L, Xiaoquan C, Yunyan X, Jianwen B, Xin G. Study on impact performances of scarf-repaired carbon fiber reinforced polymer laminates. *Journal of Reinforced Plastics and Composites.* 2015;34(1):60–71. Available from: https://doi.org/10.1177%2F0731684414562465

143. Cheng X, Zhang J, Bao J, Zeng B, Cheng Y, Hu R. Low-velocity impact performance and effect factor analysis of scarf-repaired composite laminates. *Int J Impact Eng.* 2017;111:85–93. Available from: https://doi.org/10.1016/j.ijimpeng.2017.09.004

144. Coelho SRM, Reis PNB, Ferreira JAM, Pereira AM. Effects of external patch configuration on repaired composite laminates subjected to multi-impacts. *Compos Struct.* 2017;168:259–65. Available from: http://dx.doi.org/10.1016/j.compstruct.2017.02.069

145. Soutis C, Duan DM, Goutas P. Compressive behaviour of CFRP laminates repaired with adhesively bonded external patches. *Compos Struct.* 1999;45(4):289–301. Available from: https://doi.org/10.1016/S0263-8223(99)00033-1

146. Park H, Kong C. A study on low velocity impact damage evaluation and repair technique of small aircraft composite structure. *Compos Part A Appl Sci Manuf.* 2011;42(9):1179–88. Available from: http://dx.doi.org/10.1016/j.compositesa.2011.05.002

147. Falzon BG. Impact damage and repair of composite structures. *The Aeronautical Journal.* 2009;113(1145):431–45. Available from: https://doi.org/10.1017/S0001924000003109

148. Finn SR, He YF, Springer GS, Lee HJ. Compressive Strength of Damaged and Repaired Composite Plates. *J Compos Mater.* 1992;26(12):1796–825. Available from: https://doi.org/10.1177%2F002199839202601207

149. Ivañez I, Garcia-Castillo SK, Sanchez-Saez S, Barbero E. Experimental study of the impact behavior of repaired thin laminates with double composite patch. *Mechanics of Advanced Materials and Structures.* 2020;27(19):1701–8. Available from: https://doi.org/10.1080/15376494.2018.1524952

150. Kashfuddoja M, Ramji M. Design of optimum patch shape and size for bonded repair on damaged Carbon fibre reinforced polymer panels. *Mater Des.* 2014;54:174–83. Available from: http://dx.doi.org/10.1016/j.matdes.2013.08.043

151. Deng J, Zhou G, Bordas SPA, Xiang C, Cai D. Numerical evaluation of buckling behaviour induced by compression on patch-repaired composites. *Compos Struct.* 2017;168:582–96. Available from: http://dx.doi.org/10.1016/j.compstruct.2016.12.071

152. Tie Y, Hou Y, Li C, Zhou X, Sapanathan T, Rachik M. An insight into the low-velocity impact behavior of patch-repaired CFRP laminates using numerical and experimental approaches. *Compos Struct.* 2018;190:179–88. Available from: https://doi.org/10.1016/j.compstruct.2018.01.075

153. Liu X, Wang G. Progressive failure analysis of bonded composite repairs. *Compos Struct.* 2007;81(3):331–40. Available from: https://doi.org/10.1177%2F1464420716666400

154. Campilho RDSG, de Moura MFSF, Ramantani DA, Morais JJL, Domingues JJMS. Tensile behaviour of three-dimensional carbon-epoxy adhesively bonded single- and double-strap repairs. *Int J Adhes Adhes.* 2009;29(6):678–86. Available from: https://doi.org/10.1016/j.ijadhadh.2009.02.004

155. Kashfuddoja M, Ramji M. Assessment of local strain field in adhesive layer of an unsymmetrically repaired CFRP panel using digital image correlation. *Int J Adhes Adhes.* 2015;57:57–69. Available from: http://dx.doi.org/10.1016/j.ijadhadh.2014.10.005

156. Hu FZ, Soutis C. Strength prediction of patch-repaired CFRP laminates loaded in compression. *Compos Sci Technol.* 2000;60(7):1103–14. Available from: https://doi.org/10.1016/S0266-3538(00)00011-7

157. Hou Y, Tie Y, Li C, Sapanathan T, Rachik M. Low-velocity impact behaviors of repaired CFRP laminates: Effect of impact location and external patch configurations. *Compos B Eng.* 2019;163:669–80. Available from: https://doi.org/10.1016/j.compositesb.2018.12.153

158. Soutis C, Hu FZ. Design and performance of bonded patch repairs of composite structures. *Proc Inst Mech Eng G J Aerosp Eng.* 1997;211(4):263–71. Available from: https://doi.org/10.1243%2F0954410971532668

159. Broughton WR, Crocker LE, Gower MRL. *Design Requirements for Bonded and Bolted Composite Structures*. National Physical Laboratory. Report number: MATC(A)65, 2002.

160. Cheng P, Gong XJ, Aivazzadeh S, Xiao X. Experimental observation of tensile behavior of patch repaired composites. *Polym Test.* 2014;34:146–54. Available from: http://dx.doi.org/10.1016/j.polymertesting.2014.01.007

161. Chandler JG. *Fuselage Fix – Rewriting the Book with 787 Repair?* Available from: https://www.aviationpros.com/aircraft/maintenance-providers/mro/article/11251294/fuselage-fix-rewriting-the-book-with-787-repair [Accessed 5th April 2024].

162. George. *Meeting the challenge of composite fuselage repair* Available from: https://www.reinforcedplastics.com/content/features/meeting-the-challenge-of-composite-fuselage-repair/ [Accessed 5th April 2024].

163. Hart-Smith LJ. Bonded-bolted composite joints. *J Aircr.* 1985;22(11):993–1000. Available from: https://doi.org/10.2514/3.45237

164. Chan WS, Vedhagiri S. Analysis of composite bonded/bolted joints used in repairing. *J Compos Mater.* 2001;35(12):1045–61. Available from: https://doi.org/10.1177/002199801772662325

165. Li HCH, Callus PJ, Herszberg I. Through-thickness reinforcement repair of delaminated carbon-epoxy panels. *Compos Struct.* 2006;75(1–4):539–44. Available from: https://doi.org/10.1016/j.compstruct.2006.04.043

166. Slattery PG, McCarthy CT, O'Higgins RM. Assessment of residual strength of repaired solid laminate composite materials through mechanical testing. *Compos Struct.* 2016;147:122–30. Available from: http://dx.doi.org/10.1016/j.compstruct.2016.03.036

167. Hautier M, Lévêque D, Huchette C, Olivier P. Investigation of composite repair method by liquid resin infiltration. *Plastics, Rubber and Composites.* 2010;39(3–5):200–7. Available from: https://doi.org/10.1179/174328910X12647080902411

168. Thunga M, Larson K, Lio W, Weerasekera T, Akinc M, Kessler MR. Low viscosity cyanate ester resin for the injection repair of hole-edge delaminations in bismaleimide/carbon fiber composites. *Compos Part A Appl Sci Manuf.* 2013;52:31–7. Available from: http://dx.doi.org/10.1016/j.compositesa.2013.05.001

169. Moghe RP, Prakash R V., Sudevan D, Shambhayya HK. Characterization of resin-injection repair of impact damage in polymer matrix composite. *In: ASME 2015 International Mechanical Engineering Congress and Exposition, Proceedings (IMECE2015).* Houston, Texas; 2015.

170. Kim KS, Yoo JS, Yi YM, Kim CG. Failure mode and strength of uni-directional composite single lap bonded joints with different bonding methods. *Compos Struct.* 2006;72(4):477–85. Available from: https://doi.org/10.1016/j.compstruct.2005.01.023

171. Baldan A. Adhesively-bonded joints and repairs in metallic alloys, polymers and composite materials: Adhesives, adhesion theories and surface pretreatment. *J Mater Sci.* 2004;39:1–49. Available from: https://doi.org/10.1023/B:JMSC.0000007726.58758.e4

172. Kim JK, Kim HS, Lee DG. Investigation of optimal surface treatments for carbon/epoxy composite adhesive joints. *J Adhes Sci Technol.* 2003;17(3):329–52. Available from: https://doi.org/10.1163/156856103762864651

173. Hoang-Ngoc CT, Paroissien E. Simulation of single-lap bonded and hybrid (bolted/bonded) joints with flexible adhesive. *Int J Adhes Adhes.* 2010;30(3):117–29. Available from: http://dx.doi.org/10.1016/j.ijadhadh.2009.12.002

174. Sacchetti F, Grouve WJB, Warnet LL, Villegas IF. Effect of resin-rich bond line thickness and fibre migration on the toughness of unidirectional Carbon/PEEK joints. *Compos Part A Appl Sci Manuf.* 2018;109:197–206. Available from: https://doi.org/10.1016/j.compositesa.2018.02.035

175. Slange TK, Warnet L, Grouve WJB, Akkerman R. Influence of preconsolidation on consolidation quality after stamp forming of C/PEEK composites. *AIP Conf Proc.* 2016;1769(1):170022. Available from: https://doi.org/10.1063/1.4963578

176. Bersee HEN, Robroek LMJ. The role of the thermoplastic matrix in forming processes of composite materials. *Composites Manufacturing.* 1991;2(3–4):217–22. Available from: https://doi.org/10.1016/0956-7143(91)90143-5

177. Long AC. *Composites forming technologies*. Cambridge: Woodhead Publishing Ltd; 2007.

178. Cogswell FN. *Thermoplastic Aromatic Polymer Composites*. Melksham: Butterworth-Heinemann Ltd; 1992.

179. Okine RK. Analysis of Forming Parts from Advanced Thermoplastic Composite Sheet Materials. *Journal of Thermoplastic Composite Materials.* 1989;2(1):50–76. Available from: https://doi.org/10.1177%2F089270578900200104

180. Krebs J, Friedrich K, Bhattacharyya D. A direct comparison of matched-die versus diaphragm forming. *Compos Part A Appl Sci Manuf.* 1998;29(1–2):183–8. Available from: https://doi.org/10.1016/S1359-835X(97)82706-6

181. Burkhart A, Cramer D. Feasibility of continuous-fiber reinforced thermoplastic tailored blanks for automotive applications. *In: 5th SPE Automotive Composites Conference & Exhibition, 12-14 September 2005.* Troy, Michigan; 2005.

182. Hwang SF, Hwang KJ. Stamp forming of locally heated thermoplastic composites. *Compos Part A Appl Sci Manuf.* 2002;33(5):669–76. Available from: https://doi.org/10.1016/S1359-835X(02)00004-0

183. Bigg DM, Preston JR. Thermoplastic matrix composites. *Polym Compos.* 1989;10(4):261–8. Available from: https://doi.org/10.1002/pc.750100409

184. Zahlan N, O'Neill JM. Design and fabrication of composite components; the spring-forward phenomenon. *Composites.* 1989;20(1):77–81. Available from: https://doi.org/10.1016/0010-4361(89)90685-X

185. Hou M, Friedrich K. Stamp forming of continuous carbon fibre/polypropylene composites. *Composites Manufacturing.* 1991;2(1):3–9. Available from: https://doi.org/10.1016/0956-7143(91)90153-8

186. Scherer R, Friedrich K. Inter- and intraply-slip flow processes during thermoforming of CF/PP-laminates. *Composites Manufacturing.* 1991;2(2):92–6. Available from: https://doi.org/10.1016/0956-7143(91)90185-J

187. Wakeman MD, Zingraff L, Bourban PE, Månson JAE, Blanchard P. Stamp forming of carbon fibre/PA12 composites - A comparison of a reactive impregnation process and a commingled

yarn system. *Compos Sci Technol.* 2006;66(1):19–35. Available from: https://doi.org/10.1016/j.compscitech.2005.06.001

188. Meyer BC, Katsiropoulos Ch V., Pantelakis SpG. Hot forming behavior of non-crimp fabric peek/c thermoplastic composites. *Compos Struct.* 2009;90(2):225–32. Available from: http://dx.doi.org/10.1016/j.compstruct.2009.03.013

189. Haanappel SP, Thije R Ten, Akkerman R. Forming Predictions of Ud Reinforced Thermoplastic Laminates. *In: 14th European Conference on Composite Materials (ECCM14), 7-10 June 2010.* Budapest, Hungary; 2010. p. 367.

190. Han P, Butterfield J, Price M, Murphy A, Mullan M, Ireland N. Part Form Prediction Methods for Carbon Fibre. *In: 18th International Conference on Composite Materials (ICCM18), 21-26 August 2011.* Jeju, South Korea; 2011.

191. Han P, Butterfield J, Price M, Buchanan S, Murphy A. Experimental investigation of thermoforming carbon fibre-reinforced polyphenylene sulphide composites. *Journal of Thermoplastic Composite Materials.* 2013;28(4):529–47. Available from: https://doi.org/10.1177/0892705713486133

192. Han P, Butterfield J, Buchanan S, McCool R, Jiang Z, Price M, et al. The prediction of process-induced deformation in a thermoplastic composite in support of manufacturing simulation. *Proc Inst Mech Eng B J Eng Manuf.* 2013;227(10):1417–29. Available from: https://doi.org/10.1177/0954405413488362

193. Davey S, Das R, Cantwell WJ, Kalyanasundaram S. Forming studies of carbon fibre composite sheets in dome forming processes. *Compos Struct.* 2013;97:310–6. Available from: http://dx.doi.org/10.1016/j.compstruct.2012.10.026

194. Uriya Y, Ikeuch K, Yanagimoto J. Cold and warm V-bending test for carbon-fiber-reinforced plastic sheet. *Procedia Eng.* 2014;81:1633–8. Available from: http://dx.doi.org/10.1016/j.proeng.2014.10.203

195. Zhang Q, Gao Q, Cai J. Experimental and simulation research on thermal stamping of carbon fiber composite sheet. *Transactions of Nonferrous Metals Society of China.* 2014;24(1):217–23. Available from: http://dx.doi.org/10.1016/S1003-6326(14)63050-8

196. Gherissi A, Abbassi F, Ammar A, Zghal A. Numerical and Experimental Investigations on Deep Drawing of G1151 Carbon Fiber Woven Composites. *Applied Composite Materials.* 2016;23(3):461–76. Available from: http://dx.doi.org/10.1007/s10443-015-9468-x

197. Fortin GY, Fernlund G. Effect of tool temperature on dimensional fidelity and strength of thermoformed polyetheretherketone composites. *Polym Compos.* 2019;40(11):4376–89. Available from: https://doi.org/10.1002/pc.25300

198. Zheng B, Gao X, Li M, Deng T, Huang Z, Zhou H, et al. Formability and failure mechanisms of woven CF/PEEK composite sheet in solid-state thermoforming. *Polymers (Basel).* 2019;11(6):966. Available from: https://doi.org/10.3390/polym11060966

199. Friedrich K, Hou M. On stamp forming of curved and flexible geometry components from continuous glass fiber/polypropylene composites. *Compos Part A Appl Sci Manuf.* 1998;29(3):217–26. Available from: https://doi.org/10.1016/S1359-835X(97)00087-0

200. De Luca P, Lefébure P, Pickett AK. Numerical and experimental investigation of some press forming parameters of two fibre reinforced thermoplastics: APC2-AS4 and PEI-CETEX. *Compos Part A Appl Sci Manuf.* 1998;29(1–2):101–10. Available from: https://doi.org/10.1016/S1359-835X(97)00060-2

201. Wakeman MD, Blanchard P, Månson JAE. Void evolution during stamp-forming of thermoplastic composites. *In: 15th International Conference on Composite Materials (ICCM15), 27 June - 1 July 2005.* Durban, South Africa; 2005.

202. Harrison P, Gomes R, Curado-Correia N. Press forming a 0/90 cross-ply advanced thermoplastic composite using the double-dome benchmark geometry. *Compos Part A Appl Sci Manuf.* 2013;54:56–69. Available from: http://dx.doi.org/10.1016/j.compositesa.2013.06.014

203. Soulat D, Cheruet A, Boisse P. Simulation of continuous fibre reinforced thermoplastic forming using a shell finite element with transverse stress. *Comput Struct.* 2006;84(13–14):888–903. Available from: https://doi.org/10.1016/j.compstruc.2006.02.011

204. Salomi A, Garstka T, Potter K, Greco A, Maffezzoli A. Spring-in angle as molding distortion for thermoplastic matrix composite. *Compos Sci Technol.* 2008;68(14):3047–54. Available from: http://dx.doi.org/10.1016/j.compscitech.2008.06.024

205. Lightfoot JS, Wisnom MR, Potter K. A new mechanism for the formation of ply wrinkles due to shear between plies. *Compos Part A Appl Sci Manuf.* 2013;49:139–47. Available from: http://dx.doi.org/10.1016/j.compositesa.2013.03.002

206. Donadei V, Lionetto F, Wielandt M, Offringa A, Maffezzoli A. Effects of Blank Quality on Press-Formed PEKK/Carbon Composite Parts. *Materials.* 2018;11(7):1063. Available from: https://doi.org/10.3390/ma11071063

207. Wang P, Hamila N, Boisse P. Thermoforming simulation of multilayer composites with continuous fibres and thermoplastic matrix. *Compos B Eng.* 2013;52:127–36. Available from: http://dx.doi.org/10.1016/j.compositesb.2013.03.045

208. Yin H, Peng X, Du T, Chen J. Forming of thermoplastic plain woven carbon composites: An experimental investigation. *Journal of Thermoplastic Composite Materials.* 2013;28(5):730–42. Available from: https://doi.org/10.1177/0892705713503668

209. Hallander P, Akermo M, Mattei C, Petersson M, Nyman T. An experimental study of mechanisms behind wrinkle development during forming of composite laminates. *Compos Part A Appl Sci Manuf.* 2013;50:54–64. Available from: http://dx.doi.org/10.1016/j.compositesa.2013.03.013

210. Hineno S, Yoneyama T, Tatsuno D, Kimura M, Shiozaki K, Moriyasu T, et al. Fiber deformation behavior during press forming of rectangle cup by using plane weave carbon fiber reinforced thermoplastic sheet. *Procedia Eng.* 2014;81:1614–9. Available from: http://dx.doi.org/10.1016/j.proeng.2014.10.199

211. Haanappel SP, Ten Thije RHW, Sachs U, Rietman B, Akkerman R. Formability analyses of uni-directional and textile reinforced thermoplastics. *Compos Part A Appl Sci Manuf.* 2014;56:80–92. Available from: http://dx.doi.org/10.1016/j.compositesa.2013.09.009

212. Joppich T, Doerr D, Van Der Meulen L, Link T, Hangs B, Henning F. Layup and process dependent wrinkling behavior of PPS/CF UD tape-laminates during non-isothermal press forming into a complex component. *AIP Conf Proc.* 2016;1769(1):170012. Available from: https://doi.org/10.1063/1.4963568

213. Tatsuno D, Yoneyama T, Kawamoto K, Okamoto M. Production system to form, cut, and join by using a press machine for continuous carbon fiber-reinforced thermoplastic sheets. *Polym Compos.* 2016;39(7):2571–86. Available from: https://doi.org/10.1002/pc.24242

214. Behrens BA, Raatz A, Hübner S, Bonk C, Bohne F, Bruns C, et al. Automated Stamp Forming of Continuous Fiber Reinforced Thermoplastics for Complex Shell Geometries. *Fleischer J, Teti R, editors. Procedia CIRP.* 2017;66:113–8. Available from: http://dx.doi.org/10.1016/j.procir.2017.03.294

215. Tatsuno D, Yoneyama T, Kawamoto K, Okamoto M. Hot press forming of thermoplastic CFRP sheets. *Procedia Manuf.* 2018;15:1730–7. Available from: https://doi.org/10.1016/j.promfg.2018.07.254

216. Zenker T, Schön S. Stamp forming of thermoplastic automated fiber placement blanks: Influence of layup parameters on part quality. *AIP Conf Proc.* 2019;2113(1):020021. Available from: https://doi.org/10.1063/1.5112526

217. Lessard H, Lebrun G, Benkaddour A, Pham XT. Influence of process parameters on the thermostamping of a [0/90]12 carbon/polyether ether ketone laminate. *Compos Part A Appl Sci Manuf.* 2015;70:59–68. Available from: http://dx.doi.org/10.1016/j.compositesa.2014.12.009

218. Benkaddour A, Lebrun G, Laberge-Lebel L. Thermostamping of [0/90]n carbon/peek laminates: Influence of support configuration and demolding temperature on part consolidation. *Polym Compos.* 2018;39(9):3341–52. Available from: https://doi.org/10.1002/pc.24354

219. Schug A. *Unidirectional Fibre Reinforced Thermoplastic Composites : A Forming Study*. Doctoral dissertation. Technischen Universität München; 2019.

220. Murtagh AM, Mallon PJ. Characterisation of shearing and frictional behaviour during sheet forming. In: Bhattacharyya D. (ed.) *Composite Sheet Forming.* Elsevier; 1997. p. 163–216.

221. Friedrich K, Hou M, Krebs J. Thermoforming of continuous fibre/thermoplastic composite sheets. In: Bhattacharyya D. (ed.) *Composite Sheet Forming*. Elsevier; 1997. p. 91–162.

222. Cogswell FN. The experience of thermoplastic structural composites during processing. *Composites Manufacturing.* 1991;2(3–4):208–16. Available from: https://doi.org/10.1016/0956-7143(91)90142-4

223. Boisse P, Hamila N, Vidal-Sallé E, Dumont F. Simulation of wrinkling during textile composite reinforcement forming. Influence of tensile, in-plane shear and bending stiffnesses. *Compos Sci Technol.* 2011;71(5):683–92. Available from: http://dx.doi.org/10.1016/j.compscitech.2011.01.011

224. Potter K. Bias extension measurements on cross-plied unidirectional thermoset prepreg. *Compos Part A Appl Sci Manuf.* 2002;33(1):63–73. Available from: https://doi.org/10.1016/S1359-835X(01)00057-4

225. Sjölander J, Hallander P, Åkermo M. Forming induced wrinkling of composite laminates: A numerical study on wrinkling mechanisms. *Compos Part A Appl Sci Manuf.* 2016;81:41–51. Available from: http://dx.doi.org/10.1016/j.compositesa.2015.10.012

226. Harrison P, Abdiwi F, Guo Z, Potluri P, Yu WR. Characterising the shear-tension coupling and wrinkling behaviour of woven engineering fabrics. *Compos Part A Appl Sci Manuf.* 2012;43(6):903–14. Available from: https://doi.org/10.1016/j.compositesa.2012.01.024

227. Haanappel SP, Akkerman R. Shear characterisation of uni-directional fibre reinforced thermoplastic melts by means of torsion. *Compos Part A Appl Sci Manuf.* 2014;56:8–26. Available from: http://dx.doi.org/10.1016/j.compositesa.2013.09.007

228. Sachs U. *Friction and bending in thermoplastic composites forming processes*. PhD thesis. University of Twente; 2014.

229. American Society for Testing and Materials. ASTM D1894-14. *Standard Test Method for Static and Kinetic Coefficients of Friction of Plastic Film and Sheeting*. West Conshohocken, Pennsylvania: ASTM International; 2014.

230. Morris SR, Sun CT. An investigation of interply slip behaviour in AS4/PEEK at forming temperatures. *Composites Manufacturing.* 1994;5(4):217–24. Available from: https://doi.org/10.1016/0956-7143(94)90136-8

231. Vanclooster K, Lomov SV, Verpoest I. Investigation of interply shear in composite forming. *International Journal of Material Forming.* 2008;1:957–60. Available from: https://doi.org/10.1007/s12289-008-0216-8

232. Lebrun G, Bureau MN, Denault J. Thermoforming-stamping of Continuous Glass Fiber/Polypropylene Composites: Interlaminar and Tool-Laminate Shear Properties. *Journal of Thermoplastic Composite Materials.* 2004;17(2):137–65. Available from: https://doi.org/10.1177/0892705704035411

233. Fetfatsidis KA, Gamache LM, Gorczyca JL, Sherwood JA, Jauffrès D, Chen J. Design of an apparatus for measuring tool/fabric and fabric/fabric friction of woven-fabric composites during the thermostamping process. *International Journal of Material Forming.* 2013;6(1):1–11. Available from: https://doi.org/10.1007/s12289-011-1058-3

234. Akkerman R, Ten Thije R, Sachs U, De Rooij M. Friction in textile thermoplastic composites forming. *In: Proceedings of the 10th International Conference on Textile Composites (TEXCOMP10): Recent Advances in Textile Composites.* Lille, France; 2010. p. 271–9.

235. Murtagh AM, Lennon JJ, Mallon PJ. Surface friction effects related to pressforming of continuous fibre thermoplastic composites. *Composites Manufacturing.* 1995;6(3–4):169–75. Available from: https://doi.org/10.1016/0956-7143(95)95008-M

236. Ten Thije RHW, Akkerman R, Ubbink M, Van Der Meer L. A lubrication approach to friction in thermoplastic composites forming processes. *Compos Part A Appl Sci Manuf.* 2011;42(8):950–60. Available from: http://dx.doi.org/10.1016/j.compositesa.2011.03.023

237. Hutchings IM. *Tribology: friction and wear of engineering materials*. E. Arnold; 1992.

238. Gorczyca-Cole JL, Sherwood JA, Chen J. A friction model for thermostamping commingled glass-polypropylene woven fabrics. *Compos Part A Appl Sci Manuf.* 2007;38(2):393–406. Available from: https://doi.org/10.1016/j.compositesa.2006.03.006

239. Gorczyca JL, Sherwood JA, Liu L, Chen J. Modeling of friction and shear in thermostamping of composites - Part I. *J Compos Mater.* 2004;38(21):1911–29. Available from: https://doi.org/10.1177/0021998304048416

240. Liu S, Sinke J, Dransfeld C. An inter-ply friction model for thermoset based fibre metal laminate in a hot-pressing process. *Compos B Eng.* 2021;227:109400. Available from: https://doi.org/10.1016/j.compositesb.2021.109400

241. Lee JM, Kim BM, Lee CJ, Ko DC. A characterisation of tool-ply friction behaviors in thermoplastic composite. *Procedia Eng.* 2017;207:90–4. Available from: https://doi.org/10.1016/j.proeng.2017.10.743

242. Sachs U, Akkerman R, Haanappel SP, Ten Thije RHW, De Rooij MB. Friction in forming of UD composites. *AIP Conf Proc.* 2011;1353(1):984–9. Available from: https://doi.org/10.1063/1.3589644

243. Sachs U, Akkerman R, Fetfatsidis K, Vidal-Sallé E, Schumacher J, Ziegmann G, et al. Characterization of the dynamic friction of woven fabrics: Experimental methods and benchmark

results. *Compos Part A Appl Sci Manuf.* 2014;67:289–98. Available from: http://dx.doi.org/10.1016/j.compositesa.2014.08.026

244. Harrison P, Thije RT, Akkerman R, Long AC. Characterising and Modelling Tool-Ply Friction of Viscous Textile Composites. *World Journal of Engineering.* 2010;7(1):5–22. Available from: http://eprints.gla.ac.uk/58158/

245. Scherer R, Friedrich K. Experimental Background for Finite Element Analysis of the Interply-Slip Process during Thermoforming of Thermoplastic Composites. *In: Developments in the Science and Technology of Composite Materials, Proceedings of 4th European Conference on Composite Materials (ECCM4), 25-28 September 1990.* Stuttgart, Germany; 1990. p. 1001–6. Available from: https://doi.org/10.1007/978-94-009-0787-4_144

246. Chow S. *Frictional interaction between blank holder and fabric in stamping of woven thermoplastic composites*. Master's thesis. University of Massachusetts Lowell; 2002.

247. Akkerman R, Ubbink MP, de Rooij MB, ten Thije RHW. Tool-ply friction in thermoplastic composite forming. *International Journal of Material Forming.* 2007;1(SUPPL. 1):953–6.

248. Slange TK, Warnet LL, Grouve WJB, Akkerman R. Deconsolidation of C/PEEK blanks: on the role of prepreg, blank manufacturing method and conditioning. *Compos Part A Appl Sci Manuf.* 2018;113:189–99. Available from: https://doi.org/10.1016/j.compositesa.2018.06.034

249. Slange TK, Grouve WJB, Warnet LL, Wijskamp S, Akkerman R. Towards the combination of automated lay-up and stamp forming for consolidation of tailored composite components. *Compos Part A Appl Sci Manuf.* 2019;119:165–75. Available from: https://doi.org/10.1016/j.compositesa.2019.01.016

250. Loos AC, Dara PH. Processing of Thermoplastic Matrix Composites. *In: Thompson DO, Chimenti DE, editors. Review of Progress in Quantitative Nondestructive Evaluation.* Boston, Massachusetts: Springer; 1987. p. 1257–65. Available from: https://doi.org/10.1007/978-1-4613-1893-4_143

251. Gereke T, Döbrich O, Hübner M, Cherif C. Experimental and computational composite textile reinforcement forming: A review. *Compos Part A Appl Sci Manuf.* 2013;46(1):1–10. Available from: http://dx.doi.org/10.1016/j.compositesa.2012.10.004

252. Boisse P, Colmars J, Hamila N, Naouar N, Steer Q. Bending and wrinkling of composite fiber preforms and prepregs. A review and new developments in the draping simulations. *Compos B Eng.* 2018;141:234–49. Available from: https://doi.org/10.1016/j.compositesb.2017.12.061

253. Haanappel SP. *Forming of UD fibre reinforced thermoplastics*. PhD thesis. University of Twente; 2013.

254. Zouari B, Daniel JL, Boisse P. A woven reinforcement forming simulation method. Influence of the shear stiffness. *Comput Struct.* 2006;84(5–6):351–63. Available from: https://doi.org/10.1016/j.compstruc.2005.09.031

255. Boisse P, Hamila N, Madeo A. Modelling the development of defects during composite reinforcements and prepreg forming. *Philosophical Transactions of the Royal Society A: Mathematical, Physical and Engineering Sciences.* 2016;374(2071):1–14. Available from: https://doi.org/10.1098/rsta.2015.0269

256. Liang B, Hamila N, Peillon M, Boisse P. Analysis of thermoplastic prepreg bending stiffness during manufacturing and of its influence on wrinkling simulations. *Compos Part A Appl Sci Manuf.* 2014;67:111–22. Available from: http://dx.doi.org/10.1016/j.compositesa.2014.08.020

257. Martin TA, Bhattacharyya D, Pipes RB. Deformation characteristics and formability of fibre-reinforced thermoplastic sheets. *Composites Manufacturing.* 1992;3(3):165–72. Available from: https://doi.org/10.1016/0956-7143(92)90079-A

258. Akkerman R, Haanappel SP. Thermoplastic composites manufacturing by thermoforming. In: Boisse P. (ed.) *Advances in Composites Manufacturing and Process Design*. Elsevier Ltd.; 2015. p. 111–129.

259. Liu X, Chen F. A review of void formation and its effects on the mechanical performance of carbon fiber reinforced plastic. *Engineering Transactions.* 2016;64(1):33–51. Available from: https://api.semanticscholar.org/CorpusID:56235054

260. Ye L, Chen ZR, Lu M, Hou M. De-consolidation and re-consolidation in CF/PPS thermoplastic matrix composites. *Compos Part A Appl Sci Manuf.* 2005;36(7):915–22. Available from: https://doi.org/10.1016/j.compositesa.2004.12.006

261. Zheng B, Li M, Deng T, Zhou H, Huang Z, Zhou H, et al. Process–structure–property relationships of thermoformed woven carbon-fiber-reinforced polyether-ether-ketone composites. *Polym Compos.* 2019;40(10):3823–34. Available from: https://doi.org/10.1002/pc.25241

262. Trudel-Boucher D, Fisa B, Denault J, Gagnon P. Experimental investigation of stamp forming of unconsolidated commingled E-glass/polypropylene fabrics. *Compos Sci Technol.* 2006;66(3–4):555–70. Available from: https://doi.org/10.1016/j.compscitech.2005.05.036

263. Beehag A, Ye L. Role of cooling pressure on interlaminar fracture properties of commingled CF/PEEK composites. *Compos Part A Appl Sci Manuf.* 1996;27(3):175–82. Available from: https://doi.org/10.1016/1359-835X(95)00027-Y

264. Jiang W, Huang Z, Wang Y, Zheng B, Zhou H. Voids formation and their effects on mechanical properties in thermoformed carbon fiber fabric-reinforced composites. *Polym Compos.* 2019;40(S2):E1094–102. Available from: https://doi.org/10.1002/pc.24876

265. Sang L, Wang C, Wang Y, Wei Z. Thermo-oxidative ageing effect on mechanical properties and morphology of short fibre reinforced polyamide composites-comparison of carbon and glass fibres. *RSC Adv.* 2017;7(69):43334–44. Available from: https://doi.org/10.1039/C7RA07884F

266. Rathi S, Dahiya JB. Effect on thermal behaviour of polyamide 66/clay nanocomposites with inorganic flame retardant additives. *Indian Journal of Chemistry - Section A Inorganic, Physical,*

Theoretical and Analytical Chemistry. 2012;51A(12):1677–85. Available from: http://nopr.niscair.res.in/handle/123456789/15206

267. Dai G, Zhan L, Guan C, Huang M. The effect of moulding process parameters on interlaminar properties of CF/PEEK composite laminates. *High Perform Polym.* 2020;32(7):835–41. Available from: https://doi.org/10.1177%2F0954008320903768

268. Jar PYB, Mulone R, Davies P, Kausch HH. A study of the effect of forming temperature on the mechanical behaviour of carbon-fibre/peek composites. *Compos Sci Technol.* 1993;46(1):7–19. Available from: https://doi.org/10.1016/0266-3538(93)90076-S

269. Vu-Khanh T, Denault J. Effect of Molding Parameters on the Interfacial Strength in PEEK/Carbon Composites. *Journal of Reinforced Plastics and Composites.* 1993;12(8):916–31. Available from: https://doi.org/10.1177/073168449301200806

270. Reynolds N, Awang-Ngah S, Williams G, Hughes DJ. Direct Processing of Structural Thermoplastic Composites Using Rapid Isothermal Stamp Forming. *Applied Composite Materials.* 2020;27(1–2):107–15. Available from: https://doi.org/10.1007/s10443-020-09797-4

271. Patel P, Hull TR, McCabe RW, Flath D, Grasmeder J, Percy M. Mechanism of thermal decomposition of poly(ether ether ketone) (PEEK) from a review of decomposition studies. *Polym Degrad Stab.* 2010;95(5):709–18. Available from: https://doi.org/10.1016/j.polymdegradstab.2010.01.024

272. Montaudo G, Puglisi C, Samperi F. Primary thermal degradation processes occurring in poly(phenylenesulfide) investigated by direct pyrolysis–mass spectrometry. *J Polym Sci A Polym Chem.* 1994;32(10):1807–15. Available from: https://doi.org/10.1002/pola.1994.080321002

273. Hou M, Friedrich K, Scherer R. Optimization of stamp forming of thermoplastic composite bends. *Compos Struct.* 1994;27(1–2):157–67. Available from: https://doi.org/10.1016/0263-8223(94)90077-9

274. Land P, Crossley R, Branson D, Ratchev S. Technology review of thermal forming techniques for use in composite component manufacture. *SAE International Journal of Materials and Manufacturing.* 2016;9(1):81–9. Available from: https://doi.org/10.4271/2015-01-2610

275. Chen J, Sherwood JA, Buso P, Chow S, Lussier D. Stamping of Continuous Fiber Thermoplastic Composites. *Polym Compos.* 2000;21(4):539–47. Available from: https://doi.org/10.1002/pc.10209

276. Hou M, Friedrich K. 3-D stamp forming of thermoplastic matrix composites. *Applied Composite Materials.* 1994;1(2):135–53. Available from: https://doi.org/10.1007/BF00567575

277. Vieille B, Albouy W, Taleb L. Investigations on stamping of C/PEEK laminates: Influence on meso-structure and macroscopic mechanical properties under severe environmental conditions. *Compos B Eng.* 2014;63:101–10. Available from: http://dx.doi.org/10.1016/j.compositesb.2014.03.025

278. Gao SL, Kim JK. Cooling rate influences in carbon fibre/PEEK composites. Part 1. Crystallinity and interface adhesion. *Compos Part A Appl Sci Manuf.* 2000;31(6):517–30. Available from: https://doi.org/10.1016/S1359-835X(00)00009-9

279. Gao SL, Kim JK. Correlation among crystalline morphology of PEEK, interface bond strength, and in-plane mechanical properties of carbon/PEEK composites. *J Appl Polym Sci.* 2002;84(6):1155–67. Available from: https://doi.org/10.1002/app.10406

280. Tatsuno D, Yoneyama T, Kawamoto K, Okamoto M. Effect of Cooling Rate on the Mechanical Strength of Carbon Fiber-Reinforced Thermoplastic Sheets in Press Forming. *J Mater Eng Perform.* 2017;26(7):3482–8. Available from: https://doi.org/10.1007/s11665-017-2664-0

281. Weber J, Schlimbach J. Co-consolidation of CF/PEEK tape-preforms and CF/PEEK organo sheets to manufacture reinforcements in stamp-forming process. *Advanced Manufacturing: Polymer and Composites Science.* 2019;5(4):172–83. Available from: https://doi.org/10.1080/20550340.2019.1673961

282. Gao S-L, Kim J-K. Cooling rate influences in carbon fibre/PEEK composites. Part II: interlaminar fracture toughness. *Compos Part A Appl Sci Manuf.* 2001;32(6):763–74. Available from: https://doi.org/10.1016/S1359-835X(00)00188-3

283. Parlevliet PP, Bersee HEN, Beukers A. Residual stresses in thermoplastic composites-A study of the literature-Part I: Formation of residual stresses. *Compos Part A Appl Sci Manuf.* 2006;37(11):1847–57. Available from: https://doi.org/10.1016/j.compositesa.2005.12.025

284. SHD Composites. MTC510 Epoxy Component Prepreg. Sleaford, UK: SHD Composites; 2022.

285. American Society for Testing and Materials. ASTM D7136/D7136M – 12. *Standard Test Method for Measuring the Damage Resistance of a Fiber-Reinforced Polymer Matrix Composite to a Drop-Weight Impact Event*. West Conshohocken, Pennsylvania: ASTM International; 2015.

286. Composites World. *Woven fibres: The basics*. Available from: https://www.compositesworld.com/articles/woven-fabrics-the-basics [Accessed 6th May 2021].

287. Toray Advanced Composites. Toray Cetex TC1100 PPS Product Data Sheet. Nijverdal, The Netherlands: Toray Advanced Composites; 2021.

288. Toray Advanced Composites. *Stamp Forming Processing Guide*. Toray Advanced Composites; 2019. p. 9.

289. American Society for Testing and Materials. ASTM D7137/D7137M – 17. *Standard test method for compressive residual strength properties of damaged polymer matrix composite plates*. West Conshohocken, Pennsylvania: ASTM International, 2017.

290. Dear JP, MacGillivray JH. Strain gauging for accurate determination of K and G in impact tests. *J Mater Sci.* 1991;26:2124–32. Available from: https://doi.org/10.1007/BF00549178

291. Williams JG, Adams GC. The analysis of instrumented impact tests using a mass-spring model. *Int J Fract.* 1987;33:209–22. Available from: https://doi.org/10.1007/BF00013171

292. Dear JP. High-speed photography of impact effects in three-point bend testing of polymers. *J Appl Phys.* 1990;67(9):4304–12. Available from: https://doi.org/10.1063/1.344946

293. Liu H, Liu J, Ding Y, Hall ZE, Kong X, Zhou J, et al. A three-dimensional elastic-plastic damage model for predicting the impact behaviour of fibre-reinforced polymer-matrix composites. *Compos B Eng.* 2020;201:108389. Available from: https://doi.org/10.1016/j.compositesb.2020.108389

294. Hall ZEC, Liu J, Brooks RA, Liu H, Crocker JWM, Joesbury AM, et al. The effectiveness of patch repairs to restore the impact properties of carbon-fibre reinforced-plastic composites. *Eng Fract Mech.* 2022;270:108570. Available from: https://doi.org/10.1016/j.engfracmech.2022.108570

295. Reis L, De Freitas M. Damage growth analysis of low velocity impacted composite panels. *Compos Struct.* 1997;38(1–4):509–15.

296. Ersoy N, Potter K, Wisnom MR, Clegg MJ. An experimental method to study the frictional processes during composites manufacturing. *Compos Part A Appl Sci Manuf.* 2005;36(11):1536–44. Available from: https://doi.org/10.1016/j.compositesa.2005.02.010

297. American Society for Testing and Materials. ASTM D3518/D3518M – 18. *Standard Test Method for In-Plane Shear Response of Polymer Matrix Composite Materials by Tensile Test of a ± 45° Laminate*. West Conshohocken, Pennsylvania: ASTM International, 2007.

Appendices

Appendix A - Design of pull-out rig for inter-ply friction testing

A pull-out rig was designed to test the inter-ply friction of CF/PPS under different conditions. This rig was not used for any experimental work so a description of the design process is outlined below.

A.1 Initial ideas for friction testing machine/rig

A friction testing rig was designed in order to characterise the inter-ply frictional behaviour of material for stamp forming. Initially three options were considered after studying similar rigs in the literature [228,230–233,235,239,296]:

- Hot press in biaxial machine
- Friction sled on hot plate
- Vertical pull-out/pull-through on Universal Testing Machine

Utilising a hot press in a biaxial machine was considered a relatively simple option as the equipment was already available and the temperature and pressure would be easy to control and measure. However, issues for this option included potential space restrictions which could make attaching the samples to the horizontal pull-out actuator difficult, requiring large samples and the pull-out load cell not being accurate enough to measure the relatively small inter-ply frictional force.

Using a friction sled on a hot plate was also considered a simple option and could be undertaken in line with ASTM Standard D1894 [229], which is designed for measuring the friction coefficients between plastic films. Only relatively small samples would be required and the pressure could be easily controlled by varying the weight on top of the friction sled. Additionally, this pressure would remain uniform throughout the test. The temperature could be easily controlled through the hot plate, however, only heating from one side of the sample may cause issues due to temperature non-

uniformity throughout the sample. Furthermore, measuring the pulling force could be difficult as some connection to a Universal Testing Machine is required. Designing this connection of pulleys would likely be complex. A further issue is how to attach the composite sample to the friction sled, particularly at higher temperatures.

Creating a vertical pull-out/pull-through device on a Universal Testing Machine is a more complex solution but does allow accurate pull-out forces to be measured. Pressure can be applied relatively easily through pneumatic actuators or springs. Only small samples are required, leading to less material usage. A solution for heating the plates needs to be designed and controlling this heating system could be complex. A structure to support the set-up also needs to be designed. Measuring the temperature and pressure could also be an issue. Thermocouples can measure the temperature but the plates need to be designed to accommodate these. Pressure measurement is difficult, but strain gauges could be used. Other load cells could also be an option if they are small enough.

Overall, a vertical pull-out rig was chosen as the most appropriate design. The design will give accurate pull-out force measurements and only a relatively small amount of material is required for each test. Although it could be complex to design, the other options were expected not to give as accurate results.

A.2 Detailed design for vertical pull-out rig

Two of the main design decisions were choosing how to apply the pressure and heating.

Although some rectangular heating elements were identified, these were not flat so it was decided that the most appropriate heating method was to use a hot plate, made of mild steel due to high heat conductance and low cost. This was heated by cartridge heaters which are placed in holes drilled into the plate. To design the cartridge configuration within the hot plates, thermal simulations were undertaken using Solidworks. The time taken to heat the hot plate to the required temperature was approximated. Six 75 mm long, 6.5 mm diameter 100 W cartridges were chosen (three in each hot plate) so that a relatively even temperature distribution could be obtained at the surface of the hot plates. The cartridges were not located in the middle of the plate, but instead moved further away from

the side which contacts the sample material, see Figure A-1. This allows a more even temperature distribution to be achieved over the hot plate surface and subsequently throughout the sample. Later testing showed a relatively constant surface temperature is achieved. Thermocouples were used to accurately measure the temperature at various points in the hot plate or the samples. Holes were drilled part-way through the rear surface of the mild steel hot plate (up to 4 mm before the front surface) for the thermocouples and channels were milled from the thermocouple holes to the edges of the hot plate to accommodate the thermocouples without affecting the pressure distribution, see Figure A-1 and Figure A-2.

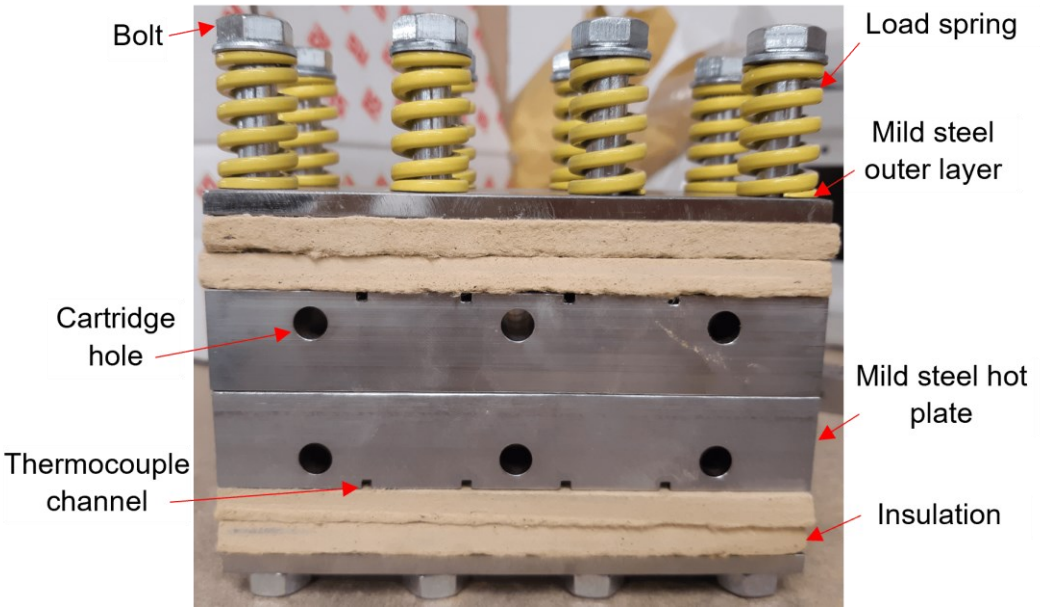


Figure A-1: Pull-out rig before the cartridges were inserted into place.

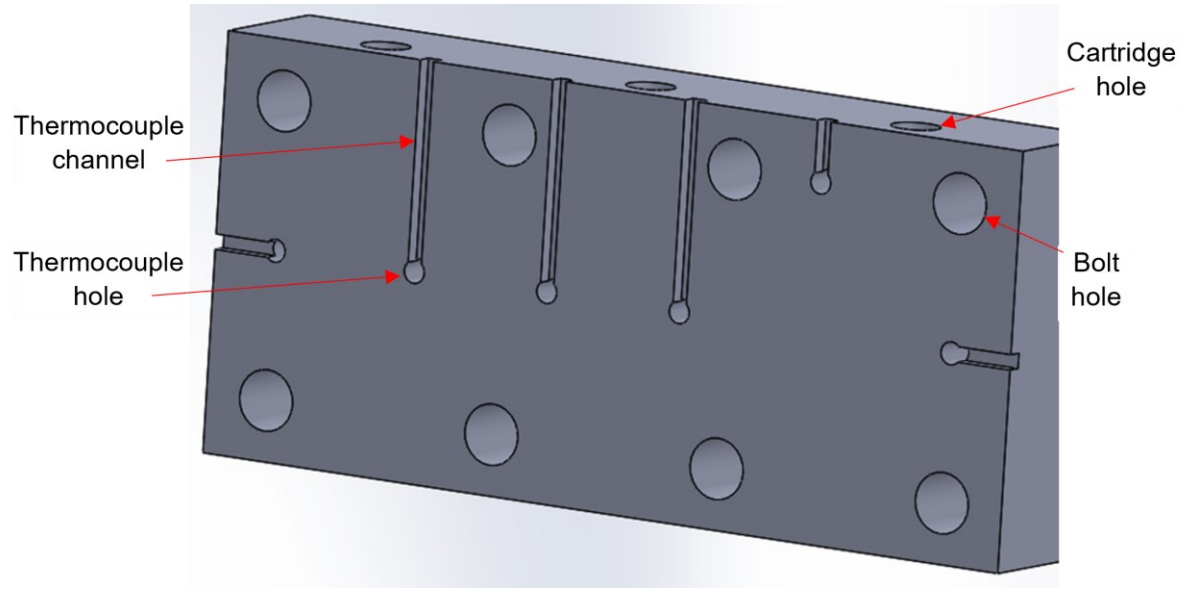


Figure A-2: Solidworks model of a single hot plate showing the thermocouple holes and channels, cartridge holes and bolt holes.

A number of potential pressure actuators were identified including pneumatic grips and air bellows, but due to the complexities involves in using these devices, springs and bolts were chosen instead. These are simple to install and use as well as being hard wearing. A variety of load cells were considered to measure the pressure being applied. However, those available were too large to be included in the rig and also may not have been able to function at the high temperatures involved in the tests. Instead, it was decided that the applied pressure could be calculated by installing strain gauges on the sides of the plates, by measuring the compression of the springs or by measuring the torque needed to tighten each bolt. To provide higher pressures of up to the intended 2 MPa, eight extra heavy load springs were chosen. At maximum safe compression, the combined load which can be applied is 6,272 N, which equates to 2.28 MPa when taking into account the pull-out area of the sample. The springs were compressed by placing a bolt inside each and through 8 holes drilled through the hot plates, see Figure A-1. The bolts also held all the parts of the rig together.

Insulation was required to reduce heat loss from the hot plates and ensure they could reach the required temperatures. Given that the insulation would have to resist compressive loads, brittle insulating blocks were not considered appropriate. Instead, two layers of millboard thermal insulation were used on either side of the hot plates, see Figure A-1, as this material can be easily machined and

cut to the required size, has a low thermal conductivity and will not fracture under compressive load. An outer layer of mild steel was used to improve the load distribution from the springs, see Figure A-1.

The general dimensions were chosen through consideration of the spring diameter required, the lengths and dimensions of cartridges available and the size of the pull-out samples. The size of the samples to test was chosen based on the sample size used in ASTM Standard D3518 [297] which governs in-plane shear testing of FRPs. These samples would be formed of three plies, two of which would be held by the bottom grip. The third ply would be pressed between the other two plies by the pull-out rig and pulled-out from between them by the top grip (i.e. only the central ply would be held by the top grip). The samples would be formed in a specially made stainless-steel mould using a hot press.

To support the pull-out rig on the Universal Testing Machine, a steel plate and four support legs were manufactured and the rig sits upon the centre of the plate, see Figure A-3. A square hole was drilled beneath the sample to allow the material to be held stationary by the lower grip of the machine. A layer of thermal insulation reduces heat transfer from the rig to the support plate. Bolts secure the pull-out rig to the plate through a block of metal at the rear of the rig. This constrains the rig and restricts any upward movement, as well as preventing the rig tipping over. Figure A-3 shows the pull-out rig in position on the Instron Universal Testing Machine (without the grips and CFRP material).

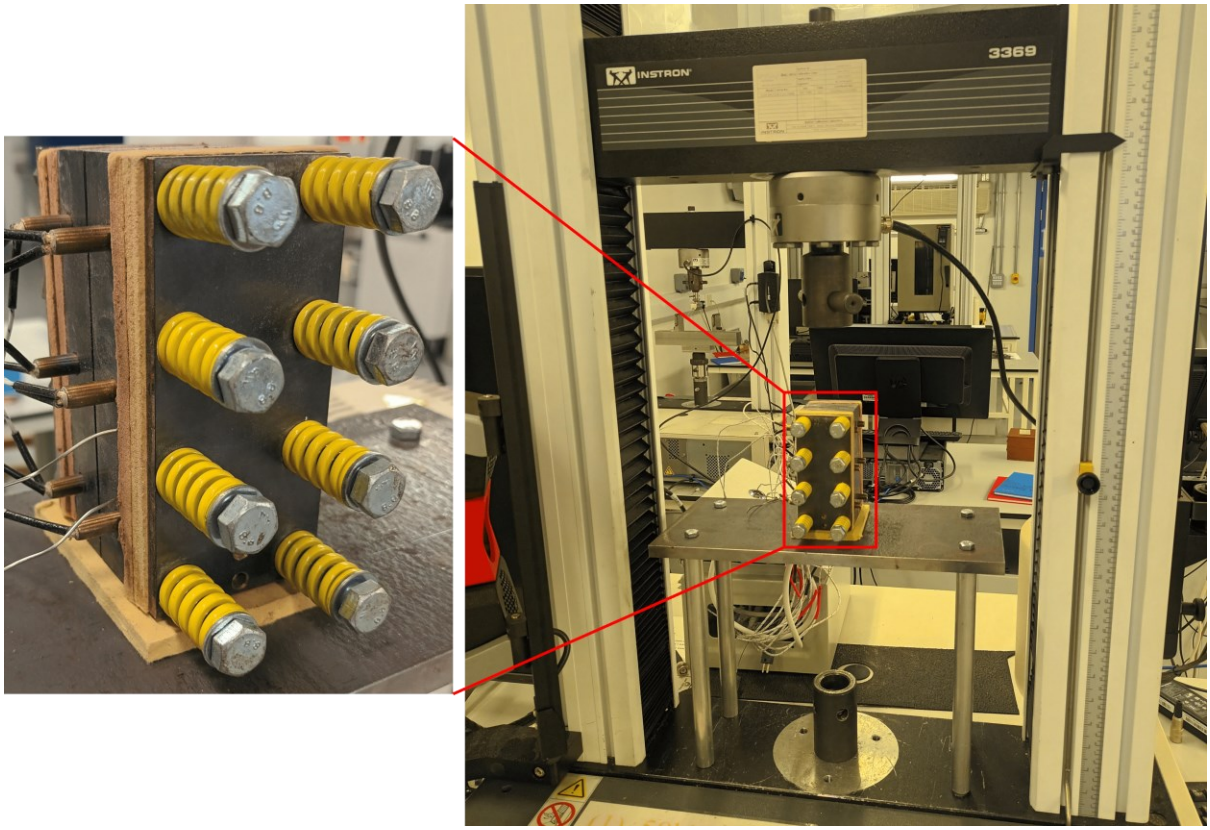


Figure A-3: Pull-out rig in position on the support plate on an Instron Universal Testing Machine. The grips and CFRP samples are not shown in this image.

A.3 Testing

The planned tests were not able to be started during the PhD.

Appendix B - Repeat data for Chapter 4

Figure B-1 shows repeat data for impacts at 5, 10 and 15 J on 2.3 mm thick CF/Epoxy panels.

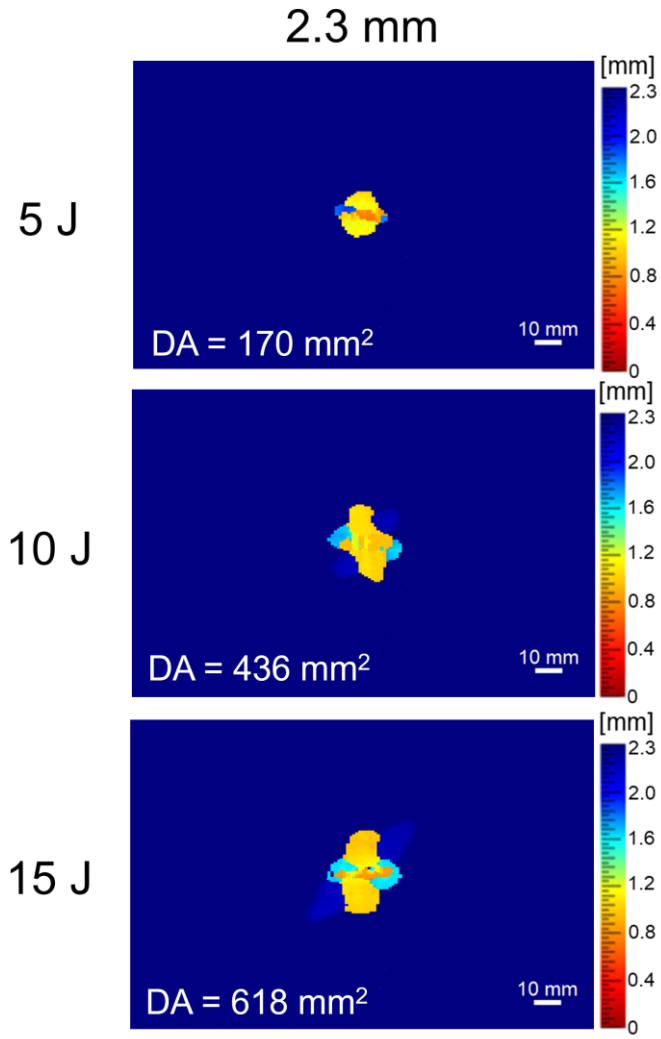


Figure B-1: C-scan damage maps obtained from the CF/Epoxy composite panels with a thickness of 2.3 mm with impact energies of 5, 10 and 15 J. The right-hand side scale indicates the location of the interlaminar delamination as a function of the depth through the thickness of the panel (0 to 2.3 mm). The footprint of the delamination damage area (DA) detected is given in the bottom left-hand corner for each panel. The bottom right of each damage map shows a 10 mm scale bar.

Figure B-2 shows repeat data from impacts at 5, 10, 15 and 20 J on 4.6 mm thick CF/Epoxy panels.

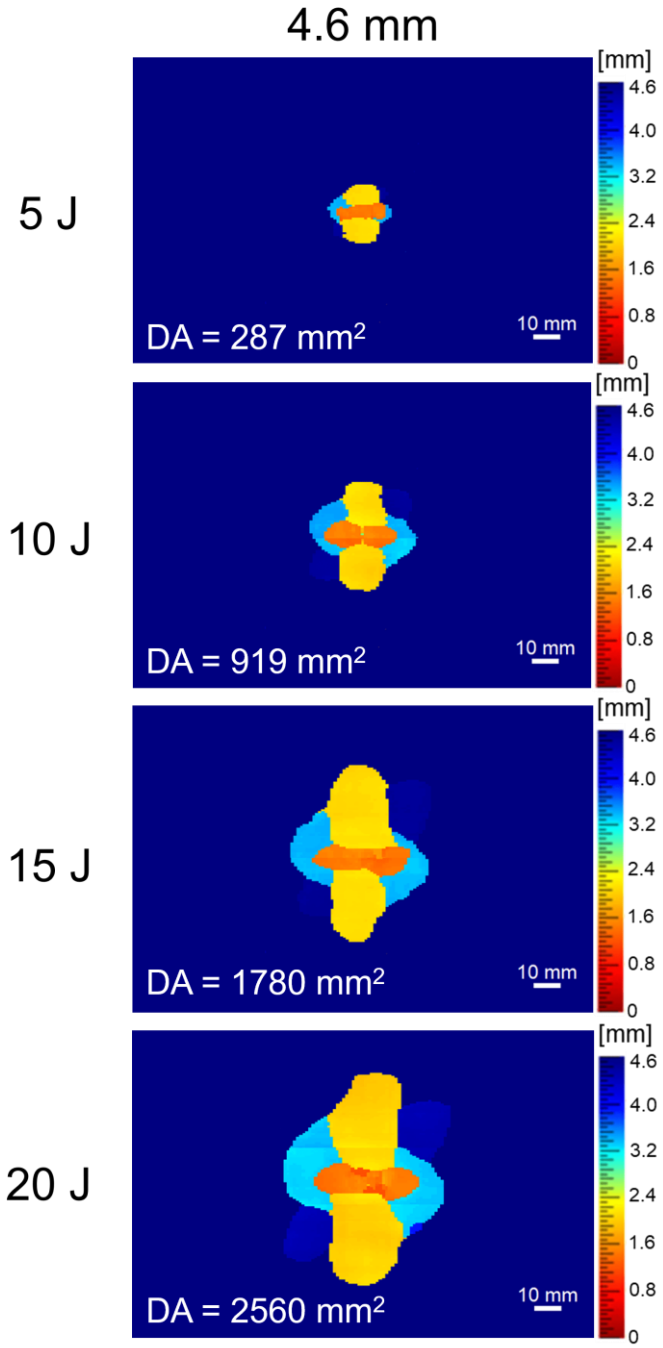


Figure B-2: C-scan damage maps obtained from the CF/Epoxy composite panels with a thickness of 4.6 mm with impact energies of 5, 10, 15 and 20 J. The right-hand side scale indicates the location of the interlaminar delamination as a function of the depth through the thickness of the panel (0 to 4.6 mm). The footprint of the delamination damage area (DA) detected is given in the bottom left-hand corner for each panel. The bottom right of each damage map shows a 10 mm scale bar.

Appendix C - Discussion of 2.3 mm thick CF/Epoxy panels impacted at 15 J

Figure C-1 presents the C-scan damage maps for the two 2.3 mm thick CF/Epoxy panels impacted multiple times at 15 J, showing the delamination damage obtained after one, two and three impacts. After the first and second impacts, the damage areas are very similar. However, after the third impacts a large difference in damage area of over 400 mm^2 is visible. This difference in damage area is investigated in this section.

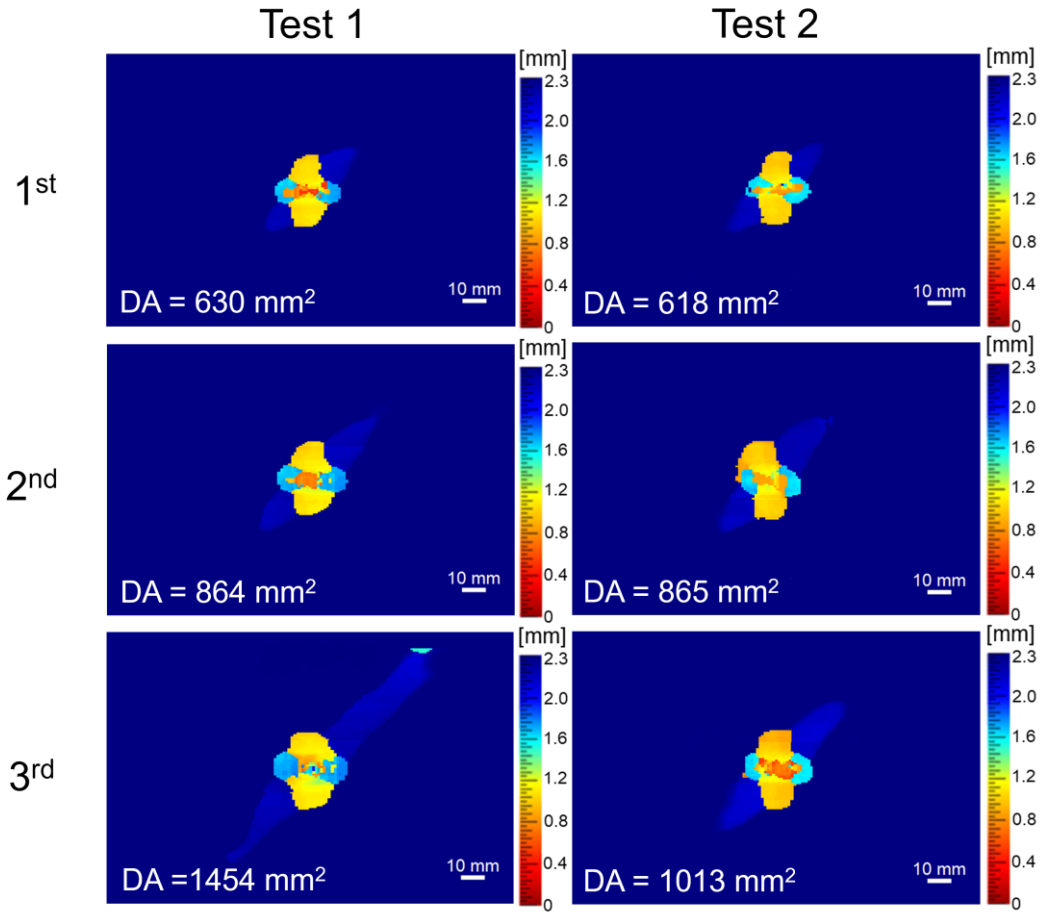


Figure C-1: C-scan damage maps obtained from the CF/Epoxy replicate composite panels with a thickness of 2.3 mm after one, two and three impacts at 15 J. The right-hand side scale indicates the location of the interlaminar delamination as a function of the depth through the thickness of the panel (0 to 2.3 mm). The footprint of the delamination damage area (DA) detected is given in the bottom left-hand corner for each panel. The bottom right of each damage map shows a 10 mm scale bar.

Figure C-2 displays (a) the load versus time and (b) the load versus displacement traces for the first impact at 15 J for the two CF/Epoxy panels. For Test 1, the first large load drop occurs at around 0.5 kN less than for Test 2. Also, Test 1 shows a slightly larger maximum displacement. This could indicate that the panel used in Test 1 is slightly weaker or contains a defect.

Similarly, Figure C-3 shows (a) the load versus time and (b) the load versus displacement traces for the second impact at 15 J for both panels. Test 1 has a lower peak load and again shows a larger maximum displacement. From Figure C-1 the delamination areas in both panels are similar, however, the indentation depths are vastly different - 0.4 mm for Test 1 versus 0.22 mm for Test 2. Also, the indentation profile for Test 1, shown in Figure 5-27, shows a rough indentation with surface damage whereas the indentation profile in Test 2 was smooth (this was not measured using the Confocal microscope). These results suggest that, although the delamination damage areas are similar, there seems to be some more damage or a defect in the Test 1 panel. In particular, the Test 1 panel may have had more severe intralaminar damage, causing the rough indentation profile and slightly affecting the maximum displacement. From Figure 5-35, the fibre fracture in the central plies likely contributed to this, provided it was caused by the second impact.

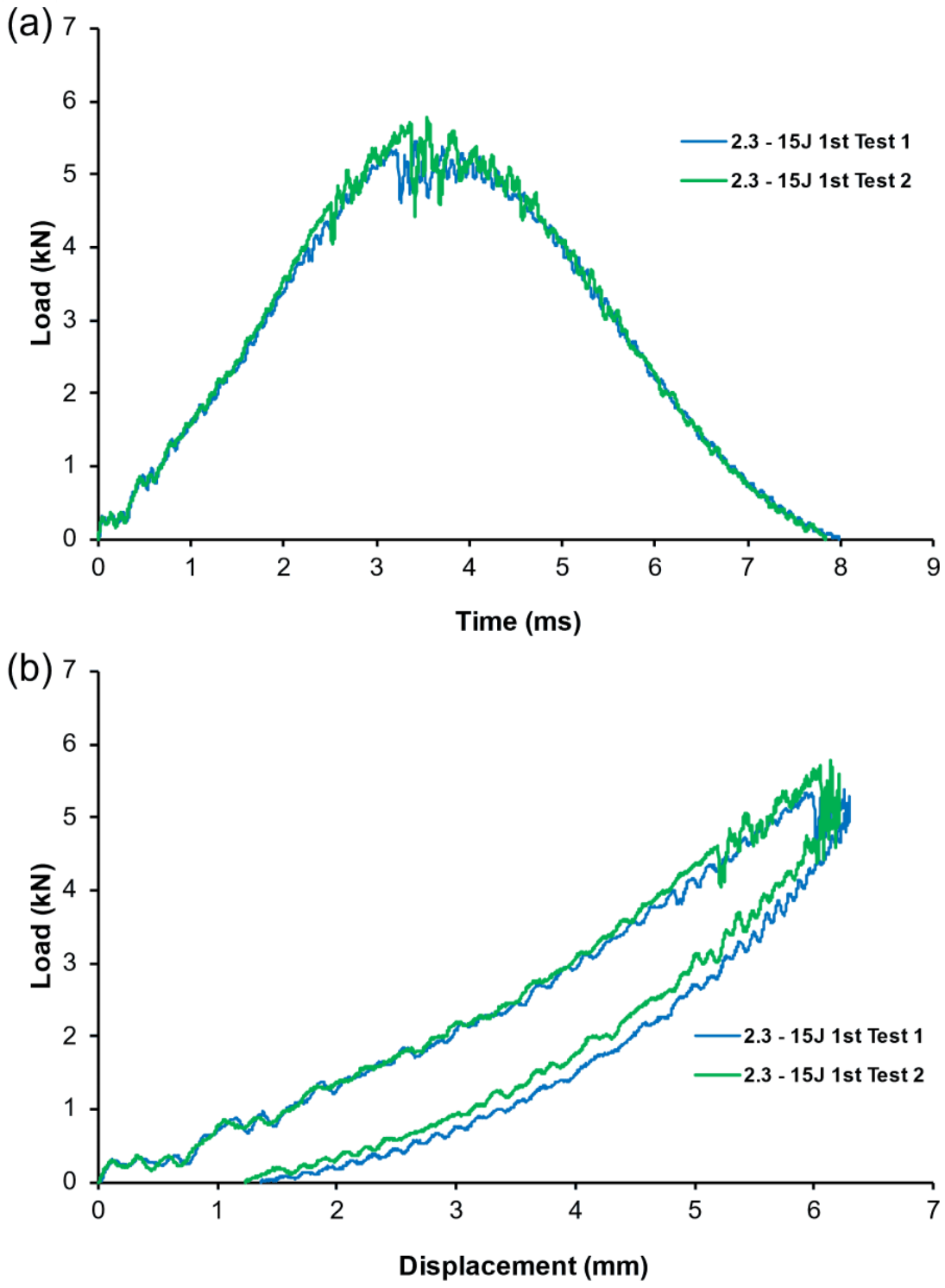


Figure C-2: (a) Load versus time traces and (b) load versus displacement traces for a first impact at 15 J on two 2.3 mm thick CF/Epoxy composite panels.

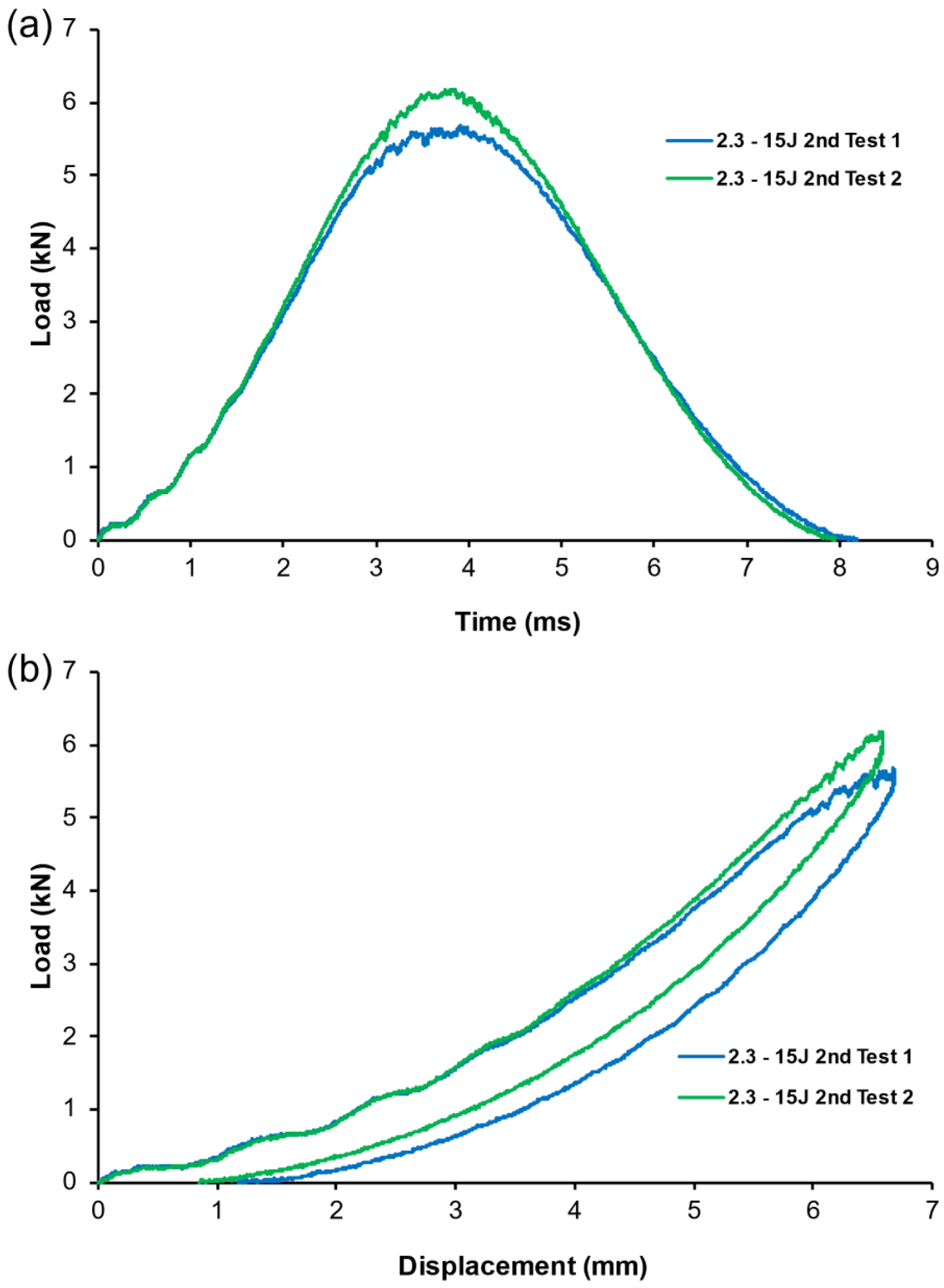


Figure C-3: (a) Load versus time traces and (b) load versus displacement traces for a second impact at 15 J on two 2.3 mm thick CF/Epoxy composite panels.

Finally, Figure C-4 shows (a) load versus time and (b) load versus displacement traces for the third impact at 15 J for both panels. These show a very different behaviour upon approach to the peak load. Whereas Test 2 exhibits a fairly elastic bell curve (similar to how the panel behaved during the second impact), Test 1 shows a drop in load indicative of impactor penetration and severe damage. The high level of damage was confirmed by both the C-scans and by observation of the rear surface where a strip of the rear-most ply had come away from the rest of the panel, see Figure 5-6. The large increase in maximum displacement for Test 1 compared to Test 2 highlights both the increase in delamination damage and the lack of resistance the panel therefore presented to the impactor. The indentation profiles and depths, shown in Figure 5-27 also highlight the large difference between the panels, with the Test 1 panel exhibiting a rough profile and depth of around 0.50 mm whereas the Test 2 panel continued to show a smooth profile with a depth of only 0.24 mm. Although the Test 1 panel may have had more severe intralaminar damage present, the large reduction in impact resistance compared to the Test 2 panel could also have been due to a defect within the panel.

These differences serve to highlight the complicated behaviour of impact damage in CFRP and how similar materials can show very different damage responses to the same impacts given only small changes in their microstructure. The sensitive nature of these panels proves how important it is to establish a thorough understanding of all aspects of impact damage production before applying findings to aircraft which are in service.

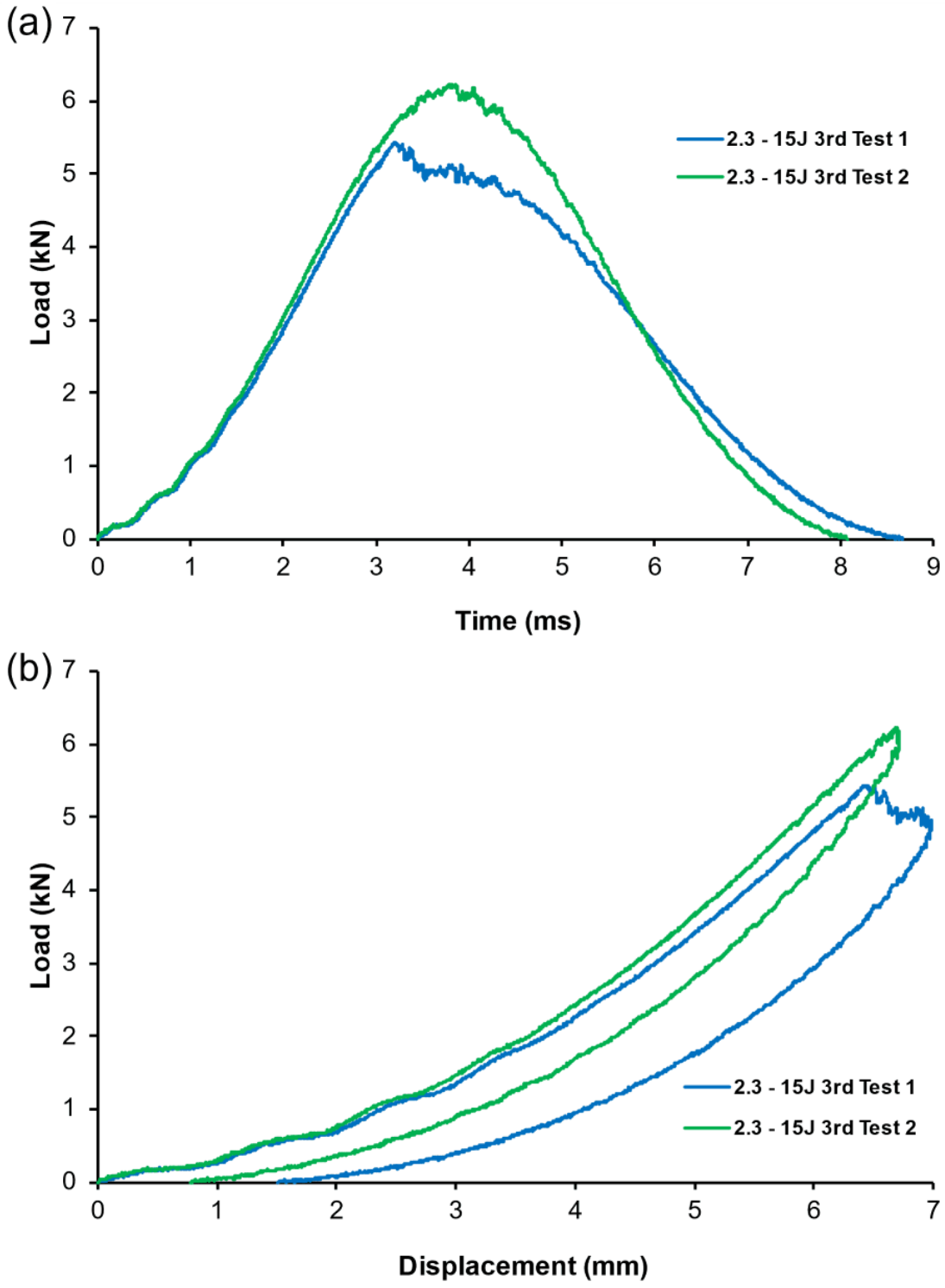


Figure C-4: (a) Load versus time traces and (b) load versus displacement traces for a third impact at 15 J on two 2.3 mm thick CF/Epoxy composite panels.

Appendix D - Load versus time and load versus displacement traces for multiple impacts at 2 J on CF/Epoxy

Load versus time and load versus displacement traces are shown in Figure D-1 for first, second and third impacts at 2 J on both thicknesses of CF/Epoxy panel. The impact traces for the 4.6 mm thick panels are very similar, which is to be expected given the lack of delamination damage formed during any of the three impacts, see Figure 4-2. In contrast, some slight differences in the traces for the 2.3 mm panels are noticeable. Firstly, the impact duration increases slightly for subsequent impacts. Secondly, the bending stiffness is slightly decreased and the maximum displacement is slightly increased for subsequent impacts. All of these observations can be explained by the small increase in delamination damage between the three impact events, see Figure 4-1, Figure 5-1 and Figure 5-4. This is discussed further in Section 5.3.2.

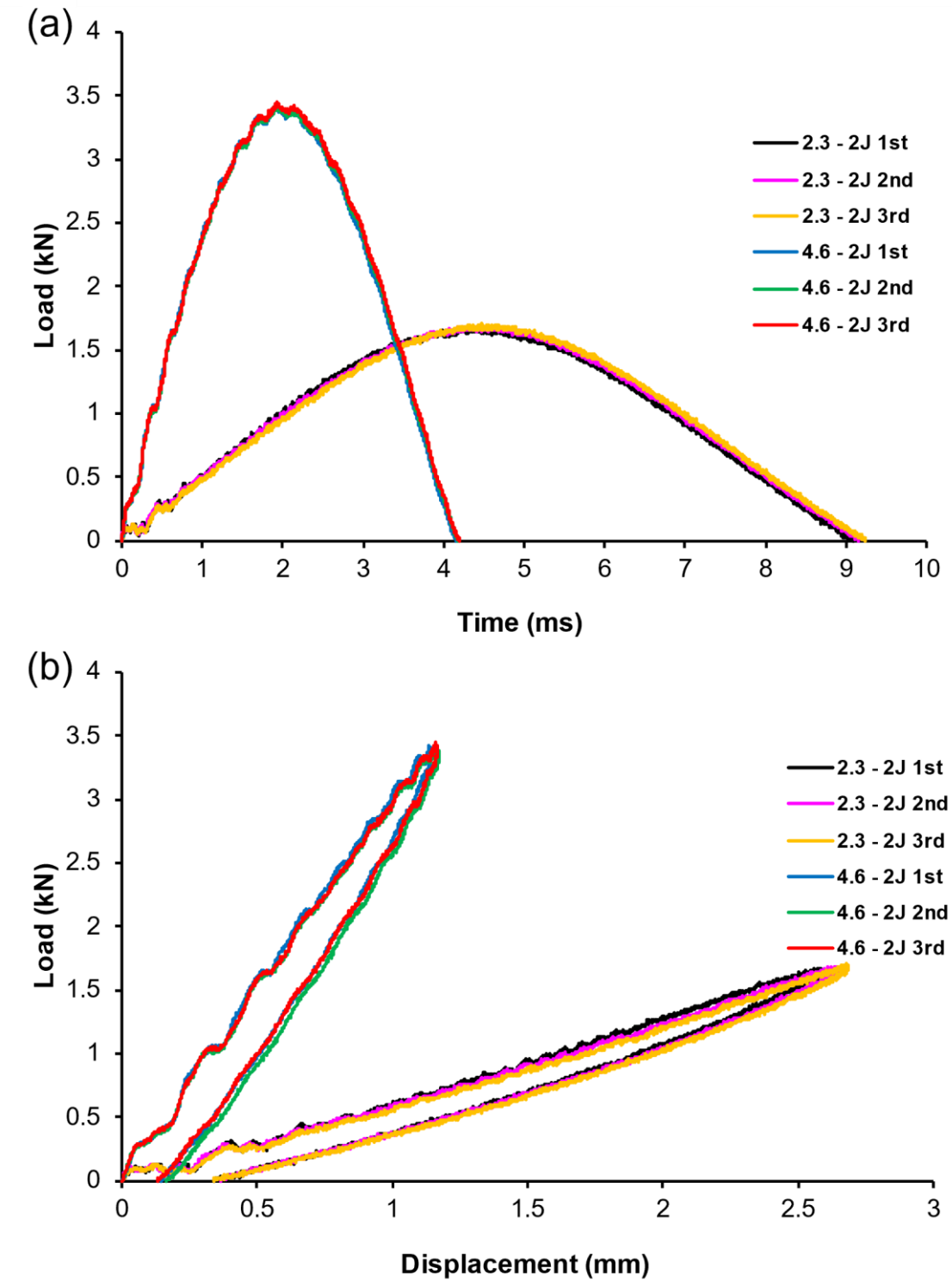


Figure D-1: (a) Load versus time traces and (b) load versus displacement traces for first, second and third impacts at 2 J on 2.3 mm and 4.6 mm thick CF/Epoxy composite panels.

Appendix E – Repeat data for Chapter 5

Figure E-1 shows repeat data for second and third impacts at 10 and 20 J on 4.6 mm thick CF/Epoxy panels.

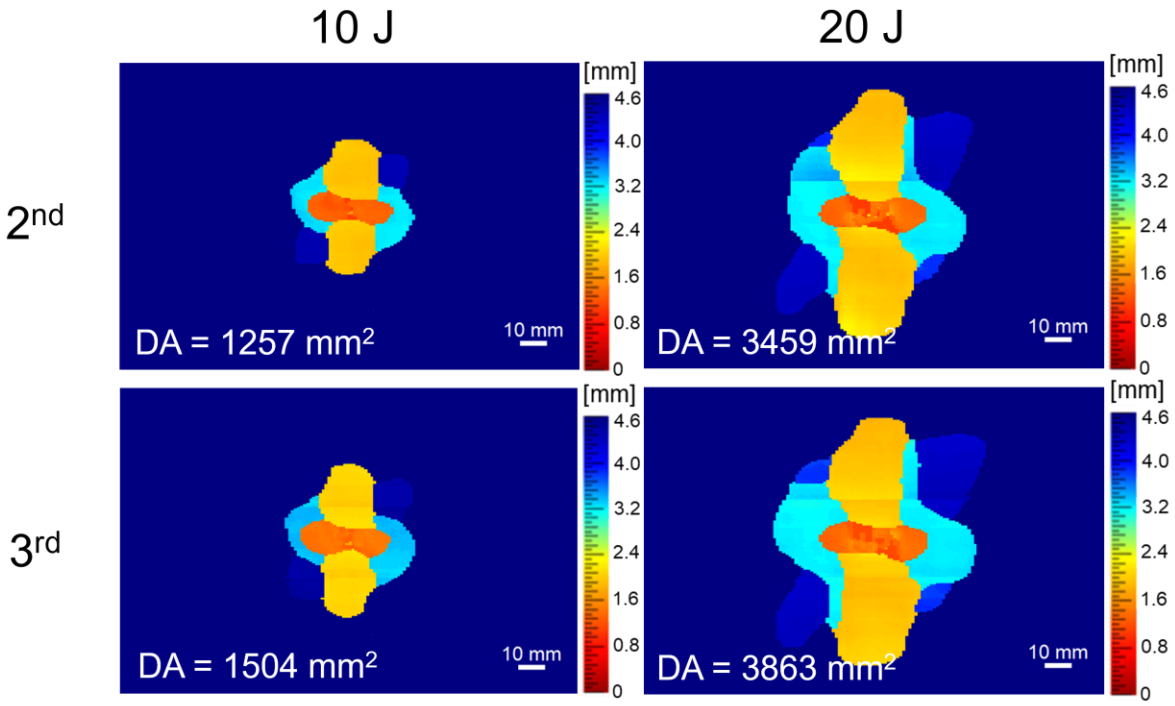


Figure E-1: C-scan damage maps obtained from the CF/Epoxy composite panels with a thickness of 4.6 mm after two and three impacts at impact energies of 10 J and 20 J. The right-hand side scale indicates the location of the interlaminar delamination as a function of the depth through the thickness of the panel (0 to 4.6 mm). The footprint of the delamination damage area (DA) detected is given in the bottom left-hand corner for each panel. The bottom right of each damage map shows a 10 mm scale bar.

Appendix F - Additional data for Chapter 6

Figure F-1 shows C-scan damage maps for CF/PPS panels after impacts at 2.15, 5.15 and 10.15 J.

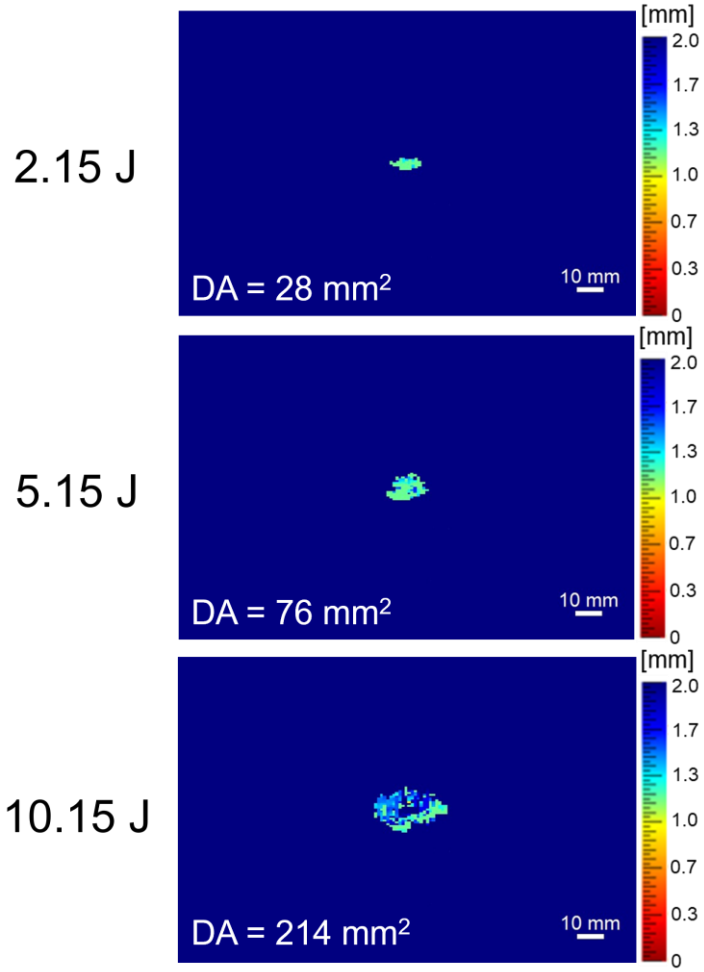


Figure F-1: C-scan damage maps obtained from the CF/PPS replicate composite panels with impact energies of 2, 5, 7.5, 10 and 12.5 J. The right-hand side scale indicates the location of the damage as a function of the depth through the thickness of the panel (0 to 2.0 mm). The footprint of the damage area (DA) detected is given in the bottom left-hand corner for each panel. The bottom right of each damage map shows a 10 mm scale bar.

Appendix G - Additional data for Chapter 7

Figure G-1, Figure G-2 and Figure G-3 show the C-scan damage maps after a first and second impact, both at 3, 6 and 9 J, respectively, on the same panel, with the two impacts separated by 10 and 30 mm. For all the C-scans shown, the right-hand side scale indicates the location of the interlaminar delamination as a function of the depth through the thickness of the panel (0 to 4.6 mm). The footprint of the delamination damage area (DA) detected is given in the bottom left-hand corner for each panel. The bottom right of each damage map shows a 10 mm scale bar.

Figure G-4 shows the C-scan damage maps after a first and second impact, both at 10, 30 and 35 J and separated by 50 mm on the same panel. The compression-after-impact (CAI) results for these panels are included in Figure 7-10(c).

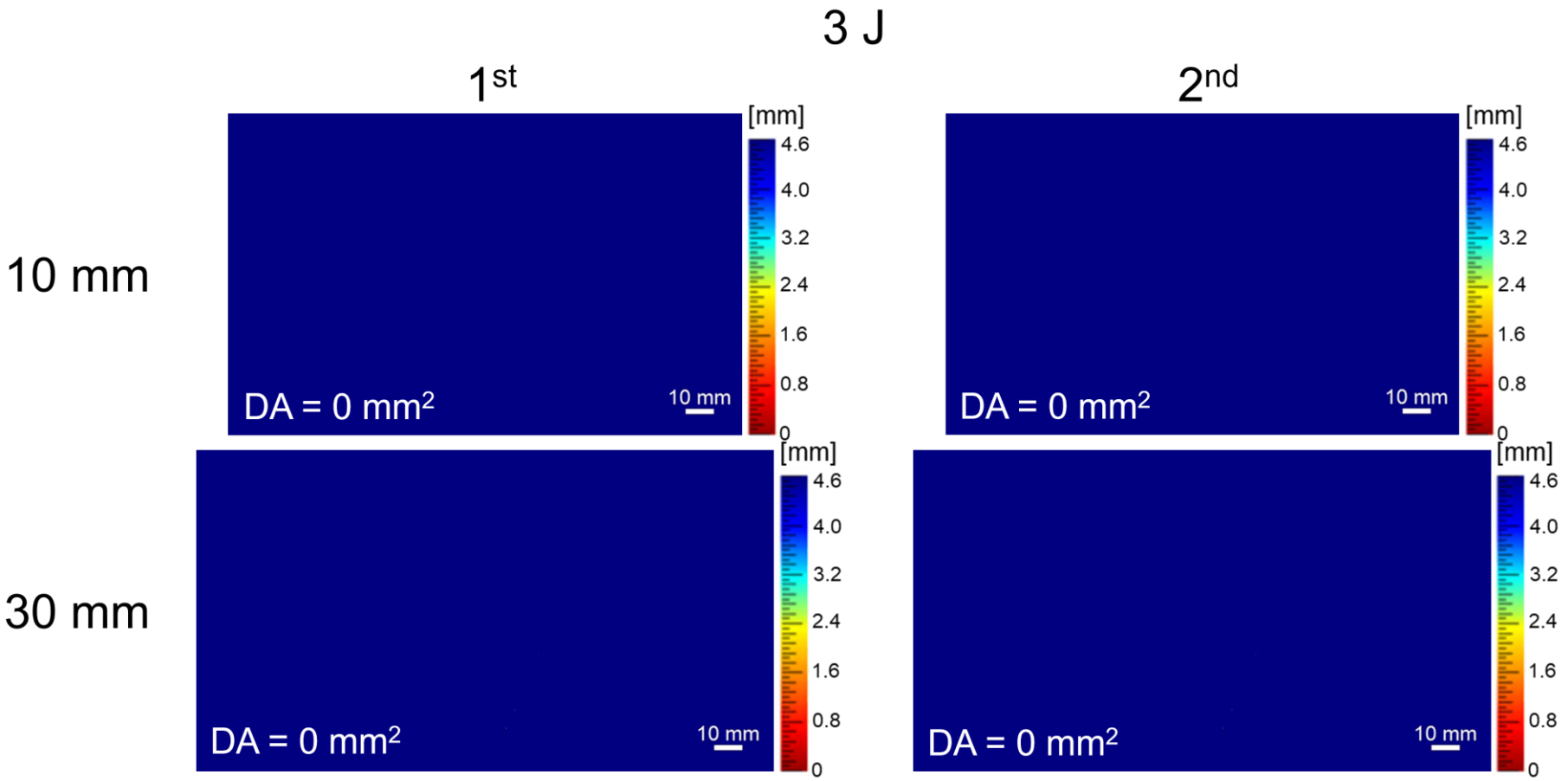


Figure G-1: C-scan damage maps obtained from the 160 and 180 mm long CF/Epoxy composite panels after one impact, and then a second impact, separated from the first by 10 and 30 mm, respectively, at an energy of 3 J.

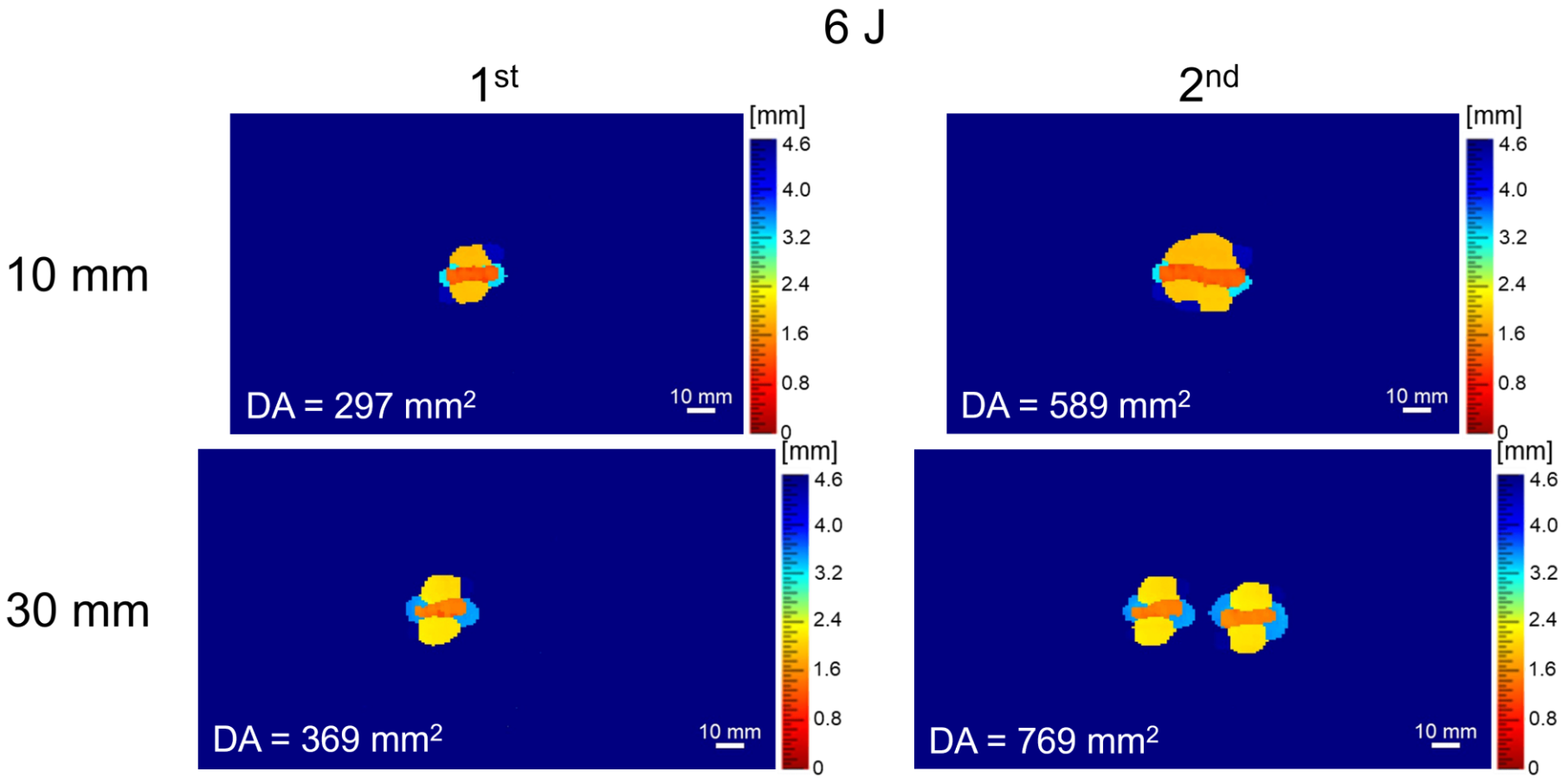


Figure G-2: C-scan damage maps obtained from the 160 and 180 mm long CF/Epoxy composite panels after one impact, and then a second impact, separated from the first by 10 and 30 mm, respectively, at an energy of 6 J.

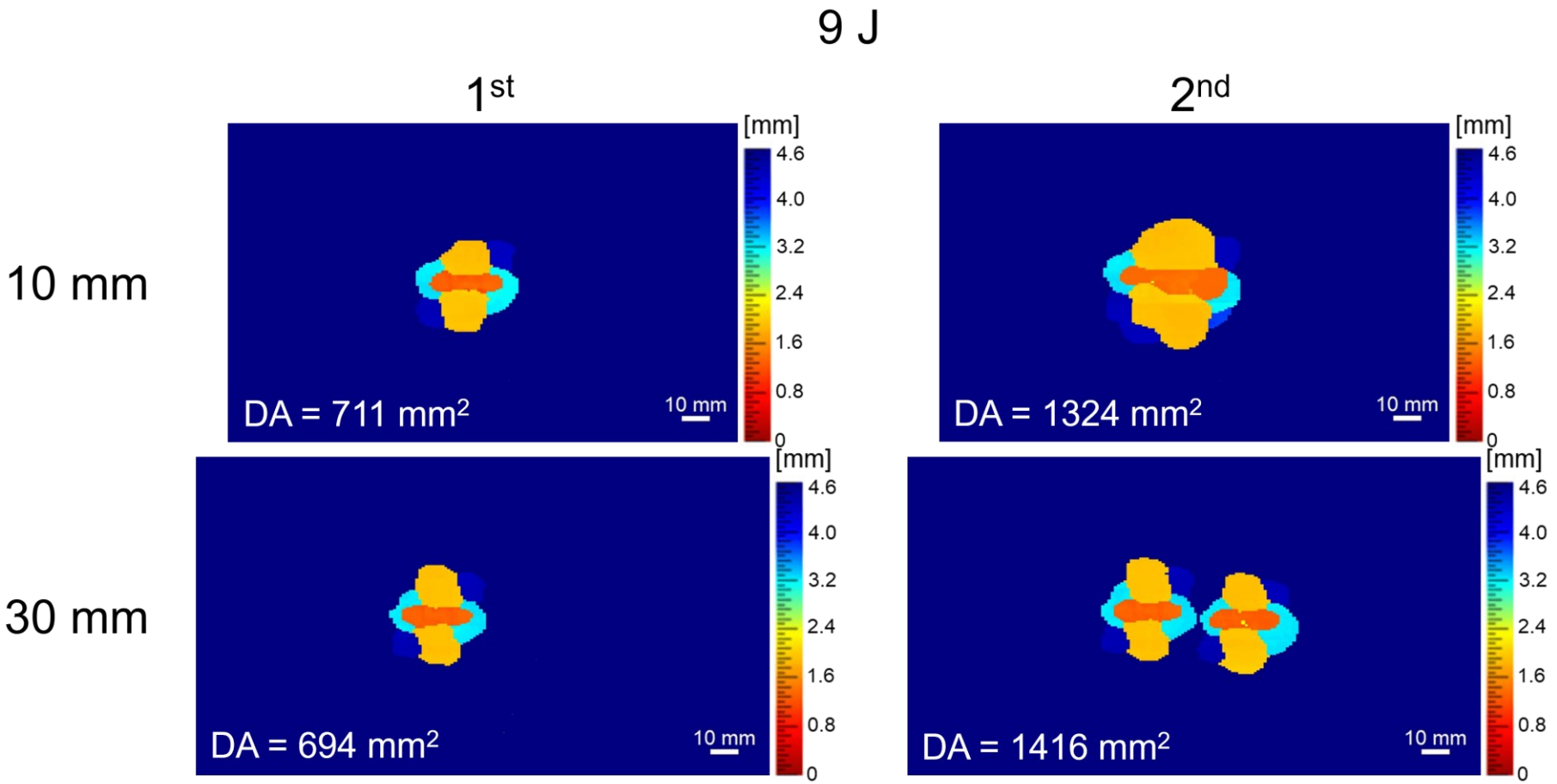


Figure G-3: C-scan damage maps obtained from the 160 and 180 mm long CF/Epoxy composite panels after one impact, and then a second impact, separated from the first by 10 and 30 mm, respectively, at an energy of 9 J.

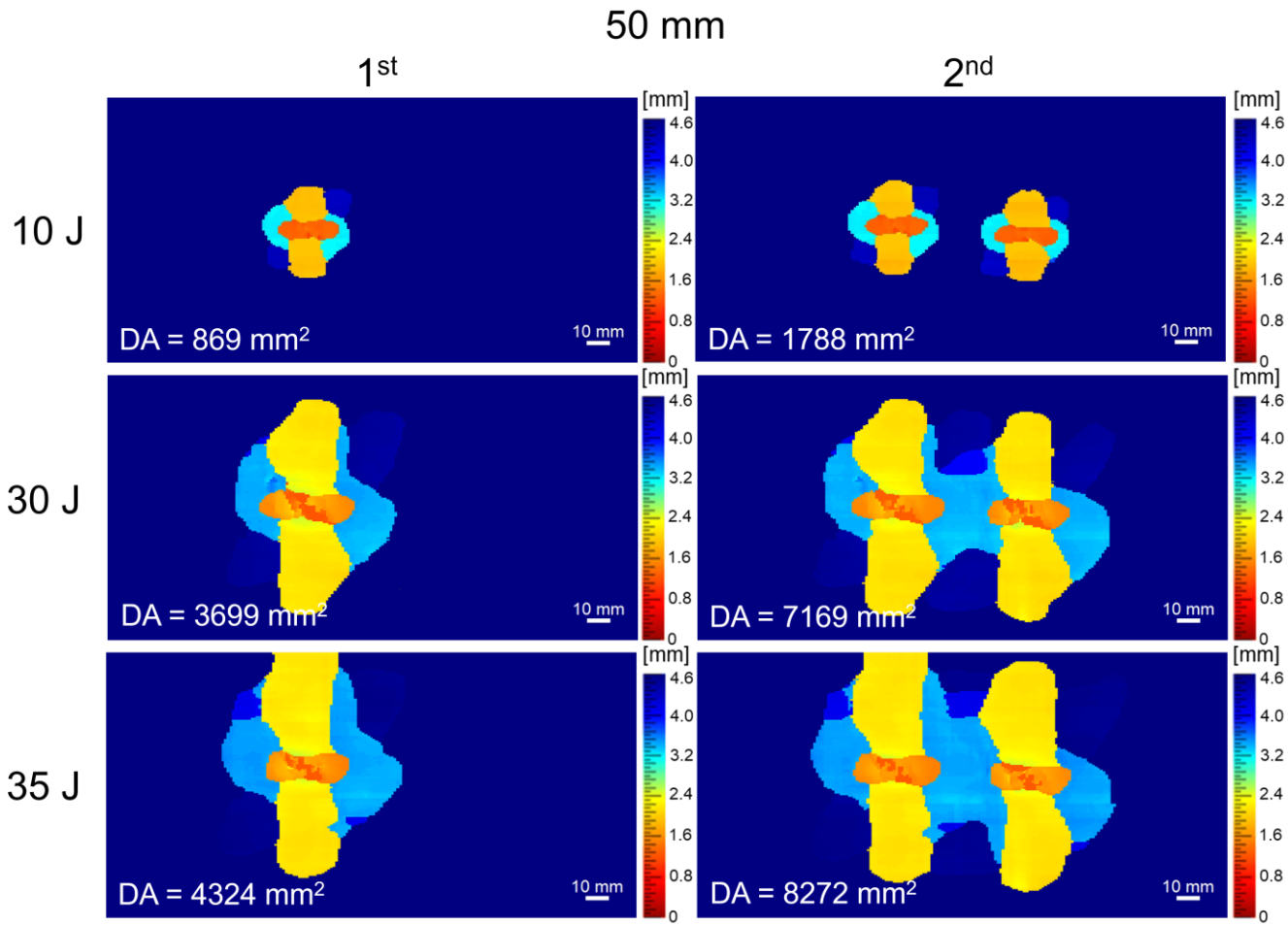


Figure G-4: C-scan damage maps obtained from the 200 mm long CF/Epoxy composite panels after one impact, and then a second impact, separated from the first by 50 mm, at impact energies of 10, 30 and 35 J.